

ÉCOLE DOCTORALE 414
INSERM UMR_S1109 – Equipe Tumor Biomechanics

THÈSE présentée par :
Gautier FOLLAIN

Soutenue le : 10 Septembre 2019

Pour obtenir le grade de : **Docteur de l'Université de Strasbourg**

Discipline : Sciences de la Vie et de la Santé

Spécialité : Biologie Cellulaire et Cancérologie

Les forces hémodynamiques contrôlent la dissémination des cellules tumorales circulantes

Hemodynamic forces control circulating tumor cells dissemination

- Volume 1 -

THÈSE dirigée par :
Dr. Jacky GOETZ

Université de Strasbourg

RAPPORTEURS :
Pr. Johanna IVASKA
Pr. Matthieu PIEL

University of Turku (Fin)
Institut Curie

EXAMINATEUR INTERNE :
Dr. Anne-Cécile Reymann

Université de Strasbourg

THANKING

First of all, I would like to thank **Ligue Contre le Cancer, University of Strasbourg** and **INSERM** (Institut National de la Santé et de la Recherche Médicale) for funding my PhD.

I thank all my family for being so supportive with me during these four years. Especially **Carine**, who accepted me in her flat at Neudorf' paradise! And **my parents**, whom welcomed us nearly all the week-ends in the relaxing family home. Many thanks for your advices and your help all along the years!

I thank my close friends for therapeutic brain drain, and open-minded questioning of my work. In alphabetic order be sure to keep them! ☺ **Ambre, Cécile, Corantin, Elowen, Manu, Marielle, Naël** (I'll come back to you later!), **Téo...**

I thank all the lab members and past-lab members of the Goetz's lab! We've been through a lot of fun together! I wish you all the best in the future! Thanks to...

Jacky, for offering me the possibility to work on this great topic and for all the effort he put in trying to make me a great scientist.

Sébastien, for all he taught me, all the personal support and his way to always put the students first. And the beers!

Naël – Partner of “La Fine Equipe” –, for this amazing duo we have been! All you taught me and all the co-work we did!

Vincent, for teaching me to never forget the bright face of the moon. And the beers!

Olivier, for all technical supports and the good vibes.

The baby students and the students I could work with **Claire, Yohan, Cédric, Edona and Valentin** - May the force be with you!

Luc for his problem-solving power, dearest colleague **Maria** for the plaquetas challenge, **Ignacio** for the barbecue (and electronic microscopy), **Kelly, Shima, Benjamin, Annabel, Patricia, Nina, Guillaume**, ... for all !

A special thanks to **Pascal**, for teaching me how to use the upright SP5 (<3) and how to eat properly at noon!

And another special thanks to **Kerstin** from Peri's Lab in EMBL, who saved my PhD providing zebrafish embryos during quite a long time!

I thank **all the collaborators** of the different projects we worked on. Especially **Vanesa and Raphael** that offered me the chance to work on Zika virus! ;-)

Finally, I thank **J. Ivaska, A-C. Reymann and M. Piel** for accepting to be part of this great jury!

RESUME EN FRANÇAIS

Introduction

La progression tumorale est un processus complexe, composé de plusieurs étapes clés, aboutissant à l'apparition de métastases généralement responsables du décès des patients. Elle commence par le développement d'une tumeur primaire d'où certaines cellules s'échappent. Ces cellules se propagent en utilisant les systèmes lymphatiques et vasculaires et atteignent ainsi des organes distants. La colonisation de ces organes conduit à la formation de tumeurs secondaires, les métastases. De nombreuses évidences suggèrent que l'apparition de lésions métastatiques est induite par des caractéristiques intrinsèques aux cellules tumorales ainsi que par des facteurs environnementaux organes-spécifiques. Cet organotropisme, proposé sous la forme de l'hypothèse du « seed and soil » par S. Paget, est très étudié d'un point de vue médical, biologique et chimique, afin de comprendre et d'anticiper la progression tumorale chez les patients. Cependant, ces études ne prennent que rarement en compte la contribution de facteurs biomécaniques. Par exemple, l'augmentation de la pression interstitielle dans les tumeurs solides primaires va être moteur de l'invasion, l'architecture vasculaire va guider les cellules tumorales circulantes vers un premier lit capillaire, très souvent un organe hautement métastatique (les poumons dans les cancers du sein, le foie pour les cancers colorectaux, ...). A l'échelle des capillaires sanguins, les paramètres hémodynamiques et la topographie des vaisseaux (ramifications, diamètre interne, ...) influencent les sites d'arrêt des cellules tumorales. En général, ces aspects sont connus, mais leurs réels impacts biologiques ne sont que peu décrits *in vivo*.

Dans notre laboratoire, nous approchons toutes les étapes de la cascade métastatique sous un angle biomécanique. Au cours de ma thèse, j'ai étudié l'influence des facteurs hémodynamiques lors de l'arrêt, l'adhésion et l'extravasation (sortie des vaisseaux vers le stroma) de cellules tumorales circulantes (CTC), précédant la colonisation métastatique. Pour cela, nous avons combiné la microscopie corrélative intravitale (*correlative light and electron microscopy* - CLEM), l'imagerie à grande vitesse et des outils biophysiques tels que des pincettes optiques, appliqués aux embryons de poisson zèbre et à des modèles microfluidiques. L'objectif principal de notre projet a

été de démontrer le rôle central des paramètres de la circulation sanguine dans ces étapes.

Résultats

Nous avons commencé ce projet en examinant le rôle de la circulation sanguine sur les trois étapes : arrêt, adhésion et extravasation des CTC. Pour ce faire, nous exploitons les avantages des embryons de poisson zèbre à 2 jours post-fécondation (transparence optique, lignées transgéniques fluorescentes tissu-spécifiques, manipulation simple...). Nos résultats montrent que l'ajustement du débit sanguin affecte toutes les étapes. Tout d'abord, en observant des CTCs directement lors de l'injection (Follain et al. *MMB* 2018), nous avons observé que de faibles forces d'écoulement permettent un arrêt des cellules tumorales alors que des forces d'écoulement élevées maintiennent les cellules dans la circulation. De plus, en utilisant les pinces optiques *in vivo* (Harlepp et al. *MBoC* 2017) et *in vitro*, nous avons identifié un seuil de vitesse de flux permis à l'arrêt des CTC autour de 400 $\mu\text{m/sec}$ (ceci indépendamment des arrêts liés à l'occlusion des petits vaisseaux sanguins par les cellules tumorales). Nous avons ensuite développé une cartographie quantitative de l'adhésion stable des CTC 3h post-injection (hpi) de manière statistique. Ces données nous ont permis de conclure que les forces de flux modifient de manière significative l'emplacement privilégié d'adhésion des CTC. En menant une étude similaire à 24hpi, nous avons observé l'effet du flux sur l'extravasation. Remarquablement, une diminution des vitesses d'écoulement réduit fortement l'extravasation des cellules tumorales, suggérant un rôle central des forces d'écoulement dans la transmigration des CTC. En utilisant notre approche de microscopie corrélative intravitale, nous avons caractérisé le remodelage endothérial - dépendant du flux - autour des cellules tumorales comme processus d'extravasation des CTC. Nous avons démontré l'apport majeur des cellules endothéliales dans ce processus. Les cellules endothéliales sont capables de migrer de manière intra-luminale et d'envelopper totalement les cellules arrêtées. Cela conduit finalement à l'exclusion des cellules tumorales du flux sanguin et au maintien de l'homéostasie avec le retour d'une perfusion normale du vaisseau. Nous n'avons pas établi quelle voie de signalisation permettait la mise en place de ce processus, mais nous pensons que l'adhésion des cellules tumorales, la sécrétion de facteurs solubles par la cellule tumorale et/ou directement la capacité des cellules

endothéliales à sentir de faibles variations de flux peuvent être responsables. Globalement, ces résultats démontrent que les profils hémodynamiques régulent les étapes importantes de la cascade métastatique ([Follain et al. DevCell 2018](#)).

Sur la base de ces résultats, nous avons poursuivi nos investigations et conduit deux projets complémentaires. Premièrement, nous avons inhibé le remodelage endothérial autour des cellules tumorales en ciblant la voie des VEGF récepteurs ([Follain et al. En prep](#)). Nous avons utilisé une approche pharmacologique : traitement avec du Sunitinib, un inhibiteur de cette voie. Nous avons totalement bloqué le remodelage endothérial *in vitro* et dans les embryons de poisson zèbre. Nous avons ensuite validé nos résultats dans le modèle murin, où nous avons observé une baisse significative de l'extravasation et de la colonisation métastatique. Ces résultats ouvrent une voie thérapeutique nouvelle puisque ce processus est une cible potentielle. Deuxièmement, nous nous sommes concentrés sur les phases d'arrêt et d'adhésion stable des cellules tumorales en circulation, et avons décrit un processus d'arrêt et d'adhésion en deux étapes *in vivo* ([Osmani et al. Cell report 2019](#)). Nos résultats montrent que l'adhésion des cellules tumorales a un impact direct sur la croissance métastatique. Dans le cas de nos cellules, des récepteurs à faible force de liaison tels que CD44 et ITGB3 sont nécessaires pour la phase d'arrêt, mais pas pour l'adhésion stable. À l'opposé, des forces de liaison élevées (plus lentes à s'engager) permettent une adhésion stable, en particulier par l'intermédiaire du récepteur ITGA5B1. Le ligand de ce récepteur est la fibronectine, une protéine de la matrice extracellulaire, dont nous avons quantifié la présence sur la surface apicale des cellules endothéliales. De plus, la présence apicale de la fibronectine est corrélée, elle aussi, au flux *in vitro* et *in vivo*. L'ensemble de ces résultats montrent le rôle central, mais encore mal caractérisé, du flux sanguin dans la cascade métastatique.

Enfin, j'ai participé à de nombreux projets collaboratifs basés sur l'emploi du modèle poisson zèbre. Je commenterai brièvement ces collaborations qui élargissent mon projet sur divers aspects de la biologie cellulaire et d'échanges multidisciplinaires. Tout d'abord, sur le suivi *in vivo* des vésicules extracellulaires ([Verweij et al Dev. Cell 2019](#)), en particulier d'origine tumorale ([Hyenne et al. Dev. Cell 2019](#)). Ces vésicules sont fortement sécrétées par les cellules tumorales et possèdent un potentiel de signalisation cellulaire qui peut être lié à la formation de niches pré-métastatiques.

Ensuite, nous avons utilisé le modèle poisson zèbre pour étudier l'extravasation de monocytes infectés par des virus ZIKV, dans le contexte d'une étude de la propagation du virus dans le cerveau ([Nunez et al. En révision](#)). Enfin, nous avons développé plusieurs projets liés au marquage fluorescent *in vivo* : 1. Marquage de populations cellulaires spécifiques, par *barcoding* fluorescent ([Andreiuk et al Small 2017](#)), 2. et plus fondamentalement, l'utilisation de silice pour réduire la cytotoxicité de quantum dots ([Perton et al. JCIS 2018](#)).

Conclusion

Cette thèse a fait l'objet de plusieurs articles scientifiques et mis en évidence l'impact des aspects biomécaniques sur la progression métastatique.

- 1- Le flux sanguin contrôle l'arrêt, l'adhésion et l'extravasation des cellules tumorales en circulation. Ce point ouvre la voie à de très nombreuses questions à l'interface entre la physique des fluides et la capacité biologique des cellules à sentir/réagir à ce stimulus.
- 2- Les CTC utilisent tout leur répertoire d'adhésion pour s'arrêter et adhérer activement à la paroi du vaisseau dans un contexte *in vivo*.
- 3- La description du remodelage endothérial en tant que processus actif d'extravasation et la mise en évidence d'une voie de signalisation ouvrant la perspective d'un traitement pour l'inhiber.

Au sein du laboratoire, cette thèse nous a permis de développer et de mettre en place plusieurs méthodes utilisant le poisson zèbre et la microfluidique. Celles-ci permettent aujourd'hui au projet de progresser vers l'étude d'autres paramètres biophysiques tels que la rigidité des cellules tumorales et la résistance aux forces de cisaillement du flux sanguin.

ABBREVIATIONS

General:

CAF: cancer associated fibroblast
CAM: cancer associated macrophage
CLEM: correlative light electron microscopy
CSC: cancer stem cell
CV: caudal vein
DA: dorsal aorta
DNA: deoxyribonucleic acid
ECM: extracellular matrix
EV: extracellular vesicle
GF: growth factor
IBMX: isobutyl methylxanthine
ISV: intersegmental vessels
QD: quantum dot
MMP: matrix metalloproteinase
NIRB: near-infrared branding
NK: natural killer cell
NO: nitric oxide
PCR: polymerase chain reaction
PDMS: polydimethylsiloxane
PICA: primitive internal carotid artery
RNA: ribonucleic acid
RNAi: RNA interference
RNAseq: RNA sequencing
ROI: region of interest
ROS: reactive oxygen species
T-ALL: T-cell lymphoblastic leukemia
TIC: tumor-initiated cell
TMEM: Tumor microenvironment of metastasis
YSL: yolk syncytial layer
μ-CT: micro computed tomography

Animals and cell lines:

B16F10: mouse melanoma cells
D2A1: mouse mammary carcinoma cell (highly metastatic)
D2OR: mouse mammary carcinoma cell (non-metastatic)
HUVEC: human umbilical vein endothelial cells
MDA-213-MB: human breast cancer cells
NSG mouse: NOD Scid Gamma mouse (immunodeficient line)
RBC: red blood cells
ZMEL: zebrafish melanoma cells

Recurrent proteins:

Cad. (VE-; E-; P-): cadherin (vascular endothelial-; epithelial-; platelet- (also CDH3))
CD44: cluster of differentiation 44 (adhesion receptor)
CD63: cluster of differentiation 63 (tetraspanin)
EGF: epidermal growth factor
FGF: fibroblast growth factor
ICAM: inter cellular adhesion molecule
ITG: integrin (adhesion receptor)
MUC-1: mucin-1 (adhesion receptor)
P53: protein 53 (tumor suppressor gene)
PECAM: Platelets endothelial cell adhesion molecule (also CD31)
PDGF: platelet-derived growth factor
PSGL1: P-selectin glycoprotein ligand (also CD162)
RhoA: Ras homolog gene A (small GTPase)
ROCK: Rho associated kinase protein
Sel. (E-; L-; P): selectin (endothelial-; leukocyte-; platelet-)
TGF-β: tumor growth factor beta
TNF-α: tumor necrosis factor alpha
VCAM: vascular cell adhesion molecule
VEGF: vascular endothelial growth factor

TABLE OF CONTENTS

THANKING	3
RESUME EN FRANÇAIS.....	4
ABBREVIATIONS	9
TABLE OF CONTENTS.....	10
FIGURES AND BOXES.....	12
INTRODUCTION	15
I - GENERAL INTRODUCTION TO CANCER RESEARCH.....	16
A) CANCER DEFINITION AND CLINICAL IMPACT.....	16
B) COMMON FEATURES OF CANCER	18
D) HETEROGENEITY AND COMPLEXITY OF THE DISEASE	24
i) PRIMARY TUMOR HETEROGENEITY.....	24
ii) GIVING RISE TO METASTATIC HETEROGENEITY	25
iii) SINGLE-CELL LEVEL TO TACKLE TUMOR HETEROGENEITY	28
II - THE METASTATIC STEPS PRECEDING ENTRY INTO THE CIRCULATION	30
A) TUMOR GROWTH INITIATION	30
B) INVASION	31
C) INTRAVASATION.....	35
III - FACTORS IMPACTING THE METASTATIC SPREADING	37
A) BIOLOGICAL FACTORS IMPACTING THE METASTATIC SPREADING	37
B) MECHANICAL FACTORS IMPACTING THE METASTATIC SPREADING	39
C) MULTIFACTORIAL TUMOR DISSEMINATION	41
IV - FOCUS ON THE BIOMECHANICS OF ARREST, ADHESION AND EXTRAVASATION	42
A) SURVIVAL IN THE CIRCULATION	42
i) SINGLE CIRCULATING TUMOR CELL SURVIVAL	44
ii) CELL INTERACTION-BASED SURVIVAL	45
B) CIRCULATING TUMOR CELLS ARREST AND STABLE ADHESION.....	47
i) LEUKOCYTES ROLLING AND DIAPEDESIS	47
ii) PHYSICAL TRAPPING INDUCING TUMOR CELL ARREST	48
iii) ACTIVE ADHESION DURING TUMOR CELL ARREST	51
iv) STABLE ADHESION OF TUMOR CELLS	54
C) TUMOR CELLS EXTRAVASATION	57
i) FROM LEUKOCYTE MODEL TO TUMOR CELL EXTRAVASATION	57
ii) ENDOTHELIAL CELLS INVOLVEMENT IN THE EXTRAVASATION	60
TECHNICAL APPROACHES.....	65
USE OF ZEBRAFISH EMBRYOS.....	66
HISTORICAL DIGRESSION	68
ZEBRAFISH AS A CANCER MODEL	70
ZEBRAFISH IN OUR EXPERIMENTS	74

USE OF MICROFLUIDICS	81
MICROFLUIDICS APPLIED TO BIOLOGY.....	81
MICROFLUIDICS IN OUR PROJECT	83
USE OF OPTICAL TWEEZING	85
PRINCIPLE AND CALIBRATION.....	85
OPTICAL TWEEZING APPLICATIONS TO CANCER.....	87
OPTICAL TWEEZING IN OUR PROJECT.....	88
RESULTS	89
HEMODYNAMIC FORCES TUNE THE ARREST, ADHESION AND EXTRAVASATION OF CIRCULATING TUMOR CELLS	90
METASTATIC TUMOR CELLS EXPLOIT THEIR ADHESION REPERTOIRE TO COUNTERACT TO FORCES DURING INTRAVASCULAR ARREST.....	135
IMPAIRING FLOW-MEDIATED ENDOTHELIAL REMODELING REDUCES EXTRAVASATION OF TUMOR CELLS	177
COLLABORATIVE WORKS	213
STUDY (TUMOR) EXTRACELLULAR VESICLES <i>IN VIVO</i>	213
CELL LABELLING <i>IN VIVO</i>.....	215
ZEBRAFISH AS A HUMAN DISEASE MODEL TO LOOK AT EXTRAVASATION	217
DISCUSSION.....	219
I- PHYSICAL CONSTRAINTS DURING ARREST, ADHESION AND EXTRAVASATION	220
II- BLOOD FLOW AND ACTIVE ADHESION	222
III- BLOOD FLOW, CELL ADHESION AND ENDOTHELIAL REMODELING	223
IV- ENDOTHELIAL REMODELING APPLICATION TO CLINIC.....	225
BIBLIOGRAPHY	227
ANNEXES.....	257
ANNEX 1: SEEING IS BELIEVING – MULTI-SCALE SPATIO-TEMPORAL IMAGING TOWARDS <i>IN VIVO</i> CELL BIOLOGY	258
ANNEX 2: USING ZEBRAFISH EMBRYO TO DISSECT THE EARLY STEPS OF THE METASTASIS CASCADE	275
ANNEX 3: HEMODYNAMIC FORCES CAN BE ACCURATELY MEASURED <i>IN VIVO</i> WITH OPTICAL TWEEZERS	293
ANNEX 4: LIVE TRACKING OF INTER-ORGAN COMMUNICATION BY ENDOGENOUS EXOSOME <i>IN VIVO</i> .	303
ANNEX 5: STUDY THE FATE OF TUMOR EXTRACELLULAR VESICLES AT HIGH SPATIOTEMPORAL RESOLUTION USING THE ZEBRAFISH EMBRYO.....	327
ANNEX 6: FLUORESCENT POLYMER NANOPARTICLES FOR CELL BARCODING <i>IN VITRO</i> AND <i>IN VIVO</i> .	355
ANNEX 7: WRAPPED STELLATE SILICA NANOCOMPOSITES AS BIOCOMPATIBLE LUMINESCENT NANOPLATFORMS ASSESSED <i>IN VIVO</i>	369
ANNEX 8: ZIKA VIRUS ENHANCES MONOCYTE ADHESION AND TRANSMIGRATION, FAVORING VIRAL DISSEMINATION TO THE CNS.....	385

FIGURES AND BOXES

Figure 1: 2018 FRM report

Figure 2: Hallmarks of cancer

Figure 3: Typical tumor microenvironment

Figure 4: Step-wise progression of cancer

Figure 5: Clonal expansion of the tumor

Figure 6: Spatial spreading heterogeneity of cancer

Figure 7: Temporal spreading heterogeneity induced by dormancy

Figure 8: Example of single CTCs isolation experiments

Figure 9: Example of fluorescent barcoding approach

Figure 10: Difference between cell of origin and cancer stem cell

Figure 11: Cell migration mechanism

Figure 12: Migration strategy depending on the confinement

Figure 13: Single vs collective migration

Figure 14: Intravital acquisition of tumor intravasation

Figure 15: Premetastatic niche formation

Figure 16: The vascular architecture partially explains the repartition of metastases

Figure 17: Blood flow, physical constrain and adhesion force

Figure 18: Analysis of tumor cell fate

Figure 19: Fragmentation of arrested cells

Figure 20: Leukocyte rolling and diapedesis

Figure 21: CTCs intravascular arrest through occlusion *in vivo*

Figure 22: *In vitro* microfluidic studies on cell passing through physical constraints

Figure 23: Clusters of CTCs squeezing in narrow channel

Figure 24: Transmembrane receptor CD44

Figure 25: Integrins

Figure 26: Intraluminal fibronectin deposit

Figure 27: Model of leukocyte diapedesis

Figure 28: Extravasation of tumor cells

Figure 29: Tumor cells induce the necrosis of endothelial cells to transmigrate

Figure 30: Invasive cell protrusion during cell extravasation

Figure 31: Endothelial remodeling driving extravasation

Figure 32: Angiopellosis driving extravasation

Figure 33: Angiophagy leading to extravasation

Figure 34: Endothelialisation of arrested tumor cells
Figure 35: Tech. Approach – Zebrafish historical digression
Figure 36: Tech. Approach – Zebrafish as a cancer model
Figure 37: Tech. Approach – Zebrafish relevance for cancer study
Figure 38: Tech. Approach – Our approach using zebrafish embryos
Figure 39: Tech. Approach – High resolution Imaging
Figure 40: Tech. Approach – Microfluidics applications
Figure 41: Tech. Approach – Optical tweezers

Box 1: CD44 in cancer progression
Box 2: Integrins in cancer progression
Box 3: Animal model in cancer research

INTRODUCTION

I tried to build this introduction as we designed my PhD project. Cancer is a generally well-known disease but 1. Its large variability prevents the development of efficient therapeutic protocols. 2. The mechanistic description of specific steps in its progression is still incomplete. Facing this heterogeneity and dissecting the key steps is a challenge to which many researchers are confronted nowadays (**CHAPTER I**). In this aim, in my lab, we develop innovative imaging approaches applied to animal models. By this means, we can observe tumor cell behavior at the single cell level in a relevant environment during cancer progression. My thesis focuses on the impact of blood flow in the last steps of the metastatic cascade. That's why I chose to treat separately the origin of tumor initiation, the local invasion and the intravasation of tumor cells (**CHAPTER II**) from the tumor systemic dissemination strictly speaking. Then, I describe the various factors influencing tumor dissemination in order to insist on the importance of considering biomechanical factors (**CHAPTER III**) before I deal with my main object. That is the circulation, the arrest, the adhesion and the extravasation of circulating tumor cells just preceding the metastatic outgrowth (**CHAPTER IV**).

I - GENERAL INTRODUCTION TO CANCER

RESEARCH

A) CANCER DEFINITION AND CLINICAL IMPACT.

Cancer regroups a wide variety of diseases characterized by the anarchic proliferation of cells. In the case of leukemia (blood cancer), tumor cells are systemically spread without the formation of a tumor mass (Sell, 2005). At the opposite, for instance with glioblastoma (brain cancer), a tumor mass forms, but rarely spreads outside the brain (Beauchesne, 2011). In between, there are many types of cancers called “solid tumor” (mainly regrouping sarcoma (stromal cancer) and carcinoma (epithelial cancer)): These cancers are characterized by the formation of a tumor mass (the primary tumor), that can evolve, invade its surrounding stroma and potentially give rise to metastases (secondary tumor foci) (Nguyen et al., 2009; Valastyan and Weinberg, 2011).

Theoretically, tumors can form anywhere in the body. However, the most frequent locations are the organs in contact with external environment or highly vascularized: skin, respiratory system, digestion tracts and brain. The proliferation of cells disturbs homeostasis, recruits stromal cells and progressively modifies the microenvironment. In most of the case, at the macroscopic level, it creates an undifferentiated and/or

stiffer tissue (due to the high density of cells and alteration of the extracellular matrix composition), that is the basis for diagnosis (Chang et al., 2011; Youk et al., 2014).

Currently in France and in many other developed countries, cancer is the first cause of mortality, surpassing cardiovascular diseases.

In France in 2017, there was 150 000 cancer-related deaths (Fig. 1). Even more striking, according to the national cancer institute (InCA), 1 over 3 men and 1 over 4 women will eventually develop cancer. Most frequent cancers for men are prostate, lung (the most lethal) and colorectal cancers. While for women, it is mostly breast (the most lethal), colon and lungs which are affected (InCA report 2017). Importantly, in France, we estimate between 14 000 and 30 000 the new cases per year, with half of them engaging vital prognosis. To note, it is now well established that there are environmental risk factors (smoking, alcohol, high-fat diet, lack of physical activities, pollution...), that merge with genetic factors to drastically increase the risk to develop cancer. One of the strongest examples would be that 90% of lung cancer are related to smoking.

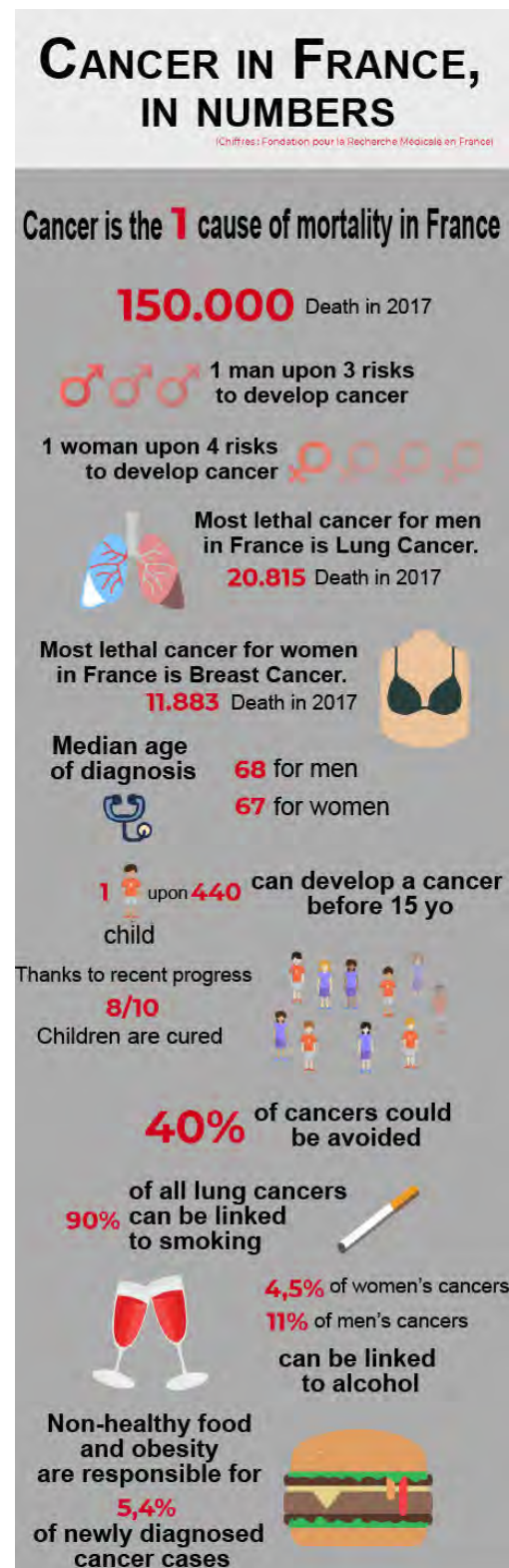


Fig 1: 2018 FRM (Fondation pour la Recherche Médical) report graphical abstract. Extracted from www frm org.

Especially in the case of carcinoma, the formation of a primary tumor mass is not the main cause of death. In most of the cases, it is possible to use surgery and complementary treatments to recover. Indeed, in 90% of the case, lethality comes from the formation of metastases (Gupta and Massagué, 2006; Steeg, 2006). They arise through the dissemination of tumor cells from the primary tumor, that circulate in the body fluids (blood, lymph) and potentially colonize distant organs. The life-threatening potential of metastases comes from the fact that: 1. Many metastases localize in vital organs, among which lungs, liver and brain (Gupta and Massagué, 2006). 2. Metastases are also difficult to remove by surgery, either because of side-damage risks or because they form a large number of small-sized lesions. However, the formation of metastases is a complex process, going through many steps that tumor cells have to fully master, while surviving the immune system (Nguyen et al., 2009).

B) COMMON FEATURES OF CANCER

Despite the wide variety of cancers, common features have been highlighted in the past. In “Hallmarks of Cancer”, Hanahan and Weinberg give a complete scientific definition of cancer disease (**Fig. 2** - (Hanahan and Weinberg, 2000, 2011)). First of all, the characteristics that cancer cells acquire to survive and form a primary tumor arise from random genetic mutations (1). These are induced by the pressure that the immune system and the microenvironment parameters exert on abnormal cells (Fidler, 1990). In the selection process, different mutations giving rise to different survival/proliferation mechanism will support the appearance of several clones of cancer cells. Before developing this point in the next section, I will briefly present the common traits that tumor cells must have to grow a primary tumor.

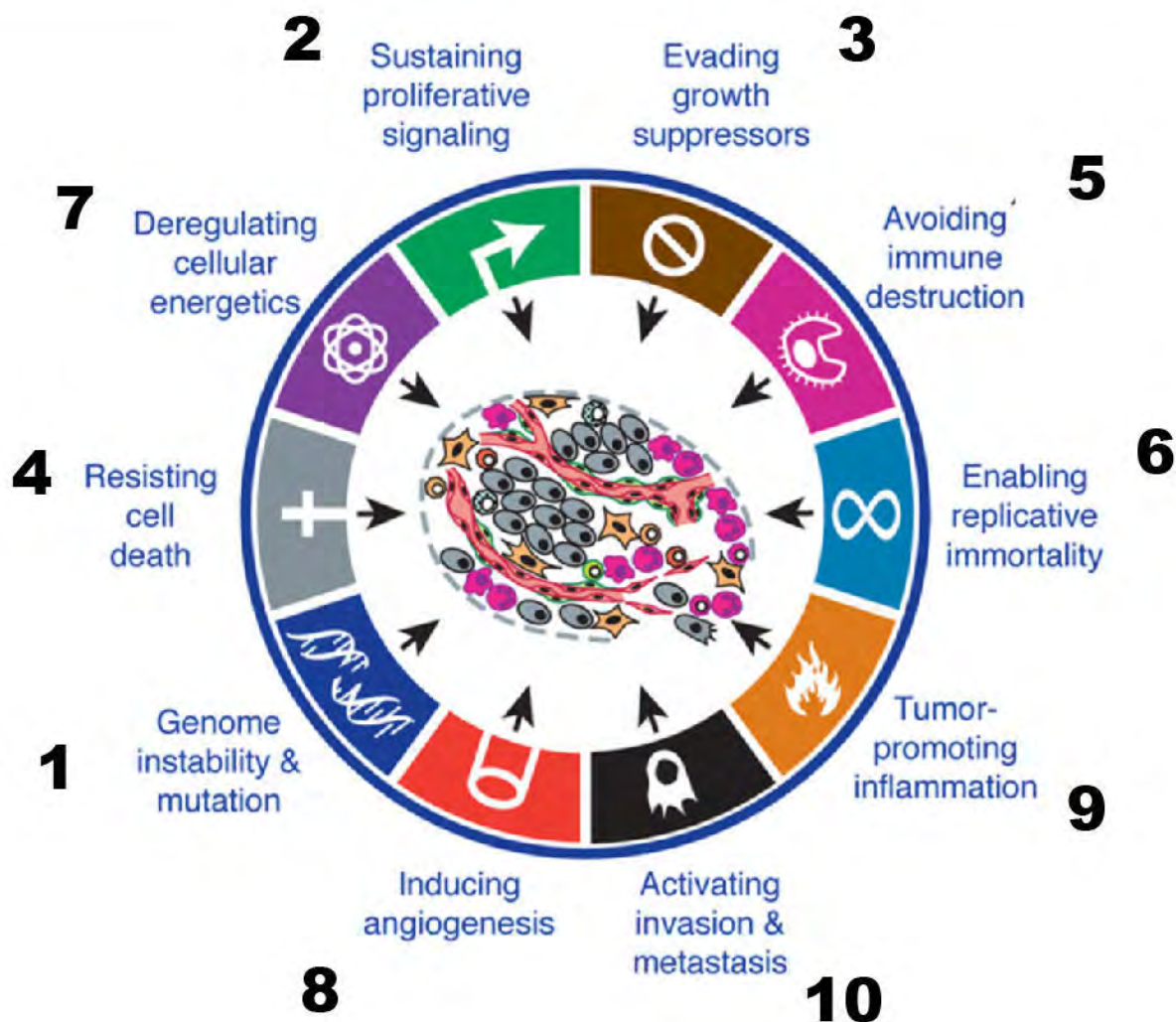


Fig. 2: Hallmarks of cancer from Hanahan and Weinberg. Corresponding numbers are commented in the text. Adapted from Hanahan and Weinberg, 2011.

The needs for cancer cells to form the primary tumor are (**Fig. 2**):

(2) Sustained proliferation thanks to Growth Factor (GF), through:

- Autocrine production (Fedi, 1997). This was shown for brain cancer cells producing PDGF and TNF- α to sustain their growth.
- Hypersensitivity to stromal cells GF (paracrine signaling), classically achieved by overexpression of the receptors. For instance, the overexpression of EGFR in stomach, brain and breast tumor (Slamon et al., 1987).
- GF independence, either through mutations that constitutively active the receptor (Fedi, 1997), or by overexpression and ligand-independent signaling (Di Fiore et al., 1987).

(3) Evading growth suppressor, with three major actors:

- Retinoblastoma protein (Rb), which is a central anti-proliferative protein: Its phosphorylation blocks cell proliferation by sequestering E2F, blocking cell cycle in G1 phase (Weinberg, 1995).
- TP53 which is also a central cell cycle blocker, sensitive to intracellular stress signals. Indeed, especially DNA damage or incomplete replication, but also metabolic stress, will converge to P53 that blocks the cell cycle before the mitosis (Finlay et al., 1989). To note, P53 can also trigger apoptosis in a specific context, which relates to the next point.
- the loss of contact inhibition: In physiologic condition, epithelial cells stop their growth in response to crowding. The exact combination of mechanical signals and biological pathway is still unclear, but carcinoma develop insensitivity to these cues (Shaw, 2009).

(4) Resisting cell death pathways, which is dependent of the activation of:

- Intrinsic signals, with the cytoplasmic entry of mitochondrial cytochromeC (Green and Reed, 1998).
- Extrinsic signals, especially the binding of FasL to its membrane receptor Fas (Ashkenazi and Dixit, 1999).

When triggered, both converge to the unlock of caspases cascade physiologically leading to apoptosis (Thornberry and Lazebnik, 1998). In the case of cancer, this pathway is unactivated at different levels. For instance, Fas is inactive in many carcinoma (Pitti et al., 1998).

(5) Evading immune cells suppression, which is related to resisting apoptosis, including from cells such as cytotoxic lymphocyte, Natural Killer (NK) cells and phagocytic cells (Vajdic and van Leeuwen, 2009). This is achieved through the co-option of the immune cells in the context of the tumor microenvironment (as discussed below) or the acquisition of resistance mechanisms (Shields et al., 2010; Yang et al., 2010).

(6) Reaching replicative immortality based on telomerase activation. Relatively independent from the 4 first hallmarks, this one stand that even if tumor cells can proliferate and survive, they will reach the physiologic limit of the length of the telomeres. To note, telomeres are repeated sequences of DNA that cap the chromosomes ends to protect the coding DNA. Each replication of the DNA induces a loss of the length of these telomeres, until they reach minimal size that blocks the proliferation of cells

(Hayflick 1997). Nevertheless, all malignant cells activate telomerase (Shay and Bacchetti, 1997), an enzyme specialized in the addition of repeated hexameres to the DNA telomeric ends (Bryan and Cech, 1999). Thus, they acquire theoretical “immortality” through unlimited cell proliferation cycles (Blasco, 2005).

(7) Reprogramming metabolism to only glycolysis. This decreases the production of ATP but favors the synthesis of more elemental bricks (amino acids and nucleosides) (Vander Heiden et al., 2009). Importantly, this activates oncogenes such as RAS and MYC (DeBerardinis et al., 2008; Jones and Thompson, 2009); linking metabolism to the other hallmarks.

(8) Inducing angiogenesis, which is necessary to bring O₂ and nutrient and evacuate CO₂ and metabolic waste to the growing number of cells in the primary tumor. This physiologic process is deregulated in tumors (Hanahan and Folkman, 1996), mainly because of the spatial concentrations of endothelial growth factors such as VEGF (Baeriswyl and Christofori, 2009). The resulting vasculature is highly abnormal with enlarged vessels, leakiness and over-branching (Baluk et al., 2005; Nagy et al., 2010).

Many of these characteristics are related to the notion of “tumor microenvironment” (9) that is the result of the growth of a primary tumor in its surrounding stroma. Importantly, its formation is progressive and tends to favor the growth of the tumor (Joyce and Pollard, 2009). It includes many types of cells, among which the different subclones of tumor cells, recruited stromal and endothelial cells and immune cells in a modified extracellular matrix (Fig. 3).

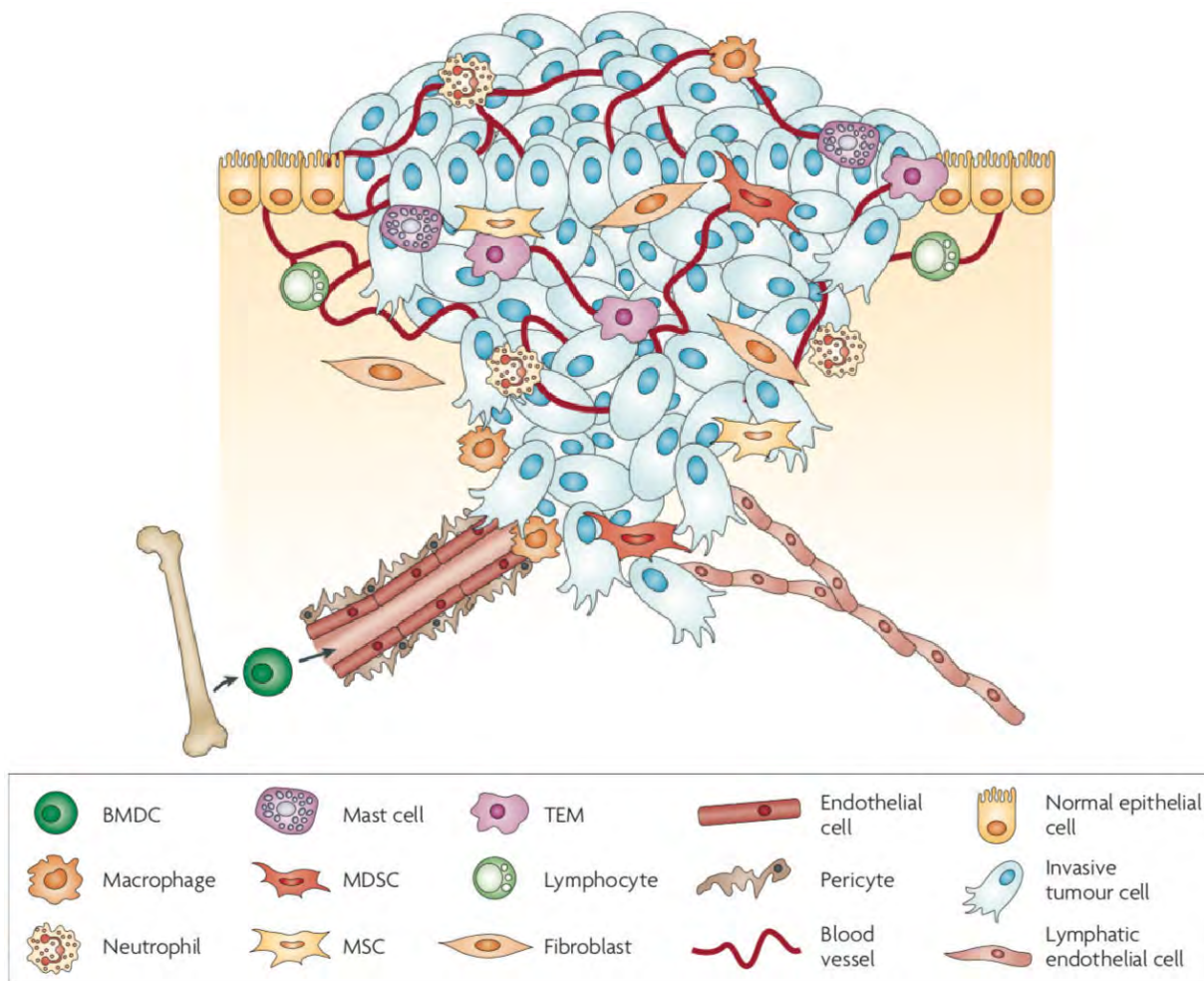


Fig. 3: Typical tumor microenvironment. Adapted from Joyce and Pollard, 2009.

In this specific context, normal cells such as fibroblast or macrophages can be influenced by tumor cells and assist them (namely turned into cancer-associated fibroblasts and cancer-associated macrophages) (Cirri and Chiarugi, 2012; Netea-Maier et al., 2018). For instance, macrophages that would in theory eliminate tumor cells, turn to pro-tumoral agents, producing growth factors and angiogenic factors in the tumor microenvironment (Condeelis and Pollard, 2006). Furthermore, in response to tumor cells presence, immune cells produce inflammatory cytokines that paradoxically increase tumor cell proliferation and survival (DeNardo et al., 2010). Also, endothelial cells in proximity to these inflammatory/remodeling signals can be perturbed. This ends in the formation of abnormal vessels (Jain, 2001; Goel et al., 2013) that are the major escape routes for tumor cell dissemination (Naxerova and Jain, 2015).

All in all, these features favor the proliferation and the dissemination of tumor cells (10) (**Fig. 4**). Some of the cells will be able to invade their stroma towards the blood and lymphatic vessels. They might be able to enter these vessels (process called intravasation) and thus be carried by the flows to distant organs. If they manage to stop in the circulation, adhere the vessels wall and extravasate (cross the endothelial barrier to reach the stroma, they might reactivate the growth of a new tumor, a metastasis (Valastyan and Weinberg, 2011). This step-wise progression will be detailed in the next chapters.

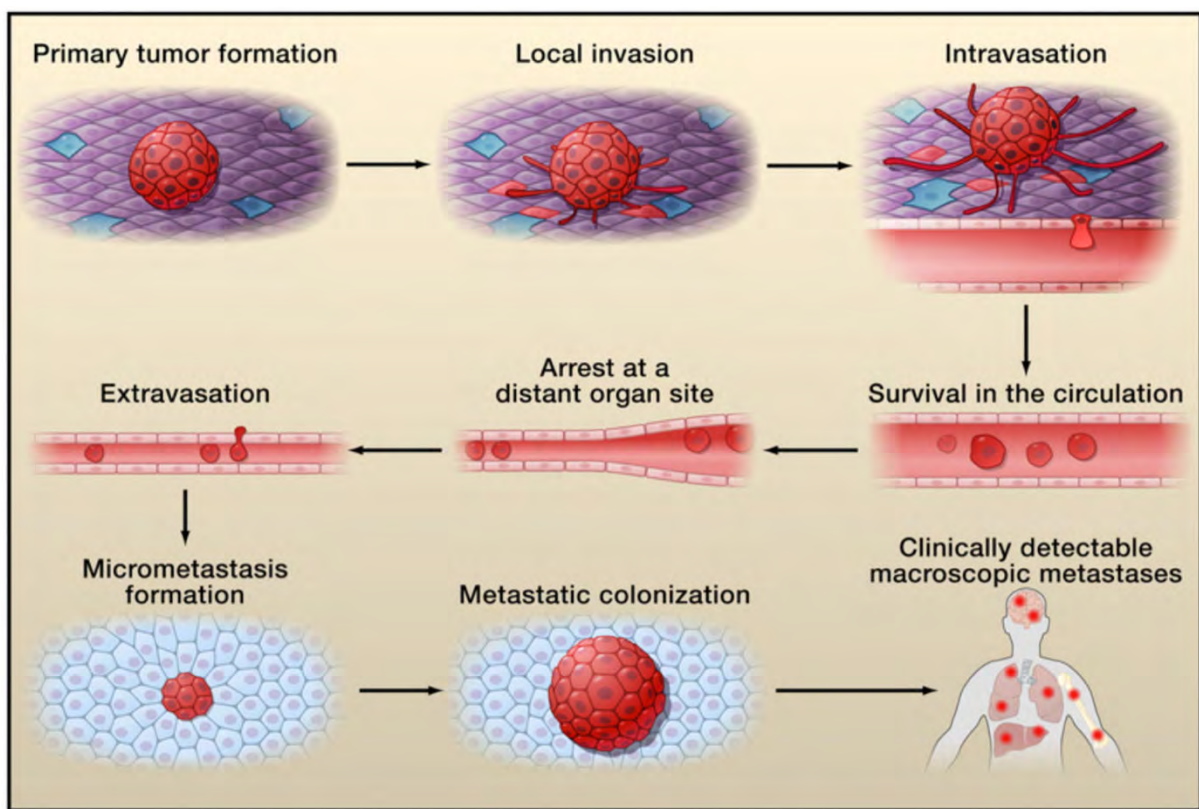


Fig.4 : Step-wise progression from the primary tumor the the formation of life-threatening metastasis. Extracted from Valastyan and Weinberg, 2011.

D) HETEROGENEITY AND COMPLEXITY OF THE DISEASE

Before entering in the description of the metastatic cascade that is at the center of my project, it is important to discuss the complexity of cancer disease. Indeed, the step-wise progression of tumor to the formation of life-threatening metastases is a simplification of the heterogeneity of cancer that originate from the primary tumor.

i) PRIMARY TUMOR HETEROGENEITY

The first level of complexity is in the primary tumor. Malignant cells and non-malignant cells forming the tumor evolve over time into a complex ecosystem (Lawson et al., 2018). In the primary tumor, the stochastic accumulation of genetic mutations (more than 10 000 somatic mutations for an advanced tumor – (Vogelstein et al., 2013) induces the apparition of distinct genetic subclones of tumor cells (McGranahan and Swanton, 2015) (Fig. 5A). Then, all along cell divisions, these cells may evolve toward a large spectrum undifferentiated to differentiated phenotypes (Tirosh et al., 2016; Treutlein et al., 2014) (Fig. 5B). Finally, the tumor heterogeneous microenvironment creates local pressures (immune cells prevalence, modified extracellular matrix, growth factor supplies...) that drives a stringent clonal selection. Thus, the most-fitted subclones proliferate while the less fitted do not (Greaves and Maley, 2012).

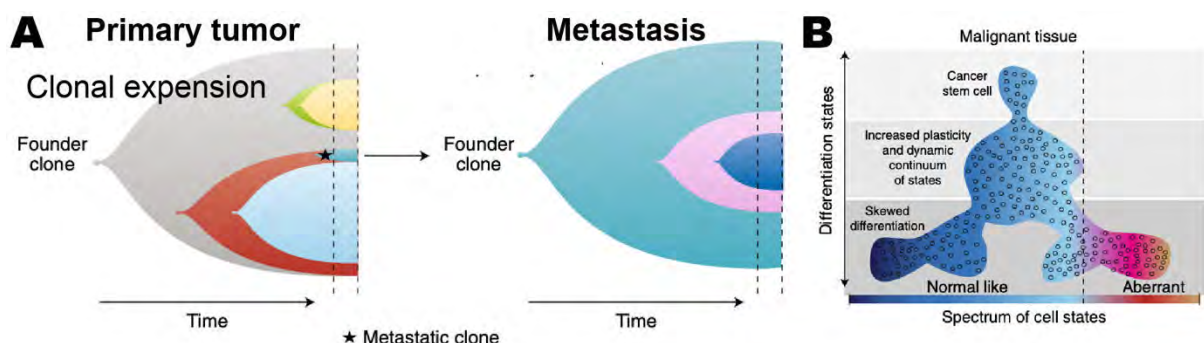


Fig. 5: **A** - Clonal expansion of the tumor. Colors indicate different clones. **B** – Heterogeneity induced by the level of differentiation of cancer cells. Adapted from Lawson et al., 2018.

In parallel, tumor cells influence locally their surrounding stromal cells (Quail and Joyce, 2013) and the composition of the extracellular matrix, increasing even more the heterogeneity of the primary tumor. Thus, a primary tumor is made of many different

cells that have different sensitivities to chemical and immunologic treatment (Carter et al., 2017) and targeting the wrong population can have disastrous outcomes. For instance, targeting the tumor mass by starving the cells through the inhibition of vascularization of the tumor leads to an increase of invasion of metastatic subclones of the tumor (Du et al., 2017). This results in promoting the presence of circulating tumor cells and subsequent metastatic seeding.

II) GIVING RISE TO METASTATIC HETEROGENEITY

The second level of complexity is the metastatic level. Indeed, from the heterogeneous pool of cell populations within the primary tumor, very few have a metastatic potential (Gerlinger et al., 2012) (**Fig. 5A**). Thus, the step-wise cancer progression (invasion, intravasation, extravasation and metastatic colonization at distance - as detailed in the next chapter) is an obvious simplification. Indeed, it doesn't take into account the spatial (from primary tumor origin to organ-specific metastasis) and the kinetic (same target organs but different relapse timings) heterogeneity of cancer spreading (Naxerova and Jain, 2015). This is a vast open question with multiple aspects:

First, in terms of spatial spreading: Cancer progression is following different routes. Current knowledge proposes three major types of blood born progression (Naxerova and Jain, 2015). 1- The linear progression which is the simplest: from the primary tumor to several “parallel” metastases (**Fig. 6A**). 2- the cascade model, in which the metastases are also shedding Circulating Tumor Cells (CTCs) that colonize more and more organs (like a flowing cascade). The major difference with the first model being the selection environment (a metastatic environment being a step to form another metastasis). 3- The parallel progression, in which early metastases and primary tumors are shedding CTCs simultaneously (**Fig. 6B**). These 3 models have been described using genomic analysis and they reveal all the real complexity of the disease. Moreover, tumor self-seeding, which is the process where metastatic cells re-colonize the primary tumor site, has been described (Kim et al., 2009), thus adding an additional layer of complexity (**Fig. 6C**). Finally, it seems that there are alternative routes leading metastatic cells dissemination from the primary tumor. Cells can alternatively reach first the lymphatic vessels around the primary tumor site, or the blood vessels (Naxerova et al., 2017; Brown et al., 2018). In the case of lymphatic transportation,

lymph nodes would allow tumor cell transfers from lymph to blood and vice versa (Pereira et al., 2018) before reaching different distant organs.

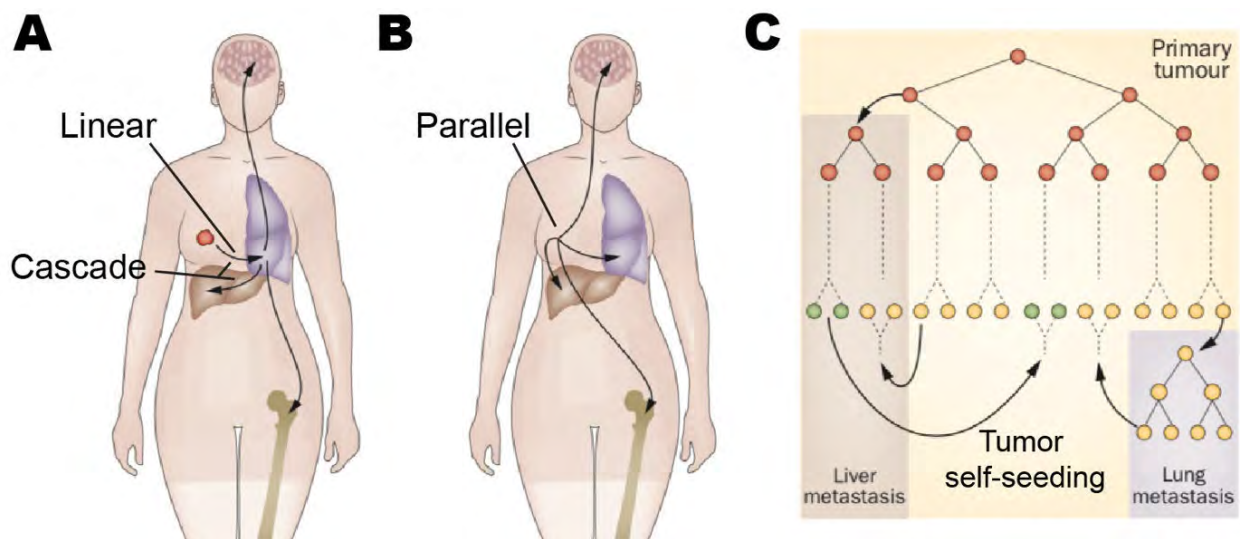


Fig. 6: Spatial spreading heterogeneity of cancer. **A** – Schematic of the Linear and Cascade models. **B** – Schematic of the Parallel model. **C** – Theoretical example of the reconstruction of cancer progression showing clonal expansion and metastasis interaction with the primary tumor. Adapted from Naxerova and Jain, 2015.

Second, in terms of temporal spreading: Several groups have shown that metastases arise from early dissemination from a non-invasive primary tumor (Hüsemann et al., 2008). Intravital imaging of *in situ* carcinoma revealed the capacity of some tumor cells to escape the tumor (Harper et al., 2016). In parallel, genome analysis confirmed that metastasis bear high similarities (up to 80% of the case in a mouse mammary cancer model) with the early primary tumor (Hosseini et al., 2016). Thus, these findings 1. drastically challenge the step-wise progression of cancer and 2. favor the parallel model of cancer spreading (Fig 6). Ultimately, this increases the tumor cell heterogeneity due to the various condition of the different metastatic organs.

Besides, it appears that a large part of tumor cells that reach distant organs are not able to proliferate, certainly due to the lack of their tumor microenvironment, or else, a non-favorable microenvironment (Gao et al., 2019). But often these tumor cells do not die. They enter in a senescence state called dormancy and might eventually re-activate if conditions turn to be more favorable (Aguirre-Ghiso, 2007; Hanahan and Weinberg,

2011) (Fig. 7). How and when these mechanisms are taking place is one of the major challenges for clinicians.

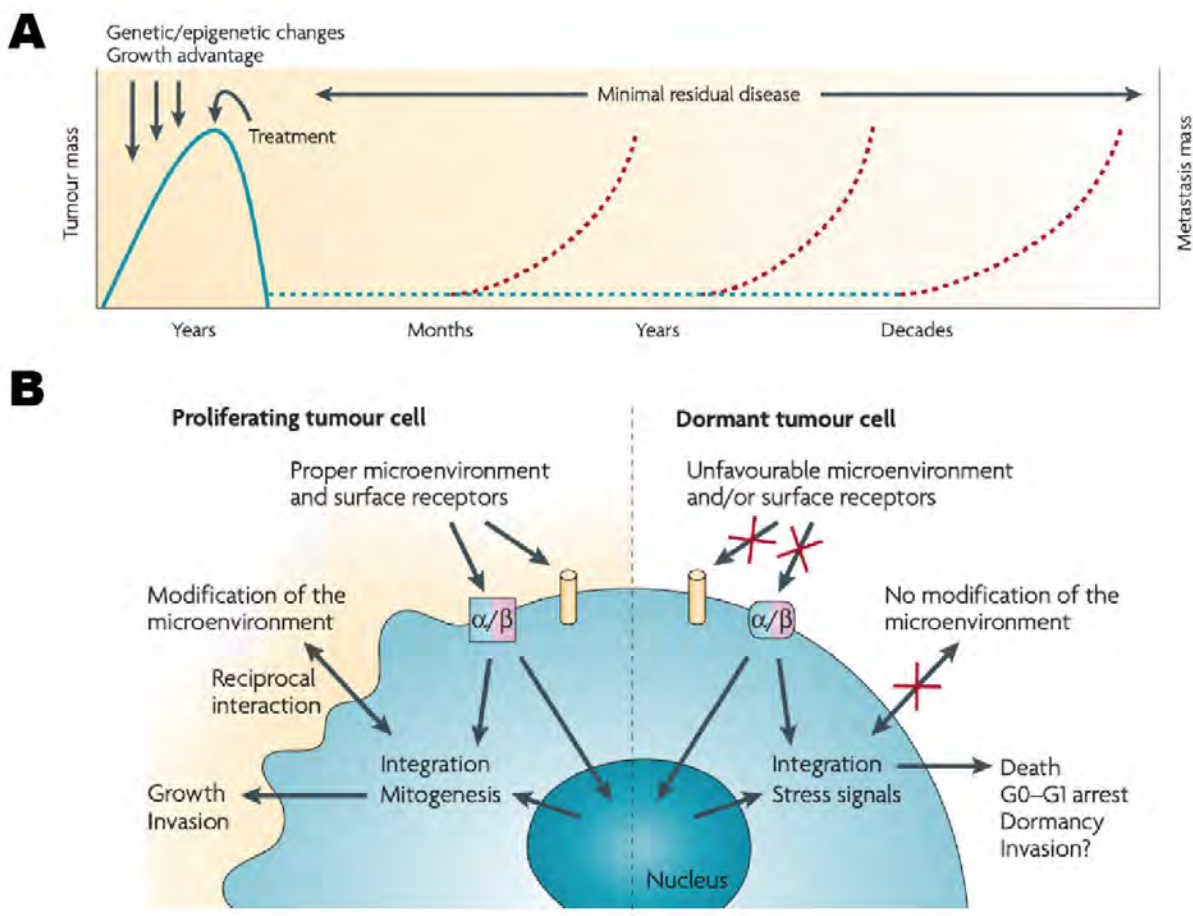


Fig. 7: Temporal spreading heterogeneity induced by dormancy. **A** – Metastatic outgrowth delay due to long dormancy phase at distance from the primary tumor. **B** – Dormancy state compared with proliferative state of tumor cell resisting apoptosis in a G0-like phase of the cell cycle. Adapted from Aguirre-Ghiso, 2007.

Finally, so far there is no consensus on the time CTCs spend in blood circulation: this ranges from a few minutes, observed during intravital imaging acquisitions in the mice (Kienast et al., 2010), up to several hours in patients (Meng et al., 2019).

All these context-dependent, spatial and temporal heterogeneities are complexifying our understanding of the disease progression. Thus, studying cancer requires the development of single cell analysis as introduced in the next section.

III) SINGLE-CELL LEVEL TO TACKLE TUMOR HETEROGENEITY

Classical approach looking at tumor growth in mouse models is now backed-up by the use of single-cell analysis. Although, these have drawbacks (small sample size, variability, massive amount of data...), it allows the targeting of a precise aspect that might be critical in tumorigenesis. Two major strategies are used to tackle tumor heterogeneity: the -omic at single cell level (DNA sequencing and RNA sequencing, proteomics, ...) and the imaging with high spatial and temporal resolutions.

Using -omic approaches, it is possible to separate cell population and have access to clonal signatures in patients (Navin et al., 2011; Carter et al., 2017) (Fig. 8). These retrospective data allow the discovery of tumor initiating or metastatic populations and pave the way to study the role of specific key genes (Polzer et al., 2014).

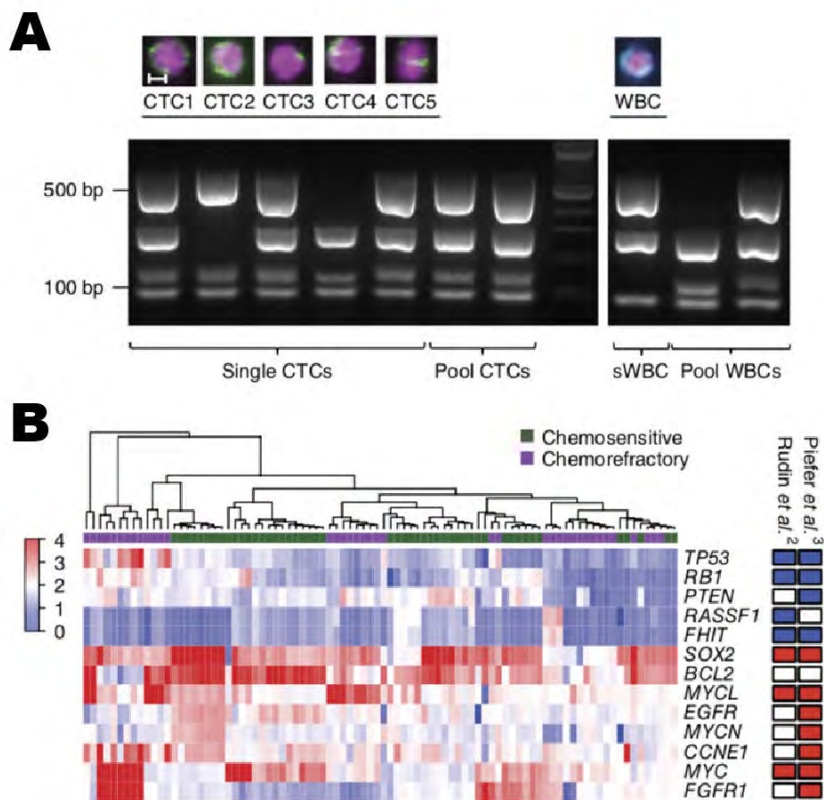


Fig. 8: Example of single CTCs isolation experiments allowing the discovery of specific gene signature of tumor cells surviving in the circulation. **A** – Image of CTCs isolated and Southern Blot separation of PCR product. **B** – Genomic data analysis comparing different CTCs on their chemosensitivity. Extracted from Carter et al., 2017.

Using imaging on animal models (such as mouse, zebrafish or drosophila), it is possible to accede to the single cell resolution. This approach is more direct, but less powerful in terms of statistical output. A recent example is the use of Dendra2 photoconvertible fluorescent protein to study the fate of a few single cells xenografted in the zebrafish (Yan et al., 2019). In recent years, imaging barcoding strategies were interestingly used to characterize the primary tumor heterogeneity (Reeves et al., 2018) (**Fig. 9A and B**), subclone disseminations (Wagenblast et al., 2015; Merino et al., 2019) and metastatic initiating populations (Krøigård et al., 2017). In these studies, cell transformations are used to induce the expression of different fluorophores in the chosen cells, before implanting them in mouse models. The fluorescent combinations of the cells at the injection site and the metastatic lesions allow the tracking and understanding of the impact of each cell populations in tumorigenesis (**Fig. 9C**).

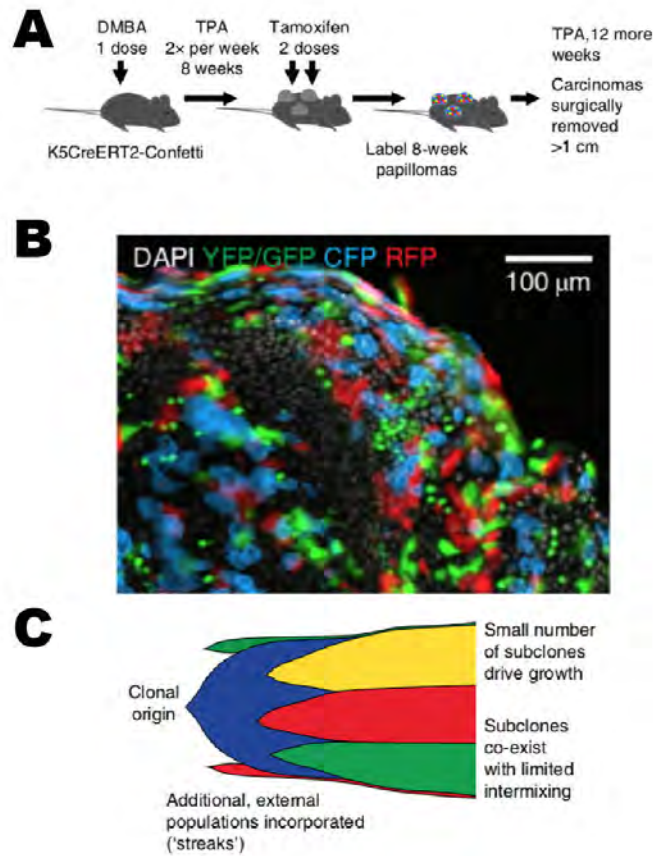


Fig. 9: Example of fluorescent barcoding approach allowing the study of tumor heterogeneity. **A** – Experimental design using inducible random recombination CRE system to give rise to different colors at the single cell level. **B** – Representative image of the results at the primary tumor, with tumor cells labelled in 3 colors. **C** – Graphical representation of the results of the experiment, showing the clonal population ratio overtime. Adapted from Reeves et al., 2018.

In parallel, imaging is necessary to characterize the tumor cell spreading from a mechanistic point of view *in vivo*. This is dependent on -omic signatures, but their understanding needs direct visualization of the tumor cells in relevant *in vivo* context. To note, this is the main focus of the lab, and the approach that we used during my PhD.

II - THE METASTATIC STEPS PRECEDING ENTRY INTO THE CIRCULATION

A) TUMOR GROWTH INITIATION

The origin of tumor formation is a complex issue to address. Most often, researchers/clinicians do not have access to the tumor initiating cells (TIC): The cells of origin of the primary tumor. To note, they can be different from “Cancer stem cells” (CSC), whose name is restricted to the cells that are sustaining tumorigenesis (i.e. mastering all the step of the metastatic cascade). In other terms, both types of cells are able to self-renew and grow a tumor, but CSC are invasive (Visvader, 2011) (Fig. 10).

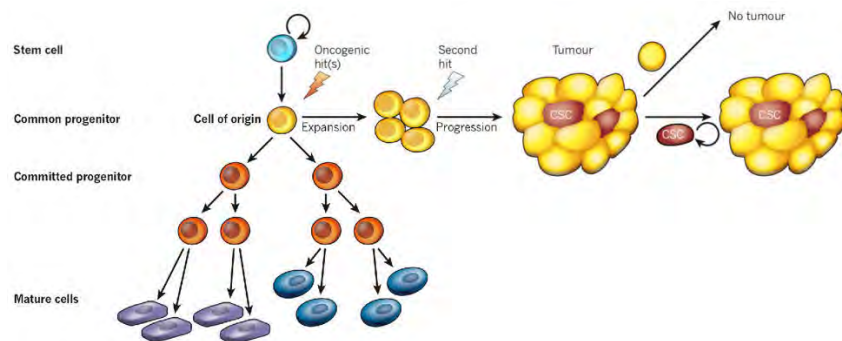


Fig. 10: Difference between cell of origin and cancer stem cell. Extracted from Visvader, 2011.

The combination of cell plasticity, DNA mutations and stromal signals are thought to initiate tumor formation:

- Cell plasticity helps understanding the apparition of TICs (Varga and Greten, 2017). Indeed, stem cells and differentiated cells are able to repair damage tissue and maintain homeostasis thanks to their ability to adapt to a context. These adaptations require the regulation of gene expressions that are “accepted” by the cells, even if they are not physiological in normal context. The same plasticity allows the progressive survival of slightly abnormal cells that can accumulate DNA mutations.

- DNA mutation is central in tumor initiation. Mutation in the non-coding (regulatory) and coding sequence can unlock and/or activate tumor formation. In general, TICs bear mutations in “Master regulator genes”. They are key genes that are sufficient (but not necessary) to induce cell transformation (Califano and Alvarez, 2017). In brief, they are either tumor suppressor (normally blocking tumor development) or oncogenes (if their activation promote tumorigenesis). For instance, Myc is a proto-oncogene (Dalla-Favera et al., 1982): Its overexpression induces the overproduction of MYC transcription activators that leads to abnormal proliferation. Or else, Tp53 that is a central actor of the cell cycle blocking in case of Cell/DNA damage. Thus, it is a tumor suppressor: its inactivation unlocks the proliferation of abnormal cells (Resnick et al., 2005).

- Finally, the interplay between cells and stroma is guiding tumor initiation. Cells are reacting to stromal signals, sometimes through a proliferation that favor tumor transformation (Plaks et al., 2015) and sustains proliferation. These signals can be local (like the presence of inflammatory macrophages (Condeelis and Pollard, 2006)) or systemic: For instance, it is the case in hormone-sensitive breast cancers, in which the presence of estrogen/progesteron activates the proliferation of cells (Dalmau et al., 2014).

According to these last points, stem cells that are responsible for the homeostatic renewal of the organs are good candidates for tumor initiation. They are responsible for DNA heritance during proliferation, they are highly sensitive to stromal signals from their niches, and the modification from stem cells to differentiated cells requires cell plasticity. Indeed, studies using spontaneous or inducible cancer mouse models could show the central role of stem cells (Visvader, 2011). This model fits the majority of colon cancer, arising from crypt stem cells. Nevertheless, most pancreatic cancers originate from differentiated luminal epithelial cells.

B) INVASION

With the proliferation of tumor cells and the formation of the tumor microenvironment, biological and physical cues turn benign and local tumor mass to invasive (malign) cancer. First, in the common case of cancer from epithelial origin (carcinoma), tumor

cells must break their basal lamina, which is considered as the limit from *in situ* to malignant tumor (Spaderna et al., 2006; Nguyen-Ngoc et al., 2012).

According to Wolf et al. the minimal pore size that a cell can go through is 10% of the nucleus cross sectional area (Wolf et al., 2013). This is called the “nuclear limits” and represent a pore of $\sim 7 \mu\text{m}^2$. In the case of more confined space (which is the case of basal lamina), cells will start expressing metalo-proteinases (MMPs) and degrade the matrix first. MMPs are either transmembrane or secreted by tumor and stromal cells (Lee and Murphy, 2004). Most often, they are associated with the formation of invasive cell protrusions called invadopodia (Paz et al., 2014) revealing the other important actor of cell invasion: the cytoskeleton.

Cell migration relies on the capacity to produce forces and to transmit them to the microenvironment (Moreau et al., 2018). Force generation comes from the actin polymerization, crosslinking and association with molecular motors such as myosin IIa (Barbier et al., 2019). The transmission of the force generated goes through friction or cell adhesion (Fig. 11). Cell adhesions involved in mechanical forces transmission rely mostly on focal adhesion, with the central role of integrins receptors (see also **box 2: Integrin** for more details about Integrins in cancer). These anchors points are both signaling activators of actin remodeling and can be enriched in transmembrane proteases (or be a favored site of secretion for soluble proteases) that favor the migration (Jacquemet et al., 2015; Mygind et al., 2018).

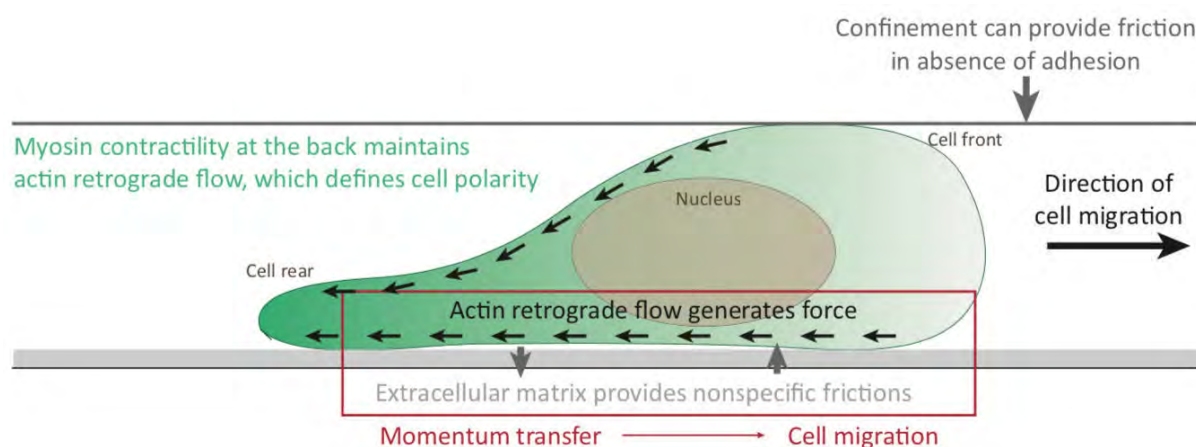


Fig. 11: Cell migration mechanism. Extracted from Moreau et al., 2018.

Interestingly, there is a wide range of coordinated MMPs' action and acto-myosin contractions that will end up in a wide variety of motility depending on the cell type:

from totally mesenchymal to totally amoeboid, as described in **Fig. 12** (Paul et al., 2017).

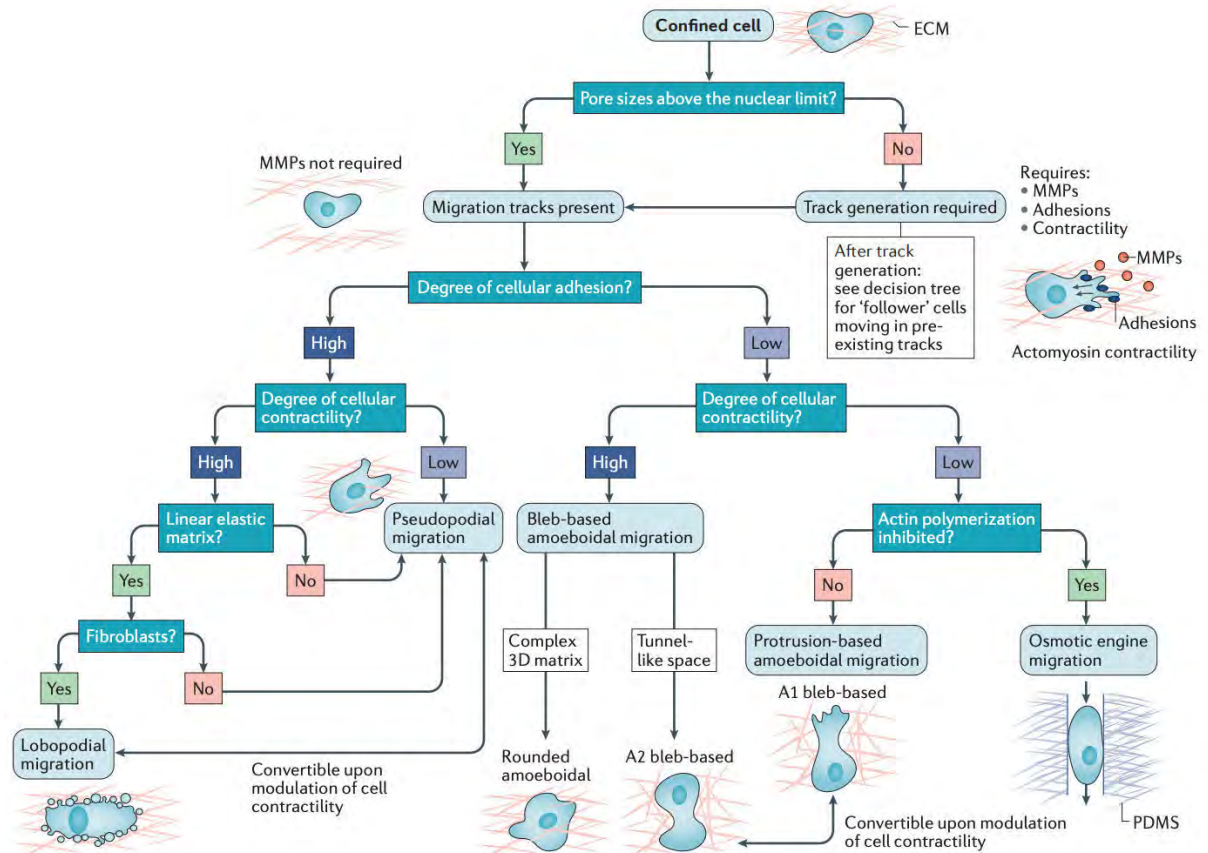


Fig. 12: Migration strategy depending on the confinement. Extracted from Paul et al., 2017.

In the case of invasive tumor cells, *in vivo* data could highlight the role of “leader cells”, that are creating paths in the stroma (Alexander et al., 2008). These cells can be tumor cells (Cheung et al., 2013) or stromal cells (for instance, cancer- associated fibroblasts (Gaggioli et al., 2007)). Then other tumor cells might use these paths of “lower confinement” to invade. This concept is classically associated with collective migration of tumor cells (**Fig. 13**), but it also impacts single cells migration, as single cells will naturally choose the paths of lower confinement (Paul et al., 2016). In the case of collective migration, they are bound to leader cells (also called migration front in this case) that they follow (Friedl and Alexander, 2011) (**Fig. 13**).

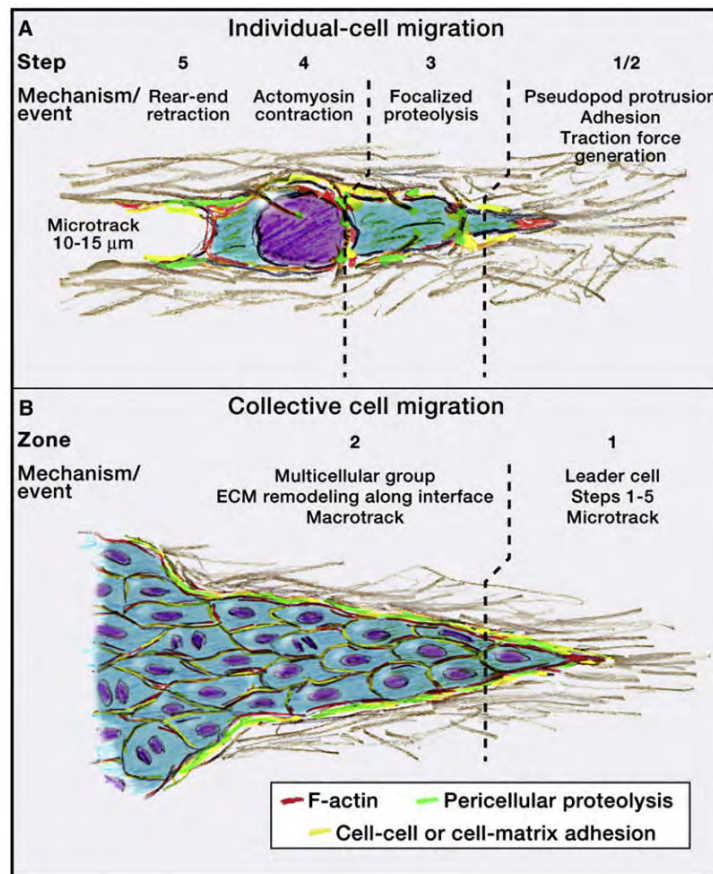


Fig. 13: Single vs collective migration. Extracted from Friedl and Alexander, 2011.

To note, the type of migration used may directly depend on the degree of the confinement and of the cancer cells' epithelial (with conservation of cell-cell adhesion) versus mesenchymal (freely migrating in the stroma) status (Pastushenko and Blanpain, 2019), which represents an additional layer of heterogeneity originating from the tumor microenvironment (Friedl and Alexander, 2011).

The tumor microenvironment can favor invasiveness through different biomechanical processes: 1. It promotes angiogenesis and lymphangiogenesis that provide escaping routes to metastases (Butler et al., 2010). 2. The matrix and cell density physically exerts pressure onto the cells (a process called solid stress – (Stylianopoulos et al., 2012) to leave the primary tumor. 3. High interstitial fluid pressure (Swartz and Fleury, 2007) induces a convective flow towards the lymphatic vessels (Cornelison et al., 2018).

c) INTRAVASATION

With the growth of the primary tumor, blood and lymphatic vessels develop towards the tumor mass. Through invasion, some of the tumor cells are able to reach the vessels and cross the endothelial barrier, a process called intravasation. Potentially, the vasculature around the primary tumor is sufficiently disrupted and permeable (with incomplete basal lamina and immature cell-cell junction) to allow tumor cells to enter by themselves (Yuan et al., 1995). Indeed, the vessels are in constant rearrangement and also often lack pericytes, these cells are part of the vessel wall, enwrapping the endothelial cells (Carmeliet and Jain, 2011). Few key proteins have been identified to intervene in this direction. For instance, the enhanced expression of Twist (promoter of the loss of cell-cell junction between tumor cells) accelerating intravasation in the context of lung cancers (Yang et al., 2004). Or, Aes (amino-terminal enhancer of split), which inhibits Notch signaling, suppressing invasion in the context of colon cancers (Sonoshita et al., 2011). Or else, the expression of actin binding protein such as an isoform of Mena protein named Mena^{INV} (Roussos et al., 2011) and N-WASP (Gligorijevic et al., 2012) that promotes invasion and intravasation of breast cancer cells.

Alternatively, several articles discussed the role of tumor-associated macrophages in this step. They showed that a tripartite complex (called TMEM) composed of a macrophage, a tumor cell and endothelial cells is at play (Wyckoff et al., 2007) (Fig. 14). The tumor cell activates the macrophage which in turn secretes inflammatory signals among which Tumor Necrosis Factor alpha ((TNF- α) – (Zervantonakis et al., 2012) disrupting endothelial junction and facilitating the tumor cell crossing (Harney et al., 2015).

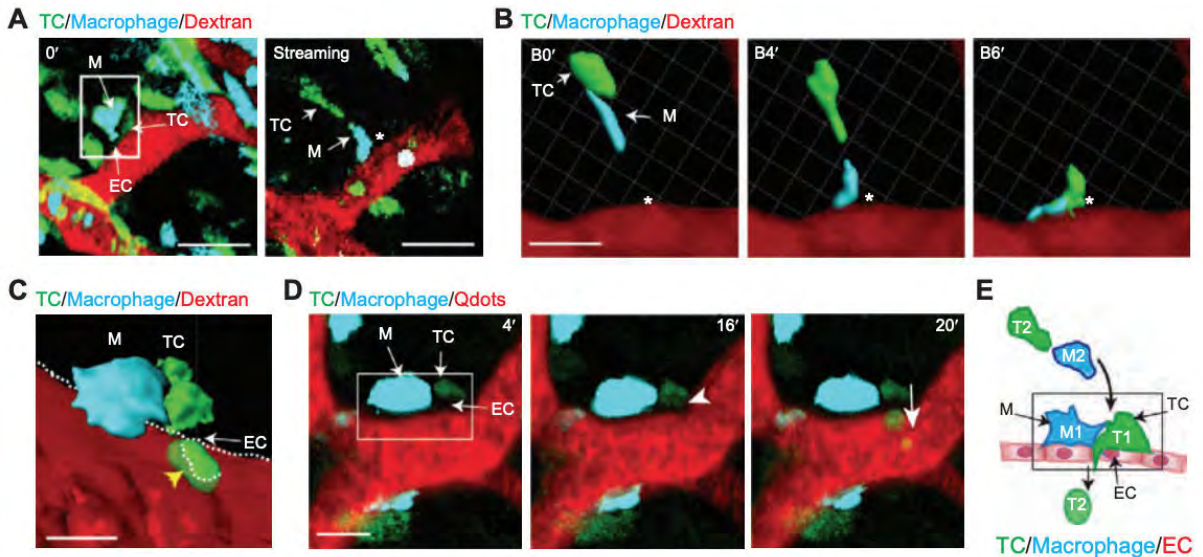


Fig. 14: Intravital acquisition of tumor intravasation. Tumor cell (green) in the process of intravasation, assisted by a tumor-associated macrophage (blue). Lumen of the vessel in red. TC= tumor cell. EC= endothelial cell. M=macrophage. Extracted from Harney et al., 2015.

After intravasation, tumor cells are in the blood or lymphatic circulation that carries them away from the primary tumor. Eventually, they will arrest, adhere and extravasate (i.e. cross the endothelial barrier) escaping the circulation (Nguyen et al., 2009). These last steps are the major focus of my works and will be developed with a biomechanic focus in chapter 4 of this introduction, after discussing the factors that influence these steps. At distant sites, cells will regrow - potentially after a phase of dormancy - and colonize the new locations, forming secondary tumors (metastases).

III - FACTORS IMPACTING THE METASTATIC SPREADING

A) BIOLOGICAL FACTORS IMPACTING THE METASTATIC SPREADING

After intravasation, tumor cells systemic spreading that triggers the apparition of metastases was described through the “seed and soil” hypothesis proposed by S. Paget in 1889 (Paget, 1889). It means that the seed (tumor cell) will only grow in a favorable soil (metastatic organs). This theory, based on the organotropism observable in all cancers, is widely accepted and described. One convincing study is from Tarin et al. in the context of ovarian cancers. In this clinical study, a palliative treatment consisting of connecting fluid excess from the tumor to jugular vein allowed the transfer of thousands of tumor cells to reach the blood flow and to spread systemically. Strikingly, the majority of the patients did not developed metastases (Tarin et al., 1984). This hypothesis takes into account the cell surface receptors, enzymes, transcription factors, chemokines, ... All are biological factors that influence the tumor cells to complete the metastatic cascade (Fidler, 2003) as illustrated in the following examples:

- 1- In the case of breast cancer cell lines (MDA-MB-231) injected intracardially into mice, Yoneda et al. could select an over-metastatic subclone of tumor cells that specifically colonize the bones. Compared to control MDA, these cells were sensitive to insulin-like growth factor 1 that is expressed in the bones (Yoneda et al., 2001).
- 2- Another example from Radinsky et al., on colon cancer: they could show the need for a combination of the expression of Epidermal Growth Factor Receptor (EGFR) and Transforming Growth Factor alpha (TGF- α) to sustain a tumor growth (Radinsky and Ellis, 1996).
- 3- For the establishment of distant metastasis, circulating factors have been identified to prime the metastatic organs, before the arrival of CTC, a process called pre-metastatic niche formation (Liu and Cao, 2016; Peinado et al., 2017). Without entering into details, accumulating evidence have shown that extracellular vesicles and other tumor derived circulating factors are impacting the biology of distant organs (endothelial adhesion receptors activation, immune cell inhibition, extracellular matrix

remodeling...) (Fig. 15). For instance, extracellular vesicles induce changes in the adhesion repertoire of lymph nodes, favoring their colonization (Hood et al., 2011) and increased lung metastasis through the inhibition of neutrophils (Liu et al., 2016) in melanoma.

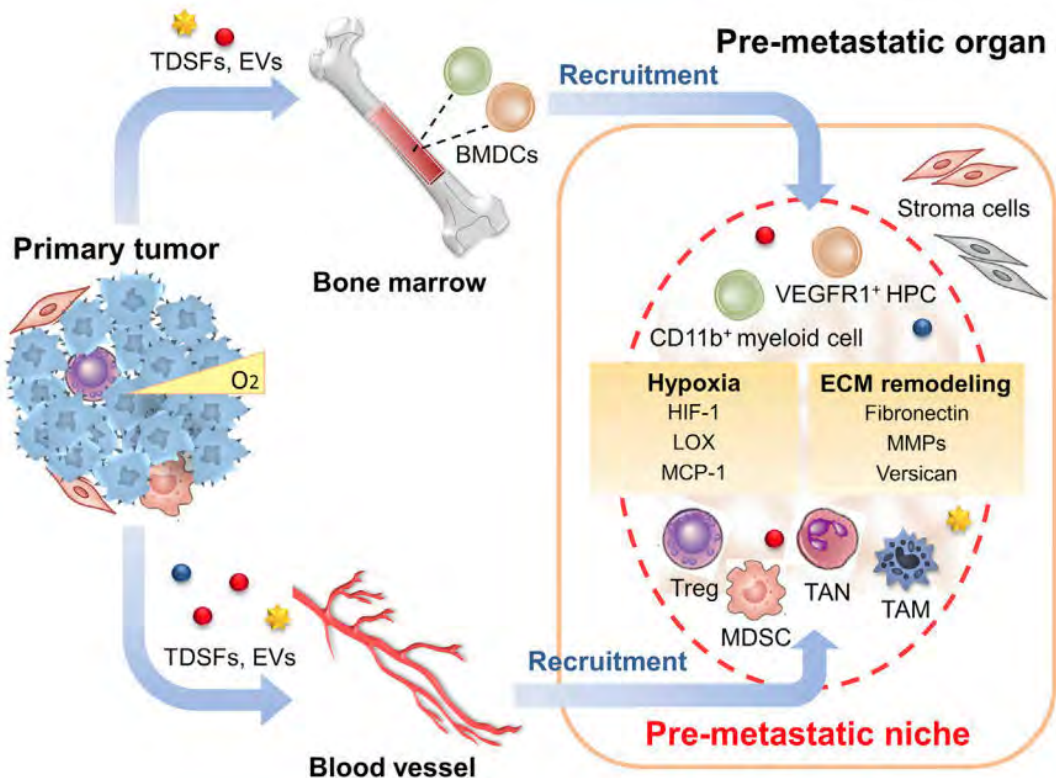


Fig 15: Premetastatic niche formation, under the influence of the primary tumor circulating factors. TDSFs = tumor derived secreted factors. EVs = extracellular vesicles. Treg, MDSC, TAN, TAM = immune system associated cells. HPC = hematopoietic progenitor cells. Extracted from Liu and Cao, 2016.

More controversially, different microenvironments transform the same tumor cells in different manners, as shown by Nakajima et al. (Nakajima et al., 1990). In their article, they revealed that the expression pattern of proteases by the same cells is influenced by the matrix composition at metastatic sites. This means that tumor cells are also able to adapt to their microenvironment, which brings the static view of the “seed and soil” hypothesis to a more complex system.

B) MECHANICAL FACTORS IMPACTING THE METASTATIC SPREADING

Multiple articles based on autopsies (Weiss, 2000), show a clear correlation between the primary tumor location and the major metastatic organs. These are the basis of the mechanical hypothesis proposed by J. Ewing in 1928 (Ewing, 1928). He stands that tumor cell dissemination and subsequent metastatic seeding are mainly driven by physical cues (Chambers et al., 2002; Wirtz et al., 2011). For instance, colon cancer patients very often develop liver metastasis (Obenauf and Massagué, 2015). Looking at the anatomic plan of the vessels, this sounds perfectly logical, as blood from the colon, carrying circulating tumor cells, will be filtered by the liver at first place (Fig. 16). In here, CTCs have to go through tiny and tortuous capillaries where they have great chances to stop. This point is linked to the probabilistic view of tumor cell arrests (Bell, 1979; Bell et al., 1984): Tumor cells have a finite chance to arrest in the circulation, based on the size of the capillary, the number and time of contact between tumor and vessel wall and the concentration of adhesion molecules at their surface (Wirtz et al., 2011). Thus, small capillaries are the most probable site of adhesion preceding the extravasation of tumor cells.

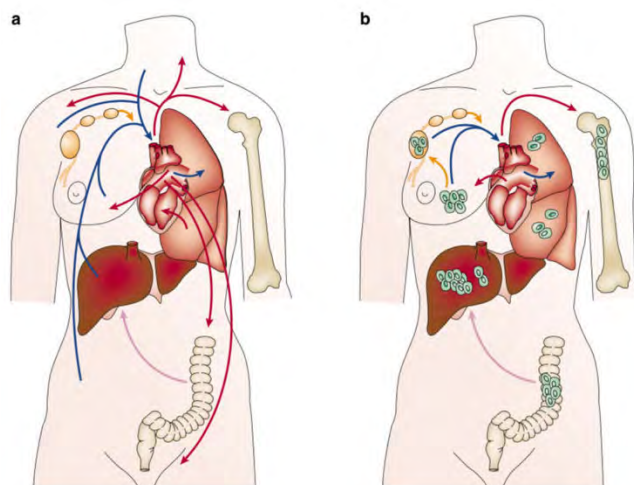


Fig. 16: The vascular architecture partially explains the repartition of metastases. The first capillary bed that tumor cells will cross, is always a major metastatic organ. For instance, liver in the case of colon cancer (by the portal vein). Extracted from Chambers et al., 2002.

All in all, three major biomechanical factors impact tumor cell arrests, stable adhesion and extravasation. Blood flow, physical constraints and active adhesion forces (Fig.

17). These three factors are acting synergistically or antagonistically. For instance, a low blood flow in a small diameter capillary (above 1 mm/sec) will maximize the number of contacts and their duration, promoting CTCs arrests (Wirtz et al., 2011). While high flow (such as an arterial flow profile up to 30 cm/sec) induces high shear forces which prevent cell adhesions.

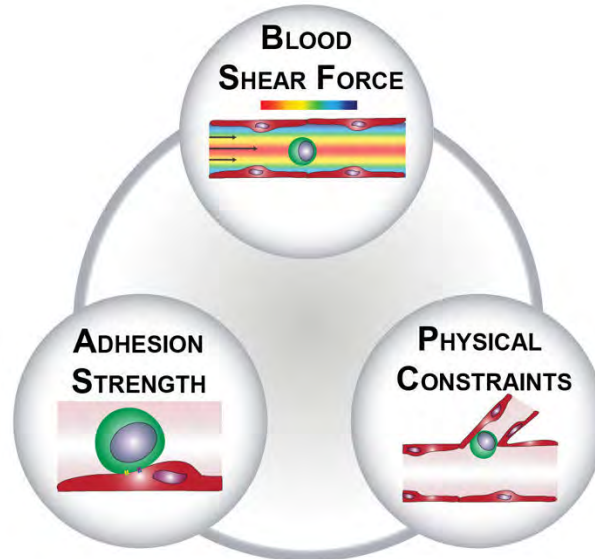


Fig 17: Blood flow, physical constrain and adhesion force are the main factors impacting CTCs arrest, adhesion and extravasation.

This hypothesis was also strengthened with the rise of biomechanics in the last decades, with the depiction of the impact of mechanical cues at the cellular level. One good example is the impact of the extracellular matrix on tumor invasion, as previously mentioned. Several groups have been working on the clinically proved extracellular matrix stiffening (Sinkus et al., 2000; Butcher et al., 2009). The ability of extracellular matrix to impact cells is shown by the difference in cell morphology that can be observed between 2D versus 3D embedded culture of the same cells. For instance, from flat to spindle-like in the case of fibroblasts (Walpita and Hay, 2002) or cuboid in the case of mammary gland cells (Streuli et al., 1991) and from monolayer to tubes in the case of endothelial cells (Folkman and Haudenschild, 1980). Cells are able to sense extracellular matrix stiffness and adapt their morphology through the remodeling of their cytoskeleton (Yeung et al., 2005). In particular, the actin cytoskeleton is at play, as the modulation of the RhoA/Rock pathway influences cell rigidity in 3D (Panorchan et al., 2006). Even more, they are able to probe the matrix stiffness during cell migration as they tend to migrate following the stiffening gradient (Lo et al., 2000; Zaman et al., 2006). In the case of cancer cells, matrix stiffening through collagen deposit and crosslinking (Szauter et al., 2005) has been associated with tumor malignancy (Paszek

et al., 2005). This was associated with increased of the integrin signaling inducing PI3K pathway activation that enhances cell migration (Levental et al., 2009).

All in all, this demonstrates that cells can feel and react to mechanical stimuli. This means that not only basic anatomical arguments validate the mechanical hypothesis, but physical cues influence the metastatic cascade at cellular level.

C) MULTIFACTORIAL TUMOR DISSEMINATION

Historically, the mechanical hypothesis was strongly challenged (Fidler, 2003) partly because the anatomical correlation is not always correct (Weiss, 2000, 1992). For instance, Breast cancer is very often linked to bone metastasis (Chambers et al., 2002; Obenauf and Massagué, 2015), a clinical fact that the mechanical hypothesis can't explained easily. Nowadays, with the knowledge acquired on cell biomechanics, the consensus is that both hypotheses are at play (Azevedo et al., 2015). The combination of favorable vessel architecture and permissive flow allowing the tumor cells to arrest are linked with biological signals that first, allow stable adhesion of the tumor cells, second help its extravasation and third activate its outgrowth. In the previous example of breast cancer metastasing in the bones, one can consider the coordinated roles of fenestrated capillary vasculature and low flow (mechanical hypothesis) with the bone cell secretion of CXCL5 chemokine (seed and soil) (Bersini et al., 2014) to activate extravasation and subsequent metastatic outgrowth.

IV - FOCUS ON THE BIOMECHANICS OF ARREST, ADHESION AND EXTRAVASATION

A) SURVIVAL IN THE CIRCULATION

After escaping from the primary tumor, cells enter either in lymphatic or in blood vessels which are an unfamiliar and harsh microenvironment. Tumor cells will then be exposed to moderate shear stress until they reach lymph nodes or another organ while passing by veins. For instance, in the case of colon cancer, cells will be transported by the portal vein to the liver. If they stay in the blood circulation, managing to go through the capillaries (of the liver in this example), they will reach the heart and the arterial flow, thus being exposed to high shear stress. It is also true in the case of breast cancer cells that do not stop in the lungs: they will be transported to the heart and reach bones, brain and liver (highly metastatic organs according to clinical data - (Obenauf and Massagué, 2015)). Thanks to this observation, it is clear that some CTCs are able to sustain the harsh intravascular microenvironment and survive until they arrest, adhere and extravasate at distance.

Luckily, CTCs that do survive in circulation and establish metastatic foci are rare (Nagrath et al., 2007) (**Fig. 18**). This was nicely showed by the work of Luzzi et al. and Cameron et al. In both these works, they used intravascular injection of tumor cells and recorded the early metastatic seeding in the afferent organ (maximizing the chance to observe metastatic foci). Their results showed that only 1 to 4% of the cells gave rise to micro-metastases (Luzzi et al., 1998; Cameron et al., 2000).

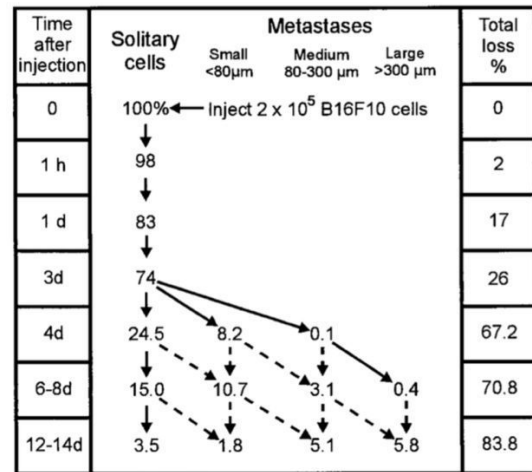
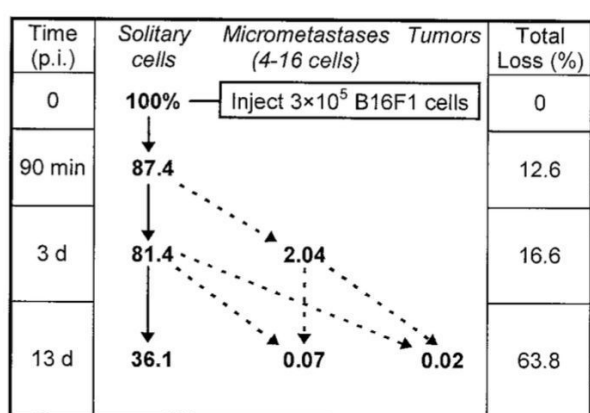


Fig. 18: **A** – Analysis of tumor cell fate in the liver after injection in the superior mesenteric vein. Extracted from Luzzi et al., 1998. **B** – Similar experiment realized in the vena cava to target the lungs. Extracted from Cameron et al., 2000.

Besides, using intravital imaging in the brain, Kienast et al. showed that most of the CTCs die before extravasating. A large number of cells get stuck in the brain capillaries post-intracardiac injection, but less than 5% successfully extravasate (Kienast et al., 2010). To note, CTCs that die or fragment in the blood flow have an impact on the surrounding vasculature (Headley et al., 2016; Entenberg et al., 2018) (Fig. 19). This means that even if these CTCs are not giving rise to metastasis, they are priming the receiving organs that might become more prone to metastatic seeding.

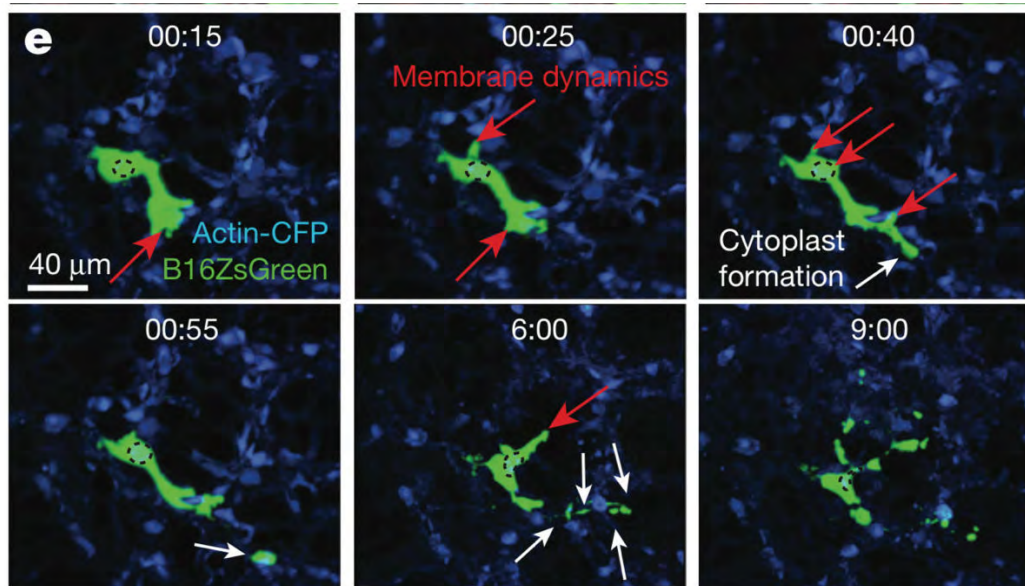


Fig. 19: Arrested cells (green) show fragmentation (white arrow) in the circulation. Extracted from Headley et al., 2016.

I) SINGLE CIRCULATING TUMOR CELL SURVIVAL

Tumor cells genomic instability and clonal selection will most likely cause the development of survival strategies during the fluid transport.

First, because they are in circulation, single CTCs will have to survive anoikis (Frisch and Scream, 2001) (apoptosis due to the lack of cell-cell/cell-matrix contact). To do so, Douma et al. showed that CTCs achieve it by the overexpression of the neurotrophic tyrosine kinase receptor B (TrkB) protein. TrkB blocks the activation of caspases apoptotic pathway *in vitro* and increases the metastatic colonization *in vivo* (Douma et al., 2004).

Second, they have to survive an increased level of Nitric Oxid (NO) and other Reactive Oxygen Species (ROS) induced by the blood flow (Harrison et al., 2006). Indeed, shear stress induces the entry of Ca in cells, its interaction with calmoduline and the activation of eNOS that produces ROS. To note, the accumulation of ROS is leading to DNA damage and rapid protein and lipid degradation (Poprac et al., 2017). To resist the ROS increase, several strategies were described. The reversible activation of the folate metabolic pathway, that increases the regeneration of NADPH to buffer the ROS (Piskounova et al., 2015). The translocation of KLF4 transcription factor, leading to the over-expression of beta-globin (HBB) which neutralizes ROS (Zheng et al., 2017). Interestingly, in this case, blood flow would be responsible for both the danger (ROS production), and the survival strategy, as KLF4 is a flow-sensitive transcription factor. Third, there is also the direct impact of flow, i.e. the destructive mechanical force of the flow. CTCs experience shear forces and collisions that can challenge their integrity. Shear stress can induce cell destruction (usually characterized as necrosis) (Mitchell et al., 2015; Regmi et al., 2017), programmed cell death (Mitchell and King, 2013; Regmi et al., 2017), cell cycle arrest (Chang et al., 2015), cytoplasmic leakage through cytoplasmic membrane breakage (Barnes et al., 2012) and DNA damage (Gong et al., 2015). In this case also, their survival strategies are now better understood. For instance, concerning membrane breakage, a calcium dependent mechanism was described for rapid closure of the membrane using lipid vesicle fusion (Terasaki et al., 1997). Otherwise, to prevent DNA damage, CTCs relies on nuclear resistance to stress, thanks to the composition of their nuclear envelope. Especially the concentration of lamin A and C was shown to be critical for nuclear rigidity (Lammerding et al., 2006; Mitchell et al., 2015), and also other actors such as

STEF/TIAM2 (guanine nucleotide exchange factor) protein complex that controls Rac1 GTPase and subsequent perinuclear actin network (Woroniuk et al., 2018). Finally, in the case of DNA damage, some mutations that result from inaccurate DNA repair were shown to be pro-survival, increasing resistance to chemotherapy (Gong et al., 2015).

II) CELL INTERACTION-BASED SURVIVAL

Alternatively, CTCs can travel as clusters (Liotta et al., 1976). Clusters are composed of tumor cells and potentially stromal cells that gathered together before intravasation (Gao et al., 2019; Liu et al., 2018c), in the circulation (Cheung et al., 2016; Liu et al., 2018c) or at arrest site (Entenberg et al., 2018). It is still unclear how they remain cohesive despite the ripping shear forces and the collisions, but several studies could identify that adhesion proteins are involved. For instance, CD44 was shown to be required (in a homophilic interaction manner) in the formation of circulating clusters of patient derived cells (Liu et al., 2018c). Also, plakoglobin, a desmosomal and adherent junction intracellular adaptor was shown to allow the formation of CTC clusters at the site of the primary tumor (Aceto et al., 2014). Both examples show that several types of receptors are involved in the formation of the clusters. Importantly, clusters are associated with increased metastatic incidence as shown in different studies (Hou et al., 2013; Aceto et al., 2014).

In the circulation, interactions with stromal and immune cells were described for their protective role when associated with tumor cells:

1- CTCs interact with cancer associated fibroblasts (Jones et al., 2013; Ao et al., 2015). This interaction and its advantages (extracellular matrix remodeling, pro-survival signals, favored invasion...) were extensively demonstrated in the tumor microenvironment (Attieh et al., 2017). Gao et al could show that this interaction persists in the context of peritoneal dissemination, providing survival advantage (Gao et al., 2019). Also, the partial depletion of CAF in the context of lung cancer cell dissemination hampers metastatic foci formation (Duda et al., 2010).

2- CTCs interact with neutrophils (Spicer et al., 2012). Co-opted neutrophils provide protection against shear stress and other immune cells (Szczerba et al., 2019), while increasing the chance of adhesion for tumor cells (Strell et al., 2007; Szczerba et al., 2019).

3- CTCs interact with platelets. Interestingly, platelets can have a positive or a negative impact on the metastatic outgrowth (Bambace and Holmes, 2011). The combination of tumor cell signals and shear stress activates platelets (Ilkan et al., 2017). First of all, thrombocytopenia (loss of platelets) was shown to correlates with reduced metastases (Gasic et al., 1968). Two major findings support this result: First, platelets can protect the tumor cells from shear stress and immune cells by forming a mechanical “shield” around tumor cells (Labelle et al., 2011, 2014). Second, activated platelets are covered with adhesion receptors that can favor the arrest of tumor cells (Frenette et al., 1995; Reymond et al., 2013). Controversially, anti-metastatic effects of platelets were also demonstrated, through the activation of some of their receptors. For instance, the depletion of GPIb, a platelet transmembrane receptor reduces the metastatic potential of melanoma cells (Erpenbeck et al., 2010). Less clearly, the integrin α 2B (called GPIIb in the context of platelets) was shown to increase CTCs arrest, but it limits cell proliferation at the metastatic sites (Echtler et al., 2017). Thus, the real impact of CTC clustering with platelets is still unclear and needs further work.

Moreover, the clustering of CTCs together also provides many resistance advantages. First, tumor cells in clusters are often polyclonal, which suggest that a cluster will have various resistance mechanisms. For instance, some of the cells can retain epithelial characteristics (assessed by the presence of keratin 14, an epithelial intermediate filament), expressing cell-cell adhesion molecule such E- and P-cadherin as well as desmosomal proteins as shown by Cheung et al. (Cheung et al., 2013, 2016). Thus, this cell population could be more prone to colonize distant organs, as clusters may have shielding effect (Cheung and Ewald, 2016). Second, tumor cells in clusters do not suffer from anoikis. This was demonstrated to be dependent on mucin interaction (MUC1) (Zhao et al., 2010) or integrins that bind and internalize ECM component blocking apoptosis (Guo and Giancotti, 2004).

Finally, independently from the cells that form the cluster, mathematical models predict that clusters roll less than single tumor cells in circulation (King et al., 2015). Also, depending on their shape, they can circulate closer to the vessel border (a process called margination - (Anderson et al., 2017; Rejniak, 2012). Both of these would statistically favor their adhesion by increasing the number of contacts between the vessel wall and the cells (Wirtz et al., 2011).

All in all, 1. Clusters are more resistant to shear stress and immune system. 2. They have greater chances to arrest thanks to physical trapping and active adhesion in small capillaries than single cells. This last point is detailed in the next section discussing the way CTCs and CTC clusters arrest and adhere to the vessel walls.

B) CIRCULATING TUMOR CELLS ARREST AND STABLE ADHESION

Arrest of a tumor cell is the moment when the cell stops in the circulation. Live imaging of this steps shows that it is highly dynamic, made of transient stops and re-circulation phases. In certain circumstances, stable adhesion occurs and definitively anchors the CTC to the vessel wall (Nguyen et al., 2009). Initial insights on the cancer cell arrest, adhesion and extravasation were provided by leukocytes rolling and diapedesis, with the speculation that most of the results could be transferred (Miles et al., 2007; Vestweber, 2015). Thus, I will start by a brief description of the leukocyte model before discussing the current knowledge about CTCs.

I) LEUKOCYTES ROLLING AND DIAPEDESIS.

Leukocyte rolling is induced by inflammatory signals from the stroma. These signals impact the endothelial cells, that express cell adhesion receptors at their surface (Wyble et al., 1997; van Wely et al., 1999). Among them, the important family of the E-selectin, L-selectin and P-selectins, that are recognized by leukocytes. These receptors have the particularity of being fast to engage, but with low binding forces (Alon et al., 1995; Marshall et al., 2003). This is what induces the rolling of the leukocytes (Brunk et al., 1996; Simon and Green, 2005). While rolling, the leukocyte slows down. This lower speed gives enough time to high binding force but low speed cell adhesion molecule to stabilize the leukocyte at the surface of the endothelium (Mayadas et al., 1993; Kong et al., 2013). Among them, the integrins are the most important (see also **box 2: Integrins** for more details about Integrins in cancer). Especially, $\alpha L\beta 2$ binding ICAM and $\alpha 4\beta 1$ binding VCAM are key in the stable adhesion of leukocytes (Oppenheimer-Marks et al., 1991; Reiss and Engelhardt, 1999; Simon et al., 2000). Finally, these adhesion molecules trigger downstream signaling in the

endothelial cells, that will favor the diapedesis (transmigration of the leukocyte through the endothelial layer) as described in the next section (Schaefer and Hordijk, 2015) (Fig. 20).

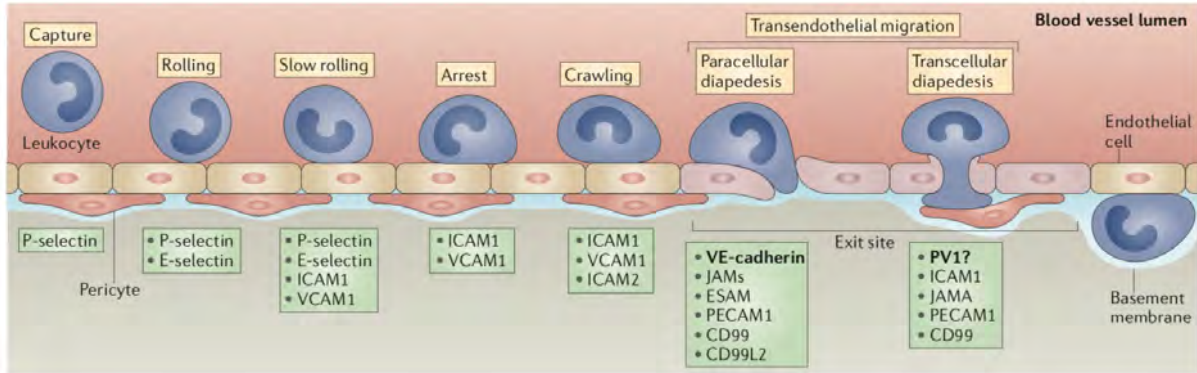


Fig. 20: Leukocyte rolling and diapedesis. Extracted from Vestweber, 2015.

Whether this knowledge can be directly transferred to CTCs arrest, adhesion and extravasation is an open question. As discussed in the following section, CTCs hijack several receptors and trigger a similar pathway to arrest and transmigrate. Nevertheless, 1. Some cell adhesion receptors are highly specific to leukocytes (among them, several integrin subunits). 2. The inflammation that induces endothelial “pro-adhesive” response is missing (not considering the concept of pre-metastatic niche discussed above) (Peinado et al., 2017). Moreover, CTCs diameters (between 10 to 15 in general) are bigger than leukocytes (8 μm), which suggest that CTCs can more easily be trapped in small capillaries.

II) PHYSICAL TRAPPING INDUCING TUMOR CELL ARREST

Intravital imaging of arrested tumor cells often show trapped cells in a tiny capillary or at a branching point (Kienast et al., 2010; Stoletov et al., 2010) (Fig. 21). Indeed, mammalian CTCs measure 8 to 15 μm in diameter, while the smallest capillaries are less than 6 μm in diameter. Thus, it is not surprising that occlusion of the vessels by CTCs has been observed in many contexts : Mouse brain for mammary cancer cells (Kienast et al., 2010), Mouse liver for ovarian cancer cells (Naumov et al., 1999), colon cancer cells (Steinbauer et al., 2003) or melanoma cell (Guba et al., 2000). To note, this occlusion process is one more stress that cells must overcome as Barbera-Guillem

et al. could show: Melanoma cells suffering membrane breakage during occlusion of the liver vessels (Barbera-Guillem et al., 1992).

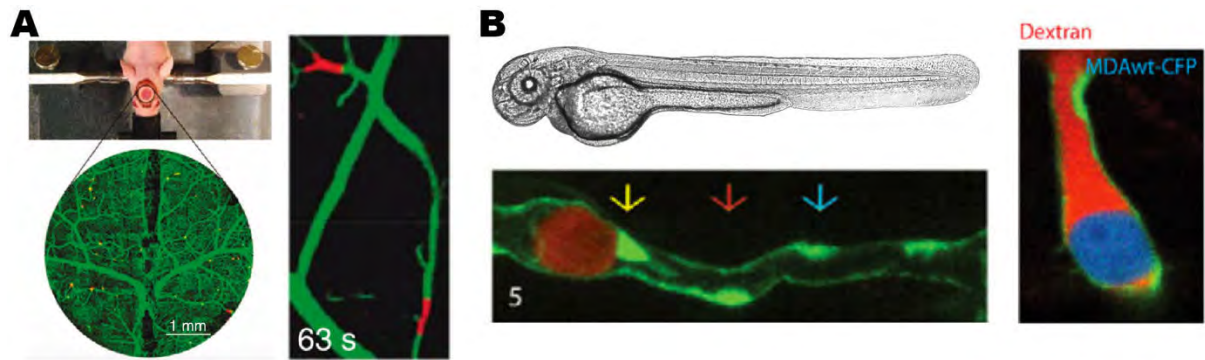


Fig 21 : CTCs intravascular arrest through occlusion *in vivo*. **A** – In the mouse brain, observed through an optical window and vessel perfusion with dextran (green); Tumor cells in red. Adapted from Kienast et al., 2010. **B** – In the zebrafish embryo. Left image: Tumor cell in red; vasculature in green. Right image: Tumor cell in blue, vasculature in green and dextran in red. Adapted from Stoletov et al., 2010.

Interestingly, this (and other mechanical disruptions of tumor cells happening in flow) induces the formation of necrotic cell debris that were linked to the transformation of the endothelial cells into pro-adhesive endothelial cells (Weis et al., 2004) and establishment of the pre-metastatic niche (Headley et al., 2016).

There is much to know relating to the stress and deformability limits of CTCs. But there is an interesting parallel to do with *in vitro* works using microfluidic chips (narrowing channels, confinement...) (Garcia-Arcos et al., 2019). Indeed, comparing the shape of CTCs in capillaries and in microfluidic, one can envision the potential knowledge transfer (**Fig 22**) : Importance of cell deformation (Lautscham et al., 2015), nuclear deformations (Thiam et al., 2016; Graham and Burridge, 2016), nuclear envelope ruptures (Denais et al., 2016; Raab et al., 2016), chromatin disruptions (Irianto et al., 2016) and subsequent DNA damages that would happen the same way *in vivo*.

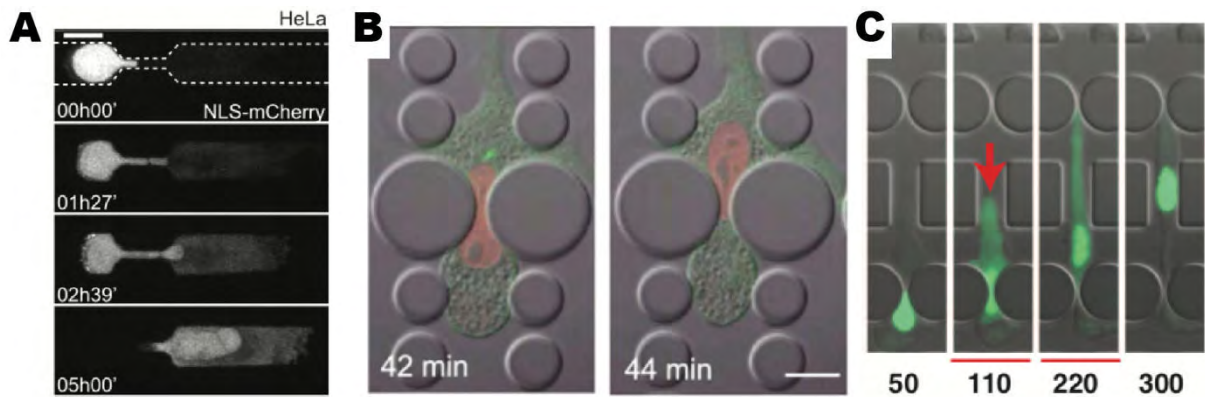


Fig. 22: *In vitro* microfluidic studies on cell passing through physical constraints. Left, extracted from Raab et al., 2016. Middle, adapted from Cao et al., 2016. Right, adapted from Denais et al., 2016.

Controversially, occlusion is not always the key factor. Orr et al. showed that melanoma cells injected in the portal vein arrest in large sinusoids of the liver (Orr et al., 2000), where no occlusion can happen (Scherbarth and Orr, 1997). Similarly, Haier and colleagues demonstrated the same arrest pattern for colon cancer cells (Haier et al., 2003). Also, efficient arrest of breast and prostate cancer cells in the bones can be blocked by inhibiting cell adhesion receptors (lectins in this case), demonstrating that cell active adhesion has more impact in this context (Glinskii et al., 2005). On the same line, Gassmann et al. were able to separate arrest and adhesion by blocking the adhesion steps, demonstrating that occlusion is not sufficient for a stable anchoring of the CTCs (Gassmann et al., 2009). Finally, occlusion was recently challenged by a study on clusters of CTCs. Au et al. could show that clusters can go through capillary-sized channels, forming a single-file shape cluster at the narrowing point without breakage of the cluster (Au et al., 2016) (Fig. 23). This study adds to the vast literature on the deformability of CTCs (Cross et al., 2007; Alibert et al., 2017) suggesting that even if the capillaries are smaller, the cells might be able to squeeze and keep flowing.

All in all, even if a physical constraint just induces transient cell trapping, it will for sure promote cell deceleration. This will increase the probability of cell arrest and subsequent stable adhesion.

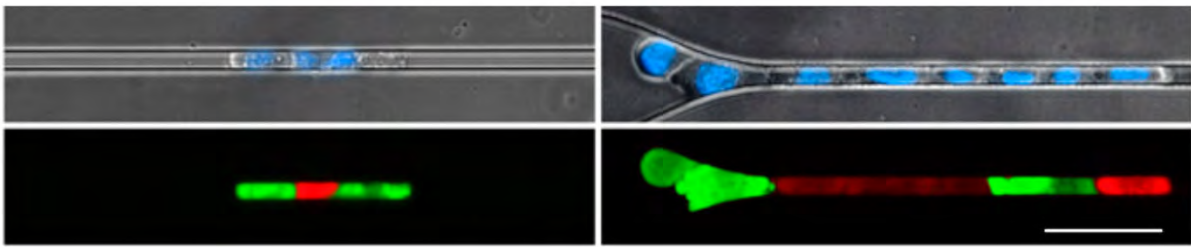


Fig. 23: Clusters of CTCs squeezing in narrow channel. Tumor cells colored in green and red to follow single cells in the cluster. Extracted from Au et al., 2016.

In summary, on the one hand, occlusion occurs *in vivo*, and is considered as the major arrest mechanism so far (Chambers et al., 2002; Gupta and Massagué, 2006). On the other hands, thanks to their reduced stiffness, CTCs are able to squeeze and thus, cell active adhesion to the vessel wall also play a role in the arrest phase.

III) ACTIVE ADHESION DURING TUMOR CELL ARREST

As described above, this step has been extensively studied in the case of leukocytes (Vestweber, 2015). In the case of tumor cells, rolling has not been precisely described so far *in vivo*, but mainly treated indirectly (without direct imaging at the single cell level) (Hiratsuka et al., 2011; Köhler et al., 2010) or *in vitro*. Moreover, intravital Imaging of arresting CTCs in the liver (Ito et al., 2001) or in the brain (Kienast et al., 2010) did not reveal cancer cell rolling. Nevertheless, E-selectin was shown to mediate breast and colon cancer cells rolling during perfusion (Tözeren et al., 1995). To note, the central role of E-selectin was shown in other studies using colon cancer cells, (showing its requirement preceding the binding of VCAM and extravasation (Auguste et al., 2007)) but was questioned by the use of blocking-antibody against selectin, that do not block the apparition of metastases (Glinskii et al., 2005).

Other *in vitro* experiments could show the prominent role of glycoproteins on the arrest of tumor cells. Among them, the central role of CD44 and CD24 interacting with E-selectin, PSGL1 interacting with P-selectin and MUC1 interacting with ICAM were described. (Strell and Entschladen, 2008; Reymond et al., 2013; Shea et al., 2017). To note, CD44 is a major adhesion receptor for both immune and tumor cells with low binding forces (Bano et al., 2016) (**Fig. 24** - please see **box 1: CD44**). It is also

overexpressed in highly metastatic cells (Baccelli et al., 2013; Boral et al., 2017). CD44 is one of the key receptors in the second article of the results section.

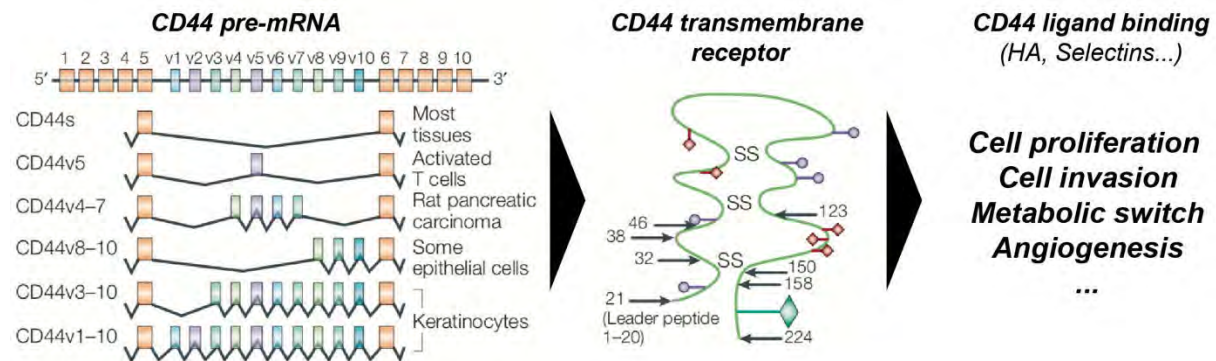


Fig 24: Transmembrane receptor CD44. Alternative splicing and mutations induce the expression of various form of CD44 impacting cell behavior. Left, splicing variants. Middle schematic of the protein. SS = disulfide bridge. Small marks = alternative post-transcriptional modification (N-glycosylation, O-glycosylation, ...) sites. HA = Hyaluronic Acid. Adapted from Ponta et al., 2003.

Otherwise, thanks to lattice light sheet microscopy (Chen et al., 2014), Liu et al. could observe intravascular crawling of breast cancer cells (Liu et al., 2018b): The cell binds metastable adhesions by sending filopodia-like structures towards the vessel wall that breaks over time. Interestingly, this highlights the presence of a low binding adhesion in the case of cancer cells, potentially allowing the binding of high-forces anchors that were also found (Shibue et al., 2012, 2013; Jacquemet et al., 2015), to definitively stabilize the tumor cells links to the wall.

Altogether, these data reveal the coordinated role of occlusion and active adhesion to counter-act the shear stress and allow CTC arrest. Once arrested, CTCs endure stronger shear forces due to the fact that they are immobile in the flow (Fan et al., 2016), and therefore must quickly engage stronger and more stable adhesions to proceed to extravasation as described in the next section.

Box 1: CD44 in cancer progression

CD44 is a transmembrane glycoprotein with a small cytoplasmic tail, a single transmembrane domain and seven highly variable extracellular domain due to numerous alternative splicing (Ponta et al., 2003; Zöller, 2011).

The principal ligand of CD44 is hyaluronic acid (most abundant component of the extracellular matrix - (Aruffo et al., 1990; Almond, 2007)), but it also binds other extracellular matrix components among which fibronectin (Bennett et al., 1995) or laminin (Naor et al., 2002) and mediate cell-cell contact binding E-selectin and L-selectin (Weber et al., 1996). To note, it can also mediate cell-cell contact thanks to the glycocalyx at the surface of the cell that contain hyaluronan epitope (Weinbaum et al., 2007). The intracellular tail interacts with cytoskeletal protein (ankyrin, ezrin, moesin, radixin – (Tsukita et al., 1994)), which regulate cell migration, cell shape but also apoptosis (Günthert et al., 1991; Cattaruzza et al., 2004).

CD44 is often deregulated in cancer, and several alternative splicing variants are associated to cancer as tumor suppressors or metastatic initiators (Naor et al., 2008; Chen et al., 2018). For instance, CD44 overexpression in colon cancer is a sign of poor prognosis (Wielenga et al., 1993), while it suppresses metastasis in the context of prostate cancer (Gao et al., 1997). To note, regulation of the expression of CD44 and its splicing variants is not fully understood. It is controlled by a complex interplay between intervention of various transcription factors (Shtivelman and Bishop, 1993), epigenetic marks (as shown by the impact of DNA methylation mutation on its expression – (Reisman et al., 2002)) and post-transcriptional actors such as miRNA (Liu et al., 2011).

CD44 is considered as a “cancer stem cell marker” (Al-Hajj et al., 2003), especially in the case of gastric cancer (Watanabe et al., 2017) because several studies showed that the subset of CD44 overexpressing cells among the primary tumor is often the metastatic one (Mani et al., 2008; Godar et al., 2008). Related to metastatic progression, CD44 is involved in adhesion and extravasation of leukocytes (Siegelman et al., 2000), a process that tumor cells hijack according to *in vitro* data (Shea et al., 2017). Moreover, Kang et al. could show that blocking CD44-dependent anchoring of tumor cells was drastically reducing the development of metastatic foci (Kang et al., 2014). Then, CD44 binding to E-selectin induces the rolling of circulating leukocytes, the first step of leukocytes extravasation (Vestweber, 2015). Interestingly, Lundell et al. showed that CD44 adhesion recruit beta-1 integrin at the contact site (Lundell et al., 1997). In this case, it reinforces the adhesion of hematopoietic stem cell in the stroma. The same mechanism could be at play for cancer cells in the circulation.

In conclusion, CD44 splicing variants certainly impact all steps of the metastatic cascade: 1. At the primary tumor as an extracellular matrix binding/sensor protein. 2. During circulating tumor cell spreading, as it binds to the endothelial cells and could favor intravascular arrest *in vivo*.

IV) STABLE ADHESION OF TUMOR CELLS

Similarly to leukocytes (McEver and Zhu, 2010; Wirtz et al., 2011), while arresting, CTCs have to engage new type of adhesions with endothelial cells. These adhesions are characterized, by the involvement of a higher magnitude of energy meaning stronger and more stable bounds (but with longer activation rates) which requires longer arrest time to form and strengthen. Integrins are thought to be the main actors in this step (Miles et al., 2007; Desgrosellier and Cheresh, 2010) (**Fig 25** - Please see also **box 2: Integrins**). Importantly, depending on the integrin heterodimer, they will be able to engage strong and stable adhesion that can be quantified (Roca-Cusachs et al., 2009; Bharadwaj et al., 2017).

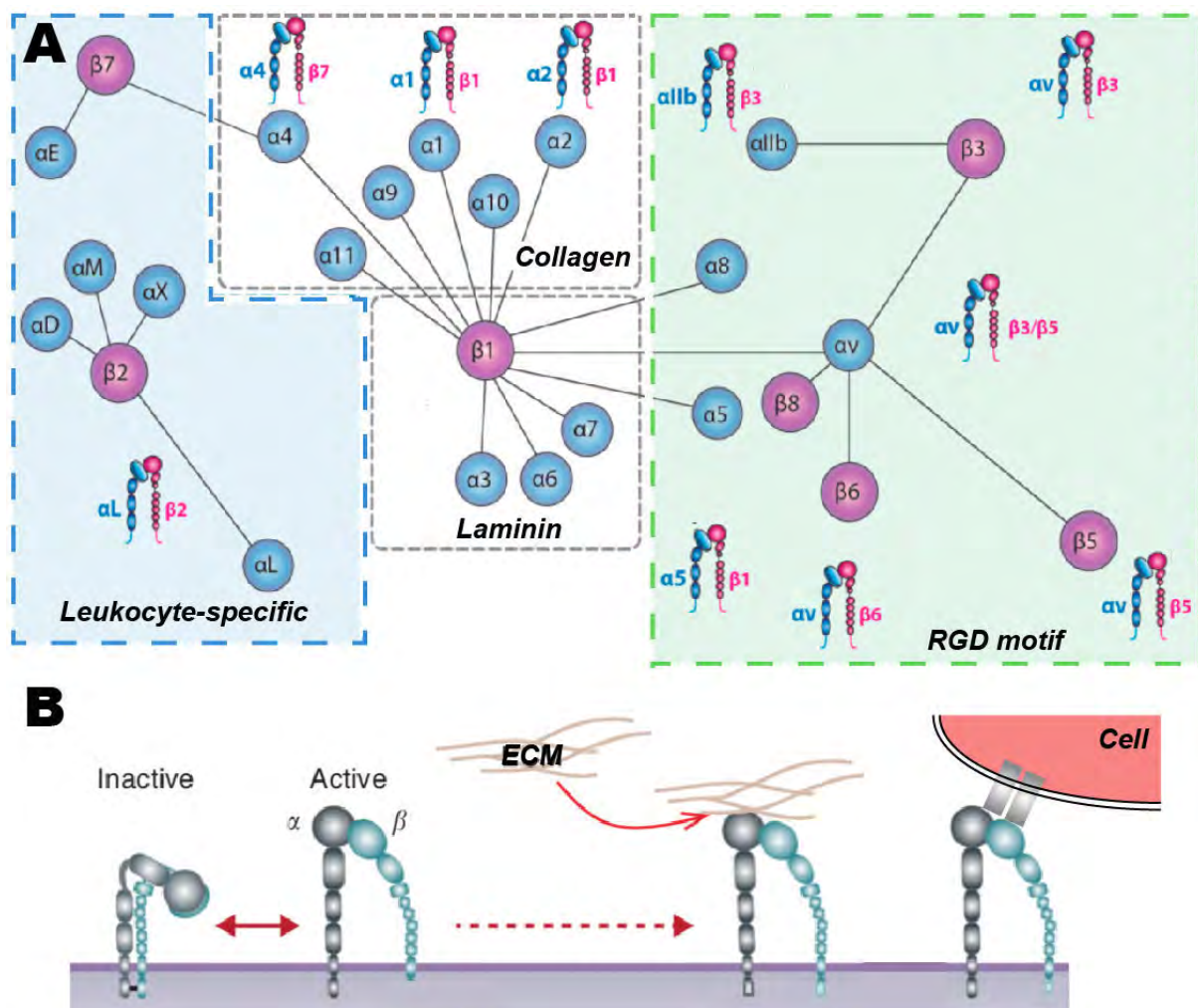


Fig. 25: Integrins. **A** - Integrins heterodimers ligand specificity. Adapted from Raab-Westphal et al., 2017. **B** – Integrin activation and binding at the membrane. Adapted from Hamidi et al., 2016.

Box 2: Integrins in cancer progression

Integrins are fundamental adhesion receptors sensitive to chemical and physical stimuli, playing central roles in cell proliferation and cell migration (Hamidi and Ivaska, 2018). Integrins comprise 24 transmembrane heterodimers made of 18 alpha and 8 beta subunits. Typical subunits are made of 1000 to 750 amino acids with a short intracellular tail, a single membrane-spanning domain and a large multidomain extracellular part (Campbell and Humphries, 2011). Alpha and beta subunits associate in various manner that dictate their ligand specificity (Humphries, 2006) and adhesion strength (Puklin-Faucher and Sheetz, 2009; Eibl, 2013) in the endoplasmic reticulum. Then, they traffic through the Golgi and reach the plasma membrane in an inactive form. Among the most studied, they principally get activated when binding to RGD (Arginine-Glycine-Asparagine) motif-containing extracellular matrices, collagen and laminin. This triggered complex signaling pathways through more than 200 proteins called “integrin adhesome” (Horton et al., 2016).

In the case of cancer, integrins expression levels are often (Desgroiselle and Cheresh, 2010; Hamidi et al., 2016), but their specific roles are not fully understood. To note, this is due to a complex regulation system including recycling in endosomal compartments and to the fact that their impact depends on the microenvironmental conditions (Kechagia et al., 2019). For instance, integrin αVβ6 activates Transforming Growth Factor beta (TGF-β) (Ludlow et al., 2005). In a physiologic context, it blocks proliferation (so could be seen as a tumor suppressor) but this αVβ6 integrin also promotes metastatic outgrowth according to clinical data (breast cancer) (Moore et al., 2014).

In primary tumors, integrins are central in the extracellular matrix remodeling: 1. They can upregulate metalloproteinases which degrade the extracellular matrix (Munshi and Stack, 2006). 2. They activate cancer associated fibroblasts which are the major actors of matrix homeostasis (Attieh et al., 2017). Then, when the matrix is modified (denser and more cross-linked) (Acerbi et al., 2015), integrins are part of the mechanoreceptors that will activate tumor cell proliferation (White et al., 2004) and invasion, guiding tumor cells to escape the primary tumor (activation of migration machinery (Rubashkin et al., 2014), activation of matrix degradation (Beaty and Condeelis, 2014; Destaing et al., 2011),...).

In the circulation, integrins can block anoikis. Several articles showed that they bind structural (Mana et al., 2016) and non-structural components (Huang et al., 2017) of the extracellular matrix, that are endocytosed and inhibit apoptosis. Otherwise, they are central in the arrest and adhesion step, as they are responsible for the binding to endothelial cells or extracellular matrix comprising the vessel wall. Among others, in vivo study of lung metastasis foci formation could show that active αVβ3 increase lung metastasis (Felding-Habermann et al., 2001). Or else, In vitro studies showed could dissect the major role of β4 integrin in the case of colon carcinoma (Laferrière et al., 2004), α4β1 in the case of melanoma cells (Klemke et al., 2007) or β1 and αVβ3 in prostate cancer (Barthel et al., 2013).

Finally, they play a role, triggering cell signaling in the endothelial cells and in tumor cells, favoring the extravasation step (Stoletov et al., 2010; Reymond et al., 2012) and the breakage the basal lamina (Chen et al., 2016). For instance, their association with Angiopoietin 2 in the endothelial cell disrupt the vessel wall (Parikh et al., 2006). Or else, the association between α5 integrin and Neuropilin 2 in pancreatic cancer cells promote adhesion and extravasation (Cao et al., 2013).

Altogether, integrins are central in the tumor progression. They are sensitive to biological and physical cues and finely regulates tumor cells and tumor microenvironment.

Interestingly enough, several studies could directly link arrest and adhesion in the context of cancer cells. For instance, CD44 mediated contact between breast cancer cells and endothelial cells triggers the expression of $\alpha L\beta 2$ and $\alpha 4\beta 1$ integrins, strictly following the leukocyte model (Wang et al., 2005). Several other heterodimers were described as involved in CTC adhesion to the endothelium in various cancer contexts. Non-exhaustively, $\alpha 4\beta 1$ is expressed by cancer cells and binds to luminal VCAM at the surface of endothelial cells (Klemke et al., 2007) (again, similarly to leukocytes (Carman and Springer, 2004)). Or else, $\beta 4$ integrin (potentially with $\alpha 6$ subunit – (Abdel-Ghany et al., 2003)) is required for colon cancer cell adhesion in the liver vasculature (Laferrière et al., 2004). Alternatively, $\alpha 3\beta 1$ and $\alpha 6\beta 1$ are expressed *in vitro* by breast/mammary and melanoma cancer cell lines (MDA, 4T1, A375) to bind laminins (Wang et al., 2005; Chen et al., 2016). This suggest that tumor cells are able to contact the basal lamina under the endothelial cells, something that is not clearly understood so far. Last of this list, the $\alpha 5\beta 1$ binding fibronectin from the basal extracellular matrix (Huvaneers et al., 2008) or the apical side of the vessel (as Barbazan and colleagues described recently - (Barbazán et al., 2017)) (**Fig. 26**) was also described to allow stable adhesions of cancer cells. To note, this heterodimer is studied *in vivo* in the second part of the result chapter.

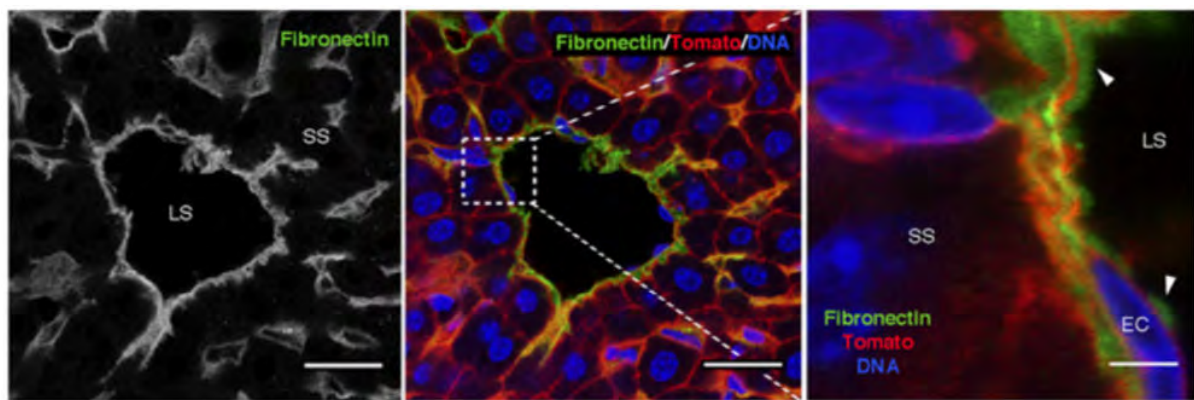


Fig. 26: Intraluminal fibronectin deposit (green). LS: Luminal side. SS: Stomal side. Extracted from Barbazán et al., 2017.

Finally, based on the leukocyte model, adhesion receptors signaling through ligand binding (such as integrins) activate signaling pathways that influence tumor and endothelial cells and might favor transmigration (Miles et al., 2007). This was

particularly well demonstrated in the case of $\beta 1$ integrin, whose inhibition decreases metastatic outgrowth, and activation increases it (Kato et al., 2012).

c) TUMOR CELLS EXTRAVASATION

Tumor cells extravasation is the migration of tumor cells from the lumen to the stroma, crossing the endothelial barrier.

i) FROM LEUKOCYTE MODEL TO TUMOR CELL EXTRAVASATION

In the case of leucocytes, transmigration was extensively studied (Fig. 27). Two paths of extravasation have been described: The paracellular (between endothelial cells) (Vestweber, 2012) and the transcellular transmigration (through the endothelial cell body) which is less described (Carman and Springer, 2004). In brief, downstream signaling of the binding of $\alpha L\beta 2$ and $\alpha 4\beta 1$ to ICAM and VCAM respectively, results in the activation of Rho-GTPases through ROCK (Rho effector kinase) (Sahai and Marshall, 2002). Then, Rho-GTPases trigger the disruption of endothelial cell adherent junctions (Dejana et al., 1999; Hordijk et al., 1999) and activate actin network reorganization (Thompson et al., 2002; Lyck et al., 2003).

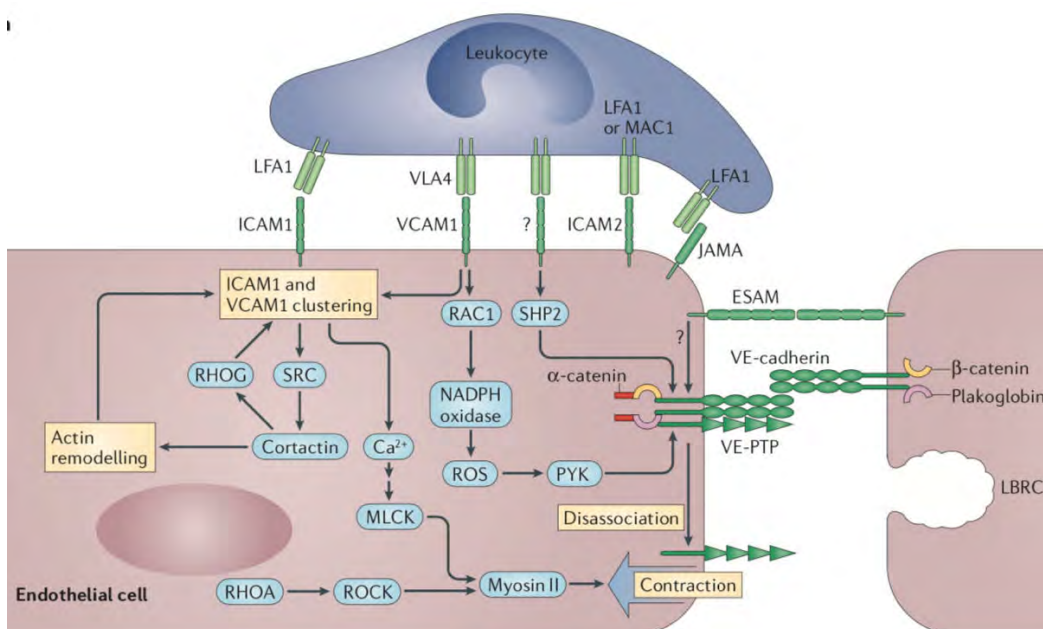


Fig. 27: Model of leukocyte diapedesis. Extracted from Vestweber, 2015.

In parallel, mechanical cues are also important in this step. Schaefer et al. have shown that rolling adhesions and stable adhesions between a leukocyte and endothelial cells pull on the endothelial cells (due to shear forces) and the mechano-transduction of the signal induces endothelial cell-stiffening that triggers the opening of cell junctions (Schaefer et al., 2014). The combination of all this, allows the transmigration of the leukocyte (Braga, 2002; Vestweber, 2015). To note, blocking of VE-Cadherin or PECAM at the cell-cell junction was shown to impair the diapedesis of leukocytes (Corada et al., 2001).

Following up on the idea that cancer cells phenocopy leucocytes, transmigration through diapedesis was observed *in vitro* using microfluidic models (Chen et al., 2013). Most of the work shows paracellular extravasation (Heyder et al., 2002; Reymond et al., 2012), with the central role of endothelial cell-cell junction disruptions (**Fig. 28**).

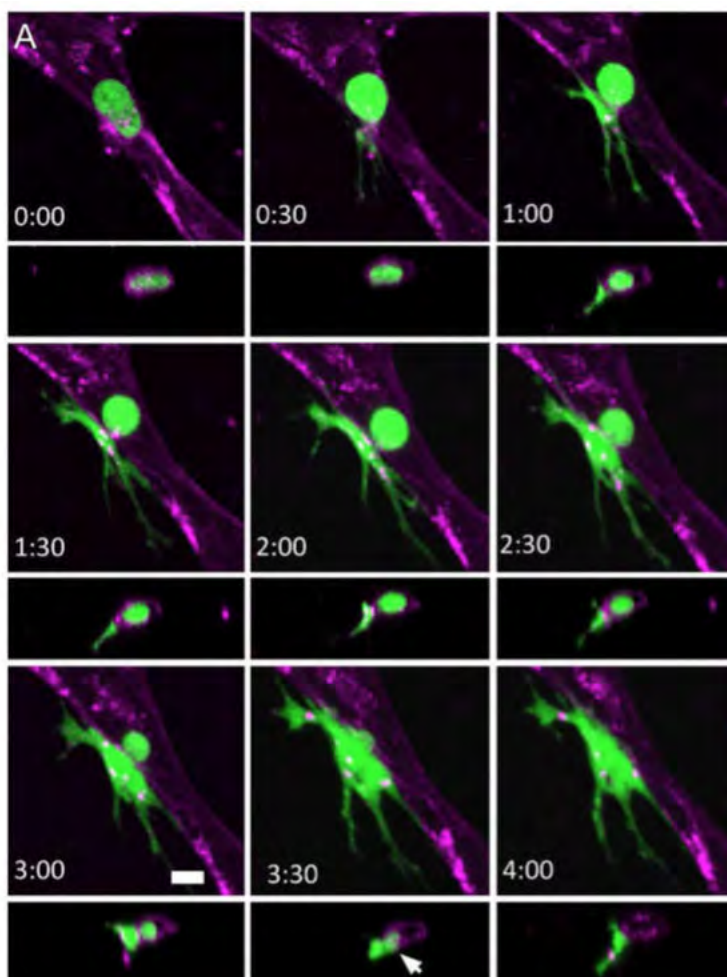


Fig. 28: Extravasation of tumor cells (green) through paracellular transmigration. Endothelial cells in purple. Extracted Chen et al., 2013.

Li et al. could show that Rho-GTPase are also involved in the transmigration of lung cancer cells through the blood brain barrier (Li et al., 2006) and Kusama et al. could show it with breast cancer cells (Kusama et al., 2006). Nevertheless, whereas leukocyte diapedesis is completed in 2h (Liao et al., 1995), cancer cell transmigration was observed in 3.5h for bladder carcinoma cells (Heyder et al., 2002) (, 5h for melanoma cells (Voura et al., 1998) *in vitro*. Strikingly, intravital imaging revealed that ovarian cancer cells needed 24h, melanoma cells 8h and colon cancer cells a few minutes to extravasate. Thus, there are various mechanisms that are at play in the context of CTCs.

Furthermore, tumor cells were shown to induce endothelial retraction (non-physiological rupture of the vessel wall) or even apoptosis or necrosis of endothelial cells (Kebers et al., 1998; Strilic et al., 2016) (Fig. 29). In some cases, this could be linked with the secretion of VEGF by the tumor cells (Senger et al., 1986; Fukumura and Jain, 2007) causing the remodeling of the actin cytoskeleton and, among others, triggering VE-cadherin/β-catenine complex to leave the junctions (Hoeben, 2004; Miles et al., 2007). Moreover, Padua and colleague could show that lung carcinoma cells are expressing angiopoietine-4 that induce the disruption of endothelial cell-cell junction and leakiness of the vessels (Padua et al., 2008).

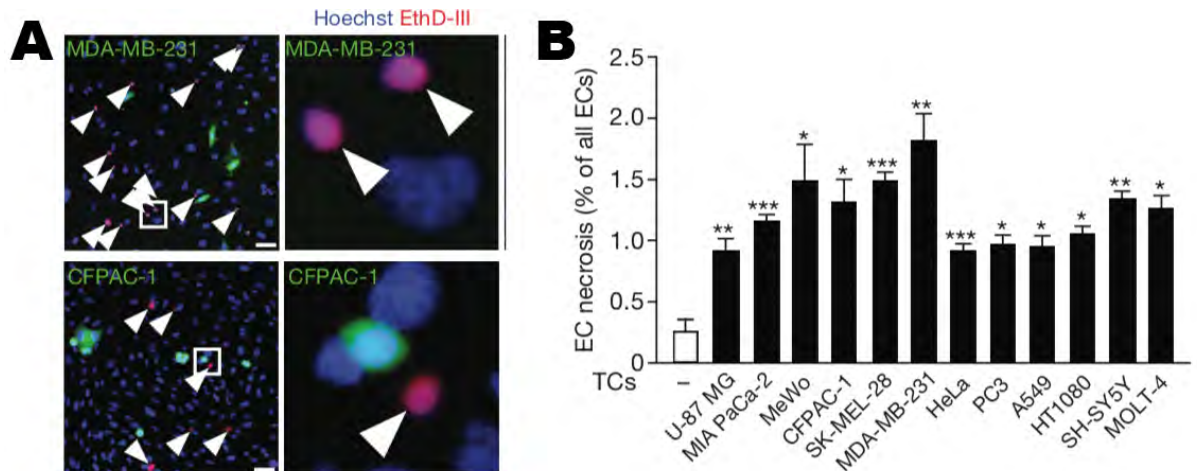


Fig. 29: Tumor cells induce the necrosis of endothelial cells to transmigrate. **A** – Representative image of dying endothelial cells (red label) with MDA-MB-231 breast cancer cells (top) and CFPAC-1 pancreatic cell (bottom). **B** – Quantification of the endothelial cell death using several cell lines of various origins. Extracted from Strilic et al., 2016.

Finally, when tumor cells cross the endothelial layer, they are confronted with the basal lamina of the vessel. The breaching of the last barrier before entering in the stroma and potentially seeding metastasis has been poorly studied. It presumably uses the same strategies that tumor cells use during intravasation, mainly enzymatic degradation of the basal lamina in a combination of proteinase and cell protrusions (Vlodavsky et al., 1982; Fidler, 2003). Leong et al. demonstrated that acto-myosin contractility allowing the formation of invasive protrusions is necessary for tumor cells transmigration (Leong et al., 2014; Williams et al., 2019) (Fig. 30). Even before crossing the endothelial cells, these protrusions go through the endothelial layer (using an uncharacterized mechanism) to start degrading the extravascular matrix thanks to transmembrane metalo-proteinases. To note, the breakage of basal lamina induces the release of stored growth factors such as FGF, VEGF and TGF- β , that would favor the establishment of the metastasis (Nakajima et al., 1988).

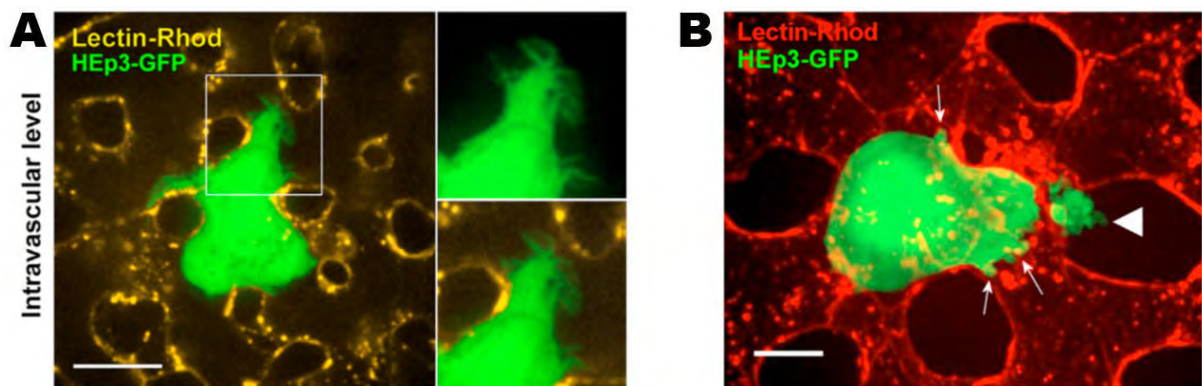


Fig 30: Invasive cell protrusion during cell extravasation. **A** – Arrested tumor cell (Green) sending intravascular filopodia-like structures. **B** – Tumor cells protrusions (small arrows) and apparition of one bigger protrusion crossing the endothelial wall and degrading the extravascular matrix (white arrow head). Extracted from Leong et al., 2014.

II) ENDOTHELIAL CELLS INVOLVEMENT IN THE EXTRAVASATION

Very few articles consider the active remodeling of endothelial cells to help the diapedesis of leukocytes. Only the local reorganization of the cytoskeleton allowing the formation of a “cup-shape” was described to favor the extravasation (Reglero-Real et al., 2012). In these articles, researchers showed that a4b1 bindings result in the local

rearrangement of cortical actin cytoskeleton that maximizes the contact between leukocyte and endothelial cells.

In addition, other cells recruit more drastic endothelial cells remodeling in which endothelial cells are partially detached from the basal lamina and migrate towards the lumen around the extravasating cell. Major works come from the extravasation of neutrophils and stem cells (like hematopoietic stem cells during development). To transmigrate, neutrophils induce endothelial “dome formation”: Endothelial cells enwrap the neutrophils before opening towards the stroma (Phillipson et al., 2008) (Fig. 31). Neutrophil bindings through integrin αL induce the association of the lymphocyte-specific protein 1 (LSP1 - an actin binding protein) to the actin cytoskeleton in the endothelial cells that trigger the remodeling (Petri et al., 2011). Interestingly, this mechanism maintains maximal vascular impermeability (reducing blood leakage), as the endothelial cells are keeping cell-cell contact during the process.

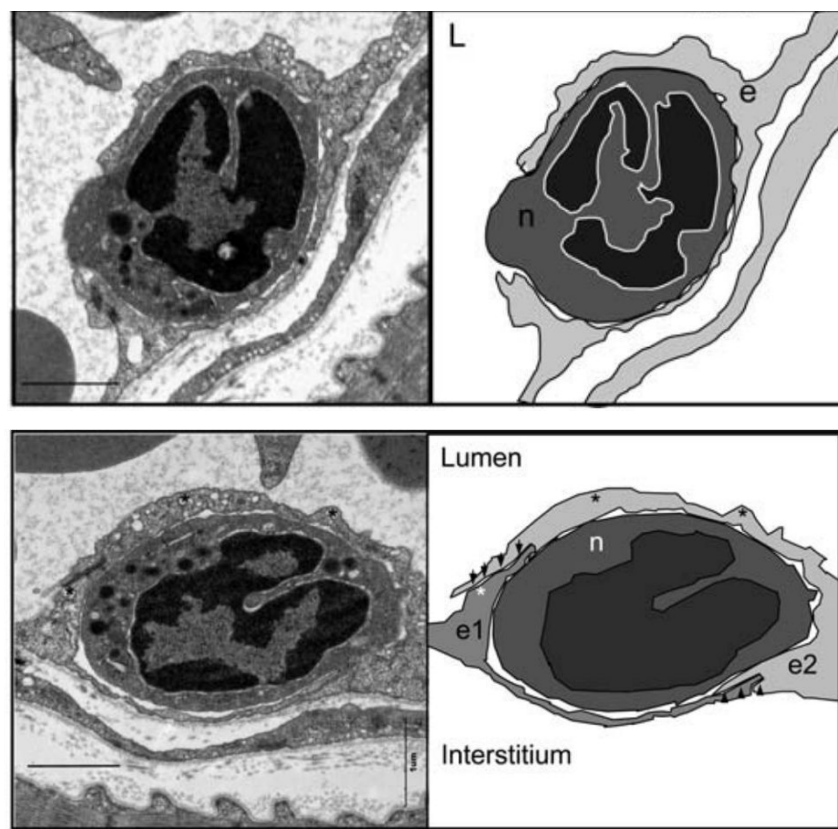


Fig. 31: Endothelial remodeling driving extravasation. Transmission electron microscopy images and schematics of endothelial dome formation around arrested neutrophil. L=Lumen, e=endothelial cell, n=neutrophil. Adapted from Phillipson et al., 2008.

The same kind of mechanism was observed in the context of stem cells homing in the zebrafish model (Allen et al., 2017) (Fig. 32). Allen et al. could show that integrin αL is involved in endothelial remodeling (that they called “angiopellosis”), but the downstream signaling cascade was not studied. Along the same line of evidence, cardiac stem cells injected intracardially in mice were tracked using intravital microscopy by Cheng et al. They described endothelial remodeling driving extravasation in this context (Cheng et al., 2012). In their study, they could show two important determinants of endothelial remodeling :1 Inhibition of integrin binding blocks the endothelial remodeling. 2. metalo-proteinases allow the detachment of the endothelial cells from the basal lamina.

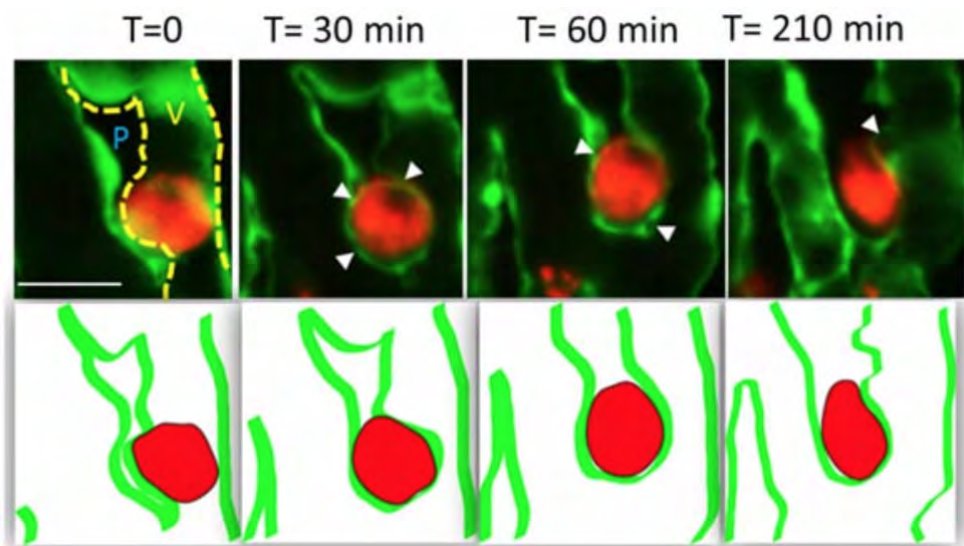


Fig. 32: Angiopellosis driving extravasation. Image sequence showing the angiopellosis mechanism, leading to the extravasation of cardiac stem cells (red) in the zebrafish embryo. Endothelial cell labelled in green. P= parenchymal tissue, V=vasculature lumen. Extracted from Allen et al., 2017.

Otherwise, endothelial remodeling was also described as a physiological response of the endothelium to maintain blood perfusion and thus the homeostasis of blood vascular system. Indeed, it is occurring around fibrin clots and platelet aggregates that may accumulate in the lumen (Lam et al., 2010; Grutzendler et al., 2014). Endothelial cells are able to engulf these wastes to keep the vessels well perfused, in a

phenomenon called “angiophagy” (Fig. 33). However, the signaling pathway that trigger vascular remodeling in this context remains to be determined.

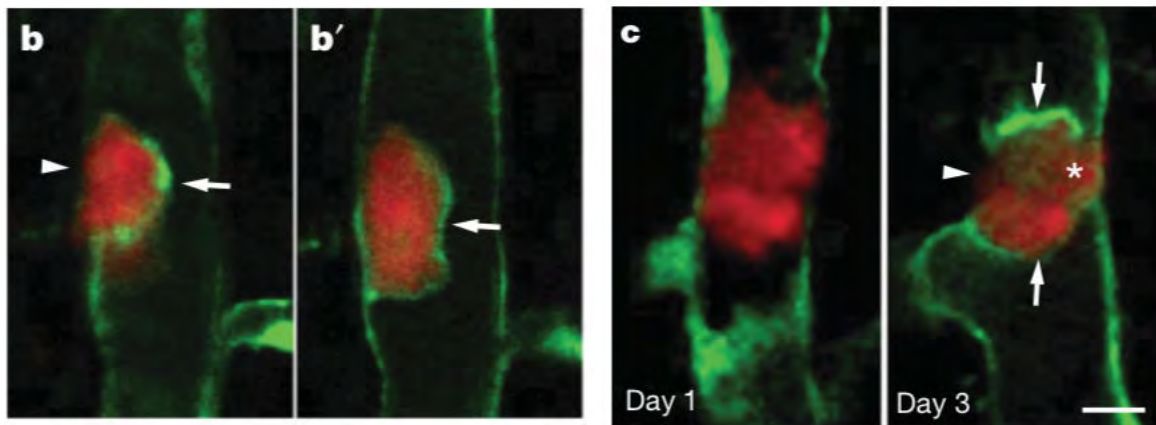


Fig. 33: Angiophagy leading to extravasation. Representative images of fibrin clot (red) eliminated from the lumen through the process called angiophagy in the mouse brain. Endothelial cells labelled in green. Extracted from Lam et al., 2010.

Finally, endothelial remodeling has been described as occurring around arrested tumor cells. This was shown using electron microscopy by Lapis et al in the 80s (Lapis et al., 1988) (Fig. 34A). They linked this process to intussusception, a process described in developmental biology in which endothelial cells divide their lumen into two (from 1 vessel to 2 parallel vessels) (Makanya et al., 2009). Later, Paku and colleagues published a study on “endothelialization”, using Lewis lung carcinoma cells (Fig. 34B). Using electron microscopy from 1h post injection of tumor cells to 48h (6 time points), they quantified the extravasation in lung, kidney, liver, adrenals and brains. Interestingly, the same cells show very different extravasation capacity in the different organs, but also different extravasation mechanism. Indeed, while endothelial remodeling is the major process in lung and liver, only partial endothelial remodeling and endothelial retraction were observed in the adrenals, and very few extravasations in the brain. To note, according to their data, “endothelialisation” requires 6 to 11 hours to be completed (Paku et al., 2000).

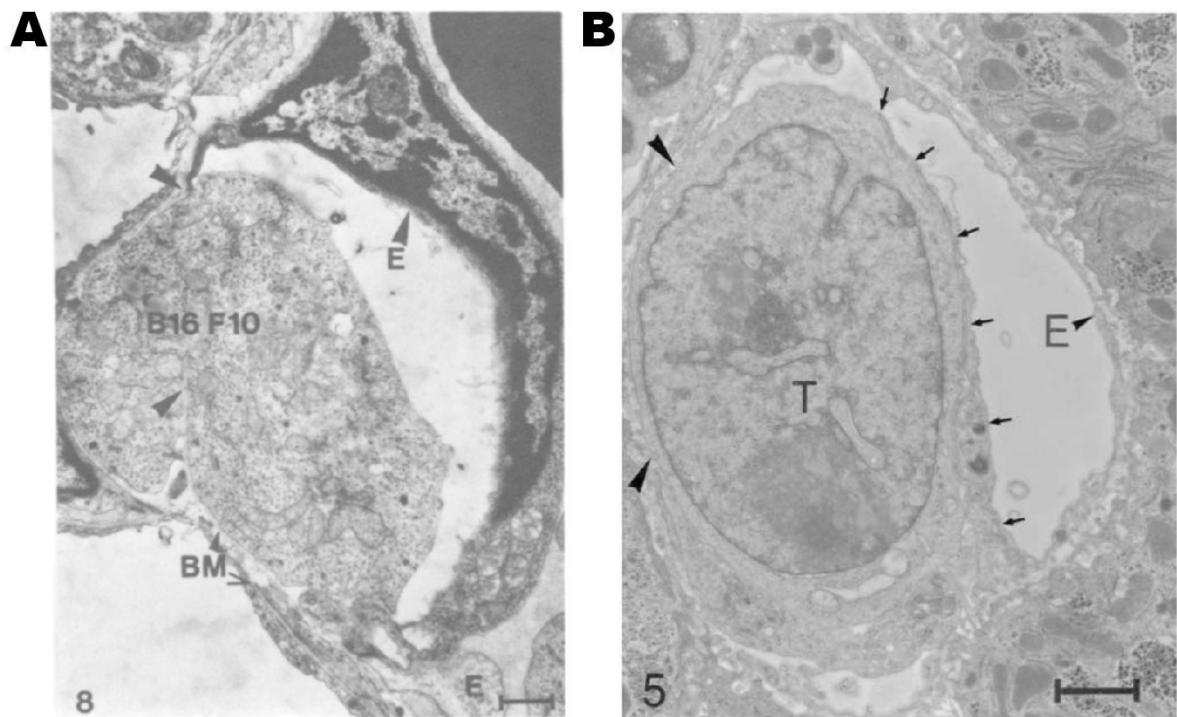


Fig. 34: Endothelialisation of arrested tumor cells. A – Melanoma cells during the process of endothelialisation leading to extravasation. Extracted from Lapis et al., 1988. B – Lewis lung carcinoma cells in the process of endothelialisation. Arrows indicate a layer of endothelial cell that fully enwrap the tumor cell. Extracted from Paku et al., 2000.

All in all, in the case of cancer cells, the factors and the signaling pathways are not described. It is not clear yet if tumor cells are hijacking a physiologic cleaning mechanism (angiophagy) or activating adhesion receptors signaling pathway like stem cell (angiopellosis). Moreover, as shown by Strilic et al., the nature of the relation between tumor and endothelial cells is not clear as tumor cells can locally induce the death of endothelial cells to favor their extravasation (Strilic et al., 2016). Moreover, the extravasation step is non-mandatory for cancer progression. Indeed, Al-Mehdi et al described intravascular metastatic outgrowth (Al-Mehdi et al., 2000), in which no extravasation is taking place before the metastatic seeding. This gives rise to massive intravascular emboli (described decades ago (Kinjo, 1978; Kawaguchi and Nakamura, 1986)) that can progressively merge with the organs.

In conclusion, little is known about endothelial remodeling around arrested tumor cells. The dissection of this mechanism over time requires relevant *in vivo* models, as discussed in the following part.

TECHNICAL APPROACHES

**TO STUDY CTCS ARREST AND EXTRAVASATION AT
HIGH RESOLUTION**

Putting human cells into culture dish to study human diseases is problematic for several reasons. First because, cells loose parts of their characteristics *in vitro* (Duval et al., 2017). Second, even the best set up fails to totally reconstitute *in vivo* environment (for instance, non-physiologic perfusion in the context of extravasation study in microfluidic (Chen et al., 2013)). Both means that cells are experiencing uncontrolled stresses besides the chosen experiment. Thus, it is necessary to use animal models to study cell behavior *in vivo*. Several animal models have shown interesting characteristic in cancer research, even if mouse is the gold standard (please also see **box 3: animal model in cancer research**). In this chapter, I will describe the advantage of zebrafish as a cancer model, especially to study the last steps of the metastatic cascade.

USE OF ZEBRAFISH EMBRYOS

Zebrafish (*Danio rerio*) is a 4-5 cm vertebrate from the Cyprinidae (Freshwater fish) super-family. It is native from calm rivers of South Asia, where it lives in small shoals. In captivity/laboratory, it is easy to maintain, only needing clean and oxygenized water, fish food and daylight cycles. It can live up to 3 years (Parichy, 2015).

Today, zebrafish is a well-established animal model in research fields such as neurology, developmental biology and cancer. It has many advantages: Small size, high fecundity (approximatively 2 years of laying – between 50 to 300 eggs per cross), transparency, rapid and external embryonic development, many shared organs with humans... Thus, it is fit to reverse and forward genetic, genetic screening, chemical screening and phenotypic analysis (Berghmans et al., 2005a). To note, the CRISPR/Cas9 system is well implemented for knock-in, knock-out and point mutation insertion, and common experimental protocols are established (molecular biology, staining, cell transplantations...). Besides, various advanced light imaging approaches (as we discussed in a review during my PhD – (Follain et al., 2016) – please see [annex 1: Seeing is believing – multi-scale spatio-temporal imaging towards *in vivo* cell biology](#)) can be applied to this model at embryonic, juvenile and adult stages. Indeed, many tissue/cell specific promoters were used to produce fluorescent transgenic zebrafish lines. The one I used the is *Tg(Fl1a:eGFP)* from an AB background (one of the wildtype strand) : eGFP highly expressed in endothelial cells and few hematopoietic stem cells (Lawson and Weinstein, 2002). Moreover, some fluorescent

Box 3: Animal models in cancer research

Mouse models are the gold standard for cancer research. Compared to other mammalian models it is smaller, inexpensive to maintain, has a large offspring and is technically perfectly established (protocols, facilities, genetic approaches...) (Cheon and Orsulic, 2011). A plethora of transgenic lines have been developed to mimic human cancer disease, either spontaneous, inducible or coupled with tumor cells injections to recapitulate nearly all the steps and types of cancer. Nowadays, cell-specific and time-specific mutation can be achieved using homologous recombination and inducible CRE-Lox systems (Metzger and Chambon, 2001) to reconstitute a specific aspect of the metastatic cascade. Moreover, recent technical development of intravital imaging using optical windows (Dondossola et al., 2018; Entenberg et al., 2018; Warren et al., 2018) allows us to observe cancer cells in a relevant context. Alternative animal models were developed to tackle mouse limitations: Cost, low throughput, inaccurate recapitulation of human cancer, questionable ethic...

First, *Gallus gallus*, and more specifically the chicken eggs are well known in the cancer field for the Chorio-Allantoic Membrane (CAM) assay (van Marion et al., 2016). Opening the egg shell after two days post-fertilization, it is possible to use the growing vascular system to recapitulate tumor angiogenic growth and tumor progression (circulation, intravasation and extravasation) (Ribatti, 2014). It has the advantages to be highly cost effective, very simple, naturally immunodeficient (Deryugina and Kiosses, 2017) and accessible for manipulation and high-resolution microscopy (Anca Maria et al., 2011). For instance, Leong et al used it to characterize invadopodia (degradative cancer cell protrusion) formation during extravasation (Leong et al., 2014). Major drawbacks of this experiment are that tools adapted to chick biology are still lacking (genetic tools and specific antibodies for instance) and experiments cannot last more than ~10 days due to the development of the chick (from the ovocyte to the chick in 21 days only), which impairs the long term observation of metastatic outgrowth (Anca Maria et al., 2011).

Second, based on the fact that cancer is at first, a genetic disease, *Drosophila melanogaster* can be a very good model. Indeed, most of the cell signaling pathway have been extensively studied in this model (Hippo, HedgeHog, Wnt, Notch, ... - (Perrimon et al., 2016)) and generation of mutants is straightforward (Li et al., 2014). Thus, Drosophila is a good model to study specific gene roles and test pharmacologic substance (Sonoshita and Cagan, 2017). Moreover, drosophila is widely used for its compatibility with high resolution imaging (Chen et al., 2014; Lye et al., 2015; Stegmaier et al., 2016). Few examples could show the potential of drosophila in cancer research at the cellular level. For instance, on tumor initiation, studying the ability of single mutation to transform normal to neoplastic tissue (Janic et al., 2010; Miles et al., 2011). Or else, on the metastatic development, grafting cancer cells in an adult animal that form lethal metastasis within 12 days (Beaucher et al., 2007). Nevertheless, Drosophila has a very different immune system compared to mammals and lacks many anatomical structures, especially it has no closed blood circulation systems, so it can't be used to study the metastatic dissemination through the vasculature (FlyBase).

Third, *Ceanorhabditis elegans* (small nematode used mainly in developmental biology) has shown some interesting features for the cancer field (Stuelten et al., 2018). As for drosophila, several key steps of cancer progression can be modeled in this animal, even if in this case, they are only indirect (only the germline cells could show over proliferation). For instance, the "anchor cell" of *C. elegans* will break through its basal lamina to migrate out of its position between uterus and vulva during development (Sherwood and Sternberg, 2003). This time- and space-controlled event is a good model for basal lamina breakage that occurs at least two times during cancer progression (intravasation and extravasation) (Rowe and Weiss, 2008). More generally, thanks to its very large offspring, short development time, ease to maintain, established cell lineage, (...) this model is perfectly suited for large genetic screenings and drug testing (Wu et al., 2016). Despite this, *C. elegans* lacks genetic/regulator complexity and anatomical structures (WormBase) that limits its relevance to the cancer field. Finally, *Danio rerio* is now well established in the cancer field (White et al., 2013). It has many advantages compared to mouse models (cost, fertility, imaging accessibility, ...) and compared to invertebrate models (anatomic plan and genetic proximity to human, longer lifespan, ...). It allows high throughput experimentations of genetic screen, drug testing, tumor growth and tumor spreading imaging at high resolution (Heilmann et al., 2015) in a relevant *in vivo* context (Amatruda et al., 2002) to model nearly all the steps of human cancers : tumor cell invasion (Lee et al., 2005), angiogenesis (Haldi et al., 2006), intravasation (Stoletov et al., 2007), extravasation (Stoletov et al., 2010)...

transgenic lines were crossed with pigmentation mutants to produce fluorescent and transparent adult fish zebrafish known as the Casper line (White et al., 2008). They allow high resolution and time lapse imaging, offering unprecedent access to biological processes *in vivo*.

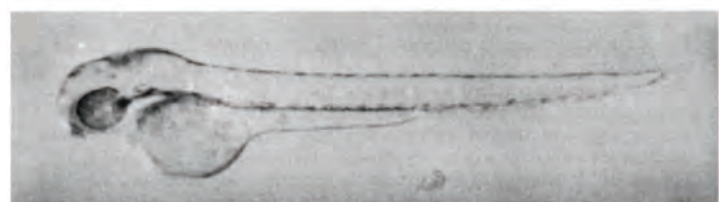
HISTORICAL DIGRESSION

Historically, the first publications on Zebrafish came from Hisaoka et al. in the 50s, working on toxicity test (Hisaoka and Hopper, 1957; Hisaoka, 1958). In the 60s, Weis et al. published the first developmental studies, on the neural tube formation (Weis, 1958). Then, in 1981, Streisinger (which is considered as the father of zebrafish in labs) published on the establishment of the first homozygous zebrafish line from wild-type background (called AB), the *Golden* line (Streisinger et al., 1981) (Fig. 35A). His seminal works showed to the scientific community that large mutagenesis screens could be achieved on this vertebrate model to create various mutant and transgenic lines.

Several researchers started to use this model in neurology (Kimmel et al., 1981; Sajovic and Levinthal, 1982), which is still a major application field, and in developmental biology. Major publications in the 80s come from Levinthal, Law, Kimmel and Warga who established the cell lineage and fate maps of the Zebrafish (Kimmel and Law, 1985a, 1985b, 1985c; Kimmel and Warga, 1986, 1987, 1988) (Fig. 35B). These observations were coupled with chemical screening approaches that gave rise to many research articles on cell migration and collective cell migration during development (Walker and Streisinger; Mullins).

The next step was achieved by C. Nüsslein-Volhard, who applied genetic screening to this model in 1993 (Granato and Nüsslein-Volhard, 1996; Nüsslein-Volhard, 1994). Her Seminal works were published in 1996 in a special issue (Haffter et al., 1996; Kane et al., 1996a, 1996b): In these articles, they described the role of key genes in the different steps of the early development of Zebrafish embryos (Fig. 35C).

In the meantime, D. Stainier started working on the cardio-vascular system of Zebrafish embryos (Stainier et al., 1996; Lee et al. 1997). His following results on the development and regenerative capacity of cardiomyocytes opened a wide research field and participated to the spreading of the zebrafish embryo.

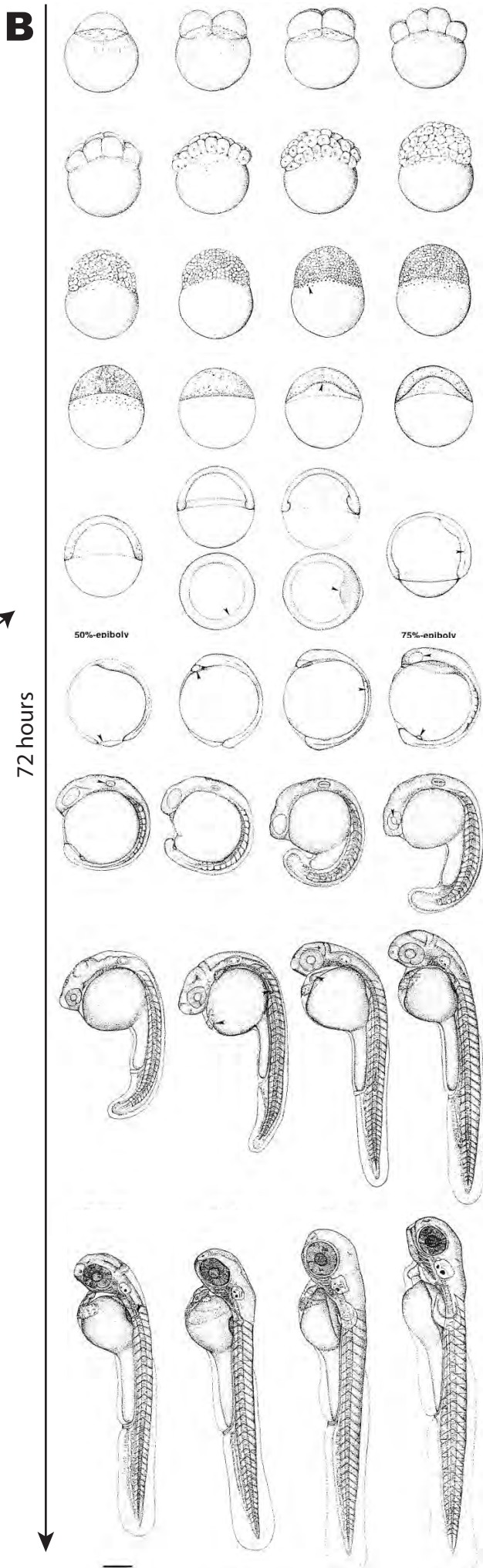


a zebrafish as it is found in the wild

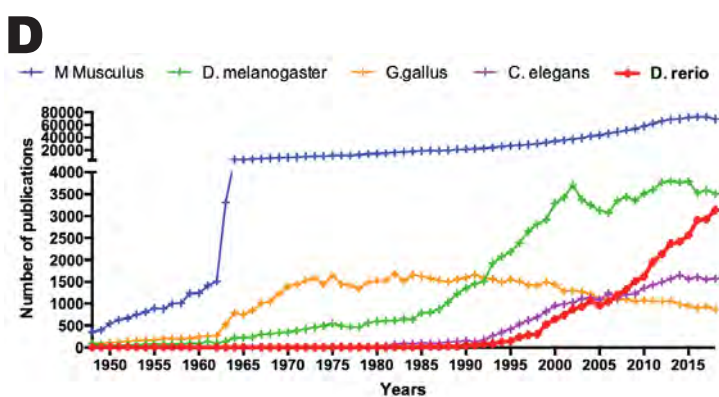
a zebrafish with the "golden" mutation

A - Pictures comparing the zebrafish wildtype (AB) (top) and the Golden line (bottom). Panel extracted from Streisinger et al., 1981. Same zebrafish at the adult stages (<https://evolution.berkeley.edu>).

B - Zebrafish major early developmental stages drawn by Kimmel and colleagues in 1995. Adapted from Kimmel et al., 1995.



C - Pictures of gastrulation mutant (ava) characterized by the team of C. Nusslein-Volhard during their genetic screen in the 90s. Extracted from Kane et al., 1996.



D - Comparison of the number of publications per years between the major animal models. Bibliometric analysis (Pubmed).

Fig. 35: Tech. Approach – Zebrafish historical digression

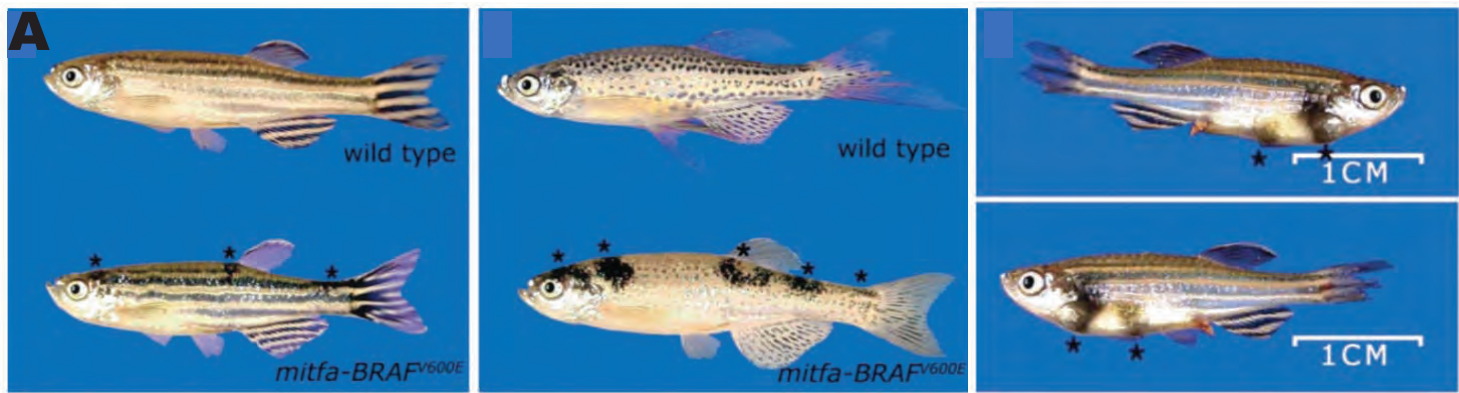
In 1999, ZFIN platform was created (Westerfield et al., 1999). It's the equivalent of the Wormbase for *C. elegans*, or Flybase for *Drosophila*, centralizing all Zebrafish knowledge on housing, crossing, lines, publications... This definitely imposed the zebrafish as a major model in developmental biology, neuroscience, cell biology and clinical science (Fig. 35D). Finally, Sanger institute started sequencing zebrafish genome in 2000 (as one of the first) and gave first results on coding sequence in 2001. To note, the complete sequence was published in 2013, demonstrating that 70% of human genes (and 82% of human genes involved in genetic disease) have at least one ortholog in zebrafish (Howe et al., 2013).

ZEBRAFISH AS A CANCER MODEL

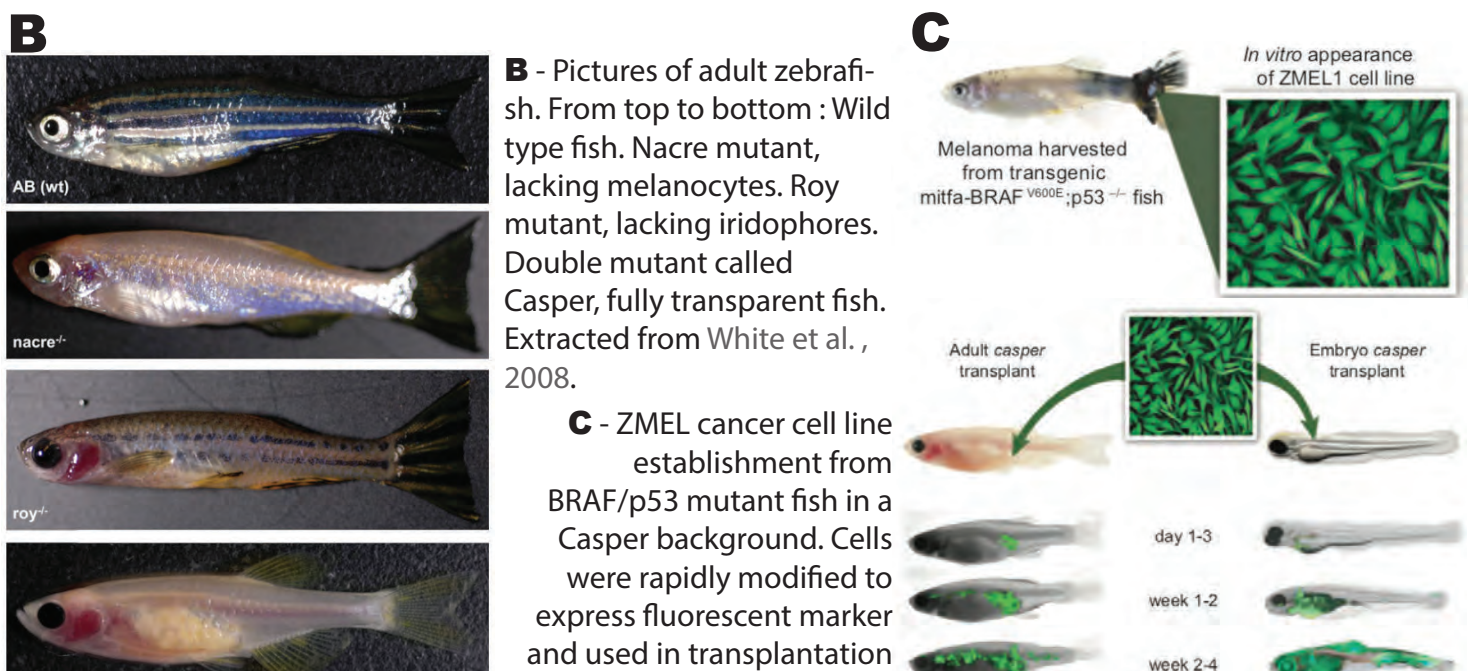
Very early on, Diethyl-nitrosamine (inducer of random mutations) was used on zebrafish (Stanton, 1965). In this study, the treated zebrafish rapidly developed lethal neoplasia in the liver. Then, other screens with other molecules could show that fish can develop skin, gastrointestinal, ovarian, pancreatic, (...) tumors (Spitsbergen et al., 2000; Moore et al., 2006). Interestingly, at the histological level, these tumors resemble human ones (Amatruda et al., 2002). Even more striking, gene enrichment analysis comparing human tumors to zebrafish tumors show strong conservation signature (Lam et al., 2006). For instance, gene signature for human liver cancer shows stronger correlation with zebrafish liver cancer than non-liver human cancer.

In parallel, screening using N-ethyl-N-nitrosourea (inducer of random point mutations) performed in the context of developmental biology (Grunwald and Streisinger, 1992) also ends up in the creation of many spontaneous cancer lines, especially when tumor suppressors are mutated: PTEN (Choorapoikayil et al., 2012), APC (Haramis et al., 2006), BRCA2 (Shive et al., 2010) or P53 (Berghmans et al., 2005b). In this last exemple, studying P53 point mutation in the zebrafish, T. Look and L. Zon showed that the same orthologous mutation was key in the development of the tumor. Namely, in the DNA binding site of P53, the loss of a lysine was blocking the association (Berghmans et al., 2005b).

In brief, in the early 2000s, the first zebrafish models for specific types of cancers were created: a melanoma model based on the major mutation found in human melanoma, $BRAF^{V600E}$ (Patton et al., 2005) (related to the work of Berghmans of p53) (Fig. 36A).

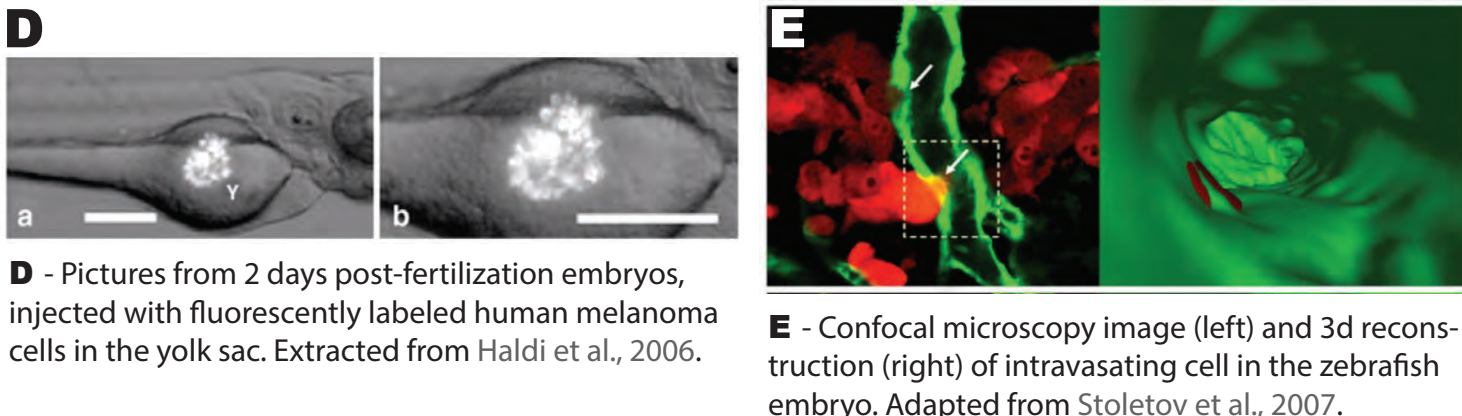


A - Pictures of adult zebrafish. On the left, comparison of *Danio rerio* vs BRAF mutant (nevi formation). In the middle, comparison of *Danio leopardo* vs BRAF mutant (nevi formation). On the right, pictures from the double mutant : BRAF and p53 (malignant tumor formation). Adapted from Patton et al., 2005.



B - Pictures of adult zebrafish. From top to bottom : Wild type fish. Nacre mutant, lacking melanocytes. Roy mutant, lacking iridophores. Double mutant called Casper, fully transparent fish. Extracted from White et al., 2008.

C - ZMEL cancer cell line establishment from BRAF/p53 mutant fish in a Casper background. Cells were rapidly modified to express fluorescent marker and used in transplantation experiments. Adapted from Heilmann et al., 2015.



D - Pictures from 2 days post-fertilization embryos, injected with fluorescently labeled human melanoma cells in the yolk sac. Extracted from Haldi et al., 2006.

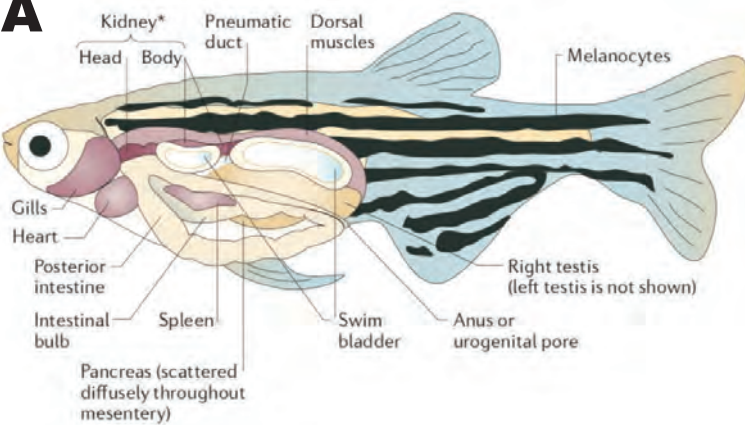
E - Confocal microscopy image (left) and 3D reconstruction (right) of intravasating cell in the zebrafish embryo. Adapted from Stoletov et al., 2007.

Fig. 36: Tech. Approach – Zebrafish as a cancer model

and a model to study leukemia (called T-ALL) (Langenau et al., 2003). To note, this melanoma model was developed exploiting the full potential of zebrafish for imaging, with the establishment of the *casper* fish line (adult transparent line – **Fig. 36B**) few years later (White et al., 2008). Recently, it allowed the isolation of the first solid tumor cell line, called ZMEL (Heilmann et al., 2015), quickly transfected to express fluorescent makers (**Fig 36C**). This paved the way to model fish cancer progression in a fish biological context. Otherwise, thanks to the ease of genetically engineered zebrafish, many other lines appeared: Neuroblastoma (Zhu et al., 2012), Pancreatic cancer (Liu and Leach, 2011), leukemia (Rudner et al., 2011), etc...

Gradually, many research groups started to use the Zebrafish in xenotransplantation experiments (Lee et al., 2005; Haldi et al., 2006; Nicoli et al., 2007; Konantz et al., 2012) (**Fig. 36D**). The major goal of such experimental approaches is to use the imaging power and screening capacity of zebrafish to study murine or human cancer cells *in vivo* (**Fig. 36E**). Classically, injections are made in the embryos (lacking adaptive immune system) in the yolk sac, in the dorsal part of the embryo, or in the duct of Cuvier to reach the circulation. Then, the major steps of the metastatic cascade can be observed: cell migration, invasion, intravasation, extravasation, colonization... Importantly, several groups have grown zebrafish at high temperature (above 28°C, their physiologic temperature) to allow the “normal” growth rate of the xenotransplanted mammalian cells. Recently, Langenau’s lab published a resource article about the possibility to grow immunodeficient zebrafish at 37°C to model cancer (Yan et al., 2019). This seminal article is bringing an equivalent of the NSG mouse model (immunodeficient gold-standard required to study human cancer cells in mice) to study cancer treatment impact at the single cell level. To note, such a fish line could be used in personalized cancer treatment: Following the implantation of human cancer cells from biopsies in fish, they could be treated with a panel of anti-cancer treatment. This would give treatment efficiency results in an *in vivo* context after only one month.

Strangely enough, despite numerous similarities and zebrafish advantages that were described during the last 20 years and the genetic proximity to human (**Fig. 37**) (Yen et al., 2014; Völkel et al., 2018), zebrafish is strongly questioned on its relevance to human diseases. Forgetting the obvious anatomical differences, the major argument comes from the fact that, already in the mouse model (phylogenetically closer to

A

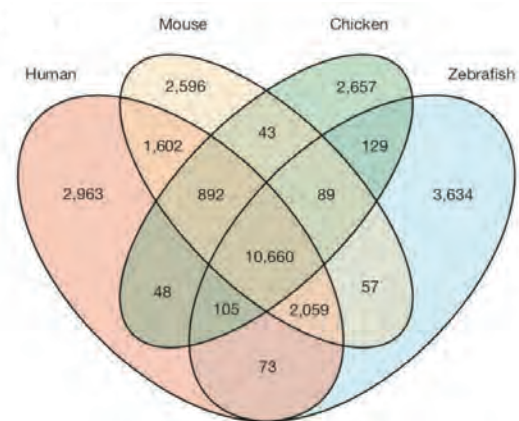
A - Schematic representation of zebrafish anatomy, showing the common traits and missing anatomical structure compared to human. Extracted from White et al., 2013.

B

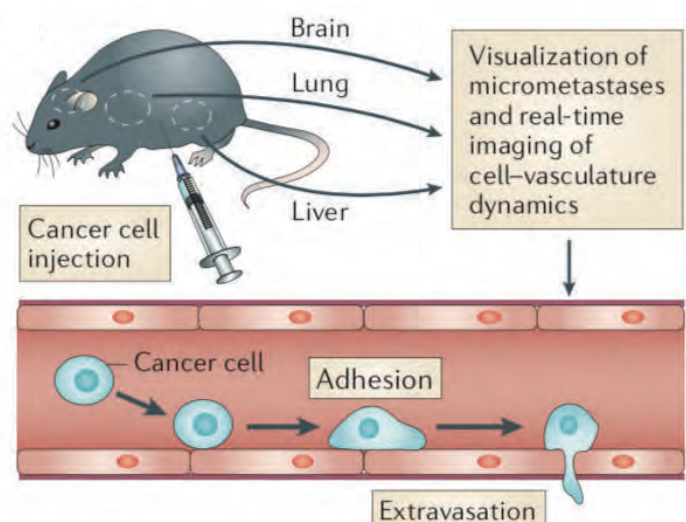
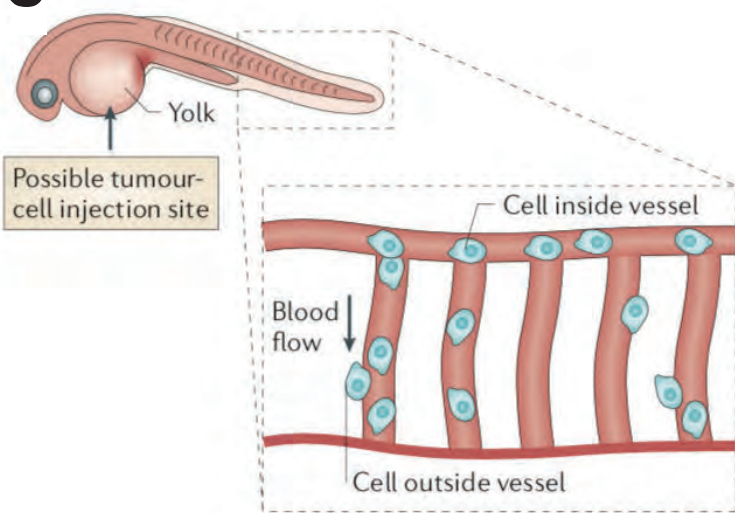
Table 2 | Comparison of human and zebrafish protein-coding genes and their orthology relationships

Relationship type	Human	Core relationship	Zebrafish	Ratio
One to one	-	9,528	-	-
One to many	3,105	-	7,078	1:2.28
Many to one	1,247	-	489	2.55:1
Many to many	743	233	934	1:1.26
Orthologous total	14,623	13,355	18,029	1:1.28
Unique	5,856	-	8,177	-
Coding-gene total	20,479	-	26,206	-

Data and orthology relationship definitions are based on Ensembl Compara version 67 (http://www.ensembl.org/info/docs/compara/homology_method.html).



B - Table comparing the protein-coding genes between human and zebrafish. On the left, the graphical representation of the common protein-coding genes between human, mouse, chicken and zebrafish. Adapted from Howe et al., 2013.

C

C - Schematic showing zebrafish embryo as a relevant alternative to the mouse model in studying cancer dissemination. Extracted from Reymond et al., 2013.

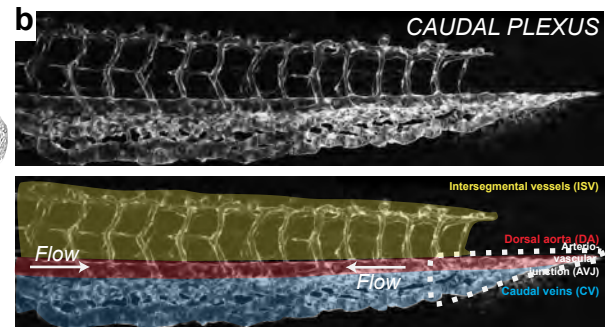
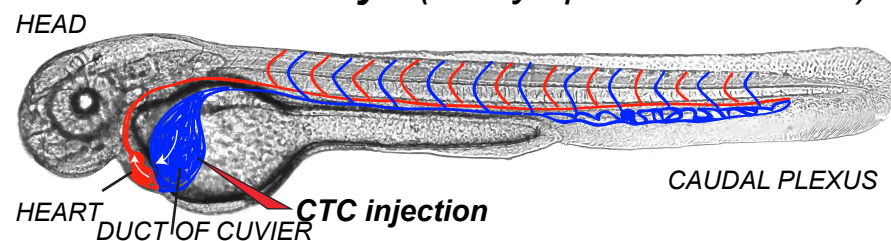
Fig. 37: Tech. Approach – Zebrafish relevance for cancer study

human), many findings failed to transfer to humans. These are pro and cons arguments, as massive differences between fish-mouse and fish-human can be observed at the genetic level (Howe et al., 2013). Nevertheless, efforts are made to “humanize” the models to make fish compatible with mammalian cells, as described above. All in all, both approaches (all-fish modeling like White et al. and 37°-Zebrafish xenotransplantation like Langenau et al.) sounds strongly relevant to study many aspects of the metastatic cascade *in vivo* at the subcellular resolution (Please see **Box 3: animal models in cancer research** for comparison between zebrafish and other animal models). An interesting approach is to confirm findings from fish experiments in mouse models (White et al., 2008) (**Fig. 37C**). This allows to test many hypotheses with experimental ease and statistical power, before using the complex and expensive mouse model (Reymond et al., 2013; Blackburn and Langenau, 2014).

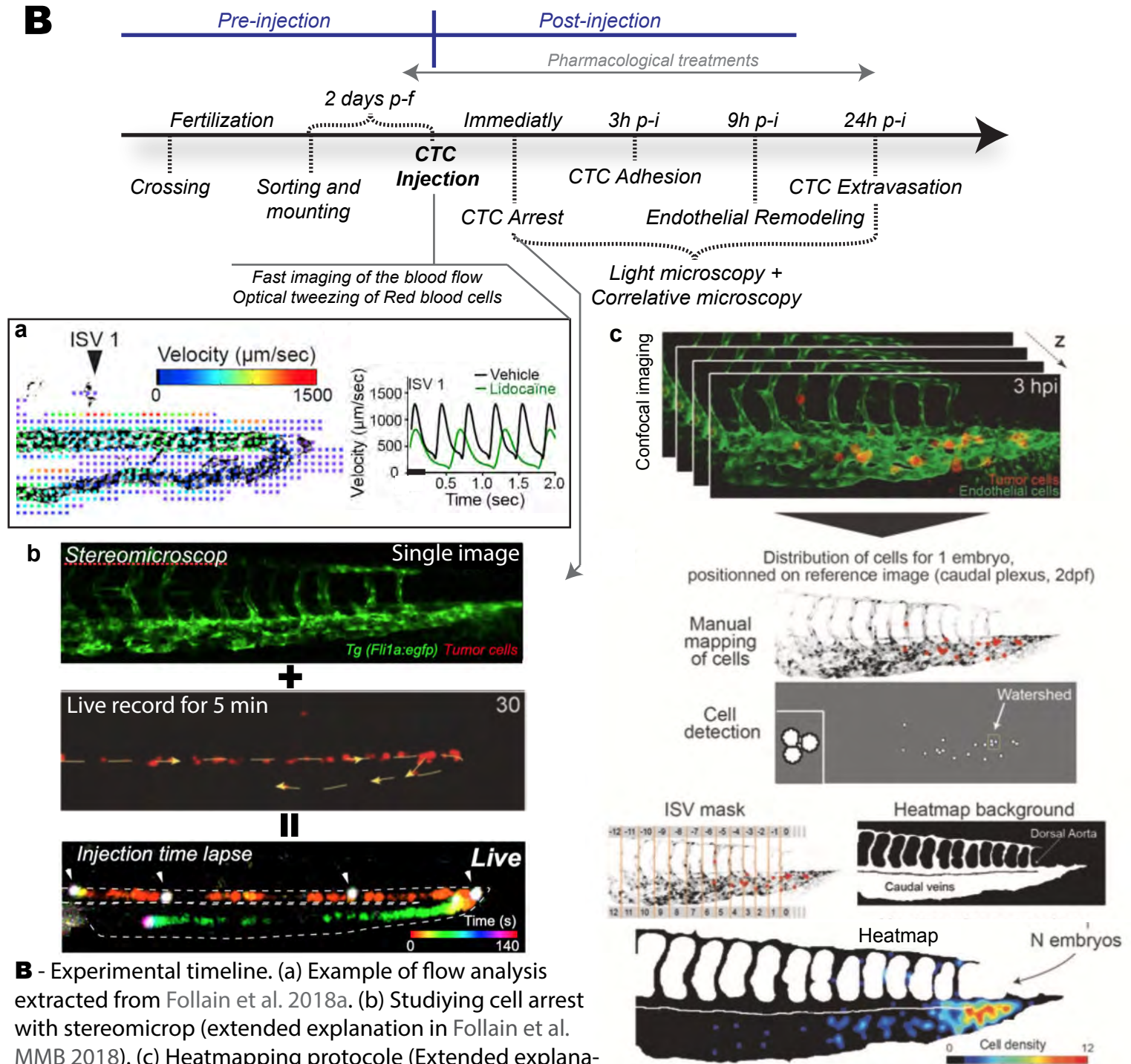
Moreover, the use of zebrafish and other alternative animal models to mice (Cagan et al., 2019) is in accordance with our times, when animal experimentation is increasingly questioned and regulated. Global principle of the 3R (replace, reduce, refine) mainly asks the researcher to replace mammalian models when it is possible, to reduce the number of animals per experience to the relevant minimum and to refine the experimental approach. Even if it is hard to defend with scientific arguments (lack of some pain-related neurons, reduced self-consciousness?..), zebrafish, especially at embryonic states, sounds like a relevant alternative. At least, the European and French political powers have built text laws in this direction (European directive 2010/63/EU ; Code rural France – REG-L2T1Ch4-Ch5).

ZEBRAFISH IN OUR EXPERIMENTS

Based on the numerous advantages of the zebrafish discussed above, we selected this model to work on the metastatic cascade during my PhD. We developed injection in the duct of Cuvier of zebrafish embryos at 2 days post-fertilization. This duct is directly connected to the heart, that pumps the cells to two arteries: The primitive internal carotid artery (PICA) going to the head and the dorsal aorta (DA) going to the tail. The vast majority of the tumor cells enter the dorsal aorta towards the caudal plexus. At the end of the tail, the dorsal aorta makes a U-turn opening to the caudal veins (CV). We call this turn “Arterio-Venous Junction” (AVJ). CV are highly ramified and composed of large and small vessels which are interconnected (**Fig. 38A**).

A**a Zebrafish embryo (2 days post-fertilization)**

A - Zebrafish embryo at 2 days post-fertilization. (a) Schematic of the blood circuit that tumor cells will follow after injection (Heart - DA - CP - CV - Heart). (b) Focus on the caudal plexus where most of the arrest occurs.

B

B - Experimental timeline. (a) Example of flow analysis extracted from Follain et al. 2018a. (b) Studying cell arrest with stereomicroscopy (extended explanation in Follain et al. MMB 2018). (c) Heatmapping protocol (Extended explanation in Follain et al. MMB 2018).

Fig. 38: Tech. Approach – Our approach using zebrafish embryos

One can see it as a capillary bed, with vessels having similar diameters as capillaries in human organs like lungs and liver (Williams et al., 1988; Isogai et al., 2001). Then, the venous capillaries gather in one single vessel, the posterior caudal vein, closing the circuit by ending in the duct of Cuvier. To sum up, this technique allows us to bypass the primary tumor growth, invasion and intravasation steps, to directly come to arrest, adhesion and extravasation of circulating tumor cells (**Fig. 38A**).

To statistically address arrest, adhesion and extravasation, we established post-injections time points ranging from directly during injection to 24 hours post injection (**Fig. 38B**). Otherwise, we could have performed time lapse imaging, but the throughput of such an approach would have been too low.

First, we developed the imaging from the injection time to 5 minutes post-injection using a stereo microscope. This allowed us to have access to the very first event of arrest in the caudal plexus. It was achieved using the camera of the stereo microscope, and the filter corresponding to cell fluorescence. For each embryo, we acquired a five minutes movie of the injection and took a picture of the vasculature of the plexus. Then, this single image was used as a background (giving a vascular architecture context to the movie) during analysis. From these movies, we could extract cell arrest number and location, cell circulation, time of arrest, stability and roughly the cell deformation (with the limit of the resolution of these wide-field images) (**Fig. 38Bb**).

Second, we used a time point at 3 hours post-injection to study the stable adhesion of tumor cells to the endothelium. Although we established that most of the arrest/circulation events are over after 5 minutes, few cells are circulating or arresting for more than one-hour post-injection. At three hours post-injection, the pattern of adhesion is definitive in most of the case. We observe no more flowing cells and we start observing extravasation behavior. Thus, we selected this time point to track stable adhesion of CTCs. We performed confocal imaging at this timepoint, and analyzed the data using heatmap and manual quantifications of number and location of cells (**Fig. 38Bc**). Heatmapping principle is to merge tumor cell dispersion in the caudal plexus of all embryos on a single image of the caudal plexus. This is possible thanks to the stereotyped vasculature of the caudal plexus. We acquired a representative image of the plexus at 2 days post-fertilization and used the Inter-Segmental Vessels (ISV) as landmarks to manually map the cells for each individual fish. Then, a MatLab

script allows the stacking from single maps to the heatmap where the color scale represents cell density per pixels (**Fig. 38Bc**).

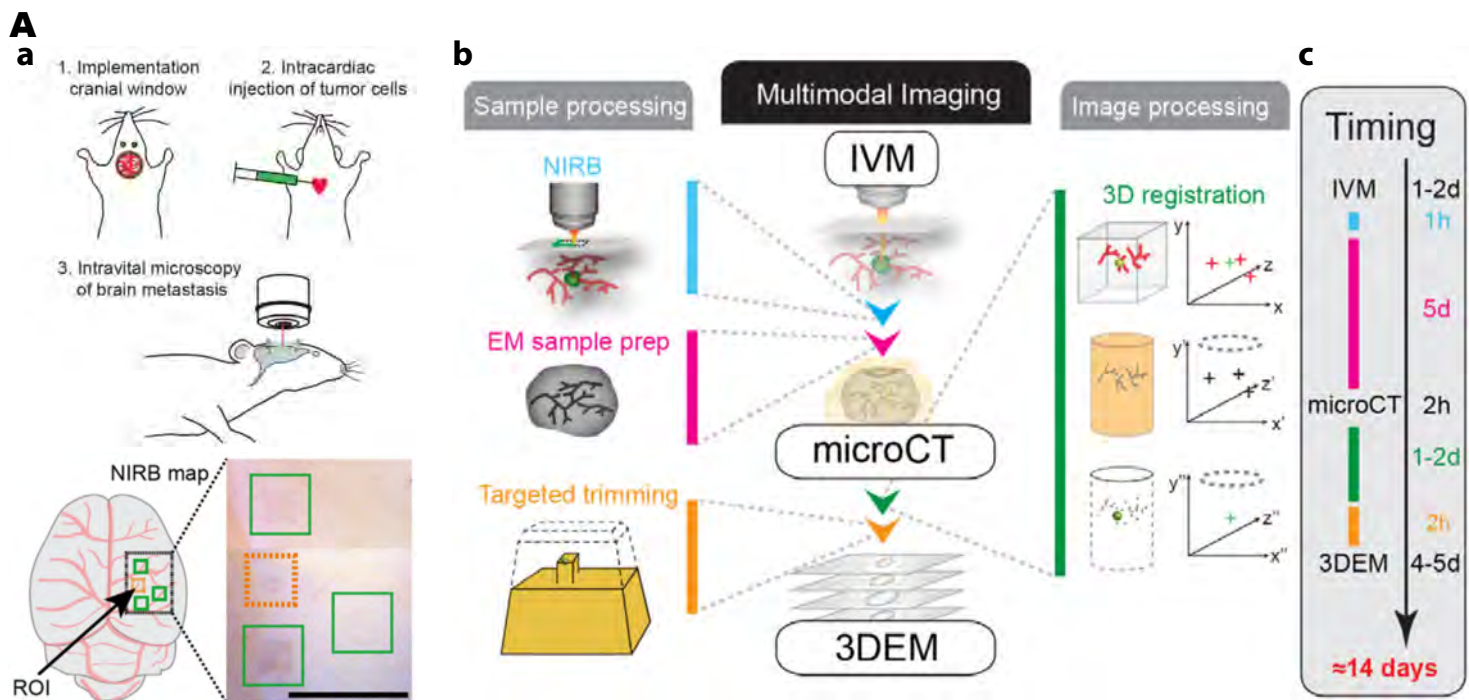
Third, we used a time point at 24 hours post-injection to quantify extravasation. This time point was selected based on D2A1 (murine mammary carcinoma) cell injection experiments. At 24 hpi, more than 95% of the cells are extravascular. Here also, we performed confocal imaging and analyzed the data using heatmapping and manual quantification of number, location and status (in or out of the vessels) (**Fig. 38Bc**).

We added an extra time point at 9 hpi, to better define the kinetic regulating the endothelial remodeling leading to extravasation of CTCs (Follain et al., 2018a). Here again, we used confocal imaging and manual image analysis.

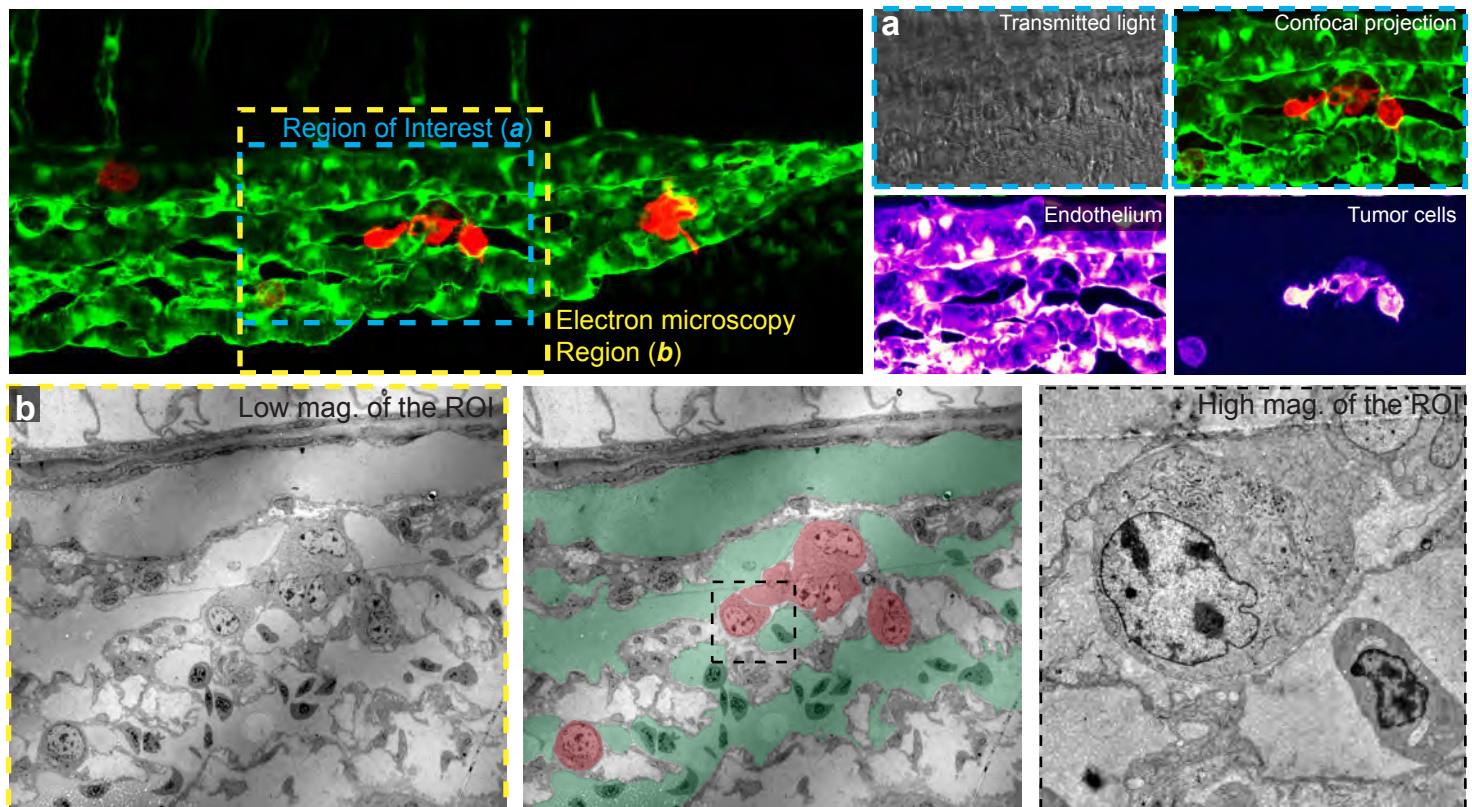
All these time points were also assessed using correlative light and electron microscopy (CLEM), as we aimed at illustrating all the phases at the best resolution *in vivo* (**Fig. 39**). CLEM allows the tracking of cellular and subcellular events combining the advantages of light and electron microscopy. Intravital light microscopy offers a large field of view over 3D region of interest, over time. Electron microscopy offers the best resolution (up to nanometric through electron tomography) over a small field of view at a given time. The combination of the two is mandatory to observe discrete events such as filopodia-like structure between endothelial and tumor cells in the circulation of the zebrafish embryos. First, by targeting the event of interest with light microscopy. Second by fixing the sample as quickly as possible. Third, processing the sample for electron microscopy. Fourth, using correlation tools to retrieve the region of interest. And fifth, imaging the region of interest with an electron microscope.

To perform CLEM, we have been applying already established methods that are reviewed in several collaborative publications (Karreman et al., 2014, 2016a, 2016b). We mainly used CLEM approach to dissect the arrest and extravasation of tumor cells in the zebrafish (**Fig. 39B**). In this case, the NIRB (laser branding technic allowing us to retrieve the ROI in mouse tissue) and the μ -cT imaging (X-ray imaging allowing us to dock the ROI in the electron microscopy resin block) were not necessary (**Fig. 39A**). All the correlations were performed using anatomical landmarks and cell shapes. Also, thanks to the relative flatness of the zebrafish caudal plexus, the in-depth correlation was straightforward (**Fig. 39B**).

To note, live imaging of 0 to 5 minutes post-injection presented above had never been published before. Thus, we were invited to publish this method by A. Gautreau (scientific coordinator for a special issue in *Methods in Molecular Biology*) at ASCB 2016. This book chapter was published in 2018 ((Follain et al., 2018b) – please see [**annex 2: Using zebrafish embryo to dissect the early steps of the metastasis cascade**](#)) and presents a more detailed version of our approaches with zebrafish embryos.



A - Schematic of the intravital correlative light and electron microscopy pipeline used in the mouse model. **(a)** Use of cranial window to observe intracardiac injected cells in the brain. **(b)** Brain dissection and NIRB branding to mark the region of interest in the brain. **(c)** Use of x-ray scan to retrieve the region of interest in depth after embedding in the resin block and serial sectioning of the region. **(d)** Typical duration of the experiment. Adapted from Karreman et al., 2016.



B - Representative image of a correlative light and electron microscopy experiment in the zebrafish embryos (unpublished data from results part). From the confocal stack **(a)** to the transmission electron microscopy image **(b)**. Correlation done using vessel architecture and recognition of mouse cancer cells.

Fig. 39: Tech. Approach – High resolution imaging

USE OF MICROFLUIDICS

Our approach using injection in zebrafish embryos also have drawbacks: 1. We do not fully control the parameters of the blood flow. 2. the architecture of the caudal plexus is quite complex, which makes it more difficult to separate the role of blood flow and physical constraints. 3. the injection induces a burst of circulating tumor cells that do not recapitulate progressive cancer cells dissemination. Thus, we developed a complementary approach using microfluidic channels. This chapter explains how microfluidics are applied to cancer and describes our approach.

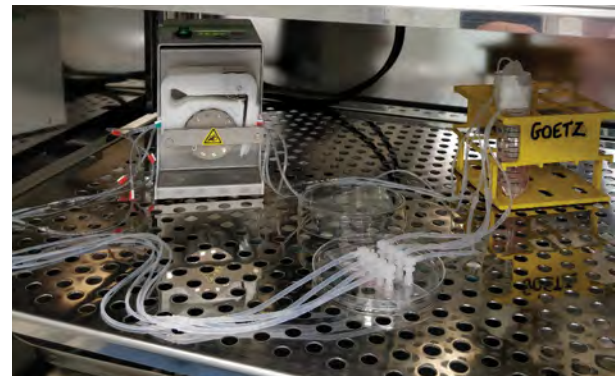
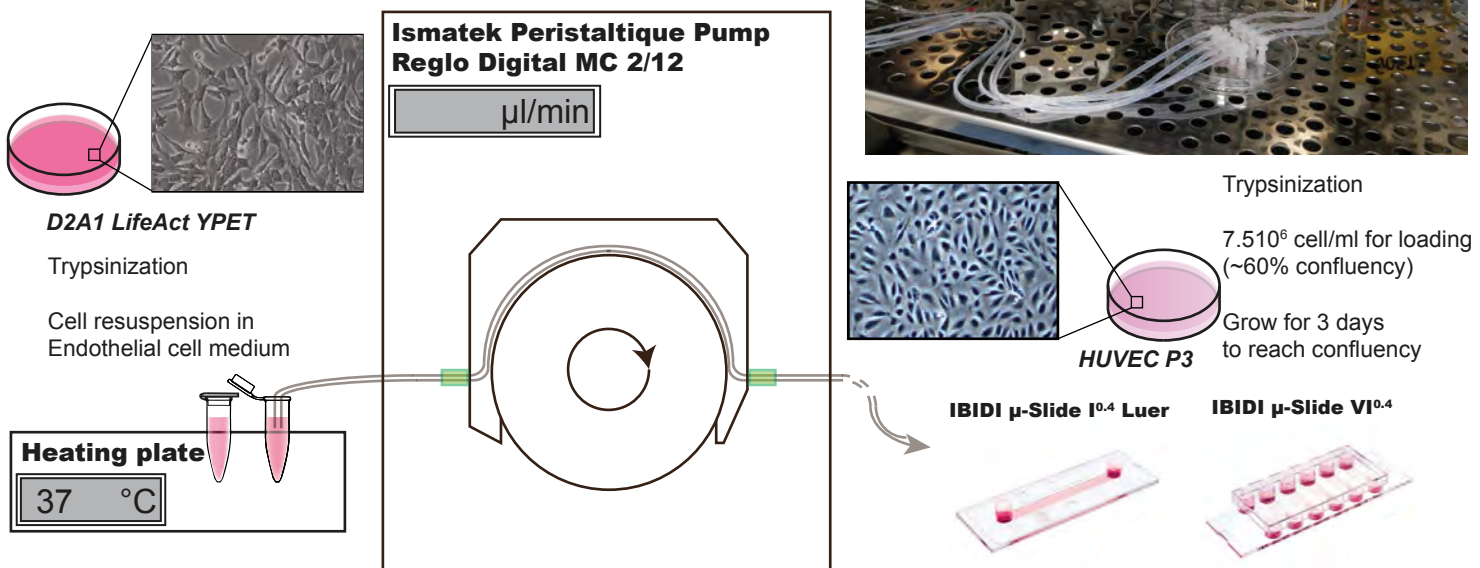
MICROFLUIDICS APPLIED TO BIOLOGY

Microfluidics applied to biology is a growing field that democratized 20 years ago. In general, microfluidic patterns are drawn by applying photolithography to a silica wafer. Then, polydimethylsiloxane (PDMS) and a cross linking agent are mixed and poured in the mold. When set, the PDMS chip and the glass microscope slide go through a plasma-cleaner before being sealed together. This microfluidic device can be perfused using small tubing. Such devices provide more functionalities than classic cell culture tools (Sontheimer-Phelps et al., 2019):

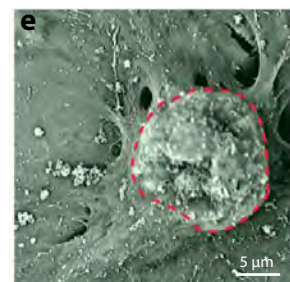
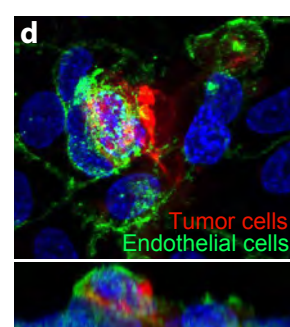
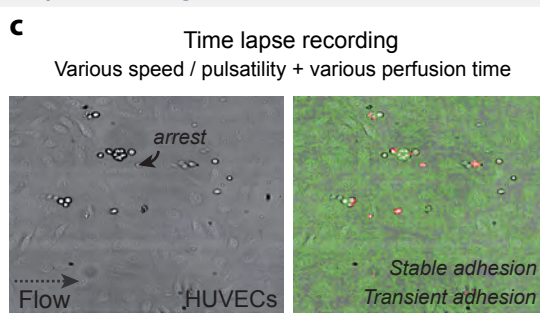
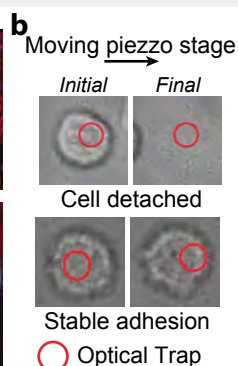
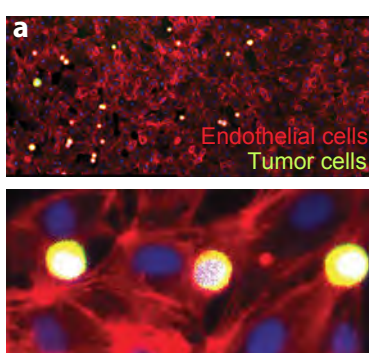
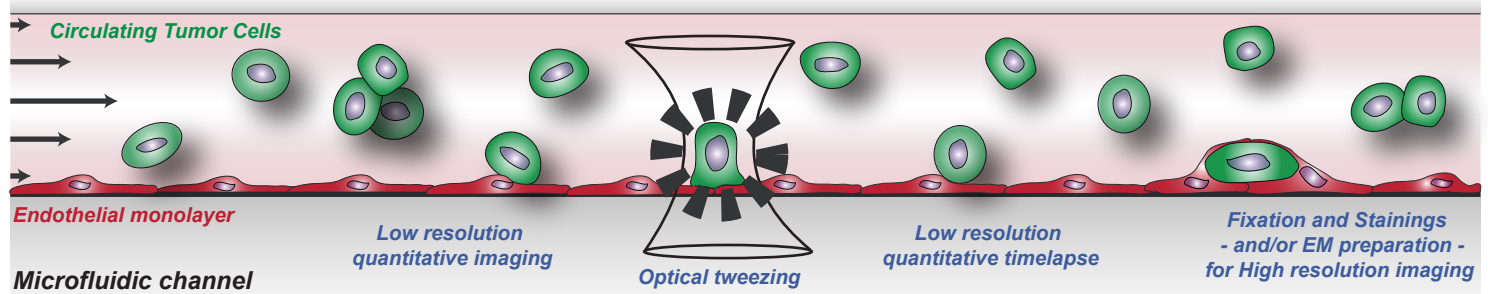
- 1- It allows single cell analysis at low cost (Paguirigan and Beebe, 2008), with a better control of the environment. In the case of soluble molecules, by perfusing a small amount of specific media, potentially in a gradient manner (Takayama et al., 2003), or in the case of protein coating with or without patterning (Shea et al., 2017).
- 2- It offers the possibility to draw any pattern of choice, that can mimic topographical and physiological situations that cells might encounter: channel bifurcation, channel narrowing (Raab et al., 2016), pores of different sizes (Irianto et al., 2016), etc....
- 3- It can also be used to recreate an environment closer to physiologic conditions, like a vessel surrounded by extracellular matrix (Bersini et al., 2014), or small organoids recapitulating physio- or pathologic cell growth (Choi et al., 2015).
- 4- It offers platforms for methodological improvements like the recent NanoJ-Fluidics for small perfusion with low loss in the context of stainings (Almada et al., 2019).
- 5- In the context of circulating tumor cells, it is used to isolate circulating tumor cells and circulating tumor clusters (Aceto et al., 2014; Hvichia et al., 2016).

A - Overview of our microfluidic set up. Top picture is showing the set up installed in the incubator (37°C/5%CO₂). We use tumor cells (harvest on the left) and the peristaltic pump (in the middle) to perfuse IBIDI channel pre-coated with HUVEC.

A



B



B - Schematic of the major applications of the set up and example pictures : **(a)** Fluorescent imaging post-perfusion and fixation (actin labeling (phalloidin-543) of the HUVEC, D2A1 life-actin YPET cells and DAPI). **(b)** Transmitted light microscopy of optical tweezing experiment. **(c)** Live recording of tumor cell arrest on HUVEC. **(d)** Immunofluorescent imaging of endothelial remodeling in vitro (PECAM labelling of HUVEC membrane, D2A1 life-act Td-Tomato cells and DAPI). **(e)** Scanning electron microscopy of endothelial remodeling in vitro.

Fig. 40: Tech. Approach – Microfluidics applications

6- Of interest for my project, it can also be perfused at different speeds, allowing various physiologic perfusions to study the direct effect of shear stress on flowing cells (Regmi et al., 2017, 2018) or adherent cells (Raghavan et al., 2014).

MICROFLUIDICS IN OUR PROJECT

During my PhD, we needed to have a system to test the effect of blood flow on the metastatic cascade in a better controlled manner than the zebrafish pharmacological treatment. Thus, we developed a simple microfluidic system in which we could set the perfusion speed at will. We used simple systems based on IBIDI® microslides (commercially available, straight channels) that we perfused with endothelial cell medium (**Fig. 40A**). We standardized the approach using fibronectin coating, Human Umbilical Vein Endothelial Cells (HUVEC) seeding and physiologic perfusion speed (**Fig. 40A**). We decided to use HUVEC because they are primary cells (closer to physiologic endothelial cells than cell lines), relatively easy to handle and compatible with transient transfection and culture in microfluidic channels.

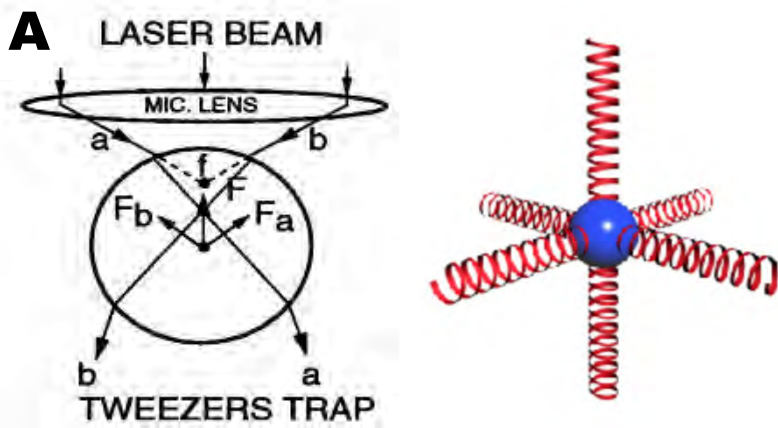
Then, this system was used in all its versatility (**Fig. 40B**): 1. We performed tumor cell perfusion at various concentrations, speeds and pulsatilities. This was live recorded to quantify arrest and stable adhesion. 2. We coupled the system with optical tweezers (see next section) to measure adhesion forces between tumor and endothelial cells. 3. We carried out fixation and staining for protein of interest and/or cell behavior (for instance, extravasation) in light microscopy, or alternatively prepared samples for electron microscopy to better characterize cell positions during tumor-associated endothelial remodeling.

USE OF OPTICAL TWEEZING

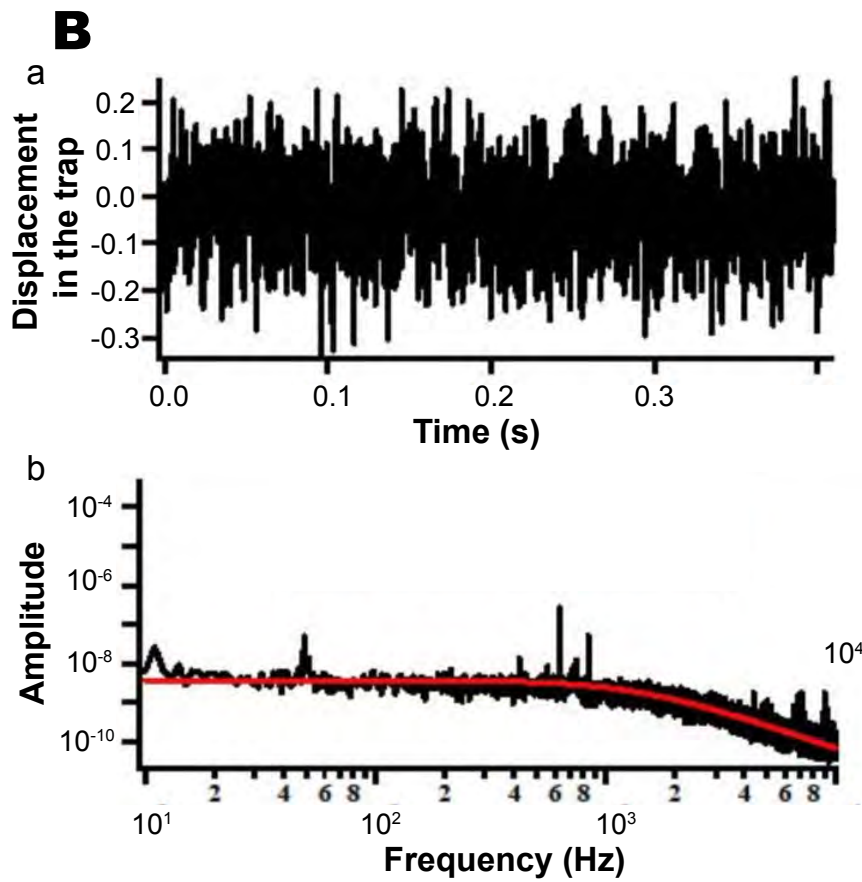
PRINCIPLE AND CALIBRATION

Optical tweezers were established by A. Ashkin in 1970 (Ashkin, 1970), with a first study in yeast biology in 1987 (Ashkin et al., 1987). It has many applications from fundamental physics to biology and Ashkin was rewarded with the 2018 Nobel Prize of Physics. The principle is quite simple: By focusing a laser beam thanks to a lens, this creates an electromagnetic gradient that exerts a maximal force to its center in three dimensions. With the condition that the particle is able to polarize (i.e. being electrically charged and orientated in accordance with the electromagnetic gradient) and do not absorb light (which would heat it), it is possible to trap it without damage. Thanks to the force gradient, it will go to the maximum density point, i.e. the focal point. Once it is trapped, it can be maintained in an equilibrium position, thanks to the photon flow: In the middle of the trap, the photons are equally refracted. When the particle shifts, the refraction is stronger on the same side, generating a reaction force on the opposite side (following the mass conservation law - 3rd Newton's Law) and the object goes back into the center. The best analogy to understand this might be to imagine a 3D spring (**Fig. 41A**): If an external force pulls in one direction, the tension increases accordingly and when the external force is removed, the object goes back to the central equilibrium position.

Complexity comes with the applications. Indeed, catching an object is straightforward, but the power of such a tool is to calibrate it and use it as a pico-dynamometer. To do so, we use a 4-quadrant diode that transforms the received light to current. When the photon flow is perturbed by the particle, the light profile sensed by the diode is modified and the current accordingly. The calibration is done on a bead at the steady state. The position data of the bead are recorded by the diode over a short time (**Fig. 41Ba**). Then, the trace position/time is transferred to the frequency regime, using Fourier's transformation (**Fig. 41Bb**). This curve gives access to the cut-off frequency, which is the limit between real values and noise (at the higher frequencies). From this cut-off frequency, it is possible to access the trap stiffness (k) (**Fig. 41Bc**). To note, *in vivo* calibration of the optical tweezer follows the same principle but is a bit more complex.



A - Schematic presenting the forces that exert the optical tweezers on a trapped bead (left). Draw illustrating the analogy with a 3d string (right).



B - Major steps used to calibrate the optical tweezers. **(a)** Graphic of the position of the bead in the trap over time, at the steady state. **(b)** Result of the Fourier's transformation: Position regarding the acquisition frequency. **(c)** Summary of the process of calibration. From (a) to (b), allowing the graphical determination of the cut-off frequency and the calculation of the trap stiffness.

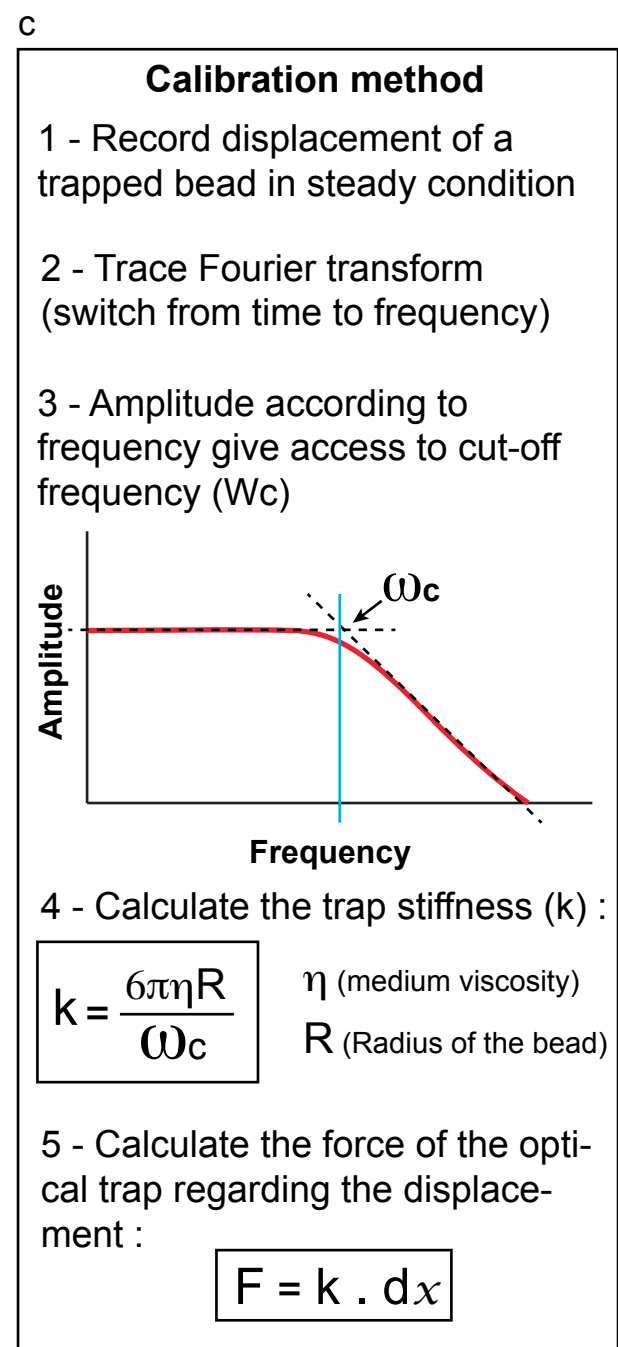


Fig. 41: Tech. Approach – Optical tweezers

This was fully described in a published article from our group ((Harlepp et al., 2017) – see [**annex 3: Hemodynamic forces can be accurately measured *in vivo* with optical tweezers**](#)).

OPTICAL TWEEZING APPLICATIONS TO CANCER

Related to our project, optical tweezers have been extensively used *in vitro*. First, they were used to measure single molecule adhesion forces. Trapping beads coated with the protein of interest, it is possible to contact a cell or a coated plate to test the binding force (For instance, $\alpha V\beta 3$ integrin binding Thy-1 in the brain - (Burgos-Bravo et al., 2018)). Also, with coated beads, it is possible to impose a cell deformation (for instance by using 2 beads stuck to a cell, with 1 fixed bead and pull on the other one (Dao et al., 2005)) and measure viscoelasticity of single cells (Rehfeldt and Schmidt, 2017). Alternatively, optical tweezing can be used to trap intracellular compartment and perform micro-rheological measurements: Wulkopf and colleague used optical tweezers to probe cell viscoelasticity by trapping lipid droplets (that thermally fluctuate more or less depending of the intracellular viscosity) during invasion. To note, data show that invasive leader cells are more viscous than the followers (Wulkopf et al., 2018). Also during cell migration, optical tweezers can be used to probe the maturation of the adhesion and the traction forces that the cell impose to the subtract (Schwingel and Bastmeyer, 2013). Finally, optical traps can be used to manipulate cells, and force their contact with other cells to study cell interaction, adhesion, immune activation... This was used by Gou et al., to bring leukocytes in contact with bone marrow cells (Gou et al., 2015).

To note, the use of optical tweezers *in vivo* is less widespread. Nevertheless, it was used to explore mechanical forces during drosophila (Bambardekar et al., 2015), or zebrafish development (Hörner et al., 2017). Moreover, it was previously used to probe hemodynamic forces through trapping of the red blood cells in mouse ears (Zhong et al., 2013) or in the zebrafish embryo ((Anton et al., 2013) – co-authored by S. Harlepp from the team).

OPTICAL TWEEZING IN OUR PROJECT

Knowing the trap stiffness (thanks to its calibration as explained above), it is possible to use the tweezers in many biophysical applications. To us, mainly three:

1- *In vitro*, to measure adhesion strengths: In this case, we trapped tumor cells at the surface of the endothelial cells, before applying a given displacement of the microscope stage. If the cell is able to resist the tearing force of the trap, it means that the cell adhesion force is stronger. If the cell detaches, depending on the distance and trap stiffness, it is possible to calculate this adhesion rupture force.

2- *In vivo*, to measure adhesion forces: On the same principle, we used optical tweezers to measure adhesion strengths in the zebrafish plexus. To note, we were not able to detach a cell in this condition, meaning that *in vivo* adhesion forces exceed ~150 pN very rapidly (maximal force of the optical tweezers) (Follain et al., 2018a) (Fig 1H).

3- *In vivo* to measure the shear forces that blood flow exerts on flowing and arrested cells intravascularly. In this case, we trapped red blood cells and studied the displacement of the RBCs in the optical trap: Knowing the trap stiffness and measuring the displacement from center to border of the trap of the RBC, we can calculate shear forces (Anton et al., 2013).

RESULTS

HEMODYNAMIC FORCES TUNE THE ARREST, ADHESION AND EXTRAVASATION OF CIRCULATING TUMOR CELLS

Scientific context

The metastatic cascade is a complex progression towards the formation of life-threatening metastases (Nguyen et al., 2009). Biological and mechanical factors are governing this progression in specific organs (Chambers et al., 2002). Despite the fact that many of these steps are happening in blood circulation, very little is known about the impact of blood flow on the circulating tumor cells arrest, adhesion and extravasation. Our current knowledge of these steps mostly comes from *in vitro* data. The common model for these phenomena comes from leukocytes rolling (arrest) and diapedesis (extravasation) (Vestweber, 2015), with the prediction that tumor cells use similar mechanisms (Chen et al., 2013). Otherwise, the few *in vivo* data from zebrafish and mouse models obtained using intravital microscopy often describe cell arrest through occlusion (without rolling) in capillary vessels (Kienast et al., 2010; Stoletov et al., 2010) and do not dissect extravasation processes. Indeed, the most admitted hypothesis about the way tumor cells arrest before extravasation, is through occlusion. This hypothesis is correlated to the fact that the tumor cell diameter can exceed the diameter of the tiny capillary vessels. Moreover, evidences showed that tumor cells can circulate as clusters, obviously larger than small capillaries. As detailed in the introduction, this hypothesis has been challenged in recent studies showing that clusters can cross capillary-like channel (Au et al., 2016). Even still, it remains the major one.

Technically, it is challenging to tackle arrest, adhesion and extravasation steps *in vivo*, as they are very hard to predict in time and space. To overcome this technical challenge, we used 2 days post fertilization zebrafish embryo as an *in vivo* model. Thanks to its multiple advantages it is possible to observe and quantitatively study these steps *at the single cell level*.

Strategic context

When I started my PhD, there was a gap in the literature, about the impact of shear stress on the metastatic cascade. Thus, we decided to study the impact of blood flow on the dissemination of metastatic cells, with the strong belief that we could statistically answer it using our approaches. Therefore, we started by impacting the flow with pharmaceutical reagents such as lidocain and IBMX to respectively decrease and increase the blood flow in embryos. Then, we injected these treated embryos with tumor cells, to follow the tumoral behavior in those conditions. We designed the study through 4 time points allowing us to highlight the arrest, stable adhesion, endothelial remodeling around adhered tumor cells and extravasation. As a plus, we used correlative light and electron microscopy to dissect the ongoing mechanisms at the best resolution.

Major outputs

Our results dissect the role of the blood flow on the last steps of the metastatic cascade, preceding the metastatic outgrowth. We scientifically demonstrated that arrest and adhesion are flow dependent in an intuitive manner: A higher flow lowers the adhesion probability imposing the cell to run further in the circulation, where the flow becomes permissive, whereas a lower flow increases the adhesion probability allowing cells to stop and remain upstream in the circulation. We could partially separate this phenotype from the occlusion by showing that arrest and adhesion happen in capillaries with higher diameter than the cellular diameter. Thanks to the electron microscopy resolution, we also showed the presence of filopodia-like structures binding endothelial to cancer cells.

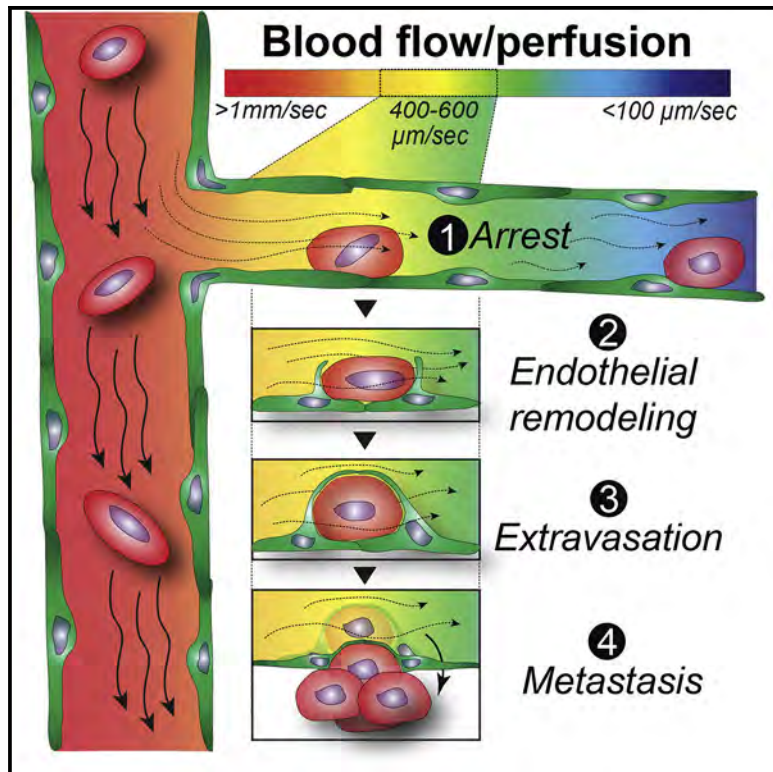
Then, we demonstrated how blood flow impacts extravasation, through the inhibition of endothelial remodeling. We documented this process at high resolution using correlative light and electron microscopy. Interestingly, we were able to show the flow-dependency of the process, and its relevance in the mouse model. Finally, we could correlate these findings with patient data: They revealed that metastasis in the brain are significantly more present at the boundary between white and grey matter. This region corresponds to the site of vascular branching and flow drop. To summarize, our descriptive works demonstrate that blood flow is a central parameter impacting metastatic spreading.

From this work, two major questions raised. 1- What kind of receptors are required by the cells to stop without occlusion? 2- What is the medical relevance of our findings? To tackle these problems, we designed two follow-up project: First, we wanted to describe quantitatively how the cell adhesion repertoire is involved *in vivo*, in the early arrest and adhesion steps. Second, we looked further to hinder the description of the endothelial remodeling with pharmaceutical drugs that block the extravasation process.

Developmental Cell

Hemodynamic Forces Tune the Arrest, Adhesion, and Extravasation of Circulating Tumor Cells

Graphical Abstract



Authors

Gautier Follain, Naël Osmani, Ana Sofia Azevedo, ..., Klaus Pantel, Sébastien Harlepp, Jacky G. Goetz

Correspondence

jacky.goetz@inserm.fr

In Brief

Follain et al. demonstrate that blood flow forces tune both the arrest and extravasation of circulating tumor cells *in vivo*. Permissive flow forces allow stable intravascular arrest of circulating tumor cells. Flow forces drive endothelial remodeling around arrested tumor cells, favoring extravasation preceding metastatic outgrowth.

Highlights

- Arrest of circulating tumor cells occurs in blood vessels with permissive flow profiles
- pN-range adhesion forces favor rapid and stable intravascular adhesion
- Flow-mediated endothelial remodeling drives extravasation of tumor cells



Hemodynamic Forces Tune the Arrest, Adhesion, and Extravasation of Circulating Tumor Cells

Gautier Follain,^{1,2,3,4,15} Naël Osmani,^{1,2,3,4,15} Ana Sofia Azevedo,^{1,2,3,4,15} Guillaume Allio,^{1,2,3,4} Luc Mercier,^{1,2,3,4} Matthia A. Karreman,⁵ Gergely Solecki,⁶ Maria Jesús García León,^{1,2,3,4} Olivier Lefebvre,^{1,2,3,4} Nina Fekonja,^{1,2,3,4} Claudia Hille,⁷ Vincent Chabannes,⁸ Guillaume Dollé,⁸ Thibaut Metivet,⁸ François Der Hovsepian,⁸ Christophe Prudhomme,⁸ Angélique Pichot,^{1,2,4} Nicodème Paul,^{1,2,4} Raphaël Carapito,^{1,2,4} Siamak Bahram,^{1,2,4} Bernhard Ruthensteiner,⁹ André Kemmling,¹⁰ Susanne Siemonsen,¹¹ Tanja Schneider,¹¹ Jens Fiehler,¹¹ Markus Glatzel,¹² Frank Winkler,⁶ Yannick Schwab,⁵ Klaus Pantel,⁷ Sébastien Harlepp,^{2,13,14} and Jacky G. Goetz^{1,2,3,4,16,17,*}

¹INSERM UMR_S1109, Strasbourg 67200, France

²Université de Strasbourg, Strasbourg 67000, France

³LabEx Medalis, Université de Strasbourg, Strasbourg 67000, France

⁴Fédération de Médecine Translationnelle de Strasbourg (FMTS), Strasbourg 67000, France

⁵Cell Biology and Biophysics Unit, European Molecular Biology Laboratory, Heidelberg 69117, Germany

⁶Department of Neurooncology, University Hospital Heidelberg, Heidelberg, 69120, Germany and Clinical Cooperation Unit Neurooncology, German Cancer Research Center (DKFZ), Heidelberg 69120, Germany

⁷Institute of Tumor Biology, University Medical Center Hamburg-Eppendorf, Martinistraße 52, Hamburg 20246, Germany

⁸LabEx IRMIA, CEMOSIS, Université de Strasbourg, Strasbourg 67000, France

⁹Zoologische Staatssammlung München, Munich 81247, Germany

¹⁰Department of Neuroradiology, University Medical Center Schleswig-Holstein, Campus Lübeck, 23535 Lübeck, Germany

¹¹Department of Diagnostic and Interventional Neuroradiology, University Medical Center Hamburg-Eppendorf, 20246 Hamburg, Germany

¹²Center for Diagnostics, Institute of Neuropathology, University Medical Center Hamburg-Eppendorf, 20246 Hamburg, Germany

¹³CNRS UMR7504, Institut de Physique et Chimie des Matériaux de Strasbourg (IPCMS), Strasbourg 67000, France

¹⁴LabEx NIE, Université de Strasbourg, Strasbourg 67000, France

¹⁵These authors contributed equally

¹⁶Twitter: @GoetzJacky

¹⁷Lead Contact

*Correspondence: jacky.goetz@inserm.fr

<https://doi.org/10.1016/j.devcel.2018.02.015>

SUMMARY

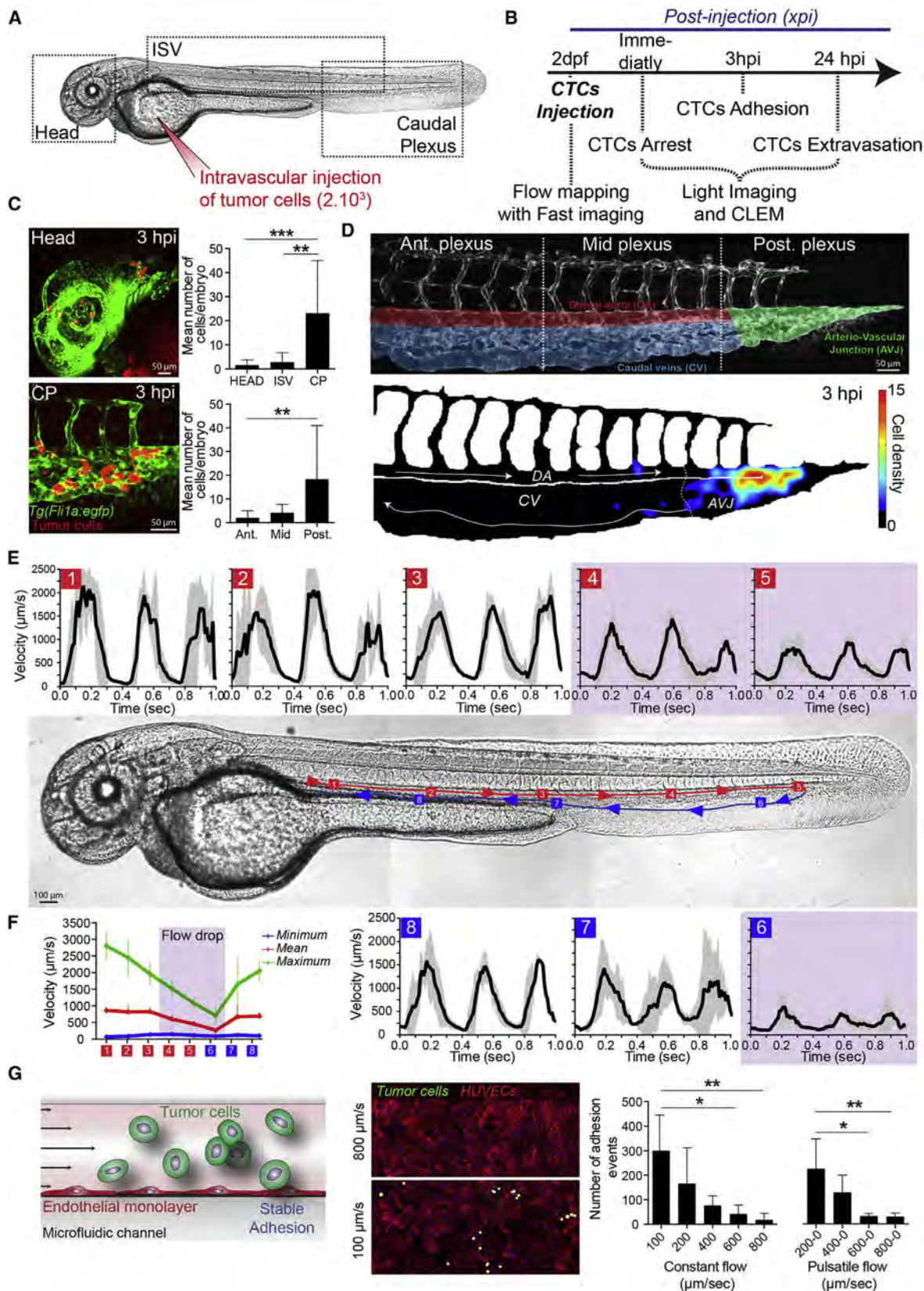
Metastatic seeding is driven by cell-intrinsic and environmental cues, yet the contribution of biomechanics is poorly known. We aim to elucidate the impact of blood flow on the arrest and the extravasation of circulating tumor cells (CTCs) *in vivo*. Using the zebrafish embryo, we show that arrest of CTCs occurs in vessels with favorable flow profiles where flow forces control the adhesion efficacy of CTCs to the endothelium. We biophysically identified the threshold values of flow and adhesion forces allowing successful arrest of CTCs. In addition, flow forces fine-tune tumor cell extravasation by impairing the remodeling properties of the endothelium. Importantly, we also observe endothelial remodeling at arrest sites of CTCs in mouse brain capillaries. Finally, we observed that human supratentorial brain metastases preferably develop in areas with low perfusion. These results demonstrate that hemodynamic profiles at metastatic sites regulate key steps of extravasation preceding metastatic outgrowth.

INTRODUCTION

Metastatic progression is a complex process resulting in the formation of lethal secondary tumors at distance from their origin (Nguyen et al., 2009). Metastatic cancer cells disseminate very efficiently throughout the body upon intravasation in the blood circulation. Recent work on breast cancer suggests that about 80% of metastases originate from early disseminated cancer cells (Harper et al., 2016; Hosseini et al., 2016). Once in the blood stream, circulating tumor cells (CTCs) may find a location favoring arrest and stable adhesion before extravasating and avoiding the hostile shear forces (Valastyan and Weinberg, 2011; Regmi et al., 2017). After extravasation, metastatic cells either remain dormant (Sosa et al., 2014) or grow successfully into life-threatening secondary tumors (Kienast et al., 2010). Although multiple mechanisms have been postulated for successful extravasation and outgrowth of metastatic cells (Chen et al., 2016b; Headley et al., 2016; Kienast et al., 2010; Strilic et al., 2016), there are only few insights on the role played by mechanical cues encountered in the blood, the main route for hematogenous metastatic dissemination.

Biomechanical forces are known to have a major impact on metastasis progression. For example, tumor cells (TCs) sense and respond to stiffening of the surrounding stroma by increasing their invasive potential (Levental et al., 2009;





(legend on next page)

Mouw et al., 2014; Paszek et al., 2005). High extravascular stress caused by tumor growth (Chauhan et al., 2013; Stylianopoulos et al., 2012) and interstitial fluid pressure (Provenzano et al., 2012) lead to vascular compression that impairs perfusion and eventually promotes tumor progression, immunosuppression, and treatment resistance. Locally, invading TCs need to overcome physical tissue constraints by cellular and nuclear deformability (Harada et al., 2014; Wolf et al., 2013), possibly inducing nuclear envelope rupture and DNA damage (Denais et al., 2016), leading eventually to inheritable genomic instability (Irianto et al., 2016). Overall, while the impact of biomechanics on tumor growth and invasion are mechanistically relatively well understood, the *in vivo* mechanisms driving survival, arrest, and successful extravasation of CTCs, preceding metastatic growth, remain to be elucidated.

Indeed, very little is known about how CTCs arrest and adhere to the endothelium of small capillaries and leave the blood stream by crossing the vascular wall. While the “seed and soil” concept states that metastasis will occur at sites where the local microenvironment is favorable (Paget, 1889), the “mechanical” concept argues that arrest and metastasis of CTCs occur at sites of optimal flow patterns (Weiss, 1992). CTCs in the blood circulation are subjected to vascular routing (Chambers et al., 2002), collisions and associations with blood cells (Labelle et al., 2014), hemodynamic shear forces (Chang et al., 2008), and physical constraints imposed by the vessel architecture (Headley et al., 2016; Kienast et al., 2010). Only CTCs capable of overcoming or exploiting the deleterious effects of shear forces will eventually arrest, adhere to, and exit the vasculature to form a secondary tumor (Wirtz et al., 2011). Nevertheless, a direct contribution of mechanical cues to the arrest and successful extravasation of CTCs has so far only been poorly studied (Wirtz et al., 2011). Therefore, new *in vivo* models, where modeling, visualization, and biophysical quantification of the extravasation parameters are easily performed, are of utmost importance for assessing whether biomechanics regulate metastatic extravasation.

Here, we aim to address the direct impact of the blood flow on the arrest and extravasation of CTCs *in vivo*. We developed an original experimental approach to measure and modulate blood flow with intravascular injection of CTCs within zebrafish embryos. We observed that blood flow controls the sequential steps of arrest, adhesion, and extravasation of CTCs *in vivo*. In parallel, using microfluidics and optical tweezers (OT), we identified the critical adhesion force (80 pN) that CTCs require

to initiate adhesion to the endothelium, which rapidly stabilizes under shear flow. This value matches the threshold dragging force measured *in vivo* at extravasation sites. Finally, we used our recently developed intravital correlative light and electronic microscopy (CLEM) (Follain et al., 2017; Karreman et al., 2016a, 2016b) to identify endothelial remodeling as one of the major extravasation mechanisms *in vivo*, and that endothelial remodeling scales with flow velocities. Overall our studies demonstrate that blood flow forces at metastatic sites regulate key steps of extravasation preceding metastatic outgrowth.

RESULTS

Arrest and Adhesion of CTCs is Favored by Permissive Flow Velocities

To test the impact of blood flow on the arrest, adhesion, and extravasation of CTCs, we experimentally modeled metastatic seeding in endothelium-labeled zebrafish embryo (*Tg(Fl1a:EGFP*)) at 2 days post-fertilization by injecting fluorescently labeled TCs in the duct of Cuvier (Figures 1A and 1B). While metastatic extravasation can be successfully tracked in this model (Stoleto et al., 2010), the zebrafish embryo further allows to combine biophysical characterization and manipulation of blood flow parameters with long-lasting and high-resolution imaging of TCs *in vivo*. We first quantified and mapped the position of arrested and stably adherent TCs (D2A1) in the zebrafish vasculature and noticed that CTCs preferentially arrested (and extravasated) in the caudal plexus (CP) (Figure 1C). Although arrest and extravasation can be also observed in inter-somatic vessels (ISV) (Figure 1C) and in the brain of zebrafish embryos (Figures 1C, S1A, and S1B; Video S1), the majority of the TCs arrest in the CP. We exploited the highly stereotyped vasculature of this region by compiling >10 embryos and quantitatively identifying a major hotspot of arrest in this region (Figure 1D), which sits between the caudal artery and the venous plexus. This was the case for multiple human (Jm1, 1675, and A431), mouse (D2A1 and 4T1), and zebrafish (ZMEL) cell lines (Figure S1C). Using fast imaging of the blood flow (100 fps) within the entire zebrafish embryo, combined with PIV (particle image velocimetry) analysis, we observed decreasing flow values in the vascular region that is permissive for CTC arrest (Figures 1E and 1F; Video S2). Accurate dissection of blood flow profiles using PIV analysis showed that flow velocity progressively decreases from the anterior dorsal aorta (DA) (position 1, maximal velocity, $v_{max} = 2,500 \mu\text{m/s}$; Figures 1E and 1F), to a minimal flow in its most posterior region

Figure 1. Arrest and Stable Adhesion of CTCs Are Favored by Permissive Blood Flow Profiles in the Zebrafish Embryo

(A and B) Experimental design and workflow. xpi, min or hr post-injection (mpi) or (hpi).

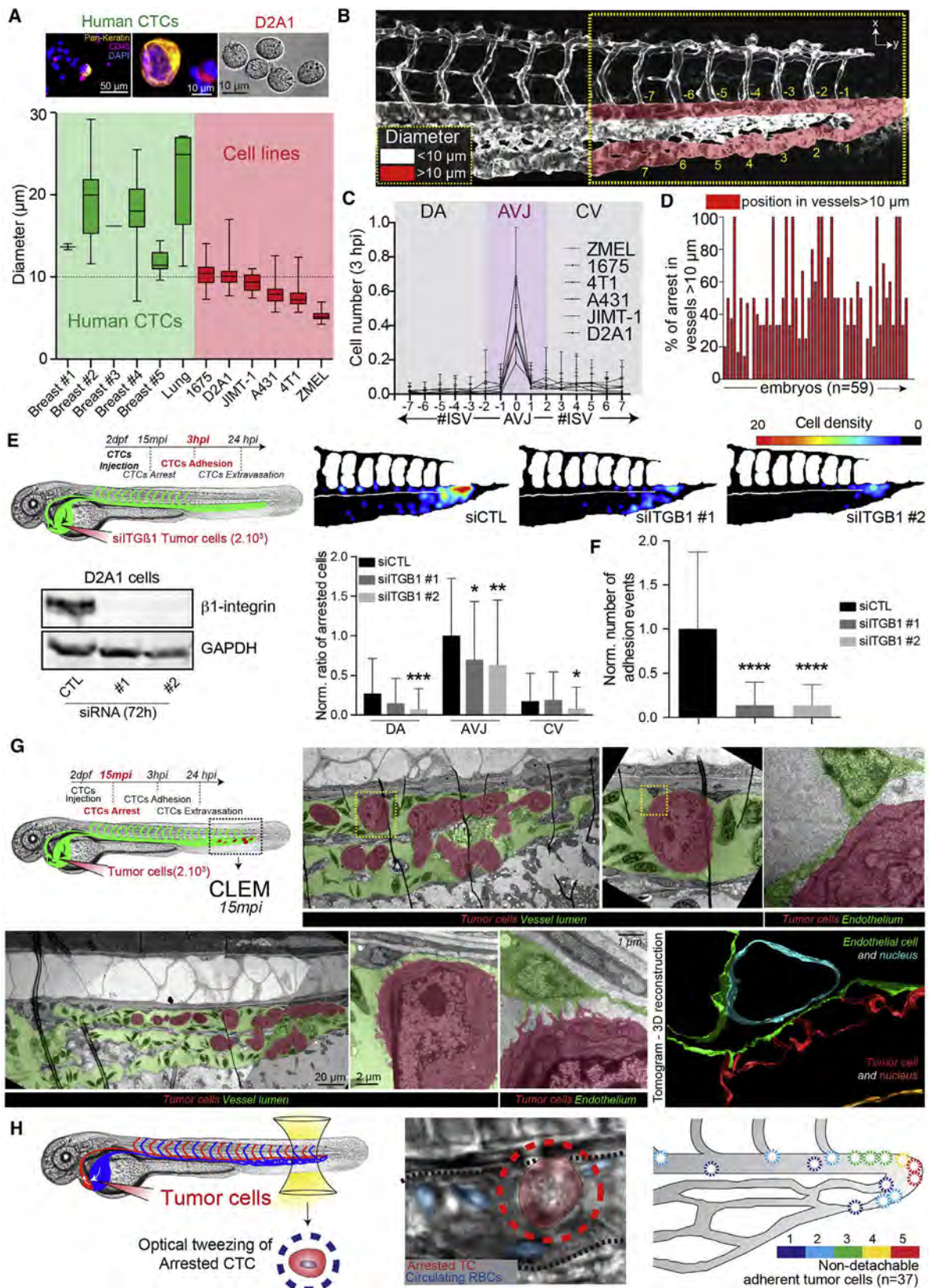
(C) Representative images (Head, head region; CP, caudal plexus) and quantification of arrested CTCs (red) in the vasculature (green) of the zebrafish embryo at 3 hpi (see also Video S1). Ant., Mid, and Post., anterior, mid, and posterior plexus as depicted in (D).

(D) High-magnification image of the vascular CP, the associated regions, and heatmap of arrested CTCs at 3 hpi ($n = 11$ embryos). AVJ, arterio-venous junction; DA, dorsal aorta; CV, caudal veins. Arrows indicate blood flow direction.

(E) Blood flow velocity measurements (PIV) in the indicated region (red and blue squares 1 to 8) of the zebrafish embryo. Arrows indicate blood flow direction (see also Videos S2 and S3).

(F) Minimum, maximum, and mean values of the blood flow velocity are plotted over the eight different regions ($n = 3$ embryos).

(G) Experimental setup, representative images, and quantification of the microfluidic approach. CTCs (green) are perfused over a monolayer of HUVECs (ECs, red) and adhesion is quantified ($n = 5$ –6 independent channel per conditions). Pulsatile flow corresponds to 0.3 s perfusion/0.3 s stop of the peristaltic pump. Values are mean \pm SD. * $p < 0.05$, ** $p < 0.01$, *** $p < 0.0001$.



(legend on next page)

(positions 5 to 6, $v_{max} = 500 \mu\text{m/s}$), which we named the arterio-venous junction (AVJ). We have shown in the past that blood flow dissipates along the vascular network of the zebrafish embryo (Anton et al., 2013). In addition, the mass conservation implies that ramification of the vessels in the AVJ further contributes to the blood flow decrease. We thus set out to model this phenomenon *in silico* using a mathematical simulation of the blood flow in the CP (see [Supplemental Information](#)). Simulation experiments reproduced the flow drop observed in the most posterior region of the CP (Figures S1D–S1H; [Video S3](#)). Also, to determine whether flow velocity can affect the CTC arrest, we developed an *in vitro* approach to mimic *in vivo* flow profiles in microfluidic channels previously coated with endothelial cells (ECs) or human umbilical vein endothelial cells (HUVECs) (Figure 1G). We observed that adhesion of CTCs to the endothelial layer was favored by reduced flow profiles (peak velocities of 100–400 $\mu\text{m/s}$) (Figure 1G), similar to those measured *in vivo* in the AVJ (Figures 1D and 1E). Using higher-flow profiles that mimic flow values obtained in the anterior DA prevented efficient adhesion of CTCs to the endothelial layer (Figure 1G), as observed *in vivo* where no adhesion could be observed in the DA between positions 1 and 4 (Figures 1D and 1E). Adhesion efficacy (and forces) of CTCs was not affected by temperature (28°C versus 37°C; Figures S2B and S2C). Taken together, these data suggest that reduced flow profiles are permissive for stable adhesion of CTCs to the endothelium, and that the threshold velocity value for efficient adhesion of CTCs ranges from 400 to 600 $\mu\text{m/s}$.

Permissive Flow Profiles Promote Stable Adhesion of CTCs to the Endothelium

Adhesion of CTCs to the endothelium is an important feature that precedes their extravasation (Reymond et al., 2013). Furthermore, mechanical constraints imposed by cell size and vessel topology likely favor the initial arrest of CTCs (Cameron et al., 2000; Kienast et al., 2010; Luzzi et al., 1998). We set out to test whether such features also contribute to arrest and adhesion in the zebrafish embryo. Our models of CTCs are composed of multiple human (Jm1, 1675, A431), mouse (D2A1, 4T1), and zebrafish (ZMEL) cell lines, whose mean diameters range from

10.23 to 5.25 μm (Figure 2A). We validated these models by comparing their values to average diameters of human CTCs isolated from breast and lung cancer patients (ranging from 7 to 29 μm) (Figure 2A). We then accurately measured mean vessel diameters of the CP of the zebrafish embryo (Figure 2B). We noticed that diameters of the highly perfused vessels (red, Figure 2B) each displayed a minimal value that exceeds the maximum size for our CTC models (10.23 μm ; Figure 2B). When injected in the embryo, our CTCs mostly arrested in the flow-permissive hotspot (AVJ), suggesting that flow drop significantly affects the arrest of CTCs (Figure 2C). Interestingly, when we correlated the position of arrested CTCs within the vasculature to the vessel size, we observed that 49% of them were located in vessels with diameters $<10.23 \mu\text{m}$ (Figure 2D). These cells could have been trapped in low-size vessels or crawled, upon arrest, into these vascular regions before extravasating. Indeed, we have observed that intravascular CTCs are capable of efficiently crawling on the vessel wall, suggesting that CTCs establish firm adhesions with the endothelium ([Video S4](#)). Moreover, stiff 10- μm polystyrene beads circulate continuously when injected in the embryo, suggesting that size restriction, although it does participate, is not a major determinant of cell arrest (Figure S2A). These observations led us to test the role of adhesion molecules in driving successful, flow-dependent arrest of CTCs. Thus, we took advantage of our *in vitro* microfluidic approach and used the OT technology to trap and stick CTCs to the EC monolayer. Doing so, we identified an average value of 80 pN for the very early adhesion forces (<1 min after adhesion of the CTCs to the endothelial layer) required for the attachment of CTCs to ECs (Figure S2C; [Video S5](#)). Interestingly, applying Stoke's law to measure the correspondence between flow and force intensity, we noted that a value of 80 pN represents an average flow value of 450 $\mu\text{m/s}$, which agrees with threshold flow values that we measured both *in vivo* and *in vitro* (Figure 1). Thus, CTCs very quickly establish adhesion forces that allow them to sustain flow velocities of 450 $\mu\text{m/s}$.

To test the role of adhesion molecules, we targeted $\beta 1$ integrins (ITGB1), known to play a central role in tumor metastasis (Seguin et al., 2015) and promote stable adhesion of CTCs to the endothelium before extravasation (Gassmann et al., 2009;

Figure 2. Arrest of CTCs Depends on Early Cellular Adhesion Forces

- (A) Quantification of the diameters of human CTCs (green, five breast cancer patients and one lung cancer patient) and 1675, D2A1, JIMT-1, A431, 4T1, and ZMEL1 cells (red) in suspension. Representative images of human CTCs and D2A1 are also provided. Human CTCs are labeled with pan-keratin (CTC marker), CD45, and DAPI (nucleus).
- (B) Representative confocal z projection image of the CP. Red shows highly perfused vessels with diameters over 10 μm .
- (C) Quantification of the number of arrested cells per ISV in the yellow dashed region depicted in (B).
- (D) Quantification of the repartition of arrested cells in the plexus of 59 embryos, between the regions of bigger (red) and smaller (white) than 10 μm vessels in diameter.
- (E) Experimental workflow and depletion of ITGB1 via small interfering RNA (siRNA) in D2A1 cells: control siRNA (siCTL) and two distinct sequences of the siRNA targeting ITGB1 (siITGB1 no. 1 and siITGB1 no. 2). Representative western blot images are shown. Heatmaps of arrested CTCs after 3 hpi are shown for CTCs transfected with siRNAs ($n = 77, 63$, and 55 , respectively). Quantification of the ratio of arrested CTCs in the indicated region is provided. Norm., normalized to siCTL AVJ.
- (F) Graph depicts the number of adhesion events (CTCs to HUVECs) quantified in our microfluidic approach (see also [Videos S6](#) and [S7](#)). Norm., normalized to siCTL.
- (G) Experimental setup of intravital CLEM performed on arrested CTCs only 15 mpi. Representative EM images of arrested CTCs (red) in vascular lumen (green) are provided from two different sections (top and bottom). A reconstruction of an electron tomogram is provided. The yellow outline highlights the area quantified in (C).
- (H) Experimental setup, representative image, and quantification of optical tweezing experiments of arrested CTCs in the AVJ ($n = 37$ arrested cells, $n > 10$ embryos) (see also [Video S7](#)).

Values are mean \pm SD. * $p < 0.05$, ** $p < 0.01$, *** $p < 0.001$, **** $p < 0.0001$.

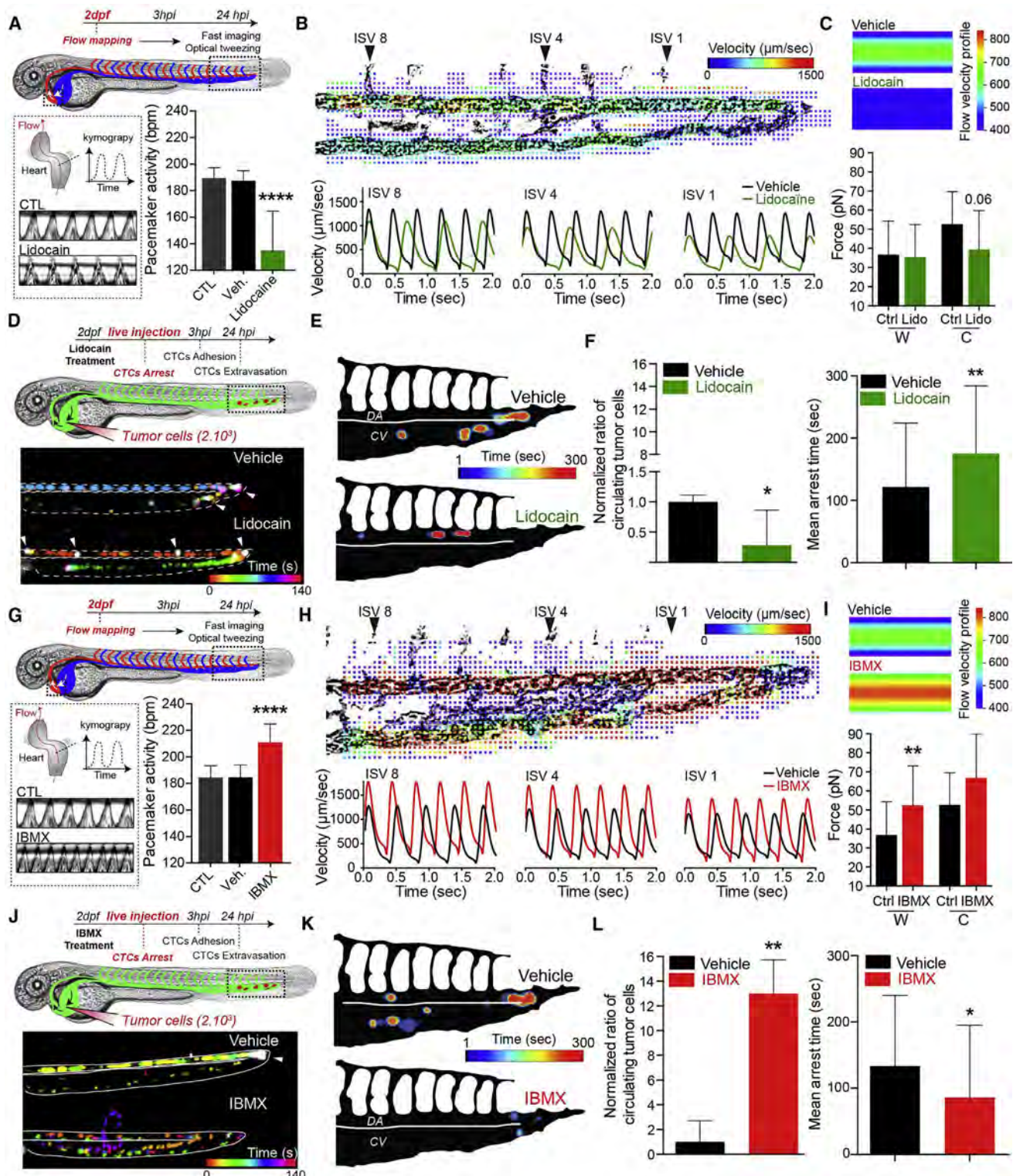


Figure 3. Modulating Blood Flow Forces Regulates Arrest of CTCs.

(A–L) Zebrafish embryos were treated with vehicle, lidocaine (A–F), or IBMX (G–L). (A and G) Experimental workflow. Heart PMA is quantified for each condition. CTL, breeding water. An additional kymograph analysis is provided. (B and H) top: images extracted from fast imaging and PIV analysis of the blood flow in the CP; region boxed in (A) and (G) (see also Videos S8–S10). Bottom: quantification of the flow profiles in the center of the DA analyzed at position ISV 8, ISV 4, and ISV1 ($n = 4/5$ embryos per condition). (C and I) Orthogonal flow velocity profile and quantification extracted from optical tweezing of RBCs in the DA under ISV 1 (W, wall; C, center) (see also Video S10). (D and J) Experimental workflow and representative images of the residency time of CTCs in the CP over a period of 5 min

(legend continued on next page)

Schlesinger and Bendas, 2015). We determined whether compromising stable adhesion mediated by $\beta 1$ integrins would affect the ability of CTCs to arrest under permissive flows. We depleted ITGB1 in our cells using a small interfering RNA approach (Figure 2E) and assessed their stable adhesion 3 hr post-injection (hpi) using a heatmap procedure over several embryos. Interestingly, while the adhesion hotspot in the AVJ is conserved, the overall number of adhesion event is significantly reduced (Figure 2E). Similar observations were made in our microfluidic system, where only 20% of ITGB1-depleted CTCs stably adhere to the EC monolayer using the same perfusion parameters (Figure 2E). Comparable values were obtained when adhesion (or detachment) of perfused CTCs to (from) ECs was forced using OT in microfluidic channels (Figure S2D; Video S6), indicating that permissive flow profiles, combined with proper adhesion forces, allow stable adhesion of CTCs to the endothelium.

To further support this hypothesis, we assessed whether adhesion events could be observed *in vivo* using intravital CLEM (Goetz et al., 2014), which allows to combine live imaging of xenografted CTCs in the zebrafish embryo with electron microscopy (EM). Interestingly, CTCs that were arrested in the zebrafish vasculature only 15 min post-injection (mpi) displayed finger-like adhesive contacts with ECs (Figure 2G). In addition, ECs displayed long protrusions when in contact with arrested CTCs (upper panels, Figure 2G). These observations suggest that integrin-dependent adhesion forces between early arrested CTCs and ECs quickly exceed stripping forces from the blood flow. We aimed to further demonstrate the contribution of early adhesion forces to flow-dependent arrest of CTCs and performed OT *in vivo*. Although OT can very efficiently trap circulating red blood cells (RBCs) in the vasculature of living zebrafish embryo (Video S7) and detach adhered CTCs from ECs *in vitro* (Figure S3B), OT was inefficient for detaching arrested CTCs *in vivo* (Figure 2H; Video S7). The inability to detach >35 arrested CTCs with OT, demonstrates that early adhesion forces rapidly exceed 200 pN (which is the technical limit of our OT setup). These results suggest that low flow forces (~80 pN) enable the arrest and stable adhesion of CTCs *in vivo*.

Pharmacological Tuning of Hemodynamic Forces Modulates Pacemaker Activity

Since the arrest of CTCs occurs at the site of permissive flow patterns, we investigated whether tuning flow forces would affect the arrest efficacy. We first tuned the zebrafish pacemaker activity (PMA) and subsequent flow forces using pharmacological treatments. We selected lidocain (Vermot et al., 2009) and isobutylmethylxanthine (IBMX) (Luca et al., 2014) to decrease or increase the (PMA), respectively (Figures 3A and 3G). Upon treatment, we assessed cardiac PMA and measured an average decrease and increase of 20% for lidocain and IBMX, respectively. Using fast imaging combined with PIV analysis we determined the resulting velocities in three positions of the DA for several embryos (ISV 1, 4, and 8) and observed that lowering

or increasing PMA with lidocain and IBMX, respectively, significantly altered flow profiles (Figures 3B and 3H; Video S8). In brief, while lidocain treatments led to lower velocities with longer times under 400 μ m/s (Figures 3B and S3A), IBMX significantly increased the maximum velocities of flow pulses and decreased the overall duration of the flow under 400 μ m/s (Figures 3H and S3A). We confirmed the impact of the two drugs on flow profiles using *in silico* 3D flow simulation (Figures S3C–S3F; Video S9). We further assessed the impact of tuning PMA on hemodynamic forces by trapping RBCs using OT in the AVJ region *in vivo* (Figure S3B; Video S10). We measured the forces exerted on trapped RBCs, both at the vessel wall and in its center, and extracted the corresponding flow profiles based on the Poiseuille law for each condition (Figure S3C). While lidocain significantly reduced flow forces in the center of the vessel, IBMX increased flow forces at the vessel wall and in the center (Figures 3C and 3I). Importantly, before taking on experiments aiming to study the behavior of CTCs in distinct flow profiles, we demonstrated that our pharmacological treatments had no impact on the vasculature architecture and permeability (Figures S4A–S4D), on the migratory and adhesive properties of TCs *in vitro* (Figures S4E–S4G), or on adhesion efficacies in our microfluidic approach (Figure S4I).

Reduced Flow Promotes Early Arrest of CTCs

We then assessed the impact of modulating flow forces on the arrest of CTCs using live and instantaneous intravital imaging upon injection (Figures 3D and 3J; Video S11). As expected, CTCs mostly arrest in the AVJ in normal flow profiles (Figures 3D, 3E, 3J, and 3K, vehicle). Interestingly, decreasing flow profiles with lidocain-induced arrest of CTCs in the anterior regions of the DA decreased the number of CTCs in the blood flow over a period of 5 mpi, and significantly increased their mean arrest time over the imaging period (Figures 3D–3F). In contrast, increasing flow profiles with IBMX drastically abrogated the arrest of CTCs in the blood flow over a period of 5 mpi and reduced their mean arrest time (Figures 3J–3L). Similar results were obtained when passivated, stiff 10- μ m polystyrene beads were injected in control embryos, suggesting that inert stiff objects are unlikely to arrest in regions with permissive flow profiles (Figure S2A). These results show that, while reduced flow forces enhance the arrest probability of CTCs, increased flow profiles are capable of impeding their early arrest.

Hemodynamic Forces Tune the Stable Intravascular Adhesion of CTCs

Because extravasation of CTCs requires stable adhesion to the vessel wall, we investigated whether tuning flow profiles would affect the stable adhesion of CTCs to the endothelium *in vivo*. We first assessed the number and location of adhered CTCs 3 hpi in a large number of embryos, making use of our heatmap protocol and the stereotyped vasculature of the zebrafish CP (Figures 4A and 4D). While normal flow conditions favored the definitive arrest in the AVJ, decreasing flow forces with lidocain

(see also Video S11). Arrowheads indicate long-lasting arrested cells (white). (E and K) Spatiotemporal quantification of the residency time of CTCs in the CP using heatmap on a representative embryo. (F and L) Quantification of the ratio of CTCs as well as the mean arrest time over a period of 5 min for embryos treated with vehicle or the indicated drug. Norm., normalized to vehicle mean. Values are mean \pm SD. *p < 0.05, **p < 0.01, ***p < 0.0001.

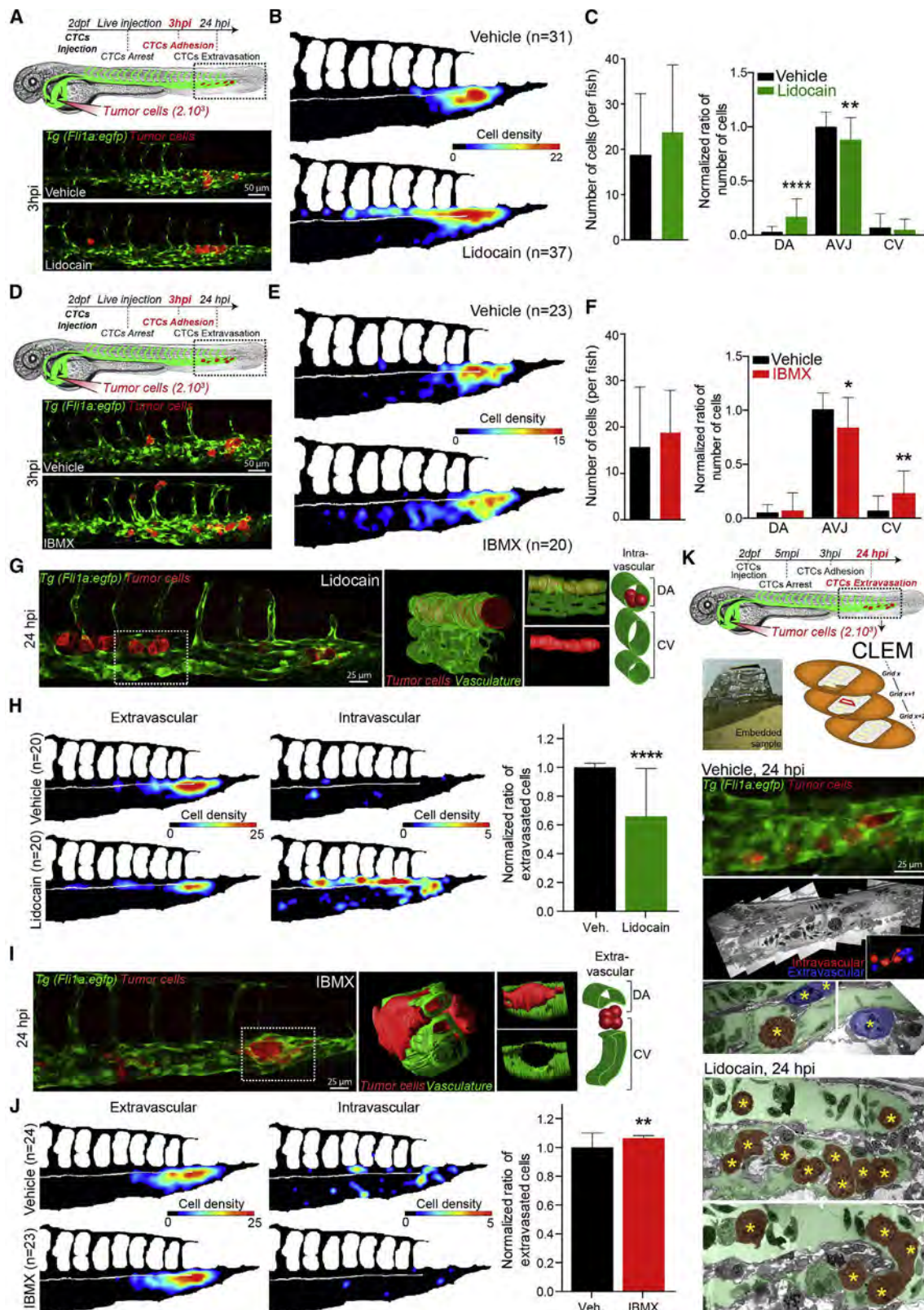


Figure 4. Modulating Blood Flow Forces Regulates Stable Adhesion and Extravasation of CTCs

Figure 4. Modulating Blood Flow Fosters Regulated Static Adhesion and Extravasation of CTCs

(A–J) Zebrafish embryos were treated with vehicle, lidocaine (A–C and G–H) or IBMX (D–F and I–J). (A and D) Experimental workflow and representative images of arrested CTCs (red) in the CP (green) of vehicle- or drug-treated embryos. (B and E) Quantification of the number and location of arrested CTCs in the CP of 3 hpi

(legend continued on next page)

stimulated the stable adhesion of CTCs in more anterior regions of the DA and reduced the proportion of CTCs arresting in the CV (Figures 4A–4C). On the contrary, increasing flow forces with IBMX impaired stable arrest in the DA and AVJ regions, and shifted definitive arrest toward venous regions of the CP (Figures 4D–4F). Thus, arrest of CTCs mostly occurs in regions with permissive flow profiles, which are shifted toward anterior regions in the DA in lidocaine-treated embryos, and toward posterior regions in the CV in IBMX-treated embryos. We further consolidated this observation by using two additional drugs known to decrease (nifedipine; Brennan, 2005) and increase (norepinephrine; Luca et al., 2014) PMA, with similar outcome without perturbing the properties of TCs (Figures S4, S5A–S5H). These data suggest that flow forces finely tune the adhesive capacity of CTCs independently of the vessel architecture.

Increased Flow Promotes Extravasation of CTCs

Once stably attached to the vessel wall, CTCs need to withstand the shear forces and undergo extravasation for metastatic outgrowth. We thus further investigated whether flow forces could affect the extravasation abilities of arrested CTCs and assessed the location and ratio of extravascular cells 24 hpi. Most of the arrested CTCs eventually undergo extravasation in normal flow conditions, while impairing flow forces with lidocain drastically reduced the number of extravascular cells. More than 60% of cells remained fully intravascular, in particular along anterior regions of the DA where CTCs mostly arrested in reduced flow conditions (Figures 4G and 4H). Impairing flow forces with lidocain only once CTCs were arrested perturbed their extravasation equally (Figure S4H). Using our CLEM protocol, we confirmed that the TCs were extravascular in normal flow conditions (Figure 4K; Video S12). Similar experiments conducted on lidocain-treated embryos showed that the vast majority of the cells remain indeed fully intravascular (Figures 4G, 4H, and 4K). In contrast, increasing flow forces with IBMX further increased the ratio of extravascular cells (close to 100%) (Figures 4I and 4J), and favored the formation of micrometastasis foci that were surrounded by the local vasculature (Figure 4I). Overall, these results show that blood flow forces enhance the extravasation abilities of CTCs.

Flow-Dependent Endothelial Remodeling Drives Extravasation of CTCs

We noticed that ECs could react very quickly to the presence of arrested CTCs (Figure 2G), and that extravasation of CTCs induces massive remodeling of the local vasculature (Figure 4I). In addition, our drugs had no effect on the behavior of the TCs (Figures S4–S5), which prompted us to investigate whether flow forces could affect the extravasation via ECs. We thus set up long-lasting (15 hr) intravital 3D confocal recordings of the behavior of TCs during extravasation (Figure 5A, Video S13).

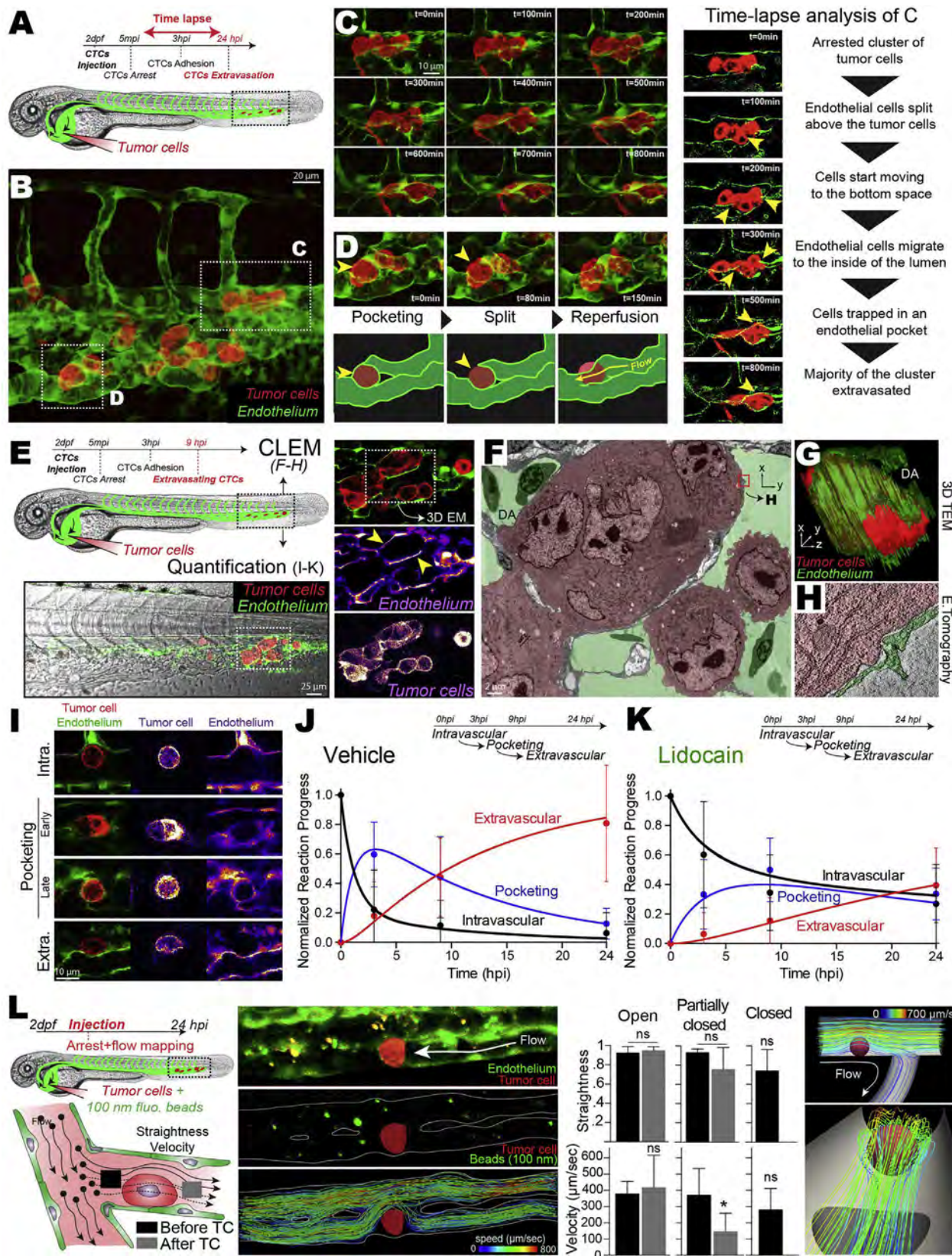
Unexpectedly, image analysis revealed that a majority of CTCs extravasated by indoctrinating the local vasculature rather than by actively transmigrating through the vessel wall by diapedesis, which is nevertheless also observed (Figures 5B–5D). Indeed, ECs remodeled around the arrested CTCs by protruding and establishing tight connections with other ECs. During this process, ECs engulf single or clusters of arrested CTCs inducing extravasation of CTCs. To gain further structural insights into this phenomenon, we performed intravital CLEM at only 9 hpi to catch an ongoing extravasation phenomenon (Figure 5E). CLEM analysis revealed that clusters of arrested CTCs are indeed fully surrounded by ECs (Figures 5F and 5G; Video S14). High-resolution images performed via electron tomography showed that ECs could establish a tight contact around the cluster of arrested CTCs (Figure 5H).

We further examined embryos 3, 9, and 24 hpi and documented the behavior of the associated ECs (pocketing) over a high number of arrested CTCs (Figure 5I), over time, and in dependence of the blood flow profiles. Interestingly, in normal flow conditions, injected CTCs that are fully intravascular are rapidly (≈ 3 hpi) accompanied by EC pocketing, which drives successful extravasation of TCs (Figure 5J). On the contrary, reduced flow significantly delays the pocketing behavior of ECs (≈ 9 hpi), impairing efficient extravasation of intravascular TCs (Figure 5K), suggesting that blood flow drives endothelial remodeling.

Although the flow profiles of the zebrafish embryo, and of blood capillaries, is characterized by very low Reynolds number, and are thus mostly laminar, we next wondered whether arrested TCs would significantly impact resulting flow profiles. We injected 100-nm fluorescent beads in the zebrafish vasculature (in addition to CTCs) and performed instantaneous high-speed confocal microscopy (100 fps) for probing flow profiles at high spatiotemporal resolution (Figure 5L). We performed individual track analysis of flowing beads, before and after the position of arrested TCs. Quantification of the tracks' straightness (1 = straight track) and velocities demonstrate that flow profiles are laminar (straightness ~ 1 , velocity ~ 400 $\mu\text{m/s}$) when reaching arrested TCs. In non-occluded vessels, flow profiles remain laminar, with no impact on flow velocity, as expected from our numerical simulations (Figures 5L and S6A). Indeed, all the streamlines follow the imposed flow direction and did not follow chaotic streamlines. In partially occluded vessels, flow profiles remain laminar, with a slight impact on flow velocity (Figure S6B). In occluded vessels, flow profiles reaching arrested CTCs are laminar (straightness ~ 1). In addition, we precisely quantified the position of arrested TCs in relation to the first fully perfused vessel: on average, arrested TCs are only separated by < 2 μm from the first flow-bearing vessel, suggesting that ECs close to arrested TCs are still exposed to laminar flow profiles (straightness ~ 1 , velocity ~ 300 $\mu\text{m/s}$) (Figure S6C). Thus, this analysis demonstrates that arrested TCs only deviate established laminar

vehicle- or drug-treated embryos, through heatmapping. (C and F) Quantification of the number of arrested CTCs per embryo as well as the ratio of arrested CTCs per region in vehicle- or drug-treated embryos, 3 hpi. Data normalized to vehicle AVJ mean ratio. (G and I) Representative images of TCs (red) in the CP (green) of 24 hpi vehicle- or drug-treated embryos are shown. 3D reconstruction and scheme of the boxed region is provided. (H and J) Quantification of the number and location of intra- and extravascular TCs in the CP of 24 hpi vehicle- or drug-treated embryos, through heatmapping and histograms. (K) Experimental workflow and CLEM analysis of 24 hpi vehicle- or lidocain-treated embryos is used for further assessing the vascular location of TCs (yellow stars) intravascular (red) or extravascular (blue) (see also Video S12).

Values are mean \pm SD. * $p < 0.05$, ** $p < 0.01$, *** $p < 0.0001$.



(legend on next page)

flows present in the vasculature. When arrested CTCs occlude the vessel, laminar flows remain in very close proximity to ECs facing arrested CTCs.

We then wondered whether this flow-dependent phenomenon could be reproduced *in vitro* and set out a microfluidic experiment where flow (with or without TCs) is perfused on a monolayer of ECs (HUVECs). Interestingly, stimulating ECs with a laminar flow of 400 $\mu\text{m/s}$ is sufficient to induce a significant protrusive activity of their dorsal surface, which we probed upon expression of a CAG-EGFP construct tagged to the plasma membrane (Figure 6A; Video S15). Similarly, the dorsal surface of ECs stimulated over 16 hr with a laminar flow of 400 $\mu\text{m/s}$ displayed characteristic protrusive structures (filopodia and/or microvilli) (Figure 6B). We then perfused CTCs and probed resulting flow profiles around arrested TCs using 100-nm fluorescent beads and high-speed imaging. As we had observed in the zebrafish embryo, arrested TCs did not drastically perturb flow profiles, but rather only deviated established laminar flows where streamlines follow the imposed flow direction and did not follow chaotic motion (Figure S6C). According to this result, CTCs were perfused over a monolayer of ECs for 10 min and incubated 16 hr under perfusion (or not, laminar flow of 400 $\mu\text{m/s}$) before assessing the behavior of ECs. We observed that flow stimulated the transmigration of TCs. Interestingly, TCs that transmigrated through the HUVEC monolayer were mostly engulfed by ECs, visualized with confocal and scanning electron microscopy, mimicking the pocketing phenomenon we had observed *in vivo* (Figures 6D and 6E). As a consequence, TCs that successfully transmigrated in the absence of flow were rarely surrounded by ECs, suggesting that they crossed the monolayer by diapedesis. These results demonstrate that the extravasation of CTCs occurs via indoctrination of the associated endothelium, and that flow forces are essential for maintaining the remodeling abilities of the vasculature.

Micrometastases Develop from Mouse Brain Capillaries with Reduced Flow Profiles

We next investigated whether blood flow forces could explain the location of successful extravasation and micrometastasis

formation in another model, the mouse brain. We used our intravital imaging setup (Kienast et al., 2010) to quantify the vascular arrest, extravasation, and growth in the mouse brain after intracardiac injection of highly metastatic TCs (Figure 7A). We analyzed a high number of TCs, from several cell lines, that successfully mastered all steps of brain metastatic cascade in brain microvessels. We measured the associated blood flow velocities of these vessels, and compared them with flow velocities within blood vessels where arrest and extravasation of CTCs never occurred (Figure 7B). Strikingly, the mean flow velocity in metastasis-proficient vessels was $628 \pm 46 \mu\text{m/s}$, which is very close to the permissive flow values we had identified in the zebrafish embryo. In contrast, mean flow velocity of metastasis-deficient vessels was much higher ($5,880 \pm 716 \mu\text{m/s}$). While vessel diameter very likely impacts arrest of CTCs in synergy with permissive flow profiles, additional data suggest that arrested CTCs preserve a mild plasma flow, allowing dextran perfusion, while being in close proximity ($<10 \mu\text{m}$) to vessels perfused with laminar flows (Figures S7A–S7D). Together, these data suggest that flow-mediated arrest of CTCs could be a new important and additional determinant of tumor metastasis.

Similar to the zebrafish embryo experiments, we performed intravital CLEM (Karreman et al., 2016a, 2016b) and investigated whether ECs were also influenced by arrested CTCs in the mouse brain. We thus conducted intracardiac injections of Jimt1 cells and recorded the position of arrested CTCs only 3 days post-injection, where most of the CTCs are still intravascular (Figure 7C). This enabled us to document the ultrastructure of the arrested TC (Figures 7C and 7D), of its associated vessel (Figures 7C and 7D), and of neighboring vessels, where no CTC could be observed (Figures 7C and 7E). Blood vessels where no arrested CTC could be observed displayed a smooth vascular wall (Figure 7E). However, ECs from the vessel containing an arrested CTC displayed a remodeling phenotype in close proximity to the arrested cell (Figure 7D). Indeed, multiple ECs could be observed protruding within the vessel lumen, establishing contacts with other cells of the vessel wall, and enwrapping the arrested TC while maintaining a lumenized vessel. These results obtained in the context of brain metastasis (BM) in the

Figure 5. Extravasation of CTCs Occurs via Flow-Dependent Endothelial Remodeling

- (A) Experimental workflow.
- (B) Extracted z projection image from 3D time-lapse analysis of the behavior of arrested TCs (red) in the CP vasculature (green) over a period of 15 hr (see also Video S13).
- (C) Multiple sequential images, over a period of 800 min, of the region boxed in (B) are displayed and commented (yellow arrowheads point to the location of the associated comment, left panel).
- (D) Multiple sequential images, over a period of 150 min, of the region boxed in (B) are displayed and commented (yellow arrowheads point to the location of the associated comment).
- (E) Experimental workflow and CLEM analysis of a 9-hpi vehicle-treated embryo. Extracted images of confocal analysis of extravasating TCs (red) at 9 hpi is performed.
- (F) Transmission electron microscopy (TEM) image of the region of interest boxed in (E), retrieved in the electron microscopy volume. A representative section is shown and color-coded for TCs (red) and vascular lumen (green) (see also Video S14).
- (G) 3D reconstruction of the serial section TEM performed over the entire regions of interest, depicting TCs (red) and associated ECs (green) (see also Video S14).
- (H) Electron tomography image extracted from 3D reconstruction over the boxed region in (F) (TC, red; ECs, green) (see also Video S14).
- (I) Representative images of TCs (red) and the associated vasculature (green) in 9 hpi embryos are shown.
- (J and K) Quantification and kinetic analysis of the mean number of events over time for vehicle- and lidocaine-treated embryos. The number of events (intravascular, pocketing, and extravascular) was quantified at 3, 9, and 24 hpi.
- (L) Experimental workflow and idealized representation (left). Embryos are injected with CTCs and 100-nm beads and imaged at high speed, before single-particle tracking analysis (middle). Corresponding quantification of tracks' straightness and velocity in three scenarios (open, partially closed, and closed) and *in silico* representation of laminar flow around arrested tumor cell (right).

Values are mean \pm SD. *p < 0.05. ns, not significant.

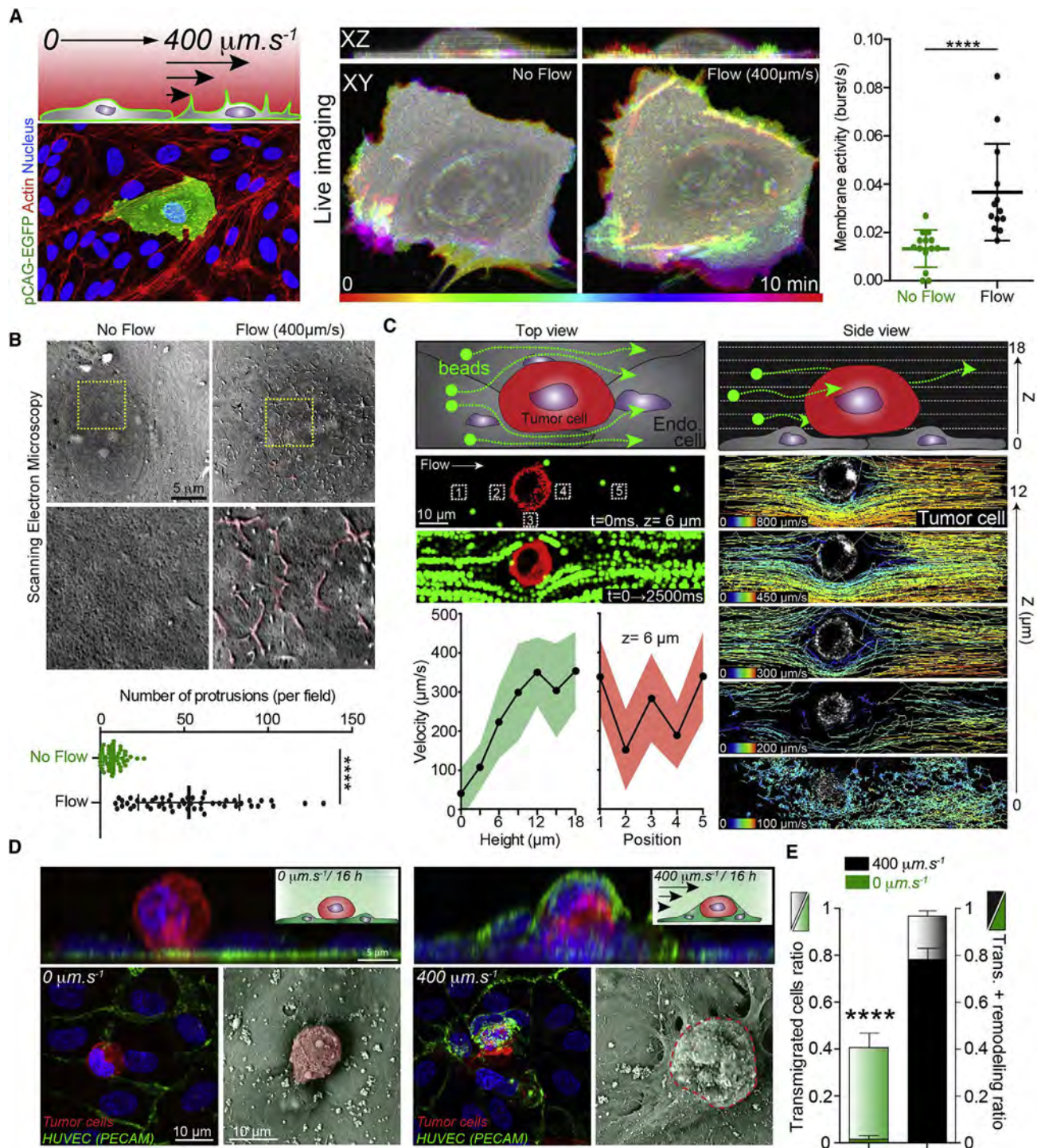


Figure 6. Laminar Flow Stimulates the Protrusive and Remodeling Activity of ECs

(A) Experimental workflow and representative image of transfected HUVECs. Representative time projection images of pCAG-EGFP expressing HUVECs in flow and no flow conditions, and quantification of the number of protrusion over time (see Video S15).

(B) SEM images and quantification showing the number of protrusion in flow versus no flow condition (16-hr treatment).

(C) Fluorescent bead (100 nm) perfusion over arrested tumor cells in the microfluidic channels. Single-particle tracking analysis from high-speed confocal acquisition at different heights (z step) (right) and quantifications (left).

(D) Immunostaining and SEM representative images of TCs (LifeAct, red) arrested on a monolayer of HUVECs (PECAM, green) is shown, in two flow conditions (0 and 400/s).

(E) Quantification of the number of transmigrated TCs and of transmigrated TCs with remodeled HUVECs.

Values are mean \pm SD. ***p < 0.0001.

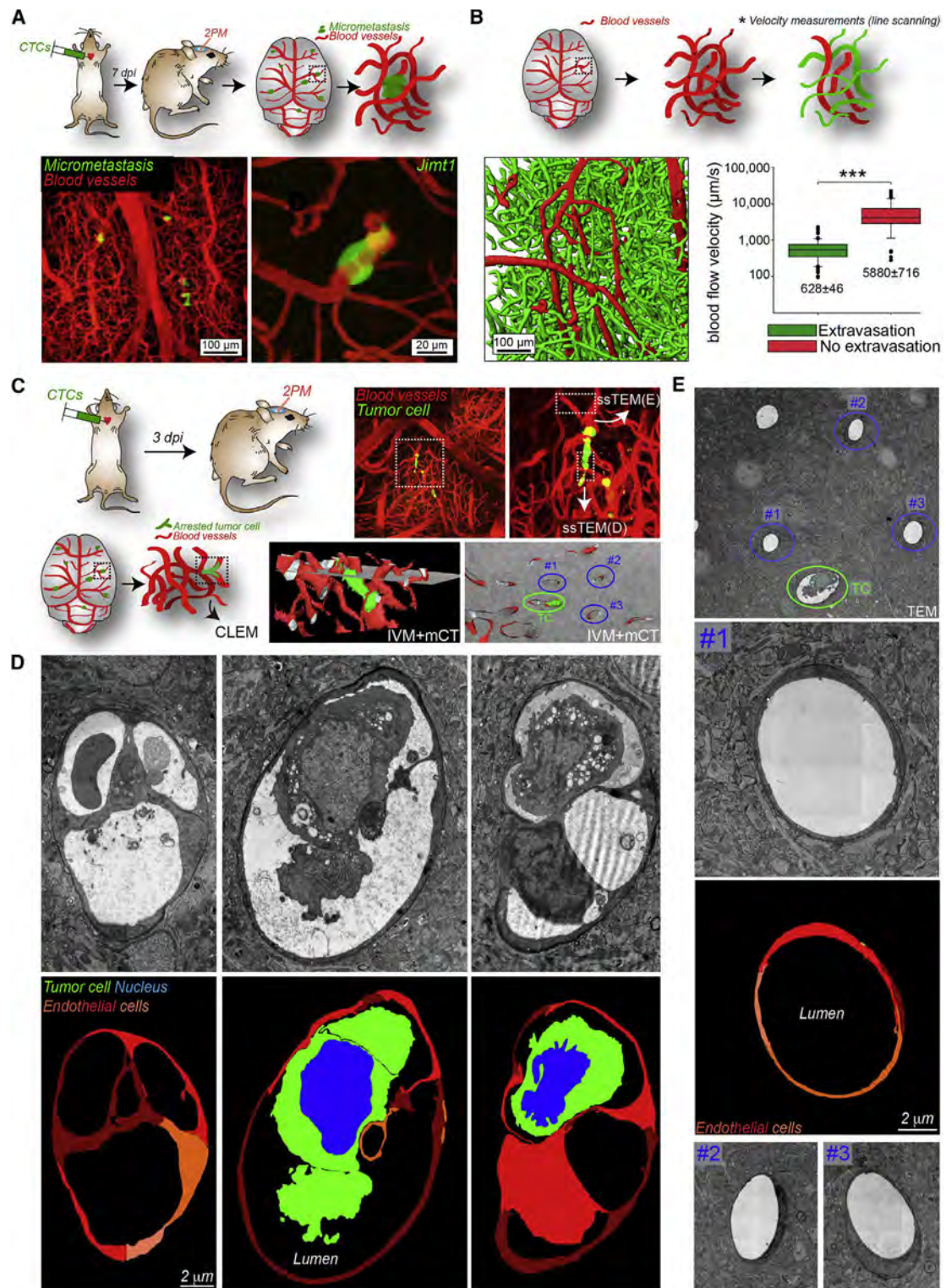


Figure 7. Permissive Flow Profiles Favor Formation of Micrometastasis in the Mouse Brain

(A) Experimental workflow and representative images of micrometastases in 7 days post-infection (dpi) mice injected with Jimt1-GFP cells (2PM, two-photon microscopy).

(B) Experimental workflow and 3D reconstruction of representative vascular network of the healthy brain. Quantification of the mean blood flow velocity in brain capillary with a diameter of 5–10 μm (highlighted in green, where extravasation preferentially takes place) and with higher diameter (highlighted in red, where extravasation is not expected).

(legend continued on next page)

mouse suggest that permissive flow profile is a very relevant mechanism driving the arrest of CTCs, leading to micrometastasis growth. In addition, the observation of early vascular remodeling in the presence of arrested CTCs, which are surrounded by plasma and laminar flows (Figures S7A–S7C), further suggests an active reaction of the endothelium to arrested cancer cells. These observations made in mouse cerebral capillaries speak for very similar mechanisms to what we have observed in zebrafish.

Blood Perfusion Controls the Location of Human Brain Metastasis

We next investigated whether blood flow perfusion would control the location of BM in humans. For this purpose, we analyzed a randomly selected cohort of 100 patients with BM ($n = 580$) in the supratentorial region of the brain (Figure 8A). The BM of each patient were segmented on contrast-enhanced T1-weighted imaging and the sum mask of all patients (Figure 8B) was co-registered with a computed tomography perfusion atlas of a healthy cohort (Figure 8C). We then performed a voxel-wise comparison of regions containing BM (BM+) and those who did not (BM−) (Figure 8D). Strikingly, BM preferably develop in regions with lower cerebral blood flow ($51 \pm 36\text{--}61$ versus $58 \pm 41\text{--}76 \text{ mL}/100 \text{ g}/\text{min}$, $p < 0.001$) and higher mean transit time ($4.6 \pm 4.3\text{--}5.1$ versus $4.5 \pm 4.2\text{--}5.0 \text{ s}$, $p < 0.001$) (Figures 8C and 8D). These results indicated that occurrence of BM is favored in brain regions with low perfusion, further demonstrating that blood flow patterns are key determinants of metastatic outgrowth.

DISCUSSION

In this work, we have unraveled for the first time the contribution of flow forces *in vivo* on mediating arrest, adhesion, and successful extravasation of CTCs, preceding metastatic outgrowth. Using the multiple advantages of the zebrafish embryo, we have identified a threshold of hemodynamic profiles ($400\text{--}600 \mu\text{m}/\text{s}$) that participates in the stable arrest of CTCs in permissive vascular regions, a prerequisite for metastasis formation (Figure 8E). These values were further confirmed *in vitro* and *in silico* using a combination of microfluidic and 3D flow simulation approaches, which were developed upon accurate *in vivo* measurements of hemodynamic forces. We have shown that these permissive flow profiles promote the formation of transient protrusions, establishing integrin-dependent adhesion of CTCs to the endothelium. This fast and weak adhesion is then quickly stabilized (less than a minute *in vitro*) to reach adhesion forces exceeding the shear forces generated by such permissive flow values. This process is impaired in regions with high shear values, where forces are significantly higher than the initial adhesion forces and CTCs are able to produce. Reduced flow forces favor arrest and metastasis in the zebrafish embryo, but also in

mouse brain capillaries. Importantly, we made similar observations in humans, where a significant reduction of blood perfusion is observed in pro-metastatic brain regions. Once arrest of CTCs within blood vessels is consolidated, TCs engage in a second step where blood flow remains essential (Figure 8E). Indeed, we have observed that blood flow is required to stimulate endothelial remodeling and subsequent pro-metastatic extravasation. While reduced flow forces allow the arrest of CTCs, they impede the remodeling potential of ECs, and significantly impair extravasation of arrested TCs. Interestingly, laminar and plasma flows are preserved in regions displaying strong occlusion by arrested TCs. Thus, pro-metastatic vascular regions are characterized by intermediate flow profiles that are sufficiently low (or reduced) to favor the arrest of CTCs, and sufficiently high to stimulate endothelial remodeling, which could be a fundamental mechanism driving metastasis formation.

While much attention has been given to the contribution of biomechanics to tumor growth and tumor invasion (Kai et al., 2016; Wirtz et al., 2011), only little evidence suggests that biomechanics could also modulate one of the most important steps of tumor progression, namely extravasation and metastatic outgrowth. However, CTCs are shed in the blood circulation and must survive in a very hostile environment, where blood shear forces could induce cell-cycle arrest (Chang et al., 2008) or even necrotic cell death (Regmi et al., 2017). In addition, CTCs frequently collide with other components of the blood and the vascular wall, reaching capillary-like vascular regions that often appear occlusive (Gassmann et al., 2009; Headley et al., 2016; Kienast et al., 2010). Size-mediated arrest of CTCs in capillaries occurs in multiple organs, such as the lung, liver, and brain (Azevedo et al., 2015). Moreover, cellular and nuclear rigidity (Harada et al., 2014) and integrity (Denais et al., 2016; Irianto et al., 2016) were recently shown to be key drivers of tumor invasion and metastasis. Our work suggests that, in addition to physical occlusion, permissive flows are sufficient to facilitate arrest of CTCs. Selectin-dependent arrest of CTCs has been observed independently of size restriction *in vivo* (Heidemann et al., 2014). In the zebrafish embryo, 50% of arrested TCs did so in vascular regions where the diameter of the vessel exceeds the diameter of TCs, excluding exclusive occlusion mechanisms. In addition, full occlusion of mouse brain capillaries is rarely observed, suggesting that blood flow or physical constraints, while they could impact synergistically, are sufficient to promote the arrest of CTCs. Further work is required to investigate the mutual contribution of cell stiffness/size, vascular architecture, and blood flow as determinant factors in arrest and extravasation of CTCs. Recent work demonstrates that clusters of CTCs, whose arrest would be favored by physical occlusion, are more potent in driving tumor metastasis (Aceto et al., 2014; Cheung and Ewald, 2016; Cheung et al., 2016). Also, we frequently observed a remarkable behavior of arrested CTCs that did not occlude the blood vessel: they crawl counter-flow along the endothelium in perfused

(C) Experimental workflow of intravital CLEM of 3 dpi arrested JIMT1br3 cells. Maximum z projections showing an arrested JIMT1br3 cell (GFP, green) and the associated vasculature (TRITC-dextran, red). Merged images of the micro-computed X-ray tomography (mCT) and the intravital imaging (IVM) volume. Vessels containing the TC is circled in green (TC) and dissected using serial section TEM in (D), normal neighboring vessels are circled in blue (nos. 1–3) and dissected in (E).

(D) Serial section TEM images and segmentation of the tumor cell (green), its nucleus (blue), and ECs (red colors) are shown. Three different z heights are provided.

(E) TEM images and segmentation of the ECs (red colors) of normal neighboring vessels are shown.

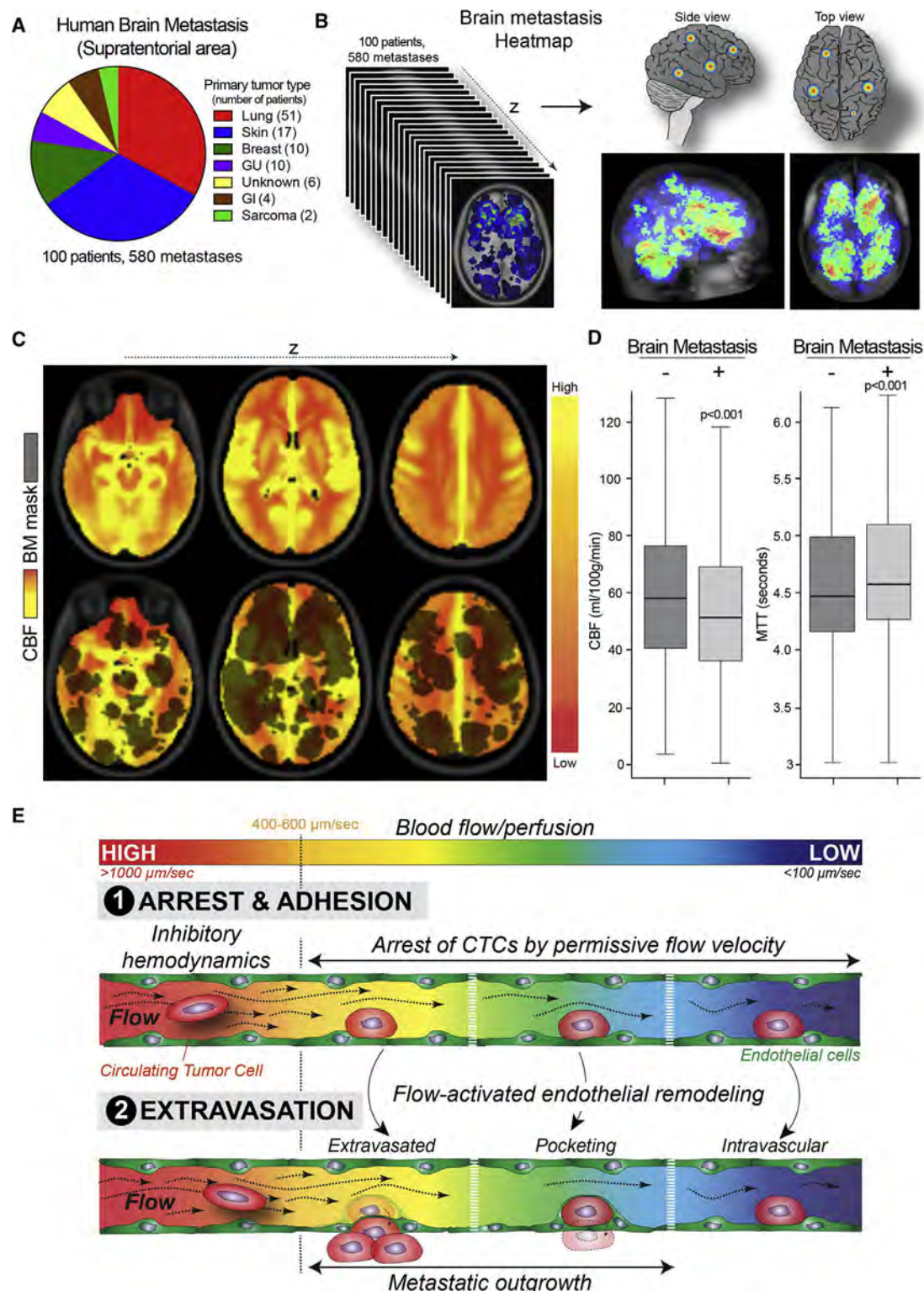


Figure 8. Blood Perfusion Controls the Location of Human brain metastasis (BMs)

(A) Number of BMs and number of patients are provided for the entire cohort.

(B and C) BM of the 100 patients were segmented semi-manually and co-registered on a CT perfusion mask from a control brain template consisting of 107 healthy patients. The cerebral blood flow (CBF) mask is displayed with red indicating a lower CBF and yellow a higher CBF. The cumulative BM is overlaid to the perfusion mask.

(D) Mean CBF and MTT (mean transit time) is displayed for the brain metastases (BM+) and the corresponding area without any BM (BM-).

(legend continued on next page)

vessels and tend to cluster intravascularly before extravasating (Video S4). This process occurs without compromising blood flow and suggests that TCs establish a cell-cell contact that could favor successful extravasation.

A fundamental observation made in our study is that reduced, or drop, in blood flow favors arrest of CTCs in multiple organisms (zebrafish, mouse, and human), preceding metastatic outgrowth. Indeed, we first identified a threshold flow velocity value of 400–600 $\mu\text{m/s}$, which favors the arrest of CTCs in the vasculature of the zebrafish embryo. Using intravital imaging and flow profiling in the mouse brain, we confirmed that brain capillaries perfused with low flow velocities (around 600 $\mu\text{m/s}$) are favorable to extravasation and outgrowth of TCs. Finally, we analyzed a cohort of 100 patients with BM, and observed that BM preferably develop in regions with lower cerebral blood perfusion. These results obtained in various organisms indicate that occurrence of metastasis is favored in vascular regions with reduced perfusion, further demonstrating that blood flow patterns are key determinants of metastatic outgrowth in the brain. Interestingly, human BM had been shown to occur preferentially in vascular border zones as well as in the gray and white matter junction (Hwang et al., 1996). These regions are located at the most distal part of the arterial tree and display sudden drops in vessel diameter, blood pressure, and blood flow, making them very susceptible to infarction and ischemia. Our results further demonstrate that such vascular networks are favorable environments for metastatic extravasation.

Another key observation from our work is that reduced flow promotes arrest of CTCs by favoring the establishment of intravascular TC-EC adhesions. Indeed, arrest of CTCs can be observed in anterior regions of the DA, when flow values are decreased and depletion of ITGB1 drastically impedes the arrest of CTCs. We identified an initial TC-EC adhesion force of 80 pN, likely mediated by a few integrin molecules. While ITGB1 favors TC protrusion into the subendothelial matrix, thereby favoring metastatic outgrowth (Chen et al., 2016a), integrin-mediated arrest of CTCs could be favored by interaction between ITGB1 and endothelial adhesion molecules, or extracellular matrix molecules localized on the luminal side of the vascular wall. Indeed, *in vitro* data suggest that CTCs hijack the leukocyte adhesion machinery and arrest using $\alpha\beta 1$ integrins to bind the VCAM-1 receptor present at the surface of ECs (Klemke et al., 2007). Furthermore, *in vivo* imaging of liver metastasis has demonstrated that, although lumen occlusion by CTCs is rather frequent, it does not account fully for the efficient extravasation, as blocking adhesion with ITGB1-blocking antibody significantly impaired stable cell arrest of CTCs (Gassmann et al., 2009). CTCs can escape mechanical entrapment in the lungs (Glinskii et al., 2005), and adhesion-mediated arrest of CTCs has been observed without signs of mechanical entrapment (Enns et al., 2004). This suggests that, although capillary size can stop CTCs, active adhesion between CTCs and the vascular wall is

required for efficient extravasation, and subsequent metastasis. Even if we have not directly visualized this in our experiments, we cannot exclude that CTCs undergo rolling, which could activate ITGB1. Further work will be required to investigate whether arrest of CTCs follows rules that are commonly used by immune cells before extravasation.

An important observation of our work is the route used by arrested CTCs to undergo extravasation. Indeed, in most of the cases, extravasation of CTCs engages massive endothelial remodeling, which encapsulates single or clusters of arrested CTCs. This phenomenon has been observed during extravasation of neutrophils and allows the vessel to reduce vascular permeability (Petri et al., 2011). We observed that pocketing or encapsulation of arrested CTCs occurs by the formation of endothelial domes, reminiscent of the ones observed for extravasation of neutrophils (Phillipson et al., 2008) and of leukocytes (Carman and Springer, 2004), which are tightly connected through EC-EC junctions (Figure 6). Recent work performed in zebrafish embryos has shown that stem cells use similar mechanisms to undergo extravasation (Allen et al., 2017). Interestingly, using intravital CLEM technology, we observed that vascular regions of arrested TCs in the mouse brain also engage massive endothelial remodeling in vessels with permissive flow profiles, suggesting that it could drive extravasation of brain metastatic cells. This reinforces the view that CTCs require a very active contribution of the endothelium to perform transmigration of the vascular wall, and challenges the classical idea that CTCs mostly use diapedesis for extravasation (Heyder et al., 2002; Khuon et al., 2010; Tremblay et al., 2008). Along this line, arrested CTCs have been observed to proliferate when attached to the luminal wall of lung blood vessels, leading to intraluminal metastatic foci that eventually passively rupture the endothelial barrier (Al-Mehdi et al., 2000). Recent work suggests that arrested CTCs are also capable of driving TC-mediated necrosis of EC and subsequent metastasis (Strilic et al., 2016), further suggesting that the vascular wall is a key contributor to efficient metastatic outgrowth. While endothelium remodeling around arrested CTCs has been observed *in vivo* in the past (Lapis et al., 1988; Stoletov et al., 2010), its importance during metastatic extravasation is still not fully appreciated (Lambert et al., 2017). Interestingly, past work has shown that cerebral microvasculature is capable of removing blood clots by a process called angiophagy, which is strikingly similar to the one we describe here. We now provide evidence that proximal blood flow, which remains laminar, actively regulates such behavior thereby promoting extravasation of CTCs (Grutzendler et al., 2014; Lam et al., 2010). Indeed, flow forces increase both *in vivo* pocketing and *in vitro* endothelial dome formation. As blood flow is known to be a key regulator of vascular homeostasis (Franco et al., 2015; Gebala et al., 2016) and angiogenesis (Goetz et al., 2014; Potente et al., 2011), it is likely that it is required during extravasation by maintaining its remodeling behavior.

(E) Graphical abstract of our study: we identified a threshold of flow velocities that are permissive for the arrest of CTCs, a prerequisite for metastasis formation. Below blood flow velocities of 400–600 $\mu\text{m/s}$, arrest and adhesion of CTCs to the endothelium is favored. This is the case *in vitro* (microfluidics), in zebrafish embryos and in mouse brain capillaries. Similar results are obtained in humans where a significant reduction of blood perfusion is observed in pro-metastatic regions. In a second step, blood flow is required to stimulate endothelial remodeling and subsequent pro-metastatic extravasation. However, although low flow allows arrest of CTCs, it impairs extravasation of arrested TCs. Thus, pro-metastatic vascular regions are characterized by flow profiles that are sufficiently low (or reduced) to favor the arrest of CTCs, and sufficiently high to stimulate endothelial remodeling.

In conclusion, we provide the first *in vivo* demonstration that blood flow, which carries tumor-shed CTCs, actively participates in both stable arrest and extravasation of CTCs, preceding metastatic outgrowth. Our work identified pre-metastatic vascular regions that are characterized by laminar flow profiles, which are permissive for the arrest of CTCs and stimulate endothelial remodeling. Our current work aims to identify the molecular mechanisms that are driven by blood flow to encapsulate arrested CTCs. This work suggests that therapies that target endothelial remodeling might be useful to impede extravasation, and subsequent outgrowth, of metastatic cells.

STAR METHODS

Detailed methods are provided in the online version of this paper and include the following:

- **KEY RESOURCES TABLE**
- **CONTACT FOR REAGENT AND RESOURCE SHARING**
- **EXPERIMENTAL MODEL AND SUBJECT DETAILS**
 - D2A1 Cells (CVCL_0190). Mouse Mammary Carcinoma (BALB/c female)
 - JIMT-1 BR3 Cells (CVCL_2077). Human Ductal Breast Carcinoma (Female) Highly Metastatic in the Brain
 - 1675 Cells (WM115, CVCL_0040). Human Melanoma (Female)
 - A431 Cells (CRL_1555). Human Skin Epidermoid Carcinoma (Female)
 - 4T1 Cells (CVCL_0125). Mouse Mammary Gland Carcinoma (BALB/c Female)
 - ZMEL1 Cells
 - Human Umbilical Vein Endothelial Cells (HUVECs)
 - Zebrafish Embryos
 - Mice
 - Human Patients
- **METHODS DETAILS**
 - Cell Culture and siRNA-Mediated Knock-down
 - Zebrafish Handling
 - Pharmacological Treatments
 - High-Speed Microscopy for Pacemaker Activity and Blood Flow Profiling
 - Intravascular Injection of CTCs in the Zebrafish Embryo
 - Confocal Imaging and Analysis
 - Heatmaps
 - Sample Preparation for Electronic Microscopy of Zebrafish Embryos
 - Microfluidic Experiments
 - Immunofluorescent Staining in the Microfluidic Channels
 - HUVEC Transfection and Live Imaging
 - High-Speed Microscopy for Blood Flow Profiling around Arrested Tumor Cells
 - Scanning Electron Microscopy on HUVEC and D2A1 in Microchannels
 - Optical Tweezers
 - Mice Experiments and Surgical Procedures
 - *In Vivo* Multiphoton Laser Scanning Microscopy (MPLSM)

- Blood Flow Velocity Measurements and Visualization of MPLSM Data
- Western Blotting
- *In Vitro* Migration and Adhesion Assays
- Mathematical Modeling and Numerical Methods for *In Silico* Experiments
- Patient Blood Collection for CTC Size Analysis
- Brain Metastasis and Blood Flow Perfusion Study
- **QUANTIFICATION AND STATISTICAL ANALYSIS**
 - Statistical Tests
 - Zebrafish Experiments
 - Mouse Experiments
 - Microfluidic and Other *In Vitro* Experiments
 - Patient's MRI for Brain Metastatic Study
- **DATA AND SOFTWARE AVAILABILITY**

SUPPLEMENTAL INFORMATION

Supplemental Information includes 7 figures and 15 videos and can be found with this article online at <https://doi.org/10.1016/j.devcel.2018.02.015>.

ACKNOWLEDGMENTS

We thank all members of the Goetz Lab for helpful discussions. We are grateful to Tsukasa Shibue (MIT) and Bob Weinberg (MIT) for providing D2A1 cells and to Richard White (MSKCC) for providing the ZMEL1 cell line. We are very much grateful to Francesca Peri (EMBL) and Kerstin Richter (EMBL) for providing zebrafish embryos. We thank Anita Michel (INSERM U949) and Fabienne Proamer (INSERM U949) from EFS imaging facility for electronic microscopy. We thank Yohan Gerber for help with the Nifedipine and Norepinephrine experiments. We thank Mourad Ismail for the fruitful discussions on flow simulation and Marie Houillon for participating in the simulation setup. We thank Martin Schrob (EMBL) for assistance with electron tomography. We thank Gertraud Orend, Vincent Hyenne (Goetz Lab), and Michaël Poirier for critical reading of the manuscript. We thank Raphaël Gaudin for providing access to the Imaris software. This work has been funded by Plan Cancer (OptoMetaTrap, to J.G. and S.H.) and CNRS IMAG'IN (to S.H., J.G., and C.P.), by the French National Cancer Institute (INCa, MetaCLEM, to J.G and S.H.), and by institutional funds from INSERM and University of Strasbourg. C.P. and V.C. were supported by the Center of Modeling and Simulation of Strasbourg (CEMOSIS), ANR MONU-Vivabrain, and the Labex IRMIA. G.F. is supported by La Ligue Contre le Cancer. N.O. is supported by Plan Cancer. L.M. is supported by an INSERM/Région Alsace PhD fellowship. A.S.A. and G.A. are supported by FRM (Fondation pour la Recherche Médicale). M.A.K. is supported by an EMBL Interdisciplinary Post-doctoral fellowship (EIPOD) under Marie Curie Actions (COFUND).

AUTHOR CONTRIBUTIONS

G.F. performed experiments and analysis, and wrote the initial version of the manuscript and figures. N.O. performed experiments and analysis and participated in manuscript writing and figure editing. A.S.A. initiated the project through experiments and analysis that set the foundations of the study. G.A. developed the heatmapping protocol and contributed to blood flow analysis, as well as processing of EM images. L.M. and O.L. participated in the mouse experiments and statistical analysis. M.A.K. and Y.S. performed EM of the mouse BM. G.S. and F.W. performed 2PSEM imaging of the mouse BM. C.H. and K.P. isolated and characterized human CTCs. N.F. performed EM in the zebrafish embryo. M.J.G.L performed SEM analysis. V.C., G.D., T.M., F.D.H., and C.P. developed the flow simulation with input from G.F., S.H., and J.G.G. A.P., N.P., R.C., and S.B. contributed to analysis of the *in vitro* experiments. B.R. and M.A.K. performed mCT experiments. A.K., S.S., T.S., J.F., M.G., and K.P. analyzed human brain metastases and blood perfusion patterns on imaging. S.H. supervised the study and performed OT experiments and analysis. J.G. conceived the project, supervised the study, performed experiments and analysis, and wrote the paper with G.F., with input from N.O. and S.H.

DECLARATION OF INTERESTS

The authors declare no competing interest.

Received: August 31, 2017

Revised: January 5, 2018

Accepted: February 16, 2018

Published: April 9, 2018

REFERENCES

Abels, B., Klotz, E., Tomandl, B.F., Kloska, S.P., and Lell, M.M. (2010). Perfusion CT in acute ischemic stroke: a qualitative and quantitative comparison of deconvolution and maximum slope approach. *AJNR Am. J. Neuroradiol.* 31, 1690–1698.

Aceto, N., Bardia, A., Miyamoto, D.T., Donaldson, M.C., Wittner, B.S., Spencer, J.A., Yu, M., Pely, A., Engstrom, A., Zhu, H., et al. (2014). Circulating tumor cell clusters are oligoclonal precursors of breast cancer metastasis. *Cell* 158, 1110–1122.

Allen, T.A., Gracieux, D., Talib, M., Tokarz, D.A., Hensley, M.T., Cores, J., Vandergriff, A., Tang, J., de Andrade, J.B.M., Dinh, P.-U., et al. (2017). Angiopellosis as an alternative mechanism of cell extravasation. *Stem Cells* 35, 170–180.

Al-Mehdi, A.B., Tozawa, K., Fisher, A.B., Shientag, L., Lee, A., and Muschel, R.J. (2000). Intravascular origin of metastasis from the proliferation of endothelium-attached tumor cells: a new model for metastasis. *Nat. Med.* 6, 100–102.

Anton, H., Harlepp, S., Ramspacher, C., Wu, D., Monduc, F., Bhat, S., Liebling, M., Paoletti, C., Charvin, G., Freund, J.B., et al. (2013). Pulse propagation by a capacitive mechanism drives embryonic blood flow. *Development* 140, 4426–4434.

Azevedo, A.S., Follain, G., Pathabhiraman, S., Harlepp, S., and Goetz, J.G. (2015). Metastasis of circulating tumor cells: favorable soil or suitable biomechanics, or both? *Cell Adh. Migr.* 9, 345–356.

Brennan, C. (2005). Acetylcholine and calcium signalling regulates muscle fibre formation in the zebrafish embryo. *J. Cell Sci.* 118, 5181–5190.

Cameron, M.D., Schmidt, E.E., Kerkvliet, N., Nadkarni, K.V., Morris, V.L., Groom, A.C., Chambers, A.F., and MacDonald, I.C. (2000). Temporal progression of metastasis in lung: cell survival, dormancy, and location dependence of metastatic inefficiency. *Cancer Res.* 60, 2541–2546.

Carman, C.V., and Springer, T.A. (2004). A transmigratory cup in leukocyte diapedesis both through individual vascular endothelial cells and between them. *J. Cell Biol.* 167, 377–388.

Chambers, A.F., Groom, A.C., and MacDonald, I.C. (2002). Dissemination and growth of cancer cells in metastatic sites. *Nat. Rev. Cancer* 2, 563–572.

Chang, S.-F., Chang, C.A., Lee, D.-Y., Lee, P.-L., Yeh, Y.-M., Yeh, C.-R., Cheng, C.-K., Chien, S., and Chiu, J.-J. (2008). Tumor cell cycle arrest induced by shear stress: roles of integrins and Smad. *Proc. Natl. Acad. Sci. USA* 105, 3927–3932.

Chauhan, V.P., Martin, J.D., Liu, H., Lacorre, D.A., Jain, S.R., Kozin, S.V., Stylianopoulos, T., Mousa, A.S., Han, X., Adstamongkonkul, P., et al. (2013). Angiotensin inhibition enhances drug delivery and potentiates chemotherapy by decompressing tumour blood vessels. *Nat. Commun.* 4, 2516.

Chen, M.B., Lamar, J.M., Li, R., Hynes, R.O., and Kamm, R.D. (2016a). Elucidation of the roles of tumor integrin β 1 in the extravasation stage of the metastasis cascade. *Cancer Res.* 76, 2513–2524.

Chen, Q., Boire, A., Jin, X., Valiente, M., Er, E.E., Lopez-Soto, A., Jacob, L.S., Patwa, R., Shah, H., Xu, K., et al. (2016b). Carcinoma-astrocyte gap junctions promote brain metastasis by cGAMP transfer. *Nature* 533, 493–498.

Cheung, K.J., and Ewald, A.J. (2016). A collective route to metastasis: seeding by tumor cell clusters. *Science* 352, 167–169.

Cheung, K.J., Padmanabhan, V., Silvestri, V., Schipper, K., Cohen, J.D., Fairchild, A.N., Gorin, M.A., Verdone, J.E., Pienta, K.J., Bader, J.S., et al. (2016). Polyclonal breast cancer metastases arise from collective dissemination of keratin 14-expressing tumor cell clusters. *Proc. Natl. Acad. Sci. USA* 113, E854–E863.

Chudziak, J., Burt, D.J., Mohan, S., Rothwell, D.G., Mesquita, B., Antonello, J., Dalby, S., Ayub, M., Priest, L., Carter, L., et al. (2016). Clinical evaluation of a novel microfluidic device for epitope-independent enrichment of circulating tumour cells in patients with small cell lung cancer. *Analyst* 141, 669–678.

Denais, C.M., Gilbert, R.M., Isermann, P., McGregor, A.L., te Lindert, M., Weigelin, B., Davidson, P.M., Friedl, P., Wolf, K., and Lammerding, J. (2016). Nuclear envelope rupture and repair during cancer cell migration. *Science* 352, 353–358.

Enns, A., Gassmann, P., Schlüter, K., Korb, T., Spiegel, H.-U., Senninger, N., and Haier, J. (2004). Integrins can directly mediate metastatic tumor cell adhesion within the liver sinusoids. *J. Gastrointest. Surg.* 8, 1049–1059, discussion 1060.

Feyen, L., Minnerup, J., Seifarth, H., Niederstadt, T., Heindel, W., and Kemmling, A. (2010). Standardization of dynamic whole-brain perfusion CT: A comprehensive database of regional perfusion parameters. Conference: Radiological Society of North America 2010 Scientific Assembly and Annual Meeting 189–220.

Follain, G., Mercier, L., Osmani, N., Harlepp, S., and Goetz, J.G. (2017). Seeing is believing – multi-scale spatio-temporal imaging towards *in vivo* cell biology. *J. Cell Sci.* 130, 23–38.

Franco, C.A., Jones, M.L., Bernabeu, M.O., Geudens, I., Mathivet, T., Rosa, A., Lopes, F.M., Lima, A.P., Ragab, A., Collins, R.T., et al. (2015). Dynamic endothelial cell rearrangements drive developmental vessel regression. *PLoS Biol.* 13, e1002125.

Gassmann, P., Hemping-Bovenkerk, A., Mees, S.T., and Haier, J. (2009). Metastatic tumor cell arrest in the liver-lumen occlusion and specific adhesion are not exclusive. *Int. J. Colorectal Dis.* 24, 851–858.

Gebala, V., Collins, R., Geudens, I., Phng, L.-K., and Gerhardt, H. (2016). Blood flow drives lumen formation by inverse membrane blebbing during angiogenesis *in vivo*. *Nat. Cell Biol.* 18, 443–450.

Glinskii, O.V., Huxley, V.H., Glinsky, G.V., Pienta, K.J., Raz, A., and Glinsky, V.V. (2005). Mechanical entrapment is insufficient and intercellular adhesion is essential for metastatic cell arrest in distant organs. *Neoplasia* 7, 522–527.

Goetz, J.G., Steed, E., Ferreira, R.R., Roth, S., Ramspacher, C., Boselli, F., Charvin, G., Liebling, M., Wyart, C., Schwab, Y., et al. (2014). Endothelial cilia mediate low flow sensing during zebrafish vascular development. *Cell Rep.* 6, 799–808.

Grutzendler, J., Murikinati, S., Hiner, B., Ji, L., Lam, C.K., Yoo, T., Gupta, S., Hafler, B.P., Adelman, R.A., Yuan, P., et al. (2014). Angiophagy prevents early embolus washout but recanalizes microvessels through embolus extravasation. *Sci. Transl. Med.* 6, 226ra31.

Harada, T., Swift, J., Irianto, J., Shin, J.-W., Spinler, K.R., Athirasala, A., Diegmiller, R., Dingal, P.C.D.P., Ivanovska, I.L., and Discher, D.E. (2014). Nuclear lamin stiffness is a barrier to 3D migration, but softness can limit survival. *J. Cell Biol.* 204, 669–682.

Harper, K.L., Sosa, M.S., Entenberg, D., Hosseini, H., Cheung, J.F., Nobre, R., Avivar-Valderas, A., Nagi, C., Girnius, N., Davis, R.J., et al. (2016). Mechanism of early dissemination and metastasis in Her2(+) mammary cancer. *Nature*. <https://doi.org/10.1038/nature20609>.

Headley, M.B., Bins, A., Nip, A., Roberts, E.W., Looney, M.R., Gerard, A., and Krummel, M.F. (2016). Visualization of immediate immune responses to pioneer metastatic cells in the lung. *Nature* 531, 513–517.

Heidemann, F., Schildt, A., Schmid, K., Bruns, O.T., Riecken, K., Jung, C., Ittrich, H., Wicklein, D., Reimer, R., Fehse, B., et al. (2014). Selectins mediate small cell lung cancer systemic metastasis. *PLoS One* 9, e92327.

Heyder, C., Gloria-Maercker, E., Entschladen, F., Hatzmann, W., Niggemann, B., Zanker, K.S., and Dittmar, T. (2002). Realtime visualization of tumor cell/endothelial cell interactions during transmigration across the endothelial barrier. *J. Cancer Res. Clin. Oncol.* 128, 533–538.

Hosseini, H., Obradović, M.M.S., Hoffmann, M., Harper, K.L., Sosa, M.S., Werner-Klein, M., Nanduri, L.K., Werno, C., Ehrl, C., Maneck, M., et al. (2016). Early dissemination seeds metastasis in breast cancer. *Nature*. <https://doi.org/10.1038/nature20785>.

Hvichia, G.E., Parveen, Z., Wagner, C., Janning, M., Quidde, J., Stein, A., Müller, V., Loges, S., Neves, R.P.L., Stoecklein, N.H., et al. (2016). A novel microfluidic platform for size and deformability based separation and the subsequent molecular characterization of viable circulating tumor cells. *Int. J. Cancer* 138, 2894–2904.

Hwang, T.L., Close, T.P., Grego, J.M., Brannon, W.L., and Gonzales, F. (1996). Predilection of brain metastasis in gray and white matter junction and vascular border zones. *Cancer* 77, 1551–1555.

Irianto, J., Xia, Y., Pfeifer, C.R., Athirasala, A., Ji, J., Alvey, C., Tewari, M., Bennett, R.R., Harding, S.M., Liu, A.J., et al. (2016). DNA damage follows repair factor depletion and portends genome variation in cancer cells after pore migration. *Curr. Biol.* <https://doi.org/10.1016/j.cub.2016.11.049>.

Kai, F., Laklai, H., and Weaver, V.M. (2016). Force matters: biomechanical regulation of cell invasion and migration in disease. *Trends Cell Biol.* 26, 486–497.

Karreman, M.A., Hyenne, V., Schwab, Y., and Goetz, J.G. (2016a). Intravital correlative microscopy: imaging life at the nanoscale. *Trends Cell Biol.* 26, 848–863.

Karreman, M.A., Mercier, L., Schieber, N.L., Solecki, G., Allio, G., Winkler, F., Ruthensteiner, B., Goetz, J.G., and Schwab, Y. (2016b). Fast and precise targeting of single tumor cells *in vivo* by multimodal correlative microscopy. *J. Cell Sci.* 129, 444–456.

Kemmling, A., Wersching, H., Berger, K., Knecht, S., Groden, C., and Nölte, I. (2012). Decomposing the Hounsfield unit: probabilistic segmentation of brain tissue in computed tomography. *Clin. Neuroradiol.* 22, 79–91.

Khuon, S., Liang, L., Dettman, R.W., Sporn, P.H.S., Wysolmerski, R.B., and Chew, T.-L. (2010). Myosin light chain kinase mediates transcellular intravasation of breast cancer cells through the underlying endothelial cells: a three-dimensional FRET study. *J. Cell Sci.* 123, 431–440.

Kienast, Y., von Baumgarten, L., Fuhrmann, M., Klinkert, W.E.F., Goldbrunner, R., Herms, J., and Winkler, F. (2010). Real-time imaging reveals the single steps of brain metastasis formation. *Nat. Med.* 16, 116–122.

Klemke, M., Weschenfelder, T., Konstandin, M.H., and Samstag, Y. (2007). High affinity interaction of integrin alpha4beta1 (VLA-4) and vascular cell adhesion molecule 1 (VCAM-1) enhances migration of human melanoma cells across activated endothelial cell layers. *J. Cell. Physiol.* 212, 368–374.

Labelle, M., Begum, S., and Hynes, R.O. (2014). Platelets guide the formation of early metastatic niches. *Proc. Natl. Acad. Sci. USA* 111, E3053–E3061.

Lam, C.K., Yoo, T., Hiner, B., Liu, Z., and Grutzendler, J. (2010). Embolus extravasation is an alternative mechanism for cerebral microvascular recanalization. *Nature* 465, 478–482.

Lambert, A.W., Pattabiraman, D.R., and Weinberg, R.A. (2017). Emerging biological principles of metastasis. *Cell* 168, 670–691.

Lapis, K., Paku, S., and Liotta, L.A. (1988). Endothelialization of embolized tumor cells during metastasis formation. *Clin. Exp. Metastasis* 6, 73–89.

Levental, K.R., Yu, H., Kass, L., Lakins, J.N., Egeblad, M., Erler, J.T., Fong, S.F.T., Csiszar, K., Giaccia, A., Weninger, W., et al. (2009). Matrix crosslinking forces tumor progression by enhancing integrin signaling. *Cell* 139, 891–906.

Luca, E.D., Zaccaria, G.M., Hadhoud, M., Rizzo, G., Ponzini, R., Morbiducci, U., and Santoro, M.M. (2014). ZebraBeat: a flexible platform for the analysis of the cardiac rate in zebrafish embryos. *Sci. Rep.* 4, 4898.

Luzzi, K.J., MacDonald, I.C., Schmidt, E.E., Kerkvliet, N., Morris, V.L., Chambers, A.F., and Groom, A.C. (1998). Multistep nature of metastatic inefficiency: dormancy of solitary cells after successful extravasation and limited survival of early micrometastases. *Am. J. Pathol.* 153, 865–873.

Magbanua, M.J.M., Pugia, M., Lee, J.S., Jabon, M., Wang, V., Gubens, M., Marfurt, K., Pence, J., Sidhu, H., Uzgiris, A., et al. (2015). A novel strategy for detection and enumeration of circulating rare cell populations in metastatic cancer patients using automated microfluidic filtration and multiplex immunoassay. *PLoS One* 10, e0141166.

Mouw, J.K., Yui, Y., Damiano, L., Bainer, R.O., Lakins, J.N., Acerbi, I., Ou, G., Wijekoon, A.C., Levental, K.R., Gilbert, P.M., et al. (2014). Tissue mechanics modulate microRNA-dependent PTEN expression to regulate malignant progression. *Nat. Med.* 20, 360–367.

Nguyen, D.X., Bos, P.D., and Massagué, J. (2009). Metastasis: from dissemination to organ-specific colonization. *Nat. Rev. Cancer* 9, 274–284.

Nudelman, K.N.H., Wang, Y., McDonald, B.C., Conroy, S.K., Smith, D.J., West, J.D., O'Neill, D.P., Schneider, B.P., and Saykin, A.J. (2014). Altered cerebral blood flow one month after systemic chemotherapy for breast cancer: a prospective study using pulsed arterial spin labeling MRI perfusion. *PLoS One* 9, e96713.

Osswald, M., Jung, E., Sahm, F., Solecki, G., Venkataramani, V., Blaes, J., Weil, S., Horstmann, H., Wiestler, B., Syed, M., et al. (2015). Brain tumour cells interconnect to a functional and resistant network. *Nature* 528, 93–98.

Paget, S. (1889). The distribution of secondary growths in cancer of the breast. *Cancer Metastasis Rev.* 8, 98–101.

Paszek, M.J., Zahir, N., Johnson, K.R., Lakins, J.N., Rozenberg, G.I., Gefen, A., Reinhart-King, C.A., Margulies, S.S., Dembo, M., Boettiger, D., et al. (2005). Tensional homeostasis and the malignant phenotype. *Cancer Cell* 8, 241–254.

Petri, B., Kaur, J., Long, E.M., Li, H., Parsons, S.A., Butz, S., Phillipson, M., Vestweber, D., Patel, K.D., Robbins, S.M., et al. (2011). Endothelial LSP1 is involved in endothelial dome formation, minimizing vascular permeability changes during neutrophil transmigration *in vivo*. *Blood* 117, 942–952.

Phillipson, M., Kaur, J., Colarusso, P., Ballantyne, C.M., and Kubes, P. (2008). Endothelial domes encapsulate adherent neutrophils and minimize increases in vascular permeability in paracellular and transcellular emigration. *PLoS One* 3, e1649.

Potente, M., Gerhardt, H., and Carmeliet, P. (2011). Basic and therapeutic aspects of angiogenesis. *Cell* 146, 873–887.

Provenzano, P.P., Cuevas, C., Chang, A.E., Goel, V.K., Von Hoff, D.D., and Hingorani, S.R. (2012). Enzymatic targeting of the stroma ablates physical barriers to treatment of pancreatic ductal adenocarcinoma. *Cancer Cell* 21, 418–429.

Regmi, S., Fu, A., and Luo, K.Q. (2017). High shear stresses under exercise condition destroy circulating tumor cells in a microfluidic system. *Sci. Rep.* 7, 39975.

Reymond, N., d'Águia, B.B., and Ridley, A.J. (2013). Crossing the endothelial barrier during metastasis. *Nat. Rev. Cancer* 13, 858–870.

Robb, R.A. (2001). The biomedical imaging resource at Mayo Clinic. *IEEE Trans. Med. Imaging* 20, 854–867.

Schlesinger, M., and Bendas, G. (2015). Contribution of very late antigen-4 (VLA-4) integrin to cancer progression and metastasis. *Cancer Metastasis Rev.* 34, 575–591.

Schwarzbach, C.J., Schaefer, A., Ebert, A., Held, V., Bolognese, M., Kablau, M., Hennerici, M.G., and Fatar, M. (2012). Stroke and cancer: the importance of cancer-associated hypercoagulation as a possible stroke etiology. *Stroke* 43, 3029–3034.

Seguin, L., Desgroes, J.S., Weis, S.M., and Cheresh, D.A. (2015). Integrins and cancer: regulators of cancer stemness, metastasis, and drug resistance. *Trends Cell Biol.* 25, 234–240.

Shibue, T., Brooks, M.W., and Weinberg, R.A. (2013). An integrin-linked machinery of cytoskeletal regulation that enables experimental tumor initiation and metastatic colonization. *Cancer Cell* 24, 481–498.

Sosa, M.S., Bragado, P., and Aguirre-Ghiso, J.A. (2014). Mechanisms of disseminated cancer cell dormancy: an awakening field. *Nat. Rev. Cancer* 14, 611–622.

Stoleto, K., Kato, H., Zardouzian, E., Kelber, J., Yang, J., Shattil, S., and Klemke, R. (2010). Visualizing extravasation dynamics of metastatic tumor cells. *J. Cell Sci.* 123, 2332–2341.

Strilic, B., Yang, L., Albarrán-Juárez, J., Wachsmuth, L., Han, K., Müller, U.C., Pasparakis, M., and Offermanns, S. (2016). Tumour-cell-induced endothelial cell necrosis via death receptor 6 promotes metastasis. *Nature* 536, 215–218.

Stylianopoulos, T., Martin, J.D., Chauhan, V.P., Jain, S.R., Diop-Frimpong, B., Bardeesy, N., Smith, B.L., Ferrone, C.R., Horncik, F.J., Boucher, Y., et al. (2012). Causes, consequences, and remedies for growth-induced solid stress in murine and human tumors. *Proc. Natl. Acad. Sci. USA* 109, 15101–15108.

Tremblay, P.-L., Huot, J., and Auger, F.A. (2008). Mechanisms by which E-selectin regulates diapedesis of colon cancer cells under flow conditions. *Cancer Res.* 68, 5167–5176.

Valastyan, S., and Weinberg, R.A. (2011). Tumor metastasis: molecular insights and evolving paradigms. *Cell* 147, 275–292.

Vermot, J., Forouhar, A.S., Liebling, M., Wu, D., Plummer, D., Gharib, M., and Fraser, S.E. (2009). Reversing blood flows act through klf2a to ensure normal valvulogenesis in the developing heart. *PLoS Biol.* 7, e1000246.

Weiss, L. (1992). Comments on hematogenous metastatic patterns in humans as revealed by autopsy. *Clin. Exp. Metastasis* 10, 191–199.

Wirtz, D., Konstantopoulos, K., and Searson, P.C. (2011). The physics of cancer: the role of physical interactions and mechanical forces in metastasis. *Nat. Rev. Cancer* 11, 512–522.

Wolf, K., Te Lindert, M., Krause, M., Alexander, S., Te Riet, J., Willis, A.L., Hoffman, R.M., Figdor, C.G., Weiss, S.J., and Friedl, P. (2013). Physical limits of cell migration: control by ECM space and nuclear deformation and tuning by proteolysis and traction force. *J. Cell Biol.* 201, 1069–1084.

STAR★METHODS

KEY RESOURCES TABLE

REAGENT or RESOURCE	SOURCE	IDENTIFIER
Antibodies		
Anti-GAPDH: goat polyclonal (V-18)	Santa Cruz	Cat#sc-20357, Batch # L051, RRID:AB_641107
Anti-CD31: mouse monoclonal (MEM-05)	Thermo	Cat#37-0700, Batch # 72 41 99A, RRID:AB_2533295
Anti-ITG β 1: rabbit polyclonal	Millipore	Cat#AB1952, RRID:AB_91150
Donkey anti-rabbit IgG coupled to HRP	GE Healthcare	Cat#NA934-1ML, Batch # 9750792, RRID:AB_772206
Donkey anti-goat IgG coupled to HRP	Santa Cruz	Cat#sc-2020, Batch # B2316, RRID:AB_631728
Goat anti-mouse coupled to Alexa Fluor 488	Thermo	Cat#A-11029, Batch # 1008719, RRID:AB_138404
Chemicals, Peptides, and Recombinant Proteins		
IBMX (3-isobutyl-1-methylxanthine)	Sigma-Aldrich	Cat#I5879
Lidocain	Sigma-Aldrich	Cat#L7757
Norepinephrin	Sigma-Aldrich	Cat#A0937
Nifedipin	Sigma-Aldrich	Cat#N7634
Dextran FITC	Sigma-Aldrich	Cat#FD70S
Experimental Models: Cell Lines		
D2A1	Weinberg lab (HHMI)	RRID: CVCL_0190
JIMT-1 BR3	Winkler lab (DKFZ)	RRID: CVCL_2077
ZMEL-1	White lab (MSKCC)	N/A
A431	F. Salteil, (INSERM U1053)	RRID: CRL_1555
1675	F. Salteil, (INSERM U1053)	RRID: CVCL_0040
4T1	Thery lab (Curie Institute)	RRID: CVCL_0125
A2058br	Winkler lab (DKFZ)	N/A
PC14PE6br	Winkler lab (DKFZ)	N/A
H1	Winkler lab (DKFZ)	N/A
HUVEC SD	PromoCell	Cat#C14010
Experimental Models: Organisms/Strains		
Zebrafish: <i>Tg(Fli1a:eGFP)</i>	EMBL zebrafish facility (Heidelberg)	N/A
Mouse: <i>Foxn1^{nu/nu}</i>	Charles River	Cat#490
Oligonucleotides		
siRNA targeting sequence: ITGB1 (mouse) ORF, position 688, CCACAGAAGUUUACAUUA	This paper	N/A
siRNA targeting sequence: ITGB1(mouse) ORF, position 1915, GUGUGUAGGAAGAGAGAUA	This paper	N/A
Recombinant DNA		
pCAG-EGFP	Addgene	Cat#89684
Software and Algorithms		
GraphPAD Prism Commercial software	Commercial software	Version 5.04
PIV, ImageJ plugin	This paper, adapted from https://sites.google.com/site/qingzongtseng/piv	N/A
Heatmap creator (MatLab)	This paper, using published function from Y-L Tang, Dep. of Info. Manag., Chaoyang University	N/A
Free Cad	https://www.freecadweb.org/	N/A
Gmsh	http://www.gmsh.info	N/A

(Continued on next page)

Continued

REAGENT or RESOURCE	SOURCE	IDENTIFIER
AngioTK	http://www.cemosis.fr/projects/angiotk/	N/A
Feel++	http://www.feelpp.org , http://www.cemosis.fr/software/feelpp	N/A
Feel++ (fluid-structure)	http://book.feelpp.org/toolbox/fsi/	N/A
Imaris	Gaudin lab	Bitplane
Other		
100nm fluorescent beads	Polysciences	Cat#17150
10 μ m fluorescent beads	Phosphorex	Cat#2227

CONTACT FOR REAGENT AND RESOURCE SHARING

Further information and requests for resources and reagents should be directed to and will be fulfilled by the Lead Contact, Jacky G. Goetz (jacky.goetz@inserm.fr).

EXPERIMENTAL MODEL AND SUBJECT DETAILS**D2A1 Cells (CVCL_0190). Mouse Mammary Carcinoma (BALB/c female)**

Major information on the D2A1 cell line can be found following this link: http://web.expasy.org/cellosaurus/CVCL_0190. Culture conditions: 37°/5% CO₂. DMEM HG with 5% NBCS, 5% FBS, 1% NEAA-MEM, 1% Penstrep. Authentication: Injection in the nipple of mammary gland of BALB/c mice lead to mammary tumor. Cells do not show contamination to mycoplasma.

JIMT-1 BR3 Cells (CVCL_2077). Human Ductal Breast Carcinoma (Female) Highly Metastatic in the Brain

Major information on the JIMT1 cell line can be found following this link: http://web.expasy.org/cellosaurus/CVCL_2077. Culture condition: 37°/5%CO₂. DMEM HG with 10% FBS, 1% Penstrep. Authentication: Intracardiac injection in nude mice (NU/NU) lead to cerebral metastasis. Cells do not show contamination to mycoplasma.

1675 Cells (WM115, CVCL_0040). Human Melanoma (Female)

Major information on the 1675 cell line can be found following this link: https://web.expasy.org/cellosaurus/CVCL_0040. Culture condition: 37°/5%CO₂. DMEM HG with 10% FBS, 1% Penstrep. Cells do not show contamination to mycoplasma.

A431 Cells (CRL_1555). Human Skin Epidermoid Carcinoma (Female)

Major information on the A431 cell line can be found following this link: https://www.lgcstandards-atcc.org/products/all/CRL-1555.aspx?geo_country=fr. Culture conditions: 37°/5% CO₂. DMEM HG with 10% FBS, 1% Penstrep. Cells do not show contamination to mycoplasma.

4T1 Cells (CVCL_0125). Mouse Mammary Gland Carcinoma (BALB/c Female)

Major information on the 4T1 cell line can be found following this link: https://web.expasy.org/cellosaurus/CVCL_0125. Culture condition: 37°/5%CO₂. RPMI 1640 with 10% FBS, 1% Penstrep. Authentication: Injection in the nipple of mammary gland of BALB/c mice lead to mammary tumor. Cells do not show contamination to mycoplasma.

ZMEL1 Cells

Zebrafish melanoma. Culture condition: 28°/5% CO₂. DMEM HG, 10% FBS, 1% Penstrep. Cells do not show contamination to mycoplasma.

Human Umbilical Vein Endothelial Cells (HUVECs)

Primary cells from single donor, commercial vials (PromoCell) amplified before used at P4 for all experiments. Culture condition: 37°/5% CO₂. ECGM with Supplemental mix (PromoCell) and 1% Penstrep.

Zebrafish Embryos

Tg(fli1a:eGFP) Zebrafish (*Danio rerio*) embryos from a Golden background. Embryos were maintained at 28° in Danieau 0.3X medium (see next section), supplemented with 1-Phenyl-2-thiourea (Sigma-Aldrich) as previously described (Goetz et al., 2014) after 24 hours postfertilization (hpf). For all Zebrafish experiments, the offspring of one single cross was selected, based on anatomical/developmental good health. Embryos were split randomly between experimental groups. All injection experiments were carried at 48 hpf and imaged between 48 hpf and 72 hpf.

Mice

Immunodeficient 8-10 weeks old female *Foxn1^{nu/nu}* mice (Charles River, Sulzfeld, Germany) were used. Mice were housed at 22°C and have access to water and food at libitum. All work on animals has been carried out in accordance with the German Animal Protection Act after approval by the german ethics committee: Regierungspräsidium, Karlsruhe, Germany. All efforts were made to minimize animal suffering and to reduce the number of animals used. The operation of the chronic cranial window was done as previously described (Kienast et al., 2010; Osswald et al., 2015). Three weeks after window implantation tumor cells were injected intracardially.

Human Patients

For the experiments using patient blood collection for CTC size analysis, patient blood samples were acquired in accordance to the World Medical Association Declaration of Helsinki and the guidelines for experimentation with humans by the Chambers of Physicians of the State of Hamburg (“Hamburger Ärztekammer”). All patients gave informed, written consent prior to blood draw.

Human patient data showing the link between brain metastasis (BM) and perfusion pattern were obtained on a single-center cohort. The retrospective study was conducted in compliance with the local ethics committee (Ethik-Kommission der Ärztekammer Hamburg, WF-018/15) with a waiver of informed consent. To collect cases, all MRI studies from 01/2014 to 12/2016 were screened for the presence of untreated malignant intra-axial brain tumors (no previous brain surgery or radiation). In total, 407 patients met the inclusion criteria. From the entire cohort, we randomly selected 100 patients (37 women and 63 men).

METHODS DETAILS

Cell Culture and siRNA-Mediated Knock-down

D2A1 stably expressing LifeAct-RFP or LifeAct-YPET, kindly provided by Robert A. Weinberg (MIT), were grown as previously described (Shibue et al., 2013), in DMEM with 4.5 g/l glucose (Dutscher) supplemented with 5% FBS, 5% NBCS, 1% NEAA and 1% penicillin-streptomycin (Gibco). Human Umbilical Vein Endothelial Cells (HUVEC) (PromoCell) were grown in ECGM (PromoCell) supplemented with supplemental mix (PromoCell C-39215) and 1% penicillin-streptomycin (Gibco). To maximize the reproducibility of our experiments, we always used these cells at 4th passage in the microfluidic channels. siRNAs were transfected into D2A1 cells using Lipofectamine RNAiMAX (Invitrogen) following the manufacturer's instructions. Experiments were performed between 72 h and 96h post-transfection. siRNA sense sequences are the following: siCTL: GCA AAT TAT CCG TAA ATC A, siTGB1 #1: CCA CAG AAG UUU ACA UUA A, siTGB1 #2: GUG UGU AGG AAG AGA GAU A.

Zebrafish Handling

Tg(fli1a:eGFP) Zebrafish (*Danio rerio*) embryos from a Tübingen background used in the experiments were kindly provided by the group of F.Peri from EMBL (Heidelberg, Germany). Embryos were maintained in Danieu 0.3X medium (17,4 mM NaCl, 0,2 mM KCl, 0,1 mM MgSO₄, 0,2 mM Ca(NO₃)₂) buffered with HEPES 0,15 mM (pH = 7.6), supplemented with 200 µM of 1-Phenyl-2-thiourea (Sigma-Aldrich) to inhibit the melanogenesis, as previously described (Goetz et al., 2014).

Pharmacological Treatments

Drugs were added in the breeding water (Danieu 0.3X + PTU) of the embryos before mounting and injection. IBMX (3-isobutyl-1-methylxanthin) (Luca et al., 2014), lidocain (Vermot et al., 2009), nifedipin and norepinephrine (Luca et al., 2014) (Sigma) were used at 100 µM in DMSO (incubation time: 20h), 640µM in ethanol (inc. time: 2h), 5 µM in DMSO (inc. time: 2h) and 500 µM in water (inc. time: 1h) respectively. In Figure S4H, treatment was started 1h post-injection to test the impact of reducing flow forces on extravasation.

High-Speed Microscopy for Pacemaker Activity and Blood Flow Profiling

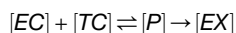
To measure the heart pacemaker activity and the associated blood flow profiles, we used the USB 3.0 uEye IDS CCD camera (IDEX) mounted on a DMIRE2 inverted microscope (Leica) using transmitted light. Heartbeats were acquired at 80 frames per second (fps) and blood flow in the tail region at 200 fps. For the whole-embryo high-speed recordings of the blood flow, acquisitions were done using an Orca Flash 4.0 cMOS camera (Hamamatsu) mounted on an IX-73 inverted microscope equipped with a UPLFLN 10X/0.3 objective (Olympus). Heartbeats were manually counted to compute the pacemaker activity. The blood flow intensity profile over time at each positions in the vasculature was analyzed using an adapted Particle Image Velocimetry (PIV) protocol from ImageJ software that is available online (<https://sites.google.com/site/qingzongtseng/piv>).

Intravascular Injection of CTCs in the Zebrafish Embryo

48 hour post-fertilization (hpf) *Tg(fli1a:eGFP)* embryos were mounted in 0.8% low melting point agarose pad containing 650 µM of tricain (ethyl-3-aminobenzoate-methanesulfonate) to immobilize the embryos. D2A1 LifeAct-RFP cells were injected with a Nanoject microinjector 2 (Drummond) and microforged glass capillaries (25 to 30 µm inner diameter) filled with mineral oil (Sigma). 23nL of a cell suspension at 100.10⁶ cells per ml were injected in the duct of Cuvier of the embryos under the M205 FA stereomicroscope (Leica), as previously described (Stoletov et al., 2010). The same protocol was used when injecting 1675, A431, JIMT1, 4T1 and ZMEL1 cells. Similarly, injection of 10 µm fluorescent beads (Phosphorex) was performed with a similar concentration of beads, pre-treated with Poly-Ethyleneglycol (sigma) at 0,1 mg/ml in PBS for 5 hours.

Confocal Imaging and Analysis

Confocal imaging was alternatively performed with an upright TCS SP5 or SP8 confocal microscope with a HC FLUOTAR L 25X/0,95 W VISIR (Leica), or with a SP2 confocal head mounted on a DMIRE2 stage with HC PL APO 20X/0,7 IMM CORR CS objective (Leica). The caudal plexus region (around 50 μ m width) was imaged with a z-step of less than 1.5 μ m for at least 20 embryos per conditions from at least 3 independent experiments. Cells dispersion was manually counted and localized (using the stereotype patterning of ISVs as reference) in the caudal plexus. The data were compiled to generate heatmaps using a custom-made MATLAB plug in (see next section). Post-processing was performed using Imaris (Bitplane), Amira (FEI) and IMOD (Boulder Laboratory, University of Colorado) for segmentation and 3D reconstruction. For the permeability assay, embryos were pharmacologically treated (as described above) and injected in the duct of Cuvier with 18,4 nl of Dextran-TRITC (500kDa), 3 hours before confocal imaging of the caudal plexus. For assessing the endothelial remodeling *in vivo*, cells were sorted in 3 groups (intravascular, pocketing and extravascular) based on confocal imaging. A kinetic analysis for the individual groups, in vehicle- and lidocain-treated embryos, was performed based on a Michaelis-Menten model, where the arrested tumor cells (TC) interact with endothelial cells (EC) that initiate pocketing (P) before undergoing extravasation (Ex):



Heatmaps

The heatmaps were generated using ImageJ (<https://imagej.nih.gov/ij/index.html>) and MATLAB (MathWorks) softwares. The adhesion/extravasation events are identified for each fish after the analysis of the confocal z-stacks with ImageJ. The position of these events is manually reported on a gray-level support image of a 2.5 days post-fertilization zebrafish plexus. Then, all the support images representing each embryo for one condition were put together in an image stack using ImageJ. The stack is read layer by layer in MATLAB and the dots representing the localization are automatically detected with the function Hough circles (Yuan-Liang Tang, Department of Information Management, Chaoyang University of Technology, Taichung, Taiwan) (<https://fr.mathworks.com/matlabcentral/fileexchange/22543-detects-multiple-disks-coins-in-an-image-using-hough-transform>) using the Circular Hough Transform based algorithm, giving in output the coordinates of the detected dots. Gaussian spots are then created at these coordinates. The amplitude of each Gaussian spot is equal to 1. The different layers of one condition are added each other by making a sum projection, and a black and white mask created with the gray level support image is applied to this sum projection. The gaussian spot amplitudes of each layers are summed to produce the heatmap. The areas of the sum projection where the gaussian spot amplitudes are higher corresponds to high density areas of adhesion/extravasation events. To produce the final heatmap, a custom colormap, inspired by the jet colormap, is applied to the sum projection. The colormap goes from black (no event) to red (high density areas).

Sample Preparation for Electronic Microscopy of Zebrafish Embryos

Correlative Light and Electron Microscopy was performed as previously described (Goetz et al., 2014). To describe ultra-structural characteristics of CTCs and the endothelium in the zebrafish embryo, chosen zebrafish embryos were chemically fixed with 2,5% glutaraldehyde and 4% paraformaldehyde in 0.1 M Cacodylate buffer (fish tails cut off in the fixative). Samples were kept in fixative at room temperature for 1-2h and stored in fixative at 4°C overnight or until further processing. Samples were rinsed in 0.1M Cacodylate buffer for 2x5min and post-fixed using 1% OsO4 in 0.1 M Cacodylate buffer, for 1h at 4°C. Then, samples were rinsed for 2x10min in 0.1M Cacodylate buffer and secondary post-fixed with 4% water solution of uranyl acetate, 1h at room temperature. Rotation was used at all steps of sample processing. Followed by 5min wash in MiliQ water, the samples were stepwise dehydrated in Ethanol (25%, 50% each 15min, 95%, 3X100% each 20min) and infiltrated in a graded series of Epon (Ethanol/Epon 3/1, 1/1, 1/3, each 45min). Samples were left in absolute Epon (EmBed812) overnight. The following day, samples were placed in a fresh absolute Epon for 1h and polymerized (flat embedded) at 60°C for 24-48h. Once polymerized, most surrounding Epon was cut off using razorblade and samples were mounted on empty Epon blocks (samples flat on the top of the blocks) and left at 60°C for 24h-48h. Semi-thin sections (200nm) were serially sectioned using ultramicrotome (Leica Ultracut UCT), collected on formvar-coated slot grids and stained with 4% water solution of uranyl acetate for 10min and Reynolds lead citrate for 3min. Semi-thin sections (200nm) were imaged with a CM120 transmission electron microscope (Philips Biotwin) operating at 120 kV. Images were recorded with Veleta 2k x 2k (Olympus-SIS) camera using iTEM software. On the same sections, Electron tomography was performed with a Tecnai F30 Field Emission Gun TEM (FEI) operating at 300 kV and equipped with an Eagle 4K camera (FEI). The F30 was controlled by Tecnai User Interface (PEOUI) and Tecnai Acquisition (TIA) software. Single-axis tomograms were obtained using SerialEM and reconstructed in eTomo, part of the IMOD software package (Boulder Laboratory, University of Colorado).

Microfluidic Experiments

Quantification of the flow-dependent adhesion of CTCs was done using six channels μ -slides VI^{0,4} pre-coated with fibronectin (IBIDI). HUVEC cells were seeded at 21 000 cells per channel (Volume = 30 μ l). Medium was changed twice a day until they reach maximal confluence (3 to 4 days). D2A1 LifeAct-GFP cells were diluted to maintain the concentration of 150 000 cells/ml of cells between the different speed conditions and perfused using a REGLO Digital MS-2/12 peristaltic pump (Ismatec) and Tygon LMT-55 tubing (IDEX) for 10 minutes before fixation with 4% PFA (Electronic Microscopy Sciences) and stainings (see below). A similar protocol was used for checking the effect of the principal pharmacological treatment (IBMX and Lidocain) and of the temperature (28°C vs 37°C) on the adhesion efficiency of tumor cells.

For endothelial remodeling experiments *in vitro*, two μ -slides I^{0.4} Luer (IBIDI) coated with fibronectin from bovine plasma at 10 μ g/ml (Sigma F-1141) were used in parallel for each experiment. After seeding the HUVEC cells, one channel was cultured under a flow of 400 μ m/sec using REGLO pump and Tygon tubing and for the other channel (no flow condition), medium was changed twice a day. At confluence, D2A1 LifeAct-RFP cells were added at a concentration of 200 000 cells/ml for 10 min. Then, tumor cells were washed using fresh medium and incubated for 16h with or without flow. Z position of the tumor cells relative to the HUVEC monolayer was determined using the piezzo stage of the confocal microscope. A similar protocol was used for checking the effect of the principal pharmacological treatment (IBMX and Lidocain) on the extravasation efficacy of tumor cells.

Immunofluorescent Staining in the Microfluidic Channels

Cells were fixed using 4% PFA (Electronic Microscopy Sciences), permeabilized with 0.2% Triton-X100 (Sigma) and quenched with 2mg/ml NaBH₄ (Sigma) 10 min at room temperature before using the following primary antibodies: rat anti-mouse CD29 (9EG7, BD), mouse anti-human CD31 monoclonal primary antibody (MEM-5, Invitrogen). Following secondary antibodies were used: goat anti-rat or mouse coupled with Alexa Fluor 488 (Invitrogen). Cells were mounted using Vectashield (Vector Laboratories). For fluorescent labelling of the HUVEC cells (Figure 1), Alexa Fluor 568 Phalloidin (Life-technologies) and DAPI (Sigma) were used.

HUVEC Transfection and Live Imaging

HUVECs cell were seeded on fibronectin-coated μ Slide I at 100000 cells/channel. The following day, pCAG-EGFP plasmid was nucleofected in HUVEC cells using Nucleofector device and Cell Line Nucleofector Kit V (Lonza) following the manufacturer's instructions and were seeded into the pre-seeded channels. Live imaging experiments performed 24h later on a DMI6000 equipped with TCS SP5 confocal module and a chamber at 37°C. the HUVEC medium was supplemented with 20 mM Hepes. Briefly, the full volume of single cells was acquired for 10 min sequentially without flow. Then, the flow was turned on at 400 μ m/s and the full volume of cells were acquired for 10 min.

High-Speed Microscopy for Blood Flow Profiling around Arrested Tumor Cells

48 hour post-fertilization (hpf) *Tg(Flt1a:eGFP)* embryos were injected with CTCs and 100-nm fluorescent beads (Invitrogen), using with a Nanoject microinjector 2 (Drummond) and microforged glass capillaries (25 to 30 μ m inner diameter) filled with mineral oil (Sigma). Positively-injected embryos were instantaneously imaged at high-speed (100 fps) using a Leica SP5 confocal microscope equipped with resonant scanner. Such imaging allowed to image arrested tumor cells as well as the displacement of flowing fluorescent beads (100 nm) in their vicinity. We have then developed automated tracking of fluorescent beads (imaged at high-speed) that is followed by single track analysis, before and after the position of arrested TCs. This was performed either using the Imaris (Bitplane) software or Fiji (Trackmate, for *in vitro* flow proving) Quantification of the tracks' straightness (net/total distance, 1=straight track) was performed, in addition to flow velocities, for measuring whether flow is laminar or chaotic/turbulent in the presence of arrested tumor cells. A similar approach was conducted *in vitro*.

Scanning Electron Microscopy on HUVEC and D2A1 in Microchannels

HUVECs were seeded in glass coverslips mounted on Ibidi sticky-slide I Luer microchannels, and then cultivated under flow with the addition of D2A1 cells as described in "microfluidic experiments" section. Cells were fixed with glutaraldehyde 2,5% (EMS) in 0.1 M sodium cacodylate buffer (pH7.4), and dehydrated in ethanol-graded series. Once in ethanol 100%, coverslips were detached from Ibidi sticky chambers. The cell-containing portion of the coverslip was tightly cut with a diamond knife in two pieces, which were irreversibly dehydrated with 1,1,1,3,3,3-hexamethylidilazane (HDMS, Merck, Millipore)/ethanol-graded series. Next, glass coverslips were mounted onto 25,4mm EM Aluminium Mounts for AMRAY (EMS, Hatfield) by using Leit-C conductive carbon cement (CCC, Plano GmbH, Germany). After proper O/N drying, samples were metallized by platinum vaporization under vacumm up to 12nm (Cressington Sputter Coater 208HR coupled to a Pfeiffer Vacum, Germany). Image acquisition was performed at high-resolution (10kV) and 7000x/ 12000x magnification on a PhenomWorld SEM desktop microscope (Phenom-World B.V, The Netherlands).

Optical Tweezers

Optical tweezing experiments were performed as previously described (Anton et al., 2013). Briefly, OT behaves as a picodynamometer where stiffness and the displacement from the steady position can be computed to extract the applied force. Optical tweezing experiments *in vitro* were performed in single channel I^{0.4} Luer μ -slides pre-coated with fibronectin (IBIDI). HUVEC cells were cultured until confluence before the experiment as described above. D2A1 were perfused at 10⁴ cells/ml at a low speed to maximize the cell trapping and avoid collision effects by other CTC. A 1064 nm laser (Navigator 1064-7Y Spectra Physics) was used to generate optical tweezers mounted on a thermostated inverted microscope equipped with a UPLFLN-P 100X/1.3 objective (Olympus). D2A1 cells attached to the HUVEC monolayer were trapped in the beam and moved away from the HUVEC monolayer by displacing a computer-controlled piezzo stage (PI P545 PNano) along the X/Y axis. The fluctuations of the cell in the trap were recorded on a quadrant diode (Thorlabs PDQ30C) and the associated spectral power density allowed the calibration of the trap stiffness. The detachment of D2A1 cells from the HUVEC monolayer was recorded using a Cmos camera (Thorlabs DCC3240C). The movies were analyzed to access the center of mass of the cell in each image. This position compared to the steady position of the cell in the trap is proportional to the force exerted on the cellular adhesion. The rupture force between D2A1 and HUVEC gave rise to a drop in the position of the trapped cell steady state and allowed to access the rupture force.

Optical tweezing experiments in the zebrafish embryo were performed as previously described (Anton et al., 2013), with slight modifications: We implemented the setup with a thermoregulated chamber ensuring the embryos to remain at 28°C. We acquired the displacement with the camera at high frame rates 200fps after having established the power spectrum from the photodiode at 20kHz resolution to calibrate the setup.

Mice Experiments and Surgical Procedures

8-10 weeks old female Nu/Nu mice (Charles River, Sulzfeld, Germany) were used to study the extravasation cascade. All efforts were made to minimize animal suffering and to reduce the number of animals used. The operation of the chronic cranial window was done as previously described (Kienast et al., 2010; Osswald et al., 2015). Three weeks after window implantation a 100 μ l cell suspension, containing 500,000 tumor cells (JIMT1br3, A2058br, PC14PE6br, H1), was injected intracardially. *In vivo* imaging was done on day 3 and day 7 after the heart injection. After imaging, the mouse was perfusion-fixed through intracardiac injection with 2.5% glutaraldehyde (Electron Microscopy Sciences, Hatfield, PA) and 2% formaldehyde (Electron Microscopy Sciences) in 0.1 M PHEM buffer (comprising 60 mM PIPES, 25 mM HEPES, 10 mM EGTA and 2 mM MgCl, pH adjusted to 6.9). Following fixation, the regions of interest (ROIs) were imaged again based on the stored stage x,y-coordinates. NIRB was performed with the same laser that had been used for *in vivo* microscopy, tuned to 800 nm wavelength, as previously described (Karreman et al., 2016b). Above the ROIs, at the level of the brain surface, a 150 \times 150 μ m² area was scanned in a single focal plane until the NIRB square became clearly visible through emission of autofluorescence in the green channel. Around the ROI, three bigger 300 \times 300 μ m² NIRB squares were drawn in non-symmetric positions to facilitate orientation and retrieval of the ROI upon dissection. The brain was removed from the skull and post-fixed by immersion in the same fixative at 4°C overnight. The following day, the fixative was replaced with 0.1 M PHEM buffer, and the brain was stored at 4°C until further processing (Karreman et al., 2016b). All animal procedures were performed in accordance with the institutional laboratory animal research guidelines after approval of the Regierungspräsidium Karlsruhe, Germany (governmental authority).

In Vivo Multiphoton Laser Scanning Microscopy (MPLSM)

In vivo imaging was performed with a Zeiss 7MP microscope (Carl Zeiss Microscopy, Jena, Germany) provided with a Coherent Chameleon Ultrall laser (Coherent, Glasgow, UK) with a 500-550 nm and a 575-610 nm band pass filter. With the wavelength of 850 nm GFP and TRITC-dextran were detected. To prevent phototoxic effects, laser power was always kept as low as possible. During the imaging process animals were anaesthetized with a low gas narcosis including 1.5% isoflurane (Baxter, Unterschleißheim, Germany) and 98.5% oxygen (Guttröff, Heidelberg, Germany). During imaging body temperature was kept constantly at 37°C by a heating pad. To acquire angiographies of brain blood vessel, 0.1 ml TRITC-dextran (500 kDa, 10 mg.ml⁻¹, Sigma-Aldrich, Munich, Germany) was injected.

Blood Flow Velocity Measurements and Visualization of MPLSM Data

The blood flow velocity was measured by a line scan with a minimum length of 10 μ m, detecting 2000 events in microvessels. At least 16 randomly chosen vessels were measured per animal. The resulting scan identifies single erythrocytes as angular black lines, where the x-axis is according to the length of the detected distance and the y-axis is the elapsed time of the measurement. The angle is converging more and more to 90° when the cells are static. By knowing the resolution of both parameters and by the measurement of the slope of 30 randomly chosen red blood cells a calculation of the mean velocity is possible, by inversion of the result.

Western Blotting

For western blotting analysis, extracts corresponding to similar cell numbers were loaded on 4-20% polyacrylamide gels (Biorad) and run under denaturing conditions. The following primary antibodies were used: ITGB1 (Millipore AB1952; rabbit), GAPDH (V-18; Goat). HRP-conjugated secondary antibodies were used with ECL (GE Healthcare) for reading using a PXi system (Syngene). Intensities were normalized over cellular GAPDH levels.

In Vitro Migration and Adhesion Assays

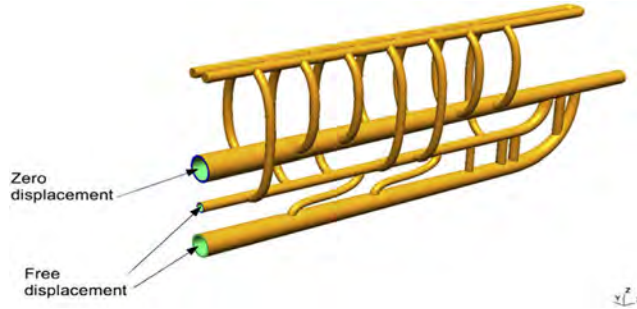
For wound healing assay, cells were cultured until confluence in 6-wells plate. The monolayer was scratched with a 20 μ l tips and medium was changed with medium supplemented with the corresponding pharmacological treatments. Pictures were taken at time = 0h, 3h, 6h, 9h and 24h. Wound closure was analyzed using ImageJ.

For adhesion assay, cells were plated at 20 000 cells/ml in 96-well plate filled with culture medium supplemented with the corresponding pharmacological treatments. After 30 min incubation, wells were washed with PBS, fixed in 4% PFA and stain with 1% violet crystal (VC, Sigma) for 1h at room temperature. VC was washed with PBS and pure DMSO was added to solubilized VC for 30 min under gentle moving. Optical density at 590nm was measured using TriStar² plate reader (Berthold).

Mathematical Modeling and Numerical Methods for *In Silico* Experiments

The *in silico* experiments presented are developed in the framework of Finite Element Embedded Library in C++, Feel++, which allows to consider a wide range of mathematical models and numerical methods and advanced techniques. It provides in particular the numerical models described in the following sections. To achieve these simulations, we followed these steps: (i) build a 3D geometry

accounting for the main features of the caudal vessel architecture of the zebrafish using a computer aided design software and generate a discrete computational domain where the entry point is ISV8, (ii) set up a fluid-structure interaction model between the blood and the endothelium in Feel++ and (iii) extract numerical flow rates and compare with *in vivo* experiments. Before getting into details for the three different steps let us introduce the notations used.



Let $I = [0, T]$ be the time interval over which we perform the *in silico* experiments, and $t \in I$ denote the time. Ω_f^t is the fluid (lumen) domain, the exponent t indicates that the domain changes over time, we work in an Eulerian setting. We denote Ω_s^* the solid (vessel) wall which is set in a Lagrangian setting. We also introduce Ω_f^* the reference fluid domain, which can be chosen as $\Omega_f^* \equiv \Omega_f^{t_0}$ where $t_0 = 0$ is the initial time. To couple the fluid and the solid dynamics, we need to formulate the fluid equations in Lagrangian coordinates. To this end, we introduce the Arbitrary Lagrangian Eulerian (ALE) framework which allows to go from the Eulerian to the Lagrangian frame and vice versa, and more specifically we define the ALE map

$$\begin{aligned} \mathcal{A}^t : \quad \Omega_f^* &\rightarrow \Omega_f^t \\ \mathbf{x}^* &\mapsto \mathbf{x} \end{aligned}$$

where \mathbf{x} is the position in Ω_f^t of the point which was at \mathbf{x}^* in Ω_f^* .

We can then define the Lagrangian derivative

$$\frac{\partial \mathbf{u}}{\partial t} \Big|_{\mathbf{x}^*} = \frac{\partial \mathbf{u}}{\partial t} \Big|_{\mathbf{x}} + (\mathbf{w} \cdot \nabla_{\mathbf{x}}) \mathbf{u}$$

where \mathbf{u} is a vector field and \mathbf{w} is the velocity of the mesh displacement defined as follows

$$\mathbf{w}(\mathbf{x}, t) = \frac{\partial \mathbf{x}}{\partial t} \left((\mathcal{A}^t)^{-1}(\mathbf{x}), t \right)$$

Variables defined in the reference frame are denoted as follows

$$\hat{\mathbf{u}} = \mathbf{u} \circ \mathcal{A}^t$$

The computational domain was built using computer aided design software to reproduce an idealized geometry obtained from the segmentation of stacks of images. The discrete computational domain, also called mesh, is built of 884221 tetrahedrons and is expressed in millimeters. The physical quantities used hereafter are accordingly adapted to this unit. In order to simulate the blood flow in the system, we have to consider the interaction between the blood and the endothelium. The blood flow is modelled using the incompressible Navier-Stokes equations and the endothelium is modelled using the Saint Venant-Kirchhoff linear elasticity model formulated in displacement/pressure due to the quasi incompressible nature of the endothelium. Both models are supplemented with boundary conditions.

The blood velocity and pressure (\mathbf{u}_f, p_f) are then given by the equation

$$\begin{aligned} \rho_f \frac{\partial \mathbf{u}_f}{\partial t} \Big|_{\mathbf{x}} + \rho_f ((\mathbf{u}_f - \mathbf{w}_f) \cdot \nabla_{\mathbf{x}}) \mathbf{u}_f - \nabla_{\mathbf{x}} \cdot \boldsymbol{\sigma}_f &= \mathbf{f}_f^t, \quad \text{in } \Omega_f^t \\ \nabla_{\mathbf{x}} \cdot \mathbf{u}_f &= 0, \quad \text{in } \Omega_f^t \end{aligned}$$

with

$$\boldsymbol{\sigma}_f = -p_f \mathbf{I} + 2\mu_f \mathbf{D}(\mathbf{u}_f)$$

$$\mathbf{D}(\mathbf{u}_f) = \frac{1}{2} (\nabla_{\mathbf{x}} \mathbf{u}_f + (\nabla_{\mathbf{x}} \mathbf{u}_f)^T)$$

and where \mathbf{f}_f^t is the volumic force density, ρ_f the blood density and μ_f the blood viscosity. The blood flow boundary conditions are an inlet Poiseuille flow in the aorta at ISV8 obtained from the experimental data and free outflow boundary conditions.

We model the arterial wall as an hyperelastic material and we use a displacement-pressure formulation following a Saint Venant-Kirchhoff material law. The displacement and pressure (\mathbf{n}_s, p_s) equations read:

$$\begin{aligned}\rho_s \frac{\partial^2 \mathbf{n}_s}{\partial t^2} - \nabla \cdot (\mathbf{F}_s \boldsymbol{\Sigma}_s) &= \mathbf{f}_s \quad \text{in } \Omega_s^* \\ \text{tr}(\mathbf{E}_s) &= \frac{1}{\lambda} p_s \quad \text{in } \Omega_s^*\end{aligned}$$

with

$$\begin{aligned}\boldsymbol{\Sigma}_s &= -p_s \mathbb{I} + 2\mu_s \mathbf{E}_s \\ \mathbf{E}_s &= \frac{1}{2} \left(\nabla \mathbf{n}_s + (\nabla \mathbf{n}_s)^T \right) + \frac{1}{2} \left((\nabla \mathbf{n}_s)^T \nabla \mathbf{n}_s \right)\end{aligned}$$

λ_s, μ_s are the Lamé coefficients defined as

$$\lambda_s = \frac{E_s \nu_s}{(1 + \nu_s)(1 - 2\nu_s)} \quad , \quad \mu_s = \frac{E_s}{2(1 + \nu_s)}$$

$\rho_s = 1.2 \cdot 10^{-6}$ kg mm³ is the endothelium density, $E_s = 3$ kg mm⁻¹ s⁻² is the Young modulus and $\nu_s = 0.49$ is the Poisson coefficient.

The FSI model is completed by matching conditions at the interface between the fluid and the structure stating the continuity of the velocity and the normal stress. These conditions read

$$\begin{aligned}\frac{\partial \mathbf{n}_s}{\partial t} - \mathbf{u}_f \circ \mathcal{A}_f^t &= 0 \quad (\text{velocity}) \\ \mathbf{F}_s \boldsymbol{\Sigma}_s \mathbf{n}_s^* + J_{\mathcal{A}_f^t} \mathbf{F}_f^{-T} \boldsymbol{\sigma}_f \mathbf{n}_f^* &= 0 \quad (\text{stress}) \\ \varphi_s^t - \mathcal{A}_f^t &= 0 \quad (\text{geometry})\end{aligned}$$

Regarding the space discretization, we use the continuous piecewise polynomials of order 2 for the velocity and order 1 for the pressure in the fluid and we use continuous piecewise polynomials of order 1 for the displacement and for the pressure in the solid. Regarding the time discretization, we use for the fluid a BDF2 (Backward Differentiation Formula) scheme and for the solid we use the Newmark scheme, both are second order in time. The time step is fixed to $\delta t = 5 \cdot 10^{-3}$ s and the final time is fixed at $T = 4$ s.

The FSI solution strategy follows a partitioned method solving at time t^n alternatively for the solid displacement \mathbf{n}_s^n and then the fluid velocity and pressure \mathbf{u}_f^n, p_f^n until convergence using a Robin-Robin coupling scheme between the fluid and the structure. The Robin-Robin coupling conditions read

$$\begin{aligned}\boldsymbol{\sigma}_s^n \mathbf{n}_s^n + \frac{\gamma \mu_f}{h} \mathbf{u}_s^n &= \frac{\gamma \mu_f}{h} \mathbf{u}_f^{n-1} - \boldsymbol{\sigma}_f^{n-1} \mathbf{n}_f \quad \text{in } \Omega_s^* \\ \boldsymbol{\sigma}_f^n \mathbf{n}_f + \frac{\gamma \mu_f}{h} \mathbf{u}_f^n &= \frac{\gamma \mu_f}{h} \mathbf{u}_s^n + \boldsymbol{\sigma}_f^{n-1} \mathbf{n}_f \quad \text{in } \Omega_f^n\end{aligned}$$

with $\mathbf{u}_s^n = \frac{\partial \mathbf{n}_s^n}{\partial t}$ and γ a parameter to choose.

In order to analyze the impact of a tumor cell attached to the endothelium on blood flow, we extracted small parts of the CAD model. In each of these, we modeled an arrested tumor cell and performed fluid dynamics only simulations in fixed geometries without the interaction with the vessel wall. The arrested tumor cell is modeled by deforming the endothelium, using a boolean difference of volumes in Gmsh (the volumes were the blood vessel and a sphere), and the whole structure was then considered rigid. The volumes were meshed entirely with Gmsh. Blood flow was simulated using the incompressible Navier-Stokes model in a fixed domain, Ω_f .

The blood velocity and pressure (\mathbf{u}_f, p_f) are then given by the equation

$$\begin{aligned}\rho_f \frac{\partial \mathbf{u}_f}{\partial t} + \rho_f (\mathbf{u}_f \cdot \nabla) \mathbf{u}_f - \nabla \cdot \boldsymbol{\sigma}_f &= \mathbf{f}_f^t, \quad \text{in } \Omega_f \\ \nabla \cdot \mathbf{u}_f &= 0, \quad \text{in } \Omega_f\end{aligned}$$

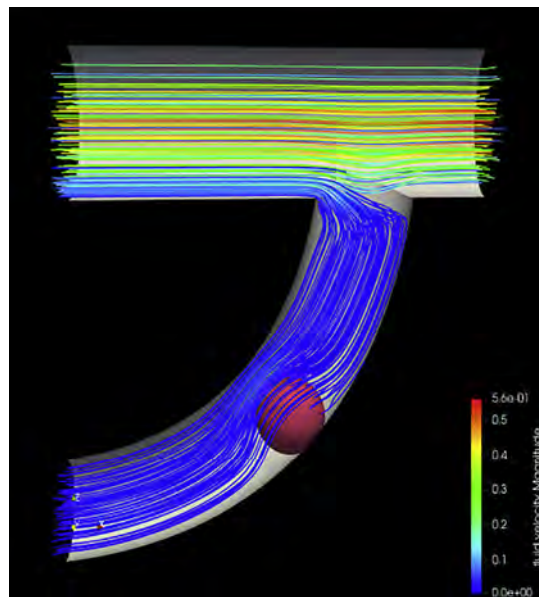
with

$$\boldsymbol{\sigma}_f = -p_f \mathbb{I} + 2\mu_f \mathbf{D}(\mathbf{u}_f)$$

$$\mathbf{D}(\mathbf{u}_f) = \frac{1}{2} \left(\nabla \mathbf{u}_f + (\nabla \mathbf{u}_f)^T \right)$$

and where \mathbf{f}_f is the volumic force density, ρ_f the blood density and μ_f the blood viscosity.

The boundary conditions are as follows: at the inlets a Poiseuille flow with a defined maximum velocity estimated from *in vivo* experiments, at the walls zero velocity condition and at the outlets free outflow condition.



In all cases, the flow remains low Reynolds with a few recirculations when the occlusion is important or total.

Patient Blood Collection for CTC Size Analysis

Patient blood samples were acquired in accordance to the World Medical Association Declaration of Helsinki and the guidelines for experimentation with humans by the Chambers of Physicians of the State of Hamburg ("Hamburger Ärztekammer"). All patients gave informed, written consent prior to blood draw. Samples were collected from 5 metastatic breast cancer patients into standard 7.5 ml ethylenediaminetetraacetic acid (EDTA) vacutainers and transferred to TransFix® (Cytomark) tubes within 2 h of sample draw. Blood was also collected from a metastatic non-small lung cancer patient directly into either CellSave® (Menarini-Silicon Biosystems), Cell-free DNA BCT® (Streck) or TransFix® preservatives for further analysis. Circulating tumor cells were isolated from whole blood sample by two size based enrichment systems: Both methods have been validated within a large European consortium of 36 partners from academia and industry, CANCER-ID (www.cancer-id.eu). The Parsortix™ system (ANGLE plc, UK) enriches tumor cells from a wide variety of blood tubes and has been described in detail in previous publications (Hvichia et al., 2016; Chudziak et al., 2016). In short, the device passes blood into a disposable cassette. This cassette narrows down to a critical gap of 6.5 μ m at which all larger cells are retained while smaller cells pass through into the waste, thus drastically reducing white blood cell and erythrocyte background. Due to their larger size and higher rigidity, tumor cells are retained at the gap and can be extracted by reversing the flow within the chamber. The enriched cell fraction is harvested into a cytopsin funnel and spun down (190 x g, 5 min). Upon drying overnight, samples can either be frozen at -80°C or directly stained by immunocytochemistry (ICC). The second size based enrichment system used to process cancer patient samples, was a novel microfluidic filtration device provided by Siemens Healthcare Diagnostics (Elkhart, IN, USA). The system uses a Hamilton STARlet™ robot (Hamilton Company, Reno Nevada) with a specifically developed software allowing for automated enrichment and staining of CTCs from whole blood (Magbanua et al., 2015). Briefly, the blood is passed through a membrane containing pores of 8 μ m, enriching for all larger cells. For this, EDTA blood samples were transferred into TransFix® preservation tubes and incubated overnight. The blood was then transferred to the device together with all reagents necessary for ICC staining of CTCs. Cytopsins generated following Parsortix™ enrichment were stained using fluorescently labeled antibodies. ICC included fixation with 4 % PFA, permeabilization with 0.1 % Triton X-100 and blocking using serum albumin. Two pan-Keratin antibodies (clone AE1/AE3, eBioScience and clone C11, Cell Signaling) were combined with a CD45 targeting antibody (REA747, Miltenyi Biotec) and DAPI for cell detection. Cytopsins were cover slipped using ProLong® Gold antifade reagent (Invitrogen). For the filtration device, we performed a single ICC staining step using a cocktail of fluorescently labeled antibodies, followed by cover slipping with ProLong® Gold antifade reagent (Invitrogen). Tumor cells were detected by targeting Dy550 labelled keratins (Pan CK – clone AE1/AE3, CK8/18 – clone UCD / PR10.11, CK19 – clone A53-B/A2), multiple Dy650 labelled white blood cell markers (CD45 – clone 9.4, CD66b – clone G10F5) and DAPI, all provided directly by Siemens Healthcare Diagnostics. Cytopsins and filtration membranes were evaluated and enumerated manually by fluorescence microscopy. CTCs were classified as pan-keratin positive, CD45 negative and DAPI positive cells. They were photographed using the AxioVision LE64 microscope software (Zeiss) which allows for measurement of lengths with its respective processing tools.

Brain Metastasis and Blood Flow Perfusion Study

Human patient data showing the link between brain metastasis (BM) and perfusion pattern were obtained on a single-center cohort. The retrospective study was conducted in compliance with the local ethics committee (Ethik-Kommission der Ärztekammer Hamburg, WF-018/15) with a waiver of informed consent. To collect cases, all MRI studies from 01/2014 to 12/2016 were screened for the presence of untreated malignant intra-axial brain tumors (no previous brain surgery or radiation). In total, 407 patients met the inclusion criteria. From the entire cohort, we randomly selected 100 patients (37 women and 63 men).

MRI was performed using a 1.5 Tesla (Magnetom® Sonata, Siemens Healthcare, Erlangen, Germany; Magnetom® Symphony, Siemens Healthcare, Erlangen, Germany, and Magnetom® Avanto, Siemens Healthcare, Erlangen, Germany) in 94 patients or a 3 Tesla scanner (Magnetom® Skyra, Siemens Healthcare, Erlangen, Germany; Ingenia, Philips Medical Systems, Best, The Netherlands) in 6 patients. Imaging protocol always included axial T1w spin echo with flow compensation and/or three-dimensional T1w gradient echo sequences following weight-adjusted Gadolinium injection (T1w+). If both sequences were acquired the latter one was used for further analysis. Sequence parameters (repetition time, echo time, inversion time, field of view, matrix, pixel size, slice thickness, interslice gap, and number of slices) varied among the different scanners. All BM were subsequently segmented semi-manually using the Analyze Software System 11.0 (Biomedical Imaging Resource, Mayo Clinic, Rochester, MN, USA) (Robb, 2001). Axial T1w+ MR images of all patients were then automatically co-registered to the Montréal Neurological Institute (MNI) brain by using the FMRIB Software Library (Analysis Group, Oxford, UK) linear registration tool. Correct registration of all T1w+ images and the segmented BM to the MNI brain was secured by visual inspection. Cluster maps comprising all BM of the respective cohort were calculated (Figure 8). Computed tomography was used to build the brain perfusion atlas. Since cancer patients often show an altered cerebral blood flow due to paraneoplastic changes or chemotherapy administration, we decided to use computed tomography (CT) perfusion data from a healthy cohort as reference (Nudelman et al., 2014; Schwarzbach et al., 2012). In brief, 107 patients were triaged by CT perfusion for symptoms of transient ischemic attack but without evidence of ischemia or any perfusion abnormality, infarction or symptoms on follow up, or vascular abnormality as reported elsewhere (Feyen et al., 2010). Quantitative perfusion maps were obtained for CBF and MTT (Abels et al., 2010). All perfusion raw data were processed in a central core-lab on a work-station dedicated for perfusion analysis (Syngo mmwp VE52A with VPCT-Neuro; Siemens Healthcare, Forchheim, Germany) with motion correction and low band temporal noise removal. Non-parenchymal voxels corresponding to bone, vasculature, calcification and cerebrospinal fluid were automatically excluded by adaptive intensity thresholding. Perfusion parameter maps were calculated based on a deconvolution model by least mean squares fitting. All perfusion maps were then affine registered to 1 mm MNI standard space by a precise registration model between the baseline time average of each CT perfusion dataset and a custom CT template in standard space using the FMRIB Software Library 5.0 (Kemmling et al., 2012). Mean voxel-wise perfusion parameter maps normalized to standard space were then registered to each individual patient in our study cohort to obtain voxel specific normal perfusion values. Absolute mean cerebral blood flow (CBF in ml/100g brain tissue/min) and mean transit time (MTT in sec) values of all BM were calculated for each voxel of the perfusion mask and each voxel with a BM. Statistical analysis was conducted using IBM SPSS Statistics® software (IBM® 2011, version 20, Armonk, New York, USA) and R (The R Foundation, version 3.3.1. Vienna, Austria). The differences in CBF and MTT between all BM and BM- voxels were compared by the independent t-test. Voxels with more than one BM were weighted according to the number of BM occurring within the voxel. The paired samples t-test was used to compare the perfusion values and the volume of the BM. If not otherwise indicated, data are given as median \pm interquartile range.

QUANTIFICATION AND STATISTICAL ANALYSIS

Statistical Tests

Statistical analysis of the results obtained during Zebrafish, Mice and microfluidic experiments were performed using the GraphPad Prism program version 5.04. The Shapiro-Wilk normality test was used to confirm the normality of the data. The statistical difference of Gaussian data sets was analyzed using the Student unpaired two-tailed t test, with Welch's correction in case of unequal variances. For data not following a Gaussian distribution, Kruskal-Wallis and Dunn's multiple comparisons post-test or the Mann-Whitney test was used. For qualitative data, the Fisher test was used. Illustrations of these statistical analyses are displayed as the mean \pm standard deviation (SD). p-values smaller than 0.05 were considered as significant. *, p < 0.05, **, p < 0.01, ***, p < 0.001, ****, p < 0.0001.

Please find below, the details related to sample size and data exclusion, replication and randomization for each experiment.

Zebrafish Experiments

The Pacemaker activities of the embryos (Figures 3A, 3G, S5A, and S5 E) had been registered during 3 to 5 experiments all along the experimentation as a control of treatment efficiency. Represented sample sizes are: n=60 Veh. Lidocain, n=78 lidocain, n=58 Veh. IBMX, n=65 IBMX, n=11 Veh. nifedipin, n=10 nifedipin, n=10 Veh Norepinephrin, n=10 Norepinephrin.

Blood flow measurement regarding pharmacological treatment using PIV/automated treatment (Figures S3A, 3B, and 3H) was done on 5 embryos from the same batch, Except for one Veh. EtOH treated embryos that was excluded during analysis, based on imaging focus default.

Blood flow measurement using PIV/automated treatment on ZF whole embryo (Figures 1E and 1F). Sample size = 3 fish. Due to the size of the whole embryo, the imaging time and cost of acquisition are very high, so we decided to limit the sample size.

Optical tweezing of adhered tumor cells (Figure 2H) were performed on 37 cells during 4 independent experiments.

Blood flow measurement using optical tweezing (Figures 3C, 3I, and S3B) was done over more than 5 embryos per condition from several treatment batch. due to the low throughput of the approach and knowing that the pacemaker activities from both vehicle condition are not significantly different, we decided to pull them as a control situation. Sample sizes for Ctrl / IBMX / Lidocain:

- number of cells in total: 75 / 54 / 54
- trapped at the wall of the DA (Figure 3C): 26 / 22 / 19
- trapped in the center of the DA (Figure 3C)": 23 / 7 / 12

All Zebrafish injection experiments at 3, 9 and 24 hours post-injection (Figures 1C, 1D, S1C, 2C–2E, 4A–4J, S4H, 5I–5K, S5B, S5C, S5G, S5F, and S5I) were repeated at least three times independently on 16 embryos per condition each time. Taking into account, the success rate of injection and imaging time limitation, this lead to the following final numbers:

- 3hpi: n=20 Veh. IBMX, n=20 IBMX, n=31 Veh. lidocain, n=37 lidocain, n=15 Veh. nifedipin, n=15 nifedipin, n=16 Veh. norepinephrine, n=21 norepinephrine. Arrest regarding the position (Figure 2D), n=59.
- 9hpi: n=22 Veh. lidocain, n=23 lidocain.
- 24hpi: n=24 Veh. IBMX, n=23 IBMX, n=20 Veh. lidocain, n=20 lidocain.
- 1675 at 3hpi, n=32 ; A431 at 3hpi, n=37 ; JIMT1 at 3hpi, n=40 ; 4T1 at 3hpi, n=40 ; ZMEL1 at 3hpi, n=28.
- Lidocain starting 1hpi, 24hpi imaging, n=19.
- Veh. lidocain starting 1hpi, 24hpi imaging, n=16.

Exception: Figures 1C–1D (ZF whole embryo 3 hours post-injection). Sample size = 11 fish/3 independent experiments. Due to the size of the whole embryo, the imaging time and cost of acquisition are very high. Adding the fact that the results were straightforward, we decided to limit the sample size.

Exception: Figure 2E (ZF injection with transfected siRNA cells). Because of the increased variability of the results, and the fact that all injected fish were take into account (including embryos bearing no arrested CTC), we reproduce the experiments five time. Total sample sizes are: n=77 siCtrl, n=63 siTGb1 #1, n=55 siTGb1 #2.

Zebrafish live injection (Figures 3D, 3E, 3F, 3J, 3K, and 3L) was done in triplicate of independent injection batch of 5 fish. This experimental procedure asks fine settings and 5 min acquisition time following the injection. The following sample size are the “final number of fish / the number of events” (= cell or small cluster of 2 to 5 cells): n=7/54 Veh. IBMX, n=3/62 IBMX, n=4/42 vehicle Lidocain, n=8/46 lidocain.

Zebrafish live injection with 10 μ m beads, Figure S2A. 2 embryos showing more than 260 events in total were took into account for the quantification.

Zebrafish flow around arrested tumor cell study using 100 μ m beads (Figures 5L and S6C) is based on high-speed imaging: n=7 “open”, n=6 “partially closed” and n=6 “closed”.

Permeability assays in the treated zebrafish (Figure S4D) were done over 8 embryos per conditions.

Vessel diameter measurements (Figures 2B and S4A–SC) were done on 1 representative control embryo (Figure 2B) and 3 embryos per condition for the comparison of the effect of the treatments (Figures S4A–S4C).

For zebrafish electronic microscopy experiments (Figures 2G, 4K, and 5E) sample size is 1. These experiments have the objective to be as descriptive as possible, reaching the best resolution existing, but not to be quantitative. The embryos, the region of interest and the timing was chosen during a dedicated injection experiment.

Mouse Experiments

For Mouse blood flow measurement (Figure 7B), results were obtained from more than 5,000 tumor cells from four different tumor cell lines (JIMT1br3, A2058br, PC14PE6br, H1). A total of 51–96 vessels from 12–13 regions (dimensions: 607.28x607.28x372.00 μ m) of 3–6 animals per group were quantified. Box plots representing median values with 10th, 25th, 75th and 90th percentiles.

For experiments described in Figure S7 (A–D), results were obtained from (A) : Distance to first perfused vessels, n=19; (C) Dextran High, n=17 vessels. Dextran low, n=7 vessels; (D) Diameter, n= 98 vessels from 4 stacks.

Microfluidic and Other *In Vitro* Experiments

Microfluidic perfusion assays (Figures 1G, 2F, S2B, S4I, 6D, and 6E) were reproduced 3 times, with independent HUVEC culture and independent siRNA transfection when used. For Figure 2F, n=62, 64 and 65 cells in siCtrl, siTGb1 #1 and siTGb1 #2 respectively.

For Figure 6E, quantification was done on n=67 cells in no flow and n=88 in flow conditions.

Exception: The data shown on the Figure 1G come from 6 independent experiments using 6-channels IBIDI μ -slides. During each experiments, all the perfusion conditions couldn't not be realized each time, so we decided to increase the number of experiments, inducing a final sample size of 5 to 6 perfused channel per condition.

Live imaging of pCAG-EGFP transfected HUVEC (Figure 6A) was done on 4 independent experiments. In total, n=14 cells for the no flow condition and n=15 cells for the flow condition.

SEM experiment (Figures 6B and 6D) was repeated in two independent experiments. For the quantification in 6B, n=15 fields for the flow and n=10 fields for the no flow condition were quantified.

Flow study experiments of 100 μm beads around arrested CTCs in the microfluidic channels (Figure 6C) were performed during 2 independent experiments. Velocity analysis was made on 6 cells.

Microfluidic assays couple with optical trapping (Figures S2C and S2D) were repeated in three independent experiments, with independent HUVEC culture and independent siRNA transfection. Represented total sample sizes (number of trapped CTC) are $n = 8$ (37°) and $n=6$ (28°) (Figure S2C) and $n=12, 13, 15$ and $n= 15, 23, 14$ cells, respectively for adhesion and detachment experiments with siRNA Integrin cells (siCtrl, siITGb1#1 and siITGb1#2 – Figure S2D).

In vitro assays (adhesion and migration - Figures S4E–S4G, S5D, and S5H) was repeated three times independently. Furthermore, adhesion assay was done in triplicate.

Western blot analysis and immunofluorescence quantification (Figures 2C and S2E) were obtained from three independent experiments as a validation for the siRNA efficiency.

Cell diameter measurement of CTCs from patients (Figure 2A) were done post-isolation from blood sample from 6 patients, resulting in $n=2, 12, 1, 53, 10, 7$ cells respectively. For 1675, D2A1, JIMT-1, A431, 4T1, ZMEL cells diameter, quantification was done using acquisitions of cells in suspension, $n>90$.

Patient's MRI for Brain Metastatic Study

Number of BM for the 100 patients are provided for the entire cohort: BM originate from various tumor types including lung cancer ($n=51$), skin cancer ($n=17$), breast cancer ($n=10$), genitourinary (GU) cancer ($n=10$), gastrointestinal (GI) cancer ($n=4$), sarcoma ($n=2$) and cancer of unknown primary ($n=6$). The differences in CBF and MTT between all BM and BM- voxels were compared by the independent t-test. Voxels with more than one BM were weighted according to the number of BM occurring within the voxel. The paired samples t-test was used to compare the perfusion values and the volume of the BM (Figures 8A–8D).

DATA AND SOFTWARE AVAILABILITY

For most of the analysis: GraphPad V5.04 to V6, PRISM - commercial dedicated software for statistical analysis.

For human patients data, statistical analysis was conducted using IBM SPSS Statistics® software (IBM® 2011, version 20, Armonk, New York, USA) and R (The R Foundation, version 3.3.1. Vienna, Austria)

Optical tweezers acquisitions were driven with Labview software and National Instruments acquisition boards. The signal analyses for the optical tweezers as for PIV were performed with IgorPro and ImageJ. The Michaelis Menten model was developed under Wolfram Mathematica. The heatmap reconstruction is a homewritten script running under Matlab (available to the scientific community).

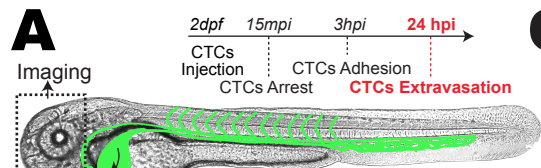
The *in silico* vasculare architecture and numerical simulation were performed with with Freecad, Gmsh, AngioTK and Feel++ (See Resource table for more information).

Probing of flow profiles around arrested tumor cells was performed using Imaris (Bitplane) as well as FIJI.

Supplemental Information

Hemodynamic Forces Tune the Arrest, Adhesion, and Extravasation of Circulating Tumor Cells

Gautier Follain, Naël Osmani, Ana Sofia Azevedo, Guillaume Allio, Luc Mercier, Matthias A. Karreman, Gergely Solecki, María Jesús García León, Olivier Lefebvre, Nina Fekonja, Claudia Hille, Vincent Chabannes, Guillaume Dollé, Thibaut Metivet, François Der Hovsepian, Christophe Prudhomme, Angélique Pichot, Nicodème Paul, Raphaël Carapito, Siamak Bahram, Bernhard Ruthensteiner, André Kemmling, Susanne Siemonsen, Tanja Schneider, Jens Fiehler, Markus Glatzel, Frank Winkler, Yannick Schwab, Klaus Pantel, Sébastien Harlepp, and Jacky G. Goetz



Tumor cells (2.10^3)

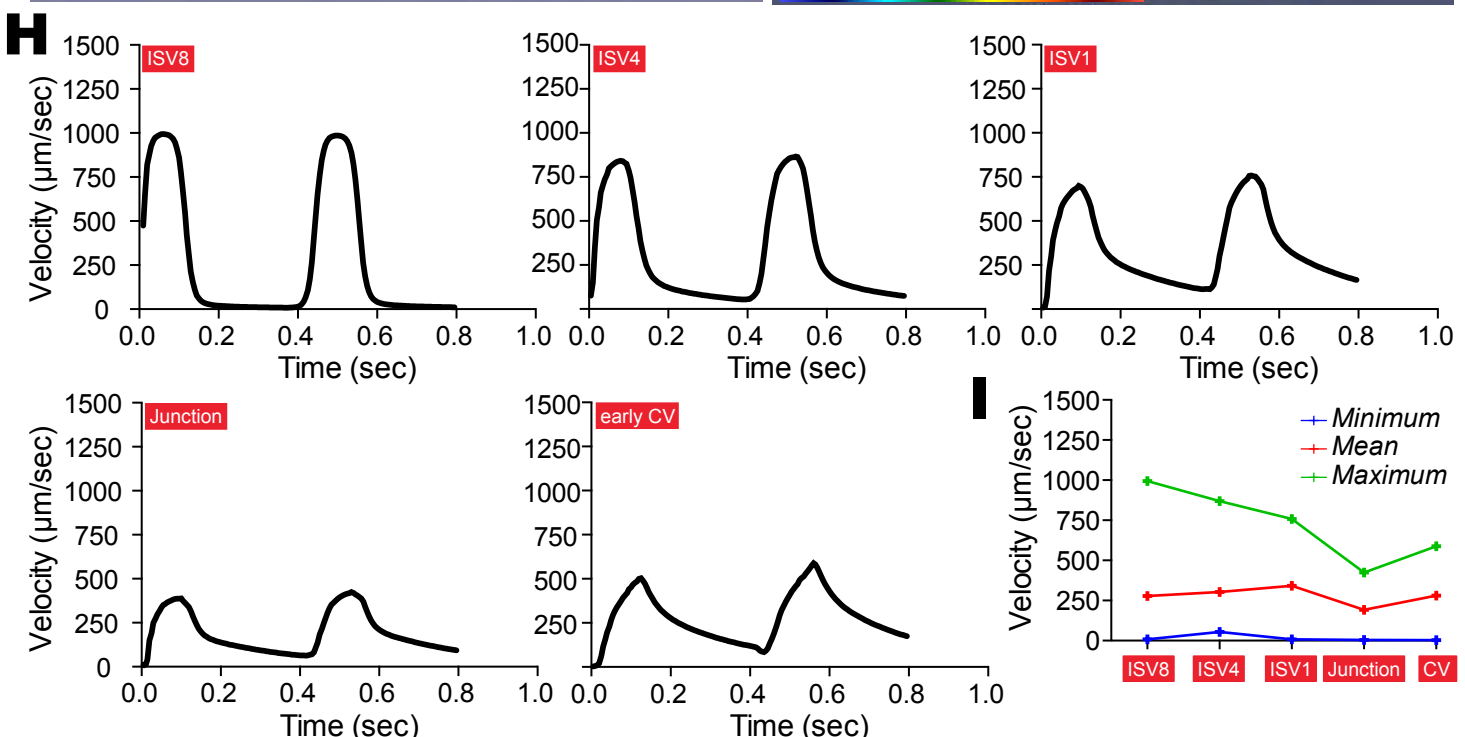
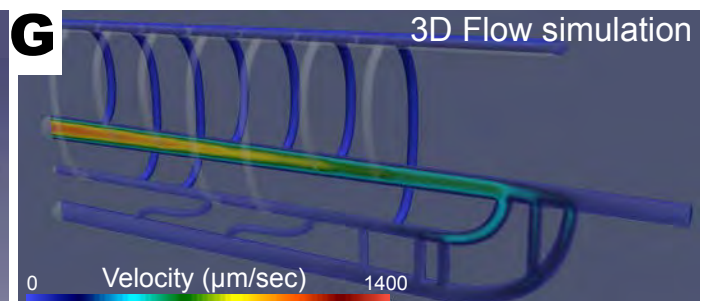
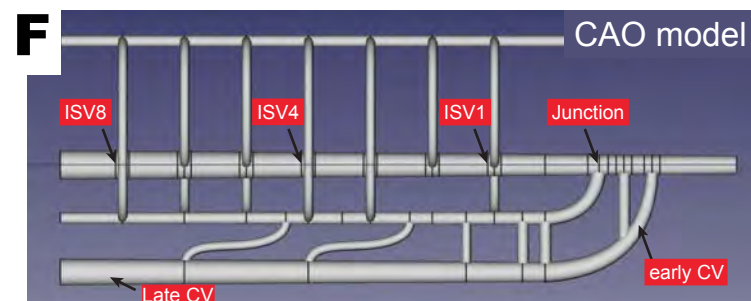
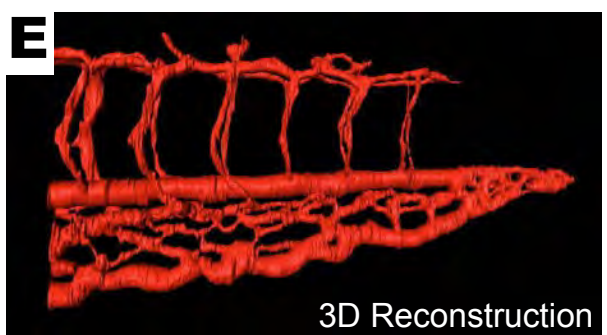
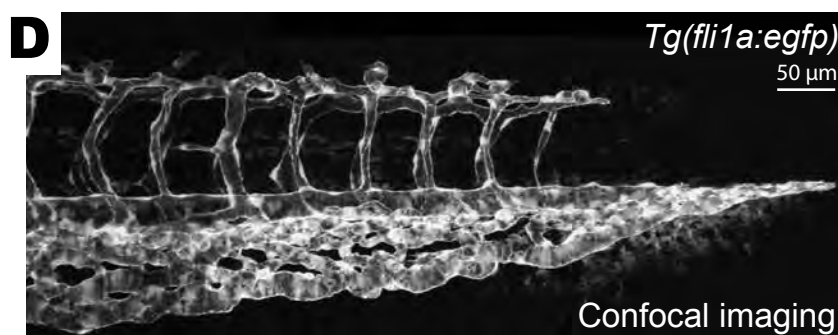
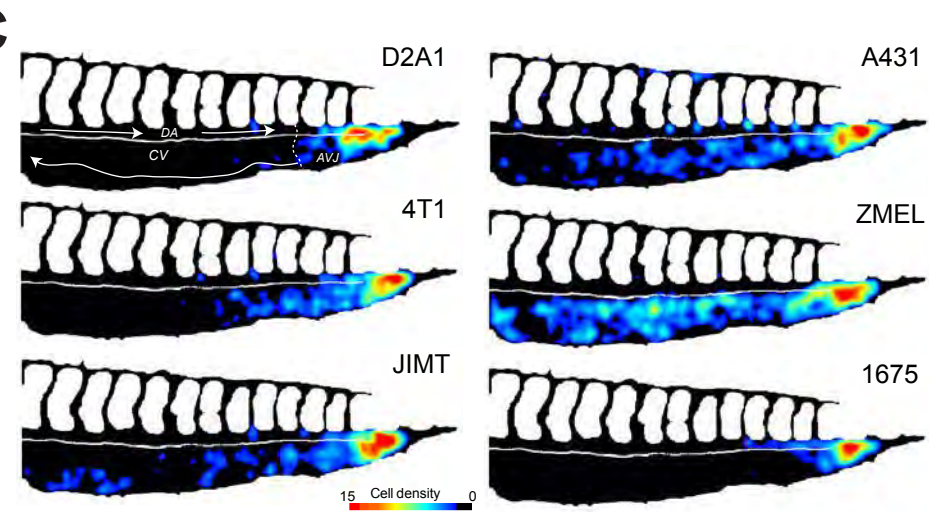
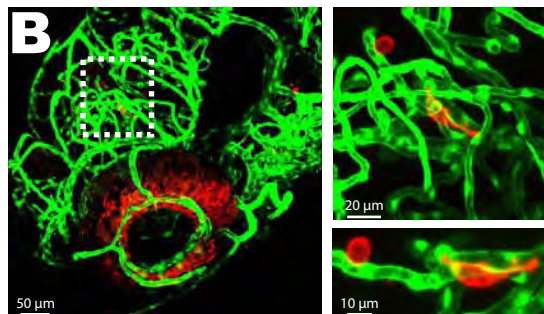


Figure S1. Related to Figure 1: CTCs arrest and extravasate in vascular regions with permissive flow profiles. (A) Experimental workflow. (B) Maximum projection of confocal stack of the zebrafish brain vasculature (green) containing extravasated TCs (red). (C) Heatmaps showing the adhesion pattern of 6 cell lines in the caudal plexus of the zebrafish embryos. (D) Confocal Z-projection of zebrafish posterior caudal plexus (CP) at 2 dpf. (E) Partial 3D segmentation (Amira) based on confocal acquisition (D). (F) Simplified AOC model of the zebrafish CP. (G) Image extracted from Movie S3, showing flow simulation results in the AOC model. (H) Velocity profiles obtained from flow simulation at several positions indicated in F. (I) Graphical representation of minimum, maximum and mean values of the blood flow velocity over the 5 positions from F.

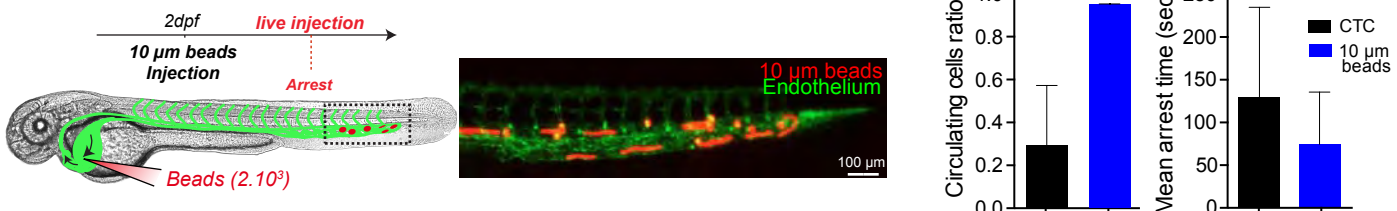
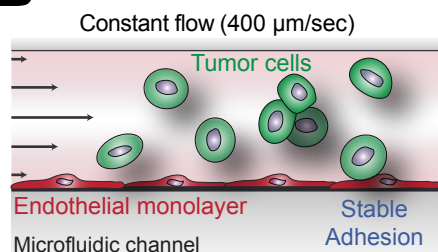
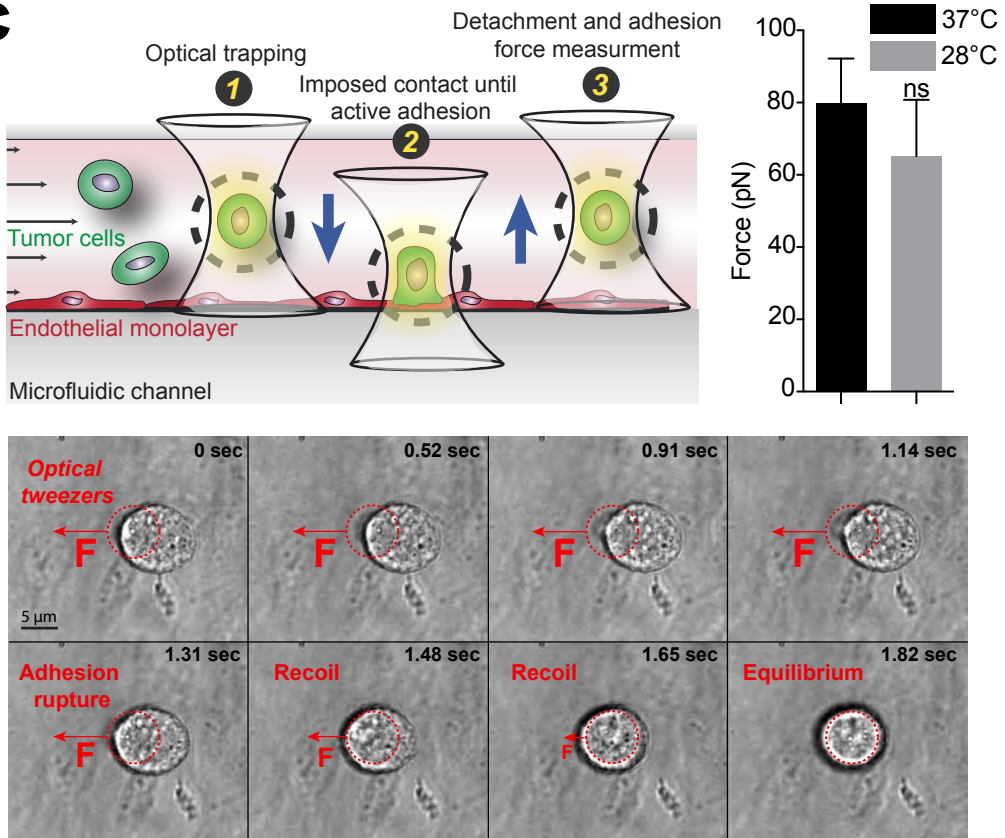
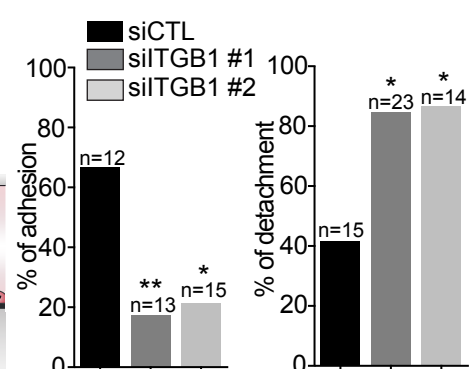
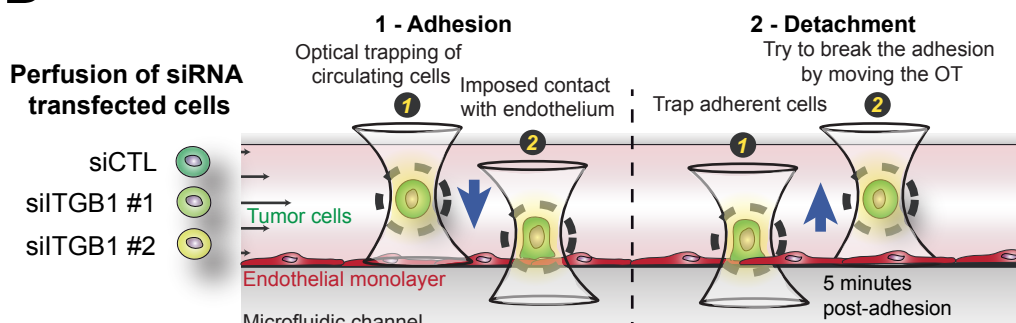
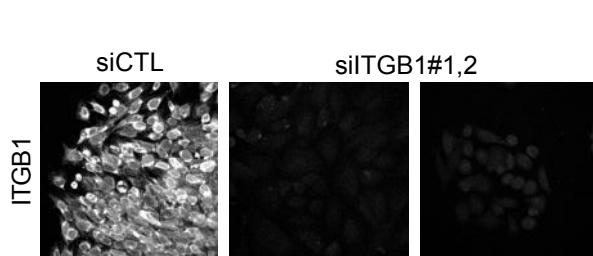
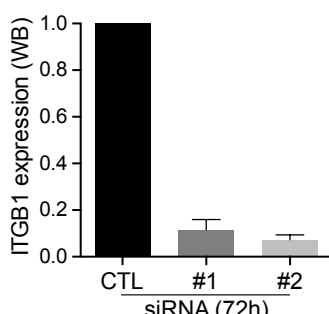
A**B****C****D****E**

Figure S2. Related to Figure 2: Permissive flow profiles allow adhesion of CTCs to ECs. (A) Experimental set up, representative image and quantifications of the 10-μm beads injection. (B) Experimental set up and results of the adhesion efficacy regarding the temperature. (C) Experimental set up and quantification of the measured adhesion rupture force (n=8 and 6) of attached TC (top). Annotated image sequence from Movie 6 showing the detachment of a TC from the endothelial monolayer (bottom). (D) Experimental set up and quantification of the ratio of effective adhesion events upon OT (left) and OT-mediated detachment events (right) using siRNA-treated TCs. (E) Quantification of the Western blot analysis in Fig.2E and representative immunostaining images from siTGB1 cells.

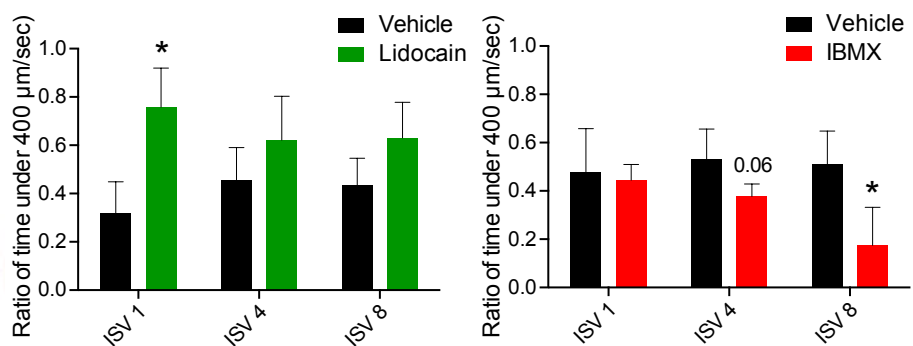
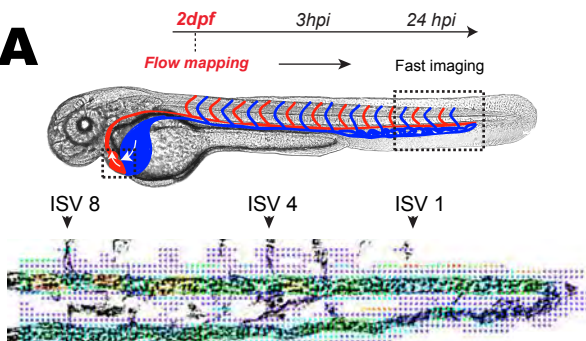
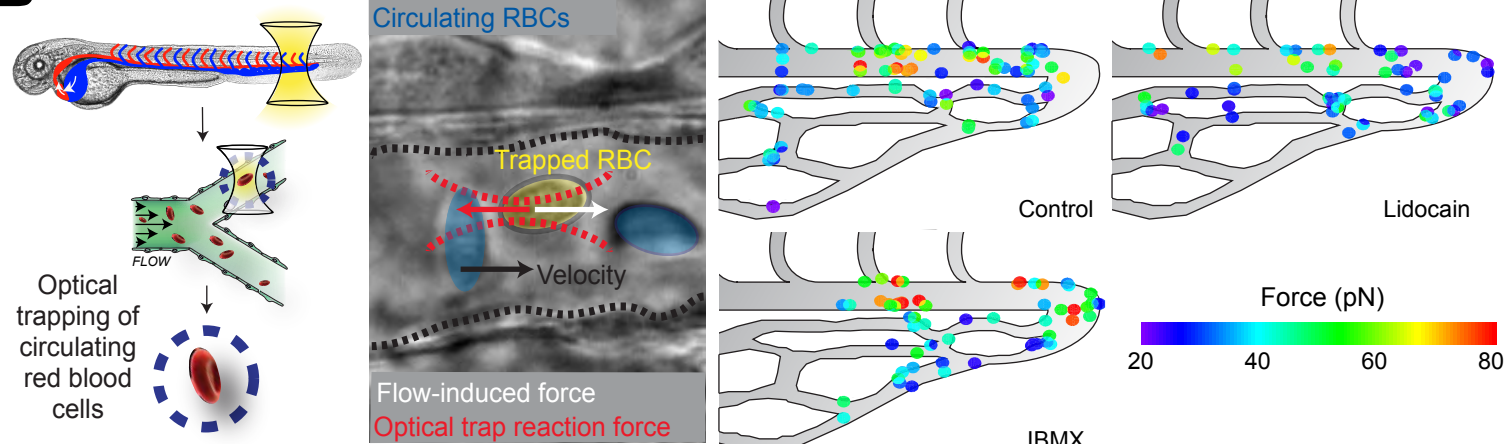
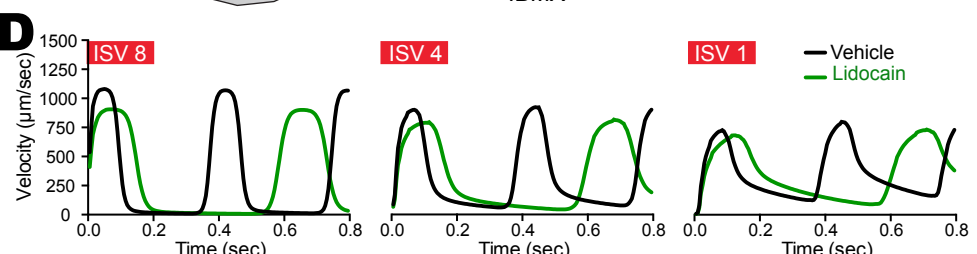
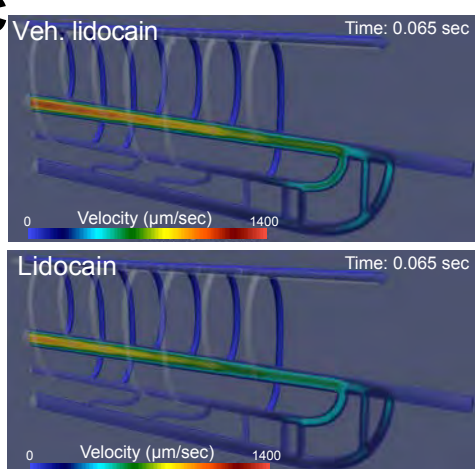
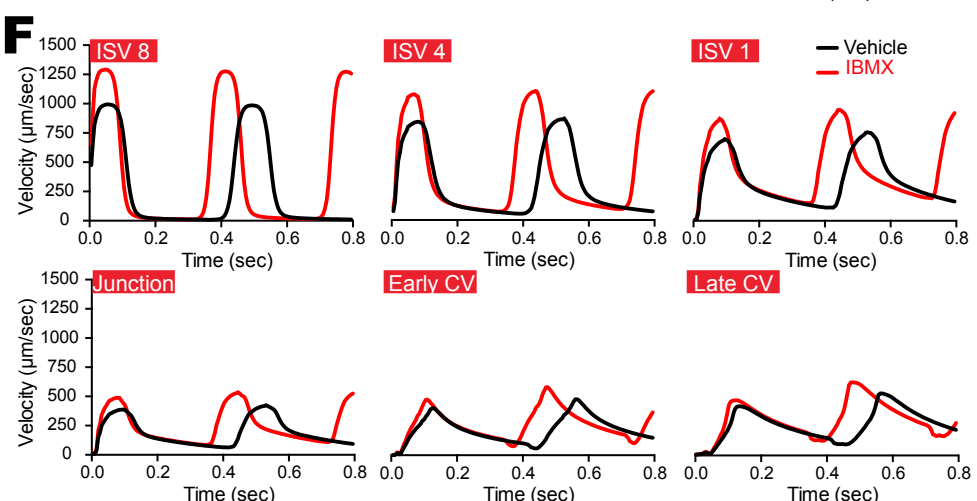
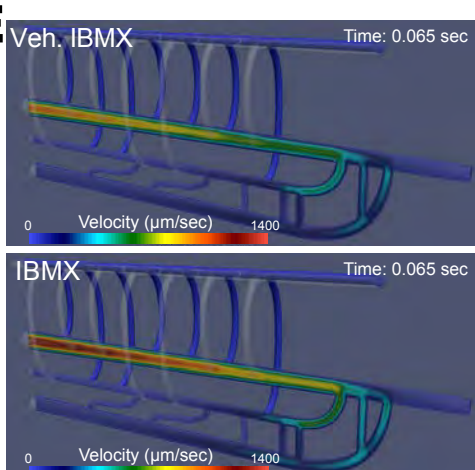
A**B****C****E**

Figure S3. Related to Figure 3: Flow tuning in vivo. (A) Experimental workflow, and a representative image of the PIV analysis in the CP. Quantification of the duration of the flow under 400 $\mu\text{m/sec}$ for each pharmacological condition in the dorsal aorta (position ISV 1, 4 and 8 from A) ($n = 4$ to 5 embryos per condition). (B) Experimental workflow of OT-mediated quantification of hemodynamic forces in vivo and annotated image showing trapped RBC in the DA (yellow) (see also Movie 11). Quantification and mapping of the flow force measured with OT on trapped RBCs for 3 conditions: lidocain, IBMX and control (breeding water). Values in A are mean \pm SD. (C and E) Image extracted from Movie 10, showing flow simulation results in the AOC model for vehicles and lidocain (C) or IBMX (E). (D and F) Velocity profiles from flow simulation at several positions for each condition (as shown in Fig.S1F).

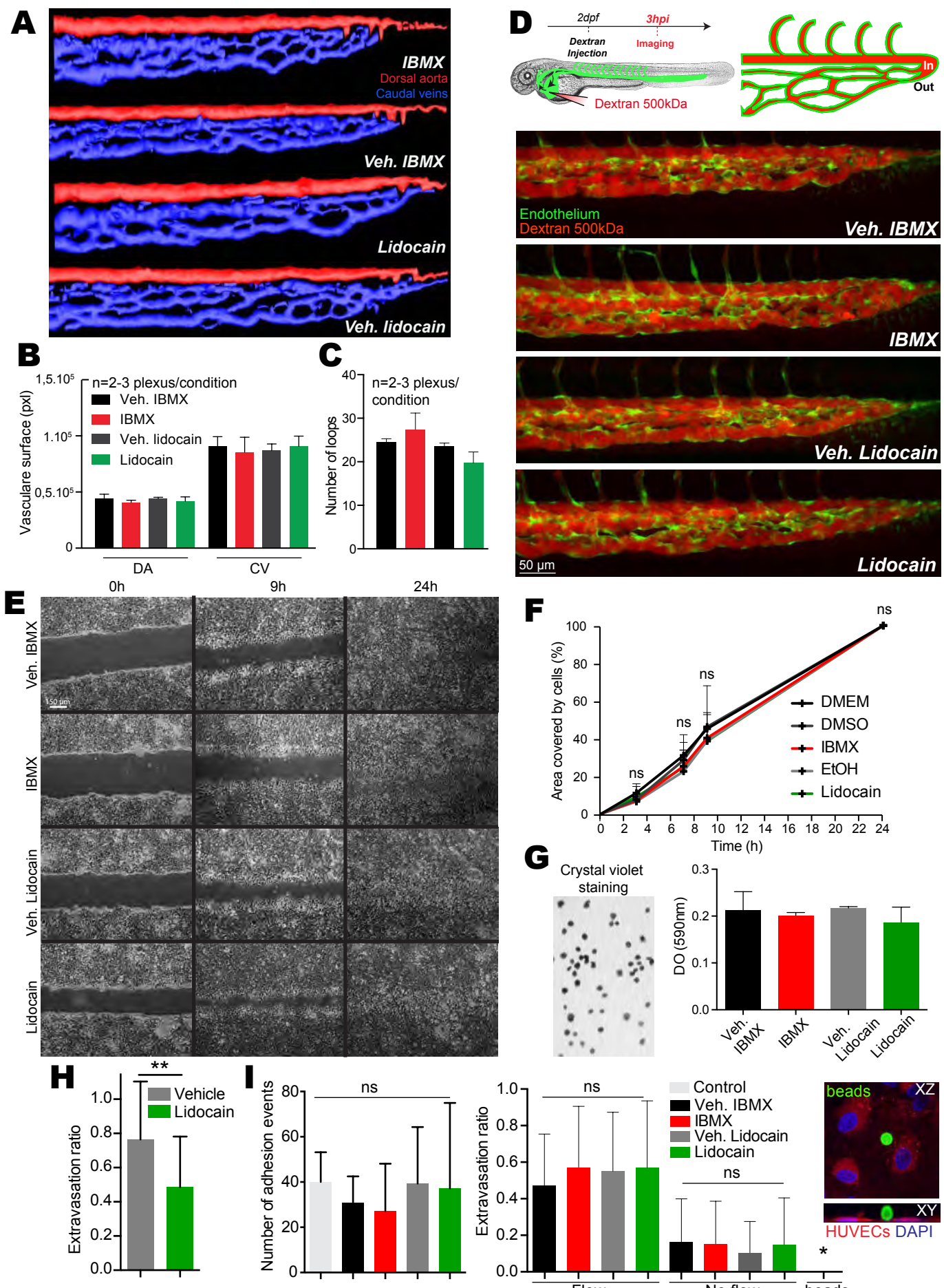


Figure S4. Related to Figure 4: Blood flow tuning does not affect the architecture of the caudal plexus or tumor cells ability to migrate and adhere. (A) 3D segmentation (IMOD) from one zebrafish posterior caudal plexus per condition (See also Movie 12). (B) Total vascular surface from dorsal aorta (DA, red on A) and caudal veins (CV, blue on A) for each condition (n=3). (C) Number of vascular loops for each condition (n=3). (D) Representative images of embryos injected with dextran 500kDa and imaged 3 hpi are shown (E) Representative images of wound closure for each condition 0, 9 and 24 hours after wound. (F) Wound closure over time (n=3). (G) Representative image of TC stained with crystal violet during the adhesion test (left). Absorbance measured at 590nm (right). (H) Number of adhesion events per field after 10 min of perfusion of tumor cells in each condition using the microfluidic channels. (I) Number of extravasated cells 16 hours post-perfusion of tumor cells (10min), with or without flow, in the microfluidic channels in each condition. In vitro experiment were done at least 3 times, in triplicate. Values in (B-C), (F-G) and (H,I) are mean + SD.

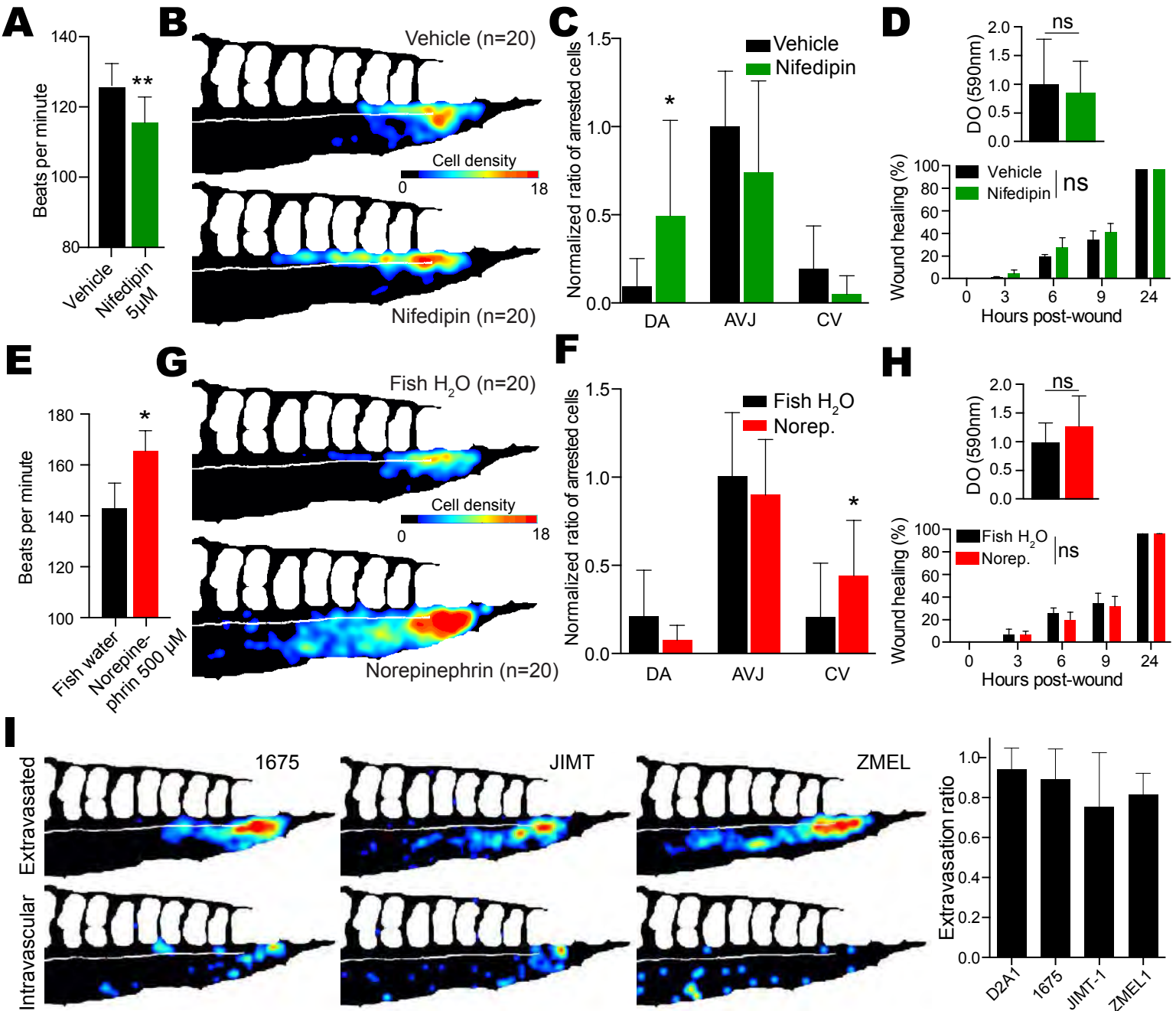


Figure S5. Related to Figure 4: Tuning PMA with two other drugs also perturb the behavior of CTCs in vivo. (A) Quantification of the PMA with nifedipin (5μM) treatment compared to vehicle. (B) Number and location of arrested CTCs 3hpi using heatmap, and quantification (C). (D) Adhesion and migration assay results of TCs assessed in presence of nifedipin. (E) Quantification of the PMA with norepinephrine (500μM) treatment compared to control. (F) Number and location of arrested CTCs 3hpi using heatmap, and quantification (G). Data normalized to vehicle AVJ mean. (H) Adhesion and migration of TCs is assessed in presence of norepinephrine. (I) Heatmaps and quantification of the extravasation efficacy of 1675, JIMT-1 and ZMEL cells 24 hpi. Values in (A), (C-F), (H-J) and (I) are mean + SD.

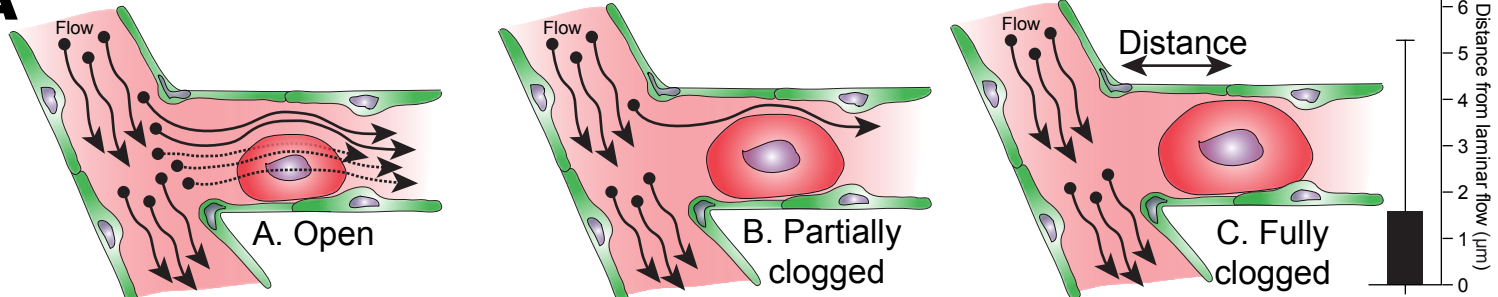
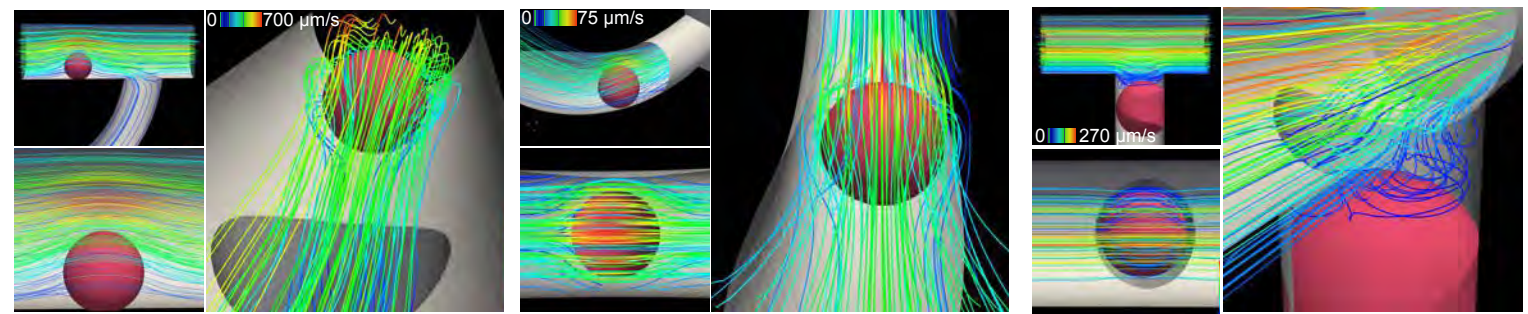
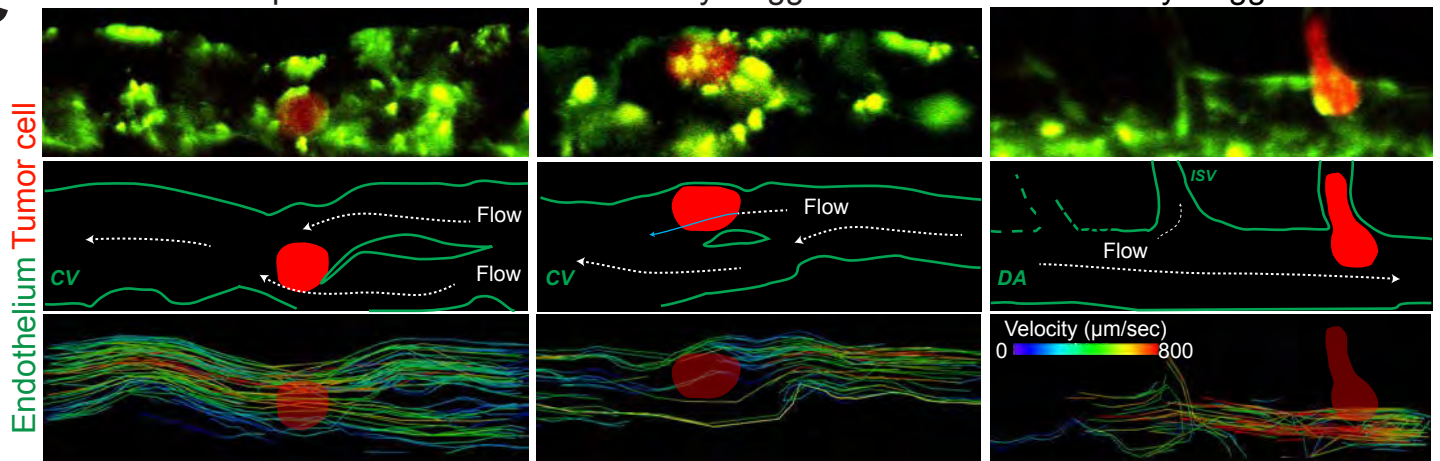
A**B****C**

Figure S6. Related to Figure 5L: Flow profiles around (and close to) arrested tumor cells in the zebrafish embryo. (A) Scheme depicting flow profiles around arrested TC in the zebrafish embryo (Open, partially clogged and clogged) and quantification of the distance between arrested TC and the first fully perfused vessel (B) Images of in silico simulations for the respective scenario (C) Images and analysis of high-speed confocal acquisitions in the zebrafish embryo. Values in (A) are mean \pm SD.

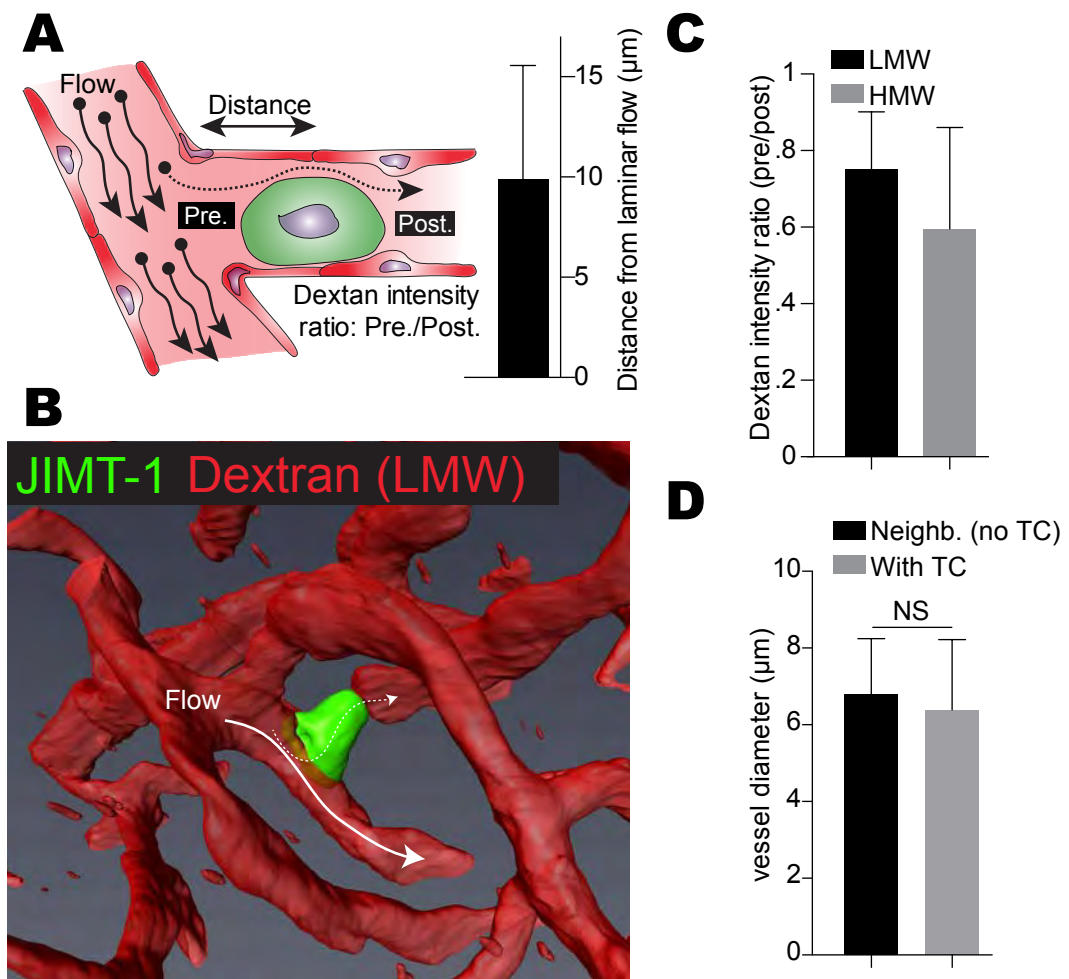


Figure S7. Related to Figure 7: Arrested CTCs in the mouse brain are in contact (or close to) with laminar flow profiles.
 (A) Scheme depicting flow profiles around arrested TC in the mouse brain and quantification of the distance between arrested TC and the first fully perfused vessel. (B) 3D image of an arrested TC in a cerebral capillary. (C) Quantification of Dextran intensity before and after the arrested TC, ratio is plotted for both High (HMW) and Low (LMW) Molecular Weight Dextran. (D) Quantification of mean vessel diameter in vessel bearing (with TC) or not (neighboring) arrested TC. Values in (A), (C), and (D) are mean + SD.

METASTATIC TUMOR CELLS EXPLOIT THEIR ADHESION REPERTOIRE TO COUNTERACT TO FORCES DURING INTRAVASCULAR ARREST.

Scientific context

Cell adhesion is central in the metastatic cascade. It allows cells to probe and migrate in the extracellular matrix towards the vessels during invasion (Friedl and Alexander, 2011; Paul et al., 2017). It also allows the tumor cells to cluster with other circulating cells (such as other tumor cells, immune cells and platelets), conferring them a higher metastatic potential (Aceto et al., 2014). Cell Adhesion is necessary to allow tumor cells to stick to the endothelium in the blood stream and to settle at secondary sites before the metastatic outgrowth. Cell adhesion receptors expressed by the tumor cells have been largely studied (Reymond et al., 2013). A large amount of publications focused on circulating tumor cells adhesion *in vitro* (Marshall et al., 2003; Shea et al., 2017; Strell and Entschladen, 2008), mainly using microfluidic devices, to dissect the role of different receptors (Felding-Habermann et al., 2001; Laferrière et al., 2004; Klemke et al., 2007). Despite this knowledge, *in vivo* significance is still largely unknown (Reymond et al., 2012; Barthel et al., 2013).

In our previous work (Follain et al., 2018a), we observed that tumor cells are contacting the endothelial cells through filopodia-like structures that strongly suggest active cell adhesion. Moreover, reproducing stable adhesion experiment (3hpi) with knocked-down cells for ITGB1 (one of the most central cell adhesion molecule), we showed that the overall number of adhered tumor cells was decreased (*Follain et al. Dev. Cell 2018 – Fig. 1E*). Thus, these results demonstrate that 1- active adhesion play a role in our data. 2- The adhesion-specific contribution is not fully dependent on blood flow: Indeed, the effect of the knocking down of $\beta 1$ integrin is not to push the cells further away (like higher flow does), but to decrease the overall number of cell arrests. These findings prompted us to develop this part of the project, by dissecting the role of adhesion receptors in arrest and stable adhesion steps *in vivo*.

Strategic context

Based on the experimental approach that we designed to study the last steps of the metastatic cascade in the zebrafish embryos (Follain et al., 2018a, 2018b) we started to address the role of circulating tumor cells adhesion receptors. We used siRNA strategy that allow transient knock-down of the target of interest to study the role of each receptor. We selected a list of receptors based on the literature (Reymond et al., 2013; Vestweber, 2015) and checked their expression by western blot in the D2A1 (highly metastatic) and D2OR (non-metastatic counterpart) cells. Then, we reproduced the previous methodology *in vivo* and complemented the results with microfluidic experiments to identify the key receptors and to dissect their roles.

Major outputs

Our results establish a two-step process for cancer cell arrest and adhesion, involving different receptors *in vivo*: For our cells, low binding forces molecules such as integrin $\beta 3$ (ITGB3) and CD44 are required during the arrest steps, whereas Integrin $\alpha 5\beta 1$ (ITGA5B1) is required to stabilize the adhesion. This is reminiscent from leukocyte transmigration, even if we never observed rolling of our CTCs at the surface of the endothelium *in vivo* and *in vitro*. Also, $\alpha 4$ integrin (central binding molecule for leucocytes to VCAM at the apical surface of endothelial cells) is not implicated in our cell lines. Further moving to mice experiments, we showed that only stable adhesion (using ITGB1 knock-down cell) impacts extravasation and subsequent metastatic outgrowth.

To note, this manuscript was first sent to *Developmental cell* where it was peer-reviewed. Editors offered us to transfer our manuscript to *Cell Report* after addressing reviewer's comments. This is the version **accepted for publication** in *Cell report* in July 2019.

Metastatic tumor cells exploit their adhesion repertoire to counteract shear forces during intravascular arrest

Naël Osmani^{1-3*}, Gautier Follain^{1-3*}, Marìa Jesús Garcia Leòn¹⁻³, Olivier Lefebvre¹⁻³, Ignacio Busnelli¹⁻³, Annabel Larnicol¹⁻³, Sébastien Harlepp¹⁻⁴, Jacky G. Goetz^{1-4#}

¹ INSERM UMR_S1109, Strasbourg, F-67000, France.

² Université de Strasbourg, Strasbourg, F-67000, France.

³ Fédération de Médecine Translationnelle de Strasbourg (FMTS), Strasbourg, F-67000, France.

⁴ Corresponding author

* These authors contributed equally to this work

Materials and correspondance, #lead author:

Jacky G. GOETZ#, jacky.goetz@inserm.fr, Sébastien HARLEPP, harlepp@unistra.fr
INSERM UMR_S1109, 67000 Strasbourg, France; Fédération de Médecine
Translationnelle de Strasbourg (FMTS), 67000 Strasbourg, France
Web: www.goetzlab.com, twitter: [@GoetzJacky](https://twitter.com/GoetzJacky)

Keywords:

Circulating tumor cell, arrest, adhesion, metastasis, biomechanics, zebrafish, integrins

SUMMARY

Cancer metastasis is a process whereby a primary tumor spreads to distant organs. We have previously demonstrated that blood flow controls the intravascular arrest of circulating tumor cells (CTCs), through stable adhesion to endothelial cells. We now aim at defining the contribution of cell adhesive potential and at identifying adhesion receptors at play. Early arrest is mediated by the formation of weak adhesion depending on CD44 and integrin $\alpha v\beta 3$. Stabilization of this arrest uses integrin $\alpha 5\beta 1$ -dependent adhesions with higher adhesion strength, which allows CTCs to stop in vascular regions with lower shear forces. Moreover, blood flow favors luminal deposition of fibronectin on endothelial cells, an integrin $\alpha 5\beta 1$ ligand. Finally, we show that only receptors involved in stable adhesion are required for subsequent extravasation and metastasis. In conclusion, we identified the molecular partners that are sequentially exploited by CTCs to arrest and extravasate in vascular regions with permissive flow regimes.

INTRODUCTION

Cancer metastasis is a complex multi-step process in which secondary tumors are formed in colonized organs ultimately leading to the death of patients (Lambert et al., 2017). Circulating tumor cells (CTCs) exploit body fluids to reach distant organs, where they will extravasate and either remain dormant or form new tumor foci (Obenauf and Massagué, 2015). The molecular receptors expressed by tumor cells and that are involved in the intravascular adhesion of CTCs have been widely studied (Reymond et al., 2013). In particular, glycoproteins involved in leukocytes rolling at the surface of the endothelium, such as selectins, are required for the adhesion of cancer cells to endothelial cells (Aigner et al., 1998; Laferrière et al., 2001). CD24, CD44, PODXL and mucins facilitate CTC adhesion to the endothelium (Aigner et al., 1998; Dallas et al., 2012; Hanley et al., 2006; Rahn et al., 2005; Shea et al., 2015). Adhesion receptors of the integrin family such as integrins $\alpha v\beta 3$, $\beta 1$ and $\beta 4$ were similarly involved in adhesion of CTCs to endothelial cells (Felding-Habermann et al., 2001; Laferrière et al., 2004; Klemke et al., 2007; Reymond et al., 2012; Barthel et al., 2013). However, the respective contribution of these receptors in intravascular arrest has rarely been challenged *in vivo* in realistic shear conditions. Furthermore, the correlation between the adhesive and the metastatic potential of CTCs is still not fully understood.

Recently, using a combination of easy-to-tune microfluidics and intravital imaging in two animal models, we have shown that blood flow tunes CTC arrest, preceding metastatic outgrowth, through a tug of war with CTC adhesion potential and thereby control their probability of intravascular arrest (Follain et al., 2018a). Using the zebrafish embryo, we observed that CTC arrest immediately upon blood circulation entry but may still be detached from the endothelium by ripping shear forces. Adhesion of CTCs is then reinforced preventing them from shear-mediated detachment. Interestingly, intravascular arrest of leukocytes is driven by weak adhesions with receptors such as CD44, while adhesions reinforcement depends on integrin-mediated bonds (Eibl et al., 2012; McEver and Zhu, 2010).

Here, we demonstrate that highly metastatic CTCs are more prone to intravascular arrest, which favors metastatic extravasation. We show that extravasation is preceded by two major steps: (i) early arrest mediated by the formation of *de novo* adhesions of weak energy (through CD44 and the integrin $\alpha v\beta 3$) and (ii) the stabilization of CTC/endothelium bond through the recruitment of adhesions with larger magnitude of energy (via the integrin $\alpha 5\beta 1$). Altogether, these 2 consecutive steps allow arrested CTCs to resist blood flow shear forces and favor metastatic extravasation.

RESULTS

CTC adhesive properties correlate with adhesion and extravasation potential

Whether intravascular arrest of CTCs determines their metastatic potential remains to be determined. We thus built on a zebrafish-based experimental metastasis workflow (Follain et al., 2018a) and compared the behavior of tumor cells with established low and high metastatic potential derived from a D2 mouse mammary hyperplastic alveolar nodule (Morris et al., 1993). While D20R cells are poorly aggressive, D2A1 cells recapitulate breast carcinoma derived lung metastasis in a BALB/C mouse syngeneic model (Shibue et al., 2013) and were shown to be metastatic in zebrafish embryos (Follain et al., 2018a).

When monitoring early arrest of these 2 cell lines, we observed a ~20% decrease in the efficiency of arrest of low-metastatic D20R, when compared to D2A1 (Figure 1A-B). While D2A1 preferentially arrested in the dorsal aorta (DA) and arterio-venous junction (AVJ), D20R were mostly observed in the AVJ and the caudal veins (CV),

further along the vascular network (Figure 1C-D). When monitoring the stable intravascular arrest at 3hpi, we confirmed that D20R were mainly found in the CV (Figure 1E-G) suggesting that they have a lower adhesive potential that prevents them from stably arresting in the DA or AVJ. Interestingly, increased arrest in the CV had been observed when flow forces were increased (Follain et al., 2018a), confirming the intricate link between shear forces and adhesive potential. We discarded the possibility that increased arrest of D2A1 cells was favored by mechanical trapping of cells with bigger size (i.e. both cell lines display similar size; ~10µm in diameter, Figure S1A). We further checked the surface expression of CD44 and ITGB1, that are respectively weak and strong force adhesion receptors. Interestingly, although expression levels were similar between the two cell lines, surface expression of CD44 and ITGB1 were respectively reduced by ~25% and ~42% in low metastatic D20R cells (Figure S1B-D). Finally, while ~98.5% of D2A1 cells were found extravascular at 24hpi, only ~32% of D20R cells did so (Figure 1H-J, S1E) in vascular regions that match their intravascular arrest location (Figure 1D,F-G,H). Altogether, this demonstrates that the metastatic potential of CTCs is directly linked to their adhesion repertoire, which dictates the efficiency of intravascular arrest.

CD44, ITGB3 and ITGB1 favor arrest of CTCs, yet only ITGB1 is required for stable adhesion to the endothelial layer

In order to conduct a molecular dissection of CTC arrest, we built on previous observations which identified a threshold flow value of 400~500 µm/s favoring CTC arrest (Follain et al., 2018a). We established a microfluidic approach to probe the CTC adhesion repertoire function in realistic shear flow conditions (Figure 2A-B). Flow-dependent adhesion of CTCs to endothelial cells was probed and challenged by tuning flow velocities as well as adhesion receptors. In control conditions, ~80% of arrested CTCs, whose arrest had been favored by decreasing flow velocities, had formed stable adhesion with the endothelial layer when challenged with increasing flow velocities (Figure 2A-C, Movie 1). Interestingly, while siRNA depletion of CD44, ITGB3 or ITGB1 compromised CTC attachment (Figure 2D, S2, Movie 2-3), only ITGB1 depletion impacted CTC stable adhesion to the endothelial layer (Figure 2D). This suggests that, while CD44 and ITGB3 favor CTC arrest, only ITGB1 allows their

stabilization on endothelial cells, in flow conditions, which mirrors their previously described adhesive potential (Bano et al., 2016; Roca-Cusachs et al., 2009).

In order to identify the α subunit (ITGA) mediating stable adhesion of CTCs, and thereby identify its ligand, we depleted ITGA4, 3 and 5 (Figure S2D,S3A). When associated to ITGB1, they respectively mediate binding to luminal VCAM (Klemke et al., 2007), to laminin (Chen et al., 2016a) and to fibronectin (Huvaneers et al., 2008) of the basal ECM. We discarded the participation of ITGA4 and observed that ITGA3 was not required for the formation of stable cell adhesion to the endothelial layer (Figure S3A-C). Only ITGA5 depletion phenocopied ITGB1 knockdown and impaired CTC attachment and the formation of stable adhesion (Figure 2D, S3A).

In order to specifically discriminate between weak metastable and stable adhesions, we used optical tweezing of adhered CTCs within microfluidic channels. This strategy allowed us to further probe the range of forces that are mediated by CD44, ITGB3 and ITGB1 by assessing the adhesive potential of cells depleted for those receptors. Upon mechanical detachment of CTCs that had established adhesion (Figure 2E), we confirmed that ~80% of control cells formed stable adhesion with the endothelium. Only ITGB1 depletion could impair the number of stable adhesion events (Figure 2F, Movie 4-6). In conclusion, while CD44, ITGB3 and ITGA5/ITGB1 both favor the initial arrest and adhesion of CTCs, only ITGA5/ITGB1 is capable of mediating stable shear-protective adhesion of CTCs to the endothelium.

CD44 and ITGB3 are required for CTC arrest *in vivo*, only ITGB1 further stabilizes adhesion to the endothelium

To further demonstrate that initial arrest can be decoupled from stable adhesion, we injected D2A1 cells in zebrafish embryo and monitored intravascular arrest using live imaging for 5 minutes (Figure 3A). Depletion of CD44 and ITGB3 impacted early adhesion of CTCs. On the contrary, depleting ITGB1 had no effect and CTCs arrested similarly the AVJ (Figure 3A-B, Movie 7-9). We carefully quantified the exact arrest duration of CTCs, which exceeded 2 minutes in control conditions. CD44- and ITGB3-depleted cells were either unable to arrest or had shorter arrest durations (Figure 3A,C) suggesting decreased adhesive abilities and/or increased sensitivity to shear forces. We further assessed the number and location of stably-adhered CTCs 3hpi and showed that depletion of CD44 or ITGB3 had no effect (Figure 2D-E). On the contrary, ITGB1 depletion drastically reduced the number of cells stably arrested

in the AVJ at 3hpi (Figure 2F). Furthermore, while ITGA4 and ITGA3 depletion did not impair CTC adhesion (Figure S3D-E), ITGA5 phenocopied ITGB1-depletion and impaired stable adhesion of CTCs (Figure 3G). This suggests that CD44/ITGB3 are required for the initial arrest while ITGA5/ITGB1 mediate stable arrest *in vivo*.

Fibronectin is a ligand for CD44 and integrins $\alpha v\beta 3$ and $\alpha 5\beta 1$ (Jalkanen and Jalkanen, 1992; Humphries, 2006). We next interrogated whether fibronectin could mediate the adhesion-dependent CTC arrest. As expected, we observed flow-dependent fibronectin deposits at the surface of endothelial cells *in vitro* (Figure S4A-B) that are independent of fibronectin expression levels (Figure S4C). Surprisingly, we observed no effect of flow forces on laminin 111 and collagen I, while it decreased both collagen IV and hyaluronan levels (Figure S4D). This suggests that flow forces, that are permissive to CTC arrest (Follain et al., 2018a), favor the deposition of fibronectin patches on the luminal side of endothelial cells. We then confirmed such observation *in vivo* and observed luminal fibronectin (Figure S4E-G). Interestingly, we found that fibronectin was more present in the DA compared to the AVJ thus correlating with higher blood flow velocities (Figure S4F) but also with the early arrest pattern of D21A (Figure 1C-D). This flow dependence was further confirmed as intravascular levels of fibronectin were massively reduced in embryos with reduced blood flow velocities upon lidocaine treatment (Figure S4E,G-H). Altogether, these observations suggest that CTCs synergistically exploit flow forces, flow-mediated deposition of fibronectin and cell surface expression of integrins for efficient intravascular arrest. Doing, they successfully resist to shear forces.

Efficient intravascular arrest dictates metastatic extravasation

Whether efficient intravascular arrest impact the ability of CTCs to extravasate and grow metastatic colonies remains to be determined. To do so, we focused on CD44 and ITGB1 as mediators of weak and stable adhesion respectively. Interestingly, while CD44 depletion had no effect on metastatic extravasation in zebrafish embryos, ITGB1 depletion significantly reduced the number of cells that underwent extravasation (Figure 4A-C). While such results confirmed the previously identified role for ITGB1 in metastatic extravasation (Stoletov et al., 2010; Chen et al., 2016b), we here provide further insight by demonstrating that ITGB1 favors pro-metastatic intravascular arrest in addition to facilitate transmigration of CTCs (Chen et al., 2016b). To further validate our observation and assess the impact on metastatic

outgrowth, we exploited the syngeneic model of lung metastasis upon tail vein injection of luciferase-expressing D2A1 cells in BALB/c mice (Figure 4D). We first carefully assessed seeding efficacy of D2A1 cells using rapid whole-animal imaging of lung signal. Doing so, we noticed that depletion of CD44 only had a mild impact on lung seeding. On the contrary, ITGB1 depletion significantly reduced the number of cells that stably reached the lungs, validating our previous observations (Fig.4E-F). *Ex vivo* imaging of lungs 13 dpi, which allows to confidently assess the impact on metastatic outgrowth, confirmed that only ITGB1 could impact the metastatic burden (Fig.4E-F). Altogether, using a unique combination of *in vitro* and two *in vivo* models, we thus demonstrate that stable intravascular arrest of CTC, which is mediated mostly by ITGB1, is a key step preceding successful metastatic outgrowth.

DISCUSSION

Establishment of metastatic foci follows intravascular journey and efficient arrest of CTCs, the latter being a key step. Although multiple tumor-intrinsic molecular machineries have now been shown to control cancer cell stemness, organotropism, metastatic potential or resistance to chemo/immunotherapy (Lambert et al., 2017), which mechanisms control the stabilization of intravascular arrest, and thereby the efficiency of tumor metastasis, remain to be fully characterized. We provide here a detailed molecular dissection of this important step by demonstrating how tumor cells exploit their own adhesion machineries, and how they exploit extrinsic factors such as blood flow, to stably arrest in specific vascular regions and favor extravasation, preceding metastatic outgrowth.

Here, we exploited recently-established techniques of intravital imaging of CTCs in the zebrafish embryo, which proves to be a very useful model for such questions (Follain et al., 2018a; White et al., 2013). We recently showed that blood flow tunes CTC arrest by a process which is encoded into a tug-of-war between blood flow-driven shear stress and the limited adhesive power of CTCs (Figure 1, Follain et al., 2018). CTC adhesion to the endothelium, preceding their exit from the bloodstream, has been extensively studied either *in vitro* (Aigner et al., 1998; Chen et al., 2016a; Giavazzi et al., 1993; Laferrière et al., 2001, 2004; Reymond et al., 2012; Tremblay et al., 2008) or *in vivo* (Hiratsuka et al., 2011; Köhler et al., 2010; Stoletov et al., 2010) for the past 30 years. These studies identified adhesion receptors used by CTCs to arrest within the bloodstream. However, such molecular dissection, at high spatio-

temporal resolution, of CTC arrest and how it dictates metastatic potential *in vivo* remains to be determined. Also, the influence of low energy versus high energy adhesion of CTCs in intravascular arrest *in vivo* remains elusive.

In the present work, we demonstrate that the metastatic potential of CTCs is, in addition to other molecular programs, controlled by their intravascular adhesive potential that dictates their arrest and thereby control their transmigration and metastatic potential. We combined microfluidics and experimental metastasis assays in zebrafish embryos to report that early arrest is mediated by CD44 and integrin $\alpha v\beta 3$. Both receptors were reported as weak energy adhesion receptors (Bano et al., 2016; Roca-Cusachs et al., 2009). Indeed, CD44 has been involved in the rolling of leukocytes along the endothelium (McEver and Zhu, 2010) and is found expressed in breast cancer CTCs with higher metastatic potential (Baccelli et al., 2013; Boral et al., 2017). Integrin $\alpha v\beta 3$, a major fibronectin ligand, has been suggested to mediate weaker adhesion involved in mechanosensing during cell migration (Roca-Cusachs et al., 2009; Bharadwaj et al., 2017). We also show that CTC/endothelium bonds are quickly stabilized to resist the shear stress from the blood flow with the formation of integrin $\alpha 5\beta 1$ dependent adhesions. These $\alpha 5\beta 1$ -dependent adhesions define more stable adhesions in cells migrating over a matrix of fibronectin as they produce larger magnitude of binding energy but also have longer bond lifetime than integrin $\alpha v\beta 3$ (Roca-Cusachs et al., 2009; Kong et al., 2009, 2013; Bharadwaj et al., 2017). These specific biomechanical properties of $\alpha 5\beta 1$ integrins are particularly relevant in a context where CTC adhesion is challenged in a tug of war by shear stress from the blood flow. Finally, we confirm that CTC stable adhesion to the endothelium is mediated by integrin $\alpha 5\beta 1$ both *in vitro* and *in vivo* in the zebrafish embryo. We recently reported that filopodia-like structures are involved in the initial arrest of CTCs (Follain et al., 2018a). Interestingly, such structures can carry adhesive receptors such as integrins $\alpha v\beta 3$ and $\alpha 5\beta 1$ (Shibue et al., 2012, 2013) suggesting that they might be exploited by CTCs to probe the surface of the endothelium and promote CTC arrest. Importantly, we validated the importance of such step in a lung metastasis assay using a syngeneic mouse model, where we combined fast evaluation of CTC seeding with careful evaluation of the metastatic outgrowth. Doing so, we show that, as expected from the zebrafish experiments, integrin $\alpha 5\beta 1$ controls lung seeding that determines the subsequent metastatic potential in mouse lungs. Altogether, we thus carefully demonstrate that organ seeding and metastatic onset of

CTCs are controlled by tumor-intrinsic factors. We also describe how CTCs can exploit permissive blood flow profiles, engage adhesion machineries to efficiently seed metastases.

Recent work suggests that CTCs can engage the laminin in the endothelial basement membrane via integrin $\alpha 3\beta 1$ and $\alpha 6\beta 1$ (Chen et al., 2016b; Wang et al., 2004). We did not observe that integrin $\alpha 3\beta 1$ is required for stable arrest (Figure S3), suggesting that its involvement might be cell line dependent. We did not test the involvement $\alpha 6\beta 1$, and thus cannot rule out its involvement. Finally, we observed that fibronectin, a ligand of CD44 and integrins $\alpha v\beta 3$ and $\alpha 5\beta 1$, is found as deposits at the surface of the endothelial layer both *in vitro* and *in vivo*, in a process which is flow-dependent (Figure S4). Fibronectin is found on the luminal side of liver blood vessels and facilitates CTC arrest in this organ (Barbazán et al., 2017). Apical fibronectin secretion by epithelial cells is essential during developmental stages such as cleft formation in mouse (Sakai et al., 2003). Fibronectin is also secreted by endothelial cells, although preferentially basally, and needed for proper vasculogenesis in the zebrafish embryo (Mana et al., 2016). Cellular exocytosis is driven by the increase in membrane tension in response to flow shear stress (Shi et al., 2018). In the zebrafish embryo, we observed a correlation between fibronectin deposits and blood flow profiles (Figure S4F). It is quite tempting to speculate that the shear stress induced by the blood flow might promote the secretion of a fibronectin adhesion platform at the luminal side of the endothelium.

Altogether, we propose that the first steps of CTC arrest are mediated by a coordination between blood flow and CTC/endothelium adhesion where: (i) blood flow shear stress challenges the finite CTC adhesion force to tune their location of arrest, (ii) CTCs differentially use their adhesion repertoire to arrest and stably adhere to the endothelial layer and (iii) only adhesions involved in arrest stabilization are required to further proceed to extravasation and metastatic outgrowth. Targeting such adhesion receptors could be relevant in order to therapeutically prevent CTC extravasation preceding metastatic colonization.

ACKNOWLEDGMENTS

We thank all members of the Goetz Lab for helpful discussions. We are grateful to Tsukasa SHIBUE and Robert WEINBERG (MIT) for providing D2A1 cells. We are very grateful to Francesca PERI and Kerstin RICHTER (EMBL) for providing

zebrafish embryos. This work has been funded by Plan Cancer (OptoMetaTrap) and CNRS IMAG'IN to S.H. and J.G. and by institutional funds from INSERM and University of Strasbourg. N.O is supported by Plan Cancer 2014-2019 (OptoMetaTrap) and the Association pour la Recherche contre le Cancer. G.F. is supported by La Ligue Contre le Cancer and University of Strasbourg. M.J.G.L is supported by INCa (National Cancer institute) and University of Strasbourg (Idex).

AUTHOR CONTRIBUTIONS

N.O. & G.F. performed most experiments and analysis. M.J.G.L performed FACS analysis. M.J.G.L and O.L performed and analyzed mice experiments. S.H. supervised the study, performed OT experiments and analysis. J.G. conceived the project and supervised the study. NO wrote the paper with input from G.F., S.H., and J.G.

DECLARATION OF INTERESTS

The authors declare no competing interests.

LEGENDS

Figure 1 – Highly-metastatic D2A1 cells are more prone to stable arrest in larger vessels than D20R cells *in vivo*. (A) Scheme of the experimental approach using 2 dpf *Tg(Flt1:EGFP)* zebrafish embryo as a metastatic cascade model. Lower panel shows blood flow in the plexus regions: dorsal aorta (DA), arterio-venous junction (AVJ) and the caudal veins (CV). (B-D) The arrest of D20R or D2A1 cells were live imaged for 5 min immediately after injection. (B) The ratio of cells stably arrested after 5 min over the total number of cells was measured. (C) The number and localization (see A) of cell arrests over the total number of arrests in the plexus was measured. The graphs show the mean \pm S.D. of 3 independent experiments. (D) Time projection of representative embryo injected with indicated cells transfected. The color code shows the arrest time of CTCs. (E-G) The adhesion pattern of D20R or D2A1 cells was imaged 3h after injection. (E) The number and localization (see A) of cells stably adhered at 3hpi was measured. The graph shows the mean \pm S.D. of 3 independent experiments. (F) Representative images of cells arrested at 3hpi. (G) The heatmaps show the quantification of the number and location of stably arrested CTCs at 3 hpi in the caudal plexus. (H-I) D20R or D2A1 cells localization pattern was

imaged 24h after injection with 3D confocal imaging. (H) The heatmaps show the quantification and location of intravascular CTCs at 24 hpi in the caudal plexus. (I) The ratio of cells extravasated (extravascular) over the total number of cells was measured. The graph shows the mean \pm S.D. of 3 independent experiments. (G) Representative images and orthoslice of cells at 24hpi. 3D rendering shows intravascular (blue) and extravascular (red) cells at 24hpi.

Figure 2 – CD44, ITGB3 and ITGB1 are involved in CTC arrest/adhesion but only ITGB1 is required for stable adhesion *in vitro*. (A) Scheme of the experimental approach for the microfluidic CTC arrest assay. (B) D2A1 were perfused into microfluidic channels containing a confluent monolayer of HUVEC cells for 2 min at the indicated speeds sequentially. The number of adhered cells is quantified and normalized to the number of cells adherent at the lowest perfusion speed (100 μ m/s). The graph shows the mean \pm S.D. of 14 independent experiments. (C) Upper panel: time projection of 2 min perfusion of D2A1 cells at 100 μ m/s showing arrested cells. Lower panel: time projection of 2 min wash step (perfusion of medium at 400 μ m/s) showing transiently arrested cells (metastable, red) or stably arrested cells (stable, green). Related to movie 1. (D) D2A1 cells were transfected with indicated siRNAs and perfused into microfluidic channels containing a confluent monolayer of HUVEC cells. The number of cells adhered normalized to siCTL was quantified (left) and the ratio of stably adhering cells was measured (right). The graphs show the mean \pm S.E.M. (left) and mean \pm S.D. (right) of 4~6 independent experiments. Related to movie 2 and 3. (E) Scheme of the experimental approach for the microfluidic CTC stable adhesion assay. (F) D2A1 cells were transfected with indicated siRNAs, perfused into microfluidic channels containing a confluent monolayer of HUVEC cells and left to attach without flow for 5 min. Attached cells were then trapped into the optical tweezer beam and was moved away using the piezo stage. The graph shows the mean \pm S.D. of 3 independent experiments. Related to movies 4 to 6.

Figure 3 – CD44 and ITGB3 are involved in CTC arrest while ITGB1 is required for stable adhesion *in vivo*. D2A1 cells were transfected with indicated siRNAs and microinjected into the duct of Cuvier of 2 dpf *Tg(Flt1:EGFP)* embryos. (A-C) Cell arrests were live imaged for 5 min immediately after injection. (A) Time projection of

representative embryo. The color code shows the arrest time of CTCs. Related to movies 7 to 9. (B) The ratio of cells stably arrested after 5 min over the total number of cells was measured. The graphs show the mean \pm S.D. of 3 independent experiments. (C) Transient arrest time of cells were measured. The graphs show the mean and min/max. of 3 independent experiments. (D-G) Cell adhesion pattern was imaged 3h after injection. The heatmaps show the quantification of the number and location of stably arrested CTCs at 3 hpi in the caudal plexus. The number of cells stably adhered in the AVJ was measured. The graphs show the mean \pm S.E.M. of 5 independent experiments.

Figure 4 – ITGB1 but not CD44 is required for extravasation in the zebrafish embryo and lung metastasis in mice. (A-C) D2A1 cells were transfected with indicated siRNAs and microinjected into the duct of Cuvier of 2 dpf *Tg(Fli1:EGFP)* embryos. Cell localization pattern was imaged 24h after injection. (B) The ratio of cells extravasated (extravascular) over the total number of cells was measured. (C) Representative images of cells at 24hpi. 3D rendering shows intravascular (blue) and extravascular (red) cells at 24hpi. (D) Scheme of the experimental approach for the mouse lung metastasis assay. (E) Representative images of D2A1-Luciferase transfected with the indicated siRNAs in lung seeding (1hpi) and metastatic outgrowth (13 dpi). (F) Quantification of the luciferase signal of D2A1-Luc transfected with the indicated siRNAs in lung seeding (1hpi, upper panel) and metastatic outgrowth (13 dpi, lower panel). The graphs show the mean and min/max. of (B) 5 of or (F) at least 2 independent experiments.

STAR*METHODS

1. KEY RESOURCES TABLE

Reagent or Resource	Source	Identifier
Chemicals, Peptides, and Recombinant Proteins		
Calcein Red-Orange	Thermo Fischer	Cat# C-34851
Lipofectamine RNAiMAX	Thermo Fischer	Cat#13778075
Lidocaine	Sigma-Aldrich	CatL7757
Antibodies		

ITGB1	Millipore	Cat#AB1952 RRID:AB_91150
ITGB3	Santa Cruz	Cat#sc-46655 RRID:AB_629167
CD44	AbCam	Cat#ab157107
GAPDH	Millipore	Cat#MAB374, RRID:AB_2107445
α -tubulin	Millipore	Cat#05-829 RRID:AB_477593
Fibronectin	AbCam	Cat#ab23750 RRID:AB_447655
Collagen IV	Takako Sasaki	
Collagen IV	Homemade	
Laminin 111	Homemade	
Hyaluronan	AbCam	Cat#ab53842 RRID:AB_881098
GFP	Roche	Cat#11814460001 RRID:AB_390913
Goat anti-mouse HRP	Jackson Immunoreseach	Cat#115-035-003 RRID:AB_10015289
Goat anti-rabbit HRP	Jackson Immunoreseach	Cat#111-035-003 RRID:AB_2313567
Rabbit anti-goat HRP	Jackson Immunoreseach	Cat#305-035-003 RRID:AB_2339400
Goat anti-mouse Alexa Fluor 488	Thermo Fischer	Cat#A-11029 RRID:AB_2534088
Goat anti-rabbit Alexa Fluor 488	Thermo Fischer	Cat#A-11034 RRID:AB_2576217
Goat anti-sheep Alexa Fluor 488	Thermo Fischer	Cat#A-11015 RRID:AB_2534082
Goat anti-rabbit Alexa Fluor 647	Thermo Fischer	Cat#A-21245 RRID:AB_2535813
Phalloidin Alexa Fluor 568	Thermo Fischer	Cat#A-12380

Experimental Models: Cell Lines		
D2A1	Weinberg lab (MIT)	RRID:CVCL_0190
D20R	Weinberg lab (MIT)	RRID:CVCL_0188
HUVEC	PromoCell	Cat#C-12203
Experimental Models: Organisms/Strains		
Tg(Fli1a:eGFP)	EMBL zebrafish facility (Heidelberg)	N/A
Oligonucleotides		
siCTL GCAAATTATCCGTAAATCA	This paper	N/A
siRNA targeting sequence: CD44 #1 UGAAGUUGGCCUGAGCAA	This paper	N/A
siRNA targeting sequence: CD44 #2 CAGCAAGAAGGGCGAGUAU	This paper	N/A
siRNA targeting sequence: ITGB1 #1 CCACAGAAGUUUACAUUAA	This paper	N/A
siRNA targeting sequence: ITGB1 #2 GUGUGUAGGAAGAGAGAU	This paper	N/A
siRNA targeting sequence: ITGA3 #1 GGACAAUGUUCGCGAUAAA	This paper	N/A
siRNA targeting sequence: ITGA3 #2 GAUAAUCCAUGGAGAGAAA	This paper	N/A
siRNA targeting sequence: ITGA4 #1 GCAAAGAGGUCCCCAGGCUA	This paper	N/A
siRNA targeting sequence: ITGA4 #2 GUGCAUGCCUCCUGUGAAA	This paper	N/A
siRNA targeting sequence: ITGA5 #1 GGACUGUGGUGAAGACAAU	This paper	N/A
siRNA targeting sequence: ITGA5 #2 CCUCAAUGCCUCUGGAAAA	This paper	N/A
Primer: ITGA3 Forward: TCAACATGGAGAACAAAGACCA	This paper	N/A
Primer: ITGA3 Reverse:	This paper	N/A

CCAACCACAGCTCAATCTCA		
Primer: ITGA4 Forward: ACTCCCCACAGGCCTTATT	This paper	N/A
Primer: ITGA4 Reverse: TCA GTC ACTTCGCAGTTATTTG	This paper	N/A
Primer: ITGA5 Forward: TCACAGGGCCTGGAGTTG	This paper	N/A
Primer: ITGA5 Reverse: TGTGTTCTGAGGCAGTAGAAC	This paper	N/A

2. LEAD CONTACT AND MATERIALS AVAILABILITY

Further information and requests for resources and reagents should be directed to and will be fulfilled by the Lead Contact, Jacky G. Goetz (jacky.goetz@inserm.fr).

3. EXPERIMENTAL MODEL AND SUBJECT DETAILS

Human Umbilical Vein Endothelial Cells (HUVECs).

Primary cells from poly-donor, commercial vials (PromoCell) amplified before used at P4 for all experiments. Culture condition: 37°C/5% CO₂. ECGM with Supplemental mix (PromoCell) and 1% Penstrep.

D2A1 cells (CVCL_0I90). Mouse mammary carcinoma (BALB/c female).

Major information on the D2A1 cell line can be found following this link: http://web.expasy.org/cellosaurus/CVCL_0I90. Culture conditions: 37°C/5% CO₂. DMEM HG with 5% NBCS, 5% FBS, 1% NEAA-MEM, 1% Penstrep. Authentication: Injection in the nipple of mammary gland of BALB/c mice lead to mammary tumor. Cells do not show contamination to mycoplasma.

D20R cells (CVCL_0I88). Mouse mammary carcinoma (BALB/c female).

Major information on the D20R cell line can be found following this link: http://web.expasy.org/cellosaurus/CVCL_0I88. Culture conditions: 37°C/5% CO₂. DMEM HG with 5% NBCS, 5% FBS, 1% NEAA-MEM, 1% Penstrep. Cells do not show contamination to mycoplasma.

Zebrafish embryos

Tg(fli1a:EGFP) Zebrafish (*Danio rerio*) embryos from a Golden background. Embryos were maintained at 28° in Danieau 0.3X medium (see next section), supplemented with 1-Phenyl-2-thiourea (Sigma-Aldrich) after 24 hours post fertilization (hpf). For all Zebrafish experiments, the offspring of one single cross was selected, based on anatomical/developmental good health. Embryos were split randomly between experimental groups. All injection experiments were carried at 48 hpf and imaged between 48 hpf and 72 hpf.

4. METHODS DETAILS

Cell culture and siRNA-mediated knock-down

D2A1 and D20R were provided by Robert A. Weinberg (MIT). D2A1 cells stably expressing LifeAct-TdTomato or Luciferase were obtained using lentiviral transfection. D20R cells were stained using calcein red-orange following the manufacturer's instructions (Thermo Fischer). Cells were grown, as previously described (Shibue et al. Cancer Cell 2013), in DMEM with 4.5 g/l glucose (Dutscher) supplemented with 5% FBS, 5% NBCS, 1% NEAA, 1% penicillin-streptomycin (Gibco). Human Umbilical Vein Endothelial Cells (HUVEC) (PromoCell) were grown in ECGM (PromoCell) supplemented with supplemental mix (PromoCell C-39215) and 1% penicillin-streptomycin (Gibco). To maximize the reproducibility of our experiments, we always used these cells at 4th passage in the microfluidic channels. siRNAs were transfected into D2A1 cells using Lipofectamine RNAiMAX (Thermo) following the manufacturer's instructions. Experiments were performed between 72 hours and 96 hours post-transfection.

Microfluidic CTC adhesion live imaging

Quantification of the flow-dependent adhesion of CTCs was done using six channels μ -slides VI^{0,4} Luer (IBIDI). Channels were coated with bovine plasma fibronectin at 10 μ g/ml (Sigma). HUVEC cells were seeded at 30 000 cells per channel. Medium was changed twice a day until they reach maximal confluence (3 to 4 days). 3 days after siRNA transfection, D2A1 LifeAct-TdTomato cells were resuspended at a concentration of 10^6 cells/ml. Cells were perfused using a REGLO Digital MS-2/12 peristaltic pump (Ismatec), Tygon LMT-55 3-stop tubing (IDEX), 0.5 and 1.6 mm silicon tubing and elbow Luer connectors (IBIDI). For live imaging, the HUVEC

medium was supplemented with 20 mM HEPES. D2A1 adhesion was imaged for 2 minutes at different speeds using a Leica DMIRE2 inverted microscope equipped with a 20X objective (Leica), a USB 3.0 μ Eye IDS CCD camera (IDEX) and a 37°C heating chamber.

Analysis of the flow response of ECM deposits in microfluidic channels

Two μ -slides I^{0.4} Luer (IBIDI) microfluidic channels were used in parallel during the course of the experiment. Channels were coated with bovine plasma fibronectin at 10 μ g/ml (Sigma). HUVEC cells were seeded at 100 000 cells per channel. Medium was changed twice a day until they reach maximal confluence (3 to 4 days). Then one channel was cultured under a flow of 400 μ m/sec for 16h using a REGLO Digital MS-2/12 peristaltic pump (Ismatec), Tygon LMT-55 3-stop tubing (IDEX), 0.5- and 1.6-mm silicon tubing and elbow Luer connectors (IBIDI). The medium of the other channel (no flow condition) was gently changed manually. Cells were fixed using 4% PFA (Electronic Microscopy Sciences), permeabilized with 0.2% Triton-X100 (Sigma) and quenched with 2mg/ml NaBH4 (Sigma) 10 min at room temperature. Cells were then incubated for 1h with rabbit anti-fibronectin antibody (AbCam), rabbit anti-collagen IV, rabbit anti-collagen I (gift from Takako Sasaki, Oita University, Japan), rabbit anti-laminin 111 or sheep anti-hyaluronan (AbCam) followed with goat anti-rabbit coupled with Alexa Fluor 488 and phalloidin coupled with Alexa Fluor 561 (Invitrogen). Cells were mounted using Vectashield (Vector Laboratories). For each individual field of view in no flow and flow conditions, the mean signal of the green channel (ECM) was thresholded and measured and then normalized to the average signal in the no flow condition.

Optical tweezers

Optical tweezing experiments were performed as previously described (Follain et al., 2018a). Briefly, experiments *in vitro* were performed in single microfluidic channel μ -slide I^{0.4} Luer (IBIDI), covered with HUVEC, as described before. 3 days after siRNA transfection, D2A1 LifeAct-TdTomato were perfused at 10⁶ cells/ml at a low speed to maximize the cell adhesion to HUVEC. Cells were left to adhere for 5 min without flow. A 1064 nm laser (Navigator 1064-7Y Spectra Physics) was used to generate optical tweezers mounted on a thermostated inverted microscope equipped with a UPLFLN-P 100X/1.3 objective (Olympus). D2A1 cells attached to the HUVEC

monolayer were trapped in the beam and moved away from the HUVEC monolayer by displacing a computer-controlled piezo stage (PI P545 PNano) along the X/Y axis. The detachment of D2A1 cells from the HUVEC monolayer was recorded using a CMOS camera (Thorlabs DCC3240C). Optical tweezers acquisitions were driven with Labview software and National Instruments acquisition boards.

Zebrafish handling

Tg(fli1a:EGFP) Zebrafish (*Danio rerio*) embryos were used in the experiments. Embryos were maintained in Danieau 0.3X medium (17,4 mM NaCl, 0,2 mM KCl, 0,1 mM MgSO₄, 0,2 mM Ca(NO₃)₂) buffered with HEPES 0,15 mM (pH = 7.6), supplemented with 200 µM of 1-Phenyl-2-thiourea (Sigma-Aldrich) to inhibit the melanogenesis, as previously described (Goetz et al., 2014).

Intravascular injection of CTCs in the zebrafish embryo

48 hours post-fertilization (hpf) *Tg(Fli1a:EGFP)* embryos were mounted in 0.8% low melting point agarose pad containing 650 µM of tricain (ethyl-3-aminobenzoate-methanesulfonate) to immobilize the embryos. D2A1 LifeAct-TdTomato cells were injected with a Nanoject microinjector 2 (Drummond) and microforged glass capillaries (25 to 30 µm inner diameter) filled with mineral oil (Sigma). 18nL of a cell suspension at 100.10⁶ cells per ml were injected in the duct of Cuvier of the embryos under the M205 FA stereomicroscope (Leica).

Caudal plexus Imaging was performed with the M205 FA stereomicroscope equipped with a DFC3000 G CCD camera (Leica). For cell adhesion experiments, single images of individual caudal plexus regions were acquired for each individual embryo 3 hours post injection. For early cell arrest experiments only the red channel (corresponding to injected cell marker, Td-Tomato) is recorded during injection. Image capture is started simultaneously with the injection itself, for 5 minutes.

***In vivo* CTC adhesion analysis and heatmaps generation**

The heatmaps were generated using ImageJ (<https://imagej.nih.gov/ij/index.html>) and MATLAB (MathWorks) softwares. The adhesion events are identified for each fish after the analysis of the confocal z-stacks with ImageJ. The position of these events is manually reported on a gray-level support image of a 2.5 days post-fertilization zebrafish plexus. Then, all the support images representing each embryo for one

condition were put together in an image stack using ImageJ. The stack is read layer by layer in MATLAB and the dots representing the localization are automatically detected with the function Hough circles (Yuan-Liang Tang, Department of Information Management, Chaoyang University of Technology, Taichung, Taiwan) (<https://fr.mathworks.com/matlabcentral/fileexchange/22543-detects-multiple-disks--coins--in-an-image-using-hough-transform>) using the Circular Hough Transform based algorithm, giving in output the coordinates of the detected dots. Gaussian spots are then created at these coordinates (see Follain et al., 2018b for more detailed protocol). For the cell density heatmaps, we added an additional step which consists in dividing the final map by the total number of arrested cells. To produce the final heatmap, a custom colormap, inspired by the jet colormap, is applied to the sum projection. The colormap goes from black (no event) to red (high density areas).

Analysis of the flow response of fibronectin deposits in zebrafish embryos

Drugs were added in the breeding water (Danieau 0.3X + PTU) of the embryos prior to fixation. Lidocain (Sigma) was used at 640µM in ethanol and incubated for 2h. Embryos were fixed using 4% PFA (Electronic Microscopy Sciences) overnight at 4°C. The day after PFA was gently removed and embryos were then incubated in methanol for 2 days at -20°C. Embryos were rehydrated with successive baths: 75% MeOH/25% PBS, 50% MeOH/50% PBS and 25% MeOH/75% for 5 minutes at room temperature without agitation. Embryos were then washed 4 times with PBS 1% Triton X-100 for 5 minutes with gentle rocking agitation. Embryos were blocked then in PBS 1% Triton X-100 0.5% BSA 1% normal goat serum for 4h at room temperature with gentle rocking agitation. Embryos were incubated with primary antibodies diluted in blocking buffer overnight at 4°C under gentle rocking agitation. The following antibodies were used: rabbit anti-fibronectin (AbCam), mouse anti-GFP (Roche, clones 7.1 & 13.1). Embryos were then washed in successive baths of PBS 1% Triton X-100 with gentle rocking agitation as follow: 1 brief, 5 x 5 min and 3 x 20 min. Embryos were blocked in PBS 1% Triton X-100 0.5% BSA 1% normal goat serum for 2h at room temperature with gentle rocking agitation. Embryos were then incubated with goat anti-rabbit coupled to Alexa Fluor 647 and anti-mouse coupled to Alexa Fluor 488 in blocking reagent for 2h at room temperature under gentle rocking agitation. Embryos were washed as previously described. For imaging, embryos were mounted in 0.8% low melting point agarose pad.

Light Sheet Microscopy

To image the whole fish immunostained for endogenous fibronectin, we used a home built light sheet microscope based on the development described for the OpenSPIM technology. Briefly a fiber connected laser source (RGB-iFLEXVIPER - Qioptics) is scanned through a galvanometer (GVS212_M - Thorlabs) before crossing two conjugated lenses feeding the illumination objective (EC PLAN NEOFLUAR 5X/0.16 - Zeiss). The orthogonal detection uses a detection objective (W-PLAN APOCHROMAT 20XW/1.0 - Zeiss) linked to a tube lens that builds the image on a cMOS camera (Camera ORCA Flash 4.0 - Hamamatsu). The signal is filtered out with fluorescent emission filters that select the bandwidth of observation. The sample is moved with a motorized translation stage (MP285 - Sutter Instruments) allowing to scan the sample through different slices.

Metastatic early seeding and growth in the lungs

Subconfluent D2A1 cells expressing luciferase (*Photinus pyralis*) were treated with siRNA as described in a previous section. For this experiment, siCTL, siCD44 #2 and siTGB1 #2 were used. Cells were washed with PBS (Gibco), detached using a 0.25% trypsin-0.02% EDTA solution (Gibco), filtered with Filcon cup 30µm (BD), washed in DMEM containing 10% fetal calf serum, resuspended in serum-free media and kept on ice until injection. Viability was determined by trypan blue exclusion and was always more than 90%. Cells (2×10^5) in 100 µl of serum-free DMEM were injected per mouse through the lateral tail vein by using a 25-gauge needle. *In vivo* bioluminescence imaging of mice lungs was immediately performed after tumor cells inoculation to establish initial lung seeding. Early time point was recorded 1h after CTC injection. Subsequent imaging time point was performed at 13 days after lung dissection. In brief, a D-luciferin solution (150 mg/kg) was injected intraperitoneally to the isofluorane-anesthetized (Zoetis) mice. 5 min after luciferin injection, a bioluminescence image was acquired with an IVIS Lumina III (Perkin Elmer) imaging system and then analyzed using the Living Image software (Perkin Elmer). The rate of total light emission of the lung metastatic area was calculated and expressed as numbers of photons counted during the whole acquisition time (5 min) and normalized to the initial photon count measured immediately after CTC injection for each individual mouse (t0).

Flow cytometry

Expression analysis of surface markers on D20R and D2A1 cell lines was determined by standard protocols. Briefly, subconfluent cells were harvested by mild trypsinization, washed, resuspended in FACS staining buffer (PBS, 1% BSA; 1% FBS) and filtered (30um) prior analysis. FITC-labelled anti-mouse CD44 (IM7; eBioscience) or APC-labeled CD29 (HMb1-1; eBioscience) mAbs and their corresponding isotype controls (rat IgG2bk-FITC, eB149/10H5 or hamster IgG-APC, eBio299arm , eBioscience) were added in FACS staining solution and incubated for 10 minutes at 4°C. Flow cytometry acquisition was performed using a BD LSRFortessa X cytometer with FACSDiva software. Flow cytometry data analysis was performed using FlowJo vX (LLC software).

Cell size measure

Cells were washed with PBS, trypsinized and resuspended in medium at a density of 10^6 cells/ml. 2 ml of cell suspension was set in 6 well plates and pictures from cells in suspension were taken using an inverted cell culture microscope. Images were calibrated using a micrometric slide. Cell size was measured using Image J.

Western blotting

Extracts corresponding to similar cell numbers were loaded on 4-20% polyacrylamide gels (Biorad) and run under denaturing conditions. The following primary antibodies were used: ITGB1 (Millipore AB1952; rabbit), CD44 (AbCam ab157107; rabbit), ITGB3 (Santa Cruz sc-53351; mouse), GAPDH (Millipore MAB374; mouse). HRP-conjugated secondary antibodies were used with ECL (GE Healthcare) for reading using a PXi system (Syngene). Intensities were normalized over cellular GAPDH levels.

RT-qPCR

Total RNAs were extracted from transfected cell using TRI Reagent (Molecular Research Center). Total cDNAs were prepared using the High Capacity cDNA Reverse Transcription Kit (Applied Biosystems). Semi-quantitative PCR was performed using the 7500 real-time PCR system.

The expression of GAPDH as a housekeeping gene was used for each individual sample using a TaqMan probe for mouse GAPDH (Life Technologies) and the FastStart Universal Probe Master (ROX) Mix (Roche). The expression of individual gene of interest were assessed in cells transfected with control siRNAs or siRNA targeting the gene of interest using custom made primers () and the FastStart Universal SYBR Green Probe Master (ROX) Mix (Roche). The ratio of the expression level for each siRNA knockdown condition versus a control siRNA was then calculated.

5. QUANTIFICATION AND STATISTICAL ANALYSIS

Statistical analysis

Statistical analysis of the results obtained during zebrafish, mice and microfluidic experiments were performed using the GraphPad Prism program version 5.04. The Shapiro-Wilk normality test was used to confirm the normality of the data. When comparing 2 groups, the statistical difference of Gaussian data sets was analyzed using the Student unpaired two-tailed t test, with Welch's correction in case of unequal variances. For data not following a Gaussian distribution, the Mann-Whitney test was used (Figure 1, S1, S4B-D). When comparing 3 groups, the statistical difference of non-Gaussian data sets was analyzed using the Kruskal-Wallis test with Dunn's post hoc test (Figure 2-4, S2-3). When comparing 3 groups with 2 variable parameters, the statistical difference of data sets was analyzed using the 2 way ANOVA test with Bonneferoni's post hoc test. For qualitative data, the Fisher test was used. Illustrations of these statistical analyses are displayed as the mean +/- standard deviation (SD). p-values smaller than 0.05 were considered as significant. *, p<0.05, **, p < 0.01, ***, p < 0.001, ****, p < 0.0001.

In vitro cell experiments

All experiments were reproduced at least 3 times with independent HUVEC vials for microfluidic experiments.

For live adhesion assay, number of arrested cells N for Figure 2B: N=808; for Figure 2D, siCTL=285, siCD44#1=92, siCD44#2=95; siCTL=307, siITGB3#1=144, siITGB3#2=124; siCTL=285, siITGB1#1=75, siITGB1#2=40, siCTL=152, siITGA5#1=35, siITGA5#2=36, Figure S3B-C: siCTL=285, siITGA4#1=247, siITGA4#2=203, siCTL=152, siITGA3#1=68, siITGA3#2=66.

For optical tweezer experiments, number N of cells for Figure 1F: siCTL=40, siCD44#1=57, siCD44#2=48; siCTL=50, siITGB3#1=50, siITGB3#2=50; siCTL=32, siITGB1#1=33, siITGB1#2=33.

For fibronectin flow response, number of analyzed cells N for Figure S4B: No flow=525, flow=394.

For ECM flow response for Figure S4D: number of field of view analyzed N with ~25 cells on average for Figure S4D: collagen IV no flow=29, flow=30; collagen I no flow=30, flow=30; laminin 111 no flow=30, flow=30; hyaluronan no flow=50, flow=50; fibronectin no flow=40, flow=40.

Cell size measure number N of cells for Figure S1A: D20R=38, D2A1=70.

Zebrafish experiments

All experiments were reproduced at least 3 times independently

For live arrest assay (5mpi) cells, number of embryos analyzed: D20R/D2A1 experiments in Figure 1B-C: D20R=16, D2A1=13, in Figure 3B-C: CD44 experiments siCTL=9, siCD44#1=5, siCD44#2=4, ITGB3 experiments siCTL=13, siITGB3#1=14, siITGB3#2=14, ITGB1 experiments siCTL=8, siITGB1#1=8, siITGB1#2=8; number of cells analyzed: D20R/D2A1 experiments D20R=201, D2A1=102, (CD44) siCTL=204, siCD44#1=67, siCD44#2=118, (ITGB3) siCTL=194, siITGB3#1=443, siITGB3#2=1321, (ITGB1) siCTL=65, siITGB1#1=76, siITGB1#2=65.

For stable arrest assay (3hpi), number of embryos analyzed: D20R/D2A1 experiments in Figure 1D-F D20R=66, D2A1=62, in Figure 3D-G: CD44 experiments: siCTL=100, siCD44#1=100, siCD44#2=110; ITGB3 experiments: siCTL=81, siITGB1#1=56, siITGB1#2=59; ITGB1 experiments: siCTL=77, siITGB1#1=63, siITGB1#2=55; ITGA5 experiments siCTL=64, siITGA5#1=64, siITGA5#2=62; in Figure S3B-C: ITGA3 experiments siCTL=64, siITGA3#1=54, siITGA3#2=57; ITGA4 experiments siCTL=41, siITGA4#1=45, siITGA4#2=45.

For extravasation assay (24hpi), number of embryos analyzed: D20R/D2A1 experiments in Figure 1H-I: D20R=22, D2A1=28, siRNA experiments in Figure 4B: siCTL=30, siCD44#1=15, siCD44#2=19; siITGB1#1=18, siITGB1#2=20.

For fibronectin flow response, number of analyzed embryos N for Figure S4F: non-treated (NT)=193 and for Figure S4H: non-treated (NT)=193, vehicle (EtOH)=227, lidocaine (lido)=216.

Mice experiments

All experiments were reproduced at least 3 times independently

For *in vivo* experiments (1hpi), number of mouse analyzed: siCTL=8, siCD44#2=8, siITGB1#2=8.

For *ex vivo* experiments (13 dpi), number of mouse analyzed: siCTL=12, siCD44#2=8, siITGB1#2=12.

Flow cytometry

At least 5000 cells were analyzed for each condition.

6. DATA AND SOFTWARE AVAILABILITY

For most of the analysis: GraphPad V5.04 to V6, PRISM - commercial dedicated software for statistical analysis. The heatmap reconstruction is a in-house script running under Matlab that has been published (Follain et al., 2018b). Confocal image analysis and rendering were performed using FIJI software.

SUPPLEMENTARY FIGURES LEGENDS

Figure S1 – D2A1 and D20R cell line characterization. (A) Quantification of the diameters of D20R and D2A1 cells in suspension. (B) Monoparametric flow cytometry histograms show cell membrane CD44 and ITGB1 levels at the surface of D20R and D2A1 cells after electronic gating on viable cells. FITC- or APC-labelled IgG isotype controls were used in D20R cells to set the negative population. Numbers in legends show the mean fluorescence intensity of the whole populations analyzed. (C-D) Protein extracts were prepared and immunoblotted against (C) CD44 or (D) ITGB1 and GAPDH. The relative expression was measured and normalized to D2A1 expression levels. The graph shows the mean \pm S.D. of 5 independent experiments. (E) D20R or D2A1 cells were microinjected into the duct of Cuvier of 2 dpf *Tg(Fli1:EGFP)* embryos and cell localization pattern was imaged 24h after injection with 3D confocal imaging. The heatmaps show the quantification and location of CTCs at 24 hpi in the caudal plexus. Related to figure 1.

Figure S2 – siRNAs knockdown validation after transfection. (A-D) D2A1 cells were transfected with control or (A) anti-CD44, (B) anti-ITGB3, (C) anti-ITGB1 or (D) anti-ITGA5 siRNAs. (A-C) Protein extracts were prepared 72h later and

immunoblotted against (A) CD44, (B) ITGB3, (C) ITGB1, (A,C) GAPDH or (B) α -tubulin. The graph shows the mean \pm S.D. of 5 independent experiments. (D) Total RNA extracts were prepared 48h after transfection. The expression of ITGA5 was measured using RT-qPCR. The graph shows the mean \pm S.D. of 3 independent experiments. Related to figure 2.

Figure S3 – ITGA4 and ITGA3 are not involved in CTC stable adhesion to endothelial cells. (A) D2A1 cells were transfected with indicated siRNAs. The expression of the genes of interest was measured using RT-qPCR. The graph shows the mean \pm S.D. of at least 3 independent experiments. (B-C) D2A1 cells were transfected with indicated siRNAs and perfused into microfluidic channels containing a confluent monolayer of endothelial cells (HUVEC). The number of cells adhered normalized to siCTL was quantified (left) and the ratio of stably adhering cells was measured (right). The graph shows the mean \pm S.E.M. (left) and mean \pm S.D. (right) of at least 4 independent experiments. (D-E) Quantification using heatmap of the number and location of stably arrested CTCs at 3 hpi in the caudal plexus of embryo injected with cells transfected with indicated siRNAs. The graphs show the mean \pm S.E.M. of 4 independent experiments. Related to figure 2 and 3.

Figure S4 – Flow drives the formation of luminal FN deposits. (A) HUVEC cells were grown to confluence in microfluidic channels and subjected to either no flow or a laminar flow of 400 μ m/s for 16h. Cells are immunostained for fibronectin (green), actin (red) and nucleus (blue). A y-projection of 35 single representative transversal confocal slices is shown in the bottom panel XZ. (B) The ratio of HUVEC cells with fibronectin (FN) deposits was quantified. The graphs show the mean \pm S.D. of 3 independent experiments. (C) HUVEC cells were grown to confluence in microfluidic channels and subjected to either no flow or a laminar flow of 400 μ m/s for 16h. Fibronectin (FN) expression was then quantified. A representative western blot image is shown in the upper panel. The graphs show the mean \pm S.D. of 5 independent experiments. (D) HUVEC cells were grown to confluence in microfluidic channels and subjected to either no flow or a laminar flow of 400 μ m/s for 16h. Cells were immunostained for collagen IV, collagen I, laminin 111, hyaluronan (HA) or fibronectin (FN). (right) Representative image of cells stained for collagen IV or hyaluronan (green), actin (red) and nucleus (blue). (left) For each individual field of

view, the mean signal of the green channel (ECM) was measured and normalized to the average signal in the no flow condition. The graphs show the mean \pm S.D. of 5 independent experiments. (E) Scheme of the experimental approach for the *in vivo* luminal FN quantification. (F) Fibronectin signal in the DA and the AVJ was compared. Embryos were classified as higher signal in the DA (DA>AVJ), identical (DA=AVJ) or higher in the AVJ (DA<AVJ). The graph shows the mean \pm S.D. of 6 independent experiments. (G) Representative embryos were imaged using light sheet microscopy (SPIM). (H) 2 dpf *Tg(Fli1:EGFP)* embryos were either untreated (NT) or treated for 2h with vehicle (EtOH) or lidocain at 640 μ M (Lido). The presence of fibronectin deposits in the AVJ was assessed. The graph shows the mean \pm S.D. of 6 independent experiments. Related to Figure 2 and 3.

Movie 1 – Live adhesion assay. D2A1 cells were transfected with control siRNAs. 72h later, cells were detached and perfused into microfluidic channels for 2 min at the indicated speeds. The movie is acquired at 24 fps and displayed at 72 fps. Related to Figure 2B-C.

Movie 2 – Live adhesion movie of siCTL, siCD44 and siITGB1 transfected cells. D2A1 cells were transfected with control, anti-CD44 or anti-ITGB1 siRNAs. 72h later, cells were detached and perfused into microfluidic channels. The movie shows in parallel the perfusion of the three conditions at 100 μ m/s. The movie is acquired at 24 fps and displayed at 72 fps. Related to Figure 2D.

Movie 3 – Live adhesion movie of siCTL and siITGB3 transfected cells. D2A1 cells were transfected with control or anti-ITGB3 siRNAs. 72h later, cells were detached and perfused into microfluidic channels. The movie shows in parallel the perfusion of the two conditions at 100 μ m/s. The movie is acquired at 24 fps and displayed at 72 fps. Related to Figure 2D.

Movie 4 – CD44 is not involved in stable adhesion *in vitro*. D2A1 cells were transfected with control siRNAs or anti-CD44. 72h later, cells were detached and perfused into microfluidic channels containing a confluent monolayer of endothelial cells (HUVEC) and left to attach to the endothelial layer without flow for 5 min. Attached cells were then trapped into the optical tweezer beam and the stage was

moved away using the piezo stage. The movie is acquired at 24 fps and displayed at 72 fps. Related to Figure 2F.

Movie 5 – ITGB3 is involved in stable adhesion *in vitro*. D2A1 cells were transfected with control siRNAs or anti-ITGB3. 72h later, cells were detached and perfused into microfluidic channels containing a confluent monolayer of endothelial cells (HUVEC) and left to attach to the endothelial layer without flow for 5 min. Attached cells were then trapped into the optical tweezer beam and the stage was moved away using the piezo stage. The movie was acquired at 24 fps and displayed at 72 fps. Related to Figure 2F.

Movie 6 – ITGB1 is involved in stable adhesion *in vitro*. D2A1 cells were transfected with control siRNAs or anti-ITGB1. 72h later, cells were detached and perfused into microfluidic channels containing a confluent monolayer of endothelial cells (HUVEC) and left to attach to the endothelial layer without flow for 5 min. Attached cells were then trapped into the optical tweezer beam and the stage was moved away using the piezo stage. The movie was acquired at 24 fps and displayed at 72 fps. Related to Figure 2F.

Movie 7 – CD44 is involved in CTC arrest/early adhesion *in vivo*. D2A1 cells were transfected with control or anti-CD44 siRNAs. 72h later, cells were detached and microinjected into the duct of Cuvier of 2 dpf *Tg(Fli1:EGFP)* embryos. Cell arrests was live imaged at 4 fps for 2,5 min immediately after injection. The movie is displayed at 80 fps. Related to Figure 3A-C.

Movie 8 – ITGB3 is involved in CTC arrest/early adhesion *in vivo*. D2A1 cells were transfected with control or anti-ITGB1 siRNAs. 72h later, cells were detached and microinjected into the duct of Cuvier of 2 dpf *Tg(Fli1:EGFP)* embryos. Cell arrests was live imaged at 4 fps for 2,5 min immediately after injection. The movie is displayed at 80 fps. Related to Figure 3A-C.

Movie 9 – ITGB1 is involved in CTC arrest/early adhesion *in vivo*. D2A1 cells were transfected with control or anti-ITGB1 siRNAs. 72h later, cells were detached and microinjected into the duct of Cuvier of 2 dpf *Tg(Fli1:EGFP)* embryos. Cell

arrests was live imaged at 4 fps for 2,5 min immediately after injection. The movie is displayed at 80 fps. Related to Figure 3A-C.

REFERENCES

Aigner, S., Ramos, C.L., Hafezi-moghadam, A., Lawrence, M.B., Friederichs, J., Altevogt, P., and Ley, K. (1998). CD24 mediates rolling of breast carcinoma cells on P-selectin. *FASEB J* 12, 1241–1251.

Al-Hajj, M., Wicha, M.S., Benito-Hernandez, A., Morrison, S.J., and Clarke, M.F. (2003). Prospective identification of tumorigenic breast cancer cells. *PNAS* 100, 3983–3988.

Baccelli, I., Schneeweiss, A., Riethdorf, S., Stenzinger, A., Schillert, A., Vogel, V., Klein, C., Saini, M., Bäuerle, T., Wallwiener, M., et al. (2013). Identification of a population of blood circulating tumor cells from breast cancer patients that initiates metastasis in a xenograft assay. *Nature Biotechnology* 31, 539–544.

Bano, F., Banerji, S., Howarth, M., Jackson, D.G., and Richter, R.P. (2016). A single molecule assay to probe monovalent and multivalent bonds between hyaluronan and its key leukocyte receptor CD44 under force. *Scientific Reports* 6, 34176.

Barbazán, J., Alonso-Alconada, L., Elkhatib, N., Geraldo, S., Gurchenkov, V., Glentis, A., Niel, G. van, Palmulli, R., Fernández, B., Viaño, P., et al. (2017). Liver Metastasis Is Facilitated by the Adherence of Circulating Tumor Cells to Vascular Fibronectin Deposits. *Cancer Res* 77, 3431–3441.

Barthel, S.R., Hays, D.L., Yazawa, E.M., Opperman, M., Walley, K.C., Nimrichter, L., Burdick, M.M., Gillard, B.M., Moser, M.T., Pantel, K., et al. (2013). Definition of Molecular Determinants of Prostate Cancer Cell Bone Extravasation. *Cancer Research* 73, 942–952.

Bharadwaj, M., Strohmeyer, N., Colo, G.P., Helenius, J., Beerenwinkel, N., Schiller, H.B., Fässler, R., and Müller, D.J. (2017). α V-class integrins exert dual roles on α 5 β 1 integrins to strengthen adhesion to fibronectin. *Nature Communications* 8, 14348.

Boral, D., Vishnoi, M., Liu, H.N., Yin, W., Sprouse, M.L., Scamardo, A., Hong, D.S., Tan, T.Z., Thiery, J.P., Chang, J.C., et al. (2017). Molecular characterization of breast cancer CTCs associated with brain metastasis. *Nature Communications* 8, 196.

Chen, J., Zhou, W., Jia, Q., Chen, J., Zhang, S., Yao, W., Wei, F., Zhang, Y., Yang, F., Huang, W., et al. (2016a). Efficient extravasation of tumor-repopulating cells depends on cell deformability. *Scientific Reports* 6, 19304.

Chen, M.B., Lamar, J.M., Li, R., Hynes, R.O., and Kamm, R.D. (2016b). Elucidation of the Roles of Tumor Integrin β 1 in the Extravasation Stage of the Metastasis Cascade. *Cancer Res* 76, 2513–2524.

Dallas, M.R., Liu, G., Chen, W.-C., Thomas, S.N., Wirtz, D., Huso, D.L., and Konstantopoulos, K. (2012). Divergent roles of CD44 and carcinoembryonic antigen in colon cancer metastasis. *FASEB J.* 26, 2648–2656.

Eibl, C., Grigoriu, S., Hessenberger, M., Wenger, J., Puehringer, S., Pinheiro, A.S., Wagner, R.N., Proell, M., Reed, J.C., Page, R., et al. (2012). Structural and Functional Analysis of the NLRP4 Pyrin Domain. *Biochemistry* 51, 7330–7341.

Felding-Habermann, B., O'Toole, T.E., Smith, J.W., Fransvea, E., Ruggeri, Z.M., Ginsberg, M.H., Hughes, P.E., Pampori, N., Shattil, S.J., Saven, A., et al. (2001). Integrin activation controls metastasis in human breast cancer. *Proceedings of the National Academy of Sciences* 98, 1853–1858.

Follain, G., Osmani, N., Azevedo, A.S., Allio, G., Mercier, L., Karreman, M.A., Solecki, G., Leòn, M.J.G., Lefebvre, O., Fekonja, N., et al. (2018a). Hemodynamic Forces Tune the Arrest, Adhesion, and Extravasation of Circulating Tumor Cells. *Developmental Cell* 45, 33-52.e12.

Follain, G., Osmani, N., Fuchs, C., Allio, G., Harlepp, S., and Goetz, J.G. (2018b). Using the Zebrafish Embryo to Dissect the Early Steps of the Metastasis Cascade. In *Cell Migration*, (Humana Press, New York, NY), pp. 195–211.

Giavazzi, R., Foppolo, M., Dossi, R., and Remuzzi, A. (1993). Rolling and adhesion of human tumor cells on vascular endothelium under physiological flow conditions. *Journal of Clinical Investigation* 92, 3038–3044.

Goetz, J.G., Steed, E., Ferreira, R.R., Roth, S., Ramspacher, C., Boselli, F., Charvin, G., Liebling, M., Wyart, C., Schwab, Y., et al. (2014). Endothelial Cilia Mediate Low Flow Sensing during Zebrafish Vascular Development. *Cell Reports* 6, 799–808.

Hanley, W.D., Napier, S.L., Burdick, M.M., Schnaar, R.L., Sackstein, R., and Konstantopoulos, K. (2006). Variant isoforms of CD44 are P- and L-selectin ligands on colon carcinoma cells. *FASEB J.* 20, 337–339.

Hiratsuka, S., Goel, S., Kamoun, W.S., Maru, Y., Fukumura, D., Duda, D.G., and Jain, R.K. (2011). Endothelial focal adhesion kinase mediates cancer cell homing to discrete regions of the lungs via E-selectin up-regulation. *Proceedings of the National Academy of Sciences* 108, 3725–3730.

Humphries, J.D. (2006). Integrin ligands at a glance. *Journal of Cell Science* 119, 3901–3903.

Huvaneers, S., Truong, H., Fassler, R., Sonnenberg, A., and Danen, E.H.J. (2008). Binding of soluble fibronectin to integrin 5 1 - link to focal adhesion redistribution and contractile shape. *Journal of Cell Science* 121, 2452–2462.

Jalkanen, S., and Jalkanen, M. (1992). Lymphocyte CD44 binds the COOH-terminal heparin-binding domain of fibronectin. *The Journal of Cell Biology* 116, 817–825.

Klemke, M., Weschenfelder, T., Konstandin, M.H., and Samstag, Y. (2007). High affinity interaction of integrin alpha4beta1 (VLA-4) and vascular cell adhesion molecule 1 (VCAM-1) enhances migration of human melanoma cells across activated endothelial cell layers. *J. Cell. Physiol.* 212, 368–374.

Köhler, K., Xiong, S., Brzostek, J., Mehrabi, M., Eissmann, P., Harrison, A., Cordoba, S.-P., Oddos, S., Miloserdov, V., Gould, K., et al. (2010). Matched sizes of activating and inhibitory receptor/ligand pairs are required for optimal signal integration by human natural killer cells. *PLoS ONE* 5, e15374.

Kong, F., García, A.J., Mould, A.P., Humphries, M.J., and Zhu, C. (2009). Demonstration of catch bonds between an integrin and its ligand. *The Journal of Cell Biology* 185, 1275–1284.

Kong, F., Li, Z., Parks, W.M., Dumbauld, D.W., García, A.J., Mould, A.P., Humphries, M.J., and Zhu, C. (2013). Cyclic Mechanical Reinforcement of Integrin-Ligand Interactions. *Molecular Cell* 49, 1060–1068.

Laferrière, J., Houle, F., Taher, M.M., Valerie, K., and Huot, J. (2001). Transendothelial Migration of Colon Carcinoma Cells Requires Expression of E-selectin by Endothelial Cells and Activation of Stress-activated Protein Kinase-2 (SAPK2/p38) in the Tumor Cells. *Journal of Biological Chemistry* 276, 33762–33772.

Laferrière, J., Houle, F., and Huot, J. (2004). Adhesion of HT-29 colon carcinoma cells to endothelial cells requires sequential events involving E-selectin and integrin beta4. *Clin. Exp. Metastasis* 21, 257–264.

Lambert, A.W., Pattabiraman, D.R., and Weinberg, R.A. (2017). Emerging Biological Principles of Metastasis. *Cell* 168, 670–691.

Mana, G., Clapero, F., Panieri, E., Panero, V., Böttcher, R.T., Tseng, H.-Y., Saltarin, F., Astanina, E., Wolanska, K.I., Morgan, M.R., et al. (2016). PPFIA1 drives active $\alpha 5\beta 1$ integrin recycling and controls fibronectin fibrillogenesis and vascular morphogenesis. *Nature Communications* 7, 13546.

McEver, R.P., and Zhu, C. (2010). Rolling Cell Adhesion. *Annual Review of Cell and Developmental Biology* 26, 363–396.

Morris, V.L., Tuck, A.B., Wilson, S.M., Percy, D., and Chambers, A.F. (1993). Tumor progression and metastasis in murine D2 hyperplastic alveolar nodule mammary tumor cell lines. *Clin Exp Metastasis* 11, 103–112.

Obenauf, A.C., and Massagué, J. (2015). Surviving at a Distance: Organ-Specific Metastasis. *Trends in Cancer* 1, 76–91.

Rahn, J.J., Chow, J.W., Horne, G.J., Mah, B.K., Emerman, J.T., Hoffman, P., and Hugh, J.C. (2005). MUC1 mediates transendothelial migration in vitro by ligating endothelial cell ICAM-1. *Clin. Exp. Metastasis* 22, 475–483.

Reymond, N., Im, J.H., Garg, R., Vega, F.M., Borda d'Agua, B., Riou, P., Cox, S., Valderrama, F., Muschel, R.J., and Ridley, A.J. (2012). Cdc42 promotes transendothelial migration of cancer cells through β 1 integrin. *The Journal of Cell Biology* 199, 653–668.

Reymond, N., d'Água, B.B., and Ridley, A.J. (2013). Crossing the endothelial barrier during metastasis. *Nature Reviews Cancer* 13, 858–870.

Roca-Cusachs, P., Gauthier, N.C., del Rio, A., and Sheetz, M.P. (2009). Clustering of $\alpha 5\beta 1$ integrins determines adhesion strength whereas $\alpha v\beta 3$ and talin enable mechanotransduction. *Proceedings of the National Academy of Sciences* 106, 16245–16250.

Sakai, T., Larsen, M., and Yamada, K.M. (2003). Fibronectin requirement in branching morphogenesis. *Nature* 423, 876–881.

Shea, D.J., Wirtz, D., Stebe, K.J., and Konstantopoulos, K. (2015). Distinct kinetic and mechanical properties govern mucin 16- and podocalyxin-mediated tumor cell adhesion to E- and L-selectin in shear flow. *Oncotarget* 6, 24842–24855.

Shi, Z., Gruber, Z.T., Baumgart, T., Stone, H.A., and Cohen, A.E. (2018). Cell Membranes Resist Flow. *Cell* 175, 1769–1779.e13.

Shibue, T., Brooks, M.W., Inan, M.F., Reinhardt, F., and Weinberg, R.A. (2012). The Outgrowth of Micrometastases Is Enabled by the Formation of Filopodium-like Protrusions. *Cancer Discovery* 2, 706–721.

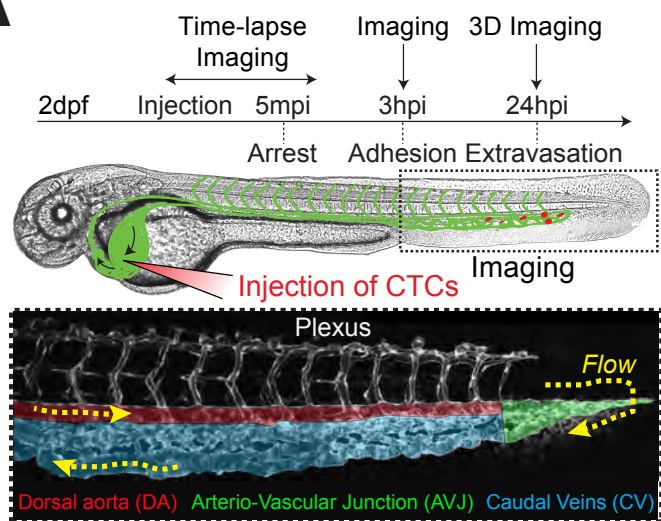
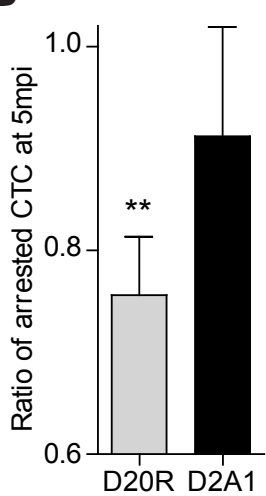
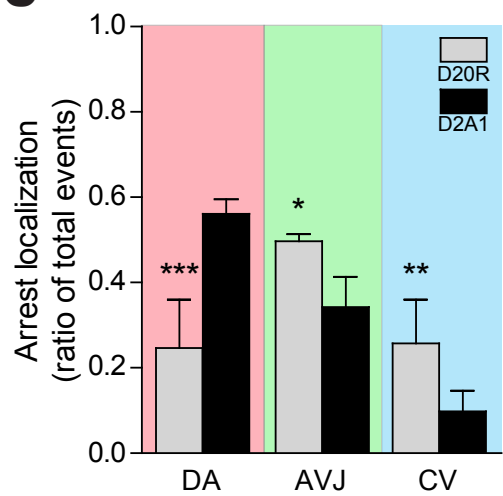
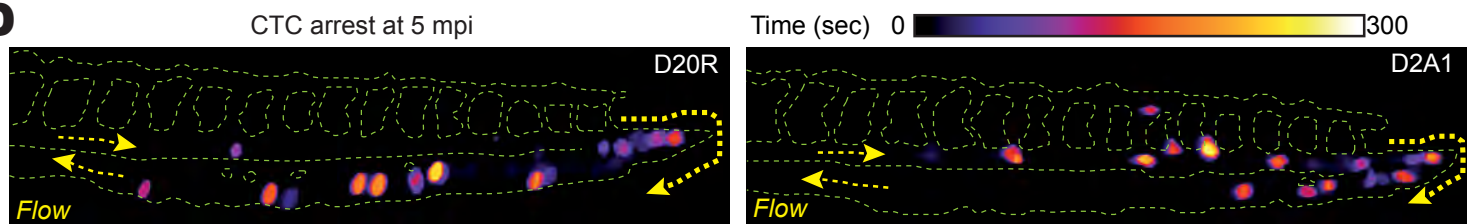
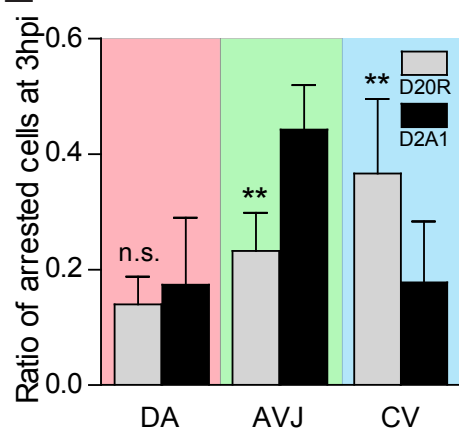
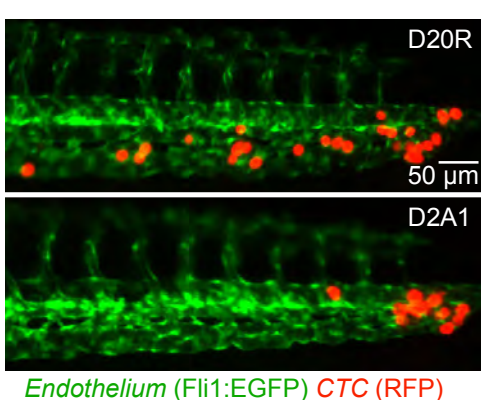
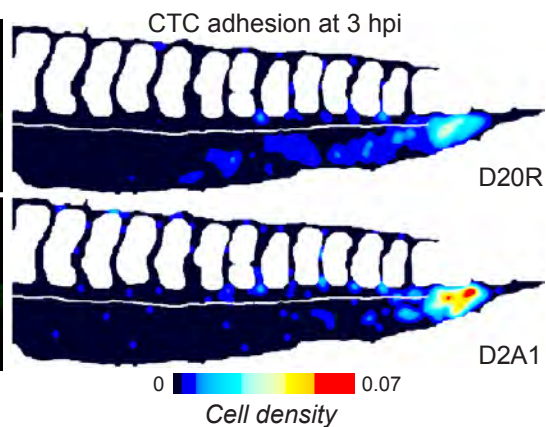
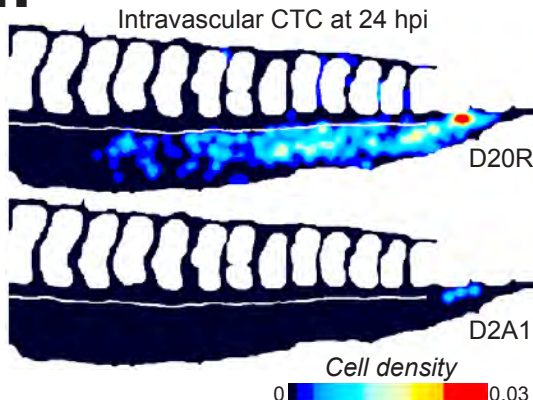
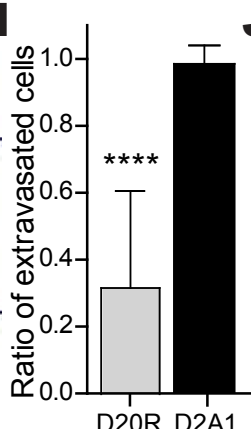
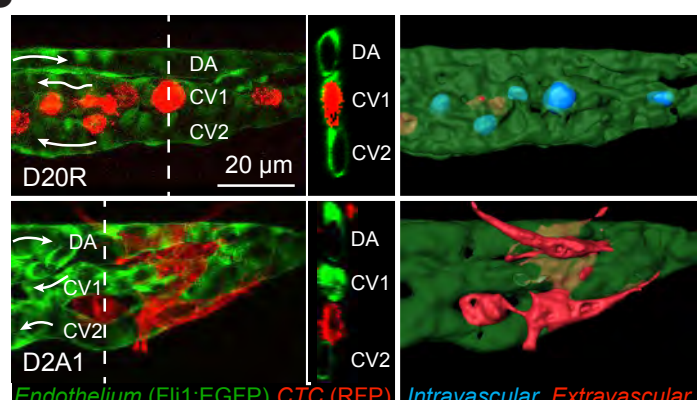
Shibue, T., Brooks, M.W., and Weinberg, R.A. (2013). An Integrin-Linked Machinery of Cytoskeletal Regulation that Enables Experimental Tumor Initiation and Metastatic Colonization. *Cancer Cell* 24, 481–498.

Stoletov, K., Kato, H., Zardouzian, E., Kelber, J., Yang, J., Shattil, S., and Klemke, R. (2010). Visualizing extravasation dynamics of metastatic tumor cells. *Journal of Cell Science* 123, 2332–2341.

Tremblay, P.-L., Huot, J., and Auger, F.A. (2008). Mechanisms by which E-Selectin Regulates Diapedesis of Colon Cancer Cells under Flow Conditions. *Cancer Research* 68, 5167–5176.

Wang, H., Fu, W., Im, J.H., Zhou, Z., Santoro, S.A., Iyer, V., DiPersio, C.M., Yu, Q.-C., Quaranta, V., Al-Mehdi, A., et al. (2004). Tumor cell $\alpha 3\beta 1$ integrin and vascular laminin-5 mediate pulmonary arrest and metastasis. *J Cell Biol* 164, 935–941.

White, R., Rose, K., and Zon, L. (2013). Zebrafish cancer: the state of the art and the path forward. *Nat Rev Cancer* 13, 624–636.

A**B****C****D****E****F****G****H****I****J****Figure 1** _Osmani et al.

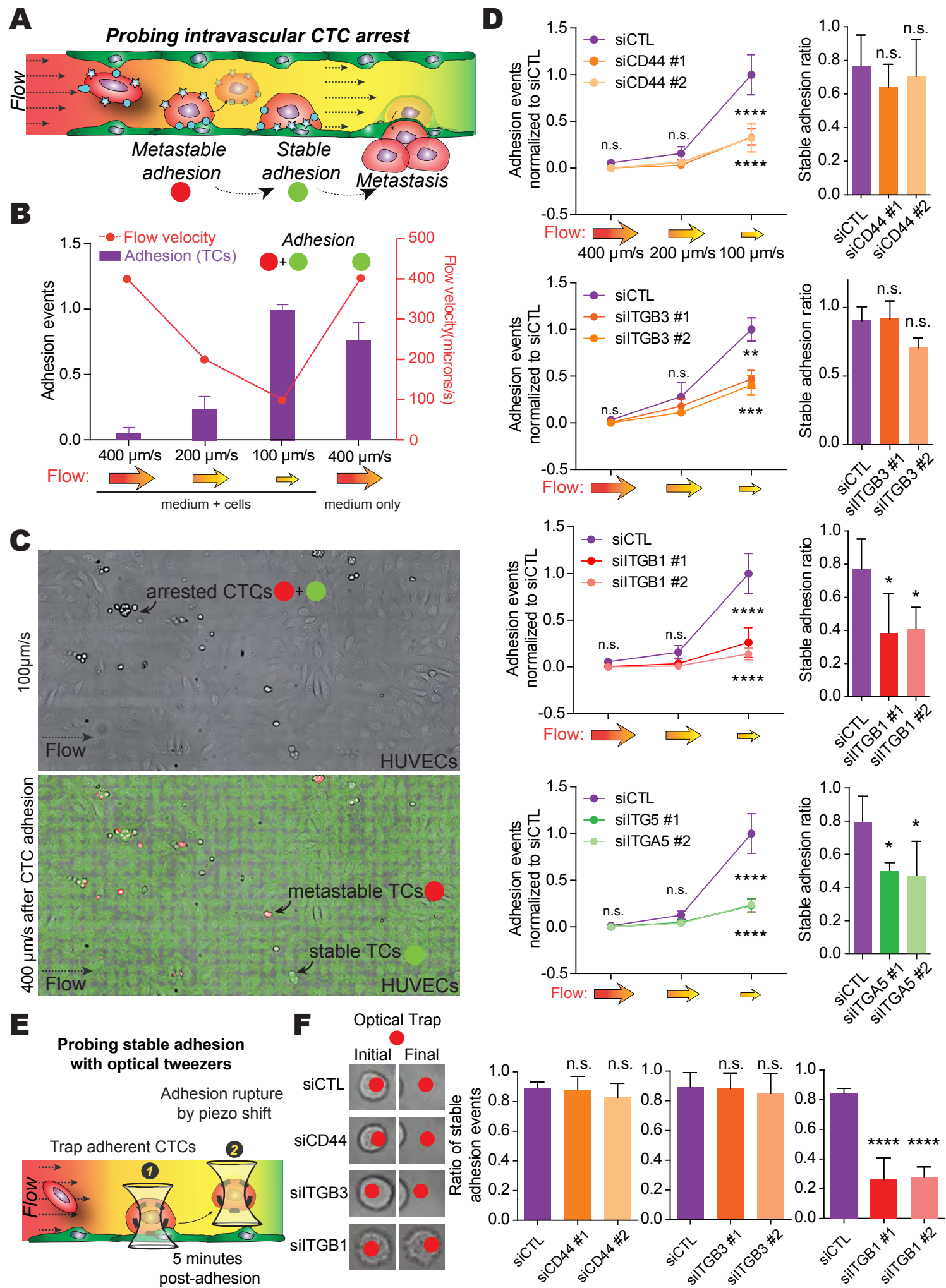
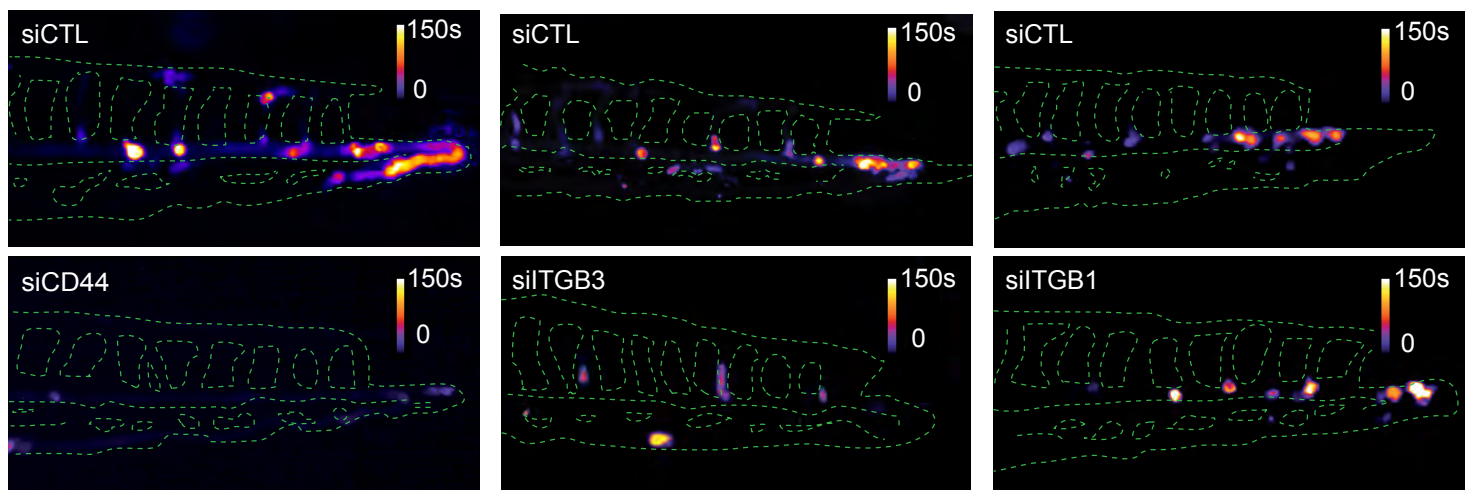
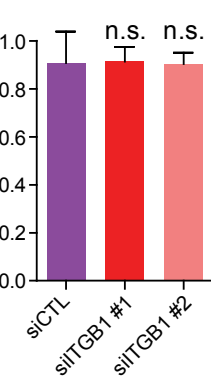
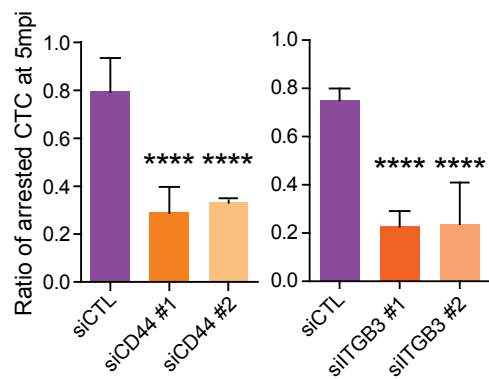
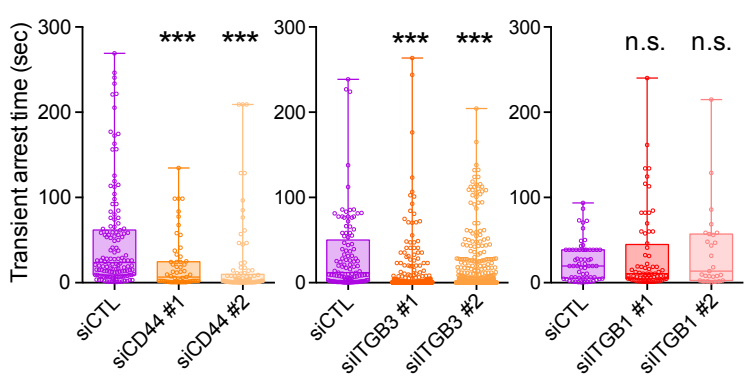
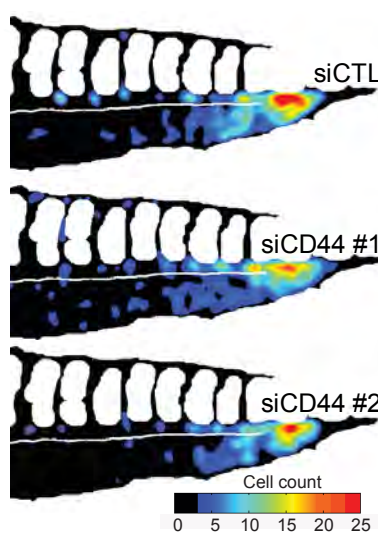
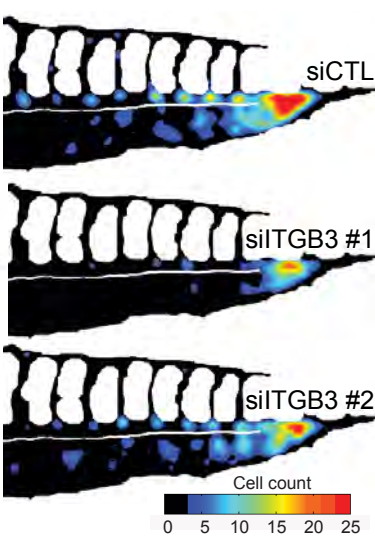
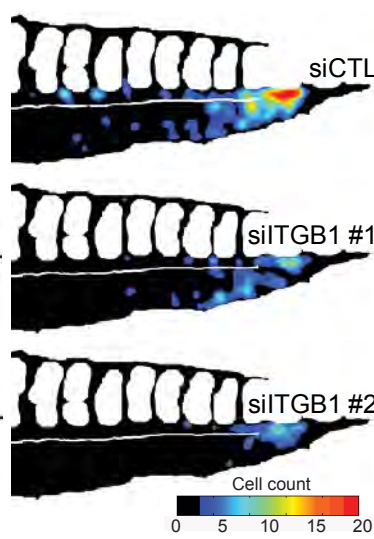
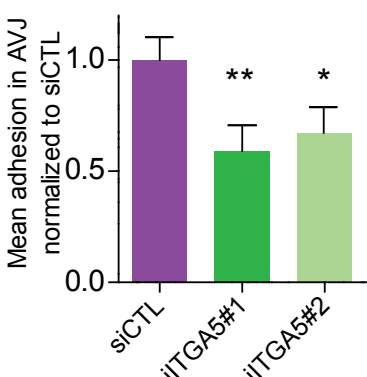
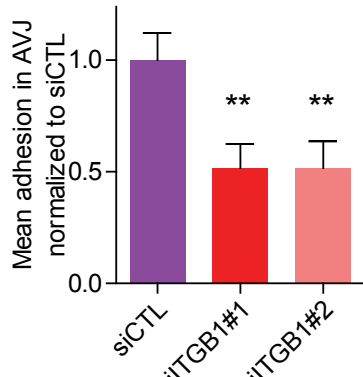
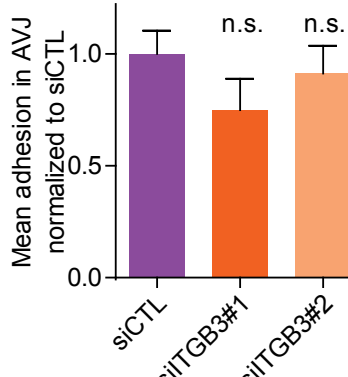
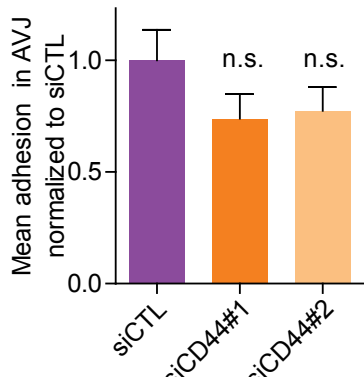
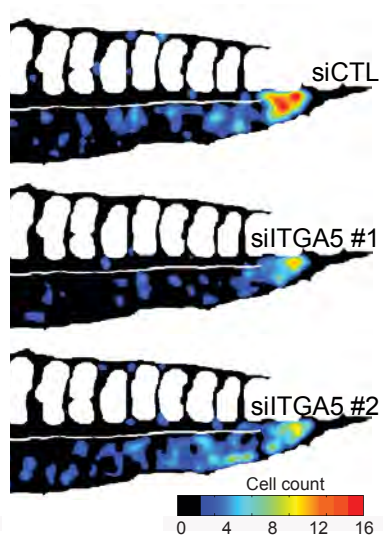


Figure 2_Osmani et al.

A**B****C****D****E****F****G****Figure 3** Osman et al.

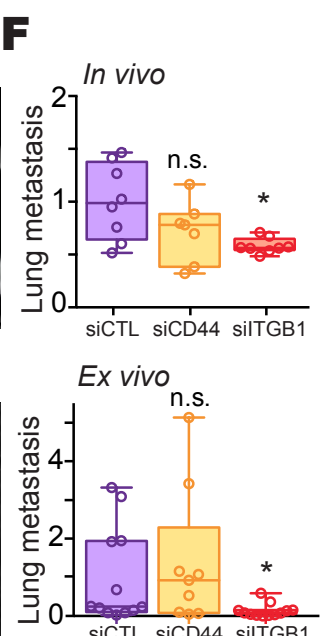
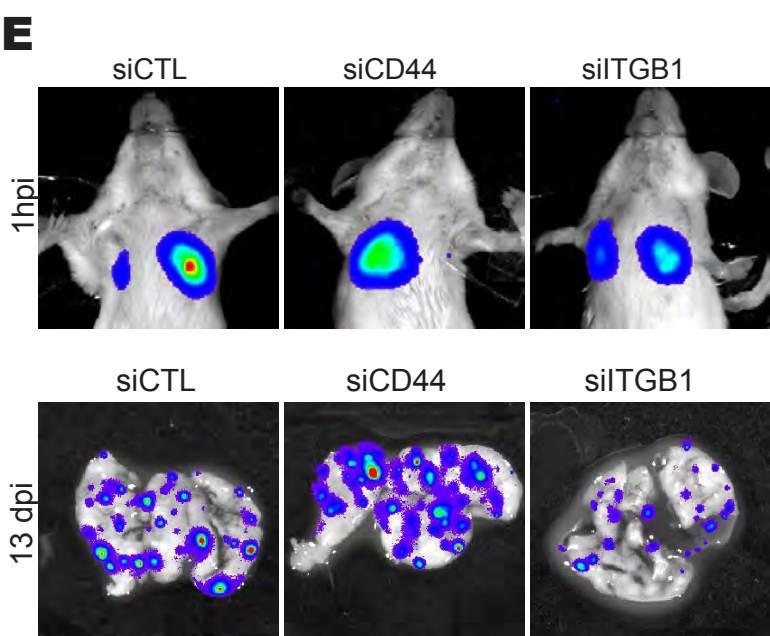
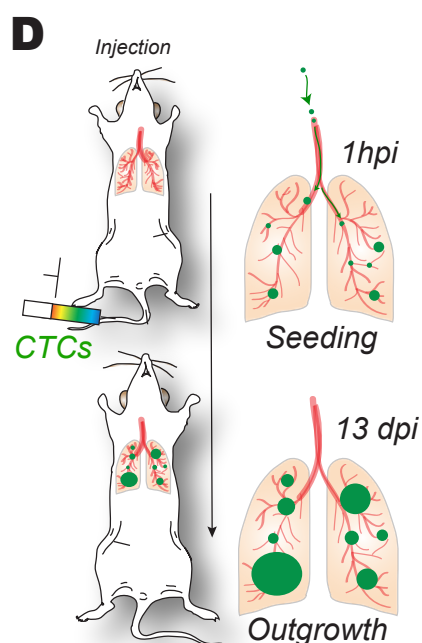
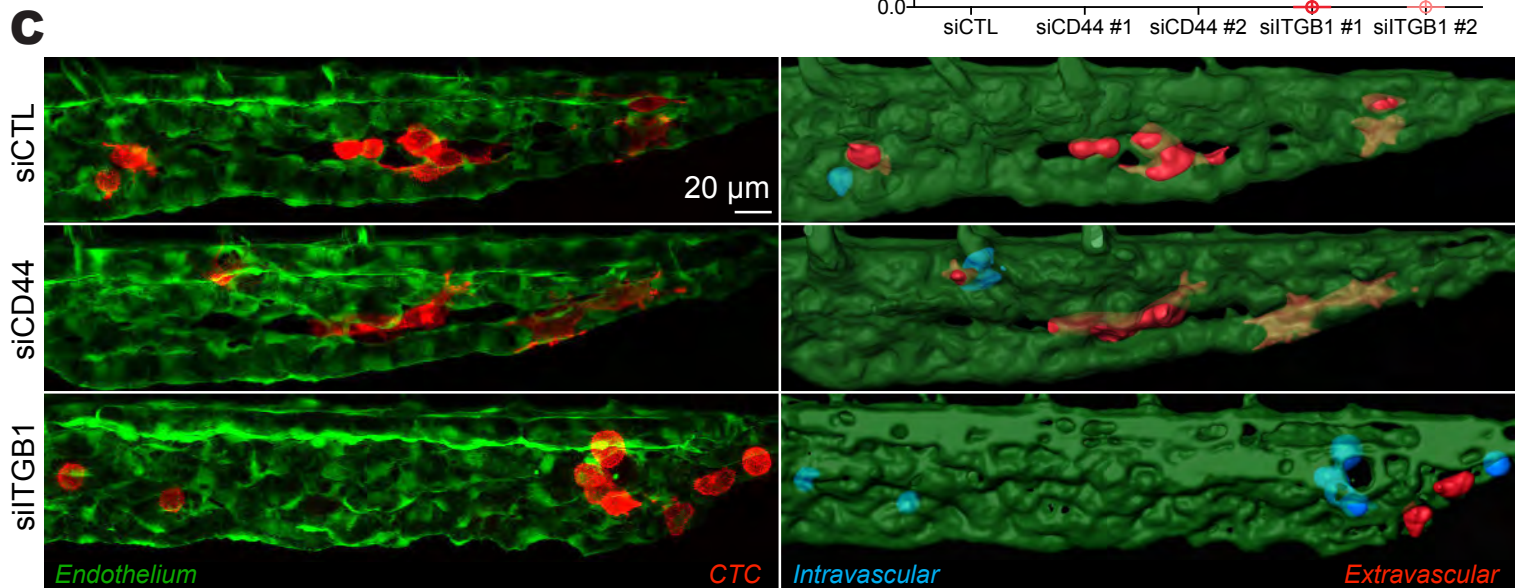
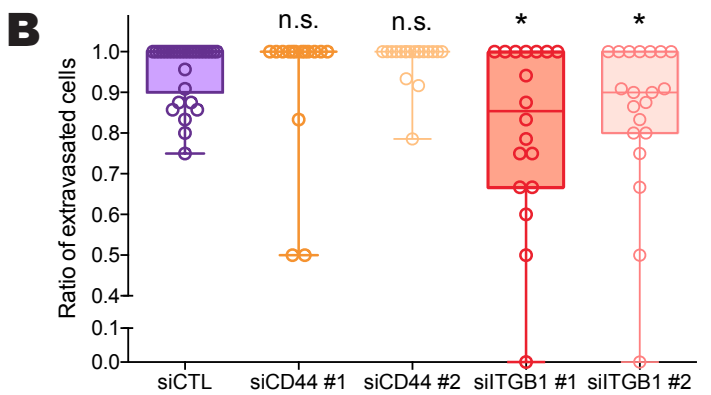
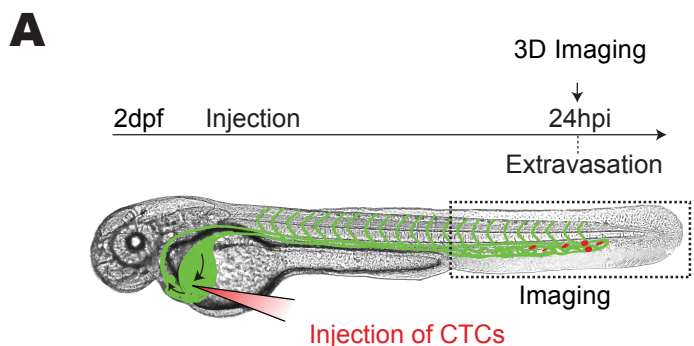


Figure 4 Osman et al.

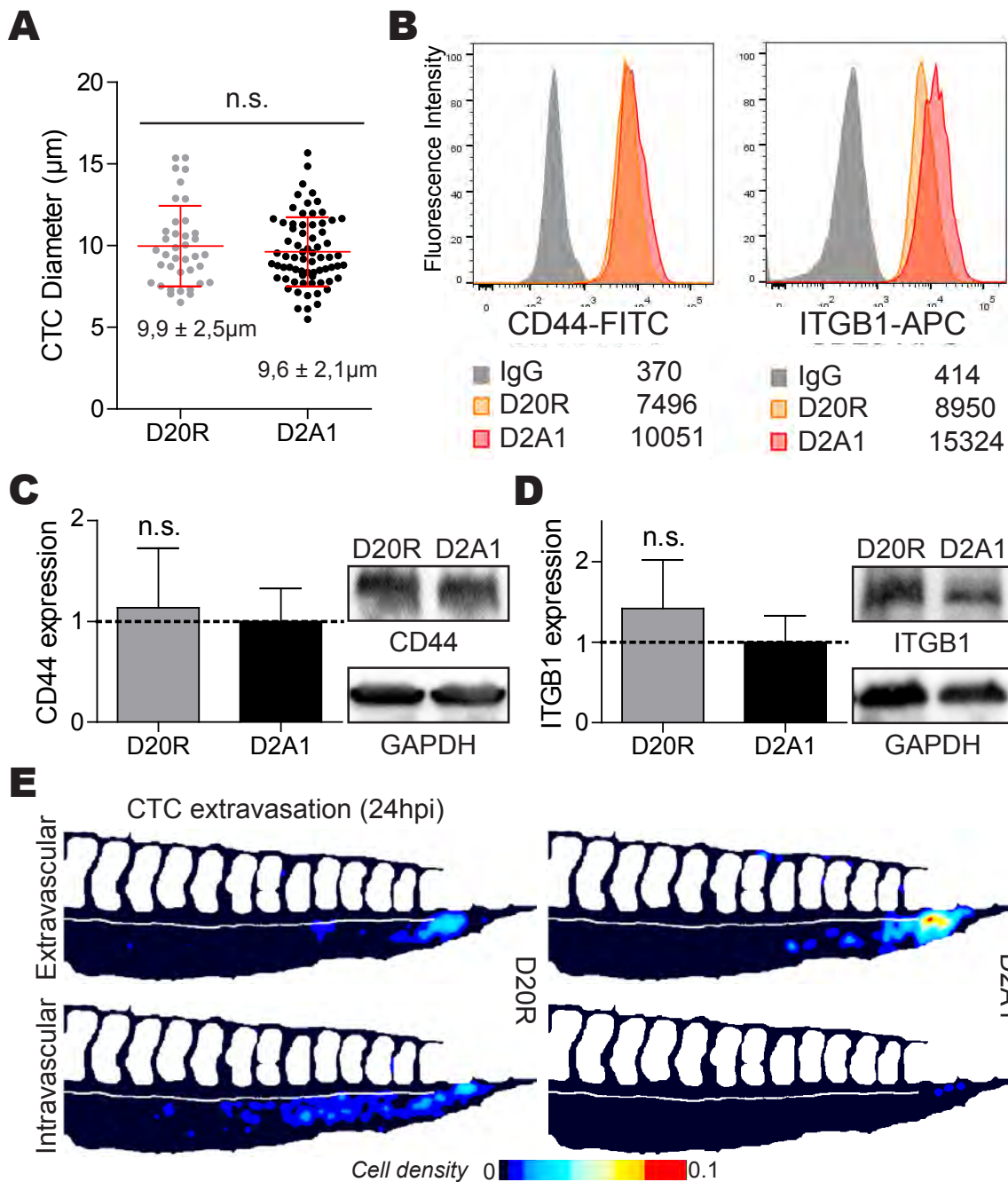
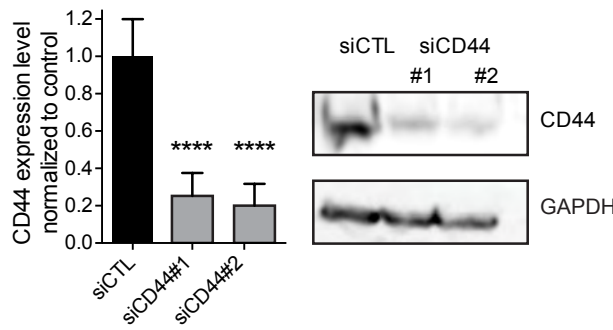
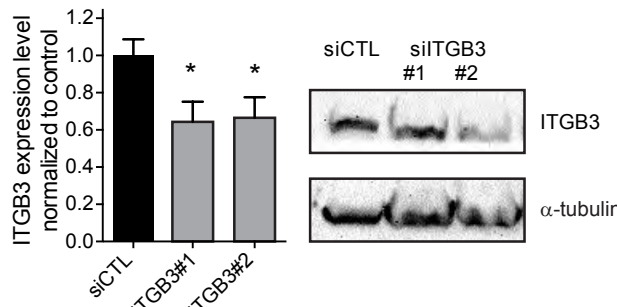
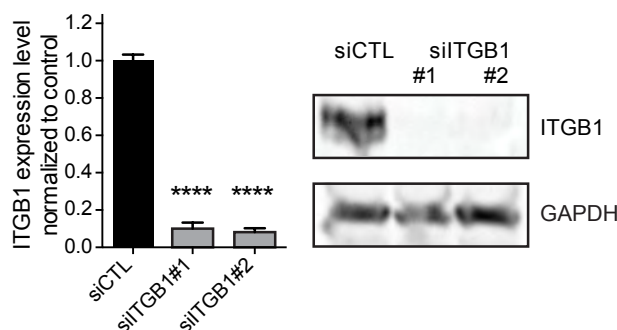
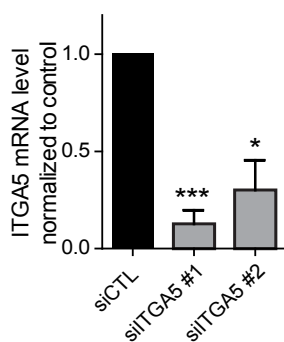


Figure S1 – D2A1 and D20R cell line characterization. (A) Quantification of the diameters of D20R and D2A1 cells in suspension. (B) Monoparametric flow cytometry histograms show cell membrane CD44 and ITGB1 levels at the surface of D20R and D2A1 cells after electronic gating on viable cells. FITC- or APC-labelled IgG isotype controls were used in D20R cells to set the negative population. Numbers in legends show the mean fluorescence intensity of the whole populations analyzed. (C-D) Protein extracts were prepared and immunoblotted against (C) CD44 or (D) ITGB1 and GAPDH. The relative expression was measured and normalized to D2A1 expression levels. The graph shows the mean \pm S.D. of 5 independent experiments. (E) D20R or D2A1 cells were microinjected into the duct of Cuvier of 2 dpf Tg(Fli1:EGFP) embryos and cell localization pattern was imaged 24h after injection with 3D confocal imaging. The heatmaps show the quantification and location of CTCs at 24 hpi in the caudal plexus. Related to figure 1H-J.

Figure S1_Osmani et al.

A**B****C****D****Figure S2 – siRNAs knockdown validation after transfection.**

(A-D) D2A1 cells were transfected with control or (A) anti-CD44, (B) anti-ITGB3, (C) anti-ITGB1 or (D) anti-ITGA5 siRNAs.

(A-C) Protein extracts were prepared 72h later and immunoblotted against (A) CD44, (B) ITGB3, (C) ITGB1, (A,C) GAPDH or (B) α-tubulin. The graph shows the mean ± S.D. of 5 independent experiments. (D) Total RNA extracts were prepared 48h after transfection. The expression of ITGA5 was measured using RT-qPCR.

The graph shows the mean ± S.D. of 3 independent experiments.

Related to figure 2.

Figure S2_Osmani et al.

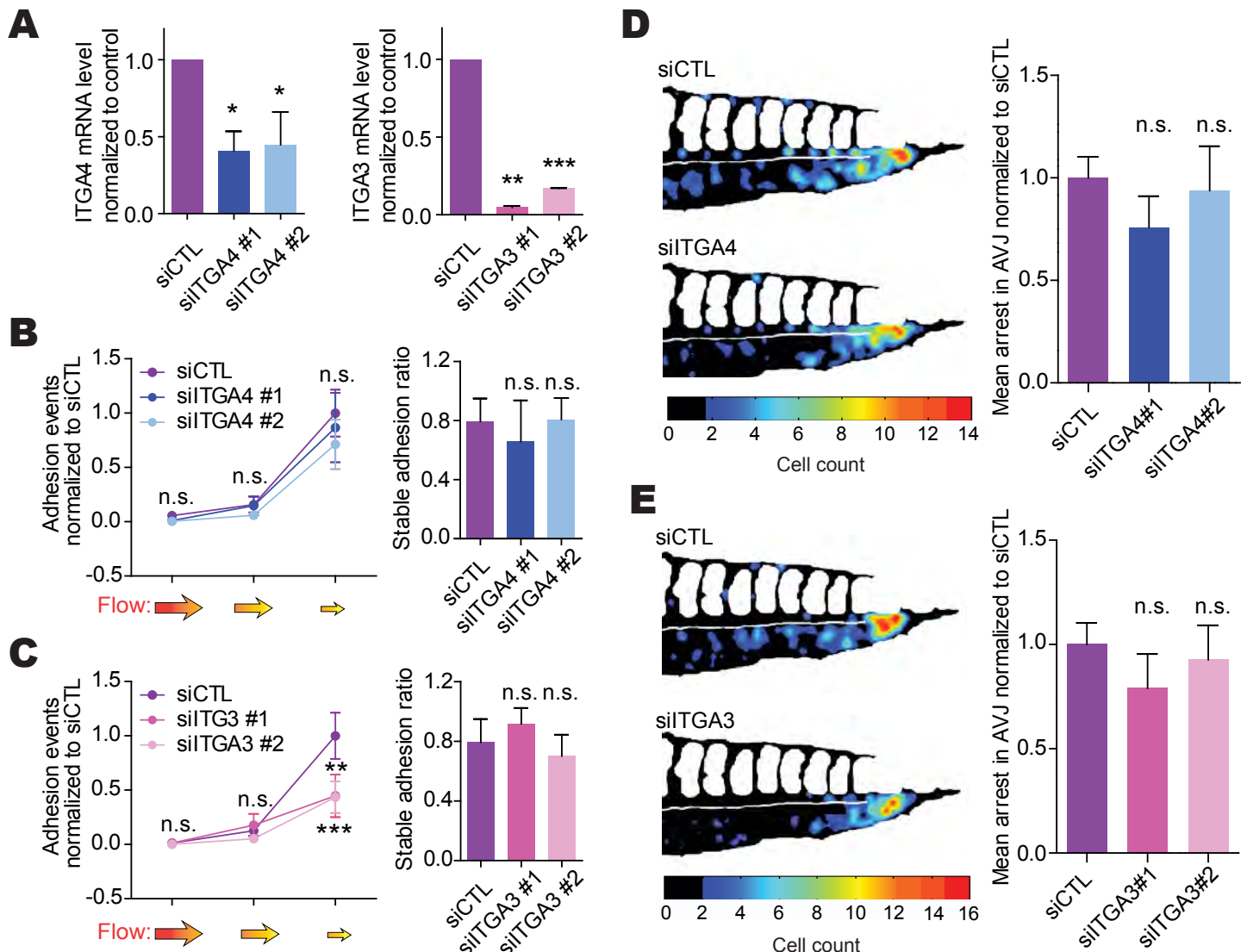


Figure S3 – ITGA4 and ITGA3 are not involved in CTC stable adhesion to endothelial cells. (A) D2A1 cells were transfected with indicated siRNAs. The expression of the genes of interest was measured using RT-qPCR. The graph shows the mean \pm S.D. of at least 3 independent experiments. (B-C) D2A1 cells were transfected with indicated siRNAs and perfused into microfluidic channels containing a confluent monolayer of endothelial cells (HUVEC). The number of cells adhered normalized to siCTL was quantified (left) and the ratio of stably adhering cells was measured (right). The graph shows the mean \pm S.E.M. (left) and mean \pm S.D. (right) of at least 4 independent experiments. (D-E) Quantification using heatmap of the number and location of stably arrested CTCs at 3 hpi in the caudal plexus of embryo injected with cells transfected with indicated siRNAs. The graphs show the mean \pm S.E.M. of 4 independent experiments. Related to figure 2 and 3.

Figure S3_Osmani et al.

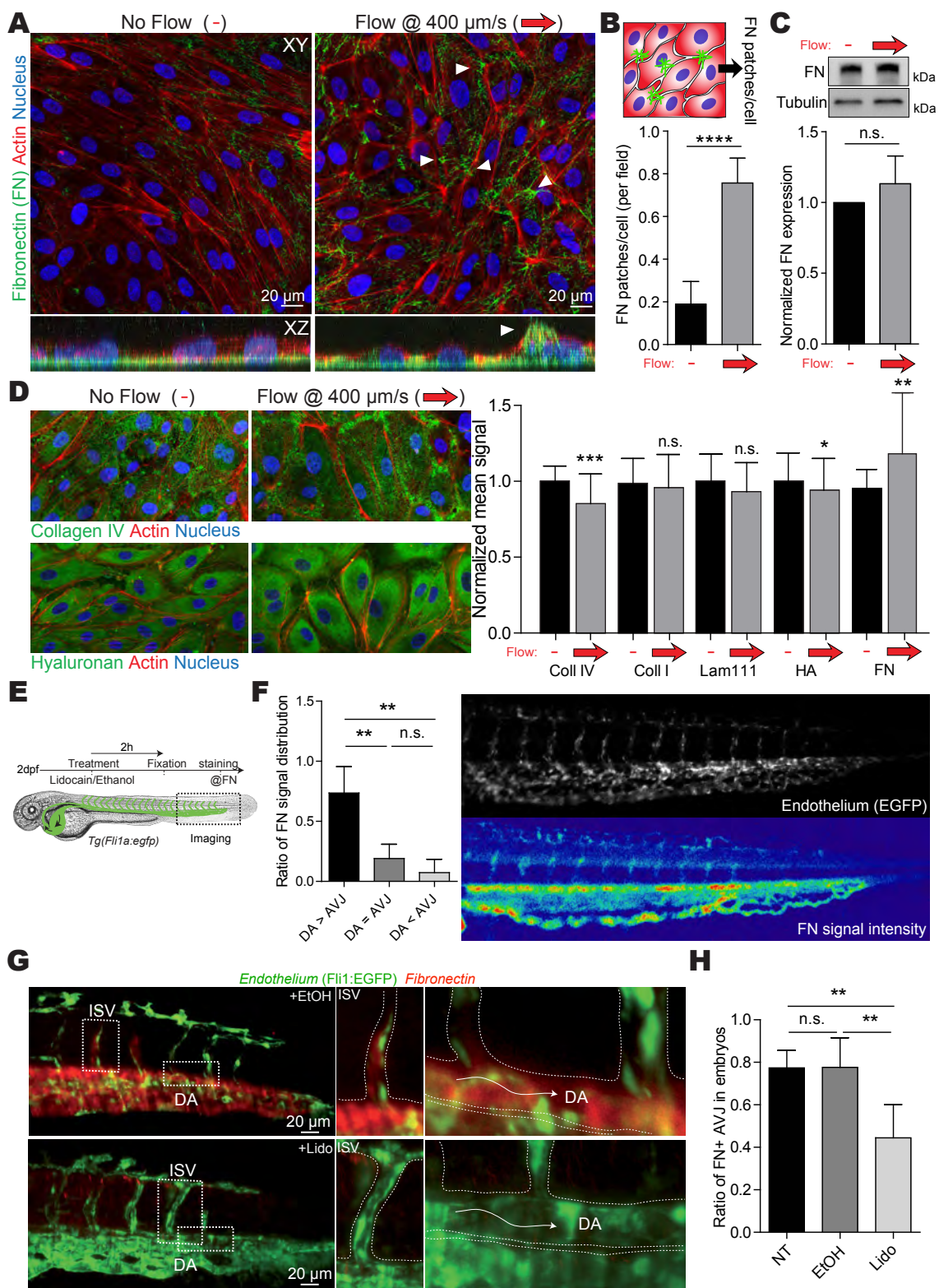


Figure S4 – Flow drives the formation of luminal FN deposits. (A) HUVEC cells were grown to confluence in microfluidic channels and subjected to either no flow or a laminar flow of 400 $\mu\text{m/s}$ for 16h. Cells are immunostained for fibronectin (green), actin (red) and nucleus (blue). A y-projection of 35 single representative transversal confocal slices is shown in the bottom panel XZ. (B) The ratio of HUVEC cells with fibronectin (FN) deposits was quantified. The graphs show the mean \pm S.D. of 3 independent experiments. (C) HUVEC cells were grown to confluence in microfluidic channels and subjected to either no flow or a laminar flow of 400 $\mu\text{m/s}$ for 16h. Fibronectin (FN) expression was then quantified. A representative western blot image is shown in the upper panel. The graphs show the mean \pm S.D. of 5 independent experiments. (D) HUVEC cells were grown to confluence in microfluidic channels and subjected to either no flow or a laminar flow of 400 $\mu\text{m/s}$ for 16h. Cells were immunostained for collagen IV, collagen I, laminin 111, hyaluronan (HA) or fibronectin (FN). (right) Representative image of cells stained for collagen IV or hyaluronan (green), actin (red) and nucleus (blue). (left) For each individual field of view, the mean signal of the green channel (ECM) was measured and normalized to the average signal in the no flow condition. The graphs show the mean \pm S.D. of 5 independent experiments. (E) Scheme of the experimental approach for the in vivo luminal FN quantification. (F) Fibronectin signal in the DA and the AVJ was compared. Embryos were classified as higher signal in the DA (DA>AVJ), identical (DA=AVJ) or higher in the AVJ (DA<AVJ). The graph shows the mean \pm S.D. of 6 independent experiments. (G) Representative embryos were imaged using light sheet microscopy (SPIM). (H) 2 dpf *Tg(Fl1:EGFP)* embryos were either untreated (NT) or treated for 2h with vehicle (EtOH) or lidocaine at 640 μM (Lido). The presence of fibronectin deposits in the AVJ was assessed. The graph shows the mean \pm S.D. of 6 independent experiments. Related to Figure 2 and 3.

IMPAIRING FLOW-MEDIATED ENDOTHELIAL REMODELING REDUCES EXTRAVASATION OF TUMOR CELLS

Scientific context

Tumor cell extravasation is the last step preceding the colonization of distant organs and the metastatic outgrowth (Nguyen et al., 2009). The leukocyte extravasation model shows several drawbacks to allow a direct extrapolation to the tumor cells behavior. First, tumor cells need to express similar receptors to successfully phenocopy leukocyte transmigration by diapedesis (Marshall et al., 2003; Kong et al., 2013). Second, diapedesis - and extravasation in general - happen in healthy tissues and vascular environment, unlike intravasation where tumor cells face abnormal vasculature (Yuan et al., 1995). Third, from a biomechanic point of view, the cell arrested in the flow is experiencing high shear stress from the blood flow (due to its arrest in the flow) and compression from vessel wall cells during transmigration while going through. Thus, it should have similar visco-elastic properties to leukocytes. Tumor cells must survive all these steps to successfully transmigrate.

Already, several studies described other paths driving cell extravasation. For instance, in the case of neutrophils, endothelial cells are recruited by the neutrophil and engulf to a closed pocket – isolated from the blood flow – before accessing the stroma (Phillipson et al., 2008). Specifically, in the zebrafish embryo caudal plexus, a similar mechanism was described for hematopoietic stem cells (Allen et al., 2017). In the context of cancer cells, we described flow-dependent remodeling of the endothelial cells around arrested tumor cells as an efficient mechanism excluding tumor cells from the lumen (Follain et al., 2018a). Importantly, we showed that this mechanism also occurs in the mouse brain around another tumor cell line. Nevertheless, we did not dig into the biological pathways involved in this process of endothelial remodeling.

Strategic context

After dissecting the flow-dependent endothelial remodeling around arrested tumor cells, we aimed at targeting it to prevent extravasation of tumor cells. To note, we did not intend to dissect the full flow-dependent signaling, but to check if it was possible to chemically block the extravasation (favored by endothelial remodeling) and the subsequent metastatic outgrowth. In other words, we initiated a set of experiments to demonstrate the medical relevance of our previous finding (Follain et al., 2018a).

Thus, we started with an RNAseq experiments on flow-treated vs no flow-treated endothelial cells to highlight the most impacted genes. This prompted us to focus on the VEGF signaling pathway, that we decided to try to block using a pan-inhibitor. We focused on Sunitinib (Sutent®), a tyrosine-kinase receptor blocker, having a strong affinity with all VEGF receptors and already tried on zebrafish embryos (Lee et al., 2009). Then we coupled our previously developed methods using zebrafish embryos (Follain et al., 2018b) and microfluidics with sunitinib treatment to study its impact on endothelial remodeling and subsequent metastatic outgrowth.

Major outputs

Our results demonstrate that endothelial remodeling is sensitive to the VEGF receptor pathway making it a potential therapeutic target. Using Sunitinib treatment, we were able to suppress endothelial remodeling *in vitro*. Interestingly, tumor cells turned to increased diapedesis under sunitinib treatment (demonstrating again the very high adaptability of cancer cells), resulting in a small decrease in term of transmigration. *In vivo*, we successfully inhibited the endothelial remodeling, that significantly reduced extravasation in the fish and in the mouse. Moreover, in the mouse model, a short early treatment with sunitinib during injection impacted the long-term (17 days) development of metastasis in the lungs.

NB: To write this manuscript, I followed the guideline of the “Short article” format of *Developmental Cell* journal. Main criteria: “The article must address a discrete point of strong significance” in a short text (25 000 characters), a maximum of 4 figures and the STAR*methods format. It has not been sent yet, thus it was never peer-reviewed. [- Blue notes -](#) indicate the points that might be modified before sending this manuscript.

Impairing flow-mediated endothelial remodeling reduces extravasation of tumor cells

- This list of authors may not be the final list -

Gautier Follain¹⁻⁴, Naël Osmani¹⁻⁴, Luc Mercier¹⁻⁴, Maria Jesus Garcia Leon¹⁻⁴, Ignacio Busnelli¹⁻⁴, Angélique Pichot¹⁻⁴, Nicodème Paul¹⁻⁴, Raphaël Carapito¹⁻⁴, Siamak Bahram¹⁻⁴, Olivier Lefebvre¹⁻⁴, Markus Glatzel, Frank Winkler, Sébastien Harlepp¹⁻⁴, Jacky G. Goetz^{1-4*}

- Affiliation list is not complete -

¹INSERM UMR_S1109, Strasbourg, F-67200, France.

²Université de Strasbourg, Strasbourg, F-67000, France.

³LabEx Medalis, Université de Strasbourg, Strasbourg, F-67000, France.

⁴Fédération de Médecine Translationnelle de Strasbourg (FMTS), Strasbourg, F-67000, France.

Materials and correspondence, lead author:

Jacky G. GOETZ, jacky.goetz@inserm.fr

INSERM UMR_S1109, 67200 Strasbourg, France; Fédération de Médecine Translationnelle de Strasbourg (FMTS), 67000 Strasbourg, France

Web: www.goetzlab.com, twitter: [@GoetzJacky](https://twitter.com/GoetzJacky)

ABSTRACT

Tumor progression and metastatic dissemination are driven by cell-intrinsic and biomechanical cues that favor the growth of life-threatening secondary tumors. We recently identified pro-metastatic vascular regions with blood flow profiles that are permissive for the arrest of CTCs. Such flow profiles also stimulate endothelial remodeling, which favors extravasation of metastatic tumor cells. Yet, how shear forces control endothelial remodeling is unknown. We thus aimed to identify, and thereby inhibit, the underlying molecular mechanisms that are driven by blood flow forces. Transcriptomic analysis revealed that blood flow significantly enhanced VEGFR signaling in endothelial cells. Using a multimodal approach (microfluidics, zebrafish and mouse), we now show that the early flow-driven endothelial response can be tuned with a pan-inhibitor of vascular remodeling, namely Sunitinib. Animals treated with low-dose of Sunitinib displayed reduced endothelial remodeling and subsequent metastatic extravasation. These results confirm the significance of metastatic extravasation through endothelial remodeling and identify means to prevent the very early stages of metastatic seeding. Altogether, this work suggests that therapies that target endothelial remodeling might be useful to impede extravasation, and subsequent outgrowth, of metastatic cells.

KEY WORDS

VEGFR, endothelial remodeling, Sunitinib, extravasation, circulating tumor cells, metastasis, blood flow.

INTRODUCTION

Metastases formation induced by advanced tumorigenic progression are the main reason for cancer-related death (Nguyen et al., 2009). It is currently well admitted that their development relies on biological and biophysical cues that influence their location and development. Indeed, adhesion molecule repertoire (Cavallaro and Christofori, 2004; Gassmann et al., 2009; Schlesinger and Bendas, 2015), vascular architecture (Headley et al., 2016; Kienast et al., 2010) and blood flow profile (Chambers et al., 2002; Wirtz et al., 2011; Follain et al., 2018) have been shown to impact the early steps of tumor cells spreading. While, the micro-environmental parameters around emerging metastasis such as growth factor, chemokines, stromal cell composition (Paget, 1889; DeNardo et al., 2010; Nagarsheth et al., 2017; Rotow and Bivona, 2017) and matrix stiffness (Paszek et al., 2005; Levental et al., 2009; Mouw et al., 2014) will permit the growth of secondary tumor.

As previously described, and as an efficient dispersion path, tumor cells go through several key steps including intravasation, blood flow carrying and extravasation to grow at distant sites (Valastyan and Weinberg, 2011; Massagué and Obenauf, 2016). Thus, a clear understanding of these steps is necessary to design relevant pharmacological approach. Recently, focusing on the extravasation step, we have been described blood flow as one of the main actors dictating the location of tumor cell extravasation and subsequent micro-metastasis formation using the zebrafish embryo (Follain et al., 2018). Importantly, we have shown endothelial remodeling around tumor cells as a prominent flow-dependent extravasation path. It relies on the ability of endothelial cells to migrate intravascularly and enclose adhered tumor cells, excluding them from the inner vasculature. As a result, this mechanism induces the re-establishment of normal perfusion pattern and “passive” extravasation of tumor cells.

The flow-dependence of endothelial remodeling prompted us to investigate the effect of flow on biological pathways activation in the endothelial cells that could be responsible for this mechanism. In the following report, we describe VEGFRs inhibition with sunitinib as a way to impair extravasation of circulating tumor cells by blocking the endothelial remodeling. Thus, our findings suggest an additional application of Sunitinib in clinic (Meadows and Hurwitz, 2012). By using RNA sequencing analysis, microfluidics and two *in vivo* models (Zebrafish and mouse), we demonstrate that

sunitinib affect an earlier step of the metastatic cascade, namely the extravasation step.

RESULT

Flow upregulate VEGF signaling pathway

As a starting point, we decided to use RNA sequencing on endothelial cells to identify flow-sensitive genes that could play a role in the endothelial remodeling process. To do so, we used previously described methods based on Human Umbilical Venous Endothelial Cells (HUVEC) culture in microfluidic channels (Follain et al., 2018). After reaching confluence, the HUVECs were culture under flow perfusion, or not, during 16 hours with a flow rate of 400 $\mu\text{m/sec}$ (Fig 1A). Of note, this speed was chosen based on our previous work and several other references that measured the flow rate contained in capillary like vessels (Ivanov et al., 1985; Anton et al., 2013; Hill et al., 2015; Sugden et al., 2017; Follain et al., 2018). These vessels are prone to circulating tumor cells (CTC) arrest and subsequent extravasation. Then, total RNA was extracted, and quantitative RNA sequencing was carried out with Gene Ontology (GO) data base.

First, results show a transcriptomic switch between cell division/cell cycle regulation in the no flow condition, to cell migration/angiogenesis in the flow condition (Fig 1B and Fig S1A), as already described in other studies (Fang et al., 2017). Second, and of major interest for us, stimulation with flow induces upregulation of genes playing a role in vascular development, angiogenesis, and response to oxidative stress that was previously link to shear stress response (Simons et al., 2016). Focusing on the GO class “Angiogenesis” (Fig 1C), applied to our list of significantly impacted gene (Fold change > 1.5 , p-value < 0.05) we observed an upregulation of only “positive regulator genes”, according to GO classes. Among others, we identified Flt1 (VEGFR1) and Kdr (VEGFR2), two VEGF receptors (VEGFR) that were strongly upregulated by the flow. Thus, we focused on the VEGFR and double-check sequencing results with real time quantitative PCR (Fig S1B). We confirm an upregulation of Flt1 and Kdr gene around two fold after flow stimulation on independent extracts. At the protein level, immunoblotting of FLT1, KDR and FLT4 (VEGFR3), of flow vs no flow HUVEC protein extracts using the same microfluidic setup (Fig 1D and F) shows an increased level of KDR and FLT4. Surprisingly, we observed no upregulation of FLT1 at the level of the

protein. In addition, we quantified Immuno-labelling on FLT1, KDR and FLT4 (**Fig 1E and 1F**). In this case, we could observe an increased signal intensity for all the three receptors.

All in All, these data prompted us to test the role of VEGFR pathways on the flow-dependent endothelial remodeling leading to extravasation of tumor cells. Moreover, we had access to human brain tissue containing metastasis on which we performed VEGFR2 immunohistochemistry (**Fig 1G and H**). Comparing signal intensity between metastatic and control brain section from biopsies, we found out that VEGFR2 is significantly overexpressed in the metastatic context (**Fig 1I and J**).

VEGF pathway inhibition with sunitinib *in vitro* suppresses endothelial remodeling

Based on our previous results, we decided to test whether blocking VEGF receptors could impact the endothelial remodeling around tumor cells. First, we performed VEGFR2 immuno-labeling of endothelial cell remodeling around CTC confirming the presence of the protein during this process (**Fig 2A**). Then, we set out experiments using microfluidic channels, coated with HUVECs in presence of flow (400 μ m/sec) with or without sunitinib treatment (**Fig 2B**). The channels were then injected with tumor cells that adhered to endothelial cells and left for 16 hours with or without flow. As previously describe, in the context of flow stimulation (Follain et al., 2018), 95% of the cells are found under the HUVEC monolayer, with visible endothelial remodeling activity in 80% of the case (**Fig 2C**). When adding 0,1 μ M of sunitinib, the number of transmigrated cells decreased, and very interestingly sunitinib suppresses the remodeling activity. Representing images from no transmigration, transmigration without remodeling and transmigration with remodeling are shown in **Fig 2D** and global repartition of the event in **Fig 2E**. These *in vitro* data confirm the role of VEGF pathway in the remodeling activity of the endothelial cells around tumor cells.

VEGF pathway inhibition with sunitinib in zebrafish embryos blocks the endothelial remodeling in a dose-dependent manner

We then decided to test the inhibition of VEGF signaling *in vivo*, using injection of tumor cells in the circulation of zebrafish embryos. Combining ease of pharmacological treatments, great imaging potential of transparent embryos and high-compatibility with mammalian tumor cell lines, the zebrafish model has proven its value to the cancer

field (Langenau et al., 2003; Patton et al., 2005; Haldi et al., 2006; Stoletov et al., 2007; White et al., 2008). Using injection of tumor cells directly in the circulation through the Duct of Cuvier of 48 hours post-fertilization (hpf) embryos, we quantitatively address the effect of sunitinib on extravasation *in vivo* (Fig 3A). As we have previously described, endothelial remodeling (ER) is a major mechanism driving extravasation of tumor cells *in vivo* (Follain et al., *Dev Cell* 2018), we classified the tumor cells into three populations: Intravascular, Pocketing (meaning in the process of extravasation through ER) and extravasated. After only 3 hours post-injection (hpi), tumor cells are stably adhered and ER is starting. Quantitative results obtained over a large number of embryos, show that sunitinib significantly slowdown this process, in a dose-dependent manner: Increasing the ratio of intravascular cells and decreasing the ratio of pocketing events (Fig 3B). At a later time point, 9 hpi (Fig S2A and S2B), we observed that the extravasation ratio of cells is significantly decrease, with most of the tumor cells remaining intravascular.

To illustrate these quantitative results, we set out a correlative light and electron microscopy (CLEM) experiment on representative embryos of both conditions (Fig S2C). In the case of vehicle, we focused on one cell in the process of ER and a cluster of cells already in contact with the stroma in the caudal plexus (Fig 3C). In the context of 5 μ M sunitinib treatment, two cells remaining intravascular are shown, with no ER initiation observable in the same region of the embryo at the same time (Fig 3D). Besides, we verified the effect of sunitinib treatments on the vascular architecture of the caudal plexus (Fig S2D) and on the blood flow pattern (Fig S2E) that could impact the ER activity. We established non-significant differences on the global architecture of the plexus, with only the most caudal ISVs not always lumenized. Nevertheless, with PIV analysis on the red blood cells, we identified a slight difference in the flow pattern: At ISV 8 (most anterior part of the DA in our analysis), the flow is not impacted. Then, in the control situation, flow drops to reach minimal values at the arterio-venous junction (at ISV 1 in our analysis – in accordance with our previous study, Follain et al. 2018). This drop is less intense in the case of sunitinib, leading to higher blood flow profile at the ISV 1. This can be explained by the reduced development of the ISV upon Sunitinib treatment as commented before. It could reduce flow dispersion normally occurring in each arterial ISV.

Finally, using multi-photon microscopy, we also quantified the tumor cell status (intra. vs extravascular) in the brain of zebrafish embryos, a region bearing a more complex

capillary-like vessel architecture (**Fig 2E**). Quantification at 3hpi shows that sunitinib also inhibit the extravasation of the tumor cells in the brain (**Fig 2F**). Taken together, these experiments demonstrate that VEGF signaling pathway play a major role in the endothelial remodeling process driving extravasation of tumor cells *in vivo*.

VEGF pathway inhibition with sunitinib reduces the number of extravasated tumor cells in the mouse brain.

Next, we investigated the impact of VEGFR inhibition with sunitinib in the mouse model. We performed sunitinib feeding to treat mice over 5 days and injected them intracardially with Jimt-1Br3 cells (selected brain metastatic clone). At day 4 post-injection, mice were sacrificed, and entire brains were dissected, sliced and stained to track extravasating tumor cells (**Fig 4A**). Representative images show that cells are either extravascular, sitting on the vessels, or still intravascular (**Fig 4B 4C**). Quantification of cells inside and outside of the vasculature in the context of control versus sunitinib treated mice reveals that sunitinib significantly decreases the extravasated ratio of the cells in the mouse brain context (**Fig 4D**). Also, using CLEM approach on brain slices, we were able to observe extravasation by endothelial remodeling in the case of control and intravascular event in the case of sunitinib (**Fig 4E**). These data confirm the importance of VEGF pathway in the extravasation step in the brain of adult mice. They also suggest a common mechanistic reason for this decrease: Inhibition of endothelial remodeling around tumor cells with Sunitinib.

Next question was the long-term effect of inhibition of VEGF pathway. Thus, we set out another experiment using the mouse model, to test if our 5 days-treatment with sunitinib would impact metastasis outgrowth. We used tail vein injection with D2A1 cells expressing luciferase (**Fig 4F**). Doing so, we maximize the number of cells reaching the lungs, the major physiologic metastatic site of these cells. Then, we injected luciferin to follow the seeding and the growth of tumor cells in the lung for 17 days. Final time point and dissected lungs from representative mice of the two conditions are shown in **Fig 4G**. Very interestingly, bioluminescent signal quantification (**Fig 4H**) shows that sunitinib treatment for 5 days significantly decreases the metastatic outgrowth in the lungs at day 17. Altogether, these results show that VEGF pathway activation is needed for efficient extravasation, and that impairing extravasation by blocking ER have a long-term effect on the metastatic spreading.

DISCUSSION

Using a combination of *in vivo* models, *in vitro* microfluidics approach and molecular biology, we demonstrated that endothelial remodeling around arrested tumor cell can be impaired by inhibiting the VEGFR pathway with Sunitinib. After showing the upregulation of VEGF receptors in the context of flow stimulation by transcriptomic analysis, we have successfully inhibited the transmigration of tumor cells in microfluidic channels covered with endothelial cells in presence of Sunitinib. Then, we have shown that Sunitinib decrease the efficiency of the endothelial remodeling process leading to extravasation of tumor cells in the zebrafish embryos at 48 hpf. Finally, using intracardiac injection on Sunitinib-treated mice, we have been able to decrease the ratio of extravasated cells in the brain and to impair subsequent metastatic growth in the lungs of mice.

These new results help in understanding previous characterization of flow-dependent endothelial remodeling driving extravasation of tumor cells (Follain et al., 2018). In our previous work, we dissected this mechanism at the best resolution *in vivo*, using correlative light and electron microscopy (CLEM) and electron tomography. Here, we describe VEGFR pathway (Stacker and Achen, 2013) as a major actor of endothelial remodeling, in a pathologic context. VEGFR pathway is still actively studied for canonical and non-canonical activation. Canonical activation is complex, due to 1. Partial ligand specificity and crosstalk between VEGF A, B, C, D or PIGF ligand and VEGFR1, R2 or R3 receptors (Domigan et al., 2015). 2. The heterodimerization of the receptors (Mac Gabhann and Popel, 2007; Nilsson et al., 2010). Interestingly, non-canonical (ligand-independent) VEGFR activation has been described (non-canonical) in the context of mechano-transduction. Modification of the shear stress profile at the apical side of the endothelial cell, due to the presence of an arrested tumor cells might be sufficient to activate VEGFR kinase cascade and transduce the signal into the nucleus (Mac Gabhann and Popel, 2007; Nilsson et al., 2010). Alternatively, the adhesion of tumor cells might induce pulling force at the surface of the endothelial cells (Conway and Schwartz, 2014). This would be an indirect effect of the blood flow that push on the arrested tumor cells. To note, it would be less probable that tumor cells secrete VEGF ligand upon arrest to induce canonical activation. Indeed, according to qPCR analysis (data not shown) measuring VEGF expression of our tumor cells, very few VEGF protein could be measured. Controversially, we can't eliminate the

hypothesis of an autocrine activation of the pathway, as proposed to maintain homeostasis by Lee et al. (Lee et al., 2007). All in all, the dissection of the ER at the level of the signaling pathway remains to be done.

Sunitinib is a tyrosine-kinase receptor inhibitor, mainly targeting VEGFR, PDGFR and c-KIT receptors that was first identified in 1999 (T. Fong et al., 1999). It is currently clinically used for several cancer treatments like renal or Gastrointestinal cancer (Younus et al., 2010). It is also in clinical trials and recent research articles for its ability to block vascular development around well-established tumors in other context and in comparison with similar drugs such as Pazopanib (Rodriguez-Vida et al., 2017; Chellappan et al., 2017). Despite positive results on tumor growth and cancer progression (Young et al., 2010), the positive impact of sunitinib was questioned in several publications: Using Sunitinib at high concentration (120 mg/kg/day) on syngeneic mice increase tumor progression of MDA 231/LM2-4 cells (Ebos et al., 2009). Also, previous work from Welti and colleagues using tail vein injection of 4T1 (mammary carcinoma from Balb/c genetic background) and RENCA (Renal carcinoma also from Balb/c) cells in syngenic model showed a negative effect with 4T1 cells, but positive with RENCA cells (Welti et al., 2012). Recently, studying the impact of sunitinib treatment on renal cancer cells, Lichner et al. have shown that sunitinib resistant cells were present as a tumor subpopulation that would lead to tumor resistance (Lichner et al., 2018). Beside, *in vitro* experiments have shown that sunitinib treatment increase cell mobility and expression of mesenchymal markers that would promote metastasis (Tomida et al., 2017). From our data, sunitinib at low concentration (40 mg/kg/day) has a positive impact on D2A1 (mammary carcinoma) cells, impairing extravasation and early metastatic growth. All in all, sunitinib seems to have a tumor cell- and host-dependent efficacy. Interestingly, previous data showed that sunitinib treatment is simplifying the tumor microvasculature, leading to increased drug delivery (Czabanka et al., 2009). To note, promising ongoing works are now orienting the use of sunitinib coupled with immunotherapy (Liu et al., 2018).

All in all, our data show that it is possible to inhibit the endothelial remodeling around arrested tumor cells *in vivo*. Thus, we provide the demonstration that endothelial remodeling is a drugable target of interest to fight cancer progression.

AUTHOR CONTRIBUTIONS – Might not be the final version –

GF and NO performed the majority of the experiments and GF performed the analysis. LM, MJGL and OL performed the mouse experiments. IB performed the CLEM procedures with input from GF and LM. AP, NP, RC and SB performed the RNAseq experiment and sequence alignment. FW provided Jimt-1 cells and scientific inputs. SH supervised the study and performed imaging. JGG conceived the project, supervised the study. GF wrote the manuscript with input from NO, SH and JGG.

ACKNOWLEDGMENTS – Might not be the final version –

We thank all members of the Goetz Lab for helpful discussions. We are grateful to Robert WEINBERG (MIT) for providing D2A1 cells, and to Frank WINKLER (DKFZ) for providing Jimt-1Br3 cells. We are very grateful to Francesca PERI (EMBL) and Kerstin RICHTER (EMBL) for providing zebrafish embryos. We thank imaging facility members from EFS Strasbourg, IGBMC and INCI for access and discussions to light and electron microscope.

FUNDINGS – Might not be the final version –

This work has been funded by Plan Cancer (OptoMetaTrap, to J.G. and S.H) and CNRS IMAG'IN (to S.H., J.G. and C.P.) and by institutional funds from INSERM and University of Strasbourg. N.O is supported by Plan Cancer. G.F. was supported by La Ligue Contre le Cancer.

REFERENCES

Anders, S., Pyl, P.T., and Huber, W. (2015). HTSeq--a Python framework to work with high-throughput sequencing data. *Bioinformatics* *31*, 166–169.

Anton, H., Harlepp, S., Ramspacher, C., Wu, D., Monduc, F., Bhat, S., Liebling, M., Paoletti, C., Charvin, G., Freund, J.B., et al. (2013). Pulse propagation by a capacitive mechanism drives embryonic blood flow. *Development* *140*, 4426–4434.

Bishop, D., Nikić, I., Brinkoetter, M., Knecht, S., Potz, S., Kerschensteiner, M., and Misgeld, T. (2011). Near-infrared branding efficiently correlates light and electron microscopy. *Nature Methods* *8*, 568–570.

Cavallaro, U., and Christofori, G. (2004). Cell adhesion and signalling by cadherins and Ig-CAMs in cancer. *Nat. Rev. Cancer* *4*, 118–132.

Chambers, A.F., Groom, A.C., and MacDonald, I.C. (2002). Metastasis: Dissemination and growth of cancer cells in metastatic sites. *Nat Rev Cancer* *2*, 563–572.

Chellappan, D.K., Chellian, J., Ng, Z.Y., Sim, Y.J., Theng, C.W., Ling, J., Wong, M., Foo, J.H., Yang, G.J., Hang, L.Y., et al. (2017). The role of pazopanib on tumour angiogenesis and in the management of cancers: A review. *Biomedicine & Pharmacotherapy* *96*, 768–781.

Conway, D.E., and Schwartz, M.A. (2014). Mechanotransduction of shear stress occurs through changes in VE-cadherin and PECAM-1 tension: Implications for cell migration. *Cell Adh Migr* *9*, 335–339.

Czabanka, M., Vinci, M., Heppner, F., Ullrich, A., and Vajkoczy, P. (2009). Effects of sunitinib on tumor hemodynamics and delivery of chemotherapy. *International Journal of Cancer* *124*, 1293–1300.

DeNardo, D.G., Andreu, P., and Coussens, L.M. (2010). Interactions between lymphocytes and myeloid cells regulate pro- versus anti-tumor immunity. *Cancer and Metastasis Reviews* *29*, 309–316.

Domigan, C.K., Ziyad, S., and Iruela-Arispe, M.L. (2015). Canonical and non-canonical VEGF pathways: New developments in biology and signal transduction. *Arterioscler Thromb Vasc Biol* *35*, 30–39.

Ebos, J.M.L., Lee, C.R., Cruz-Munoz, W., Bjarnason, G.A., Christensen, J.G., and Kerbel, R.S. (2009). Accelerated Metastasis after Short-Term Treatment with a Potent Inhibitor of Tumor Angiogenesis. *Cancer Cell* *15*, 232–239.

Fang, J.S., Coon, B.G., Gillis, N., Chen, Z., Qiu, J., Chittenden, T.W., Burt, J.M., Schwartz, M.A., and Hirschi, K.K. (2017). Shear-induced Notch-Cx37-p27 axis arrests endothelial cell cycle to enable arterial specification. *Nature Communications* *8*.

Follain, G., Osmani, N., Azevedo, A.S., Allio, G., Mercier, L., Karreman, M.A., Solecki, G., Garcia León, M.J., Lefebvre, O., Fekonja, N., et al. (2018). Hemodynamic Forces Tune the

Arrest, Adhesion, and Extravasation of Circulating Tumor Cells. *Developmental Cell* 45, 33–52.e12.

Gassmann, P., Hemping-Bovenkerk, A., Mees, S.T., and Haier, J. (2009). Metastatic tumor cell arrest in the liver–lumen occlusion and specific adhesion are not exclusive. *International Journal of Colorectal Disease* 24, 851–858.

Goetz, J.G., Steed, E., Ferreira, R.R., Roth, S., Ramspacher, C., Boselli, F., Charvin, G., Liebling, M., Wyart, C., Schwab, Y., et al. (2014). Endothelial Cilia Mediate Low Flow Sensing during Zebrafish Vascular Development. *Cell Reports* 6, 799–808.

Haldi, M., Ton, C., Seng, W.L., and McGrath, P. (2006). Human melanoma cells transplanted into zebrafish proliferate, migrate, produce melanin, form masses and stimulate angiogenesis in zebrafish. *Angiogenesis* 9, 139–151.

Headley, M.B., Bins, A., Nip, A., Roberts, E.W., Looney, M.R., Gerard, A., and Krummel, M.F. (2016). Visualization of immediate immune responses to pioneer metastatic cells in the lung. *Nature* 531, 513–517.

Hill, R.A., Tong, L., Yuan, P., Murikinati, S., Gupta, S., and Grutzendler, J. (2015). Regional Blood Flow in the Normal and Ischemic Brain Is Controlled by Arteriolar Smooth Muscle Cell Contractility and Not by Capillary Pericytes. *Neuron* 87, 95–110.

Ivanov, K.P., Kalinina, M.K., and Levkovich, Yu.I. (1985). Microcirculation Velocity Changes under Hypoxia in Brain, Muscles, Liver, and Their Physiological Significance. 10–18.

Karreman, M.A., Mercier, L., Schieber, N.L., Shibue, T., Schwab, Y., and Goetz, J.G. (2014). Correlating Intravital Multi-Photon Microscopy to 3D Electron Microscopy of Invading Tumor Cells Using Anatomical Reference Points. *PLoS ONE* 9, e114448.

Karreman, M.A., Hyenne, V., Schwab, Y., and Goetz, J.G. (2016a). Intravital Correlative Microscopy: Imaging Life at the Nanoscale. *Trends Cell Biol.* 26, 848–863.

Karreman, M.A., Mercier, L., Schieber, N.L., Solecki, G., Allio, G., Winkler, F., Ruthensteiner, B., Goetz, J.G., and Schwab, Y. (2016b). Fast and precise targeting of single tumor cells *in vivo* by multimodal correlative microscopy. *J Cell Sci* 129, 444–456.

Kienast, Y., von Baumgarten, L., Fuhrmann, M., Klinkert, W.E.F., Goldbrunner, R., Herms, J., and Winkler, F. (2010). Real-time imaging reveals the single steps of brain metastasis formation. *Nat. Med.* 16, 116–122.

Kim, D., Langmead, B., and Salzberg, S.L. (2015). HISAT: a fast spliced aligner with low memory requirements. *Nature Methods* 12, 357–360.

Koch, S., Tugues, S., Li, X., Gualandi, L., and Claesson-Welsh, L. (2011). Signal transduction by vascular endothelial growth factor receptors. *Biochem. J.* 437, 169–183.

Langenau, D.M., Traver, D., Ferrando, A.A., Kutok, J.L., Aster, J.C., Kanki, J.P., Lin, S., Prochownik, E., Trede, N.S., Zon, L.I., et al. (2003). Myc-Induced T Cell Leukemia in Transgenic Zebrafish. *Science* 299, 887–890.

Lee, S., Chen, T.T., Barber, C.L., Jordan, M.C., Murdock, J., Desai, S., Ferrara, N., Nagy, A., Roos, K.P., and Iruela-Arispe, M.L. (2007). Autocrine VEGF signaling is required for vascular homeostasis. *Cell* 130, 691–703.

Levental, K.R., Yu, H., Kass, L., Lakins, J.N., Egeblad, M., Erler, J.T., Fong, S.F.T., Csiszar, K., Giaccia, A., Weninger, W., et al. (2009). Matrix crosslinking forces tumor progression by enhancing integrin signaling. *Cell* 139, 891–906.

Lichner, Z., Saleeb, R., Butz, H., Ding, Q., Nofech-Mozes, R., Riad, S., Farag, M., Varkouhi, A.K., dos Santos, C.C., Kapus, A., et al. (2018). Sunitinib induces early histomolecular changes in a subset of renal cancer cells that contribute to resistance. *The FASEB Journal* *fj.201800596R*.

Liu, D., Qi, X., Manjunath, Y., Kimchi, E.T., Ma, L., Kaifi, J.T., Staveley-O'Carroll, K.F., and Li, G. (2018). Sunitinib and Sorafenib Modulating Antitumor Immunity in Hepatocellular Cancer.

Love, M.I., Huber, W., and Anders, S. (2014). Moderated estimation of fold change and dispersion for RNA-seq data with DESeq2. *Genome Biology* 15.

Mac Gabhann, F., and Popel, A.S. (2007). Dimerization of VEGF receptors and implications for signal transduction: a computational study. *Biophys. Chem.* 128, 125–139.

Massagué, J., and Obenauf, A.C. (2016). Metastatic colonization by circulating tumour cells. *Nature* 529, 298–306.

Meadows, K.L., and Hurwitz, H.I. (2012). Anti-VEGF Therapies in the Clinic. *Cold Spring Harb Perspect Med* 2.

Mouw, J.K., Yui, Y., Damiano, L., Bainer, R.O., Lakins, J.N., Acerbi, I., Ou, G., Wijekoon, A.C., Levental, K.R., Gilbert, P.M., et al. (2014). Tissue mechanics modulate microRNA-dependent PTEN expression to regulate malignant progression. *Nat. Med.* 20, 360–367.

Nagarsheth, N., Wicha, M.S., and Zou, W. (2017). Chemokines in the cancer microenvironment and their relevance in cancer immunotherapy. *Nature Reviews Immunology* 17, 559–572.

Nguyen, D.X., Bos, P.D., and Massagué, J. (2009). Metastasis: from dissemination to organ-specific colonization. *Nature Reviews Cancer* 9, 274–284.

Nilsson, I., Bahram, F., Li, X., Gualandi, L., Koch, S., Jarvius, M., Söderberg, O., Anisimov, A., Kholová, I., Pytowski, B., et al. (2010). VEGF receptor 2/-3 heterodimers detected in situ by proximity ligation on angiogenic sprouts. *EMBO J* 29, 1377–1388.

Paget, S. (1889). The distribution of secondary growths in cancer of the breast. *The Lancet* 133, 571–573.

Paszek, M.J., Zahir, N., Johnson, K.R., Lakins, J.N., Rozenberg, G.I., Gefen, A., Reinhart-King, C.A., Margulies, S.S., Dembo, M., Boettiger, D., et al. (2005). Tensional homeostasis and the malignant phenotype. *Cancer Cell* 8, 241–254.

Patton, E.E., Widlund, H.R., Kutok, J.L., Kopani, K.R., Amatruda, J.F., Murphey, R.D., Berghmans, S., Mayhall, E.A., Traver, D., Fletcher, C.D.M., et al. (2005). BRAF Mutations Are Sufficient to Promote Nevi Formation and Cooperate with p53 in the Genesis of Melanoma. *Current Biology* *15*, 249–254.

dela Paz, N.G., Walshe, T.E., Leach, L.L., Saint-Geniez, M., and D’Amore, P.A. (2012). Role of shear-stress-induced VEGF expression in endothelial cell survival. *J. Cell. Sci.* *125*, 831–843.

Rodriguez-Vida, A., Hutson, T.E., Bellmunt, J., and Strijbos, M.H. (2017). New treatment options for metastatic renal cell carcinoma. *ESMO Open* *2*, e000185.

Rotow, J., and Bivona, T.G. (2017). Understanding and targeting resistance mechanisms in NSCLC. *Nature Reviews Cancer* *17*, 637–658.

Schlesinger, M., and Bendas, G. (2015). Contribution of very late antigen-4 (VLA-4) integrin to cancer progression and metastasis. *Cancer and Metastasis Reviews* *34*, 575–591.

Shibue, T., Brooks, M.W., Inan, M.F., Reinhardt, F., and Weinberg, R.A. (2012). The Outgrowth of Micrometastases Is Enabled by the Formation of Filopodium-like Protrusions. *Cancer Discovery* *2*, 706–721.

Simons, M., Gordon, E., and Claesson-Welsh, L. (2016). Mechanisms and regulation of endothelial VEGF receptor signalling. *Nature Reviews Molecular Cell Biology* *17*, 611–625.

Stacker, S.A., and Achen, M.G. (2013). The VEGF signaling pathway in cancer: the road ahead. *Chin J Cancer* *32*, 297–302.

Stoletov, K., Montel, V., Lester, R.D., Gonias, S.L., and Klemke, R. (2007). High-resolution imaging of the dynamic tumor cell–vascular interface in transparent zebrafish. *PNAS* *104*, 17406–17411.

Sugden, W.W., Meissner, R., Aegeerter-Wilmsen, T., Tsaryk, R., Leonard, E.V., Bussmann, J., Hamm, M.J., Herzog, W., Jin, Y., Jakobsson, L., et al. (2017). Endoglin controls blood vessel diameter through endothelial cell shape changes in response to haemodynamic cues. *Nature Cell Biology* *19*, 653–665.

T. Fong, T.A., Shawver, L.K., Sun, L., Tang, C., App, H., Powell, T.J., Kim, Y.H., Schreck, R., Wang, X., Risau, W., et al. (1999). SU5416 Is a Potent and Selective Inhibitor of the Vascular Endothelial Growth Factor Receptor (Flk-1/KDR) That Inhibits Tyrosine Kinase Catalysis, Tumor Vascularization, and Growth of Multiple Tumor Types. *99–106*.

Tomida, C., Yamagishi, N., Nagano, H., Uchida, T., Ohno, A., Hirasaka, K., Nikawa, T., and Teshima-Kondo (2017). Antiangiogenic agent sunitinib induces epithelial to mesenchymal transition and accelerate motility of colorectal cancer cells.

Valastyan, S., and Weinberg, R.A. (2011). Tumor Metastasis: Molecular Insights and Evolving Paradigms. *Cell* *147*, 275–292.

Welti, J.C., Powles, T., Foo, S., Gourlaouen, M., Preece, N., Foster, J., Frentzas, S., Bird, D., Sharpe, K., van Weverwijk, A., et al. (2012). Contrasting effects of sunitinib within in vivo models of metastasis. *Angiogenesis* *15*, 623–641.

White, R.M., Sessa, A., Burke, C., Bowman, T., LeBlanc, J., Ceol, C., Bourque, C., Dovey, M., Goessling, W., Burns, C.E., et al. (2008). Transparent Adult Zebrafish as a Tool for In Vivo Transplantation Analysis. *Cell Stem Cell* *2*, 183–189.

Wirtz, D., Konstantopoulos, K., and Searson, P.C. (2011). The physics of cancer: the role of physical interactions and mechanical forces in metastasis. *Nature Reviews Cancer* *11*, 512–522.

Young, E., Miele, L., Tucker, K.B., Huang, M., Wells, J., and Gu, J.-W. (2010). SU11248, A selective tyrosine kinases inhibitor suppresses breast tumor angiogenesis and growth via targeting both tumor vasculature and breast cancer cells. *Cancer Biology & Therapy* *10*, 703–711.

Younus, J., Verma, S., Franek, J., and Coakley, N. (2010). Sunitinib malate for gastrointestinal stromal tumour in imatinib mesylate–resistant patients: recommendations and evidence. *Current Oncology* *17*, 4.

FIGURE LEGENDS

Figure 1: Flow favors expression of gene program driving endothelial remodeling, including VEGFRs. **A** - Experimental setup: microfluidic experiment for RNA sequencing. **B** - Results from global Gene Ontology analysis on 'biological process', showing most significantly impacted GO class. **C** – Fold changes heatmap, based on GO class: Angiogenesis, showing significantly upregulated genes in flow condition compared to no flow. **D** – Western blot results validating of RNAseq. Results showing increase level of KDR and FLT4 expression at the protein level. **E** – Representative image of flow vs no flow immunofluorescence labelling against FLT1, KDR and FLT4 (green) with DAPI (blue). **F** – Quantification associated with D and E, showing increased expression and signal intensity of VEGFRs. **G** – Experimental setup of human patient's brain biopsies with or without brain metastasis. **H** – Low magnification image of representative blood vessels in the metastatic tissue after performing immuno-histochemistry against KDR. **I** – Quantification of the presence of KDR in blood vessels, split in 3 categories: high, low and no coloration. **J** – Representative image of the 3 categories: high, low and no presence of KDR. Values are mean +/- SD. p-value < 0,05: *, < 0,01: **, < 0,0001: ****.

Figure 2: Inhibition of VEGFRs with Sunitinib impairs endothelial remodeling *in vitro*. **A** – Immuno-labelling pictures showing the presence of KDR (white) at the site of endothelial remodeling (Assessed with PECAM enrichment (green) around tumor cell (red)). Z-projections and two z-projection from side and top view are shown. **B** - Experimental setup: microfluidic channel for endothelial remodeling assay. **C** – Quantification of the normalized number of transmigrating cells and remodeling activity. **D** – Representative images of all status: No transmigration, Transmigration without remodeling evidence, Transmigration with remodeling. **E** – Pie Chart showing experimental results summary with or without Sunitinib. Values are mean +/- SD. p-value < 0,001: ***, < 0,0001: ****.

Figure 3: Inhibition of VEGFRs with Sunitinib reduces endothelial remodeling in Zebrafish embryos. **A** – Experimental setup: zebrafish injection 3hpi (hours post-injection). **B** – Quantification of intravascular, remodeling and extravasated cells 3hpi. **C** – Representative image of the caudal plexus and associated correlative light and

electron microscopy results of tumor cell *a* and *b* (white squares on **C**) in Vehicle condition. **D** - Representative image of the caudal plexus and associated correlative light and electron microscopy results of tumor cell *c* and *d* (white squares on **D**) in Sunitinib condition. **E** – Representative zebrafish head z-projection showing tumor cell status in both conditions. **G** – Quantification of extravasated cells in the head of zebrafish embryos. Values are mean +/- SD. p-value < 0,05: *, <0,01: **, < 0,001: ***, < 0,0001: ****.

Figure 4: Inhibition of VEGFRs with Sunitinib impacts extravasation and subsequent growth in mouse models. **A** – Experimental setup: Impact of sunitinib on extravasation efficacy in the brain of mice. **B** – Representative images of both conditions: Vehicle and sunitinib feeding. **C** – 3d model reconstruction from B. **D** – Quantification of the ratio of extravasated cells in both conditions. **E** – Electron microscopy and related 2D segmentation of representative tumor cells in both conditions. Intravascular with endothelial remodeling in the case of vehicle (left). Intravascular in the case of sunitinib treated mice (right). **F** – Experimental setup: Impact of sunitinib on early metastatic outgrowth in the lungs. **G** – Representative images from bioluminescent imaging of the mice and focus on the dissected lungs at day 17. **H** – Bioluminescent signal quantification results at day 2 and day 17. Values are mean +/- SD. p-value < 0,05: *, < 0,001: ***.

SUPPLEMENTAL FIGURE LEGENDS

Figure S1: A – Fold changes heatmap, based on GO class: Cell Cycle, showing significantly impacted genes in flow condition compared to no flow. **B** – RTqPCR data confirming RNA sequencing results. Top graphic shows RTqPCR results alone. Bottom graphic shows the comparison between RTqPCR and RNAseq. **C** – Fold change of expression level (RNAseq) of the major sunitinib targets in flow vs no flow condition (numbers are adjusted p-values).

Figure S2: A – Experimental setup: Zebrafish injection 9hpi. **B** - Quantification of intravascular, remodeling and extravasated cells 9 hpi. **C** – Correlation between light and electron microscopy. Top panels show detailed view of the confocal acquisition with the targeted region of interest. Lower panels show low magnification of the same

region of interest and higher magnification of an extravasated tumor cell (dash line). **D** – Representative image of caudal plexus architecture 3 hours post-treatment with sunitinib vs vehicle. **E** - Quantification of the effect of sunitinib on vessel architecture. **F** – Blood flow perfusion profiles of the same embryos (from D) and quantification (from PIV analysis) of the blood flow velocity in the dorsal aorta of 5 embryos in both conditions.

STAR*METHODS

1. KEY RESOURCES TABLE

Not mandatory for most journals

2. CONTACT FOR REAGENT AND RESOURCE SHARING

Further information and requests for resources and reagents should be directed to and will be fulfilled by the Lead Contact, Jacky G. Goetz (jacky.goetz@inserm.fr).

3. EXPERIMENTAL MODEL AND SUBJECT DETAILS

Human Umbilical Vein Endothelial Cells (HUVECs).

Primary cells from poly-donor, commercial vials (PromoCell) amplified before used at P4 for all experiments. Culture condition : 37°C/5% CO₂. ECGM with Supplemental mix (PromoCell) and 1% Penstrep.

D2A1 cells (CVCL_0190). Mouse mammary carcinoma (BALB/c female).

Major information on the D2A1 cell line can be found following this link: http://web.expasy.org/cellosaurus/CVCL_0190. Culture conditions: 37°C/5% CO₂. DMEM HG with 5% NBCS, 5% FBS, 1% NEAA-MEM, 1% Penstrep. Authentication: Injection in the nipple of mammary gland of BALB/c mice lead to mammary tumor. Cells do not show contamination to mycoplasma.

JIMT-1 BR3 cells (CVCL_2077). Human ductal breast carcinoma (Female) highly metastatic in the brain.

Major information on the JIMT-1 cell line can be found following this link: http://web.expasy.org/cellosaurus/CVCL_2077. Culture condition: 37°C/5% CO₂. DMEM HG with 10% FBS, 1% Penstrep. Authentication: Intracardiac injection in nude mice (NU/NU) lead to cerebral metastasis. Cells do not show contamination to mycoplasma.

Zebrafish embryos

Tg(fli1a:EGFP) Zebrafish (*Danio rerio*) embryos from a Golden background. Embryos were maintained at 28° in Danieu 0.3X medium (see next section), supplemented

with 1-Phenyl-2-thiourea (Sigma-Aldrich) after 24 hours post fertilization (hpf). For all Zebrafish experiments, the offspring of one single cross was selected, based on anatomical/developmental good health. Embryos were split randomly between experimental groups. All injection experiments were carried at 48 hpf and imaged between 48 hpf and 72 hpf.

Mice

BALB/C 8-10 weeks old female mice (Charles River, France) were used in all the experiments. Mice were housed at 22 C and have access to water and food at libitum. Appropriate enrichment (sterile pulp paper and coarsely litter) was provided. Physical condition of mice was monitored daily. All work on animals has been carried out in accordance with the French Animal Protection Act after approval by the french ethics committee (CREMIAS). All efforts were made to minimize animal suffering and to reduce the number of animals used.

4. METHODS DETAILS

Cell culture

D2A1 were provided by Robert A. Weinberg (MIT). Cells stably expressing LifeAct-TdTomato or Luciferase were obtained using lentiviral transfection. Cells were grown as previously described (Shibue et al., 2012), in DMEM with 4.5 g/l glucose (Dutscher) supplemented with 5% FBS, 5% NBCS, 1% NEAA and 1% penicillin-streptomycin (Gibco). Jimt-1Br3 cells were provided by Frank Winkler (DKFZ). Cells stably expressing TdTomato were culture in DMEM with 4,5 g/l glucose (Dutscher) supplemented with 10% FBS and 1% penicillin-streptomycin (Gibco). Human Umbilical Vein Endothelial Cells (HUVEC) (PromoCell) were grown in ECGM (PromoCell) supplemented with supplemental mix (PromoCell C-39215) and 1% penicillin-streptomycin (Gibco). To maximize the reproducibility of our experiments, we always used these cells at 4th passage in the microfluidic channels.

Zebrafish handling and sunitinib treatment

Tg(fli1a:EGFP) Zebrafish (*Danio rerio*) embryos were used in the experiments. Embryos were maintained in Danieau 0.3X medium (17,4 mM NaCl, 0,2 mM KCl, 0,1 mM MgSO₄, 0,2 mM Ca(NO₃)₂) buffered with HEPES 0,15 mM (pH = 7.6),

supplemented with 200 μ M of 1-Phenyl-2-thiourea (Sigma-Aldrich) to inhibit the melanogenesis, as previously described (Goetz et al., 2014). Sunitinib (Sigma-Aldrich) was added in the breeding water of the embryos directly after injection of tumor cells at the given concentration of 2 μ M or 5 μ M vs vehicle (DMSO).

Control experiments for Sunitinib effect on zebrafish embryos 48 hpf

5 μ M sunitinib treatment was tested for its potential impact on vascular architecture and/or on blood flow pattern in the caudal region. After 3 hours of treatment (sunitinib or vehicle, n=8 per conditions), we performed confocal microscopy (SP5 –Leica) and manually analyzed the conservation of the distance between intersegmental vessels and the number of vascular branching in the caudal veins. Also, we performed fast recording transmitted light imaging to applied our previously described PIV (Particule Image Velocimetry) protocol to measure the blood flow intensity in the dorsal aorta (Follain et al., 2018). Using the stereotypicity of the caudal plexus, we averaged the blood flow profile of 5 embryos in the dorsal aorta under ISV 8, 4 and 1.

Intravascular injection and imaging of CTCs in the zebrafish embryo

48 hour post-fertilization (hpf) *Tg(Fl1a:EGFP)* embryos were mounted in 0.8% low melting point agarose pad containing 650 μ M of tricain (ethyl-3-aminobenzoate-methanesulfonate) to immobilize the embryos. D2A1 LifeAct-TdTomato cells were injected with a Nanoject microinjector 2 (Drummond) and microforged glass capillaries (25 to 30 μ m inner diameter) filled with mineral oil (Sigma). 18nL of a cell suspension at 100.10⁶ cells per ml were injected in the duct of Cuvier of the embryos under the M205 FA stereomicroscope (Leica).

For caudal plexus, confocal imaging was performed with an inverted TCS SP5 confocal microscope with a 20x/0,75 (Leica). The caudal plexus region (around 50 μ m width) was imaged with a z-step of less than 1.5 μ m for at least 20 embryos per conditions from 3 independent experiments. For zebrafish head imaging, a multiphoton microscope Bruker Ultima Investigator equipped with a 25x/1.10 water immersion (Nikon) and an Insight X3 pulsed laser (Spectra Physics) was used. Cell number and situations was manually characterized (Intravascular, ongoing endothelial remodeling/pocketing, extravascular) using z-projections and orthogonal views in ImageJ.

Correlative Light and Electron Microscopy was performed to describe ultra structural characteristics of CTCs and the endothelium in the zebrafish embryo. Chosen embryos of both condition (Vehicle and Sunitinib treated) were imaged using confocal microscopy between 3 to 4 hpi. Just after imaging, they were chemically fixed and processed for EM (see dedicated section “EM preparation”).

Sunitinib treatment for mouse experiment

Mice were treated with sunitinib or control vehicle by feeding for 5 days, starting one day prior to the intracardiac or tail vein injection. Sunitinib was diluted in DMSO (vehicle) at 20 mg/ml, before 1/4 dilution in 5% Carboxy-Methyl-Cellulose (CMC) solution for gavage. Final volume around 200 μ l was calculating for each mice to reach 40 μ g sunitinib per gram of mouse daily.

Extravasation efficiency in the mouse brain

To favor the extravasation event in the brain, we performed intracardiac injection of 1.10^6 JIMT-1 Td-Tomato cells in 100 μ l of PBS, as previously described (Kienast et al., 2010). For comparing the effect of vessels remodeling on metastasis formation, mice were pretreated with Sunitinib (40 μ g/g/day) by oral gavage, starting one day before cells injection for 5 days. A second group of control mice were treated with DMSO (vehicle) the same way. Four days after cancer cells injection, mice were fixed by intracardiac injection of 4% Paraformaldehyde in PBS solution as previously described (Karreman et al., 2016b, 2016a). The brains were extracted and immersed in 4% Paraformaldehyde (Electron Microscopy Science) overnight at 4°C. The brains were cut in half along the sagittal sinus and embedded in 2% agarose gel. 100 μ m thick sagittal vibratome (Leica VT1000S) sections were collected and indexed in 24 well plates. Brain vibratome slices were then permeabilized with 1% Triton X100 (Sigma) in PBS overnight and stained with primary antibody: Rat anti-mouse CD31 (BD Pharmingen) and secondary antibody: Goat anti-Rat coupled to Alexa488 fluorophore (Thermo Fisher). Finally, brain slices were mounted between coverslips in a drop of hardening mounting reagent (Permafluor - Thermo Fisher). Confocal imaging was performed with an inverted TCS SP5 microscope (Leica) with a 40x/1.25 oil immersion objective (Leica). Cell situation (intravasacular or extravasacular) was determined based on the CD31 labelling and 3d rendering were performed using IMARIS software.

The vibratome brain slices were transitorily mounted on microscope glass slide in PBS. Cells of interest were imaged with a multiphoton microscope Bruker Ultima Investigator equipped with a 25x/1.10 water immersion (Nikon) and an Insight X3 pulsed laser (Spectra Physics). To retrieve the position of the cell of interest during the electron microscopy process we performed Near InfraRed Branding (NIRB) as previously described (Bishop et al., 2011; Karreman et al., 2014). NIRB was performed around the cells of interest, and thanks to the autofluorescence of the NIRB mark, a 1mm² piece of tissue containing the region of interest has been precisely biopsied under a fluorescent macroscope (Leica M205 FA) to be compatible for electron microscopy preparation.

EM preparation and Correlation between light and electron microscopy

The samples (Fish tails after confocal microscopy or mouse brain after NIRB) have been post fixed in a solution of 2,5% glutaraldehyde and 2% paraformaldehyde in 0.1 M Cacodylate buffer at 4°C overnight. Samples were rinsed in 0.1M Cacodylate buffer for 2x5min and post-fixed using 1% OsO₄ in 0.1 M Cacodylate buffer, for 1h at room temperature. Then, samples were rinsed for 3x5min in 0.1M Cacodylate buffer. Followed by washing 2x5min in pure water. Then, secondary post-fixed with 4% water solution of uranyl acetate, 1h at room temperature. Followed by 5 min wash in pure water, the samples were stepwise dehydrated in Ethanol (50% 3X5 min, 70% 3x10, 90% 3x10 and 100% 3x10) and infiltrated in a graded series of Epon (Ethanol abs/Epon 3/1, 1/1, 1/3, each 30min). Samples were left in absolute Epon (EmBed812 - EMS) overnight. Then, samples were placed in a fresh absolute Epon for 1h and polymerized (flat embedded) at 60°C for 24-48h. Once polymerized, most surrounding Epon was cut off using razorblade and samples were mounted on empty Epon blocks (samples flat at the surface of the blocks) and left at 60 °C for 24h-48h.

To do the correlation in 3d, semi thin sections (500nm) were obtained using glass knife in ultramicrotome LEICA UCT. Sections were placed on slide, stained with 1% borax Toluidine blue solution and checked out in the optical microscope. For mouse brain, once the branding square was localized, resin block was retrimmed and used in ultra thin sectioning. For zebrafish embryos, we applied the same protocol and used anatomical landmark to retrieve the ROI (Dorsal aorta, tumor cells...).

Ultra thin sections (100nm) were serially sectioned using ultramicrotome (Leica Ultracut UCT), collected on formvar-coated slot grids and stained with 4% water

solution of uranyl acetate for 5min and lead citrate for 3min. Ultra-thin sections were imaged with a CM120 transmission electron microscope (Philips Biotwin) operating at 120 kV. Images were recorded with Veleta 2k x 2k (Olympus-SIS) camera using iTEM software embedded and the ROI approached by serial sectioning.

Metastatic growth in the lung (biolumiscence imaging)

Subconfluent D2A1 cells expressing luciferase (*Photinus pyralis*) were washed with PBS (Gibco), detached using a 0.25% trypsin-0.02% EDTA solution (Gibco), filtered (30µm cup filcons - BD), washed in DMEM containing 10% fetal calf serum, resuspended in serum-free media and kept on ice until injection. Viability was determined by trypan blue exclusion and was always more than 90%. Cells (2 x 10⁵) in 100 µl of serum-free DMEM were injected per mouse through the lateral tail vein by using a 25-gauge needle (n = 5 mice per group). In vivo imaging of mice lungs was immediately performed after tumor cells inoculation to establish initial lung seeding. Subsequent imaging points at 1, 3, 7, 10 and 17 days after tumor cell injection were monitored. To do so, five min after intraperitoneal injection of D-luciferin solution (150 mg/kg) to the isofluorane-anesthetized (Zoetis) mice, the bioluminescence image was acquired with an IVIS Lumina III (Perkin Elmer) imaging system and then analyzed using the Living Image software (Perkin Elmer). The rate of total light emission of the lung metastatic area was calculated and expressed as numbers of photons emitted per second.

Microfluidic experiments

For endothelial remodeling experiments *in vitro*, two µ-slides I^{0.4} Luer (IBIDI) coated with fibronectin from bovine plasma at 10µg/ml (Sigma F-1141) were used in parallel for each experiment. HUVEC cells were seeded at 80 000 cells per channel. Medium was changed twice a day for 2 or 3 days, before perfusing the channels under a flow of 400µm/sec using REGLO Digital MS-2/12 peristaltic pump (Ismatec) and Tygon tubing (IDEX). Sunitinib treatment was added at a concentration of 0,1µM in flow. At confluence, D2A1 LifeAct-TdTomato cells were added at a concentration of 200 000 cells/ml for 10 min. Then, floating tumor cells were washed using fresh medium and the channels were incubated for 16 h with flow. Position of the tumor cells and presence of endothelial remodeling around tumor cells relative to the HUVEC

monolayer were determined using the piezzo stage of the confocal microscope after fixation and Immunofluorescent staining (see *next section*).

Immunofluorescent staining in the microfluidic channels

Cells were fixed using 4% PFA (Electronic Microscopy Sciences), permeabilized with 0.2% Triton-X100 (Sigma) and quenched with 2mg/ml NaBH₄ (Sigma) 10 min at room temperature before using the following primary antibodies: mouse anti-human CD31 monoclonal primary antibody (MEM-5, Invitrogen), FLT1 (ab9540 - abcam), KDR (D5B1 – Cell Signaling), FLT4 (ab51874 - abcam), PECAM (MEM-05 - Thermo). Following secondary antibodies were used: goat anti-mouse/rat/rabbit coupled with Alexa Fluor 488, Cy3, Alexa 555, Cy5 or Alexa647 (Invitrogen). Cells were mounted using Vectashield (Vector Laboratories).

RNA sequencing

3 independent couples (flow and no flow) of HUVEC samples were isolated from IBIDI μ -slides $1^{0,4}$ Luer (IBIDI) using Tri-reagent (MRC) 100 μ l of Tri-reagent was added directly in one side of the channel and aspire in the other side 5 times. This was followed by chloroform extraction and alcohol washing. Total cDNA was obtained using Thermo Fisher kit (SuperScriptTM VILOTM Master mix).

RNA integrity was assessed with the Agilent total RNA Pico Kit on a 2100 Bioanalyzer instrument (Agilent Technologies, Paolo Alto, USA). The construction of libraries was done with the "SMARTer[®] Stranded Total RNA-Seq Kit v2 - Pico Input Mammalian" (TaKaRa Bio USA, Inc., Mountain View, CA, USA) with a final multiplexing of 12 libraries according to the manufacturer's instructions. The library pool was denatured according to the Illumina protocol "Denature and Dilute Libraries Guide" and then deposited at a concentration of 1.3 pM to be sequenced on the NextSeq 500 (Illumina Inc., San Diego, CA, USA).

The transcriptome data set, composed of sequencing reads, was generated by an Illumina NextSeq instrument. The objective is to identify genes that are differentially expressed between two experimental conditions: *flow* and *no flow*. First, the data were mapped to the human genome/transcriptome (hg19) using the hisat2 software (Kim et al., 2015), a fast and sensitive alignment program. The total reads mapped were finally available in BAM format for raw read counts extraction. Next, read counts were found by the htseq-count tool of the Python package HTSeq (Anders et al., 2015) with default

parameters to generate an abundant matrix. Then, differential analyses were performed by the DESEQ2 (Love et al., 2014) package of the Bioconductor framework. Up-regulated and down-regulated genes were selected based on the adjusted p-value cutoff 10%. Finally, Gene Ontology Consortium (<http://www.geneontology.org/>) platform was used for data analysis and heatmaps creation. The heatmaps were formatted using IGOR software.

qPCR validation

3 to 7 independent couples (flow and no flow) of HUVEC samples were isolated from IBIDI μ -slides I^{0,4} (Luer Family) using Tri-reagent (MRC) followed by chloroform extraction and alcohol washing. Total cDNA was obtained using ThermoFisher kit (SuperScriptTM VILOTM Master mix). RT qPCR reactions were made using either TaqMan master mix (ThermoFisher - 4444557) or SYBR green master mix (ThermoFisher – A25742) in Applied Biosystem qPCR machine (QuantStudioTM 3 - ThermoFisher). See next table of qPCR primer sequences for Flt1, Kdr, Flt4, Notch1, Lama4 (lab designed). For Gapdh, a commercial TaqMan probe was used (ThermoFisher - 4333764F). Amplification results were normalized using Gapdh level and double Δ cT method.

Targets	Primer sequences
h Flt1 fwd	CCA GCA GCG AAA GCT TTG CG
h Flt1 rev	CTC CTT GTA GAA ACC GTC AG
h Kdr fwd	ATG ACA TTT TGA TCA TGG AGC
h Kdr rev	CCC AGA TGC CGT GCA TGA G
h Flt4 fwr	TGC AAG AGG AAG AGG AGG TCT
h Flt4 rev	CAG GCT TGG CGG GCT GTC C
h Notch1 fwd	CAG GAC GGC TGC GGC TCC TAC
h Notch1 rev	CCG CCG TTC TTG CAG GGC GAG
h Lama4 fwr	ACC TCC TCA ATC AAG CCA GA
h Lama4 rev	TCA GCC ACT GCT TCA TCA CT

Western blotting

Extracts corresponding to similar cell numbers were loaded on 4-20% polyacrylamide gels (Biorad) and run under denaturing conditions. The following primary antibodies were used: FLT1 (ab9540 - abcam), KDR (D5B1 – Cell Signaling), FLT4 (ab51874 - abcam), α -Tubulin (DM1A - Calbiochem). HRP-conjugated secondary antibodies were

used with ECL (GE Healthcare) for reading using the ChemiDoc XRS (Biorad). Intensities were normalized over α -Tubulin levels.

Immuno-histochemistry on human brain

Formalin-fixed, paraffin-embedded (FFPE) tumor samples from 19 patients with cerebral metastasis (10) or temporal cortical specimen without relevant neuropathological findings were obtained from one center in Germany. Diagnosis was based on current classification schemes. Tissue sample collection, data collection, and use were done in accordance with local ethics regulations and approval. FFPE samples were cut at a thickness of 3 μ m and immunohistochemically stained with a primary antibody to VEGFR2 (Santa Cruz, C-1158:sc504, 1:400) using an automated Ventana HX IHC system (Ventana-Roche Medical systems, Tucson, AZ, USA) following the manufacturer's instructions. Diaminobenzidine (Sigma) was used as chromogen.

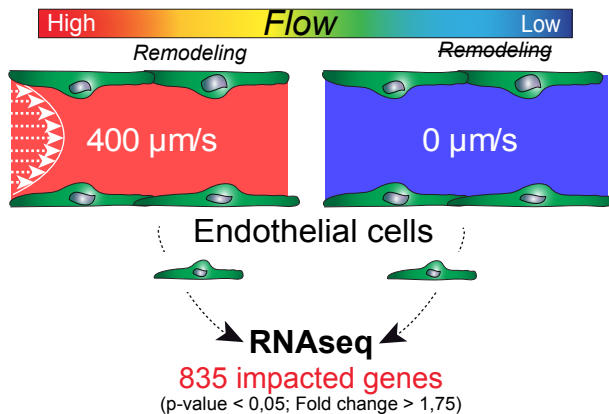
5. QUANTIFICATION AND STATISTICAL ANALYSIS

Statistical analysis of the results obtained during Zebrafish, Mice and microfluidic experiments were performed using the GraphPad Prism program version 5.04. The Shapiro-Wilk normality test was used to confirm the normality of the data. The statistical difference of Gaussian data sets was analyzed using the Student unpaired two-tailed t test, with Welch's correction in case of unequal variances. For data not following a Gaussian distribution, ANOVA multiple comparisons test or the Mann-Whitney test were used. For qualitative data, the Fisher test was used. Illustrations of these statistical analyses are displayed as the mean +/- standard deviation (SD). p-values smaller than 0.05 were considered as significant. *, p<0.05, **, p < 0.01, ***, p < 0.001, ****, p < 0.0001.

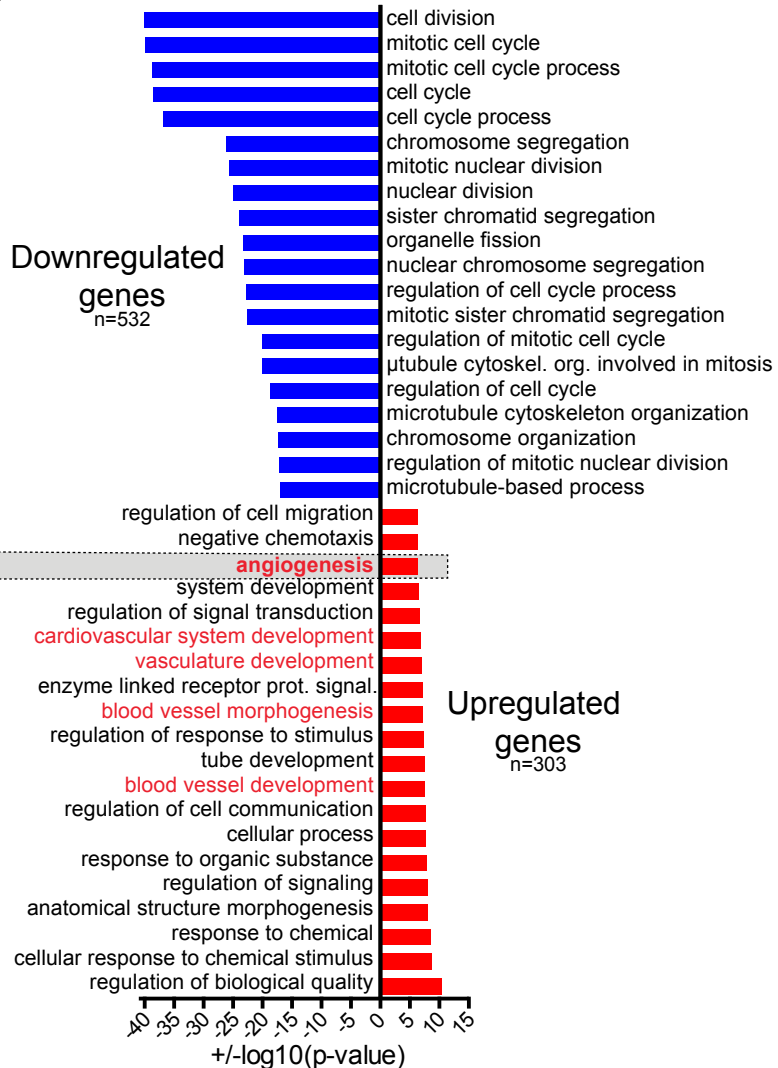
6. DATA AND SOFTWARE AVAILABILITY

For most of the analysis: GraphPad V5.04 to V6, PRISM - commercial dedicated software for statistical analysis. Confocal image analysis and rendering were performed using FIJI and Imaris (Bitplane) software. Heatmap rendering from RNAseq data was done in IgorPro. Final figures rendering was done in Adobe Illustrator.

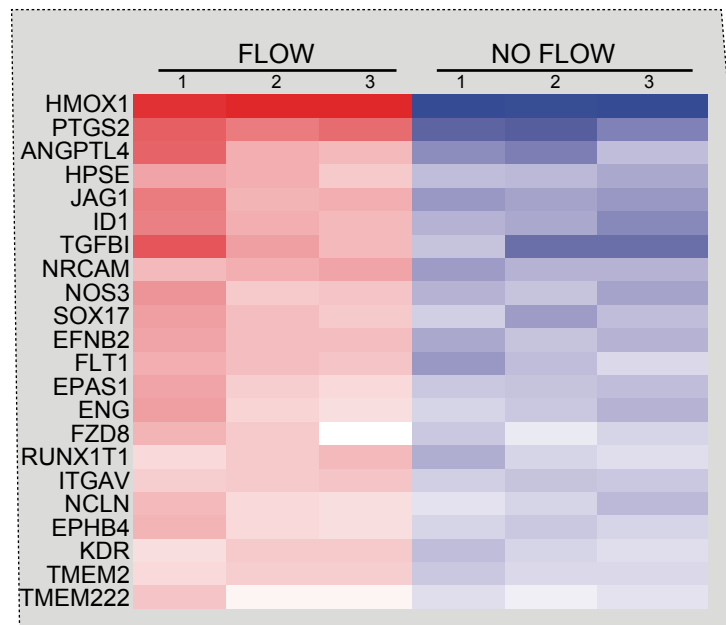
A B



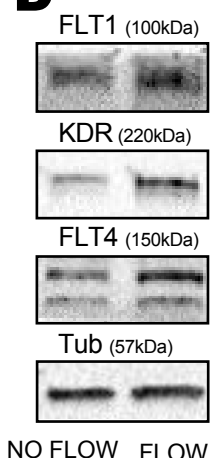
B



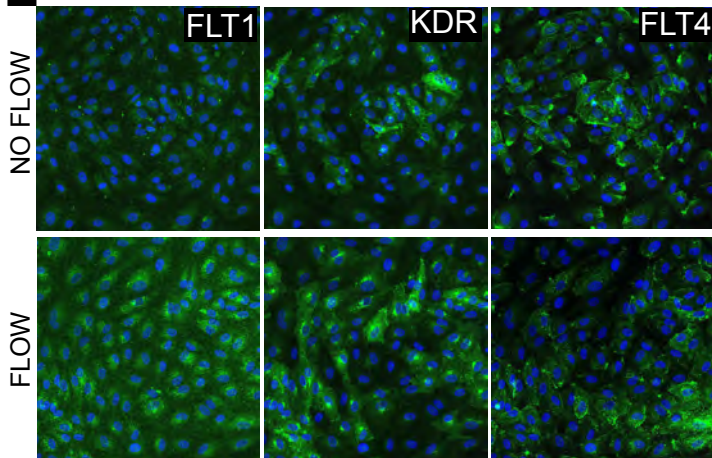
C



D



E



F

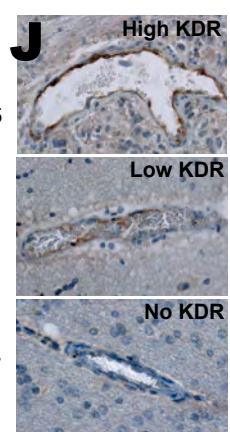
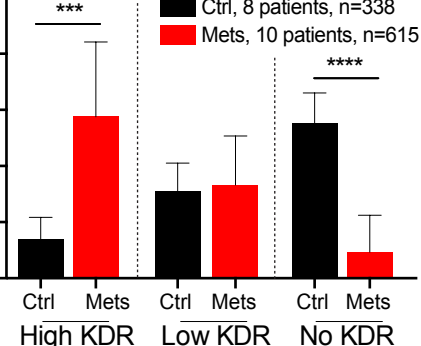
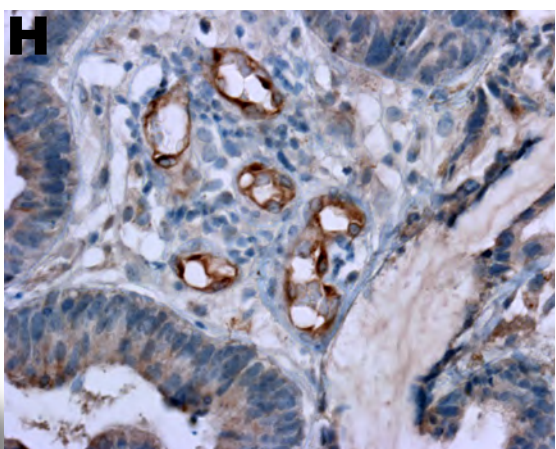
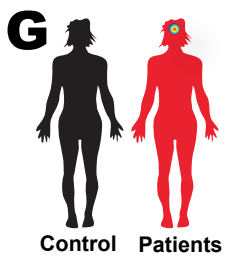
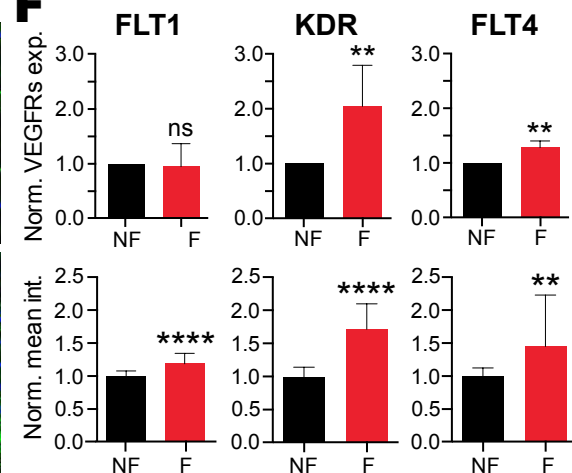
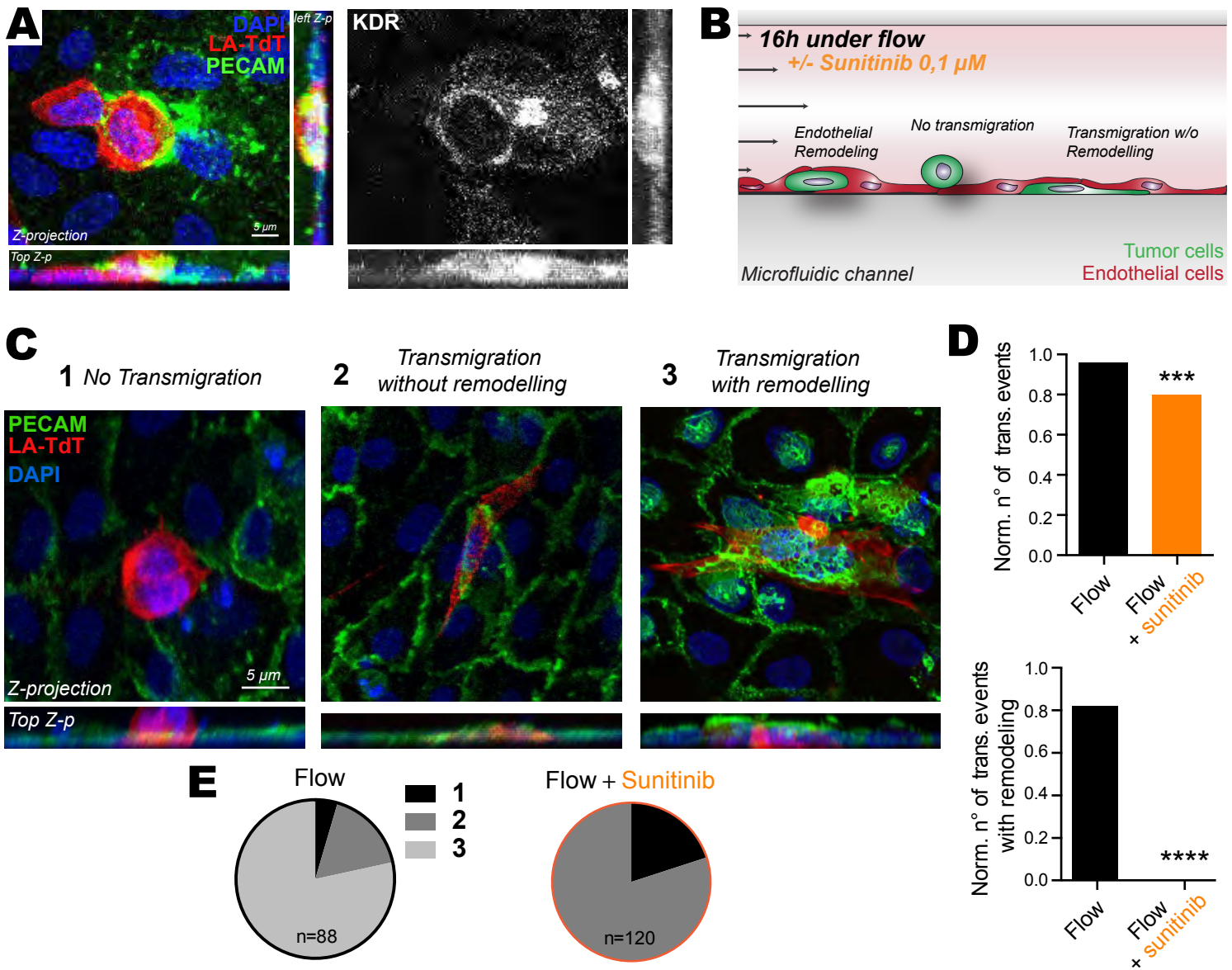
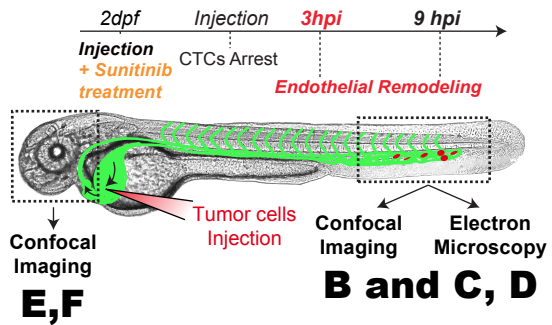
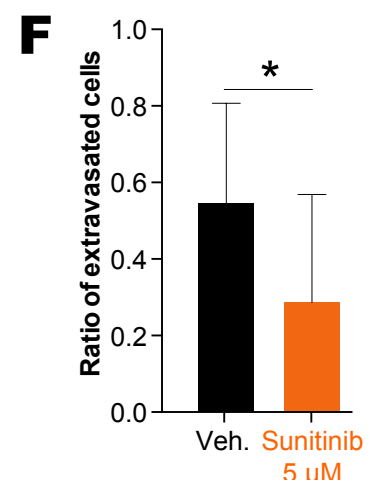
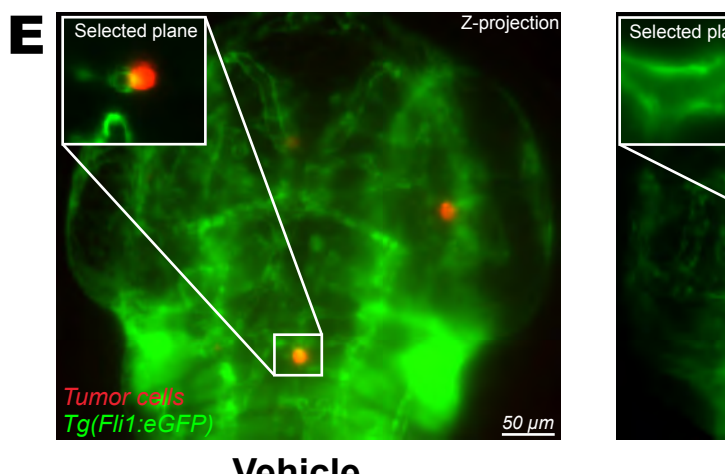
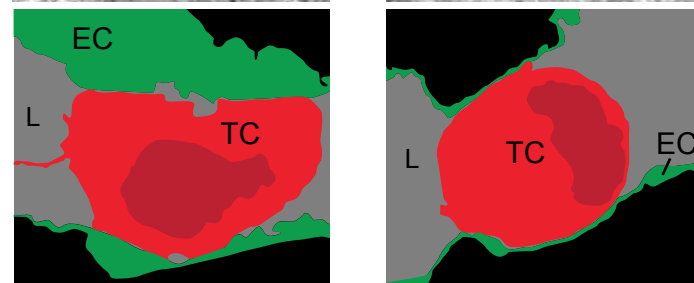
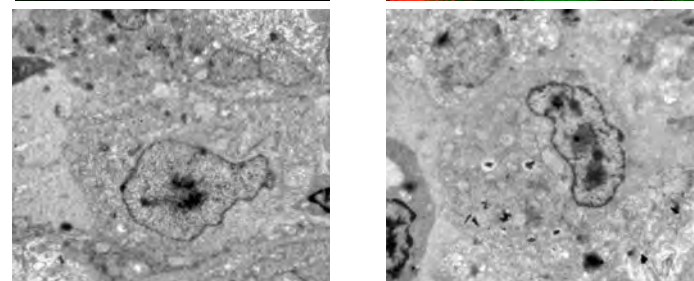
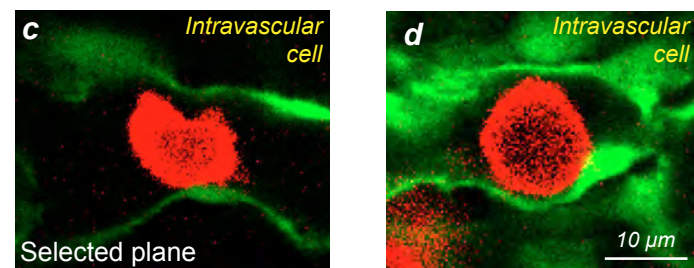
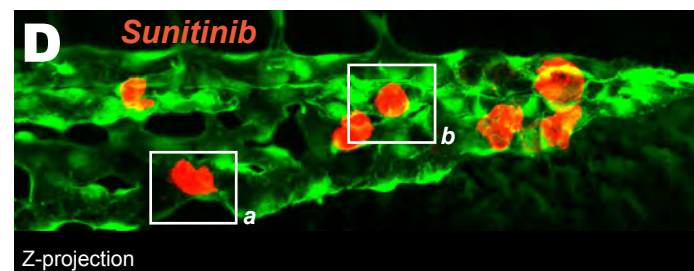
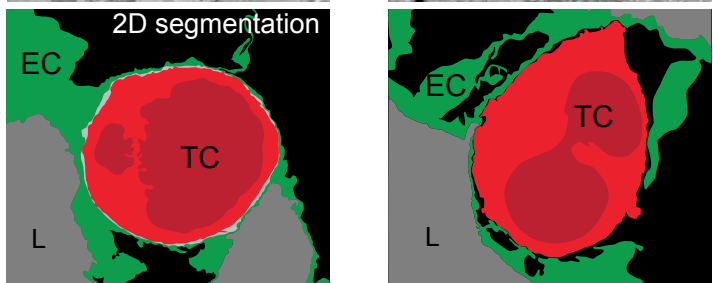
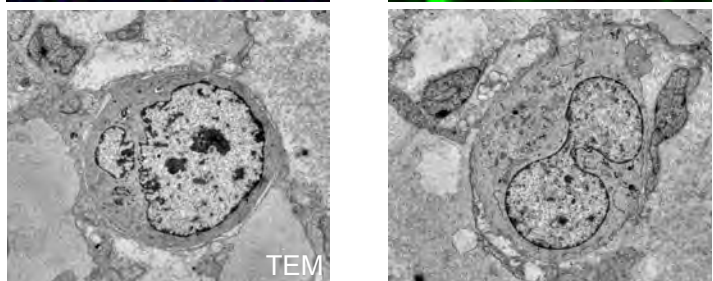
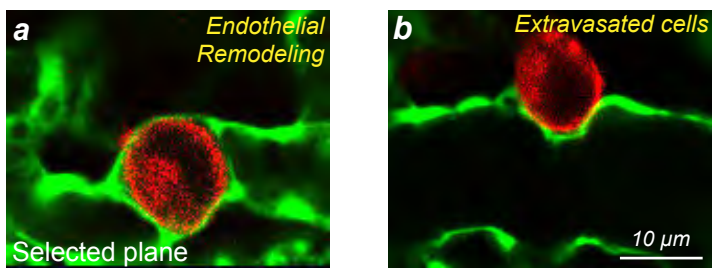
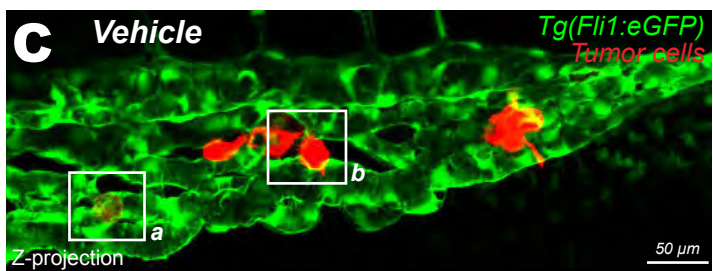
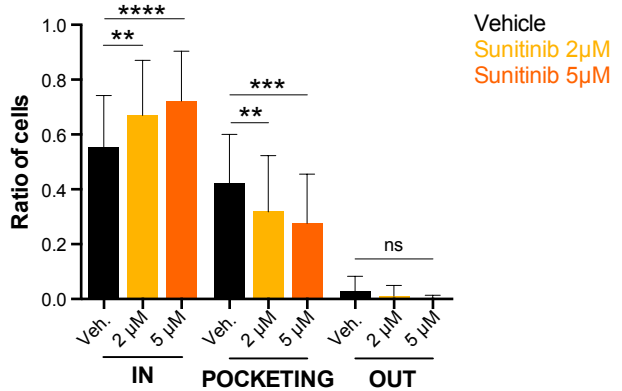
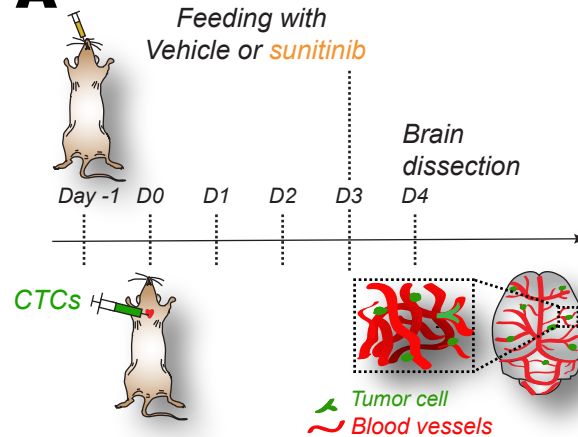
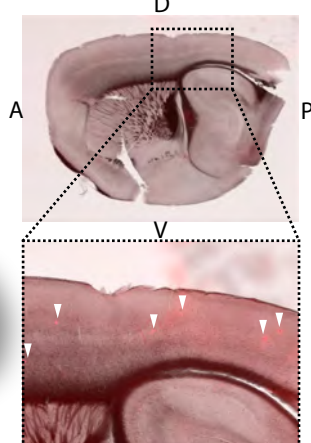
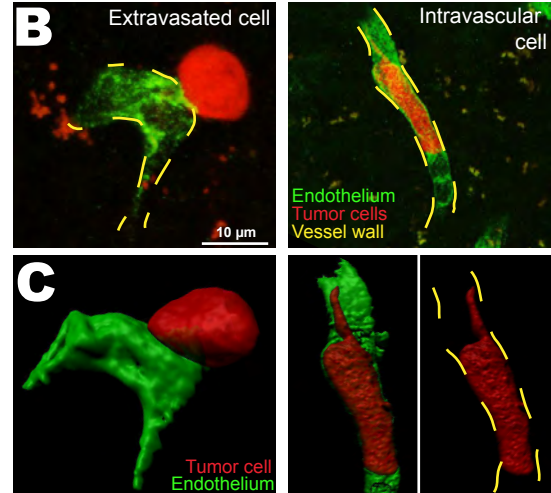
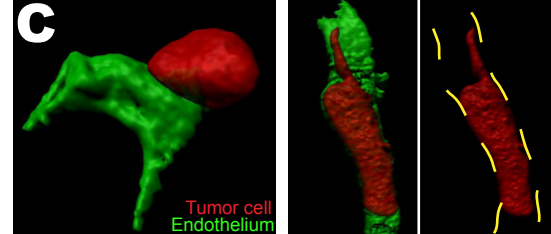
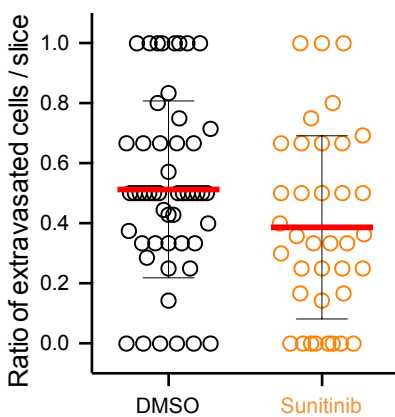
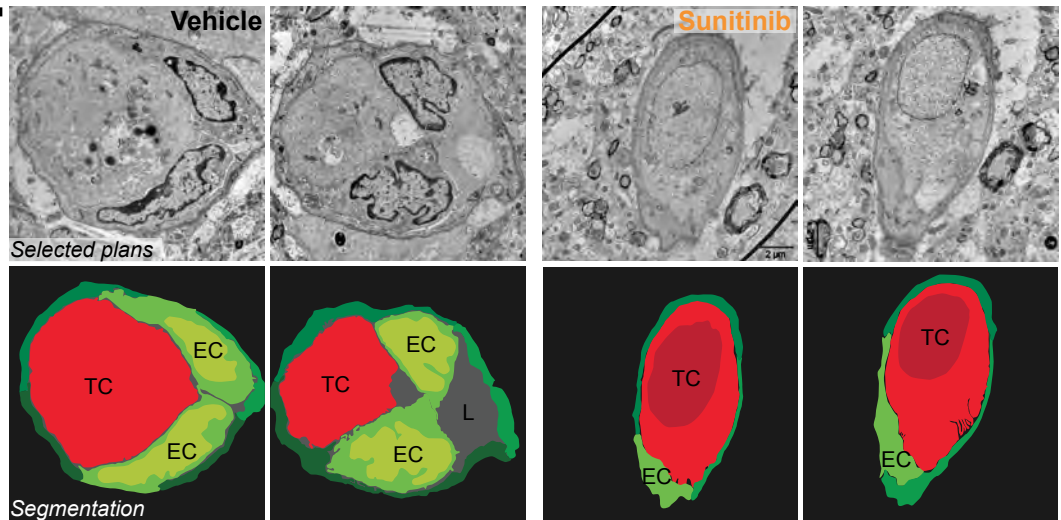
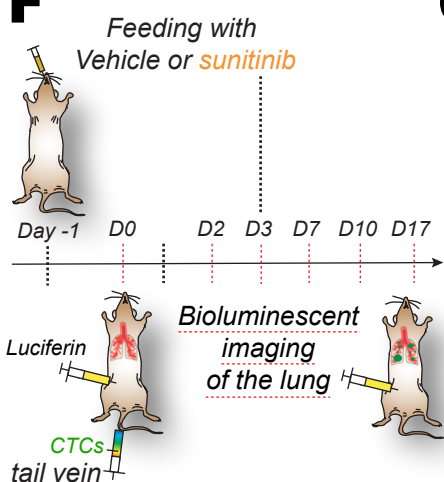
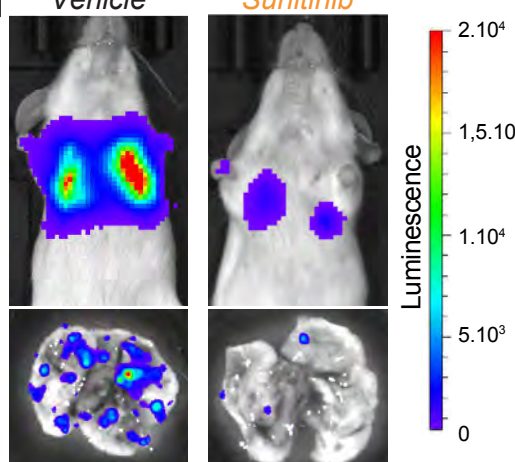
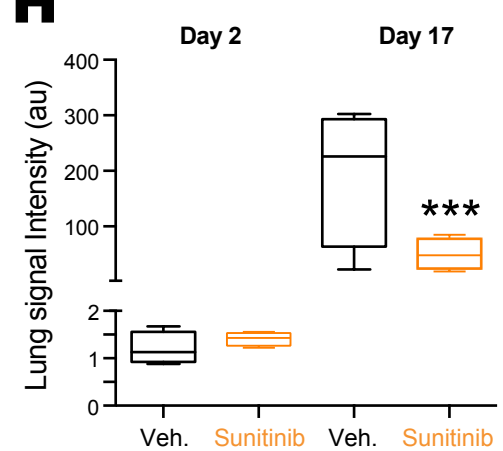


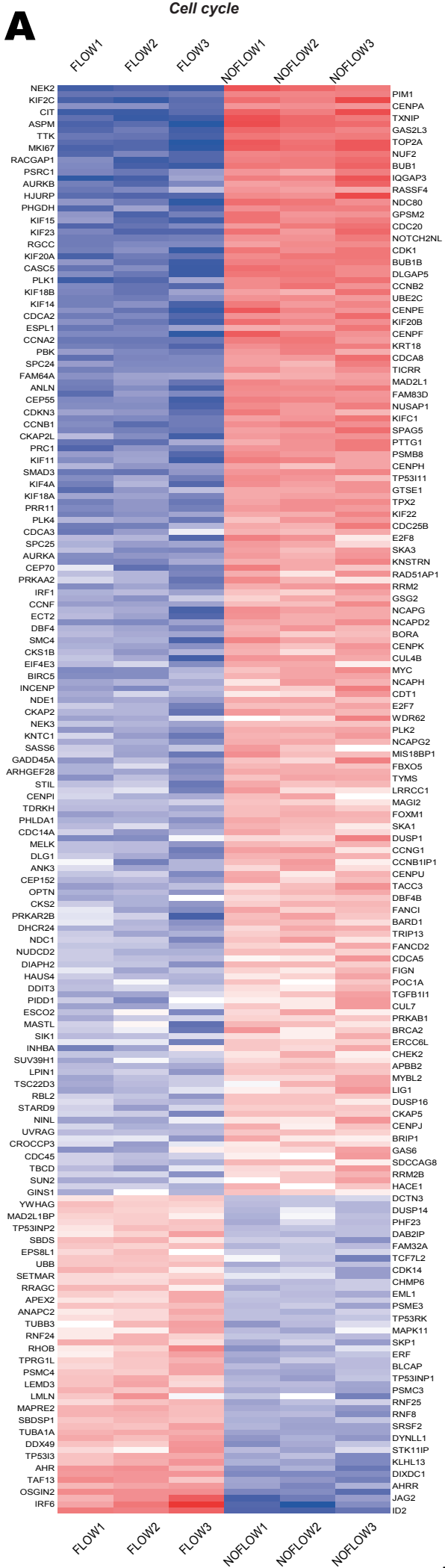
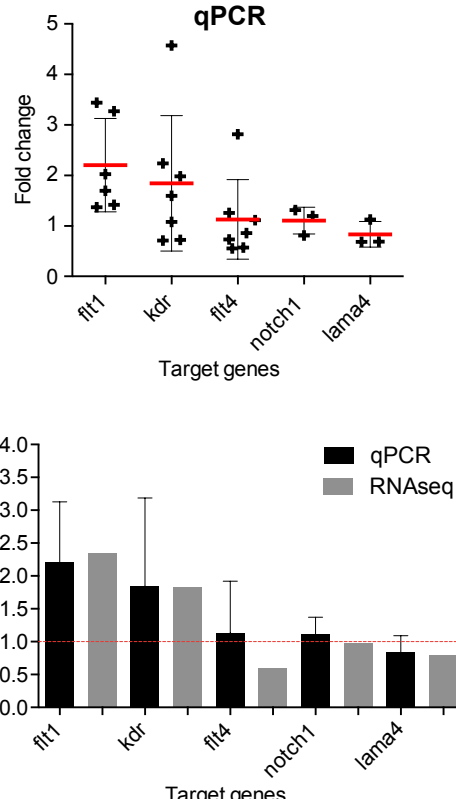
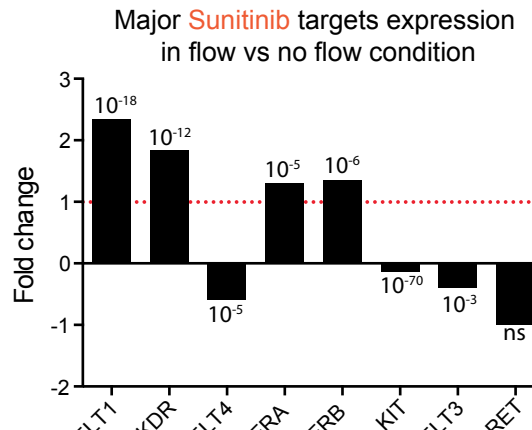
Figure 1_Follain et al.

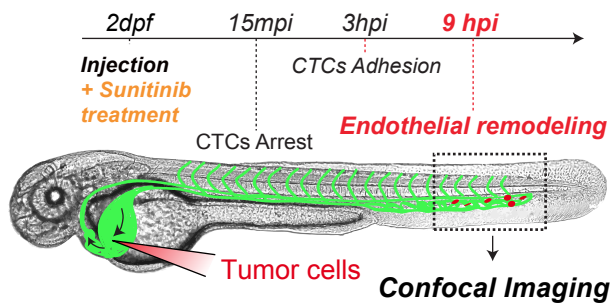
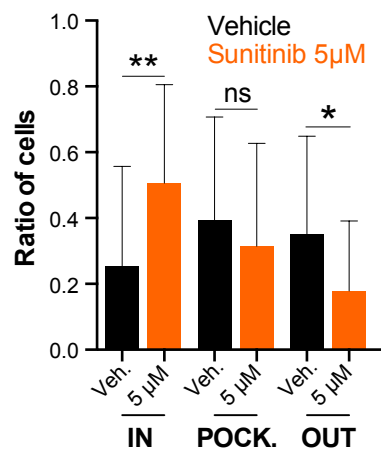
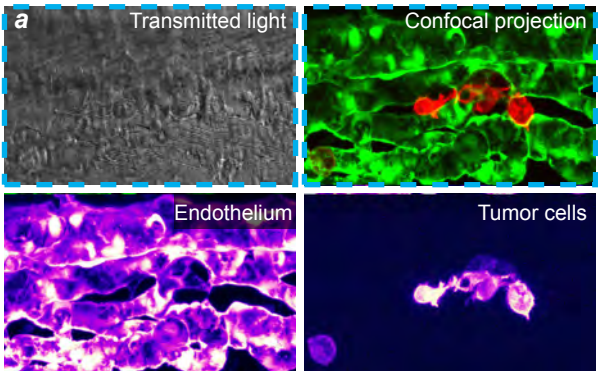
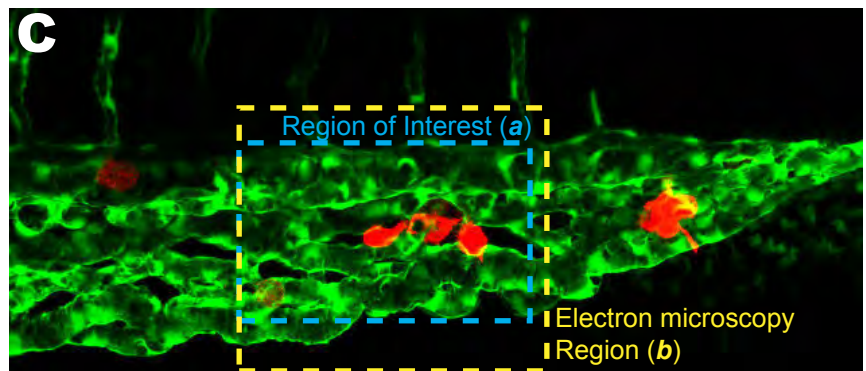
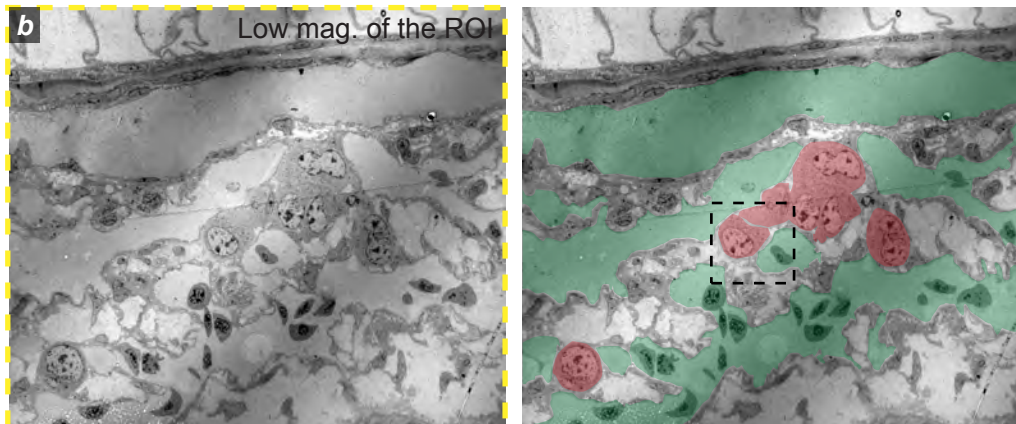


Figure_2_VEGF

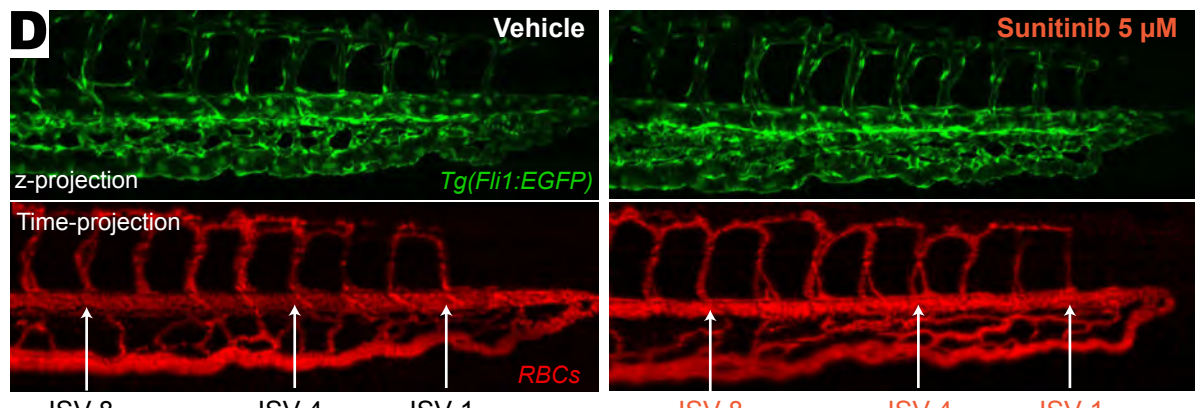
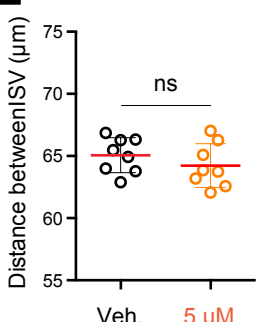
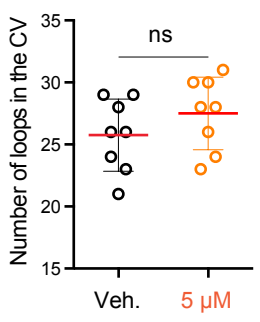
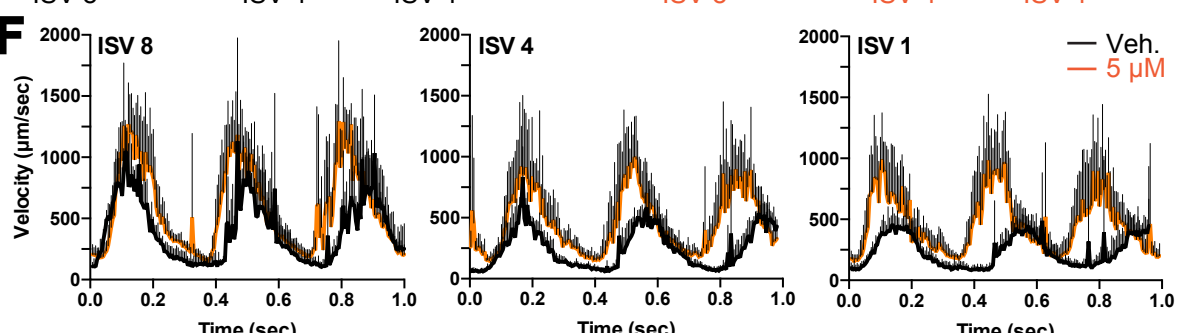
A**B****Figure_3_VEGF**

A**Vibratome sections****B****C****D****E****F****G****H****Figure_4_VEGF**

A**B****C****Figure_S1_VEGF**

A**B****C****b**

High mag. of the ROI

D**E****F****Figure_S2_VEGF**

COLLABORATIVE WORKS

During my PhD, we have been working on several collaborative studies either related with my main scientific project or to the methodology that we developed using zebrafish embryos. As they are part of my thesis work, I quickly present these works, their link to the main project and their major outputs in this section. I added all these articles/manuscripts in the [annex](#) section.

STUDY (TUMOR) EXTRACELLULAR VESICLES *IN VIVO*

Extracellular vesicles (EVs) are produced by all kind of cells and can be found in all body fluids. EVs consist on a lipid bilayer covered with transmembrane proteins and they carry cytoplasmic molecules such as proteins, RNAs and metabolites. They are important actors in distance cell-cell communication (Raposo and Stoorvogel, 2013; Tkach and Théry, 2016), thanks to their small size (50-150 nm in diameter) that eases them to reach blood and lymphatic vessels and to spread systemically. Interestingly, cancer cells are known to secrete a lot of EVs, that are enriched in pro-tumoral factors (Hyenne and Goetz, 2017). Indeed, they can transform stromal cells and stroma to tumor associated cells (Gu et al., 2012; Chow et al., 2014) and tumor microenvironment (Paggetti et al., 2015). Many studies demonstrated the role of EVs in tumor growth (Kanada et al., 2016) and on metastatic dissemination thanks to their systemic spreading (Peinado et al., 2012).

In vivo, very few is known about how EVs circulate, how they get internalized by cells, which cells undergo this uptake and how biological signaling occurs. One major limitation in the field is the ability to track such small particles *in vivo*. This drastically impairs the conclusion about their specific contribution in the metastatic cascade, especially compared to other circulating factors.

In collaboration with the group of G. Van Niel (M. Curie Institute), we worked on 1- Tracking EVs *in vivo*, using the zebrafish embryo as a model system. 2- Studying the role of tumor EVs in metastatic initiation. In our team, I participated to this project that was led by V. Hyenne.

Verweij and colleagues (Van Niel's lab) developed transgenic zebrafish embryos expressing the construct CD63:pHluorin. CD63 is a known marker for exosome (Escola et al., 1998) and pHluorin is a pH-sensitive fluorophore that is remaining in a dark state in acidic compartment but is emitting in extracellular space (Miesenböck et al., 1998). Thus, their system allowed to track EVs from endogenous production in transit. This cellular model showed that a large pool of the EVs present in the circulation are produced in the yolk syncytial layer (YSL), an embryonic structure central in cell fates and morphogenesis (Carvalho and Heisenberg, 2010). Interestingly, these EVs are uptaken by endothelial cell and vascular patrolling monocytes (Verweij et al., 2019) – see [**annex 4: Live tracking of inter-organ communication by endogenous exosome *in vivo***](#).

In parallel in our lab, we used EVs purified from fish melanoma cells (ZMEL – (Heilmann et al., 2015) that we labelled with a lipid dye (thank to another collaborative work of the team - (Collot et al., 2019) before injection in the zebrafish embryos. We were able to track circulating EVs in the blood flow and characterize their uptake by endothelial cells and patrolling monocytes. In these cells, we demonstrated that the majority of the EVs concentrate in lysosomal compartments. We also performed functional test on different transgenic embryos showing an activation and production of TNF- α (Nguyen et al., 2015), which correspond to the M2-M1 transition, often associated with the transformation of normal macrophages (M2) to cancer associated macrophage (M1) (Gordon, 2003; Biswas and Mantovani, 2010). Finally, to demonstrate the induction of premetastatic niches induced by EVs, we performed pre-injection with EVs (called priming), followed by tumor cell injection. We showed that tumor cells invade more efficiently the fish stroma and develop bigger micro-metastasis in the case of EV priming (Hyenne et al., 2019) – see [**annex 5: Study the fate of tumor extracellular vesicles at high spatiotemporal resolution using the zebrafish embryo**](#).

CELL LABELLING *IN VIVO*

Fluorescent labelling is a key in biology because it allows the tracking of cellular or subcellular elements in light microscopy. Following this idea, many cancer cell lines are modified to overexpress fluorescent protein thanks to transient transfection or homologous recombination. Besides the potential side effect of such approaches (Bolognesi and Lehner, 2018), it appears that patient-derived cells, or primary isolated cells are often very complicated to transfect. Therefore, it sounds of utmost importance to develop dyes that are stably labelling the cells/structures in an *in vivo* context. It is a wide research field at the boundary between chemistry and biology that requires easy going and low-cost *in vivo* test models. These probes have to be bright and stable to allow detection and longitudinal studies but most importantly without disclosing any cytotoxic effects. During my PhD, we worked on two different projects in this field.

*FLUORESCENT POLYMER NANOPARTICLES FOR CELL BARCODING *IN VITRO* AND *IN VIVO**

With A. Klymchenko's team (Lab. for biophotonic and pharmacology - UMR7213 - Strasbourg), we tested a barcoding approach on tumor cells, before injecting them in the zebrafish model (Andreiuk et al., 2017) – see [annex 6: Fluorescent polymer nanoparticles for cell barcoding *in vitro* and *in vivo*](#).

They developed three vital-dyes that are very bright and stable overtime *in vitro*. The advantage of these dyes is that they can be mixed at different ratios, to emit 13 different fluorescent light detectable by cell sorting. From *in vitro* experiment, we were able to label and separate 6 populations of cells (green, turquoise, blue, magenta, red, yellow) after mixing them. Then, we tested their dye *in vivo*, by injecting a mix of 6 pre-labelled wells of D2A1 cells in two days post-fertilization zebrafish embryos. We successfully observed these populations in the caudal plexus of the embryos after 3 hours post-injection.

This proof of concept experiment allowed us to envision the pre-labelling of different types of cells before injection, which is something that might be used in the future in the lab (studying clusters of tumor cells or tumor heterogeneity).

WRAPPED STELLATE SILICA NANOCOMPOSITES AS BIOCOMPATIBLE LUMINESCENT NANOPLATEFORMS ASSESSED IN VIVO

We worked with D. Mertz's team (Lab. Fr Inorganic material and chemistry – UMR7504 - Strasbourg), on the use of quantum dots as fluorescent markers.

Quantum dots (QD) are a type of dye that appears in the field of nanotechnologies. They are made of Indium or Zinc, that are both quite cytotoxic. The group of D. Mertz developed a new type of nanoparticles using QD, polysaccharids and a mesoporous silica shell that can be functionalized (potentially with anti-cancer agents). Their strategy using QD allows the fluorescent tracking of the particles, and the shell successfully blocks cytotoxicity by reducing the ability of QD to detach. We could test these nanoparticles in the lab, *in vitro* assessing the proliferation of cells, and *in vivo*, directly injecting in the zebrafish embryos. In both cases, no cytotoxic effect was observed at the higher dose (Perton et al., 2019) – see [**annex 7: Wrapped stellate silica nanocomposites as biocompatible luminescent nanoplateforms assessed in vivo**](#)).

The project is now going forward, towards the loading of these particles with anti-cancer drugs, and their controlled released using laser excitation.

ZEBRAFISH AS A HUMAN DISEASE MODEL TO LOOK AT EXTRAVASATION

Zika virus is a blood-borne pathogen, mainly known for causing neurological disorders (fetal microencephaly being the most common) to growing fetus in pregnant women. The virus reaches the fetus via physiological blood exchanges and manage to cross the blood brain barrier to reach and infect neural progenitors. It is a major public health care problem, as there is no vaccine available and no treatment. Thus, the fundamental understanding of the spreading of the virus and its action mechanism is central to design potential therapies.

During my PhD, we worked with the team of R. Gaudin (Membrane dynamics and Virus -UMR 9004 - Montpellier) on how does the Zika viruses are able to cross the endothelium. From the literature and their results, the virus could be using stromal cells (especially monocytes) as a transport to cross the blood brain barrier. This “trojan horse” strategy was previously observed with other viruses such as HIV (Gras and Kaul, 2010). To test whether this was also happening in the case of Zika, we designed a set of experiments using our established methods in the zebrafish embryos. We compared Zika-infected monocytes vs non-infected monocytes on their ability to arrest, adhere and extravasate in the zebrafish embryos after intravascular injection.

The major outcome of this work is to confirm that Zika-infected monocytes are more prone to arrest and extravasate in the zebrafish embryos. Besides, RNA sequencing experiments could show that Zika presence was affecting the adhesion repertoire of monocytes, with many receptors overexpressed. This work, actually in revision by *Nature Communication* is paving the way to potential therapeutic approach towards monocytes transmigration inhibition in the case of Zika virus infection (Nunez et al. Nat. Comm. *In revision* – see [annex 8: Zika virus enhances monocyte adhesion and transmigration, favoring viral dissemination to the CNS](#)). In the context of my PhD, this was a great occasion to test the methodology we established using the zebrafish embryos towards the study other human pathologies.

ÉCOLE DOCTORALE 414
INSERM UMR_S1109 – Equipe Tumor Biomechanics

THÈSE présentée par :
Gautier FOLLAIN

Soutenue le : 10 Septembre 2019

Pour obtenir le grade de : **Docteur de l'Université de Strasbourg**

Discipline : Sciences de la Vie et de la Santé

Spécialité : Biologie Cellulaire et Cancérologie

Les forces hémodynamiques contrôlent la dissémination des cellules tumorales circulantes

Hemodynamic forces control circulating tumor cells dissemination

- Volume 2 -

THÈSE dirigée par :
Dr. Jacky GOETZ

Université de Strasbourg

RAPPORTEURS :
Pr. Johanna IVASKA
Pr. Matthieu PIEL

University of Turku (Fin)
Institut Curie

EXAMINATEUR INTERNE :
Dr. Anne-Cécile Reymann

Université de Strasbourg

DISCUSSION AND PERSPECTIVES

During my PhD, we studied the role of blood flow on the arrest, adhesion and extravasation of circulating tumor cells. We could show that the blood flow impacts all the steps.

First, the arrest and adhesion steps only occur at sites of permissive flow profiles. Tumor cells use their adhesion repertoire to stop despite the pushing flow, in a tug of war with the shear forces. Moreover, we could show that the deposit of intravascular fibronectin patches that tumor cells use to stop are induced by flow stimulation. Second, the endothelial remodeling that we characterized as a prominent extravasation mechanism is flow-dependent. The presence of arrested tumor cell and sufficient blood flow recruit endothelial cells that migrate intraluminally in a VEGF pathway-dependent manner, ending in the extravasation of tumor cells and the normal perfusion of the blood vessels.

I- PHYSICAL CONSTRAINTS DURING ARREST, ADHESION AND EXTRAVASATION

In the work I am presenting in this manuscript, we did not focus on the role of physical constraints. Indeed, we could show in the zebrafish model that the occlusion due to bigger tumor cells than vessel diameter was only possible in 50% of the observed cases (*Follain et al. Dev. Cell 2018 – Fig. 2B*). Moreover, among these 50%, injection of 1 μ m fluorescent beads after tumor cell injection could show that occlusion was not total (*Follain et al. Dev. Cell 2018 – Fig. 5L*). Indeed, using fast confocal imaging, we observed that these beads were still flowing around arrested tumor cells, meaning that plasma flow was still present. Along the same line, a similar phenomenon was also observed during intravital imaging in the mouse brain, where perfused fluorescently-labelled low molecular weight dextran could be observed on both side of arrested cells. This is further supporting our observation that occlusion is incomplete. Nevertheless, even partial occlusion imposes massive cell deformations, as cells may either have to squeeze in a small tube-like vessel or be sticking at a branch point with a part of the cell in each branch (Kienast et al., 2010) being submitted to shear stress.

In this context, the essential role of the cell stiffness and deformability is something that must be addressed *in vivo*, as it could be pro or cons the metastatic cascade. Indeed, a very stiff cell that can't adapt to physical stress will die in the circulation

(either being ripped off or because it can't sustain extravasation), but at the opposite a too soft cell won't resist neither the high magnitude of shear stress nor collisions with blood cells and vessel walls. Thus, it is very tempting to speculate that, as there is an optimal flow velocity which favors CTC arrest, there may be a window of optimal tumor cell stiffness that favors each step of the metastatic cascade. In other words, CTCs could be able to adapt their stiffness in a short timescale.

Also, Cell deformability certainly plays a role in the extravasation of tumor cells. Especially in the case of transmigration through diapedesis (as predicted by the leukocyte model (Vestweber, 2015)), tumor cells must be able to squeeze to cross the vessel wall. Otherwise, in the case of endothelial remodeling, we can speculate that the formation of the pocket induces mechanical stress on the tumor cells that they must survive. This is something that we observed a lot in the mouse brain (and was shown previously (Kienast et al., 2010)), where most of the cells seem to fragment during extravasation though endothelial remodeling.

However *in vivo* data regarding the role of cellular stiffness in CTC extravasation are lacking. Several recent developments such as the use of cell-sized beads of various stiffness could be an approach (Taubenberger et al., 2019). Interestingly, these beads having a calibrated deformability (Girardo et al., 2018), it would also be possible to study the force that cells must sustain to survive in the circulation. In parallel, using knock-down approach, as we did for the adhesion receptors, and the zebrafish embryo, it would be possible to identify actors and their roles *in vivo*.

Indeed, cell stiffness is something that is currently investigated in the lab. We selected three targets: intermediate filament (namely vimentin being the most expressed in the case of our D2A1 cells), acto-myosin network and lamin A/C from the nuclear envelop. To test them, we use RNAi-mediated knock-down, as we did for the adhesion receptors (Osmani et al., Accepted July 2019). Applying our methodology using zebrafish embryo injections, we are studying their knock-down effect on the metastatic cascade. So far, we could show that they are decreasing cell stiffness (according to pipet assay (Pachenari et al., 2014; Alibert et al., 2017)) without drastically impacting other cell characteristics such as adhesion or proliferation. *In vivo*, we found that injected softer cells arrest less and extravasate less, something that we do not fully understand yet. To note, this project is the starting point of another PhD student project that we could train this year.

II- BLOOD FLOW AND ACTIVE ADHESION

We observed that cells were able to arrest and adhere to the vessel wall in non-occlusive conditions thanks to their adhesion repertoire *in vivo*. Interestingly, this is related to blood flow in two ways: First, only low flow forces allow the arrest and adhesion. This is a very intuitive finding but was never addressed quantitatively *in vivo*. From our results about *in vivo* flow records (*Follain et al. Dev Cell* – **Fig. 1**), we set this permissive flow around 400-500 $\mu\text{m/sec}$, which corresponds to the range of speeds that can be measured in human capillaries (Williams et al., 1988; Isogai et al., 2001). Using optical tweezers *in vitro*, we could show that a force of 80-100 pN was necessary to detach tumor cells approximately one minute post-adhesion (minimum time we could reach in our set up). We did not dissect the kinetics of the strengthening of the adhesion, which is something that is already studied *in vitro* (Balaban et al., 2001; Kong et al., 2013). But strikingly, this force corresponds to the result of the calculation of the shear force that the flow of 450 $\mu\text{m/sec}$ exerts on an arrested object in a tube of similar diameters as the tumor cells in the zebrafish vessels (Stokes' equation). In other word, the permissive flow profile that allows the arrest and the adhesion force that the cells are able to exert in a short range of time brings to the same conclusion: a flow of 400-500 $\mu\text{m/sec}$ is permissive to arrest.

Second, we showed that the same flow speed was stimulating the secretion of fibronectin at the apical side of the endothelium *in vitro* (*Osmani et al. Accepted* – **Fig. S4**). To note, apical fibronectin deposit was described during my PhD by Barbazan et al. (Barbazán et al., 2017): They could show that colon CTCs arrest in the liver vasculature using fibronectin deposits as a substrate. According to the literature, integrins $\alpha V\beta 3$ and $\alpha 5\beta 1$ are major receptors for fibronectin (Humphries et al., 2006). In agreement, we identified these same receptors as essential for both the CTC arrest and stable adhesion respectively. Thus, it is tempting to say that luminal fibronectin is driving the arrest and adhesion of our tumor cells. To note, this means that tumor cells are not adhering directly to the endothelial cells, strongly challenging the transfer from leukocyte models to cancer.

All in all, it is an interesting point because it suggests that blood flow is involved in both pro (favoring the secretion of fibronectin “adhesive platform”) and cons (with tug-of-war between pushing shear forces and adhesion force from the receptors). This

strengthened our hypothesis of the optimal blood flow window favoring the arrest and adhesion of tumor cells.

III- BLOOD FLOW, CELL ADHESION AND ENDOTHELIAL REMODELING

Using confocal time lapse imaging and Correlative Light and Electron Microscopy (CLEM), we dissected the endothelial remodeling over time and at the high resolution. We could show that this process was flow-dependent, but also that it was tumor cell-dependent, as remodeling is very strongly diminished around passivated polystyrene beads of the same diameter. This raises many open questions.

First, what is the role of specific cell adhesion at initiating endothelial remodeling?

As discussed in the previous section, integrins and CD44 are central in the arrest and adhesion phase. But, all of these are also signaling molecules (**Box 1 and 2**). Thanks to the beads, it is be possible to dissociate tumor cell signaling from the impact of blood flow on endothelial signaling. Indeed, these beads could be functionalized (Allen et al., 2017) with specific receptors and injected in zebrafish embryos to identify the specific contribution of CTC adhesion receptors in inducing the endothelial remodeling.

Otherwise, according to the leukocyte diapedesis model, the binding of integrin $\alpha 4\beta 1$ to ICAM on the endothelial cells recruit the actin machinery at the site of the adhesion (Schaefer et al., 2014), and trigger cell junction opening (Vestweber, 2015). Endothelial remodeling around arrested tumor cells also requires such mechanism involving acto-myosin network remodeling and migration into the lumen.

Second, what is the contribution of blood flow?

Having in mind the evidences that show the binding of tumor cells to apical fibronectin, it is interesting to think about indirect signaling: We can speculate that fibronectin deposit is engaged in both the endothelial and the tumor cells. In this case, the shear forces that push the tumor cells could be transmitted to the endothelial bounds to fibronectin. A similar mechanism of adhesion mediating flow forces to endothelial cells is observed in the case of leukocytes, but with the direct cell-cell contact (Yeh et al., 2018). To what extend a similar mechanism is happening in our context remains to be elucidate.

It is also possible that the arrested cells do not play a critical role. Indeed, From the field of angiogenesis, it is clear that endothelial cells can feel a broad range of physical cues from blood flow modulations including speed, pulsatile frequency, shear stress or the laminar versus turbulent nature (Franco and Gerhardt, 2017). These cues promote a physiological adaptative response which is essential for the formation of the vascular network in the embryo (including sprouting, branching and remodeling), but also for the homeostasis of the vasculature in the adult (Potente et al., 2011). In the pathologic case of atherosclerosis (narrowing of the vessels caused by inner deposits of protein/lipids and platelets aggregates), it was described that turbulent flow due to the partial occlusion activates endothelial cell migration and remodeling (Hahn and Schwartz, 2009). It is very likely that, the presence of an arrested tumor cell modifies the flow pattern and activates the same angiogenic pathways. Regarding this, we could show that the flow pattern around arrested tumor cells was indeed disturbed, but we did never observe any turbulent pattern at site of CTC arrest in the zebrafish embryos. This would require further investigation to decipher how homeostatic endothelial mechanisms influence tumor cells extravasation.

At the opposite, a possibility that cannot be ruled out is that blood flow has not a central role, but only carries the cells at the optimal spot, where endothelial cells are prone to remodel. Importantly, from our *in vitro* data, blood flow is required to stimulate the endothelial remodeling phenotypes in HUVECs. This condition of “no flow” is harder to reproduce *in vivo* (especially with the need to have flow while injecting, and to stop it after), but would be the decisive arguments to show that blood flow is required to trigger endothelial remodeling.

So far, in our model of CTC injected directly in the blood stream of the zebrafish embryo there is a finding that challenges the central role of blood flow : There is less endothelial remodeling observed in the dorsal aorta compared to the caudal veins and this remained unchanged, even when the blood flow velocities were pharmacologically tuned (*Follain et al. Dev Cell 2018 – Fig. 3*). Meaning that venous vessels in the caudal plexus are more prone to engage remodeling. This could be explained by the inherent remodeling ability of endothelial cells according to their situation. Indeed, the major arteries and veins in the human body are not subjected to remodeling, but small capillaries remodel at will, depending on the need for oxygen and nutrients around them. Indeed, in the zebrafish embryos, the dorsal aorta is not remodeled during our stages of development (48 to 72 hours post fertilization), but caudal veins are actively

remodeling. This suggest that not only the flow pattern, but also the type of vessel would impact the remodeling capacity.

All in all, a lot of work remains to 1. Dissect the mechanism of endothelial remodeling at the subcellular level (acto-myosin regulation, cell junctions opening...) and 2. Establish the impact of the biomechanical factors that trigger endothelial remodeling *in vivo*.

IV- ENDOTHELIAL REMODELING APPLICATION TO CLINIC

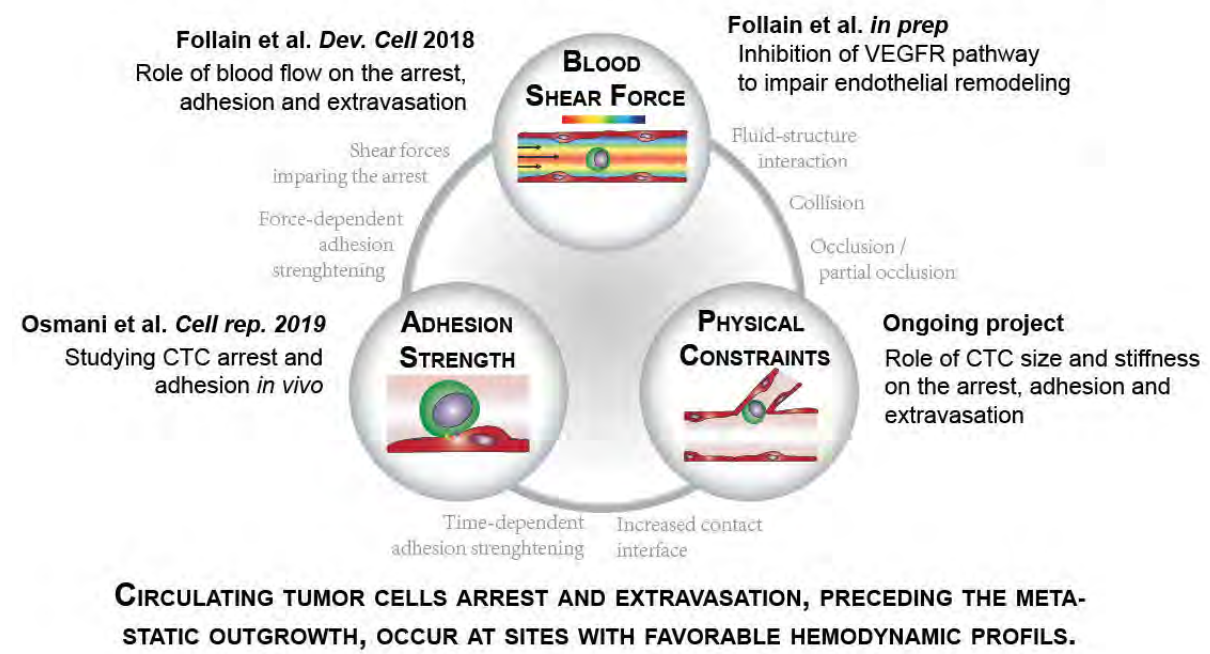
From a clinical standpoint, unravelling the signaling pathways that trigger the endothelial remodeling would be interesting, as it could provide therapeutic targets. According to our data, extravasation through this process represents more than half of the case in zebrafish embryos and happens in the mouse brain. Others could also show that it happens in mouse liver, lungs and kidney (to a smaller extend) (Paku et al., 2000). Moreover, as previously described, circulation, arrest and extravasation of tumor cells appear to be the most challenging steps of the metastatic cascade (Chambers et al., 2002). Cells are already in a harsh microenvironment, mixing apoptotic signals (anoikis, high reactive oxygen species concentration, ...) and physical stress (shear and collisions) and at the same time easily accessible for drug targeting (as drugs spreads systemically using the blood flow). Thus, blocking CTCs in the circulation by impairing their extravasation appears as a relevant strategy.

Our work shows that blocking the VEGF pathway with a pan-inhibitor (such as Sunitinib – Sutent®) at the time of tumor cell injection partially blocks the endothelial remodeling and is associated with a better survival of the mice. So, it tends to prove that reducing extravasation is a viable therapeutic approach. Nevertheless, there are major drawbacks that tone down these findings. 1. Pan-inhibitors of the VEGF pathways have been linked to increased tumor invasion (Du et al., 2017) and acceleration of the metastasis outgrowth (Ebos et al., 2009) 2. They show very harsh secondary effects (in more than 30% of the case: hypertension, low blood counts, heartburn, nausea, ...), and thus could never be used for long periods. As tumor cells are continuously shed by tumors (Kaiser, 2010), it won't be possible to target the extravasation step

specifically. Nowadays, they are used in second- or third-line treatments (advanced cancer stages) (Meadows and Hurwitz, 2012), and often coupled with an activator of the immune system. In this case, the therapeutic protocol is to starve the tumor by diminishing blood delivery (which induces the necrosis of the big tumors) and to activate immune cells to kill escaping cells from the tumor (Liu et al., 2018a). Thus, our work is rather a proof-of-concept that demonstrates that reducing the endothelial remodeling directly affects the extravasation step of the metastatic cascade and thus prevents metastatic foci formation. Undoubtedly further work should try to specifically target this mechanism.

As a concluding remark, I hope that our work during these four years participates to the demonstration that blood flow is a major factor to take into account when studying the metastatic cascade. It impacts the arrest but also the extravasation of tumor cells in close relation with physical occlusion and active adhesion.

THE MECHANICAL HYPOTHESIS



BIBLIOGRAPHY

Abdel-Ghany, M., Cheng, H.-C., Elble, R.C., Lin, H., DiBiasio, J., and Pauli, B.U. (2003). The Interacting Binding Domains of the $\beta 4$ Integrin and Calcium-activated Chloride Channels (CLCAs) in Metastasis. *J. Biol. Chem.* **278**, 49406–49416.

Acerbi, I., Cassereau, L., Dean, I., Shi, Q., Au, A., Park, C., Chen, Y.Y., Liphardt, J., Hwang, E.S., and Weaver, V.M. (2015). Human breast cancer invasion and aggression correlates with ECM stiffening and immune cell infiltration. *Integrative Biology* **7**, 1120–1134.

Aceto, N., Bardia, A., Miyamoto, D.T., Donaldson, M.C., Wittner, B.S., Spencer, J.A., Yu, M., Pely, A., Engstrom, A., Zhu, H., et al. (2014). Circulating tumor cell clusters are oligoclonal precursors of breast cancer metastasis. *Cell* **158**, 1110–1122.

Aguirre-Ghiso, J.A. (2007). Models, mechanisms and clinical evidence for cancer dormancy. *Nat. Rev. Cancer* **7**, 834–846.

Alexander, S., Koehl, G.E., Hirschberg, M., Geissler, E.K., and Friedl, P. (2008). Dynamic imaging of cancer growth and invasion: a modified skin-fold chamber model. *Histochem. Cell Biol.* **130**, 1147–1154.

Al-Hajj, M., Wicha, M.S., Benito-Hernandez, A., Morrison, S.J., and Clarke, M.F. (2003). Prospective identification of tumorigenic breast cancer cells. *Proc. Natl. Acad. Sci. U.S.A.* **100**, 3983–3988.

Alibert, C., Goud, B., and Manneville, J.-B. (2017). Are cancer cells really softer than normal cells? *Biology of the Cell* **109**, 167–189.

Allen, T.A., Gracieux, D., Talib, M., Tokarz, D.A., Hensley, M.T., Cores, J., Vandergriff, A., Tang, J., de Andrade, J.B.M., Dinh, P.-U., et al. (2017). Angiopellosis as an Alternative Mechanism of Cell Extravasation. *Stem Cells* **35**, 170–180.

Almada, P., Pereira, P.M., Culley, S., Caillol, G., Boroni-Rueda, F., Dix, C.L., Charras, G., Baum, B., Laine, R.F., Leterrier, C., et al. (2019). Automating multimodal microscopy with NanoJ-Fluidics. *Nature Communications* **10**, 1223.

Al-Mehdi, A.B., Tozawa, K., Fisher, A.B., Shientag, L., Lee, A., and Muschel, R.J. (2000). Intravascular origin of metastasis from the proliferation of endothelium-attached tumor cells: a new model for metastasis. *Nature Medicine* **6**, 100–102.

Almond, A. (2007). Hyaluronan. *Cell. Mol. Life Sci.* **64**, 1591–1596.

Alon, R., Hammer, D.A., and Springert, T.A. (1995). Lifetime of the P-selectin- carbohydrate bond and its response to tensile force in hydrodynamic flow. *374*, 4.

Amatruda, J.F., Shepard, J.L., Stern, H.M., and Zon, L.I. (2002). Zebrafish as a cancer model system. *Cancer Cell* **1**, 229–231.

Anca Maria, C., Ribatti, D., and Raica, M. (2011). A brief history of angiogenesis assays. *The International Journal of Developmental Biology* **55**, 377–382.

Anderson, K.J., de Guillebon, A., Hughes, A.D., Wang, W., and King, M.R. (2017). Effect of circulating tumor cell aggregate configuration on hemodynamic transport and wall contact. *Mathematical Biosciences* **294**, 181–194.

Andreiuk, B., Reisch, A., Lindecker, M., Follain, G., Peyriéras, N., Goetz, J.G., and Klymchenko, A.S. (2017). Fluorescent Polymer Nanoparticles for Cell Barcoding *In Vitro* and *In Vivo*. *Small* **13**.

Anton, H., Harlepp, S., Ramspacher, C., Wu, D., Monduc, F., Bhat, S., Liebling, M., Paoletti, C., Charvin, G., Freund, J.B., et al. (2013). Pulse propagation by a capacitive mechanism drives embryonic blood flow. *Development* **140**, 4426–4434.

Ao, Z., Shah, S.H., Machlin, L.M., Parajuli, R., Miller, P.C., Rawal, S., Williams, A.J., Cote, R.J., Lippman, M.E., Datar, R.H., et al. (2015). Identification of cancer associated fibroblasts in circulating blood from patients with metastatic breast cancer. *Cancer Res* 1633.2015.

Aruffo, A., Stamenkovic, I., Melnick, M., Underhill, C.B., and Seed, B. (1990). CD44 is the principal cell surface receptor for hyaluronate. *Cell* 61, 1303–1313.

Ashkenazi, A., and Dixit, V.M. (1999). Apoptosis control by death and decoy receptors. *Curr. Opin. Cell Biol.* 11, 255–260.

Ashkin, A. (1970). Acceleration and Trapping of Particles by Radiation Pressure. *Phys. Rev. Lett.* 24, 156–159.

Ashkin, A., Dziedzic, J.M., and Yamane, T. (1987). Optical trapping and manipulation of single cells using infrared laser beams. *Nature* 330, 769–771.

Attieh, Y., Clark, A.G., Grass, C., Richon, S., Pocard, M., Mariani, P., Elkhatib, N., Betz, T., Gurchenkov, B., and Vignjevic, D.M. (2017). Cancer-associated fibroblasts lead tumor invasion through integrin- β 3-dependent fibronectin assembly. *J. Cell Biol.* 216, 3509–3520.

Au, S.H., Storey, B.D., Moore, J.C., Tang, Q., Chen, Y.-L., Javaid, S., Sarioglu, A.F., Sullivan, R., Madden, M.W., O'Keefe, R., et al. (2016). Clusters of circulating tumor cells traverse capillary-sized vessels. *Proceedings of the National Academy of Sciences* 113, 4947–4952.

Auguste, P., Fallavollita, L., Wang, N., Burnier, J., Bikfalvi, A., and Brodt, P. (2007). The Host Inflammatory Response Promotes Liver Metastasis by Increasing Tumor Cell Arrest and Extravasation. *The American Journal of Pathology* 170, 1781–1792.

Azevedo A.S., Follain G., Patthabhiraman S., Harlepp S., Goetz J.G. (2015). Metastasis of circulating tumor cells: Favorable soil or suitable biomechanics, or both? *Cell Adhesion and Migration* 27, 1-12

Bacchelli, I., Schneeweiss, A., Riethdorf, S., Stenzinger, A., Schillert, A., Vogel, V., Klein, C., Saini, M., Bäuerle, T., Wallwiener, M., et al. (2013). Identification of a population of blood circulating tumor cells from breast cancer patients that initiates metastasis in a xenograft assay. *Nature Biotechnology* 31, 539–544.

Baeriswyl, V., and Christofori, G. (2009). The angiogenic switch in carcinogenesis. *Semin. Cancer Biol.* 19, 329–337.

Balaban, N.Q., Schwarz, U.S., Riveline, D., Goichberg, P., Tzur, G., Sabanay, I., Mahalu, D., Safran, S., Bershadsky, A., Addadi, L., et al. (2001). Force and focal adhesion assembly: a close relationship studied using elastic micropatterned substrates. *Nature Cell Biology* 3, 466.

Baluk, P., Hashizume, H., and McDonald, D.M. (2005). Cellular abnormalities of blood vessels as targets in cancer. *Curr. Opin. Genet. Dev.* 15, 102–111.

Bambace, N.M., and Holmes, C.E. (2011). The platelet contribution to cancer progression. *J. Thromb. Haemost.* 9, 237–249.

Bambardekar, K., Clément, R., Blanc, O., Chardès, C., and Lenne, P.-F. (2015). Direct laser manipulation reveals the mechanics of cell contacts *in vivo*. *PNAS* 112, 1416–1421.

Bano, F., Banerji, S., Howarth, M., Jackson, D.G., and Richter, R.P. (2016). A single molecule assay to probe monovalent and multivalent bonds between hyaluronan and its key leukocyte receptor CD44 under force. *Scientific Reports* 6, 34176.

Barbazán, J., Alonso-Alconada, L., Elkhatib, N., Geraldo, S., Gurchenkov, V., Glentis, A., Niel, G. van, Palmulli, R., Fernández, B., Víaño, P., et al. (2017). Liver Metastasis Is Facilitated by the Adherence of Circulating Tumor Cells to Vascular Fibronectin Deposits. *Cancer Res* 77, 3431–3441.

Barbera-Guillem, E., Smith, I., and Weiss, L. (1992). Cancer-cell traffic in the liver. I. Growth kinetics of cancer cells after portal-vein delivery. *International Journal of Cancer* 52, 974–977.

Barbier, L., Sáez, P.J., Attia, R., Lennon-Duménil, A.-M., Lavi, I., Piel, M., and Vargas, P. (2019). Myosin II Activity Is Selectively Needed for Migration in Highly Confined Microenvironments in Mature Dendritic Cells. *Front. Immunol.* 10.

Barnes, J.M., Nauseef, J.T., and Henry, M.D. (2012). Resistance to Fluid Shear Stress Is a Conserved Biophysical Property of Malignant Cells. *PLoS ONE* 7, e50973.

Barthel, S.R., Hays, D.L., Yazawa, E.M., Opperman, M., Walley, K.C., Nimrichter, L., Burdick, M.M., Gillard, B.M., Moser, M.T., Pantel, K., et al. (2013). Definition of Molecular Determinants of Prostate Cancer Cell Bone Extravasation. *Cancer Research* 73, 942–952.

Beaty, B.T., and Condeelis, J. (2014). Digging a little deeper: The stages of invadopodium formation and maturation. *European Journal of Cell Biology* 93, 438–444.

Beaucher, M., Goodliffe, J., Hersperger, E., Trunova, S., Frydman, H., and Shearn, A. (2007). Drosophila brain tumor metastases express both neuronal and glial cell type markers. *Dev. Biol.* 301, 287–297.

Beauchesne, P. (2011). Extra-neural metastases of malignant gliomas: myth or reality? *Cancers (Basel)* 3, 461–477.

Bell, G.I. (1979). A theoretical model for adhesion between cells mediated by multivalent ligands. *Cell Biochem Biophys* 1, 133–147.

Bell, G.I., Dembo, M., and Bongrand, P. (1984). Cell adhesion. Competition between nonspecific repulsion and specific bonding. *Biophys J* 45, 1051–1064.

Bennett, K.L., Modrell, B., Greenfield, B., Bartolazzi, A., Stamenkovic, I., Peach, R., Jackson, D.G., Spring, F., and Aruffo, A. (1995). Regulation of CD44 binding to hyaluronan by glycosylation of variably spliced exons. *The Journal of Cell Biology* 131, 1623–1633.

Berghmans, S., Jette, C., Langenau, D., Hsu, K., Stewart, R., Look, T., and Kanki, J.P. (2005a). Making waves in cancer research: new models in the zebrafish. *BioTechniques* 39, 227–237.

Berghmans, S., Murphey, R.D., Wienholds, E., Neuberg, D., Kutok, J.L., Fletcher, C.D.M., Morris, J.P., Liu, T.X., Schulte-Merker, S., Kanki, J.P., et al. (2005b). *tp53* mutant zebrafish develop malignant peripheral nerve sheath tumors. *Proc. Natl. Acad. Sci. U.S.A.* 102, 407–412.

Bersini, S., Jeon, J.S., Dubini, G., Arrigoni, C., Chung, S., Charest, J.L., Moretti, M., and Kamm, R.D. (2014). A Microfluidic 3D *In Vitro* Model for Specificity of Breast Cancer Metastasis to Bone. *Biomaterials* 35, 2454–2461.

Bharadwaj, M., Strohmeyer, N., Colo, G.P., Helenius, J., Beerenswinkel, N., Schiller, H.B., Fässler, R., and Müller, D.J. (2017). α V-class integrins exert dual roles on α 5 β 1 integrins to strengthen adhesion to fibronectin. *Nat Commun* 8, 14348.

Biswas, S.K., and Mantovani, A. (2010). Macrophage plasticity and interaction with lymphocyte subsets: cancer as a paradigm. *Nat. Immunol.* 11, 889–896.

Blackburn, J.S., and Langenau, D.M. (2014). Zebrafish as a model to assess cancer heterogeneity, progression and relapse. *Disease Models & Mechanisms* 7, 755–762.

Blasco, M.A. (2005). Telomeres and human disease: ageing, cancer and beyond. *Nat. Rev. Genet.* 6, 611–622.

Bolognesi, B., and Lehner, B. (2018). Reaching the limit. *ELife* 7, e39804.

Boral, D., Vishnoi, M., Liu, H.N., Yin, W., Sprouse, M.L., Scamardo, A., Hong, D.S., Tan, T.Z., Thiery, J.P., Chang, J.C., et al. (2017). Molecular characterization of breast cancer CTCs associated with brain metastasis. *Nature Communications* 8, 196.

Braga, V.M.M. (2002). Cell-cell adhesion and signalling. *Curr. Opin. Cell Biol.* 14, 546–556.

Brown, M., Assen, F.P., Leithner, A., Abe, J., Schachner, H., Asfour, G., Bago-Horvath, Z., Stein, J.V., Uhrin, P., Sixt, M., et al. (2018). Lymph node blood vessels provide exit routes for metastatic tumor cell dissemination in mice. *Science* 359, 1408–1411.

Brunk, D.K., Goetz, D.J., and Hammer, D.A. (1996). Sialyl Lewis(x)/E-selectin-mediated rolling in a cell-free system. *Biophys J* 71, 2902–2907.

Bryan, T.M., and Cech, T.R. (1999). Telomerase and the maintenance of chromosome ends. *Curr. Opin. Cell Biol.* 11, 318–324.

Burgos-Bravo, F., Figueroa, N.L., Casanova-Morales, N., Quest, A.F.G., Wilson, C.A.M., and Leyton, L. (2018). Single-molecule measurements of the effect of force on Thy-1/av β 3-integrin interaction using nonpurified proteins. *MBoC* 29, 326–338.

Butcher, D.T., Alliston, T., and Weaver, V.M. (2009). A tense situation: forcing tumour progression. *Nat. Rev. Cancer* 9, 108–122.

Butler, J.M., Kobayashi, H., and Rafii, S. (2010). Instructive role of the vascular niche in promoting tumour growth and tissue repair by angiocrine factors. *Nat Rev Cancer* 10, 138–146.

Cagan, R.L., Zon, L.I., and White, R.M. (2019). Modeling Cancer with Flies and Fish. *Developmental Cell* 49, 317–324.

Califano, A., and Alvarez, M.J. (2017). The recurrent architecture of tumour initiation, progression and drug sensitivity. *Nature Reviews Cancer* 17, 116–130.

Cameron, M.D., Schmidt, E.E., Kerkvliet, N., Nadkarni, K.V., Morris, V.L., Groom, A.C., Chambers, A.F., and MacDonald, I.C. (2000). Temporal progression of metastasis in lung: cell survival, dormancy, and location dependence of metastatic inefficiency. *Cancer Research* 60, 2541–2546.

Campbell, I.D., and Humphries, M.J. (2011). Integrin Structure, Activation, and Interactions. *Cold Spring Harbor Perspectives in Biology* 3, a004994–a004994.

Cao, X., Moeendarbary, E., Isermann, P., Davidson, P.M., Wang, X., Chen, M.B., Burkart, A.K., Lammerding, J., Kamm, R.D., and Shenoy, V.B. (2016). A Chemomechanical Model for Nuclear Morphology and Stresses during Cell Transendothelial Migration. *Biophysical Journal* 111, 1541–1552.

Cao, Y., Hoeppner, L.H., Bach, S., E, G., Guo, Y., Wang, E., Wu, J., Cowley, M.J., Chang, D.K., Waddell, N., et al. (2013). Neuropilin-2 Promotes Extravasation and Metastasis by Interacting with Endothelial 5 Integrin. *Cancer Research* 73, 4579–4590.

Carman, C.V., and Springer, T.A. (2004). A transmigratory cup in leukocyte diapedesis both through individual vascular endothelial cells and between them. *The Journal of Cell Biology* 167, 377–388.

Carmeliet, P., and Jain, R.K. (2011). Molecular mechanisms and clinical applications of angiogenesis. *Nature* 473, 298–307.

Carter, L., Rothwell, D.G., Mesquita, B., Smowton, C., Leong, H.S., Fernandez-Gutierrez, F., Li, Y., Burt, D.J., Antonello, J., Morrow, C.J., et al. (2017). Molecular analysis of circulating tumor cells identifies distinct copy-number profiles in patients with chemosensitive and chemorefractory small-cell lung cancer. *Nat. Med.* 23, 114–119.

Carvalho, L., and Heisenberg, C.-P. (2010). The yolk syncytial layer in early zebrafish development. *Trends Cell Biol.* 20, 586–592.

Cattaruzza, S., Schiappacassi, M., Kimata, K., Colombatti, A., and Perris, R. (2004). The globular domains of PG-M/versican modulate the proliferation-apoptosis equilibrium and invasive capabilities of tumor cells. *FASEB J.* 18, 779–781.

Chambers, A.F., Groom, A.C., and MacDonald, I.C. (2002). Metastasis: Dissemination and growth of cancer cells in metastatic sites. *Nat Rev Cancer* 2, 563–572.

Chang, J.M., Moon, W.K., Cho, N., Yi, A., Koo, H.R., Han, W., Noh, D.-Y., Moon, H.-G., and Kim, S.J. (2011). Clinical application of shear wave elastography (SWE) in the diagnosis of benign and malignant breast diseases. *Breast Cancer Res. Treat.* 129, 89–97.

Chang, W., Worman, H.J., and Gundersen, G.G. (2015). Accessorizing and anchoring the LINC complex for multifunctionality. *The Journal of Cell Biology* 208, 11–22.

Chen, B.-C., Legant, W.R., Wang, K., Shao, L., Milkie, D.E., Davidson, M.W., Janetopoulos, C., Wu, X.S., Hammer, J.A., Liu, Z., et al. (2014). Lattice light-sheet microscopy: Imaging molecules to embryos at high spatiotemporal resolution. *Science* 346, 1257998.

Chen, C., Zhao, S., Karnad, A., and Freeman, J.W. (2018). The biology and role of CD44 in cancer progression: therapeutic implications. *J Hematol Oncol* 11, 64.

Chen, M.B., Whisler, J.A., Jeon, J.S., and Kamm, R.D. (2013). Mechanisms of tumor cell extravasation in an *in vitro* microvascular network platform. *Integr Biol (Camb)* 5, 1262–1271.

Chen, M.B., Lamar, J.M., Li, R., Hynes, R.O., and Kamm, R.D. (2016). Elucidation of the Roles of Tumor Integrin β 1 in the Extravasation Stage of the Metastasis Cascade. *Cancer Res.* 76, 2513–2524.

Cheng, K., Shen, D., Xie, Y., Cingolani, E., Malliaras, K., and Marbán, E. (2012). Brief Report: Mechanism of Extravasation of Infused Stem Cells. *STEM CELLS* 30, 2835–2842.

Cheon, D.-J., and Orsulic, S. (2011). Mouse Models of Cancer. *Annu. Rev. Pathol. Mech. Dis.* 6, 95–119.

Cheung, K.J., and Ewald, A.J. (2016). A collective route to metastasis: Seeding by tumor cell clusters. *Science* 352, 167–169.

Cheung, K.J., Gabrielson, E., Werb, Z., and Ewald, A.J. (2013). Collective invasion in breast cancer requires a conserved basal epithelial program. *Cell* 155, 1639–1651.

Cheung, K.J., Padmanabhan, V., Silvestri, V., Schipper, K., Cohen, J.D., Fairchild, A.N., Gorin, M.A., Verdone, J.E., Pienta, K.J., Bader, J.S., et al. (2016). Polyclonal breast cancer metastases arise from collective dissemination of keratin 14-expressing tumor cell clusters. *Proceedings of the National Academy of Sciences* 113, E854–E863.

Choi, Y., Hyun, E., Seo, J., Blundell, C., Kim, H.C., Lee, E., Lee, S.H., Moon, A., Moon, W.K., and Huh, D. (2015). A microengineered pathophysiological model of early-stage breast cancer. *Lab Chip* 15, 3350–3357.

Choorapoikayil, S., Kuiper, R.V., de Bruin, A., and den Hertog, J. (2012). Haploinsufficiency of the genes encoding the tumor suppressor Pten predisposes zebrafish to hemangiosarcoma. *Dis Model Mech* 5, 241–247.

Chow, A., Zhou, W., Liu, L., Fong, M.Y., Champer, J., Van Haute, D., Chin, A.R., Ren, X., Gugiu, B.G., Meng, Z., et al. (2014). Macrophage immunomodulation by breast cancer-derived exosomes requires Toll-like receptor 2-mediated activation of NF- κ B. *Sci Rep* 4, 5750.

Cirri, P., and Chiarugi, P. (2012). Cancer-associated-fibroblasts and tumour cells: a diabolic liaison driving cancer progression. *Cancer Metastasis Rev.* 31, 195–208.

Collot, M., Ashokkumar, P., Anton, H., Boutant, E., Faklaris, O., Galli, T., Mély, Y., Danglot, L., and Klymchenko, A.S. (2019). MemBright: A Family of Fluorescent Membrane Probes for Advanced Cellular Imaging and Neuroscience. *Cell Chem Biol* 26, 600-614.e7.

Condeelis, J., and Pollard, J.W. (2006). Macrophages: obligate partners for tumor cell migration, invasion, and metastasis. *Cell* 124, 263–266.

Corada, M., Liao, F., Lindgren, M., Lampugnani, M.G., Breviario, F., Frank, R., Muller, W.A., Hicklin, D.J., Bohlen, P., and Dejana, E. (2001). Monoclonal antibodies directed to different regions of vascular endothelial cadherin extracellular domain affect adhesion and clustering of the protein and modulate endothelial permeability. *Blood* 97, 1679–1684.

Cornelison, R.C., Brennan, C.E., Kingsmore, K.M., and Munson, J.M. (2018). Convective forces increase CXCR4-dependent glioblastoma cell invasion in GL261 murine model. *Sci Rep* 8, 17057.

Cross, S.E., Jin, Y.-S., Rao, J., and Gimzewski, J.K. (2007). Nanomechanical analysis of cells from cancer patients. *Nature Nanotech* 2, 780–783.

Dalla-Favera, R., Bregni, M., Erikson, J., Patterson, D., Gallo, R.C., and Croce, C.M. (1982). Human c-myc onc gene is located on the region of chromosome 8 that is translocated in Burkitt lymphoma cells. *Proc. Natl. Acad. Sci. U.S.A.* 79, 7824–7827.

Dalmau, E., Armengol-Alonso, A., Muñoz, M., and Seguí-Palmer, M.Á. (2014). Current status of hormone therapy in patients with hormone receptor positive (HR+) advanced breast cancer. *The Breast* 23, 710–720.

Dao, M., Lim, C.T., and Suresh, S. (2005). Mechanics of the human red blood cell deformed by optical tweezers. *Journal of the Mechanics and Physics of Solids* 53, 2259–2280.

DeBerardinis, R.J., Lum, J.J., Hatzivassiliou, G., and Thompson, C.B. (2008). The biology of cancer: metabolic reprogramming fuels cell growth and proliferation. *Cell Metab.* 7, 11–20.

Dejana, E., Bazzoni, G., and Lampugnani, M.G. (1999). Vascular endothelial (VE)-cadherin: only an intercellular glue? *Exp. Cell Res.* 252, 13–19.

Denais, C.M., Gilbert, R.M., Isermann, P., McGregor, A.L., te Lindert, M., Weigelin, B., Davidson, P.M., Friedl, P., Wolf, K., and Lammerding, J. (2016). Nuclear envelope rupture and repair during cancer cell migration. *Science* 352, 353–358.

DeNardo, D.G., Andreu, P., and Coussens, L.M. (2010). Interactions between lymphocytes and myeloid cells regulate pro- versus anti-tumor immunity. *Cancer and Metastasis Reviews* 29, 309–316.

Deryugina, E.I., and Kiosses, W.B. (2017). Intratumoral Cancer Cell Intravasation Can Occur Independent of Invasion into the Adjacent Stroma. *Cell Rep* 19, 601–616.

Desgrosellier, J.S., and Cheren, D.A. (2010). Integrins in cancer: biological implications and therapeutic opportunities. *Nat Rev Cancer* 10, 9–22.

Destraing, O., Block, M.R., Planus, E., and Albiges-Rizo, C. (2011). Invadosome regulation by adhesion signaling. *Current Opinion in Cell Biology* 23, 597–606.

Di Fiore, P.P., Pierce, J.H., Kraus, M.H., Segatto, O., King, C.R., and Aaronson, S.A. (1987). erbB-2 is a potent oncogene when overexpressed in NIH/3T3 cells. *Science* 237, 178–182.

Dondossola, E., Alexander, S., Holzapfel, B.M., Filippini, S., Starbuck, M.W., Hoffman, R.M., Navone, N., De-Juan-Pardo, E.M., Logothetis, C.J., Hutmacher, D.W., et al. (2018). Intravital microscopy of osteolytic progression and therapy response of cancer lesions in the bone. *Sci Transl Med* 10.

Douma, S., van Laar, T., Zevenhoven, J., Meuwissen, R., van Garderen, E., and Peeper, D.S. (2004). Suppression of anoikis and induction of metastasis by the neurotrophic receptor TrkB. *Nature* 430, 1034–1039.

Du, Y., Liu, J.-Q., Tang, J., Ge, J., Chen, Y., Cheng, K., Ding, J., Li, Z.-K., and Liu, J.-Y. (2017). Acquired tumor cell resistance to sunitinib by increased invasion and epithelial-mesenchymal transition in LL/2 murine lung cancer. *Oncotarget* 8.

Duda, D.G., Duyverman, A.M.M.J., Kohno, M., Snuderl, M., Steller, E.J.A., Fukumura, D., and Jain, R.K. (2010). Malignant cells facilitate lung metastasis by bringing their own soil. *PNAS* 107, 21677–21682.

Duval, K., Grover, H., Han, L.-H., Mou, Y., Pegoraro, A.F., Fredberg, J., and Chen, Z. (2017). Modeling Physiological Events in 2D vs. 3D Cell Culture. *Physiology (Bethesda)* 32, 266–277.

Ebos, J.M.L., Lee, C.R., Cruz-Munoz, W., Bjarnason, G.A., Christensen, J.G., and Kerbel, R.S. (2009). Accelerated Metastasis after Short-Term Treatment with a Potent Inhibitor of Tumor Angiogenesis. *Cancer Cell* 15, 232–239.

Echtler, K., Konrad, I., Lorenz, M., Schneider, S., Hofmaier, S., Plenagl, F., Stark, K., Czermak, T., Tîrnicieriu, A., Eichhorn, M., et al. (2017). Platelet GPIIb supports initial pulmonary retention but inhibits subsequent proliferation of melanoma cells during hematogenous metastasis. *PLoS ONE* 12, e0172788.

Eibl, R.H. (2013). Single-Molecule Studies of Integrins by AFM-Based Force Spectroscopy on Living Cells. 137–169.

Entenberg, D., Voiculescu, S., Guo, P., Borriello, L., Wang, Y., Karagiannis, G.S., Jones, J., Baccay, F., Oktay, M., and Condeelis, J. (2018). A permanent window for the murine lung enables high-resolution imaging of cancer metastasis. *Nature Methods* 15, 73–80.

Erpenbeck, L., Nieswandt, B., Schön, M., Pozgajova, M., and Schön, M.P. (2010). Inhibition of platelet GPIb alpha and promotion of melanoma metastasis. *J. Invest. Dermatol.* 130, 576–586.

Escola, J.-M., Kleijmeer, M.J., Stoorvogel, W., Griffith, J.M., Yoshie, O., and Geuze, H.J. (1998). Selective Enrichment of Tetraspan Proteins on the Internal Vesicles of Multivesicular Endosomes and on Exosomes Secreted by Human B-lymphocytes. *J. Biol. Chem.* 273, 20121–20127.

Ewing, J. (1928). Neoplastic diseases. A treatise on tumors. : The American Journal of the Medical Sciences.

Fan, R., Emery, T., Zhang, Y., Xia, Y., Sun, J., and Wan, J. (2016). Circulatory shear flow alters the viability and proliferation of circulating colon cancer cells. *Scientific Reports* 6, 27073.

Fedi, P. (1997). Growth factors and cancer.

Felding-Habermann, B., O'Toole, T.E., Smith, J.W., Fransvea, E., Ruggeri, Z.M., Ginsberg, M.H., Hughes, P.E., Pampori, N., Shattil, S.J., Saven, A., et al. (2001). Integrin activation controls metastasis in human breast cancer. *Proceedings of the National Academy of Sciences* 98, 1853–1858.

Fidler, I.J. (1990). Critical factors in the biology of human cancer metastasis: twenty-eighth G.H.A. Clowes memorial award lecture. *Cancer Res.* 50, 6130–6138.

Fidler, I.J. (2003). The pathogenesis of cancer metastasis: the “seed and soil” hypothesis revisited. *Nat. Rev. Cancer* 3, 453–458.

Finlay, C.A., Hinds, P.W., and Levine, A.J. (1989). The p53 proto-oncogene can act as a suppressor of transformation. *Cell* 57, 1083–1093.

Folkman, J., and Haudenschild, C. (1980). Angiogenesis *in vitro*. *Nature* 288, 551–556.

Follain, G., Mercier, L., Osmani, N., Harlepp, S., and Goetz, J.G. (2016). Seeing is believing: multi-scale spatio-temporal imaging towards *in vivo* cell biology. *J Cell Sci* jcs.189001.

Follain, G., Osmani, N., Azevedo, A.S., Allio, G., Mercier, L., Karreman, M.A., Solecki, G., Garcia Leòn, M.J., Lefebvre, O., Fekonja, N., et al. (2018a). Hemodynamic Forces Tune the Arrest, Adhesion, and Extravasation of Circulating Tumor Cells. *Developmental Cell* 45, 33-52.e12.

Follain, G., Osmani, N., Fuchs, C., Allio, G., Harlepp, S., and Goetz, J.G. (2018b). Using the Zebrafish Embryo to Dissect the Early Steps of the Metastasis Cascade. *Methods Mol. Biol.* 1749, 195–211.

Franco, C.A., and Gerhardt, H. (2017). Morph or Move? How Distinct Endothelial Cell Responses to Blood Flow Shape Vascular Networks. *Developmental Cell* 41, 574–576.

Frenette, P.S., Johnson, R.C., Hynes, R.O., and Wagner, D.D. (1995). Platelets roll on stimulated endothelium *in vivo*: an interaction mediated by endothelial P-selectin. *Proceedings of the National Academy of Sciences* 92, 7450–7454.

Friedl, P., and Alexander, S. (2011). Cancer Invasion and the Microenvironment: Plasticity and Reciprocity. *Cell* 147, 992–1009.

Frisch, S.M., and Sreaton, R.A. (2001). Anoikis mechanisms. *Current Opinion in Cell Biology* 13, 555–562.

Fukumura, D., and Jain, R.K. (2007). Tumor microvasculature and microenvironment: Targets for anti-angiogenesis and normalization. *Microvascular Research* 74, 72–84.

Gaggioli, C., Hooper, S., Hidalgo-Carcedo, C., Grosse, R., Marshall, J.F., Harrington, K., and Sahai, E. (2007). Fibroblast-led collective invasion of carcinoma cells with differing roles for RhoGTPases in leading and following cells. *Nat. Cell Biol.* 9, 1392–1400.

Gao, A.C., Lou, W., Dong, J.T., and Isaacs, J.T. (1997). CD44 is a metastasis suppressor gene for prostatic cancer located on human chromosome 11p13. *Cancer Res.* 57, 846–849.

Gao, Q., Yang, Z., Xu, S., Li, X., Yang, X., Jin, P., Liu, Y., Zhou, X., Zhang, T., Gong, C., et al. (2019). Heterotypic CAF-tumor spheroids promote early peritoneal metastasis of ovarian cancer. *J Exp Med* 216, 688–703.

Garcia-Arcos, J.M., Chabrier, R., Deygas, M., Nader, G., Barbier, L., Sáez, P.J., Mathur, A., Vargas, P., and Piel, M. (2019). Reconstitution of cell migration at a glance. *J Cell Sci* 132, jcs225565.

Gasic, G.J., Gasic, T.B., and Stewart, C.C. (1968). Antimetastatic effects associated with platelet reduction. *Proc Natl Acad Sci U S A* 61, 46–52.

Gassmann, P., Hemping-Bovenkerk, A., Mees, S.T., and Haier, J. (2009). Metastatic tumor cell arrest in the liver-lumen occlusion and specific adhesion are not exclusive. *Int J Colorectal Dis* 24, 851–858.

Gerlinger, M., Rowan, A.J., Horswell, S., Math, M., Larkin, J., Endesfelder, D., Gronroos, E., Martinez, P., Matthews, N., Stewart, A., et al. (2012). Intratumor heterogeneity and branched evolution revealed by multiregion sequencing. *N. Engl. J. Med.* 366, 883–892.

Girardo, S., Träber, N., Wagner, K., Cojoc, G., Herold, C., Goswami, R., Schlüßler, R., Abuhattum, S., Taubenberger, A., Reichel, F., et al. (2018). Standardized microgel beads as elastic cell mechanical probes. *J. Mater. Chem. B* 6, 6245–6261.

Gligorijevic, B., Wyckoff, J., Yamaguchi, H., Wang, Y., Roussos, E.T., and Condeelis, J. (2012). N-WASP-mediated invadopodium formation is involved in intravasation and lung metastasis of mammary tumors. *Journal of Cell Science* 125, 724–734.

Glinskii, O.V., Huxley, V.H., Glinsky, G.V., Pienta, K.J., Raz, A., and Glinsky, V.V. (2005). Mechanical Entrapment Is Insufficient and Intercellular Adhesion Is Essential for Metastatic Cell Arrest in Distant Organs. *Neoplasia* 7, 522–527.

Godar, S., Ince, T.A., Bell, G.W., Feldser, D., Donaher, J.L., Bergh, J., Liu, A., Miu, K., Watnick, R.S., Reinhardt, F., et al. (2008). Growth-inhibitory and tumor-suppressive functions of p53 depend on its repression of CD44 expression. *Cell* 134, 62–73.

Goel, S., Gupta, N., Walcott, B.P., Snuderl, M., Kesler, C.T., Kirkpatrick, N.D., Heishi, T., Huang, Y., Martin, J.D., Ager, E., et al. (2013). Effects of Vascular-Endothelial Protein Tyrosine Phosphatase Inhibition on Breast Cancer Vasculature and Metastatic Progression. *JNCI J Natl Cancer Inst* 105, 1188–1201.

Gong, C., Liu, B., Yao, Y., Qu, S., Luo, W., Tan, W., Liu, Q., Yao, H., Zou, L., Su, F., et al. (2015). Potentiated DNA Damage Response in Circulating Breast Tumor Cells Confers Resistance to Chemotherapy. *J Biol Chem* 290, 14811–14825.

Gordon, S. (2003). Alternative activation of macrophages. *Nat. Rev. Immunol.* 3, 23–35.

Gou, X., Wang, R., Lam, S.S.Y., Hou, J., Leung, A.Y.H., and Sun, D. (2015). Cell adhesion manipulation through single cell assembly for characterization of initial cell-to-cell interaction. *BioMedical Engineering OnLine* 14, 114.

Graham, D.M., and Burridge, K. (2016). Mechanotransduction and nuclear function. *Current Opinion in Cell Biology* 40, 98–105.

Granato, M., and Nüsslein-Volhard, C. (1996). Fishing for genes controlling development. *Curr. Opin. Genet. Dev.* 6, 461–468.

Gras, G., and Kaul, M. (2010). Molecular mechanisms of neuroinvasion by monocytes-macrophages in HIV-1 infection. *Retrovirology* 7, 30.

Greaves, M., and Maley, C.C. (2012). Clonal evolution in cancer. *Nature* 481, 306–313.

Green, D.R., and Reed, J.C. (1998). Mitochondria and apoptosis. *Science* 281, 1309–1312.

Grunwald, D.J., and Streisinger, G. (1992). Induction of recessive lethal and specific locus mutations in the zebrafish with ethyl nitrosourea. *Genet. Res.* 59, 103–116.

Grutzendler, J., Murikinati, S., Hiner, B., Ji, L., Lam, C.K., Yoo, T., Gupta, S., Hafler, B.P., Adelman, R.A., Yuan, P., et al. (2014). Angiophagy prevents early embolus washout but recanalizes microvessels through embolus extravasation. *Sci Transl Med* 6, 226ra31.

Gu, Z., Li, Y., Lee, P., Liu, T., Wan, C., and Wang, Z. (2012). Protein Arginine Methyltransferase 5 Functions in Opposite Ways in the Cytoplasm and Nucleus of Prostate Cancer Cells. *PLOS ONE* 7, e44033.

Guba, M., Bosserhoff, A.-K., Steinbauer, M., Abels, C., Anthuber, M., Buettner, R., and Jauch, K.-W. (2000). Overexpression of melanoma inhibitory activity (MIA) enhances extravasation and metastasis of A-mel 3 melanoma cells *in vivo*. *British Journal of Cancer* 83, 1216.

Günthert, U., Hofmann, M., Rudy, W., Reber, S., Zöller, M., Haussmann, I., Matzku, S., Wenzel, A., Ponta, H., and Herrlich, P. (1991). A new variant of glycoprotein CD44 confers metastatic potential to rat carcinoma cells. *Cell* 65, 13–24.

Guo, W., and Giancotti, F.G. (2004). Integrin signalling during tumour progression. *Nat Rev Mol Cell Biol* 5, 816–826.

Gupta, G.P., and Massagué, J. (2006). Cancer Metastasis: Building a Framework. *Cell* 127, 679–695.

Haffter, P., Granato, M., Brand, M., Mullins, M.C., Hammerschmidt, M., Kane, D.A., Odenthal, J., Kelsh, R.N., Furutani-Seiki, M., Vogelsang, E., et al. (1996). The identification of genes with unique and essential functions in the development of the zebrafish, *Danio rerio*. 17.

Hahn, C., and Schwartz, M.A. (2009). Mechanotransduction in vascular physiology and atherogenesis. *Nature Reviews Molecular Cell Biology* 10, 53–62.

Haier J., Korb T., Hotz B., Spiegel H.U., Senninger N. (2003). An intravital model to monitor steps of metastatic tumor cell adhesion within the hepatic microcirculation. *J Gastrointest Surg* 7, 507-514

Haldi, M., Ton, C., Seng, W.L., and McGrath, P. (2006). Human melanoma cells transplanted into zebrafish proliferate, migrate, produce melanin, form masses and stimulate angiogenesis in zebrafish. *Angiogenesis* 9, 139–151.

Hamidi, H., Pietilä, M., and Ivaska, J. (2016). The complexity of integrins in cancer and new scopes for therapeutic targeting. *Br J Cancer* 115, 1017–1023.

Hamidi, H., and Ivaska, J. (2018). Every step of the way: integrins in cancer progression and metastasis. *Nat Rev Cancer* 18, 533–548.

Hanahan, D., and Folkman, J. (1996). Patterns and emerging mechanisms of the angiogenic switch during tumorigenesis. *Cell* 86, 353–364.

Hanahan, D., and Weinberg, R.A. (2000). The Hallmarks of Cancer. *Cell* 100, 57–70.

Hanahan, D., and Weinberg, R.A. (2011). Hallmarks of Cancer: The Next Generation. *Cell* 144, 646–674.

Haramis, A.-P.G., Hurlstone, A., van der Velden, Y., Begthel, H., van den Born, M., Offerhaus, G.J.A., and Clevers, H.C. (2006). Adenomatous polyposis coli-deficient zebrafish are susceptible to digestive tract neoplasia. *EMBO Rep* 7, 444–449.

Harlepp, S., Thalmann, F., Follain, G., Goetz, J.G., and Théry, M. (2017). Hemodynamic forces can be accurately measured *in vivo* with optical tweezers. *MBoC* 28, 3252–3260.

Harney, A.S., Arwert, E.N., Entenberg, D., Wang, Y., Guo, P., Qian, B.-Z., Oktay, M.H., Pollard, J.W., Jones, J.G., and Condeelis, J.S. (2015). Real-Time Imaging Reveals Local, Transient Vascular Permeability, and Tumor Cell Intravasation Stimulated by TIE2hi Macrophage–Derived VEGFA. *Cancer Discovery*.

Harper, K.L., Sosa, M.S., Entenberg, D., Hosseini, H., Cheung, J.F., Nobre, R., Avivar-Valderas, A., Nagi, C., Girnius, N., Davis, R.J., et al. (2016). Mechanism of early dissemination and metastasis in Her2+ mammary cancer. *Nature* 540, 588–592.

Harrison, D.G., Widder, J., Grumbach, I., Chen, W., Weber, M., and Searles, C. (2006). Endothelial mechanotransduction, nitric oxide and vascular inflammation. *Journal of Internal Medicine* 259, 351–363.

Headley, M.B., Bins, A., Nip, A., Roberts, E.W., Looney, M.R., Gerard, A., and Krummel, M.F. (2016). Visualization of immediate immune responses to pioneer metastatic cells in the lung. *Nature* 531, 513–517.

Heilmann, S., Ratnakumar, K., Langdon, E.M., Kansler, E.R., Kim, I.S., Campbell, N.R., Perry, E.B., McMahon, A.J., Kaufman, C.K., van Rooijen, E., et al. (2015). A Quantitative System for Studying Metastasis Using Transparent Zebrafish. *Cancer Research* 75, 4272–4282.

Heyder, C., Gloria-Maercker, E., Entschladen, F., Hatzmann, W., Niggemann, B., Zänker, K.S., and Dittmar, T. (2002). Realtime visualization of tumor cell/endothelial cell interactions during transmigration across the endothelial barrier. *J. Cancer Res. Clin. Oncol.* 128, 533–538.

Hiratsuka, S., Goel, S., Kamoun, W.S., Maru, Y., Fukumura, D., Duda, D.G., and Jain, R.K. (2011). Endothelial focal adhesion kinase mediates cancer cell homing to discrete regions of the lungs via E-selectin up-regulation. *Proc. Natl. Acad. Sci. U.S.A.* **108**, 3725–3730.

Hisaka, f (1958). The Effects of 2-Acetylaminofluorene on the Embryonic Development of the Zebrafish. *Cancer Research* **18**, 19.

Hisaka, K.K., and Hopper, A.F. (1957). Some effects of barbituric and diethylbarbituric acid on the development of the zebra fish, *Brachydanio rerio*. *The Anatomical Record* **129**, 297–307.

Hoeben, A. (2004). Vascular Endothelial Growth Factor and Angiogenesis. *Pharmacological Reviews* **56**, 549–580.

Hood, J.L., San, R.S., and Wickline, S.A. (2011). Exosomes released by melanoma cells prepare sentinel lymph nodes for tumor metastasis. *Cancer Res.* **71**, 3792–3801.

Hordijk, P.L., Anthony, E., Mul, F.P., Rientsma, R., Oomen, L.C., and Roos, D. (1999). Vascular-endothelial-cadherin modulates endothelial monolayer permeability. *Journal of Cell Science* **112**, 1915–1923.

Hörner, F., Meissner, R., Polali, S., Pfeiffer, J., Betz, T., Denz, C., and Raz, E. (2017). Holographic optical tweezers-based *in vivo* manipulations in zebrafish embryos. *J Biophotonics* **10**, 1492–1501.

Horton, E.R., Humphries, J.D., James, J., Jones, M.C., Askari, J.A., and Humphries, M.J. (2016). The integrin adhesome network at a glance. *J Cell Sci* **129**, 4159–4163.

Hosseini, H., Obradović, M.M.S., Hoffmann, M., Harper, K.L., Sosa, M.S., Werner-Klein, M., Nanduri, L.K., Werno, C., Ehrl, C., Maneck, M., et al. (2016). Early dissemination seeds metastasis in breast cancer. *Nature* **540**, 552–558.

Hou, H.W., Warkiani, M.E., Khoo, B.L., Li, Z.R., Soo, R.A., Tan, D.S.-W., Lim, W.-T., Han, J., Bhagat, A.A.S., and Lim, C.T. (2013). Isolation and retrieval of circulating tumor cells using centrifugal forces. *Scientific Reports* **3**, 1259.

Howe, K., Clark, M.D., Torroja, C.F., Torrance, J., Berthelot, C., Muffato, M., Collins, J.E., Humphray, S., McLaren, K., Matthews, L., et al. (2013). The zebrafish reference genome sequence and its relationship to the human genome. *Nature* **496**, 498–503.

Huang, Y.-T., Lan, Q., Lorusso, G., Duffey, N., and Rüegg, C. (2017). The matricellular protein CYR61 promotes breast cancer lung metastasis by facilitating tumor cell extravasation and suppressing anoikis. *Oncotarget* **8**.

Humphries, J.D. (2006). Integrin ligands at a glance. *Journal of Cell Science* **119**, 3901–3903.

Humphries, J.D., Byron, A., and Humphries, M.J. (2006). INTEGRIN LIGANDS. *J Cell Sci* **119**, 3901–3903.

Hüsemann, Y., Geigl, J.B., Schubert, F., Musiani, P., Meyer, M., Burghart, E., Forni, G., Eils, R., Fehm, T., Riethmüller, G., et al. (2008). Systemic spread is an early step in breast cancer. *Cancer Cell* **13**, 58–68.

Huvaneers, S., Truong, H., Fässler, R., Sonnenberg, A., and Danen, E.H.J. (2008). Binding of soluble fibronectin to integrin alpha5 beta1 - link to focal adhesion redistribution and contractile shape. *J. Cell. Sci.* **121**, 2452–2462.

Hvichia, G.E., Parveen, Z., Wagner, C., Janning, M., Quidde, J., Stein, A., Müller, V., Loges, S., Neves, R.P.L., Stoecklein, N.H., et al. (2016). A novel microfluidic platform for size and deformability based separation and the subsequent molecular characterization of viable circulating tumor cells. *Int. J. Cancer* **138**, 2894–2904.

Hyenne, V., and Goetz, J.G. (2017). Extracellular vesicles on the wire. *Cell Adh Migr* 11, 121–123.

Hyenne, V., Ghoroghi, S., Collot, M., Bons, J., Follain, G., Harlepp, S., Mary, B., Bauer, J., Mercier, L., Busnelli, I., et al. (2019). Studying the Fate of Tumor Extracellular Vesicles at High Spatiotemporal Resolution Using the Zebrafish Embryo. *Developmental Cell* 48, 554–572.e7.

Ilkan, Z., Wright, J.R., Goodall, A.H., Gibbins, J.M., Jones, C.I., and Mahaut-Smith, M.P. (2017). Evidence for shear-mediated Ca²⁺ entry through mechanosensitive cation channels in human platelets and a megakaryocytic cell line. *J Biol Chem* 292, 9204–9217.

Irianto, J., Pfeifer, C.R., Bennett, R.R., Xia, Y., Ivanovska, I.L., Liu, A.J., Greenberg, R.A., and Discher, D.E. (2016). Nuclear constriction segregates mobile nuclear proteins away from chromatin. *Molecular Biology of the Cell* 27, 4011–4020.

Isogai, S., Horiguchi, M., and Weinstein, B.M. (2001). The vascular anatomy of the developing zebrafish: an atlas of embryonic and early larval development. *Dev. Biol.* 230, 278–301.

Ito, S., Nakanishi, H., Ikehara, Y., Kato, T., Kasai, Y., Ito, K., Akiyama, S., Nakao, A., and Tatematsu, M. (2001). Real-time observation of micrometastasis formation in the living mouse liver using a green fluorescent protein gene-tagged rat tongue carcinoma cell line. *International Journal of Cancer* 93, 212–217.

Jacquemet, G., Hamidi, H., and Ivaska, J. (2015). Filopodia in cell adhesion, 3D migration and cancer cell invasion. *Current Opinion in Cell Biology* 36, 23–31.

Jain, R.K. (2001). Normalizing tumor vasculature with anti-angiogenic therapy: a new paradigm for combination therapy. *Nat. Med.* 7, 987–989.

Janic, A., Mendizabal, L., Llamazares, S., Rossell, D., and Gonzalez, C. (2010). Ectopic expression of germline genes drives malignant brain tumor growth in *Drosophila*. *Science* 330, 1824–1827.

Jones, R.G., and Thompson, C.B. (2009). Tumor suppressors and cell metabolism: a recipe for cancer growth. *Genes Dev.* 23, 537–548.

Jones, M.L., Siddiqui, J., Pienta, K.J., and Getzenberg, R.H. (2013). Circulating fibroblast-like cells in men with metastatic prostate cancer. *Prostate* 73, 176–181.

Joyce, J.A., and Pollard, J.W. (2009). Microenvironmental regulation of metastasis. *Nat Rev Cancer* 9, 239–252.

Kaiser, J. (2010). Cancer's Circulation Problem. *Science* 327, 1072–1074.

Kanada, M., Bachmann, M.H., and Contag, C.H. (2016). Signaling by Extracellular Vesicles Advances Cancer Hallmarks. *Trends Cancer* 2, 84–94.

Kane, D.A., Maischein, H.-M., Brand, M., Furutani-Seiki, M., Granato, M., Haffter, P., Hammerschmidt, M., Heisenberg, C.-P., Jiang, Y.-J., Kelsh, R.N., et al. (1996a). The zebrafish early arrest mutants. 10.

Kane, D.A., Hammerschmidt, M., Mullins, M.C., Maischein, H.-M., and Brand, M. (1996b). The zebrafish epiboly mutants. 9.

Kang, H.-J., Kendrick, S., Hecht, S.M., and Hurley, L.H. (2014). The Transcriptional Complex Between the BCL2 i-Motif and hnRNP LL Is a Molecular Switch for Control of Gene Expression That Can Be Modulated by Small Molecules. *J Am Chem Soc* 136, 4172–4185.

Karreman, M.A., Mercier, L., Schieber, N.L., Shibue, T., Schwab, Y., and Goetz, J.G. (2014). Correlating Intravital Multi-Photon Microscopy to 3D Electron Microscopy of Invading Tumor Cells Using Anatomical Reference Points. *PLoS ONE* 9, e114448.

Karreman, M.A., Mercier, L., Schieber, N.L., Solecki, G., Allio, G., Winkler, F., Ruthensteiner, B., Goetz, J.G., and Schwab, Y. (2016a). Fast and precise targeting of single tumor cells *in vivo* by multimodal correlative microscopy. *J Cell Sci* 129, 444–456.

Karreman, M.A., Hyenne, V., Schwab, Y., and Goetz, J.G. (2016b). Intravital Correlative Microscopy: Imaging Life at the Nanoscale. *Trends Cell Biol.* 26, 848–863.

Kato, H., Liao, Z., Mitsios, J.V., Wang, H.-Y., Deryugina, E.I., Varner, J.A., Quigley, J.P., and Shattil, S.J. (2012). The Primacy of $\beta 1$ Integrin Activation in the Metastatic Cascade. *PLoS ONE* 7, e46576.

Kawaguchi, T., and Nakamura, K. (1986). Analysis of the lodgement and extravasation of tumor cells in experimental models of hematogenous metastasis. *Cancer Metast Rev* 5, 77–94.

Kebers, F., Lewalle, J.M., Desreux, J., Munaut, C., Devy, L., Foidart, J.M., and Noël, A. (1998). Induction of endothelial cell apoptosis by solid tumor cells. *Exp. Cell Res.* 240, 197–205.

Kechagia, J.Z., Ivaska, J., and Roca-Cusachs, P. (2019). Integrins as biomechanical sensors of the microenvironment. *Nat. Rev. Mol. Cell Biol.*

Kienast, Y., von Baumgarten, L., Fuhrmann, M., Klinkert, W.E.F., Goldbrunner, R., Herms, J., and Winkler, F. (2010). Real-time imaging reveals the single steps of brain metastasis formation. *Nat. Med.* 16, 116–122.

Kim, M.-Y., Oskarsson, T., Acharyya, S., Nguyen, D.X., Zhang, X.H.-F., Norton, L., and Massagué, J. (2009). Tumor self-seeding by circulating cancer cells. *Cell* 139, 1315–1326.

Kimmel, C., and Law, R.D. (1985a). I. Cell Lineage of Zebrafish Blastomeres'. 8.

Kimmel, C., and Law, R. (1985b). II. Cell Lineage of Zebrafish Blastomeres. 8.

Kimmel, C.B., and Law, R.D. (1985c). III Cell lineage of zebrafish blastomeres. Clonal analyses of the blastula and gastrula stages. *Dev. Biol.* 108, 94–101.

Kimmel, C.B., and Warga, R.M. (1986). Gastrula of the Zebrafish. 5.

Kimmel, C.B., and Warga, R.M. (1987). Cell lineages generating axial muscle in the zebrafish embryo. *Nature* 327, 234–237.

Kimmel, C.B., and Warga, R.M. (1988). Cell lineage and developmental potential of cells in the zebrafish embryo. *Trends in Genetics* 4, 68–74.

Kimmel, C.B., Sessions, S.K., and Kimmel, R.J. (1981). Morphogenesis and synaptogenesis of the zebrafish mauthner neuron. *The Journal of Comparative Neurology* 198, 101–120.

King, M.R., Phillips, K.G., Mitrugno, A., Lee, T.-R., de Guillebon, A.M.E., Chandrasekaran, S., McGuire, M.J., Carr, R.T., Baker-Groberg, S.M., Rigg, R.A., et al. (2015). A physical sciences network characterization of circulating tumor cell aggregate transport. *American Journal of Physiology - Cell Physiology* 308, C792–C802.

Kinjo, M. (1978). Lodgement and extravasation of tumour cells in blood-borne metastasis: an electron microscope study. *Br J Cancer* 38, 293–301.

Klemke, M., Weschenfelder, T., Konstandin, M.H., and Samstag, Y. (2007). High affinity interaction of integrin $\alpha 4\beta 1$ (VLA-4) and vascular cell adhesion molecule 1 (VCAM-1) enhances migration of human melanoma cells across activated endothelial cell layers. *J. Cell. Physiol.* 212, 368–374.

Köhler, S., Ullrich, S., Richter, U., and Schumacher, U. (2010). E-/P-selectins and colon carcinoma metastasis: first *in vivo* evidence for their crucial role in a clinically relevant model of spontaneous metastasis formation in the lung. *Br J Cancer* 102, 602–609.

Konantz, M., Balci, T.B., Hartwig, U.F., Dellaire, G., André, M.C., Berman, J.N., and Lengerke, C. (2012). Zebrafish xenografts as a tool for *in vivo* studies on human cancer. *Annals of the New York Academy of Sciences* 1266, 124–137.

Kong, F., Li, Z., Parks, W.M., Dumbauld, D.W., García, A.J., Mould, A.P., Humphries, M.J., and Zhu, C. (2013). Cyclic Mechanical Reinforcement of Integrin–Ligand Interactions. *Molecular Cell* 49, 1060–1068.

Krøigård, A.B., Larsen, M.J., Brasch-Andersen, C., Lænkholm, A.-V., Knoop, A.S., Jensen, J.D., Bak, M., Mollenhauer, J., Thomassen, M., and Kruse, T.A. (2017). Genomic Analyses of Breast Cancer Progression Reveal Distinct Routes of Metastasis Emergence. *Sci Rep* 7, 43813.

Kusama, T., Mukai, M., Tatsuta, M., Nakamura, H., and Inoue, M. (2006). Inhibition of transendothelial migration and invasion of human breast cancer cells by preventing geranylgeranylation of Rho. *Int. J. Oncol.* 29, 217–223.

Labelle, M., Begum, S., and Hynes, R.O. (2011). Direct Signaling between Platelets and Cancer Cells Induces an Epithelial-Mesenchymal-Like Transition and Promotes Metastasis. *Cancer Cell* 20, 576–590.

Labelle, M., Begum, S., and Hynes, R.O. (2014). Platelets guide the formation of early metastatic niches. *PNAS* 111, E3053–E3061.

Laferrière, J., Houle, F., and Huot, J. (2004). Adhesion of HT-29 colon carcinoma cells to endothelial cells requires sequential events involving E-selectin and integrin β 4. *Clin Exp Metastasis* 21, 257–265.

Lam, C.K., Yoo, T., Hiner, B., Liu, Z., and Grutzendler, J. (2010). Embolus extravasation is an alternative mechanism for cerebral microvascular recanalization. *Nature* 465, 478–482.

Lam, S.H., Wu, Y.L., Vega, V.B., Miller, L.D., Spitsbergen, J., Tong, Y., Zhan, H., Govindarajan, K.R., Lee, S., Mathavan, S., et al. (2006). Conservation of gene expression signatures between zebrafish and human liver tumors and tumor progression. *Nat. Biotechnol.* 24, 73–75.

Lammerding, J., Fong, L.G., Ji, J.Y., Reue, K., Stewart, C.L., Young, S.G., and Lee, R.T. (2006). Lamins A and C but Not Lamin B1 Regulate Nuclear Mechanics. *Journal of Biological Chemistry* 281, 25768–25780.

Langenau, D.M., Traver, D., Ferrando, A.A., Kutok, J.L., Aster, J.C., Kanki, J.P., Lin, S., Prochownik, E., Trede, N.S., Zon, L.I., et al. (2003). Myc-Induced T Cell Leukemia in Transgenic Zebrafish. *Science* 299, 887–890.

Lapis, K., Paku, S., and Liotta, L.A. (1988). Endothelialization of embolized tumor cells during metastasis formation. *Clinical & Experimental Metastasis* 6, 73–89.

Lautscham, L.A., Kämmerer, C., Lange, J.R., Kolb, T., Mark, C., Schilling, A., Strissel, P.L., Strick, R., Gluth, C., Rowat, A.C., et al. (2015). Migration in Confined 3D Environments Is Determined by a Combination of Adhesiveness, Nuclear Volume, Contractility, and Cell Stiffness. *Biophysical Journal* 109, 900–913.

Lawson, N.D., and Weinstein, B.M. (2002). *In Vivo* Imaging of Embryonic Vascular Development Using Transgenic Zebrafish. *Developmental Biology* 248, 307–318.

Lawson, D.A., Kessenbrock, K., Davis, R.T., Pervolarakis, N., and Werb, Z. (2018). Tumour heterogeneity and metastasis at single-cell resolution. *Nature Cell Biology* 20, 1349.

Lee, M.-H., and Murphy, G. (2004). Matrix metalloproteinases at a glance. *Journal of Cell Science* 117, 4015–4016.

Lee, L.M.J., Seftor, E.A., Bonde, G., Cornell, R.A., and Hendrix, M.J.C. (2005). The fate of human malignant melanoma cells transplanted into zebrafish embryos: Assessment of migration and cell division in the absence of tumor formation. *Dev. Dyn.* 233, 1560–1570.

Lee, R.K.K., Stainier, D.Y.R., Weinstein, B.M., and Fishman, M.C. Cardiovascular development in the zebrafish. 6.

Lee, S.L.C., Rouhi, P., Jensen, L.D., Zhang, D., Ji, H., Hauptmann, G., Ingham, P., and Cao, Y. (2009). Hypoxia-induced pathological angiogenesis mediates tumor cell dissemination, invasion, and metastasis in a zebrafish tumor model. *Proc Natl Acad Sci U S A* 106, 19485–19490.

Leong, H.S., Robertson, A.E., Stoletov, K., Leith, S.J., Chin, C.A., Chien, A.E., Hague, M.N., Ablack, A., Carmine-Simmen, K., McPherson, V.A., et al. (2014). Invadopodia are required for cancer cell extravasation and are a therapeutic target for metastasis. *Cell Rep* 8, 1558–1570.

Levental, K.R., Yu, H., Kass, L., Lakins, J.N., Egeblad, M., Erler, J.T., Fong, S.F.T., Csiszar, K., Giaccia, A., Weninger, W., et al. (2009). Matrix Crosslinking Forces Tumor Progression by Enhancing Integrin Signaling. *Cell* 139, 891–906.

Li, B., Zhao, W.-D., Tan, Z.-M., Fang, W.-G., Zhu, L., and Chen, Y.-H. (2006). Involvement of Rho/ROCK signalling in small cell lung cancer migration through human brain microvascular endothelial cells. *FEBS Letters* 580, 4252–4260.

Li, S., Wang, H., and Groth, C. (2014). Drosophila neuroblasts as a new model for the study of stem cell self-renewal and tumour formation. *Biosci. Rep.* 34.

Liao, F., Huynh, H.K., Eiroa, A., Greene, T., Polizzi, E., and Muller, W.A. (1995). Migration of monocytes across endothelium and passage through extracellular matrix involve separate molecular domains of PECAM-1. *J. Exp. Med.* 182, 1337–1343.

Liotta, L.A., Saidel, M.G., and Kleinerman, J. (1976). The significance of hematogenous tumor cell clumps in the metastatic process. *Cancer Res.* 36, 889–894.

Liu, C., Kelnar, K., Liu, B., Chen, X., Calhoun-Davis, T., Li, H., Patrawala, L., Yan, H., Jeter, C., Honorio, S., et al. (2011). The microRNA miR-34a inhibits prostate cancer stem cells and metastasis by directly repressing CD44. *Nat. Med.* 17, 211–215.

Liu, S., and Leach, S.D. (2011). Screening pancreatic oncogenes in zebrafish using the Gal4/UAS system. *Methods Cell Biol.* 105, 367–381.

Liu, Y., and Cao, X. (2016). Characteristics and Significance of the Pre-metastatic Niche. *Cancer Cell* 30, 668–681.

Liu, D., Qi, X., Manjunath, Y., Kimchi, E.T., Ma, L., Kaifi, J.T., Staveley-O'Carroll, K.F., and Li, G. (2018a). Sunitinib and Sorafenib Modulating Antitumor Immunity in Hepatocellular Cancer. 15.

Liu, T.-L., Upadhyayula, S., Milkie, D.E., Singh, V., Wang, K., Swinburne, I.A., Mosaliganti, K.R., Collins, Z.M., Hiscock, T.W., Shea, J., et al. (2018b). Observing the cell in its native state: Imaging subcellular dynamics in multicellular organisms. *Science* 360, eaaq1392.

Liu, X., Taftaf, R., Kawaguchi, M., Chang, Y.-F., Chen, W., Entenberg, D., Zhang, Y., Gerratana, L., Huang, S., Patel, D.B., et al. (2018c). Homophilic CD44 Interactions Mediate Tumor Cell Aggregation and Polyclonal Metastasis in Patient-Derived Breast Cancer Models. *Cancer Discov.*

Liu, Y., Gu, Y., Han, Y., Zhang, Q., Jiang, Z., Zhang, X., Huang, B., Xu, X., Zheng, J., and Cao, X. (2016). Tumor Exosomal RNAs Promote Lung Pre-metastatic Niche Formation by Activating Alveolar Epithelial TLR3 to Recruit Neutrophils. *Cancer Cell* 30, 243–256.

Lo, C.M., Wang, H.B., Dembo, M., and Wang, Y.L. (2000). Cell movement is guided by the rigidity of the substrate. *Biophys. J.* 79, 144–152.

Ludlow, A., Yee, K.O., Lipman, R., Bronson, R., Weinreb, P., Huang, X., Sheppard, D., and Lawler, J. (2005). Characterization of integrin β 6 and thrombospondin-1 double-null mice. *J Cellular Mol Med* 9, 421–437.

Lundell, B.I., McCarthy, J.B., Kovach, N.L., and Verfaillie, C.M. (1997). Activation of β 1 integrins on CML progenitors reveals cooperation between β 1 integrins and CD44 in the regulation of adhesion and proliferation. *Leukemia* 11, 822.

Luzzi, K.J., MacDonald, I.C., Schmidt, E.E., Kerkvliet, N., Morris, V.L., Chambers, A.F., and Groom, A.C. (1998). Multistep Nature of Metastatic Inefficiency. *The American Journal of Pathology* 153, 865–873.

Lyck, R., Reiss, Y., Gerwin, N., Greenwood, J., Adamson, P., and Engelhardt, B. (2003). T-cell interaction with ICAM-1/ICAM-2 double-deficient brain endothelium *in vitro*: the cytoplasmic tail of endothelial ICAM-1 is necessary for transendothelial migration of T cells. *Blood* 102, 3675–3683.

Lye, C.M., Blanchard, G.B., Naylor, H.W., Muresan, L., Huisken, J., Adams, R.J., and Sanson, B. (2015). Mechanical Coupling between Endoderm Invagination and Axis Extension in Drosophila. *PLoS Biol* 13, e1002292.

Makanya, A.N., Hlushchuk, R., and Djonov, V.G. (2009). Intussusceptive angiogenesis and its role in vascular morphogenesis, patterning, and remodeling. *Angiogenesis* 12, 113.

Manz, G., Clapero, F., Panieri, E., Panero, V., Böttcher, R.T., Tseng, H.-Y., Saltarin, F., Astanina, E., Wolanska, K.I., Morgan, M.R., et al. (2016). PPFIA1 drives active α 5 β 1 integrin recycling and controls fibronectin fibrillogenesis and vascular morphogenesis. *Nat Commun* 7, 13546.

Mani, S.A., Guo, W., Liao, M.-J., Eaton, E.N., Ayyanan, A., Zhou, A.Y., Brooks, M., Reinhard, F., Zhang, C.C., Shipitsin, M., et al. (2008). The epithelial-mesenchymal transition generates cells with properties of stem cells. *Cell* 133, 704–715.

van Marion, D.M.S., Domanska, U.M., Timmer-Bosscha, H., and Walenkamp, A.M.E. (2016). Studying cancer metastasis: Existing models, challenges and future perspectives. *Critical Reviews in Oncology/Hematology* 97, 107–117.

Marshall, B.T., Long, M., Piper, J.W., Yago, T., McEver, R.P., and Zhu, C. (2003). Direct observation of catch bonds involving cell-adhesion molecules. *Nature* 423, 190–193.

Mayadas, T.N., Johnson, R.C., Rayburn, H., Hynes, R.O., and Wagner, D.D. (1993). Leukocyte rolling and extravasation are severely compromised in P selectin-deficient mice. *Cell* 74, 541–554.

McEver, R.P., and Zhu, C. (2010). Rolling cell adhesion. *Annu. Rev. Cell Dev. Biol.* 26, 363–396.

McGranahan, N., and Swanton, C. (2015). Biological and therapeutic impact of intratumor heterogeneity in cancer evolution. *Cancer Cell* 27, 15–26.

Meadows, K.L., and Hurwitz, H.I. (2012). Anti-VEGF Therapies in the Clinic. *Cold Spring Harb Perspect Med* 2.

Meng, K., Yang, H., Wang, Y., and Sun, D. (2019). Modeling and Control of Single-Cell Migration Induced by a Chemoattractant-Loaded Microbead. *IEEE Trans Cybern* 49, 427–439.

Merino, D., Weber, T.S., Serrano, A., Vaillant, F., Liu, K., Pal, B., Di Stefano, L., Schreuder, J., Lin, D., Chen, Y., et al. (2019). Barcoding reveals complex clonal behavior in patient-derived xenografts of metastatic triple negative breast cancer. *Nat Commun* 10, 766.

Metzger, D., and Chambon, P. (2001). Site- and Time-Specific Gene Targeting in the Mouse. *Methods* 24, 71–80.

Miesenböck, G., Angelis, D.A.D., and Rothman, J.E. (1998). Visualizing secretion and synaptic transmission with pH-sensitive green fluorescent proteins. *Nature* 394, 192.

Miles, F.L., Pruitt, F.L., Golen, K.L. van, and Cooper, C.R. (2007). Stepping out of the flow: capillary extravasation in cancer metastasis. *Clin Exp Metastasis* 25, 305–324.

Miles, W.O., Dyson, N.J., and Walker, J.A. (2011). Modeling tumor invasion and metastasis in *Drosophila*. *Dis Model Mech* 4, 753–761.

Mitchell, M.J., and King, M.R. (2013). Fluid Shear Stress Sensitizes Cancer Cells to Receptor-Mediated Apoptosis via Trimeric Death Receptors. *New J Phys* 15, 015008.

Mitchell, M.J., Denais, C., Chan, M.F., Wang, Z., Lammerding, J., and King, M.R. (2015). Lamin A/C deficiency reduces circulating tumor cell resistance to fluid shear stress. *American Journal of Physiology-Cell Physiology* 309, C736–C746.

Moore, J.L., Rush, L.M., Breneman, C., Mohideen, M.-A.P.K., and Cheng, K.C. (2006). Zebrafish genomic instability mutants and cancer susceptibility. *Genetics* 174, 585–600.

Moore, K.M., Thomas, G.J., Duffy, S.W., Warwick, J., Gabe, R., Chou, P., Ellis, I.O., Green, A.R., Haider, S., Brouilette, K., et al. (2014). Therapeutic Targeting of Integrin $\alpha v\beta 6$ in Breast Cancer. *JNCI: Journal of the National Cancer Institute* 106.

Moreau, H.D., Piel, M., Voituriez, R., and Lennon-Duménil, A.-M. (2018). Integrating Physical and Molecular Insights on Immune Cell Migration. *Trends in Immunology* 39, 632–643.

Mullins, C. Mutational approaches to studying embryonic formation in the zebrafish. 7.

Munshi, H.G., and Stack, M.S. (2006). Reciprocal interactions between adhesion receptor signaling and MMP regulation. *Cancer Metastasis Rev* 25, 45–56.

Mygind, K.J., Schwarz, J., Sahgal, P., Ivaska, J., and Kveiborg, M. (2018). Loss of ADAM9 expression impairs $\beta 1$ integrin endocytosis, focal adhesion formation and cancer cell migration. *J Cell Sci* 131, jcs205393.

Nagrath, S., Sequist, L.V., Maheswaran, S., Bell, D.W., Irimia, D., Ulkus, L., Smith, M.R., Kwak, E.L., Digumarthy, S., Muzikansky, A., et al. (2007). Isolation of rare circulating tumour cells in cancer patients by microchip technology. *Nature* 450, 1235–1239.

Nagy, J.A., Chang, S.-H., Shih, S.-C., Dvorak, A.M., and Dvorak, H.F. (2010). Heterogeneity of the Tumor Vasculature. *Semin Thromb Hemost* 36, 321–331.

Nakajima, M., Irimura, T., and Nicolson, G.L. (1988). Heparanases and tumor metastasis. *Journal of Cellular Biochemistry* 36, 157–167.

Nakajima, M., Morikawa, K., Fabra, A., Bucana, C.D., and Fidler, I.J. (1990). Influence of Organ Environment on Extracellular Matrix Degradative Activity and Metastasis of Human Colon Carcinoma Cells. *JNCI Journal of the National Cancer Institute* 82, 1890–1898.

Naor, D., Nedvetzki, S., Golan, I., Melnik, L., and Faitelson, Y. (2002). CD44 in cancer. *Crit Rev Clin Lab Sci* 39, 527–579.

Naor, D., Wallach-Dayan, S.B., Zahalka, M.A., and Sionov, R.V. (2008). Involvement of CD44, a molecule with a thousand faces, in cancer dissemination. *Semin. Cancer Biol.* 18, 260–267.

Naumov, G.N., Wilson, S.M., MacDonald, I.C., Schmidt, E.E., Morris, V.L., Groom, A.C., Hoffman, R.M., and Chambers, A.F. (1999). Cellular expression of green fluorescent protein, coupled with high-resolution *in vivo* videomicroscopy, to monitor steps in tumor metastasis. *J. Cell. Sci.* 112 (Pt 12), 1835–1842.

Navin, N., Kendall, J., Troge, J., Andrews, P., Rodgers, L., McIndoo, J., Cook, K., Stepansky, A., Levy, D., Esposito, D., et al. (2011). Tumour evolution inferred by single-cell sequencing. *Nature* 472, 90–94.

Naxerova, K., and Jain, R.K. (2015). Using tumour phylogenetics to identify the roots of metastasis in humans. *Nat Rev Clin Oncol* 12, 258–272.

Naxerova, K., Reiter, J.G., Brachtel, E., Lennerz, J.K., Wetering, M. van de, Rowan, A., Cai, T., Clevers, H., Swanton, C., Nowak, M.A., et al. (2017). Origins of lymphatic and distant metastases in human colorectal cancer. *Science* 357, 55–60.

Netea-Maier, R.T., Smit, J.W.A., and Netea, M.G. (2018). Metabolic changes in tumor cells and tumor-associated macrophages: A mutual relationship. *Cancer Letters* 413, 102–109.

Nguyen, D.X., Bos, P.D., and Massagué, J. (2009). Metastasis: from dissemination to organ-specific colonization. *Nature Reviews Cancer* 9, 274–284.

Nguyen, M.O., Jalan, M., Morrow, C.A., Osman, F., and Whitby, M.C. (2015). Recombination occurs within minutes of replication blockage by RTS1 producing restarted forks that are prone to collapse. *ELife* 4, e04539.

Nguyen-Ngoc, K.-V., Cheung, K.J., Brenot, A., Shamir, E.R., Gray, R.S., Hines, W.C., Yaswen, P., Werb, Z., and Ewald, A.J. (2012). ECM microenvironment regulates collective migration and local dissemination in normal and malignant mammary epithelium. *PNAS* 109, E2595–E2604.

Nicoli, S., Ribatti, D., Cotelli, F., and Presta, M. (2007). Mammalian Tumor Xenografts Induce Neovascularization in Zebrafish Embryos. *Cancer Res* 67, 2927–2931.

Nusslein-Volhard, C. (1994). Of flies and fishes. *Science* 266, 572–574.

Obenauf, A.C., and Massagué, J. (2015). Surviving at a Distance: Organ-Specific Metastasis. *Trends in Cancer* 1, 76–91.

Oppenheimer-Marks, N., Davis, L.S., Bogue, D.T., Ramberg, J., and Lipsky, P.E. (1991). Differential utilization of ICAM-1 and VCAM-1 during the adhesion and transendothelial migration of human T lymphocytes. *The Journal of Immunology* 147, 2913–2921.

Orr, F.W., Wang, H.H., Lafrenie, R.M., Scherbarth, S., and Nance, D.M. (2000). Interactions between cancer cells and the endothelium in metastasis. *J. Pathol.* 190, 310–329.

Pachenari, M., Seyedpour, S.M., Jamaleki, M., Babazadeh Shayan, S., Taranejoo, S., and Hosseinkhani, H. (2014). Mechanical properties of cancer cytoskeleton depend on actin filaments to microtubules content: investigating different grades of colon cancer cell lines. *J Biomech* 47, 373–379.

Padua, D., Zhang, X.H.-F., Wang, Q., Nadal, C., Gerald, W.L., Gomis, R.R., and Massagué, J. (2008). TGF β Primes Breast Tumors for Lung Metastasis Seeding through Angiopoietin-like 4. *Cell* 133, 66–77.

Paget, S. (1889). The distribution of secondary growths in cancer of the breast. *The Lancet* 133, 571–573.

Paggetti, J., Haderk, F., Seiffert, M., Janji, B., Distler, U., Ammerlaan, W., Kim, Y.J., Adam, J., Lichter, P., Solary, E., et al. (2015). Exosomes released by chronic lymphocytic leukemia cells induce the transition of stromal cells into cancer-associated fibroblasts. *Blood* 126, 1106–1117.

Paguirigan, A.L., and Beebe, D.J. (2008). Microfluidics meet cell biology: bridging the gap by validation and application of microscale techniques for cell biological assays. *Bioessays* 30, 811–821.

Paku, S., Döme, B., Tóth, R., and Timár, J. (2000). Organ-specificity of the extravasation process: an ultrastructural study. *Clinical & Experimental Metastasis* 18, 481–492.

Panorchan, P., Lee, J.S.H., Kole, T.P., Tseng, Y., and Wirtz, D. (2006). Microrheology and ROCK Signaling of Human Endothelial Cells Embedded in a 3D Matrix. *Biophysical Journal* 91, 3499–3507.

Parichy, D.M. (2015). Advancing biology through a deeper understanding of zebrafish ecology and evolution. *ELife* 4, e05635.

Parikh, S.M., Mammoto, T., Schultz, A., Yuan, H.-T., Christiani, D., Karumanchi, S.A., and Sukhatme, V.P. (2006). Excess Circulating Angiopoietin-2 May Contribute to Pulmonary Vascular Leak in Sepsis in Humans. *PLoS Med* 3, e46.

Pastushenko, I., and Blanpain, C. (2019). EMT Transition States during Tumor Progression and Metastasis. *Trends in Cell Biology* 29, 212–226.

Paszek, M.J., Zahir, N., Johnson, K.R., Lakins, J.N., Rozenberg, G.I., Gefen, A., Reinhart-King, C.A., Margulies, S.S., Dembo, M., Boettiger, D., et al. (2005). Tensional homeostasis and the malignant phenotype. *Cancer Cell* 8, 241–254.

Patton, E.E., Widlund, H.R., Kuto, J.L., Kopani, K.R., Amatruda, J.F., Murphey, R.D., Berghmans, S., Mayhall, E.A., Traver, D., Fletcher, C.D.M., et al. (2005). BRAF Mutations Are Sufficient to Promote Nevi Formation and Cooperate with p53 in the Genesis of Melanoma. *Current Biology* 15, 249–254.

Paul, C.D., Hung, W.-C., Wirtz, D., and Konstantopoulos, K. (2016). Engineered Models of Confined Cell Migration. *Annual Review of Biomedical Engineering* 18, 159–180.

Paul, C.D., Mistriotis, P., and Konstantopoulos, K. (2017). Cancer cell motility: lessons from migration in confined spaces. *Nat. Rev. Cancer* 17, 131–140.

Paz, H., Pathak, N., and Yang, J. (2014). Invading one step at a time: the role of invadopodia in tumor metastasis. *Oncogene* 33, 4193–4202.

Peinado, H., Alečković, M., Lavotshkin, S., Matei, I., Costa-Silva, B., Moreno-Bueno, G., Hergueta-Redondo, M., Williams, C., García-Santos, G., Ghajar, C.M., et al. (2012). Melanoma exosomes educate bone marrow progenitor cells toward a pro-metastatic phenotype through MET. *Nature Medicine* 18, 883–891.

Peinado, H., Zhang, H., Matei, I.R., Costa-Silva, B., Hoshino, A., Rodrigues, G., Psaila, B., Kaplan, R.N., Bromberg, J.F., Kang, Y., et al. (2017). Pre-metastatic niches: organ-specific homes for metastases. *Nat. Rev. Cancer* 17, 302–317.

Pereira, E.R., Kedrin, D., Seano, G., Gautier, O., Meijer, E.F.J., Jones, D., Chin, S.-M., Kitahara, S., Bouts, E.M., Chang, J., et al. (2018). Lymph node metastases can invade local blood vessels, exit the node, and colonize distant organs in mice. *Science* 359, 1403–1407.

Perrimon, N., Bonini, N.M., and Dhillon, P. (2016). Fruit flies on the front line: the translational impact of *Drosophila*. *Dis Model Mech* 9, 229–231.

Perton, F., Harlepp, S., Follain, G., Parkhomenko, K., Goetz, J.G., Bégin-Colin, S., and Mertz, D. (2019). Wrapped stellate silica nanocomposites as biocompatible luminescent nanoplatforms assessed *in vivo*. *Journal of Colloid and Interface Science* 542, 469–482.

Petri, B., Kaur, J., Long, E.M., Li, H., Parsons, S.A., Butz, S., Phillipson, M., Vestweber, D., Patel, K.D., Robbins, S.M., et al. (2011). Endothelial LSP1 is involved in endothelial dome formation, minimizing vascular permeability changes during neutrophil transmigration *in vivo*. *Blood* 117, 942–952.

Phillipson, M., Kaur, J., Colarusso, P., Ballantyne, C.M., and Kubis, P. (2008). Endothelial Domes Encapsulate Adherent Neutrophils and Minimize Increases in Vascular Permeability in Paracellular and Transcellular Emigration. *PLOS ONE* 3, e1649.

Piskounova, E., Agathocleous, M., Murphy, M.M., Hu, Z., Huddlestun, S.E., Zhao, Z., Leitch, A.M., Johnson, T.M., DeBerardinis, R.J., and Morrison, S.J. (2015). Oxidative stress inhibits distant metastasis by human melanoma cells. *Nature* 527, 186–191.

Pitti, R.M., Marsters, S.A., Lawrence, D.A., Roy, M., Kischkel, F.C., Dowd, P., Huang, A., Donahue, C.J., Sherwood, S.W., Baldwin, D.T., et al. (1998). Genomic amplification of a decoy receptor for Fas ligand in lung and colon cancer. *Nature* 396, 699–703.

Plaks, V., Kong, N., and Werb, Z. (2015). The cancer stem cell niche: how essential is the niche in regulating stemness of tumor cells? *Cell Stem Cell* 16, 225–238.

Polzer, B., Medoro, G., Pasch, S., Fontana, F., Zorzino, L., Pestka, A., Andergassen, U., Meier-Stiegen, F., Czyz, Z.T., Alberter, B., et al. (2014). Molecular profiling of single circulating tumor cells with diagnostic intention. *EMBO Mol Med* 6, 1371–1386.

Ponta, H., Sherman, L., and Herrlich, P.A. (2003). CD44: From adhesion molecules to signalling regulators. *Nat Rev Mol Cell Biol* 4, 33–45.

Poprac, P., Jomova, K., Simunkova, M., Kollar, V., Rhodes, C.J., and Valko, M. (2017). Targeting Free Radicals in Oxidative Stress-Related Human Diseases. *Trends in Pharmacological Sciences* 38, 592–607.

Potente, M., Gerhardt, H., and Carmeliet, P. (2011). Basic and therapeutic aspects of angiogenesis. *Cell* 146, 873–887.

Puklin-Faucher, E., and Sheetz, M.P. (2009). The mechanical integrin cycle. *Journal of Cell Science* 122, 179–186.

Quail, D.F., and Joyce, J.A. (2013). Microenvironmental regulation of tumor progression and metastasis. *Nat. Med.* 19, 1423–1437.

Raab, M., Gentili, M., de Belly, H., Thiam, H.R., Vargas, P., Jimenez, A.J., Lautenschlaeger, F., Voituriez, R., Lennon-Duménil, A.M., Manel, N., et al. (2016). ESCRT III repairs nuclear envelope ruptures during cell migration to limit DNA damage and cell death. *Science* 352, 359–362.

Raab-Westphal, S., Marshall, J., and Goodman, S. (2017). Integrins as Therapeutic Targets: Successes and Cancers. *Cancers* 9, 110.

Radinsky, R., and Ellis, L.M. (1996). Molecular determinants in the biology of liver metastasis. *Surg. Oncol. Clin. N. Am.* 5, 215–229.

Raghavan, V., Rbaibi, Y., Pastor-Soler, N.M., Carattino, M.D., and Weisz, O.A. (2014). Shear stress-dependent regulation of apical endocytosis in renal proximal tubule cells mediated by primary cilia. *PNAS* 111, 8506–8511.

Raposo, G., and Stoorvogel, W. (2013). Extracellular vesicles: Exosomes, microvesicles, and friends. *J Cell Biol* 200, 373–383.

Reeves, M.Q., Kandyba, E., Harris, S., Del Rosario, R., and Balmain, A. (2018). Multicolour lineage tracing reveals clonal dynamics of squamous carcinoma evolution from initiation to metastasis. *Nat Cell Biol* 20, 699–709.

Reglero-Real, N., Marcos-Ramiro, B., and Millán, J. (2012). Endothelial membrane reorganization during leukocyte extravasation. *Cell. Mol. Life Sci.* 69, 3079–3099.

Regmi, S., Fu, A., and Luo, K.Q. (2017). High Shear Stresses under Exercise Condition Destroy Circulating Tumor Cells in a Microfluidic System. *Scientific Reports* 7, 39975.

Regmi, S., Fung, T.S., Lim, S., and Luo, K.Q. (2018). Fluidic shear stress increases the anti-cancer effects of ROS-generating drugs in circulating tumor cells. *Breast Cancer Res. Treat.* 172, 297–312.

Rehfeldt, F., and Schmidt, C.F. (2017). Physical probing of cells. *J. Phys. D: Appl. Phys.* *50*, 463001.

Reiss, Y., and Engelhardt, B. (1999). T cell interaction with ICAM-1-deficient endothelium *in vitro*: transendothelial migration of different T cell populations is mediated by endothelial ICAM-1 and ICAM-2. *Int. Immunol.* *11*, 1527–1539.

Rejniak, K.A. (2012). Investigating dynamical deformations of tumor cells in circulation: predictions from a theoretical model. *Front Oncol* *2*, 111.

Reisman, D.N., Strobeck, M.W., Betz, B.L., Sciariotta, J., Funkhouser, W., Murchardt, C., Yaniv, M., Sherman, L.S., Knudsen, E.S., and Weissman, B.E. (2002). Concomitant down-regulation of BRM and BRG1 in human tumor cell lines: differential effects on RB-mediated growth arrest vs CD44 expression. *Oncogene* *21*, 1196–1207.

Resnick, M.A., Tomso, D., Inga, A., Menendez, D., and Bell, D. (2005). Functional diversity in the gene network controlled by the master regulator p53 in humans. *Cell Cycle* *4*, 1026–1029.

Reymond, N., Im, J.H., Garg, R., Vega, F.M., Borda d'Agua, B., Riou, P., Cox, S., Valderrama, F., Muschel, R.J., and Ridley, A.J. (2012). Cdc42 promotes transendothelial migration of cancer cells through β 1 integrin. *J Cell Biol* *199*, 653–668.

Reymond, N., d'Água, B.B., and Ridley, A.J. (2013). Crossing the endothelial barrier during metastasis. *Nat Rev Cancer* *13*, 858–870.

Ribatti, D. (2014). The chick embryo chorioallantoic membrane as a model for tumor biology. *Experimental Cell Research* *328*, 314–324.

Roca-Cusachs, P., Gauthier, N.C., del Rio, A., and Sheetz, M.P. (2009). Clustering of 5 1 integrins determines adhesion strength whereas v 3 and talin enable mechanotransduction. *Proceedings of the National Academy of Sciences* *106*, 16245–16250.

Roussos, E.T., Balsamo, M., Alford, S.K., Wyckoff, J.B., Gligorijevic, B., Wang, Y., Pozzuto, M., Stobezki, R., Goswami, S., Segall, J.E., et al. (2011). Mena invasive (MenaINV) promotes multicellular streaming motility and transendothelial migration in a mouse model of breast cancer. *Journal of Cell Science* *124*, 2120–2131.

Rowe, R.G., and Weiss, S.J. (2008). Breaching the basement membrane: who, when and how? *Trends Cell Biol.* *18*, 560–574.

Rubashkin, M.G., Cassereau, L., Bainer, R., DuFort, C.C., Yui, Y., Ou, G., Paszek, M.J., Davidson, M.W., Chen, Y.-Y., and Weaver, V.M. (2014). Force Engages Vinculin and Promotes Tumor Progression by Enhancing PI3K Activation of Phosphatidylinositol (3,4,5)-Triphosphate. *Cancer Res* *74*, 4597–4611.

Rudner, L.A., Brown, K.H., Dobrinski, K.P., Bradley, D.F., Garcia, M.I., Smith, A.C.H., Downie, J.M., Meeker, N.D., Look, A.T., Downing, J.R., et al. (2011). Shared acquired genomic changes in zebrafish and human T-ALL. *Oncogene* *30*, 4289–4296.

Sahai, E., and Marshall, C.J. (2002). ROCK and Dia have opposing effects on adherens junctions downstream of Rho. *Nat. Cell Biol.* *4*, 408–415.

Sajovic, P., and Levinthal, C. (1982). Visual response properties of zebrafish tectal cells. *Neuroscience* *7*, 2427–2440.

Schaefer, A., and Hordijk, P.L. (2015). Cell-stiffness-induced mechanosignaling - a key driver of leukocyte transendothelial migration. *Journal of Cell Science* *128*, 2221–2230.

Schaefer, A., Riet, J. te, Ritz, K., Hoogenboezem, M., Anthony, E.C., Mul, F.P.J., Vries, C.J. de, Daemen, M.J., Figdor, C.G., Buul, J.D. van, et al. (2014). Actin-binding proteins differentially regulate endothelial cell stiffness, ICAM-1 function and neutrophil transmigration. *J Cell Sci* *127*, 4470–4482.

Scherbarth, S., and Orr, F.W. (1997). Intravital videomicroscopic evidence for regulation of metastasis by the hepatic microvasculature: effects of interleukin-1alpha on metastasis and the location of B16F1 melanoma cell arrest. *Cancer Res.* 57, 4105–4110.

Schwingel, M., and Bastmeyer, M. (2013). Force Mapping during the Formation and Maturation of Cell Adhesion Sites with Multiple Optical Tweezers. *PLOS ONE* 8, e54850.

Sell, S. (2005). Leukemia: stem cells, maturation arrest, and differentiation therapy. *Stem Cell Rev* 1, 197–205.

Senger, D.R., Perruzzi, C.A., Feder, J., and Dvorak, H.F. (1986). A highly conserved vascular permeability factor secreted by a variety of human and rodent tumor cell lines. *Cancer Res.* 46, 5629–5632.

Shaw, R.J. (2009). Tumor suppression by LKB1: SIK-ness prevents metastasis. *Sci Signal* 2, pe55.

Shay, J.W., and Bacchetti, S. (1997). A survey of telomerase activity in human cancer. *Eur. J. Cancer* 33, 787–791.

Shea, D.J., Li, Y.W., Stebe, K.J., and Konstantopoulos, K. (2017). E-selectin-mediated rolling facilitates pancreatic cancer cell adhesion to hyaluronic acid. *The FASEB Journal* 31, 5078–5086.

Sherwood, D.R., and Sternberg, P.W. (2003). Anchor Cell Invasion into the Vulval Epithelium in *C. elegans*. *Developmental Cell* 5, 21–31.

Shibue, T., Brooks, M.W., Inan, M.F., Reinhardt, F., and Weinberg, R.A. (2012). The outgrowth of micrometastases is enabled by the formation of filopodium-like protrusions. *Cancer Discov* 2, 706–721.

Shibue, T., Brooks, M.W., and Weinberg, R.A. (2013). An integrin-linked machinery of cytoskeletal regulation that enables experimental tumor initiation and metastatic colonization. *Cancer Cell* 24.

Shields, J.D., Kourtis, I.C., Tomei, A.A., Roberts, J.M., and Swartz, M.A. (2010). Induction of lymphoidlike stroma and immune escape by tumors that express the chemokine CCL21. *Science* 328, 749–752.

Shive, H.R., West, R.R., Embree, L.J., Azuma, M., Sood, R., Liu, P., and Hickstein, D.D. (2010). brca2 in zebrafish ovarian development, spermatogenesis, and tumorigenesis. *Proc. Natl. Acad. Sci. U.S.A.* 107, 19350–19355.

Shtivelman, E., and Bishop, J.M. (1993). The human gene AHNAK encodes a large phosphoprotein located primarily in the nucleus. *J. Cell Biol.* 120, 625–630.

Siegelman, M.H., Stanescu, D., and Estess, P. (2000). The CD44-initiated pathway of T-cell extravasation uses VLA-4 but not LFA-1 for firm adhesion. *J. Clin. Invest.* 105, 683–691.

Simon, S.I., and Green, C.E. (2005). Molecular mechanics and dynamics of leukocyte recruitment during inflammation. *Annu Rev Biomed Eng* 7, 151–185.

Simon, S.I., Hu, Y., Vestweber, D., and Smith, C.W. (2000). Neutrophil tethering on E-selectin activates beta 2 integrin binding to ICAM-1 through a mitogen-activated protein kinase signal transduction pathway. *J. Immunol.* 164, 4348–4358.

Sinkus, R., Lorenzen, J., Schrader, D., Lorenzen, M., Dargatz, M., and Holz, D. (2000). High-resolution tensor MR elastography for breast tumour detection. *Phys Med Biol* 45, 1649–1664.

Slamon, D.J., Clark, G.M., Wong, S.G., Levin, W.J., Ullrich, A., and McGuire, W.L. (1987). Human breast cancer: correlation of relapse and survival with amplification of the HER-2/neu oncogene. *Science* 235, 177–182.

Sonoshita, M., Aoki, M., Fuwa, H., Aoki, K., Hosogi, H., Sakai, Y., Hashida, H., Takabayashi, A., Sasaki, M., Robine, S., et al. (2011). Suppression of Colon Cancer Metastasis by Aes through Inhibition of Notch Signaling. *Cancer Cell* 19, 125–137.

Sonoshita, M., and Cagan, R.L. (2017). Modeling Human Cancers in Drosophila. In *Current Topics in Developmental Biology*, (Elsevier), pp. 287–309.

Sontheimer-Phelps, A., Hassell, B.A., and Ingber, D.E. (2019). Modelling cancer in microfluidic human organs-on-chips. *Nat Rev Cancer* 19, 65–81.

Spaderna, S., Schmalhofer, O., Hlubek, F., Berx, G., Eger, A., Merkel, S., Jung, A., Kirchner, T., and Brabletz, T. (2006). A Transient, EMT-Linked Loss of Basement Membranes Indicates Metastasis and Poor Survival in Colorectal Cancer. *Gastroenterology* 131, 830–840.

Spicer, J.D., McDonald, B., Cools-Lartigue, J.J., Chow, S.C., Giannias, B., Kubes, P., and Ferri, L.E. (2012). Neutrophils Promote Liver Metastasis via Mac-1–Mediated Interactions with Circulating Tumor Cells. *Cancer Res* 72, 3919–3927.

Spitsbergen, J.M., Tsai, H.W., Reddy, A., Miller, T., Arbogast, D., Hendricks, J.D., and Bailey, G.S. (2000). Neoplasia in zebrafish (*Danio rerio*) treated with N-methyl-N'-nitro-N-nitrosoguanidine by three exposure routes at different developmental stages. *Toxicol Pathol* 28, 716–725.

Stainier, D.Y., Fouquet, B., Chen, J.-N., Warren, K.S., Weinstein, B.M., Meiler, S.E., Mohideen, M.A., Neuhauss, S.C., Solnica-Krezel, L., Schier, A.F., et al. (1996). Mutations affecting the formation and function of the cardiovascular system in the zebrafish embryo. *Development* 123, 285–292.

Stanton, M.F. (1965). Diethylnitrosamine-Induced Hepatic Degeneration and Neoplasia in the Aquarium Fish, *Brachydanio rerio*. *J Natl Cancer Inst* 34, 117–130.

Steeg, P.S. (2006). Tumor metastasis: mechanistic insights and clinical challenges. *Nat Med* 12, 895–904.

Stegmaier, J., Amat, F., Lemon, W.C., McDole, K., Wan, Y., Teodoro, G., Mikut, R., and Keller, P.J. (2016). Real-Time Three-Dimensional Cell Segmentation in Large-Scale Microscopy Data of Developing Embryos. *Developmental Cell* 36, 225–240.

Steinbauer, M., Guba, M., Cernaianu, G., Köhl, G., Cetto, M., Kunz-Schughart, L.A., Geissler, E.K., Falk, W., and Jauch, K.-W. (2003). GFP-transfected tumor cells are useful in examining early metastasis *in vivo*, but immune reaction precludes long-term tumor development studies in immunocompetent mice. *Clin. Exp. Metastasis* 20, 135–141.

Stoletov, K., Montel, V., Lester, R.D., Gonias, S.L., and Klemke, R. (2007). High-resolution imaging of the dynamic tumor cell–vascular interface in transparent zebrafish. *PNAS* 104, 17406–17411.

Stoletov, K., Kato, H., Zardouzian, E., Kelber, J., Yang, J., Shattil, S., and Klemke, R. (2010). Visualizing extravasation dynamics of metastatic tumor cells. *J Cell Sci* 123, 2332–2341.

Streisinger, G., Walker, C., Dower, N., Knauber, D., and Singer, F. (1981). Production of clones of homozygous diploid zebra fish (*Brachydanio rerio*). *Nature* 291, 293–296.

Strell, C., and Entschladen, F. (2008). Extravasation of leukocytes in comparison to tumor cells. *Cell Commun Signal* 6, 10.

Strell, C., Lang, K., Niggemann, B., Zaenker, K.S., and Entschladen, F. (2007). Surface molecules regulating rolling and adhesion to endothelium of neutrophil granulocytes and MDA-MB-468 breast carcinoma cells and their interaction. *Cellular and Molecular Life Sciences* 64, 3306–3316.

Streuli, C.H., Bailey, N., and Bissell, M.J. (1991). Control of mammary epithelial differentiation: basement membrane induces tissue-specific gene expression in the absence of cell-cell interaction and morphological polarity. *J. Cell Biol.* 115, 1383–1395.

Strilic, B., Yang, L., Albarrán-Juárez, J., Wachsmuth, L., Han, K., Müller, U.C., Pasparakis, M., and Offermanns, S. (2016). Tumour-cell-induced endothelial cell necroptosis via death receptor 6 promotes metastasis. *Nature* 536, 215–218.

Stuelten, C.H., Parent, C.A., and Montell, D.J. (2018). Cell motility in cancer invasion and metastasis: insights from simple model organisms. *Nat Rev Cancer* 18, 296–312.

Stylianopoulos, T., Martin, J.D., Chauhan, V.P., Jain, S.R., Diop-Frimpong, B., Bardeesy, N., Smith, B.L., Ferrone, C.R., Hor nicek, F.J., Boucher, Y., et al. (2012). Causes, consequences, and remedies for growth-induced solid stress in murine and human tumors. *PNAS* 109, 15101–15108.

Swartz, M.A., and Fleury, M.E. (2007). Interstitial Flow and Its Effects in Soft Tissues. *Annu. Rev. Biomed. Eng.* 9, 229–256.

Szauter, K.M., Cao, T., Boyd, C.D., and Csiszar, K. (2005). Lysyl oxidase in development, aging and pathologies of the skin. *Pathol. Biol.* 53, 448–456.

Szczerba, B.M., Castro-Giner, F., Vetter, M., Krol, I., Gkountela, S., Landin, J., Scheidmann, M.C., Donato, C., Scherrer, R., Singer, J., et al. (2019). Neutrophils escort circulating tumour cells to enable cell cycle progression. *Nature* 566, 553–557.

Takayama, S., Ostuni, E., LeDuc, P., Naruse, K., Ingber, D.E., and Whitesides, G.M. (2003). Selective Chemical Treatment of Cellular Microdomains Using Multiple Laminar Streams. *Chemistry & Biology* 10, 123–130.

Tarin, D., Price, J.E., Kettlewell, M.G.W., Souter, R.G., Vass, A.C.R., and Crossley, B. (1984). Mechanisms of Human Tumor Metastasis Studied in Patients with Peritoneovenous Shunts. 10.

Taubenberger, A.V., Girardo, S., Träber, N., Fischer-Friedrich, E., Kräter, M., Wagner, K., Kurth, T., Richter, I., Haller, B., Binner, M., et al. (2019). 3D microenvironment stiffness regulates tumor spheroid growth and mechanics via p21 and ROCK. *BioRxiv* 586784.

Terasaki, M., Miyake, K., and McNeil, P.L. (1997). Large plasma membrane disruptions are rapidly resealed by Ca²⁺-dependent vesicle–vesicle fusion events. *The Journal of Cell Biology* 139, 63–74.

Thiam, H.-R., Vargas, P., Carpi, N., Crespo, C.L., Raab, M., Terriac, E., King, M.C., Jacobelli, J., Alberts, A.S., Stradal, T., et al. (2016). Perinuclear Arp2/3-driven actin polymerization enables nuclear deformation to facilitate cell migration through complex environments. *Nature Communications* 7, 10997.

Thompson, P.W., Randi, A.M., and Ridley, A.J. (2002). Intercellular adhesion molecule (ICAM)-1, but not ICAM-2, activates RhoA and stimulates c-fos and rhoA transcription in endothelial cells. *J. Immunol.* 169, 1007–1013.

Thornberry, N.A., and Lazebnik, Y. (1998). Caspases: enemies within. *Science* 281, 1312–1316.

Tirosh, I., Venteicher, A.S., Hebert, C., Escalante, L.E., Patel, A.P., Yizhak, K., Fisher, J.M., Rodman, C., Mount, C., Filbin, M.G., et al. (2016). Single-cell RNA-seq supports a developmental hierarchy in human oligodendrogloma. *Nature* 539, 309–313.

Tkach, M., and Théry, C. (2016). Communication by Extracellular Vesicles: Where We Are and Where We Need to Go. *Cell* 164, 1226–1232.

Tözeren, A., Kleinman, H.K., Grant, D.S., Morales, D., Mercurio, A.M., and Byers, S.W. (1995). E-selectin-mediated dynamic interactions of breast- and colon-cancer cells with endothelial-cell monolayers. *Int. J. Cancer* 60, 426–431.

Treutlein, B., Brownfield, D.G., Wu, A.R., Neff, N.F., Mantalas, G.L., Espinoza, F.H., Desai, T.J., Krasnow, M.A., and Quake, S.R. (2014). Reconstructing lineage hierarchies of the distal lung epithelium using single-cell RNA-seq. *Nature* 509, 371–375.

Tsukita, S., Oishi, K., Sato, N., Sagara, J., Kawai, A., and Tsukita, S. (1994). ERM family members as molecular linkers between the cell surface glycoprotein CD44 and actin-based cytoskeletons. *J. Cell Biol.* 126, 391–401.

Vajdic, C.M., and van Leeuwen, M.T. (2009). Cancer incidence and risk factors after solid organ transplantation. *Int. J. Cancer* 125, 1747–1754.

Valastyan, S., and Weinberg, R.A. (2011). Tumor Metastasis: Molecular Insights and Evolving Paradigms. *Cell* 147, 275–292.

Vander Heiden, M.G., Cantley, L.C., and Thompson, C.B. (2009). Understanding the Warburg effect: the metabolic requirements of cell proliferation. *Science* 324, 1029–1033.

Varga, J., and Greten, F.R. (2017). Cell plasticity in epithelial homeostasis and tumorigenesis. *Nature Cell Biology* 19, 1133–1141.

Verweij, F.J., Revenu, C., Arras, G., Dingli, F., Loew, D., Pegtel, D.M., Follain, G., Allio, G., Goetz, J.G., Zimmermann, P., et al. (2019). Live Tracking of Inter-organ Communication by Endogenous Exosomes *In Vivo*. *Dev. Cell* 48, 573–589.e4.

Vestweber, D. (2012). Relevance of endothelial junctions in leukocyte extravasation and vascular permeability: Diapedesis and endothelial junctions. *Annals of the New York Academy of Sciences* 1257, 184–192.

Vestweber, D. (2015). How leukocytes cross the vascular endothelium. *Nature Reviews Immunology* 15, 692–704.

Visvader, J.E. (2011). Cells of origin in cancer. *Nature* 469, 314–322.

Vlodavsky, I., Ariav, Y., Atzmon, R., and Fuks, Z. (1982). Tumor cell attachment to the vascular endothelium and subsequent degradation of the subendothelial extracellular matrix. *Exp. Cell Res.* 140, 149–159.

Vogelstein, B., Papadopoulos, N., Velculescu, V.E., Zhou, S., Diaz, L.A., and Kinzler, K.W. (2013). Cancer genome landscapes. *Science* 339, 1546–1558.

Völkel, P., Dupret, B., Bourhis, X.L., and Angrand, P.-O. (2018). Le modèle poisson zèbre dans la lutte contre le cancer. *Med Sci (Paris)* 34, 345–353.

Voura, E.B., Sandig, M., and Siu, C.H. (1998). Cell-cell interactions during transendothelial migration of tumor cells. *Microsc. Res. Tech.* 43, 265–275.

Wagenblast, E., Soto, M., Gutiérrez-Ángel, S., Hartl, C.A., Gable, A.L., Maceli, A.R., Erard, N., Williams, A.M., Kim, S.Y., Dickopf, S., et al. (2015). A model of breast cancer heterogeneity reveals vascular mimicry as a driver of metastasis. *Nature* 520, 358–362.

Walker, C., and Streisinger, G. INDUCTION OF MUTATIONS BY γ -RAYS IN PREGONIAL GERM CELLS OF ZEBRAFISH EMBRYOS. 12.

Walpita, D., and Hay, E. (2002). Studying actin-dependent processes in tissue culture. *Nat. Rev. Mol. Cell Biol.* 3, 137–141.

Wang, H.-S., Hung, Y., Su, C.-H., Peng, S.-T., Guo, Y.-J., Lai, M.-C., Liu, C.-Y., and Hsu, J.-W. (2005). CD44 cross-linking induces integrin-mediated adhesion and transendothelial migration in breast cancer cell line by up-regulation of LFA-1 (alpha L beta2) and VLA-4 (alpha4beta1). *Exp. Cell Res.* 304, 116–126.

Warren, S.C., Nobis, M., Magenau, A., Mohammed, Y.H., Herrmann, D., Moran, I., Vennin, C., Conway, J.R., Mélénec, P., Cox, T.R., et al. (2018). Removing physiological motion from intravital and clinical functional imaging data. *ELife* 7, e35800.

Watanabe, T., Okumura, T., Hirano, K., Yamaguchi, T., Sekine, S., Nagata, T., and Tsukada, K. (2017). Circulating tumor cells expressing cancer stem cell marker CD44 as a diagnostic biomarker in patients with gastric cancer. *Oncol Lett* 13, 281–288.

Weber, G.F., Ashkar, S., Glimcher, M.J., and Cantor, H. (1996). Receptor-ligand interaction between CD44 and osteopontin (Eta-1). *Science* 271, 509–512.

Weinbaum, S., Tarbell, J.M., and Damiano, E.R. (2007). The structure and function of the endothelial glycocalyx layer. *Annu Rev Biomed Eng* 9, 121–167.

Weinberg, R.A. (1995). The retinoblastoma protein and cell cycle control. *Cell* 81, 323–330.

Weis, J.S. (1958). Analysis of the development of the nervous system of the zebrafish, *Brachydanio rerio*. 13.

Weis, S., Cui, J., Barnes, L., and Cheresh, D. (2004). Endothelial barrier disruption by VEGF-mediated Src activity potentiates tumor cell extravasation and metastasis. *The Journal of Cell Biology* 167, 223–229.

Weiss, L. (1992). Comments on hematogenous metastatic patterns in humans as revealed by autopsy. *Clin. Exp. Metastasis* 10, 191–199.

Weiss, L. (2000). Patterns of metastasis. *Cancer and Metastasis Reviews* 19, 281–301.

van Wely, C.A., Beverley, P.C., Brett, S.J., Britten, C.J., and Tite, J.P. (1999). Expression of L-selectin on Th1 cells is regulated by IL-12. *J. Immunol.* 163, 1214–1221.

Westerfield, M., Doerry, E., and Douglas, S. (1999). Zebrafish in the Net. *Trends in Genetics* 15, 248–249.

White, D.E., Kurpios, N.A., Zuo, D., Hassell, J.A., Blaess, S., Mueller, U., and Muller, W.J. (2004). Targeted disruption of beta1-integrin in a transgenic mouse model of human breast cancer reveals an essential role in mammary tumor induction. *Cancer Cell* 6, 159–170.

White, R., Rose, K., and Zon, L. (2013). Zebrafish cancer: the state of the art and the path forward. *Nat. Rev. Cancer* 13, 624–636.

White, R.M., Sessa, A., Burke, C., Bowman, T., LeBlanc, J., Ceol, C., Bourque, C., Dovey, M., Goessling, W., Burns, C.E., et al. (2008). Transparent Adult Zebrafish as a Tool for *In Vivo* Transplantation Analysis. *Cell Stem Cell* 2, 183–189.

Wielenga, V.J., Heider, K.H., Offerhaus, G.J., Adolf, G.R., van den Berg, F.M., Ponta, H., Herrlich, P., and Pals, S.T. (1993). Expression of CD44 variant proteins in human colorectal cancer is related to tumor progression. *Cancer Res.* 53, 4754–4756.

Williams, K.C., Cepeda, M.A., Javed, S., Searle, K., Parkins, K.M., Makela, A.V., Hamilton, A.M., Soukhtehzari, S., Kim, Y., Tuck, A.B., et al. (2019). Invadopodia are chemosensing protrusions that guide cancer cell extravasation to promote brain tropism in metastasis. *Oncogene*.

Williams, S., Wasserman, S., W Rawlinson, D., I Kitney, R., H Smaje, L., and E Tooke, J. (1988). Dynamic measurement of human capillary pressure. *Clinical Science (London, England : 1979)* 74, 507–512.

Wirtz, D., Konstantopoulos, K., and Searson, P.C. (2011). The physics of cancer: the role of physical interactions and mechanical forces in metastasis. *Nature Reviews Cancer* 11, 512–522.

Wolf, K., Lindert, M. te, Krause, M., Alexander, S., Riet, J. te, Willis, A.L., Hoffman, R.M., Figdor, C.G., Weiss, S.J., and Friedl, P. (2013). Physical limits of cell migration: Control by ECM space and nuclear deformation and tuning by proteolysis and traction force. *J Cell Biol* 201, 1069–1084.

Woroniuk, A., Porter, A., White, G., Newman, D.T., Diamantopoulou, Z., Waring, T., Rooney, C., Strathdee, D., Marston, D.J., Hahn, K.M., et al. (2018). STEF/TIAM2-mediated Rac1 activity at the nuclear envelope regulates the perinuclear actin cap. *Nature Communications* 9, 2124.

Wu, L., Zhou, B., Oshiro-Rapley, N., Li, M., Paulo, J.A., Webster, C.M., Mou, F., Kacergis, M.C., Talkowski, M.E., Carr, C.E., et al. (2016). An Ancient, Unified Mechanism for Metformin Growth Inhibition in *C. elegans* and Cancer. *Cell* 167, 1705-1718.e13.

Wullkopf, L., West, A.-K.V., Leijnse, N., Cox, T.R., Madsen, C.D., Oddershede, L.B., and Erler, J.T. (2018). Cancer cells' ability to mechanically adjust to extracellular matrix stiffness correlates with their invasive potential. *Mol. Biol. Cell* 29, 2378-2385.

Wyble, C.W., Hynes, K.L., Kuchibhotla, J., Marcus, B.C., Hallahan, D., and Gewertz, B.L. (1997). TNF- α and IL-1 Upregulate Membrane-Bound and Soluble E-Selectin through a Common Pathway. *Journal of Surgical Research* 73, 107-112.

Wyckoff, J.B., Wang, Y., Lin, E.Y., Li, J.-f., Goswami, S., Stanley, E.R., Segall, J.E., Pollard, J.W., and Condeelis, J. (2007). Direct Visualization of Macrophage-Assisted Tumor Cell Intravasation in Mammary Tumors. *Cancer Research* 67, 2649-2656.

Yan, C., Brunson, D.C., Tang, Q., Do, D., Iftimia, N.A., Moore, J.C., Hayes, M.N., Welker, A.M., Garcia, E.G., Dubash, T.D., et al. (2019). Visualizing Engrafted Human Cancer and Therapy Responses in Immunodeficient Zebrafish. *Cell* 177, 1903-1914.e14.

Yang, J., Mani, S.A., Donaher, J.L., Ramaswamy, S., Itzykson, R.A., Come, C., Savagner, P., Gitelman, I., Richardson, A., and Weinberg, R.A. (2004). Twist, a Master Regulator of Morphogenesis, Plays an Essential Role in Tumor Metastasis. *Cell* 117, 927-939.

Yang, L., Pang, Y., and Moses, H.L. (2010). TGF-beta and immune cells: an important regulatory axis in the tumor microenvironment and progression. *Trends Immunol.* 31, 220-227.

Yeh, Y.-T., Serrano, R., François, J., Chiu, J.-J., Li, Y.-S.J., Del Álamo, J.C., Chien, S., and Lasheras, J.C. (2018). Three-dimensional forces exerted by leukocytes and vascular endothelial cells dynamically facilitate diapedesis. *Proc. Natl. Acad. Sci. U.S.A.* 115, 133-138.

Yen, J., White, R.M., and Stemple, D.L. (2014). Zebrafish models of cancer: progress and future challenges. *Curr Opin Genet Dev* 24, 38-45.

Yeung, T., Georges, P.C., Flanagan, L.A., Marg, B., Ortiz, M., Funaki, M., Zahir, N., Ming, W., Weaver, V., and Janmey, P.A. (2005). Effects of substrate stiffness on cell morphology, cytoskeletal structure, and adhesion. *Cell Motil. Cytoskeleton* 60, 24-34.

Yoneda, T., Williams, P.J., Hiraga, T., Niewolna, M., and Nishimura, R. (2001). A bone-seeking clone exhibits different biological properties from the MDA-MB-231 parental human breast cancer cells and a brain-seeking clone *in vivo* and *in vitro*. *J. Bone Miner. Res.* 16, 1486-1495.

Youk, J.H., Son, E.J., Gweon, H.M., Kim, H., Park, Y.J., and Kim, J.-A. (2014). Comparison of strain and shear wave elastography for the differentiation of benign from malignant breast lesions, combined with B-mode ultrasonography: qualitative and quantitative assessments. *Ultrasound Med Biol* 40, 2336-2344.

Yuan, F., Dellian, M., Fukumura, D., Leunig, M., Berk, D.A., Torchilin, V.P., and Jain, R.K. (1995). Vascular permeability in a human tumor xenograft: molecular size dependence and cutoff size. *Cancer Res.* 55, 3752-3756.

Zaman, M.H., Trapani, L.M., Sieminski, A.L., Siemeski, A., Mackellar, D., Gong, H., Kamm, R.D., Wells, A., Lauffenburger, D.A., and Matsudaira, P. (2006). Migration of tumor cells in 3D matrices is governed by matrix stiffness along with cell-matrix adhesion and proteolysis. *Proc. Natl. Acad. Sci. U.S.A.* 103, 10889-10894.

Zervantonakis, I.K., Hughes-Alford, S.K., Charest, J.L., Condeelis, J.S., Gertler, F.B., and Kamm, R.D. (2012). Three-dimensional microfluidic model for tumor cell intravasation and endothelial barrier function. *PNAS* *109*, 13515–13520.

Zhao, Q., Barclay, M., Hilkens, J., Guo, X., Barrow, H., Rhodes, J.M., and Yu, L.-G. (2010). Interaction between circulating galectin-3 and cancer-associated MUC1 enhances tumour cell homotypic aggregation and prevents anoikis. *Molecular Cancer* *9*, 154.

Zheng, Y., Miyamoto, D.T., Wittner, B.S., Sullivan, J.P., Aceto, N., Jordan, N.V., Yu, M., Karabacak, N.M., Comaills, V., Morris, R., et al. (2017). Expression of β -globin by cancer cells promotes cell survival during blood-borne dissemination. *Nature Communications* *8*, 14344.

Zhong, M.-C., Wei, X.-B., Zhou, J.-H., Wang, Z.-Q., and Li, Y.-M. (2013). Trapping red blood cells in living animals using optical tweezers. *Nat Commun* *4*, 1768.

Zhu, S., Lee, J.-S., Guo, F., Shin, J., Perez-Atayde, A.R., Kutok, J.L., Rodig, S.J., Neuberg, D.S., Helman, D., Feng, H., et al. (2012). Activated ALK collaborates with MYCN in neuroblastoma pathogenesis. *Cancer Cell* *21*, 362–373.

Zöller, M. (2011). CD44: can a cancer-initiating cell profit from an abundantly expressed molecule? *Nat Rev Cancer* *11*, 254–267.

ANNEXES

**ANNEX 1: SEEING IS BELIEVING – MULTI-SCALE SPATIO-TEMPORAL IMAGING
TOWARDS *IN VIVO* CELL BIOLOGY**

SPECIAL ISSUE: 3D CELL BIOLOGY

COMMENTARY

Seeing is believing – multi-scale spatio-temporal imaging towards *in vivo* cell biology

Gautier Follain^{1,2,3,4,*}, Luc Mercier^{1,2,3,4,*}, Naël Osmani^{1,2,3,4,*}, Sébastien Harlepp^{2,5,6,*} and Jacky G. Goetz^{1,2,3,4,‡}

ABSTRACT

Life is driven by a set of biological events that are naturally dynamic and tightly orchestrated from the single molecule to entire organisms. Although biochemistry and molecular biology have been essential in deciphering signaling at a cellular and organismal level, biological imaging has been instrumental for unraveling life processes across multiple scales. Imaging methods have considerably improved over the past decades and now allow to grasp the inner workings of proteins, organelles, cells, organs and whole organisms. Not only do they allow us to visualize these events in their most-relevant context but also to accurately quantify underlying biomechanical features and, so, provide essential information for their understanding. In this Commentary, we review a palette of imaging (and biophysical) methods that are available to the scientific community for elucidating a wide array of biological events. We cover the most-recent developments in intravital imaging, light-sheet microscopy, super-resolution imaging, and correlative light and electron microscopy. In addition, we illustrate how these technologies have led to important insights in cell biology, from the molecular to the whole-organism resolution. Altogether, this review offers a snapshot of the current and state-of-the-art imaging methods that will contribute to the understanding of life and disease.

KEY WORDS: Cell biology, Imaging, *In vivo* imaging, 1PEM, 2PEM, CLEM, LSF, SIM, SPIM, STED microscopy

Introduction

Understanding complex and integrated cellular behaviors can be performed at various levels. The post-genomic era led to the development of numerous ‘omics’ efforts with the ambitious goal of predicting and, thereby, anticipating the treatment of clinical phenotypes by integrating multi-scale information from the patient. This concept of personalized and precision medicine faces the challenge to integrate the extremely large amount of available ‘omics’ biomedical data for the development of personalized treatments to cure patients in a routine day-to-day clinical practice. Cell biology is playing a main role in the understanding of clinical phenotype at a cellular scale. Performing *in vivo* cell biology aims to understand a disease at a subcellular scale and to integrate this information into the wider context of a tissue or an organ. Although

multi-omic approaches can grasp snapshots of a disease at multiple scales, they are often restricted to a selected time-point that does not fully represent the dynamics of cells and tissues. Thanks to the recent development of fast and high-resolution imaging approaches, *in vivo* models, gene editing, cell and biomaterial engineering, as well as high-throughput procedures, it is now possible to probe and understand – at multiple scales – the link between subcellular phenomenon and cell phenotype, both in normal or pathophysiological contexts. Because pathologies often emanate from subcellular and dynamic events that are then integrated in tissues, access to the full cellular organization is required, in 3D and in real-time, and within its most relevant context.

In this Commentary, we aim to provide a snapshot of existing as well as recent developments in live-cell imaging, which now makes the concept of *in vivo* cell biology a reachable target. Here, *in vivo* refers to imaging performed in whole living animals. Because animal models are central in understanding cellular phenotypes that are essential to development or disease progression, we start by summarizing the basics of intravital imaging, which aims to visualize an event of interest in its most representative biological context. We particularly emphasize recent developments in nonlinear microscopy, which offers means to image cellular and micro-environmental behaviors in a non-invasive manner. Because phototoxicity is an important criterium in performing live *in vivo* cell biology, we then summarize the recent development and latest improvements in light-sheet microscopy, which offers unprecedented information at the organismal scale for small animals. Cell biology is tightly linked to biomechanics and has led to the emergence of a widespread concept of mechanobiology that aims to unravel the contribution of mechanical forces to biological events and disease. We thus also provide a glimpse of the existing biophysical methods that can be applied to *in vivo* cell biology and highlight some of their applications (see Box 1). We continue by describing the recent developments in super-resolution imaging and illustrate the recent developments with some biological applications that clearly suggest that *in vivo* super-resolution can be reached within the next few years. Finally, because the highest resolution can still not be obtained on living animals, we conclude by discussing the recent progress made in correlative light and electron microscopy (CLEM), including in the area of intravital correlative microscopy, which offers access to high-resolution imaging of cellular events *in vivo*. We also provide a summary table that, for each technology, lists the advantages and limitations, the resolution that can be achieved, the technical difficulties and the key applications in cell biology (Table 1).

Intravital imaging – tracking biological events *in vivo* within higher organisms

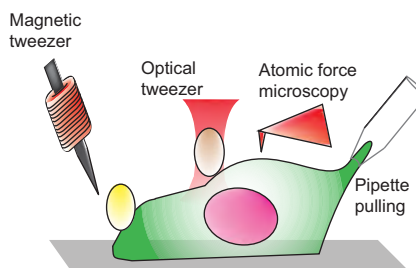
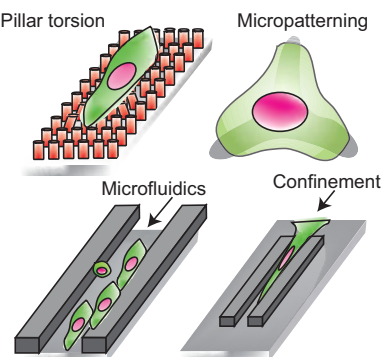
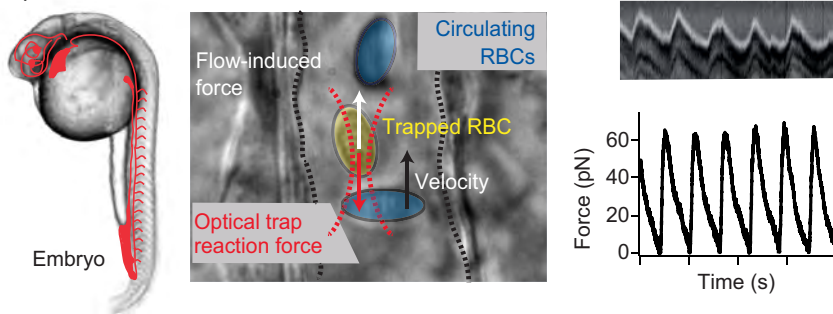
Dynamic visualization of biological processes in their natural environment is an important challenge for cell biologists. There is an obvious difference between the thickness of samples that are

¹Microenvironmental Niche in Tumorigenesis and Targeted Therapy, Inserm U1109, MN3T, Strasbourg F-67200, France. ²Université de Strasbourg, Strasbourg F-67000, France. ³LabEx Medalis, Université de Strasbourg, Strasbourg, F-67000, France. ⁴Fédération de Médecine Translationnelle de Strasbourg (FMTS), Strasbourg F-67000, France. ⁵DON: Optique ultrarapide et nanophotonique, IPCMS UMR7504, Strasbourg 67000, France. ⁶LabEx NIE, Université de Strasbourg, Strasbourg F-67000, France.

*These authors contributed equally to this work

†Author for correspondence (jacky.goetz@inserm.fr)

‡J.G.G., 0000-0003-2842-8116

Box 1. A snapshot of the available biophysical tools for assessing cellular forces**A Manipulating tools****B Micropatterning tools****C Optical tweezers *in vivo***

In addition to imaging cell behavior, a wide palette of biophysical tools is available to cell biologists when assessing and quantifying cellular mechanical forces. Whereas these tools are mostly suited for assessing forces *in vitro* (for theoretical background, see e.g. Neuman and Nagy, 2008; Kim et al., 2009; Ahmed et al., 2015) (panels A and B), some can be applied *in vivo* and to offer detailed quantification of forces in living animals (panel C). (A) Magnetic tweezers originate from the interaction of a magnetic bead fixed to the cell membrane with a magnetic field gradient (Tanase et al., 2007; Salerno et al., 2010). Historically used *in vitro* to measure mechanical properties at the single molecule (Graves et al., 2015; Strick et al., 1996) or at the single cell level (Collins et al., 2014; Marjoram et al., 2016), magnetic tweezers have recently shown their efficacy in measuring forces *in vivo* during embryonic development (Brunet et al., 2013; Desprat et al., 2008). Optical tweezers require a strongly focused laser beam that generates a 3D trap, which behaves as a spring (Ashkin, 1997). This optical technique has originally been used for *in vitro* measurement of viscoelastic properties of single molecules (Klajner et al., 2010; Smith et al., 1996) or single cells (Ashkin and Dziedzic, 1987; Ashkin et al., 1987; Dao et al., 2003). Recently, this technique has been applied *in vivo* for quantifying cell junction elasticity (Bambardekar et al., 2015; Sugimura et al., 2016) and proepicardial cell adhesion (Peralta et al., 2013), as well as for trapping circulating blood cells, thereby addressing haemodynamic forces in zebrafish (Anton et al., 2013) and mouse (Zhong et al., 2013). In atomic force microscopy (AFM), a cantilever is transiently brought in contact with the cell surface (Tartibí et al., 2015), cell nuclei (Lanzicher et al., 2015), or biological material such as cell-derived matrices (Tello et al., 2016). The analysis of its deflection over contact is linked to the exerted force and the mechanical response of the cell, which are mostly viscoelastic (Young modulus and viscosity). Even though this contact technique is mostly adapted to *in vitro* samples obtained either through cell culture (Kuznetsova et al., 2007; Ossola et al., 2015) or biopsies (Plodinec et al., 2012), AFM can be also used *in vivo*; for example, in mouse blood vessels (Mao et al., 2009). Micropipette pulling consists in locally aspirating the cell through a microforged pipette and in following the deformation for single cells (Guilak et al., 2000; Hochmuth, 2000; Chivukula et al., 2015) or for clusters of cells (Guevorkian et al., 2010, 2011). Traction force microscopy (Schwarz and Soiné, 2015) and pillar deformation (Khare et al., 2015) use calibrated soft substrates. Upon spreading, cells exert forces, which subsequently deform the substrate; these deformations inform about the localization and the amount of applied forces (Balaban et al., 2001; Gupta et al., 2015). (B) The development of improved micropatterning approaches allows the precise assessment of how surface topography influences the behavior of intracellular organelles or the cytoskeleton (Théry et al., 2006; Versaevel et al., 2012). The fast-evolving field of microfluidics has recently been used to assess how fluid forces (Perrault et al., 2015; Vartanian et al., 2008), mechanical confinement (Liu et al., 2015) or topological constrictions (Raab et al., 2016; Thiam et al., 2016) influence the behavior of cells. Measuring the migration time through confined 3D geometry provides information regarding cellular migration over topological constrictions (Thiam et al., 2016). Thus, when combined with imaging approaches, these biophysical tools offer a quantitative approach to the study of biomechanical events. (C) Optical tweezers can be applied *in vivo* on a zebrafish embryo. Focusing the laser spot in the vasculature allows the trapping of red blood cells (RBC). Pulsatility of the blood flow is visible upon kymographic analysis of the RBC displacement in the trap. This displacement is proportional to the drag force that RBCs are subjected to.

mounted on glass slides *in vitro* and whole living organisms. Here, intravital imaging refers to *in vivo* imaging within higher organisms, such as rats and mice. However, similar technologies can be used for imaging embryos and, thereby, can exploit the advantages provided by nonlinear microscopy (see below). The main drawback of conventional widefield microscopy applied to voluminous samples

is that it is impossible to provide clear and sharp images. Indeed, imaging quality within the focal plane is highly perturbed by out-of-plane scattered light. To circumvent this problem, Marvin Minsky developed – already more than fifty years ago – the first prototype of a confocal scanning microscope (Minsky, 1961). Modern confocal microscopes work on the principle of point scanning, whereby the

Table 1. Pros and cons of current imaging technologies

	1/2PEM	LSFM	Super Resolution	CLEM
Sample type	Fixed and/or live single cells up to higher organisms (mouse, rat)	Fixed and/or live single cells to embryos (ZF, fly, etc.)	Fixed and/or live single cells to embryos (ZF, fly, etc.)	Live to fixed sample Single cells to higher organisms (mouse, rat)
Resolution	200–2 nm	Cellular to subcellular	Subcellular to single molecule	nanometer
Speed	High	High to very high	Low	Very low
Penetration	Very high when using 2PEM	High	Low	Limited by light microscopy
Data volume	Small	Large	Large for PALM/STORM Small for SIM and STED	Large
Technical difficulty	Animal handling under the microscope	Data acquisition and processing	Data processing for PALM/STORM and SIM	Finding the ROI again between imaging modalities, time-consuming
Main advantage	Most-established method, easy, versatile	Best compromise between resolution and speed ratio	Best localization (sub-diffraction limited)	Best overall resolution when combined with electron tomography
Specific feature	1PEM: Better resolution compared to widefield microscopy 2PEM: In-depth long-term imaging of mice, fluorescent imaging and label-free imaging	Long-term 3D imaging with high-speed or high 3D resolution SPIM: Multiview imaging increases 3D acquisition speed DSLM: More suitable for super-resolution technologies	STED: Increased resolution for any 1PEM and 2PEM sample compatible with confocal imaging SIM: Fast 2D and 3D sub-diffraction imaging PALM/STORM: single-molecule resolution, single-particle tracking	Compatible with any <i>in vivo</i> model Requires manpower Requires access to sophisticated EM technologies for 3DEM
Biological application	Cancer biology, developmental biology, neurosciences, stem cell biology	Cell biology, developmental biology, neurosciences	Cell biology, developmental biology, neurosciences, biophysics	Cancer biology, developmental biology, neurosciences, stem cell biology
Commercially available	Yes	Yes	Yes	No (<i>in vivo</i>), Yes (<i>in vitro</i>)

1PEM, one-photon excitation microscopy; 2PEM, two-photon excitation microscopy; 3DEM, 3-dimension electron microscopy; CLEM, correlative light and electron microscopy; DSLM, digitally scanned light-sheet microscopy; LSF, light-sheet fluorescence microscopy; PALM, photo-activated localization microscopy; ROI, region of interest; SIM, structured illumination microscopy; SPIM, single plane illumination microscopy; STED, stimulated emission depletion; STORM, stochastic optical reconstruction microscopy; ZF, zebrafish.

sample is scanned by a laser spot, i.e. confocal laser scanning microscopy (CLSM) (Fig. 1A). The emitted light from the focal plane is selected through a pinhole and optically conjugated with the focal plane before being detected on sensitive photodetectors. Although this technology has provided a tremendous amount of biological insights, it was limited by its acquisition speed, which was not sufficiently fast to capture dynamic subcellular events. Acquisition speed has recently been improved by the coupled development of resonant scanners and sensitive detectors. Accelerated acquisition regimes can also be achieved by using spinning disk confocal microscopy (SDCM). Instead of scanning the sample point-by-point, SDCM is capable of acquiring multiple points at the same time (Fig. 1A), on a charge-coupled device (CCD) camera, thus increasing the data acquisition rate. The main drawback of SDCM is the cross-talk between pinholes; this can be circumvented by increasing the inter-pinhole distance or by decreasing the out-of-focus light by using two-photon excitation

(Shimojawa et al., 2013). Both CLSM and SDCM have been ground-breaking for imaging *in vitro* as well as *in vivo*; for instance, relatively thin model systems (Fig. 1C), such as tissue explants and organoids, or small organisms, such as *Caenorhabditis elegans* (Nguyen et al., 2016) or zebrafish embryos (Kissa and Herbomel, 2010). Recent advances in CLSM have led to the development of the so-called Airyscan concept (Zeiss), whose detector array allows to efficiently collect the photons from the entire Airy diffraction image with confocal resolution owing to the intrinsic size of each detector. Thus, when coupled to ultra-sensitive detectors, Airyscan exploits an increase in photon yield to improve sensitivity, speed or resolution (<http://blogs.zeiss.com/microscopy/news/en-zeiss-lsm-880-airyscan-introducing-fast-acquisition-mode/>).

CLSM has been successfully used for imaging microcirculation in the rat brain (Villringer et al., 1994) and astrocytes in the mouse brain (Pérez-Alvarez et al., 2013). SDCM has been used to describe the recruitment of platelets in several mouse organs, including brain,

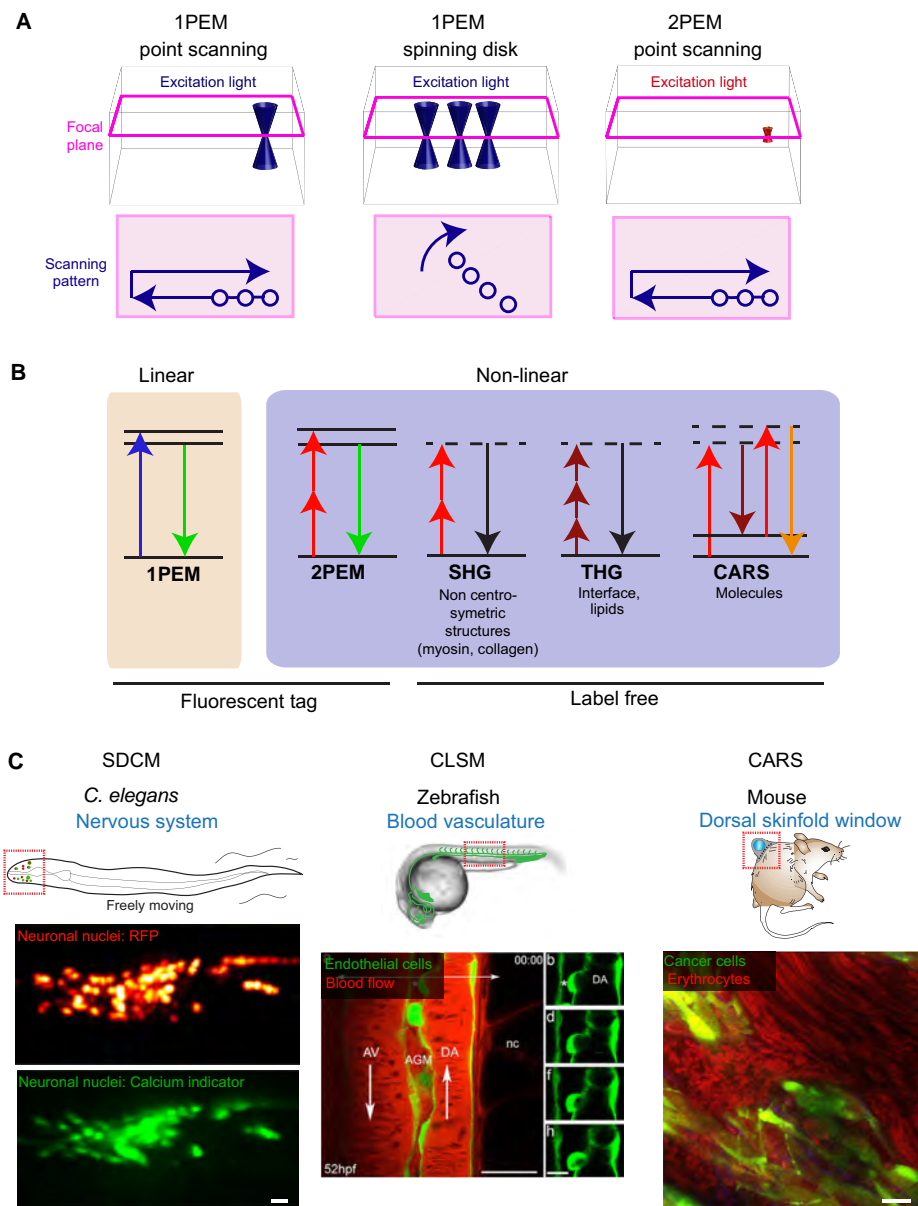


Fig. 1. Technical considerations and biological applications of intravital imaging. (A) Comparison between one-photon excitation microscopy (1PEM) and two-photon excitation microscopy (2PEM). In 1PEM, the excitation light illuminates the focus (pink line) and out-of-focus planes, and a pinhole is needed to eliminate the signal originating from the out-of-focus planes. In 2PEM, excitation occurs only at the focus plane (pink line) and a pinhole is not required because the excitation is already confocal. As shown in the illustrations at the bottom, 1PEM and 2PEM point scanning create the image of the sample by imaging one point at a time, whereas the spinning disk performs multiple acquisitions simultaneously. (B) Jablonski diagram of linear and nonlinear processes. 1PEM: the molecule is excited by absorbing a photon; after internal conversion the molecule returns to its ground state and emits a red-shifted photon. 2PEM: the molecule is excited by absorbing two photons at the same time; it returns to the ground state by emitting one photon of energy that is higher than that of the excitation photons. Second harmonic generation (SHG): two photons are scattered by a molecule and emit one photon of half the excitation wavelength. Third harmonic generation (THG): three photons are scattered by a molecule and produce one photon of a third of the excitation wavelength. Coherent anti-stokes Raman spectroscopy (CARS): a pump photon (first red arrow, pointing up) excites the molecule to a virtual state before a second photon (referred to as Stokes photon; brown arrow pointing down), forces the de-excitation of the molecule to above ground state. A third photon from the pump beam (second red arrow, pointing up) is used to elevate the molecule to a new virtual state, from which it will relax and emit a blue-shifted photon (orange arrow pointing down). (C) Biological applications of linear and nonlinear microscopy processes. Left: spinning disk confocal microscopy (SDCM) is used for ultra-fast neuronal calcium imaging in a freely moving *C. elegans*. (Red: neuronal nuclei; green: the protein calcium sensor GCaMP6s). Scale bar: 10 µm. Adapted with permission from Nguyen et al., 2016. Middle: confocal laser scanning microscope (CLSM) used for long-term (>70 h) time-lapse imaging of zebrafish vasculature, highlighting the emergence of a hematopoietic stem cell in the ventral wall of the dorsal aorta (green). Scale bars: 25 µm (left panel), 10 µm (right panel). Adapted with permission from Kissa and Herbomel, 2010. Right: multimodal nonlinear microscopy used to study tumor mass and vascularization within a skinfold dorsal chamber in mouse. Red, erythrocytes imaged by using CARS; green, cancer cells imaged by using 2PEM. Scale bar: 15 µm. Adapted with permission from Lee et al., 2015.

liver and cremaster muscle (Jenne et al., 2011). Nevertheless, most of the visible light is absorbed (Boulnois, 1986) and scattered by tissues, thus limiting depth in intravital confocal microscopy to the organ surface of an animal (<100 μm in thickness) (Masedunskas et al., 2012; see also Fig. 1C). In order to be able to image relevant biological events deeper in tissues, researchers took advantage of the optical transparency of the tissues in the near-infrared or infrared wavelengths (Boulnois, 1986) and of the discovery of pulsed lasers to develop two-photon microscopy (Helmchen and Denk, 2005), thereby making it possible to image deeper into the tissues of living animals.

Multiphoton microscopy for imaging *in vivo*

The principle of two-photon absorption was originally described in 1931 (Göppert-Mayer, 1931) but it took until 1963 for the first pulsed laser to be developed (Peticolas et al., 1963); later on, this turned into the first two-photon laser scanning microscope (Denk et al., 1990). In classic CLSM, the energy carried by a single laser photon allows the excitation of fluorophores, whereas in two-photon excitation microscopy (2PEM), each photon carries half the energy and, thus, the excitation requires the simultaneous absorption of two photons (Fig. 1B). For this purpose, the photon density has to be high, both in time (femtosecond laser pulses) and in space (through the usage of lenses with high numerical aperture). Compared to classic CLSM, 2PEM can achieve non-invasive, deep imaging in voluminous live samples owing to several properties. First, the nonlinear properties of the multiphoton absorption confine the excitation to a small volume (Fig. 1A), resulting in an enhanced signal-to-background-noise ratio and a lesser phototoxicity (Helmchen and Denk, 2005). Second, infrared light is less-well absorbed and scattered by biological tissues, and allows deeper imaging than when regular one-photon excitation (1PE) microscopy (hereafter referred to as 1PEM) is applied. Because the excitation is limited to the focal plane, the photo-toxicity typically induced by 1PEM is drastically reduced. Pinholes are not required in two-photon excitation (2PE) microscopy (hereafter referred to as 2PEM), which makes it possible to use non-descanned detectors that can be placed closer to the sample, thereby enhancing the signal. Together, these advantages allow imaging of biological phenomena that take place deep within a living organism. For example, 2PEM can easily image through the skin of living mice, and has been used for tracking xenografted cancer cells and their immune responses in mouse ear skin (Li et al., 2012), and for tracking features of muscle diseases in neuromuscular junctions (Mercier et al., 2016). Skin pigmentation can be – owing to light absorption – a major barrier in optimized imaging, and imaging windows have been developed for rodents to reach the deeper organs. This technique has been particularly useful in cancer biology for the imaging of subcutaneous tumors (using the dorsal skin-fold chamber), lungs (Headley et al., 2016), brain (Kienast et al., 2010) and abdominal organs, such as the intestine (Ritsma et al., 2014) or the liver (Ritsma et al., 2012), as well as mammary tumors (Zomer et al., 2015). Although regular 2PEM allows penetration of up to 1 mm into tissues (Theer et al., 2003), improved imaging depths through scattering tissues (the heterogeneity of biological tissues leads to photon absorption and re-direction, without any loss in energy, that can create imaging artifacts) can be obtained by increasing the wavelength of excitation to >1000 nm with optical parametric oscillators (Kobat et al., 2011). Furthermore, the use of powerful pulsed femtosecond lasers opened the door to nonlinear microscopy, which has the unique ability to provide endogenous signals from living non-labeled scattering tissues (discussed below).

Label-free intravital imaging

The most-commonly used techniques to perform intravital imaging require the presence of fluorescently labeled molecules and, therefore, do not allow the imaging of endogenous non-labeled structures and their physiological environment. Below, we discuss several nonlinear microscopy methods that exploit the physical and optical properties of molecules, as well as advanced optics, for the imaging of non-labeled material within living tissues.

Second harmonic generation microscopy (SHG) (Fig. 1B) is the most popular nonlinear imaging technique and has first been described in 1963 (Franken et al., 1961). SHG allows to visualize endogenous, non-centrosymmetric molecules, such as collagen and myosin, which upon light scattering produce a photon at half the incident wavelength. SHG has been proven to be a highly useful technology for the non-invasive intravital imaging of the collagen-rich microenvironment during tumor invasion (Wang et al., 2002), of muscle defects in the mouse ear (Mercier et al., 2016) and of zebrafish embryos (Ramsperger et al., 2015). Furthermore, nanoparticles generating second harmonics have been used *in vivo* and represent new imaging tools (Grange et al., 2011; Pantazis et al., 2010).

Third harmonic generation (THG) microscopy (Fig. 1B) is a non-linear scattering process that originates from the polarization properties of the excited volume and from variations of the refraction index in that volume, such as in water–lipid and water–protein interfaces found, for instance, in cellular membranes and extracellular matrix structures (Weigelin et al., 2016). THG is mostly used in tumor biology to visualize ECM structures (Alexander et al., 2013) but has also been used to image lipid bodies in *Drosophila melanogaster* embryos (Débarre et al., 2006). Another label-free imaging approach relies on the Raman effect (also known as Raman scattering), i.e. the inelastic scattering of a photon upon interaction with matter, which has first been described in 1928 by Raman and Krishnan, 1928. Coherent anti-Stokes Raman scattering (CARS) microscopy detects structures by simultaneously illuminating a sample with a pump and a Stokes beam, upon which a pump and a Stokes photon match the energy of the excited vibrational state of a molecule within the sample. A second pump photon is used to elevate the molecule to another virtual state before relaxation of the molecule causes an emission of photons (anti-Stokes emission) that is shifted into the blue spectrum (Fig. 1B). Intravital CARS microscopy has been applied to *C. elegans* to examine the impact of genetic variations in metabolic pathways on lipid storage (Hellerer et al., 2007) (Fig. 1C). One of the great advantages of using nonlinear microscopy *in vivo* is the possibility of combining fluorescent signals with information obtained from endogenous, unlabeled structures. For example, SHG and CARS have been combined with 2PEM in the imaging of tumors within dorsal skin-fold chambers, and have provided access to tissue structures (SHG), cancer cell behavior (2PEM) and blood flow measurement (CARS) *in vivo* (Lee et al., 2015).

Yet, although the field of intravital imaging in higher organisms has expanded tremendously in the past few years, this approach, nevertheless, suffers from drawbacks associated with light absorption and scattering that impair its use for high-resolution imaging of subcellular events of interest. These limitations can be circumvented by using the CLEM approaches we discuss in the last section of this review. However, imaging of less voluminous samples or organisms can be performed with several approaches described in the following sections.

Light-sheet fluorescence microscopy (LSFM)

An important concern in modern cell biology is the ability to perform observations over long periods of time to follow, for example, processes during embryonic development. This can now be achieved by using light-sheet fluorescence microscopy (LSFM). LSFM was originally developed to overcome the resolution limitations of conventional fluorescence microscopy, in which the resolution is diffraction limited, with the axial resolution being about twice that of the lateral resolution. LSFM is an optical imaging technique, initially based on a plane excitation that is obtained by focusing a laser beam through a cylindrical lens, while the detection is performed in an orthogonal plane (Reynaud et al., 2008). This optical geometry retains the same diffraction resolution limitation in the detection plane but offers the same resolution in the excitation axis. Nowadays, complementary metal oxide semiconductor (cMOS) cameras are used to ensure a detection of the entire field at high speed and high resolution, way beyond the detection obtained with scanning technologies. Thus, owing to a reduced acquisition time as well as the simultaneous and selective illumination of the detection plane, LSFM significantly decreases the phototoxicity and photobleaching compared to classic confocal microscopy (Keller and Ahrens, 2015; Lim et al., 2014; Pampaloni et al., 2015; Weber and Huisken, 2011); it is therefore highly useful in imaging dynamic events that take place in small and transparent organisms and embryos. In this section, we briefly focus on the two main technological strategies that have been developed to achieve this specific illumination, single plane illumination microscopy (SPIM) and digitally scanned light-sheet microscopy (DSLM). We also provide a snapshot of their current use by describing some of the biological insights that LSFM have made possible.

Single plane illumination microscopy (SPIM)

Single plane illumination microscopy (SPIM) is the first version of LSFM; here, a cylindrical lens focusing light orthogonally to the observation plane creates the light sheet (Fig. 2A). This technology is suitable for imaging of entire animals and was highlighted already in 2004 as a means to image deep inside living zebrafish and *Drosophila* embryos. Indeed, LSFM turned out to be highly efficient in following morphogenetic events for several hours at high resolution, high speed and without photo-damaging the embryos (Huisken et al., 2004). LSFM has since continuously evolved, resulting in the development of optical systems that use several illumination and detection paths, such as multiview (MuVi)-SPIM (Krzic et al., 2012) or SimView SPIM (Tomer et al., 2012). These techniques are based on a dual light-sheet system that can switch between four different light pathways in less than 50 ms. This setup allows the acquisition of four, nearly simultaneous images from different regions in the sample (scanned in one dimension by using a piezo stage), thus making it possible to image a large-volume sample for instance a *Drosophila* embryo in 35 s (Tomer et al., 2012) (Fig. 2B). Alternatively, if the acquisition rate is not limiting, LSFM can be coupled to a sample holder mounted on a rotational stage (Jakob et al., 2016).

The potential of SPIM for high-speed *in vivo* imaging has been elegantly demonstrated for the developing Zebrafish heart – this being a very challenging task owing to its small size (250 μ m) and its high beat frequency of 2–4 Hz (Mickoleit et al., 2014). Subsequently, multi-view SPIM strategy (named here ‘IsoView’) was successfully used to study the development of the *Drosophila* embryo and the brain of Zebrafish larvae, with an unprecedented spatio-temporal resolution (Fig. 2C). Here, the authors compared

their setup with lattice light-sheet microscopy (see below) to emphasize the superior imaging depth and acquisition speed their particular approach can afford (Chhetri et al., 2015). In addition, SPIM has been combined with laser ablation (optical damaging of cells or intracellular region by using a powerful and focused laser) to unravel mechanical coupling of two important morphogenetic events in *Drosophila*: endoderm invagination and axis extension (Lye et al., 2015). In addition, several groups have implemented SPIM to accelerate commonly performed imaging. For example, MuVi-SPIM together with a customized software package can be used to increase acquisition speed and analysis by several orders of magnitude, which allows to – almost instantaneously – record individual cell shapes over an entire embryo (Stegmaier et al., 2016).

Digitally scanned light-sheet microscopy (DSLM)

In DSLM, the illumination plane is obtained by deflecting the beam with a galvanometric mirror through the excitation objective (Fig. 2D). Here, 3D volumes are obtained by 2D scanning methods. This method was pioneered by the Stelzer group in 2008 and has been applied for imaging the early stages of development of zebrafish embryos (Keller et al., 2008). In this study, the authors successfully reconstructed in 3D the collective migration patterns of several cell type precursors during gastrulation with an unprecedented temporal and *x/y* resolution. When combined with Bessel beams and/or multiphoton illumination, an increase in spatial resolution can be obtained. Bessel beam illumination is an alternative method to the typical Gaussian beam illumination and consists of feeding back the focal plane of the excitation objective with an annular illumination (Planchon et al., 2011). However, Bessel illumination creates side lobes (i.e. lateral intensity peaks) in the illumination plane, which impair reaching the desired resolution. Therefore, in addition to the Bessel illumination, it is currently possible to use diffractive optics that generate a structured illumination convoluted to the Bessel beam (Gustafsson et al., 2008); this allows image acquisition below the diffraction limit (Gao et al., 2012). Moreover, this setup strongly benefits from a two-photon illumination with associated increased penetration and decreased photobleaching and/or phototoxicity (Truong et al., 2011); this drastically reduces the risk of adversely affecting the physiology of the event studied (Ahrens et al., 2013; Wolf et al., 2015). A recent, but main update in this field was provided by the group of Eric Betzig with the demonstration of the lattice light-sheet microscopy (Chen et al., 2014) as an improvement of Bessel beam LSFM. In this setup, a fast-switching, spatial light modulator is used to generate the Bessel beam mask before it enters in the excitation objective. This permits a tremendous gain of speed at a resolution that is equivalent to that obtained with SIM (Chen et al., 2014; see below). More recently, by using the same strategy of coupling super-resolution and LSFM, lattice light-sheet–point accumulation for imaging of nanoscale topography (PAINT) microscopy has been introduced (Fig. 2E). Although image acquisition may take several days, this technique makes it possible to extend the 3D visualization of single-molecule localizations in thicker and more voluminous samples, such as in dividing cells (Legant et al., 2016).

At the moment, there are only few examples for biological applications of the latest versions of DSLM. For example, lattice light-sheet microscopy has been used to study the microtubule organization during HeLa cell division *in vitro* (Yamashita et al., 2015). Owing to the superior temporal and spatial resolution that can be achieved (below the diffraction limit and with a time interval of <1 s), the authors provided new insights into the growth

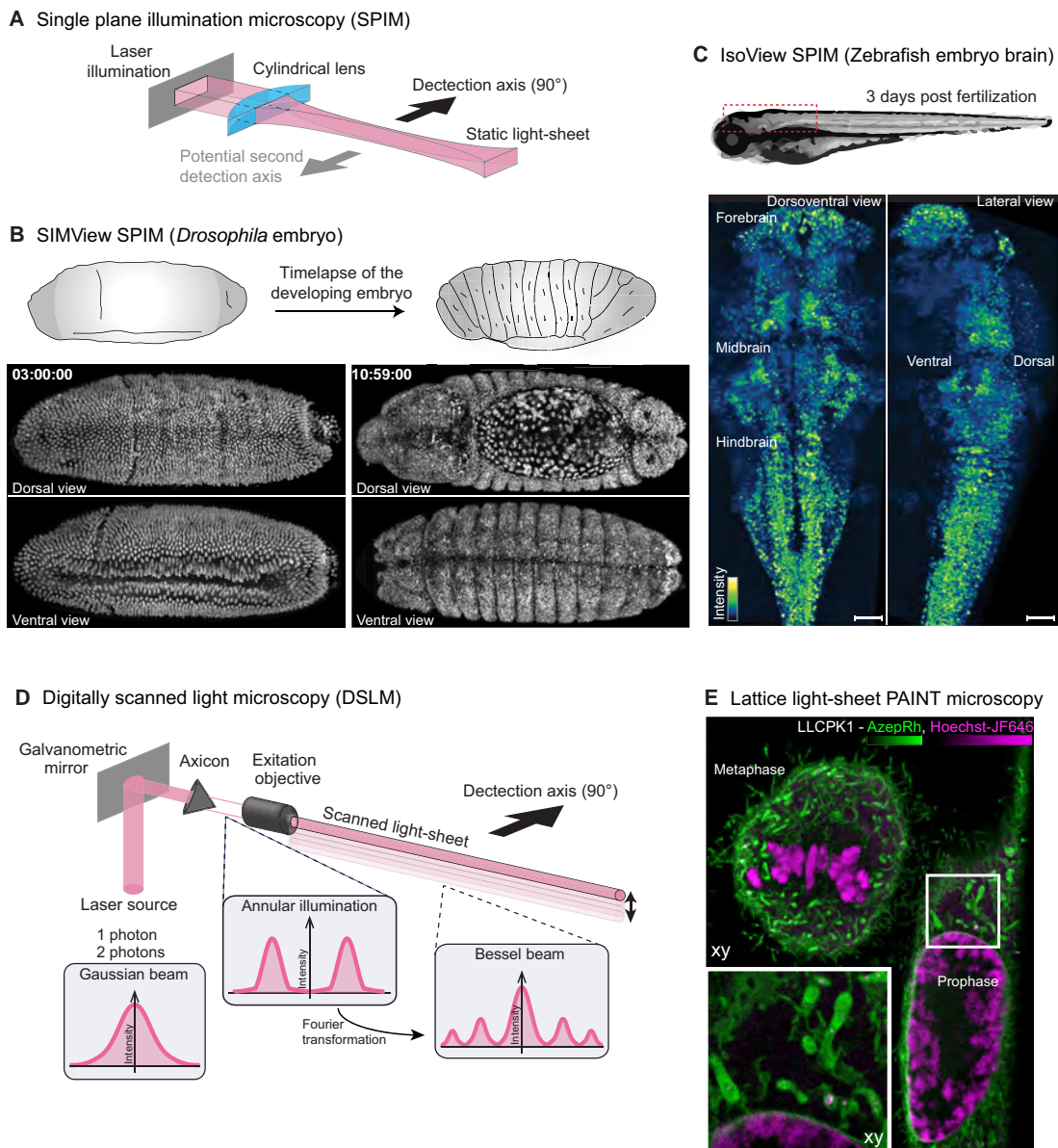


Fig. 2. Light-sheet microscopy and examples of biological applications. (A) Optics setup for SPIM. A cylindrical lens induces the formation of the light-sheet that can be scanned in 1D for volumetric imaging. Arrows indicate the detection axes (black arrow, usual 90° detection axis; gray arrow, potential second objective position for multiview SPIM). (B) SIMView SPIM imaging of nuclei during the development of *Drosophila* embryo, illustrating the possibility to carry out long-term image acquisition without photo-damage or photobleaching; adapted with permission from Tomer et al., 2012. (C) IsoView SPIM of zebrafish embryo brain (using a nuclear GCaMP6 Ca²⁺ probe), illustrating the power of this technique to record volumetric data *in vivo* at high speed and high resolution. Scale bars: 50 µm. Adapted with permission from Chhetri et al., 2015. (D) Illustration of the optical setup for Bessel beam digitally scanned light microscopy (DSLM), for which the beam is scanned in 2D for imaging in three dimensions. Laser source can be either one or two photons. The insets show the evolution of the laser intensity profile (Gaussian beam) through the axicon (a type of lens with a conical surface), leading to annular illumination, as well as the beam profile after being focused through the excitation objective. The Bessel profile is created at that step. (E) Imaging of dividing porcine kidney cells by using PAINT DSLM. DNA is labeled with Hoechst-JF₆₄₆, intracellular membranes are labeled with AzepRh. At cost of acquisition speed and a complex post-processing procedure, this technology allows so-far-unprecedented 3D resolution of a wide field of view. Adapted with permission from Legant et al., 2016.

mechanisms of microtubules. In addition, by imaging living zebrafish embryos with LSFM, the interaction between Schwann cells and axons during neuron damage repair was observed *in vivo* (Xiao et al., 2015). More recently, two-photon Bessel beam light-sheet microscopy was optimized to study how cells

maintained in a 3D culture mechanically react to changes in their microenvironment, at a subcellular level and without spatial constraint (Welf et al., 2016). Taken together, these recent studies demonstrate that LFSM is a particularly promising tool for studying mechano- and cell biology.

Requirements for LSFM

It is important to emphasize here that LSFM is extremely demanding with regard to computing resources owing to the large datasets that need to be handled. Image acquisition generates hundreds of gigabytes that need to be stored quickly. Thereafter, post-processing and reconstructions in three dimensions require enormous computer resources. These computing demands need to be consciously addressed in the future to ensure LSFM is amenable to cell biologists. In addition, only few commercial systems that are available for the wider scientific community currently exist for LSFM. This is mainly due to the fact that optical setups are typically designed and mounted in order to address a specific biological question of interest.

Taken together, there is, however, no doubt that LSFM will be used more widely in the coming decade. Thanks to its versatility, it offers multiple advances over other imaging approaches, such as increased spatio-temporal resolution with significantly reduced phototoxicity and/or photobleaching at all scales (Fig. 2B,C and E; Table 1), from *in toto* imaging of small animals with SPIM, to studying subcellular compartments in detail with DSLM.

Super-resolution microscopy – digging below the light-diffraction

Fluorescence microscopy has become one of the most useful tools for cell biologists owing to its non-invasive properties and high versatility. The past decades have witnessed significant technological improvements of microscopy setups regarding sensitivity and acquisition speed, as well as the development of brighter and more photostable fluorescent probes. These developments shifted fluorescence microscopy – which was mainly used for descriptive purposes – towards a more quantitative approach, in which the careful analysis of the large datasets allowed the deciphering of complex cellular processes at the biological and physical level. However, conventional fluorescence imaging is limited by light diffraction to a resolution (i.e. the minimal distance at which two physically distinct objects will appear as separated) of ~ 200 nm in the x/y plane (lateral resolution) and ~ 600 nm along the z axis (axial resolution), which is several orders of magnitude above the size of single proteins. Thus, reaching a resolution of a few tens of nanometers had been a main quest for microscopy optics experts and imaging computer scientists, and ultimately led to the 2014 Nobel Prize being awarded to Eric Betzig, Stefan Hell and William Moerner for their essential contributions in the development of super-resolution microscopy or nanoscopy. Furthermore, since 2007 the introduction of commercially available systems has granted the cell biology community access to these new tools, opening the door to a new era of cellular and sub-cellular imaging. Because subcellular and biomechanical processes are fast, dynamic and reversible in nature, they require fast imaging techniques to be monitored (Eyckmans et al., 2011; Hoffman et al., 2011; Janmey and Miller, 2011). Thus, we will introduce here nanoscopy approaches that can be used to study subcellular and biomechanical mechanisms by describing selected examples.

Stimulated emission depletion (STED) microscopy

An important quest for cell biologists is to have access to live and high-resolution imaging of their favorite fluorescent proteins or molecules. This can now be performed by using stimulated emission depletion (STED), which facilitates, for example, live intracellular vesicular trafficking in multiple situations. STED microscopy works on the basis of a scanning confocal microscope,

where resolution is improved by using a doughnut-shaped depletion beam that is shifted into the red-light spectrum, which ‘wraps’ the excitation beam (Fig. 3A). In this configuration, fluorophores illuminated by the depletion beam are forced to return to ground state and emit at depletion wavelength, which is filtered out, while the ‘nondepleted’ fluorophores at the center, emit normally. This optical trick result in a smaller emission volume and increases the lateral resolution to 20–70 nm (Klar et al., 2000; Willig et al., 2007). When live imaging is desired, speed acquisition may be reduced by relying on higher laser output. However, increased laser power will ultimately lead to increased phototoxicity. The use of continuous wave (CW) beams and time-gated detection allows the effective use of reduced laser powers and efficient increased resolution, thereby making gated CW STED compatible with live imaging (Willig et al., 2007; Westphal et al., 2008; Vicidomini et al., 2011).

STED was effectively used to monitor vesicular trafficking in real-time in living cultured neurons (Westphal et al., 2008), image GFP-labeled neurons in *Caenorhabditis elegans* (Rankin et al., 2011) and, more recently, follow the trafficking of EGFP-labeled vesicles in living neurons in *Drosophila* larvae with a rate above 100 frames per second (Schneider et al., 2015). These examples suggest that STED microscopy is well suited to image fast and dynamic processes in small transparent organisms, such as *C. elegans*, *Drosophila melanogaster* or zebrafish embryos. However, when considering higher organisms, conventional lasers are not able to perform intravital imaging, and confocal microscopes must be coupled to selective plane illumination microscopy (SPIM) or multiphoton excitation (discussed above). For instance, a combination of STED and SPIM was used to image >100 μm deep into the tissues of entire zebrafish embryos, resulting in a 40–250% improvement of resolution (Friedrich et al., 2011; Scheul et al., 2014; Friedrich and Harms, 2015). Axial resolution, which is often a limiting factor when using light-sheet illumination, has recently been significantly improved with reversible saturable or switchable optical linear fluorescence transitions (RESOLFT) nanoscopy and, thus, offers access to high-speed imaging with lowered laser power (Hoyer et al., 2016). 2PE lasers have a better penetrance into the tissue (<1 mm) and reduced photo-damaging, and the resulting laser spot is spread less along the z axis, thus providing a better axial resolution (Denk et al., 1990; Helmchen and Denk, 2005). 2PE-STED allowed, for example, to monitor, in real-time, the dynamics of neurons within the brain of living mice through a cranial window (Fig. 3D) to a depth of 15–90 μm and with a resolution of ~ 40 –90 nm (Berning et al., 2012; Takasaki et al., 2013; Willig et al., 2014; Coto Hernández et al., 2016). The major technical challenge is based on the fact that efficient STED requires a perfect alignment of the excitation and depletion beams. However, as tissues are not homogenous, imaging of deeper layers unavoidably decreases resolution (Takasaki et al., 2013).

Structured illumination microscopy (SIM)

Although image reconstruction remains very complex and artifact-prone, structured illumination microscopy (SIM) is the simplest of the super-resolution techniques. It works in the basis of a wide-field microscope into which a grating pattern is inserted into the light path. By generating interferences (i.e. Moiré fringes), SIM provides access to spatial information regarding the fluorescence signal. The pattern is rotated at predefined angles, and several images are acquired, usually nine to 15 (Fig. 3B). The spatial information revealed by each frame is then computed to reconstruct a sub-diffraction image, which allows to double the resolution compared

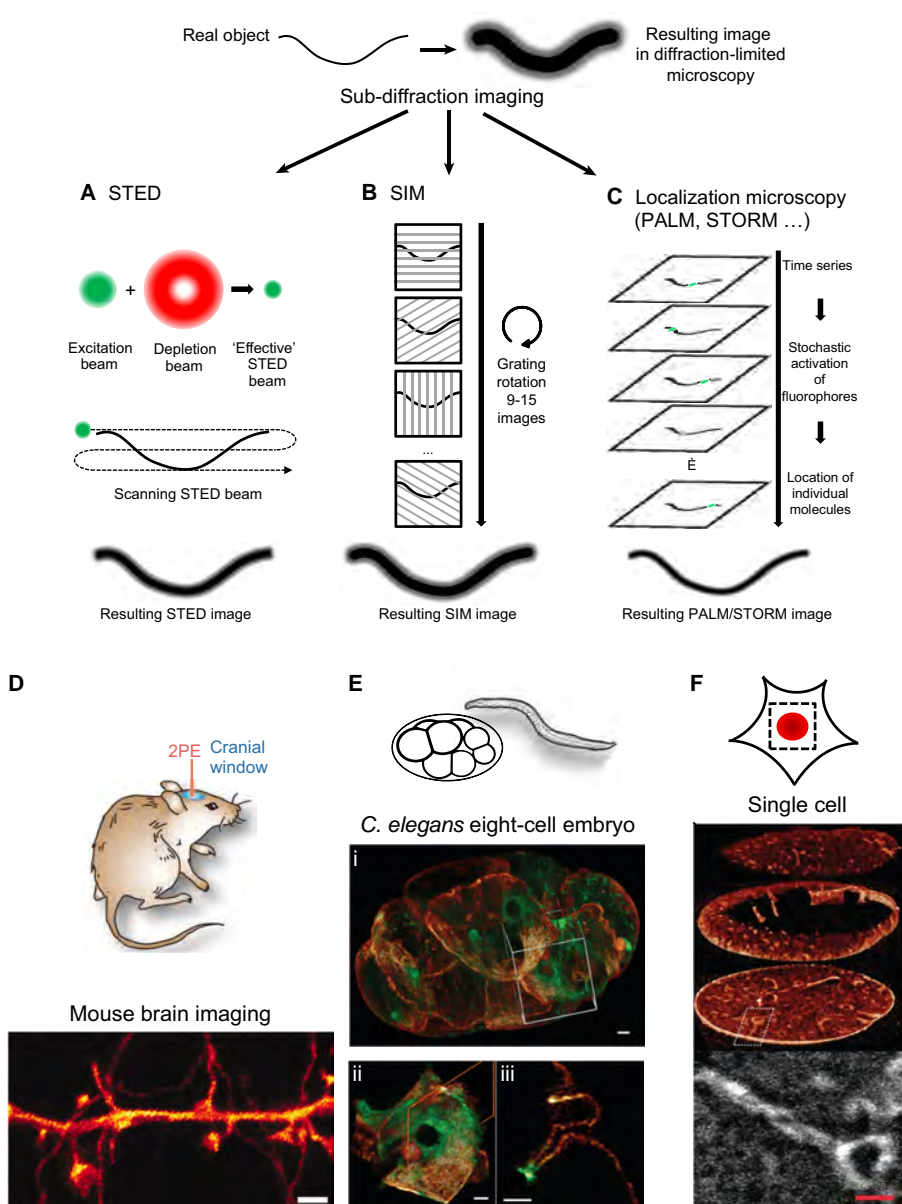


Fig. 3. Super-resolution microscopy and its biological applications. (A) Stimulated emission depletion (STED) microscopy is achieved on the basis of a line-scanning confocal microscope, in which the resolution is increased by using a second red-shifted depletion beam that 'depletes' unwanted activated fluorophores at the edges of the diffracted excitation beam. This results in a detection size in the focal plane reduced to the tens of nanometers. (B) Structured illumination microscopy (SIM) microscopy is a widefield microscopy technique. Here, increased resolution is achieved by introducing a diffraction grating in the optical path. The grating is then turned to selected angles and the sub-diffraction image is reconstructed from all the images acquired (typically 9 to 15). (C) Localization microscopy techniques, such as PALM and STORM, achieve high resolution by excitation of stochastic fluorophores coupled with computer-assisted high-precision localization of individual molecules. (D) Direct STED imaging of live mouse brain through an observation window at a depth of 10–15 µm, 2PE, two-photon excitation. Adapted with permission from Berning et al., 2012. Scale bar: 1 µm. (E) *C. elegans* eight-cell embryo expressing GFP-myosin and mCherry-membrane marker. (i) Live image using SIM combined with Bessel beam illumination. (ii) Cropped view from the 3D section in i. (iii) Single-plane view corresponding to the orange plane in ii, showing a cytokinetic ring. Adapted with permission from Gao et al., 2012. Scale bar: 2 µm. (F) 3D rendering of the nuclear envelope of U2OS cell expressing Dendra2–LaminA excited with dithered lattice light-sheet illumination and acquired with 3D PALM (top). Super-resolution maximum-intensity projection of the boxed area (bottom). Adapted with permission from Chen et al., 2014. Scale bar: 1 µm.

to conventional microscopy (Gustafsson, 2000). Alternatively, to protect living samples from excessive light exposure, the nonlinearity of photo-convertible fluorescent proteins can be used with SIM to achieve a similar resolution (Rego et al., 2012; Li et al., 2015). Furthermore, by engineering the grating to create three coherent beams, which form an illumination pattern varying laterally and axially or by using multifocal illumination patterns, the resolution can also be improved by a factor of two in all directions (Gustafsson et al., 2008; York et al., 2012).

Since SIM works on the basis of wide-field imaging and thus requires only a few planes to reconstruct a sub-diffraction image, it is probably the best-suited live-imaging approach to monitor dynamic events at subcellular level. However, one should keep in mind that resolving structures of <50–100 nm in size remains a difficult task. Nevertheless, SIM was successfully used to monitor

the dynamics of subcellular structures and organelles, such as mitochondria, clathrin-coated vesicles, microtubules and actin cytoskeleton in living cells, both in 2D and 3D at a speed of up to 11 frames per second (Fiolka et al., 2012; Kner et al., 2009; Shao et al., 2011). More recently, up to 200 frames were obtained in <0.5 s by using total internal reflexion fluorescence (TIRF) with a high numerical aperture objective in order to limit out-of-focus excitation and to increase the axial resolution on the basal side of the sample (Li et al., 2015). The use of cMOS cameras, which are faster than regular electron multiplying CCD (EMCCD) cameras, helps to further improve the number of frames acquired per second and allows the 3D recording of the entire volume of a single cell in culture within ~1 s (Fiolka et al., 2012). Recently, 3D-SIM has been combined with lattice light-sheet illumination and achieved a similar rate of acquisition with less invasive light exposure (Li et al.,

2015). Furthermore, the combination of SIM and Bessel beam plane illumination was used to image the development of a *C. elegans* embryo (Fig. 3E), and the chromosomal rearrangement in a *Drosophila* syncytium with a three- to fivefold increase in resolution and an image acquisition speed that captured the total volume of the embryo within 1 s (Gao et al., 2012). Furthermore, multifocal plane illumination SIM was used to image the dynamics of the endoplasmic reticulum in cultured cells at 100 frames per second, or of the blood flow in zebrafish at 37 frames per second (York et al., 2013).

Localization microscopy

Localization microscopy encompasses a family of techniques that allows the precise localization of fluorophores at single-molecule level; here, the precision directly reflects the number of photons emitted by a single source. The sub-diffraction image is then reconstructed from the localizations obtained for the single fluorophores. These techniques rely on the possibility to excite only a few fluorophores within the image plane, rather than all of them; this makes it possible to differentiate between fluorophores, whose distance is below the diffraction limit. This is achieved by photo-manipulation of fluorophores, i.e. by turning them on or off (Fig. 3C). In photo-activated localization microscopy (PALM), photo-manipulation is mediated by using photo-activatable fluorescent proteins (Betzig et al., 2006; Hess et al., 2006), whereas stochastic optical localization microscopy (STORM) uses a pair of organic dyes, of which one - following Förster resonance energy transfer (FRET) - activates the second one, which is imaged until it is switched off (Heinlein et al., 2005; Rust et al., 2006). Furthermore, direct STORM (dSTORM) allows the localization of single molecules by photoswitching an organic dye between its fluorescent and non-fluorescent state (Heilemann et al., 2005, 2008). Altogether, localization microscopy is the most efficient sub-diffraction technique with a lateral resolution $<10\text{--}20\text{ nm}$ (Betzig et al., 2006; Hess et al., 2006). Localization microscopy has also been implemented for 3D imaging, and several technical approaches have been used to achieve sub-diffraction 3D imaging. For instance, in combination with PALM, simultaneous detection of each imaged focal plane and of a second plane that is 350 nm closer to the objective, improves the axial resolution to 75 nm (Juette et al., 2008). In addition, combination of multifocal excitation and localization microscopy has demonstrated the simultaneous imaging of a 4- μm volume within single cells with a resolution of $20\times 20\times 50\text{ nm}$ (Hajj et al., 2014).

The main drawback of localization microscopy is that the sub-diffraction resolution is achieved by localizing single fluorophores over time, which makes it less suitable for imaging fast dynamic processes. However, localization microscopy can be used for high-resolution single-particle tracking (spt) (Manley et al., 2008), which can be very useful for understanding key cell biological events. For example, spt-PALM has recently been applied to track integrins within and outside of focal adhesions, and to quantify their diffusive properties (Rossier et al., 2012). Furthermore, this approach was used to demonstrate that the mechanical properties of the glycocalyx layer promote focal adhesion growth by channeling membrane-associated integrins into clusters (Paszek et al., 2014). In another example, 3D PALM was used in *Drosophila* embryos to analyze the clustering of E-cadherin at cell–cell junctions (Truong Quang et al., 2013). In addition, PALM has been combined with confocal correlation microscopy for high-resolution mapping of glutamate receptors in individual neurons that had been annotated by standard confocal microscopy in *C.*

elegans (Vangindertael et al., 2015). As live imaging also requires imaging at high speeds in order to be able to track dynamic events, faster cMOS cameras have been developed that allow the recording of fast events at high-resolution (Huang et al., 2013). Moreover, 3D PALM has recently been combined with lattice light-sheet illumination to image single cells in culture (Fig. 3F), as well as mouse stem cells spheroids at high speed (Chen et al., 2014). Taken together, although super-resolution imaging offers new possibilities in live and *in vivo* cell biology, there are still some limitations that impede obtaining nanoscale resolution of these events (Table 1).

Correlative light and electron microscopy (CLEM) – moving towards nanoscale resolution of dynamic *in vivo* phenomena

The most interesting biological events usually occur only infrequently and involve single molecules or organelles that are separated by only few nanometers. The perfect imaging approach, thus, would make it possible to obtain macroscopic views of tissues and structures and, at wish, to easily zoom into the most-discrete details or subcellular structures, organelles or proteins. As discussed above, live imaging with light microscopy is extremely useful to characterize the dynamics of cellular events *in vivo* and allows imaging of living samples in 3D, but it only has a limited spatial resolution. Electron microscopy (EM) achieves a much higher resolution but, generally, allows the imaging of fixed specimen with a limited screening ability. This makes it a challenging technique when studying rare objects such as single metastatic cells within a full organ (lung, brain, liver). CLEM combines live confocal microscopy with EM for the characterization of biological samples at high spatial and temporal resolution (de Boer et al., 2015) (Fig. 4A). CLEM can be used for virtually any biological event that can either be imaged (Goetz et al., 2014) or quantified by using biophysical approaches. The main bottleneck of the approach is the challenge to align the region of interest (ROI) that has been identified by light microscopy with the EM image. However, the increasing popularity of CLEM has led to the development of novel procedures and microscopy setups, although these were mainly developed to retrieve the ROI within a small sample, e.g. thin sections of cells or tissue to be imaged with transmission EM. The difficulty to accurately align the ROI within samples that have a complex 3D organization, such as large cells, embryos, small organisms or tissues, is still a major hurdle. Here, we will discuss the recent developments in CLEM by providing a snapshot of available procedures and techniques that help to reliably track biological events of interest at the highest spatial and temporal resolutions. We and others have recently contributed to the significant progress in the field of correlative light- and electron microscopy, by combining intravital imaging of entire organisms with EM, which we here refer to as intravital CLEM (Goetz et al., 2014, 2015; Karreman et al., 2014, 2016; Maco et al., 2013). Intravital CLEM enabled important discoveries in several areas of life science, such as cell biology (Avinoam et al., 2015), neuroscience (Allegra Mascaro et al., 2013; Maco et al., 2013), cancer research (Karreman et al., 2016), virology (Hellström et al., 2015) and developmental biology (Durdú et al., 2014; Goetz et al., 2014), and is highly likely to contribute to future breakthroughs in biological research.

Ground-breaking *in vitro* CLEM

CLEM has primarily and successfully been applied to *in vitro* situations. By preserving the fluorescence signal within a resin-embedded block for its easy correlation with the EM image, the Briggs group has established a ground-breaking technique that

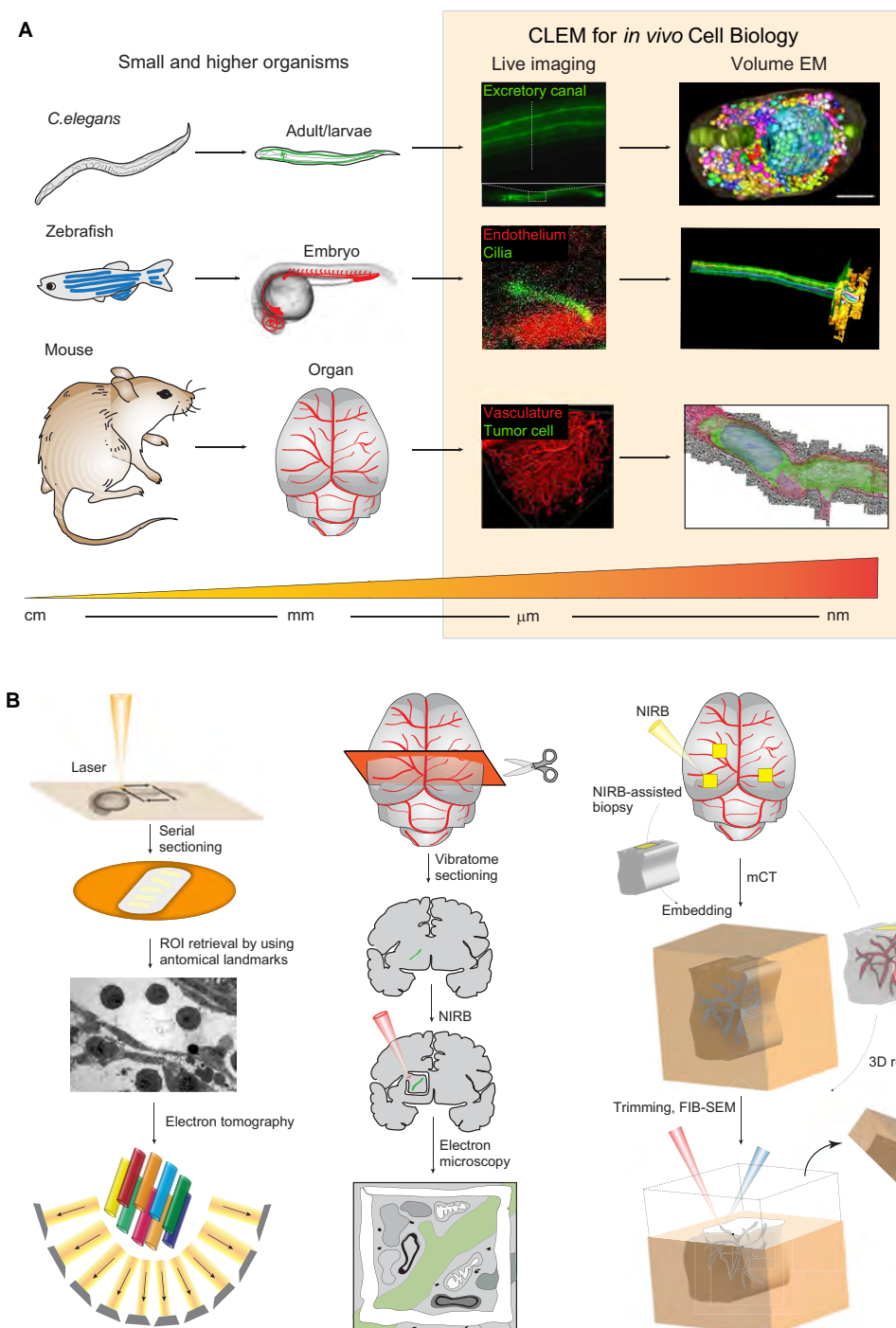


Fig. 4. Intravital CLEM and its biological applications. (A) Examples of intravital CLEM performed on *C. elegans*, zebrafish embryos and mice. In *C. elegans*, intravital CLEM has been used to study the ultrastructure and formation of the excretory canal by using correlative fluorescence and volume EM (serial electron tomography). Adapted with permission from Kolotuev et al., 2013. In the zebrafish embryo, CLEM was used to dissect the ultrastructure of endothelial cilia that sense and transduce blood flow forces. Adapted with permission from Goetz et al., 2014. In mice, we recently developed a multimodal approach that combines intravital 2PEM imaging, X-ray micro-computed tomography (mCT) and focused ion beam scanning EM (FIB-SEM; see panel B); this made it possible to retrieve single brain metastatic cells for their dissection at high-resolution. Adapted with permission from Karreman et al., 2016. (B) A snapshot of the existing intravital CLEM procedures. Targeted ultramicrotomy, and subsequent volume EM, can be performed upon laser carving in the flat-embedded resin sample (left). Alternatively, near-infrared branding (NIRB)-guided marks can be physically drawn on vibratome sections of the mouse brain for guiding ultramicrotomy and/or volume EM (middle). NIRB can also be used for whole-organ ‘tattooing’ (e.g. ear, brain) and thereby guide the biopsy of the region of interest (ROI) in voluminous samples, such as the mouse brain. Resin-embedded ROIs are then scanned by using mCT, the volumes are then registered and the position of the ROIs retrieved; this allows 3DEM by using FIB-SEM (right).

allowed them time-lapse recordings of endocytosis gaining ultrastructural information from resin sections imaged by applying electron tomography (Kukulski et al., 2011, 2012). These elegant studies elucidated how proteins that control membrane budding, such as clathrin, actin and amphiphysin, drive invagination, elongation and fission of endocytic vesicles. Further work using CLEM showed that vesicle budding appears to involve the assembly of clathrin adaptors (Skuzny et al., 2015) and the bending of a dynamic preassembled clathrin coat (Avinoam et al., 2015). Similar approaches of preserving the fluorescence signal have been used in CLEM of zebrafish embryos (Nixon et al., 2009), *C. elegans* (Watanabe et al., 2011) and mammalian cells (Paez-Segala et al., 2015; Peddie et al., 2014). CLEM can also be performed thanks to the development of bimodal probes, such as the mini singlet oxygen generator (miniSOG) (Shu et al., 2011) and proteins of the ascorbate peroxidase (APX) family, in particular APEX2 (Lam et al., 2015). MiniSOG is a fluorescent flavoprotein that, when genetically encoded, is used as a versatile tag that emits fluorescence and, in response to illumination, generates singlet oxygen that transforms diaminobenzidine into electron-dense precipitates that can be imaged by using EM. The engineered peroxidase APEX, by contrast, can be used for EM and proximity labeling upon its fusion to a protein of interest, (Mick et al., 2015). Alternatively, events or regions of interest can be tracked over the two imaging modalities, with recording of coordinates imprinted on the culture dish, by using either commercialized (Al Jord et al., 2014) or laser-micropatterned culture substrates (Spiegelhalter et al., 2010). This method allows the fast freezing (e.g. high-pressure freezing) of dynamic events within seconds for their ultrastructural characterization. A similar approach has recently been used to characterize centriole duplication in multi-ciliated ependymal cells, which grow multiple motile cilia that efficiently propel the cerebrospinal fluid in brain ventricles. By combining live super-resolution imaging of ependymal progenitors by using EM, Al Jord and colleagues could show that multiple centrioles derive from the pre-existing progenitor cell centrosome following multiple rounds of procentriole seeding, thereby unraveling an unexpected centriolar asymmetry that differs from the archetypal duplication program found in other ciliated cells (Al Jord et al., 2014). Similarly, *in vitro* CLEM has been combined with the 3D electron microscopy (3DEM) technique focused ion beam scanning electron microscopy (FIB-SEM) to show that invadopodia of cancer cells potentially mature in response to a mechanical interplay with the nucleus (Revach et al., 2015). Their EM data revealed that invadopodia are composed of actin bundles that interact with and indent the nucleus at the apical side. Finally, many of the issues that are encountered when retrieving the ROI in EM after light microscopy and sample transfer can be avoided by using integrated microscopes that are specially designed for CLEM studies; the latter also allow the combination of atomic force microscopy and EM (for a review see de Boer et al., 2015).

CLEM of multicellular and 3D samples – probing biomechanics at high resolution

A major gap in cell biology is to understand cell biological events in a realistic pathophysiological context. This can only be approached by using light microscopy in living animals, i.e. intravital imaging. Although single-photon and light-sheet imaging allow to image small organisms, such as *Drosophila*, *C. elegans* and zebrafish embryos at any depth, the event of interest might be beyond the imaging depth of the fluorescence microscope in higher organisms, such as mice. As discussed above, this can be easily overcome by

surgical implantation of imaging windows and the use of multi-photon microscopy (Helmchen and Denk, 2005), which permits to acquire high-quality fluorescent images deep inside animals (see above).

However, most organs are not directly optically accessible and require surgical procedures to expose the tissue of interest, as is employed in neuroscience (Dombeck et al., 2007) and cancer research (Ellenbroek and van Rheenen, 2014). The second, and biggest, challenge resides in the difficulty to retrieve the ROI in voluminous resin-embedded 3D samples (up to a few mm³). In small organisms and embryos, anatomical landmarks, such as fluorescent or visible structures that have been imaged *in vivo* can be utilized to provide key anchor points for pinpointing the event of interest in the resin-embedded tissue (Durdu et al., 2014; Goetz et al., 2014, 2015; Kolotuev et al., 2010, 2013; Müller-Reichert et al., 2007). This has proven to be very useful in zebrafish embryos for correlating the blood flow that is sensed by endothelial cilia to their inner ultrastructure (Fig. 4A,B). In addition to anatomical landmarks, artificial markers can be carved in the resin, which – upon superimposition with the intravital image – facilitate targeted ultramicrotomy by EM. Of note, laser etching had been originally pioneered on glass coverslips for micropatterning-assisted CLEM of cells (Spiegelhalter et al., 2010). In resin- and flat-embedded small organisms, it facilitates the retrieval of a precise ROI located within the intravital image and, for instance, afforded the characterization of how fibroblast growth factor (FGF) activity controls the frequency at which rosette-like mechanosensory organs, e.g. the zebrafish lateral line primordium, are deposited through the assembly of microluminal structures that constrain FGF signaling (Durdu et al., 2014). Studies performed in *C. elegans* provide additional examples of laser-assisted targeted ultramicrotomy; these have helped to further clarify at high resolution the formation of excretory canals, as well as the contribution of exosomes to alae formation (Hyenne et al., 2015) (Fig. 4A). Laser etching can also be used directly on hydrated tissues to precisely locate the ROI. This technology, called near-infrared branding (NIRB) has been developed a few years ago and enables to highlight the position of the ROI, either owing to laser-induced autofluorescence or upon photooxidation of the NIRB mark (Bishop et al., 2011) (Fig. 4B). In that study, by using NIRB on brain vibratome sections, single cortical dendritic spines that had been previously recorded in a living mouse could be dissected at unprecedented resolution (Bishop et al., 2011). Furthermore, NIRB-guided retrieval of the ROI in vibratome sections allows to combine intravital imaging with 3DEM, such as FIB-SEM, which was shown to provide nanoscale isotropic imaging of axons and dendrites (Maco et al., 2013). Combined with state-of-the-art optogenetic tools, intravital CLEM holds great promises for resolving long-standing questions in brain connectivity. For instance, NIRB has recently been customized to perform tissue surface ‘tattooing’, which facilitates the retrieval of the ROI before embedding (Karreman et al., 2014) (Fig. 4B). However, although this approach allows to selectively target the ROI-contained volume in *x* and *y* direction, the *z*-position within the block cannot be estimated from it, and serial sectioning throughout the block is required for ROI retrieval. Combined with anatomical landmarks, NIRB-assisted tattooing of the mouse ear skin was used to precisely correlate intravital imaging of subcutaneous tumors with high-resolution electron tomography (Karreman et al., 2014). However, these techniques do not provide the opportunity to predict where the ROI is within the resin-embedded sample; being able to achieve this would greatly increase throughput and facilitate *en bloc* imaging, which is of utmost importance when working with

high-volume samples. One way to circumvent this issue is to implement a third imaging modality to map the resin-embedded ROI and thereby predict the position of the ROI by cross-correlating the topology of anatomical landmarks. This opportunity is provided by X-ray micro-computed tomography (microCT), which uses the presence of heavy metals, such as osmium – and which are required for EM – to resolve a number of anatomical structures, such as the vasculature, hair follicles and collagen fibers (Karreman et al., 2016). This approach has been used on brain vibratome sections and allowed to locate photo-oxidized neuronal structures (Bushong et al., 2015). Moreover, microCT can be used on voluminous samples, such as brain biopsies, and allows to accurately resolve the brain capillary architecture. We have recently shown that implementing microCT as an intermediate step between intravital imaging of brain metastasis and FIB-SEM allows the high-resolution imaging of single metastatic cells (Karreman et al., 2016). The combination of state-of-the-art light and intravital microscopy techniques together with the growing approaches for 3DEM will provide scientists with an unprecedented toolbox that can help to resolve – *in vivo* and at very high resolution – many of the current questions surrounding cell biology. We believe that intravital CLEM has the potential to provide the link between cell biology and relevant pathophysiological contexts and, undoubtedly, will become the next-generation microscopy for *in vivo* cell biologists (Table 1).

Conclusions

We have summarized here the imaging approaches that are currently used for studying any cell biological event of interest. Cell biologists are now in the great position to have access to a wide and still-growing palette of fast, non-invasive, high-resolution, label-free technologies that make true '*in vivo* cell biology' a goal that is within reach in the near future. It is of utmost importance to continue to pursue the development of high-resolution and animal-suitable imaging approaches in order to visualize the cell biology of any given disease within an animal model. This giant leap forward will enable us to model, image, quantify and understand the complexity of cell biology within its most relevant contexts, thereby contributing to the wealth of knowledge and to the design of optimal therapeutic strategies to deal with life-threatening pathologies.

Acknowledgements

The authors thank all the members of the Goetz lab for useful insights and discussions as well as proofreading.

Competing interests

The authors declare no competing or financial interests.

Funding

This work has been supported by research grants from the French National Cancer Institute (Institut National Du Cancer, INCa) and the Ligue Contre le Cancer (J.G.G.), the Plan Cancer, by institutional funding from Institut National de la Santé et de la Recherche Médicale (Inserm) and the Université de Strasbourg (Idex, investissements d'avenir), and by the LAbEx NIE (grant number: ANR-11-LABX-0058_NIE). L.M. is supported by an INSERM/Région Alsace Ph.D fellowship and G. F. is supported by a Ligue contre le Cancer Ph.D fellowship, N.O. is supported by funding from Plan Cancer.

References

Ahmed, W. W., Fodor, É. and Betz, T. (2015). Active cell mechanics: measurement and theory. *Biochim. Biophys. Acta Mol. Cell Res.* **1853**, 3083–3094.

Ahrens, M. B., Orger, M. B., Robson, D. N., Li, J. M. and Keller, P. J. (2013). Whole-brain functional imaging at cellular resolution using light-sheet microscopy. *Nat. Methods* **10**, 413–420.

Al Jord, A., Lemaître, A.-I., Delgehyr, N., Faucourt, M., Spassky, N. and Meunier, A. (2014). Centriole amplification by mother and daughter centrioles differs in multiciliated cells. *Nature* **516**, 104–107.

Alexander, S., Weigelin, B., Winkler, F. and Friedl, P. (2013). Preclinical intravital microscopy of the tumour-stroma interface: invasion, metastasis, and therapy response. *Curr. Opin. Cell Biol.* **25**, 659–671.

Allegra Mascaro, A. L., Cesare, P., Sacconi, L., Grasselli, G., Mandolesi, G., Maco, B., Knott, G. W., Huang, L., De Paola, V., Strata, P. et al. (2013). In vivo single branch axotomy induces GAP-43-dependent sprouting and synaptic remodeling in cerebellar cortex. *Proc. Natl. Acad. Sci. USA* **110**, 10824–10829.

Anton, H., Harlepp, S., Ramspacher, C., Wu, D., Monduc, F., Bhat, S., Liebling, M., Paoletti, C., Charvin, G., Freund, J. B. et al. (2013). Pulse propagation by a capacitive mechanism drives embryonic blood flow. *Development* **140**, 4426–4434.

Ashkin, A. (1997). Optical trapping and manipulation of neutral particles using lasers. *Proc. Natl. Acad. Sci. USA* **94**, 4853–4860.

Ashkin, A. and Dziedzic, J. (1987). Optical trapping and manipulation of viruses and bacteria. *Science* **235**, 1517–1520.

Ashkin, A., Dziedzic, J. M. and Yamane, T. (1987). Optical trapping and manipulation of single cells using infrared laser beams. *Nature* **330**, 769–771.

Avinoam, O., Schorb, M., Beese, C. J., Briggs, J. A. G. and Kaksonen, M. (2015). ENDOCYTOSIS. Endocytic sites mature by continuous bending and remodeling of the clathrin coat. *Science* **348**, 1369–1372.

Balaban, N. Q., Schwarz, U. S., Riveline, D., Goichberg, P., Tzur, G., Sabanay, I., Mahalu, D., Safran, S., Bershadsky, A., Addadi, L. et al. (2001). Force and focal adhesion assembly: a close relationship studied using elastic micropatterned substrates. *Nat. Cell Biol.* **3**, 466–472.

Bambadekar, K., Clément, R., Blanc, O., Chardès, C. and Lenne, P.-F. (2015). Direct laser manipulation reveals the mechanics of cell contacts *in vivo*. *Proc. Natl. Acad. Sci. USA* **112**, 1416–1421.

Berning, S., Willig, K. I., Steffens, H., Dibaj, P. and Hell, S. W. (2012). Nanoscopy in a living mouse brain. *Science* **335**, 551–551.

Betzig, E., Patterson, G. H., Sougrat, R., Lindwasser, O. W., Olenych, S., Bonifacino, J. S., Davidson, M. W., Lippincott-Schwartz, J. and Hess, H. F. (2006). Imaging intracellular fluorescent proteins at nanometer resolution. *Science* **313**, 1642–1645.

Bishop, D., Nikić, I., Brinkoetter, M., Knecht, S., Potz, S., Kerschensteiner, M. and Misgeld, T. (2011). Near-infrared branding efficiently correlates light and electron microscopy. *Nat. Methods* **8**, 568–570.

Boulnois, J.-L. (1986). Photophysical processes in recent medical laser developments: a review. *Lasers Med. Sci.* **1**, 47–66.

Brunet, T., Bouclet, A., Ahmadi, P., Mitrossilis, D., Driuez, B., Brunet, A.-C., Henry, L., Serman, F., Béalle, G., Ménager, C. et al. (2013). Evolutionary conservation of early mesoderm specification by mechanotransduction in Bilateria. *Nat. Commun.* **4**, 2821.

Bushong, E. A., Johnson, D. D., Kim, K.-Y., Terada, M., Hatori, M., Peltier, S. T., Panda, S., Merkle, A. and Ellisman, M. H. (2015). X-ray microscopy as an approach to increasing accuracy and efficiency of serial block-face imaging for correlated light and electron microscopy of biological specimens. *Microsc. Microanal.* **21**, 231–238.

Chen, B.-C., Legant, W. R., Wang, K., Shao, L., Milkie, D. E., Davidson, M. W., Janetopoulos, C., Wu, X. S., Hammer, J. A., Liu, Z. et al. (2014). Lattice light-sheet microscopy: imaging molecules to embryos at high spatiotemporal resolution. *Science* **346**, 1257998.

Chhetri, R. K., Amat, F., Wan, Y., Höckendorf, B., Lemon, W. C. and Keller, P. J. (2015). Whole-animal functional and developmental imaging with isotropic spatial resolution. *Nat. Methods* **12**, 1171–1178.

Chivukula, V. K., Krog, B. L., Nauseef, J. T., Henry, M. D. and Vigmostad, S. C. (2015). Alterations in cancer cell mechanical properties after fluid shear stress exposure: a micropipette aspiration study. *Cell Health Cytoskelet.* **7**, 25–35.

Collins, C., Osborne, L. D., Guilluy, C., Chen, Z., O'Brien, E. T., III, Reader, J. S., Burridge, K., Superfine, R. and Tzima, E. (2014). Haemodynamic and extracellular matrix cues regulate the mechanical phenotype and stiffness of aortic endothelial cells. *Nat. Commun.* **5**, 3984.

Coto Hernández, I., Castello, M., Lanzanò, L., d'Amora, M., Bianchini, P., Diaspro, A. and Vicidomini, G. (2016). Two-photon excitation STED microscopy with time-gated detection. *Sci. Rep.* **6**, 19419.

Dao, M., Lim, C. T. and Suresh, S. (2003). Mechanics of the human red blood cell deformed by optical tweezers. *J. Mech. Phys. Solids* **51**, 2259–2280.

de Boer, P., Hoogenboom, J. P. and Giepmans, B. N. G. (2015). Correlated light and electron microscopy: ultrastructure lights up! *Nat. Methods* **12**, 503–513.

Débarre, D., Supatto, W., Pena, A.-M. M., Fabre, A., Tordjmann, T., Combettes, L., Schanne-Klein, M. -C. and Beaurepaire, E. (2006). Imaging lipid bodies in cells and tissues using third-harmonic generation microscopy. *Nat. Methods* **3**, 47–53.

Denk, W., Strickler, J. H. and Webb, W. W. (1990). Two-photon laser scanning fluorescence microscopy. *Science* **248**, 73–76.

Desprat, N., Supatto, W., Pouille, P.-A., Beaurepaire, E. and Farge, E. (2008). Tissue deformation modulates twist expression to determine anterior midgut differentiation in *Drosophila* embryos. *Dev. Cell* **15**, 470–477.

Dombeck, D. A., Khabbaz, A. N., Collman, F., Adelman, T. L. and Tank, D. W. (2007). Imaging large-scale neural activity with cellular resolution in awake, mobile mice. *Neuron* **56**, 43–57.

Durdu, S., Iskar, M., Revenu, C., Schieber, N., Kunze, A., Bork, P., Schwab, Y. and Gilmour, D. (2014). Luminal signalling links cell communication to tissue architecture during organogenesis. *Nature* **515**, 120–124.

Ellenbroek, S. I. J. and van Rheenen, J. (2014). Imaging hallmarks of cancer in living mice. *Nat. Rev. Cancer* **14**, 406–418.

Eyckmans, J., Boudou, T., Yu, X. and Chen, C. S. (2011). A Hitchhiker's guide to mechanobiology. *Dev. Cell* **21**, 35–47.

Fiolka, R., Shao, L., Rego, E. H., Davidson, M. W. and Gustafsson, M. G. L. (2012). Time-lapse two-color 3D imaging of live cells with doubled resolution using structured illumination. *Proc. Natl. Acad. Sci. USA* **109**, 5311–5315.

Franken, P. A., Hill, A. E., Peters, C. W. and Weinreich, G. (1963). Generation of optical harmonics. *Phys. Rev. Lett.* **118**.

Friedrich, M. and Harms, G. S. (2015). Axial resolution beyond the diffraction limit of a sheet illumination microscope with stimulated emission depletion. *J. Biomed. Opt.* **20**, 106006–106006.

Friedrich, M., Gan, Q., Ermolayev, V. and Harms, G. S. (2011). STED-SPIM: stimulated emission depletion improves sheet illumination microscopy resolution. *Biophys. J.* **100**, L43–L45.

Gao, L., Shao, L., Higgins, C. D., Poulton, J. S., Peifer, M., Davidson, M. W., Wu, X., Goldstein, B. and Betzig, E. (2012). Noninvasive imaging beyond the diffraction limit of 3D dynamics in thickly fluorescent specimens. *Cell* **151**, 1370–1385.

Goetz, J. G., Steed, E., Ferreira, R. R., Roth, S., Ramspacher, C., Boselli, F., Charvin, G., Liebling, M., Wyart, C., Schwab, Y. et al. (2014). Endothelial cilia mediate low flow sensing during zebrafish vascular development. *Cell Rep.* **6**, 799–808.

Goetz, J. G., Monduc, F., Schwab, Y. and Vermot, J. (2015). Using correlative light and electron microscopy to study zebrafish vascular morphogenesis. *Methods Mol. Biol.* **1189**, 31–46.

Göppert-Mayer, M. (1931). Über Elementarakte mit zwei Quantensprüngen. *Ann. Phys.* **401**, 273–294.

Grange, R., Lanvin, T., Hsieh, C.-L., Pu, Y. and Psaltis, D. (2011). Imaging with second-harmonic radiation probes in living tissue. *Biomed. Opt. Express* **2**, 2532–2539.

Graves, E. T., Duboc, C., Fan, J., Stransky, F., Leroux-Coyau, M. and Strick, T. R. (2015). A dynamic DNA-repair complex observed by correlative single-molecule nanomanipulation and fluorescence. *Nat. Struct. Mol. Biol.* **22**, 452–457.

Guevorkian, K., Colbert, M.-J., Durth, M., Dufour, S. and Brochard-Wyart, F. (2010). Aspiration of biological viscoelastic drops. *Phys. Rev. Lett.* **104**, 218101.

Guevorkian, K., Gonzalez-Rodriguez, D., Carlier, C., Dufour, S. and Brochard-Wyart, F. (2011). Mechanosensitive shivering of model tissues under controlled aspiration. *Proc. Natl. Acad. Sci. USA* **108**, 13387–13392.

Guilak, F., Tedrow, J. R. and Burgkart, R. (2000). Viscoelastic properties of the cell nucleus. *Biochem. Biophys. Res. Commun.* **269**, 781–786.

Gupta, M., Kocgozlu, L., Sarangi, B. R., Margadant, F., Ashraf, M. and Ladoux, B. (2015). Micropillar substrates: a tool for studying cell mechanobiology. *Methods Cell Biol.* **125**, 289–308.

Gustafsson, M. G. L. (2000). Surpassing the lateral resolution limit by a factor of two using structured illumination microscopy. *J. Microsc.* **198**, 82–87.

Gustafsson, M. G. L., Shao, L., Carlton, P. M., Wang, C. J. R., Golubovskaya, I. N., Cande, W. Z., Agard, D. A. and Sedat, J. W. (2008). Three-dimensional resolution doubling in wide-field fluorescence microscopy by structured illumination. *Biophys. J.* **94**, 4957–4970.

Hajji, B., Wisniewski, J., El Beheiry, M., Chen, J., Revyakin, A., Wu, C. and Dahan, M. (2014). Whole-cell, multicolor superresolution imaging using volumetric multifocus microscopy. *Proc. Natl. Acad. Sci. USA* **111**, 17480–17485.

Headley, M. B., Bins, A., Nip, A., Roberts, E. W., Looney, M. R., Gerard, A. and Krummel, M. F. (2016). Visualization of immediate immune responses to pioneer metastatic cells in the lung. *Nature* **531**, 513–517.

Heilemann, M., Margeat, E., Kasper, R., Sauer, M. and Tinnefeld, P. (2005). Carbocyanine dyes as efficient reversible single-molecule optical switch. *J. Am. Chem. Soc.* **127**, 3801–3806.

Heilemann, M., van de Linde, S., Schüttelpejz, M., Kasper, R., Seefeldt, B., Mukherjee, A., Tinnefeld, P. and Sauer, M. (2008). Subdiffraction-resolution fluorescence imaging with conventional fluorescent probes. *Angew. Chem. Int. Ed.* **47**, 6172–6176.

Heinlein, T., Biebricher, A., Schlüter, P., Roth, C. M., Herten, D.-P., Wolfrum, J., Heilemann, M., Müller, C., Tinnefeld, P. and Sauer, M. (2005). High-resolution colocalization of single molecules within the resolution gap of far-field microscopy. *ChemPhysChem* **6**, 949–955.

Hellerer, T., Axäng, C., Brackmann, C., Hillertz, P., Pilon, M. and Enejder, A. (2007). Monitoring of lipid storage in *Caenorhabditis elegans* using coherent anti-Stokes Raman scattering (CARS) microscopy. *Proc. Natl. Acad. Sci. USA* **104**, 14658–14663.

Hellström, K., Viihinen, H., Kallio, K., Jokitalo, E. and Ahola, T. (2015). Correlative light and electron microscopy enables viral replication studies at the ultrastructural level. *Methods* **90**, 49–56.

Helmchen, F. and Denk, W. (2005). Deep tissue two-photon microscopy. *Nat. Methods* **2**, 932–940.

Hess, S. T., Girirajan, T. P. K. and Mason, M. D. (2006). Ultra-high resolution imaging by fluorescence photoactivation localization microscopy. *Biophys. J.* **91**, 4258–4272.

Hochmuth, R. M. (2000). Micropipette aspiration of living cells. *J. Biomed. Eng.* **33**, 15–22.

Hoffman, B. D., Grashoff, C. and Schwartz, M. A. (2011). Dynamic molecular processes mediate cellular mechanotransduction. *Nature* **475**, 316–323.

Hoyer, P., de Medeiros, G., Balázs, B., Norlin, N., Besir, C., Hanne, J., Kräusslich, H.-G., Engelhardt, J., Sahl, S. J., Hell, S. W. et al. (2016). Breaking the diffraction limit of light-sheet fluorescence microscopy by RESOLFT. *Proc. Natl. Acad. Sci. USA* **113**, 3442–3446.

Huang, F., Hartwich, T. M. P., Rivera-Molina, F. E., Lin, Y., Duim, W. C., Long, J. J., Uchil, P. D., Myers, J. R., Baird, M. A., Mothes, W. et al. (2013). Video-rate nanoscopy using sCMOS camera-specific single-molecule localization algorithms. *Nat. Methods* **10**, 653–658.

Huisken, J., Swoger, J., Bene, F. D., Wittbrodt, J. and Stelzer, E. H. K. (2004). Optical sectioning deep inside live embryos by selective plane illumination microscopy. *Science* **305**, 1007–1009.

Hyenne, V., Apaydin, A., Rodriguez, D., Spiegelhalter, C., Hoff-Yoessel, S., Diem, M., Tak, S., Lefebvre, O., Schwab, Y., Goetz, J. G. et al. (2015). RAL-1 controls multivesicular body biogenesis and exosome secretion. *J. Cell Biol.* **211**, 27–37.

Jakob, P. H., Kehler, J., Flood, P., Wiegel, C., Hasselmann, U., Meissner, M., Stelzer, E. H. K. and Reynaud, E. G. (2016). A 3-D cell culture system to study epithelia functions using microcarriers. *Cytotechnology*. [Epub ahead of print] doi:10.1007/s10616-015-9935-0

Janmey, P. A. and Miller, R. T. (2011). Mechanisms of mechanical signaling in development and disease. *J. Cell Sci.* **124**, 9–18.

Jenne, C. N., Wong, C. H. Y., Petri, B. and Kubes, P. (2011). The use of spinning-disk confocal microscopy for the intravital analysis of platelet dynamics in response to systemic and local inflammation. *6*, e25109.

Juette, M. F., Gould, T. J., Lessard, M. D., Mlodzianoski, M. J., Nagpure, B. S., Bennett, B. T., Hess, S. T. and Bewersdorf, J. (2008). Three-dimensional sub-100 nm resolution fluorescence microscopy of thick samples. *Nat. Methods* **5**, 527–529.

Karreman, M. A., Mercier, L., Schieber, N. L., Shibue, T., Schwab, Y. and Goetz, J. G. (2014). Correlating intravital multi-photon microscopy to 3D electron microscopy of invading tumor cells using anatomical reference points. *PLoS ONE* **9**, e114448.

Karreman, M. A., Mercier, L., Schieber, N. L., Solecki, G., Allio, G., Winkler, F., Ruthensteiner, B., Goetz, J. G. and Schwab, Y. (2016). Fast and precise targeting of single tumor cells in vivo by multimodal correlative microscopy. *J. Cell Sci.* **129**, 444–456.

Keller, P. J. and Ahrens, M. B. (2015). Visualizing whole-brain activity and development at the single-cell level using light-sheet microscopy. *Neuron* **85**, 462–483.

Keller, P. J., Schmidt, A. D., Wittbrodt, J. and Stelzer, E. H. K. (2008). Reconstruction of Zebrafish early embryonic development by scanned light sheet microscopy. *Science* **322**, 1065–1069.

Khare, S. M., Awasthi, A., Venkataraman, V. and Koushika, S. P. (2015). Colored polydimethylsiloxane micropillar arrays for high throughput measurements of forces applied by genetic model organisms. *Biomicrofluidics* **9**, 014111.

Kienast, Y., von Baumgarten, L., Fuhrmann, M., Klinkert, W. E. F., Goldbrunner, R., Herms, J. and Winkler, F. (2010). Real-time imaging reveals the single steps of brain metastasis formation. *Nat. Med.* **16**, 116–122.

Kim, D.-H., Wong, P. K., Park, J., Levchenko, A. and Sun, Y. (2009). Microengineered Platforms for Cell Mechanobiology. *Annu. Rev. Biomed. Eng.* **11**, 203–233.

Kissa, K. and Herbomel, P. (2010). Blood stem cells emerge from aortic endothelium by a novel type of cell transition. *Nature* **464**, 112–115.

Klajner, M., Hebraud, P., Sirlin, C., Gaiddon, C. and Harlepp, S. (2010). DNA binding to an anticancer Organo-Ruthenium complex. *J. Phys. Chem. B* **114**, 14041–14047.

Klar, T. A., Jakobs, S., Dyba, M., Egner, A. and Hell, S. W. (2000). Fluorescence microscopy with diffraction resolution barrier broken by stimulated emission. *Proc. Natl. Acad. Sci. USA* **97**, 8206–8210.

Kner, P., Chhun, B. B., Griffis, E. R., Winoto, L. and Gustafsson, M. G. L. (2009). Super-resolution video microscopy of live cells by structured illumination. *Nat. Methods* **6**, 339–342.

Kobat, D., Horton, N. G. and Xu, C. (2011). In vivo two-photon microscopy to 1.6-mm depth in mouse cortex. *J. Biomed. Opt.* **16**, 106014.

Kolotuev, I., Schwab, Y. and Labouesse, M. (2010). A precise and rapid mapping protocol for correlative light and electron microscopy of small invertebrate organisms. *Biol. Cell* **102**, 121–132.

Kolotuev, I., Hyenne, V., Schwab, Y., Rodriguez, D. and Labouesse, M. (2013). A pathway for unicellular tube extension depending on the lymphatic vessel determinant Prox1 and on osmoregulation. *Nat. Cell Biol.* **15**, 157–168.

Krzic, U., Gunther, S., Saunders, T. E., Streichan, S. J. and Hufnagel, L. (2012). Multiview light-sheet microscope for rapid *in toto* imaging. *Nat. Methods* **9**, 730–733.

Kukulski, W., Schorb, M., Welsch, S., Picco, A., Kaksonen, M. and Briggs, J. A. G. (2011). Correlated fluorescence and 3D electron microscopy with high sensitivity and spatial precision. *J. Cell Biol.* **192**, 111–119.

Kukulski, W., Schorb, M., Kaksonen, M. and Briggs, J. A. G. (2012). Plasma membrane reshaping during endocytosis is revealed by time-resolved electron tomography. *Cell* **150**, 508–520.

Kuznetsova, T. G., Starodubtseva, M. N., Yegorenkov, N. I., Chizhik, S. A. and Zhdanov, R. I. (2007). Atomic force microscopy probing of cell elasticity. *Micron* **38**, 824–833.

Lam, S. S., Martell, J. D., Kamer, K. J., Deerinck, T. J., Ellisman, M. H., Mootha, V. K. and Ting, A. Y. (2015). Directed evolution of APEX2 for electron microscopy and proximity labeling. *Nat. Methods* **12**, 51–54.

Lanzicher, T., Martinelli, V., Puzzi, L., Del Favero, G., Codan, B., Long, C. S., Mestroni, L., Taylor, M. R. G. and Sbaizero, O. (2015). The cardiomyopathy lamin A/C D192G mutation disrupts whole-cell biomechanics in cardiomyocytes as measured by atomic force microscopy loading-unloading curve analysis. *Sci. Rep.* **5**, 13388.

Lee, M., Downes, A., Chau, Y.-Y., Serrels, B., Hastie, N., Elfick, A., Brunton, V., Frame, M. and Serrels, A. (2015). In vivo imaging of the tumor and its associated microenvironment using combined CARS/2-photon microscopy. *IntraVital* **4**, e1055430.

Legant, W. R., Shao, L., Grimm, J. B., Brown, T. A., Milkie, D. E., Avants, B. B., Lavis, L. D. and Betzig, E. (2016). High-density three-dimensional localization microscopy across large volumes. *Nat. Methods* **13**, 359–365.

Li, J. L., Goh, C. C., Keeble, J. L., Qin, J. S., Roediger, B., Jain, R., Wang, Y., Chew, W. K., Weninger, W. and Ng, L. G. (2012). Intravital multiphoton imaging of immune responses in the mouse ear skin. *Nat. Protoc.* **7**, 221–234.

Li, D., Shao, L., Chen, B.-C., Zhang, X., Zhang, M., Moses, B., Milkie, D. E., Beach, J. R., Hammer, J. A., Pasham, M. et al. (2015). Extended-resolution structured illumination imaging of endocytic and cytoskeletal dynamics. *Science* **349**, aab3500.

Lim, J., Lee, H. K., Yu, W. and Ahmed, S. (2014). Light sheet fluorescence microscopy (LSFM): past, present and future. *Analyst* **139**, 4758–4768.

Liu, Y.-J., Le Berre, M., Lautenschlaeger, F., Maiuri, P., Callan-Jones, A., Heuzé, M., Takaki, T., Voituriez, R. and Piel, M. (2015). Confinement and low adhesion induce fast amoeboid migration of slow mesenchymal cells. *Cell* **160**, 659–672.

Lye, C. M., Blanchard, G. B., Naylor, H. W., Muresan, L., Huisken, J., Adams, R. J. and Sanson, B. (2015). Mechanical coupling between endoderm invagination and axis extension in *Drosophila*. *PLoS Biol.* **13**, e1002292.

Maco, B., Holtmaat, A., Cantoni, M., Kreshuk, A., Straehle, C. N., Hamprecht, F. A. and Knott, G. W. (2013). Correlative in vivo 2 photon and focused ion beam scanning electron microscopy of cortical neurons. *PLoS ONE* **8**, e67405.

Maker, P. D. and Terhune, R. W. (1965). Study of optical effects due to an induced polarization third order in the electric field strength. *Phys. Rev.* **137**, 801–818.

Manley, S., Gillette, J. M., Patterson, G. H., Shroff, H., Hess, H. F., Betzig, E. and Lippincott-Schwartz, J. (2008). High-density mapping of single-molecule trajectories with photoactivated localization microscopy. *Nat. Methods* **5**, 155–157.

Mao, Y., Sun, Q., Wang, X., Ouyang, Q., Han, L., Jiang, L. and Han, D. (2009). In vivo nanomechanical imaging of blood-vessel tissues directly in living mammals using atomic force microscopy. *Appl. Phys. Lett.* **95**, 013704.

Marjoram, R. J., Guilluy, C. and Burridge, K. (2016). Using magnets and magnetic beads to dissect signaling pathways activated by mechanical tension applied to cells. *Methods* **94**, 19–26.

Masedunskas, A., Milberg, O., Porat-Shliom, N., Sramkova, M., Wigand, T., Amorphimolotham, P. and Weigert, R. (2012). Intravital microscopy: a practical guide to imaging intracellular structures in live animals. *BioArchitecture* **2**, 143–157.

Mercier, L., Böhm, J., Fekonja, N., Allio, G., Lutz, Y., Koch, M., Goetz, J. G. and Laporte, J. (2016). In vivo imaging of skeletal muscle in mice highlights muscle defects in a mouse model of myotubular myopathy. *IntraVital* **5**, e1168553.

Mick, D. U., Rodrigues, R. B., Leib, R. D., Adams, C. M., Chien, A. S., Gygi, S. P. and Nachury, M. V. (2015). Proteomics of primary cilia by proximity labeling. *Dev. Cell* **35**, 497–512.

Mickoleit, M., Schmid, B., Weber, M., Fahrbach, F. O., Hombach, S., Reischauer, S. and Huisken, J. (2014). High-resolution reconstruction of the beating zebrafish heart. *Nat. Methods* **11**, 919–922.

Minsky, M. (1961). Microscopy apparatus. U.S. Patent 3,013,467.

Müller-Reichert, T., Srayko, M., Hyman, A., O'Toole, E. T. and McDonald, K. (2007). Correlative light and electron microscopy of early *Caenorhabditis elegans* embryos in mitosis. *Methods Cell Biol.* **79**, 101–119.

Neuman, K. C. and Nagy, A. (2008). Single-molecule force spectroscopy: optical tweezers, magnetic tweezers and atomic force microscopy. *Nat. Methods* **5**, 491–505.

Nguyen, J. P., Shipley, F. B., Linder, A. N., Plummer, G. S., Liu, M., Setru, S. U., Shaevitz, J. W. and Leifer, A. M. (2016). Whole-brain calcium imaging with cellular resolution in freely behaving *Caenorhabditis elegans*. *Proc. Natl. Acad. Sci. USA* **113**, E1074–E1081.

Nixon, S. J., Webb, R. I., Floetenmeyer, M., Schieber, N., Lo, H. P. and Parton, R. G. (2009). A single method for cryofixation and correlative light, electron microscopy and tomography of zebrafish embryos. *Traffic* **10**, 131–136.

Ossola, D., Amarouch, M.-Y., Behr, P., Vörös, J., Abriel, H. and Zambelli, T. (2015). Force-controlled patch clamp of beating cardiac cells. *Nano Lett.* **15**, 1743–1750.

Paez-Segala, M. G., Sun, M. G., Shtengel, G., Viswanathan, S., Baird, M. A., Macklin, J. J., Patel, R., Allen, J. R., Howe, E. S., Piszczeck, G. et al. (2015). Fixation-resistant photoactivatable fluorescent proteins for CLEM. *Nat. Methods* **12**, 215–218, 4 p following 218.

Pampaloni, F., Chang, B.-J. and Stelzer, E. H. K. (2015). Light sheet-based fluorescence microscopy (LSFM) for the quantitative imaging of cells and tissues. *Cell Tissue Res.* **360**, 129–141.

Pantazis, P., Maloney, J., Wu, D. and Fraser, S. E. (2010). Second harmonic generating (SHG) nanoprobes for in vivo imaging. *Proc. Natl. Acad. Sci. USA* **107**, 14535–14540.

Paszek, M. J., DuFort, C. C., Rossier, O., Bainer, R., Mouw, J. K., Godula, K., Hudak, J. E., Lakins, J. N., Wijekoon, A. C., Cassereau, L. et al. (2014). The cancer glyocalyx mechanically primes integrin-mediated growth and survival. *Nature* **511**, 319–325.

Peddie, C. J., Liv, N., Hoogenboom, J. P. and Collinson, L. M. (2014). Integrated light and scanning electron microscopy of GFP-expressing cells. *Methods Cell Biol.* **124**, 363–389.

Peralta, M., Steed, E., Harlepp, S., González-Rosa, J. M., Monduc, F., Arizaga-Cosano, A., Cortés, A., Rayón, T., Gómez-Skarmeta, J.-L., Zapata, A. et al. (2013). Heartbeat-driven pericardial fluid forces contribute to epicardium morphogenesis. *Curr. Biol.* **23**, 1726–1735.

Pérez-Alvarez, A., Araque, A. and Martín, E. D. (2013). Confocal microscopy for astrocyte in vivo imaging: recycle and reuse in microscopy. *Front. Cell Neurosci.* **7**, 51.

Perrault, C. M., Brugues, A., Bazellieres, E., Ricco, P., Lacroix, D. and Trepat, X. (2015). Traction forces of endothelial cells under slow shear flow. *Biophys. J.* **109**, 1533–1536.

Peticolas, W. L., Goldsborough, J. P. and Rieckhoff, K. E. (1963). Double photon excitation in organic crystals. *Phys. Rev. Lett.* **10**, 43–45.

Planchon, T. A., Gao, L., Milkie, D. E., Davidson, M. W., Galbraith, J. A., Galbraith, C. G. and Betzig, E. (2011). Rapid three-dimensional isotropic imaging of living cells using Bessel beam plane illumination. *Nat. Methods* **8**, 417–423.

Plodinec, M., Loparic, M., Monnier, C. A., Obermann, E. C., Zanetti-Dallenbach, R., Oertel, P., Hytyla, J. T., Aebi, U., Bentires-Alj, M., Lim, R. Y. and Schoenenberger, C. A. (2012). *Nat. Nanotechnol.* **11**, 57–65.

Raab, M., Gentili, M., de Belly, H., Thiam, H. R., Vargas, P., Jimenez, A. J., Lautenschlaeger, F., Voituriez, R., Lennon-Duménil, A. M., Manel, N. et al. (2016). ESCRT III repairs nuclear envelope ruptures during cell migration to limit DNA damage and cell death. *Science* **352**, 359–362.

Raman, C. V. and Krishnan, K. S. (1928). A new type of secondary radiation. *Nature* **121**, 501–502.

Ramspacher, C., Steed, E., Boselli, F., Ferreira, R., Faggianelli, N., Roth, S., Spiegelhalter, C., Messaddeq, N., Trinh, L., Liebling, M. et al. (2015). Developmental alterations in heart biomechanics and skeletal muscle function in desmin mutants suggest an early pathological root for desminopathies. *Cell Rep.* **11**, 1564–1576.

Rankin, B. R., Moneron, G., Wurm, C. A., Nelson, J. C., Walter, A., Schwarzer, D., Schroeder, J., Colón-Ramos, D. A. and Hell, S. W. (2011). Nanoscopy in a living multicellular organism expressing GFP. *Biophys. J.* **100**, L63–L65.

Rego, E. H., Shao, L., Macklin, J. J., Winoto, L., Johansson, G. A., Kamps-Hughes, N., Davidson, M. W. and Gustafsson, M. G. L. (2012). Nonlinear structured-illumination microscopy with a photoswitchable protein reveals cellular structures at 50-nm resolution. *Proc. Natl. Acad. Sci. USA* **109**, E135–E143.

Revach, O.-Y., Weiner, A., Rechav, K., Sabanay, I., Livne, A. and Geiger, B. (2015). Mechanical interplay between invadopodia and the nucleus in cultured cancer cells. *Sci. Rep.* **5**, 9466.

Reynaud, E. G., Kržič, U., Greger, K. and Stelzer, E. H. K. (2008). Light sheet-based fluorescence microscopy: more dimensions, more photons, and less photodamage. *HFSP J.* **2**, 266–275.

Ritsma, L., Steller, E. J. A., Beerling, E., Loomans, C. J. M., Zomer, A., Gerlach, C., Vrisekoop, N., Seinstra, D., van Gorp, L., Schäfer, R. et al. (2012). Intravital microscopy through an abdominal imaging window reveals a pre-micrometastasis stage during liver metastasis. *Sci. Transl. Med.* **4**, 158ra145.

Ritsma, L., Ellenbroek, S. I. J., Zomer, A., Snippert, H. J., de Sauvage, F. J., Simons, B. D., Clevers, H. and van Rheenen, J. (2014). Intestinal crypt homeostasis revealed at single-stem-cell level by in vivo live imaging. *Nature* **507**, 362–365.

Rossier, O., Octeau, V., Sibarita, J.-B., Leduc, C., Tessier, B., Nair, D., Gatterdam, V., Destaing, O., Albigès-Rizo, C., Tampé, R. et al. (2012). Integrins $\beta 1$ and $\beta 3$ exhibit distinct dynamic nanoscale organizations inside focal adhesions. *Nat. Cell Biol.* **14**, 1057–1067.

Rust, M. J., Bates, M. and Zhuang, X. (2006). Sub-diffraction-limit imaging by stochastic optical reconstruction microscopy (STORM). *Nat. Methods* **3**, 793-796.

Salerno, D., Brogioli, D., Cassina, V., Turchi, D., Beretta, G. L., Seruggia, D., Ziano, R., Zunino, F. and Mantegazza, F. (2010). Magnetic tweezers measurements of the nanomechanical properties of DNA in the presence of drugs. *Nucleic Acids Res.* **38**, 7089-7099.

Scheul, T., Wang, I. and Vial, J.-C. (2014). STED-SPIM made simple. *Opt. Express* **22**, 30852.

Schneider, J., Zahn, J., Maglione, M., Sigrist, S. J., Marquard, J., Chojnacki, J., Kräusslich, H.-G., Sahl, S. J., Engelhardt, J. and Hell, S. W. (2015). Ultrafast, temporally stochastic STED nanoscopy of millisecond dynamics. *Nat. Methods* **12**, 827-830.

Schwarz, U. S. and Soiné, J. R. D. (2015). Traction force microscopy on soft elastic substrates: a guide to recent computational advances. *Biochim. Biophys. Acta Mol. Cell Res.* **1853**, 3095-3104.

Shao, L., Kner, P., Rego, E. H. and Gustafsson, M. G. L. (2011). Super-resolution 3D microscopy of live whole cells using structured illumination. *Nat. Methods* **8**, 1044-1046.

Shimozawa, T., Yamagata, K., Kondo, T., Hayashi, S., Shitamukai, A., Konno, D., Matsuzaki, F., Takayama, J., Onami, S., Nakayama, H. et al. (2013). Improving spinning disk confocal microscopy by preventing pinhole cross-talk for intravital imaging. *Proc. Natl. Acad. Sci. USA* **110**, 3399-3404.

Shu, X., Lev-Ram, V., Deerinck, T. J., Qi, Y., Ramko, E. B., Davidson, M. W., Jin, Y., Ellisman, M. H. and Tsien, R. Y. (2011). A genetically encoded tag for correlated light and electron microscopy of intact cells, tissues, and organisms. *PLoS Biol.* **9**, e1001041.

Skuzny, M., Desfosses, A., Prinz, S., Dodonova, S. O., Giers, A., Uetrecht, C., Jakobi, A. J., Abella, M., Hagen, W. J. H., Schulz, J. et al. (2015). An organized co-assembly of clathrin adaptors is essential for endocytosis. *Dev. Cell* **33**, 150-162.

Smith, S. B., Cui, Y. and Bustamante, C. (1996). Overstretching B-DNA: the elastic response of individual double-stranded and single-stranded DNA molecules. *Science* **271**, 795-799.

Spiegelhalter, C., Tosch, V., Hentsch, D., Koch, M., Kessler, P., Schwab, Y. and Laporte, J. (2010). From dynamic live cell imaging to 3D ultrastructure: novel integrated methods for high pressure freezing and correlative light-electron microscopy. *PLoS ONE* **5**, e9014.

Stegmaier, J., Amat, F., Lemon, W. C., McDole, K., Wan, Y., Teodoro, G., Mikut, R. and Keller, P. J. (2016). Real-time three-dimensional cell segmentation in large-scale microscopy data of developing embryos. *Dev. Cell* **36**, 225-240.

Strick, T. R., Allemand, J.-F., Bensimon, D., Bensimon, A. and Croquette, V. (1996). The elasticity of a single supercoiled DNA molecule. *Science* **271**, 1835-1837.

Sugimura, K., Lenne, P.-F. and Graner, F. (2016). Measuring forces and stresses in situ in living tissues. *Development* **143**, 186-196.

Takasaki, K. T., Ding, J. B. and Sabatini, B. L. (2013). Live-cell superresolution imaging by pulsed STED two-photon excitation microscopy. *Biophys. J.* **104**, 770-777.

Tanase, M., Biais, N. and Sheetz, M. (2007). Magnetic tweezers in cell biology. *Methods Cell Biol.* **83**, 473-493.

Taríbí, M., Liu, Y. X., Liu, G.-Y. and Komvopoulos, K. (2015). Single-cell mechanics – An experimental-computational method for quantifying the membrane-cytoskeleton elasticity of cells. *Acta Biomater.* **27**, 224-235.

Tello, M., Spené, C., Hemmerlé, J., Mercier, L., Fabre, R., Allio, G., Simon-Assmann, P. and Goetz, J. G. (2016). Generating and characterizing the mechanical properties of cell-derived matrices using atomic force microscopy. *Methods* **94**, 85-100.

Teer, P., Hasan, M. T. and Denk, W. (2003). Two-photon imaging to a depth of 1000 μ m in living brains by use of a Ti:Al2O3 regenerative amplifier. *28*, 1022-1024.

Théry, M., Pépin, A., Dressaire, E., Chen, Y. and Bornens, M. (2006). Cell distribution of stress fibres in response to the geometry of the adhesive environment. *Cell Motil. Cytoskeleton* **63**, 341-355.

Thiam, H.-R., Vargas, P., Carpi, N., Crespo, C. L., Raab, M., Terriac, E., King, M. C., Jacobelli, J., Alberts, A. S., Stradal, T. et al. (2016). Perinuclear Arp2/3-driven actin polymerization enables nuclear deformation to facilitate cell migration through complex environments. *Nat. Commun.* **7**, 10997.

Tomer, R., Khairy, K., Amat, F. and Keller, P. J. (2012). Quantitative high-speed imaging of entire developing embryos with simultaneous multiview light-sheet microscopy. *Nat. Methods* **9**, 755-763.

Truong, T. V., Supatto, W., Koos, D. S., Choi, J. M. and Fraser, S. E. (2011). Deep and fast live imaging with two-photon scanned light-sheet microscopy. *Nat. Methods* **8**, 757-760.

Truong Quang, B.-A., Mani, M., Markova, O., Lecuit, T. and Lenne, P.-F. (2013). Principles of E-cadherin supramolecular organization in vivo. *Curr. Biol.* **23**, 2197-2207.

Vangindertael, J., Beets, I., Rocha, S., Dedecker, P., Schoofs, L., Vanhoorelbeke, K., Hofkens, J. and Mizuno, H. (2015). Super-resolution mapping of glutamate receptors in *C. elegans* by confocal correlated PALM. *Sci. Rep.* **5**, 13532.

Vartanian, K. B., Kirkpatrick, S. J., Hanson, S. R. and Hinds, M. T. (2008). Endothelial cell cytoskeletal alignment independent of fluid shear stress on micropatterned surfaces. *Biochem. Biophys. Res. Commun.* **371**, 787-792.

Versaevel, M., Grevesse, T. and Gabriele, S. (2012). Spatial coordination between cell and nuclear shape within micropatterned endothelial cells. *Nat. Commun.* **3**, 671.

Vicidomini, G., Moneron, G., Han, K. Y., Westphal, V., Ta, H., Reuss, M., Engelhardt, J., Eggeling, C. and Hell, S. W. (2011). Sharper low-power STED nanoscopy by time gating. *Nat. Methods* **8**, 571-573.

Villringer, A., Them, A., Lindauer, U., Einhaupl, K. and Dirnagl, U. (1994). Capillary perfusion of the rat brain cortex. *Circ. Res.* **75**, 55-62.

Wang, W., Wyckoff, J. B., Frohlich, V. C., Oleynikov, Y., Hüttelmaier, S., Zavadil, J., Cermak, L., Bottinger, E. P., Singer, R. H., White, J. G. et al. (2002). Single cell behavior in metastatic primary mammary tumors correlated with gene expression patterns revealed by molecular profiling. *Cancer Res.* **62**, 6278-6288.

Watanabe, S., Punge, A., Hollopeter, G., Willig, K. I., Hobson, R. J., Davis, M. W., Hell, S. W. and Jorgensen, E. M. (2011). Protein localization in electron micrographs using fluorescence nanoscopy. *Nat. Methods* **8**, 80-84.

Weber, M. and Huisken, J. (2011). Light sheet microscopy for real-time developmental biology. *Curr. Opin. Genet. Dev.* **21**, 566-572.

Weigelin, B., Bakker, G.-J. and Friedl, P. (2016). Third harmonic generation microscopy of cells and tissue organization. *J. Cell Sci* **129**, 245-255.

Weisshart, K. (2014). The basic principle of airy scanning. *Zeiss*.

Welf, E. S., Driscoll, M. K., Dean, K. M., Schäfer, C., Chu, J., Davidson, M. W., Lin, M. Z., Danuser, G. and Fiolka, R. (2016). Quantitative multiscale cell imaging in controlled 3D microenvironments. *Dev. Cell* **36**, 462-475.

Westphal, V., Rizzoli, S. O., Lauterbach, M. A., Kamrin, D., Jahn, R. and Hell, S. W. (2008). Video-rate far-field optical nanoscopy dissects synaptic vesicle movement. *Science* **320**, 246-249.

Willig, K. I., Harke, B., Medda, R. and Hell, S. W. (2007). STED microscopy with continuous wave beams. *Nat. Methods* **4**, 915-918.

Willig, K. I., Steffens, H., Gregor, C., Herholt, A., Rossner, M. J. and Hell, S. W. (2014). Nanoscopy of filamentous actin in cortical dendrites of a living mouse. *Biophys. J.* **106**, L01-L03.

Wolf, S., Supatto, W., Debrégeas, G., Mahou, P., Kruglik, S. G., Sintes, J.-M., Beaupréaire, E. and Candelier, R. (2015). Whole-brain functional imaging with two-photon light-sheet microscopy. *Nat. Methods* **12**, 379-380.

Xiao, Y., Faucher, A., Pola-Morell, L., Heddleston, J. M., Liu, T.-L., Chew, T.-L., Sato, F., Sehara-Fujisawa, A., Kawakami, K. and López-Schier, H. (2015). High-resolution live imaging reveals axon-glia interactions during peripheral nerve injury and repair in zebrafish. *Dis. Model. Mech.* **8**, 553-564.

Yamashita, N., Morita, M., Legant, W. R., Chen, B.-C., Betzig, E., Yokota, H. and Mimori-Kiyosue, Y. (2015). Three-dimensional tracking of plus-tips by lattice light-sheet microscopy permits the quantification of microtubule growth trajectories within the mitotic apparatus. *J. Biomed. Opt.* **20**, 101206-101206.

York, A. G., Parekh, S. H., Nogare, D. D., Fischer, R. S., Temprine, K., Mione, M., Chitnis, A. B., Combs, C. A. and Shroff, H. (2012). Resolution doubling in live, multicellular organisms via multifocal structured illumination microscopy. *Nat. Methods* **9**, 749-754.

York, A. G., Chandris, P., Nogare, D. D., Head, J., Wawrzusin, P., Fischer, R. S., Chitnis, A. and Shroff, H. (2013). Instant super-resolution imaging in live cells and embryos via analog image processing. *Nat. Methods* **10**, 1122-1126.

Zhong, M.-C., Wei, X.-B., Zhou, J.-H., Wang, Z.-Q. and Li, Y.-M. (2013). Trapping red blood cells in living animals using optical tweezers. *Nat. Commun.* **4**, 1768.

Zomer, A., Maynard, C., Verweij, F. J., Kamermans, A., Schäfer, R., Beerling, E., Schiffelers, R. M., de Wit, E., Berenguer, J., Ellenbroek, S. I. J. et al. (2015). In Vivo imaging reveals extracellular vesicle-mediated phenocopying of metastatic behavior. *Cell* **161**, 1046-1057.

ANNEX 2: USING ZEBRAFISH EMBRYO TO DISSECT THE EARLY STEPS OF THE METASTASIS CASCADE



Chapter 15

Using the Zebrafish Embryo to Dissect the Early Steps of the Metastasis Cascade

Gautier Follain, Naël Osmani, Cédric Fuchs, Guillaume Allio, Sébastien Harlepp, and Jacky G. Goetz

Abstract

Most cancers end up with the death of patients caused by the formation of secondary tumors, called metastases. However, how these secondary tumors appear and develop is only poorly understood. A fine understanding of the multiple steps of the metastasis cascade requires *in vivo* models allowing high spatiotemporal analysis of the behavior of metastatic cells. Zebrafish embryos combine several advantages such as transparency, small size, stereotyped anatomy, and easy handling, making it a very powerful model for cell and cancer biology, and *in vivo* imaging analysis. In the following chapter, we describe a complete procedure allowing *in vivo* imaging methods, at high throughput and spatiotemporal resolution, to assess the behavior of circulating tumor cells (CTCs) in an experimental metastasis assay. This protocol provides access, for the first time, to the earliest steps of tumor cell seeding during metastasis formation.

Key words Zebrafish, Circulating tumor cells (CTCs), Metastasis, Injection, Live imaging

1 Introduction

Metastasis progression is a complex multistep process leading to the colonization of distant organs by tumor cells, which will further develop into life-threatening secondary tumors [1]. Cell migration and invasion drive most of the steps involved in the formation of metastases. Once cancer cells acquire an invasive potential, they will (1) colonize the surrounding stroma, (2) reach neighboring vessels and enter blood circulation (intravasation), (3) be transported to distant organs, (4) stop and exit (extravasation) and (5) invade the organs and settle to secondary metastatic sites.

Gautier Follain and Naël Osmani contributed equally to this work.

Electronic Supplementary Material: The online version of this chapter (https://doi.org/10.1007/978-1-4939-7701-7_15) contains supplementary material, which is available to authorized users.

Several in vitro approaches modeling these steps have shed light on the cellular dynamics as well as the molecular pathways involved [2]. However, they often fail to reproduce the complexity of the in vivo microenvironment and thus lack physiological relevance. On the other hand, the mouse model has been extensively used for the past decades to elucidate cancer progression in a more physiopathologically relevant context. These approaches include (1) xenograft of tumor cells in mice to study stromal invasion, and intravasation [3, 4], (2) intracardiac or tail vein injection of tumor cells to model circulating tumor cells (CTC) blood transport, extravasation, and metastatic niche colonization [5, 6] or (3) genetically engineered mouse models, which resume all the steps from the initial tumor formation to metastasis formation in specific organs [7]. However, these approaches often lack the time resolution required to study the complex dynamics of metastasis as it is extremely difficult, money and time-consuming to track and record these rare events in mice. Most importantly, none of these methods allow tracking of the earliest steps of tumor cell seeding in vascular structures. Moreover, these methods are unable to tune the microenvironmental parameters (such as blood flow forces) while offering the possibility to compile observations over a high number of individuals.

Therefore, the use of small transparent organisms, which are more adapted to intravital imaging, is now emerging as new models in cancer biology. The xenograft of tumor cells into the chick embryo chorioallantoic membrane (CAM), which has no immune system during the early developmental stage, has been used to monitor specifically tumor angiogenesis as well as the metastatic cascade [8, 9]. However, the lack of transgenic tools makes the CAM model less suitable for specific intravital imaging. Moreover, the nonstereotyped vasculature hinders high-throughput visualization of single cell behaviors. The zebrafish, and its embryo, have recently emerged as a promising model for cancer research [10–18]. Its embryo is transparent with a high-breeding ability and has an immature immune system making it compatible with tumor xenograft similarly to the CAM. It displays a highly stereotyped vasculature allowing high throughput analysis of tumor cell behavior over several embryos. In addition, there is also a large panel of molecular tools. These include the use of morpholinos [19] to transiently knock down gene expression or the use of knockout/knockin (TALEN and CRISPR/Cas9) to specifically alter gene expression or create cell-type specific fluorescent transgenic lines [20–22].

In this chapter, we propose an original method using the zebrafish embryo as an experimental metastasis model (Fig. 1), which allows the dissection of (1) the early steps of metastasis formation (cell arrest and stable adhesion to the endothelium), (2) CTC exit, through extravasation, from the blood stream and (3) the seeding of the nearby stroma and the formation of micro-metastases with high spatiotemporal resolution. This method enables, for the first time, the study of the behavior of single CTC

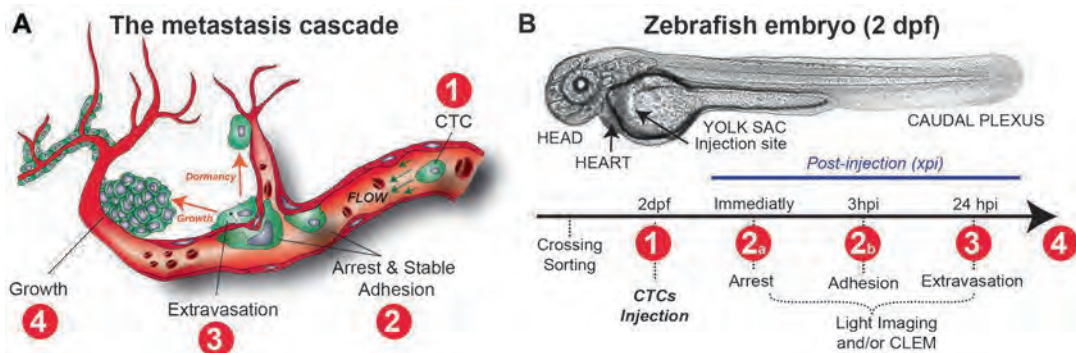


Fig. 1 Zebrafish embryos as a new experimental metastasis model. **(a)** Schematic representation of the last steps of the metastatic cascade: circulating tumor cells, carried by the blood flow, arresting and stably adhering to the endothelial cells before extravasating and forming metastasis. **(b)** Zebrafish embryo, 2 days post-fertilization (dpf) (transmitted light imaging) and global experimental timeline from breeding to CTC injection and imaging of the embryos

or small clusters of CTC in perfused vessels, and thereby offers an unprecedented window to the understanding of the earliest mechanisms that tumor cells have evolved to stop and escape from shear forces, preceding metastatic outgrowths.

2 Materials

2.1 Zebrafish Transgenic and Cell Lines

Ideally, one should use ZF transgenic lines with fluorescent reporters stably expressed in the endothelium to label the vasculature. We mostly use the *Tg(fli1a:EGFP)* transgenic line [23] (see Note 1). This protocol is designed for studying the metastatic behavior of tumor cells (cell lines or primaries; from zebrafish, mouse or human origin). Each line will differ in its ability to adhere and extravasate and one could assess this potential by comparing cells with knock-down or overexpression of any gene of interest (using siRNA or shRNA approaches). In addition, this protocol is perfectly suited for assessing the behavior of any protein/organelle of interest, provided that a corresponding stably fluorescent cell line can be established.

2.2 Zebrafish Handling and Injection Solutions

1. Danieau stock (30×): 1.74 mol/L NaCl, 21 mmol/L KCl, 12 mmol/L MgSO₄, 18 mmol/L Ca(NO₃)₂, HEPES 150 mmol/L in water.
2. Danieau (0.3×): The stock solution is diluted 1:100 in water before use (0.3×).
3. PTU stock (50×): 15 g of phenylthiourea (Sigma) in 100 mL of Danieau 0.3×, dissolve by heating at 60 °C under agitation. Stock is stored as 10 mL aliquots at -20 °C.
4. Danieau/PTU: 1 aliquot of PTU is added to 490 mL Danieau 0.3× before use (see Note 2).

5. Danieau/PTU/tricaine: Tricaine stock (25×): 210 mg in 49 mL of water, adjust pH to 7 (for example, using Tris 1 M pH 9.4). Store the stock as 1 mL aliquots at -20 °C. One aliquot is added to 24 mL Danieau/PTU before use (see Note 3). For confocal imaging, use 0.5× Danieau/PTU/Tricaine to prevent fish movement.
6. LMP Agarose 0.8%: Low Melting Point agarose at 0.8% (m/v) in Danieau 0.3× is used to immobilize the embryos during mounting and imaging. It is stored as aliquots of 24 mL at room temperature. For use, melt at 80 °C, cool down and maintain to 40 °C before adding 1 aliquot of Tricaine stock. Further proceed with mounting.
7. Mineral oil (Sigma) is needed to fill the injection glass capillary before injection (see Note 4).

2.3 Cell Preparation

Use the appropriate medium for your cell line of choice, supplemented with usual additives. Cells can be prepared for injection in their cell culture medium or in PBS. PBS 1× or PBS 1× supplemented with 0.526 mM EDTA. EDTA is used to wash the cell before trypsinization. Use the trypsin concentration usually chosen to detach cells (for us: trypsin-EDTA 0.05% to 0.25% in PBS).

2.4 Equipment (Fig. 2)

1. Classical culture room equipment: To prepare the cells, classical culture room equipment is needed: hood, incubator, centrifuge, cell counter and microscope.
2. Capillary puller: To pull the microneedle from glass capillaries, a micropipette puller is needed (Shutter instrument). We recommend using glass capillaries with 0.53 mm inner diameter (ID) and 1.14 mm outer diameter (OD) (Drummond). After pulling, microneedles are microforged to reach a 20–25 µm ID tip (see Note 5).
3. Embryos mounting (Fig. 2a, b): Heating block, transfer pipets, tweezers, petri Dishes (10 to 15 cm in diameter) and 35 mm glass-bottom dishes, uncoated (MatTek).
4. Nanoinjection (Fig. 2c): We used the Nanoject II (Drummond) that is perfectly suited for injecting ZF embryos. We combine the microinjector with the following stereomicroscope.
5. Microscopy (Fig. 2d): The stereomicroscope Leica M205FA equipped with the LAS AF 4.0 software is used for injection and live imaging. The detailed setup composition is the following: fluorescent excitation lamp (Mercury short-arc reflector lamp, EL6000), GFP filter (Ex. 450–490/Em. 500–550) and ET-C filter (Ex. 533–557/Em. 570–640), Plan APO objective 20x (10450028), camera (DFC3000 G), heating plate system (MATS).
6. Confocal microscopy: Any confocal microscope of choice would be appropriate. We are familiar with SP2/5/8 confocal

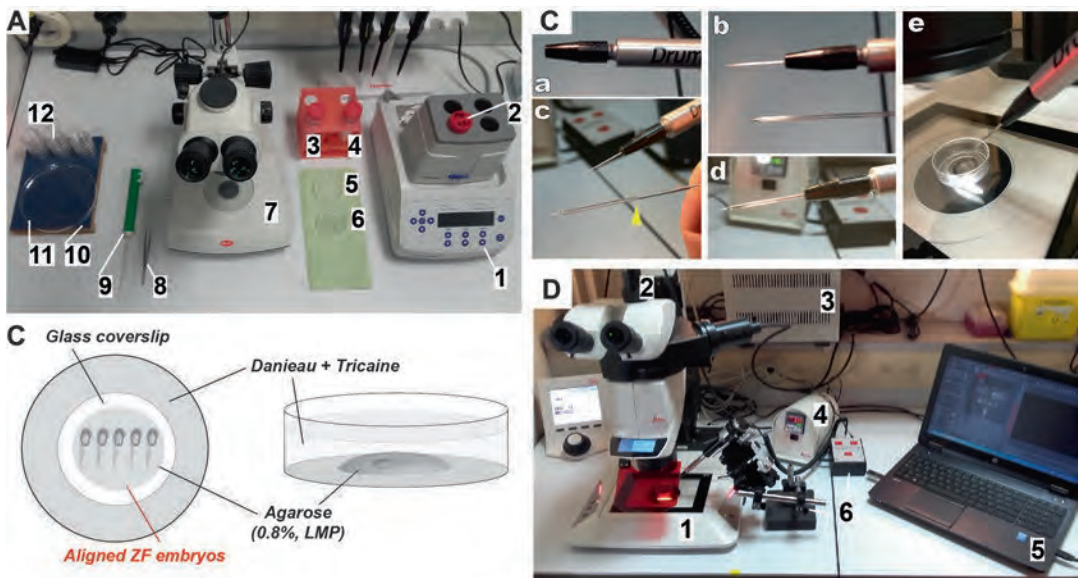


Fig. 2 Material for mounting and injection. (A) Example of bench organization used to mount the embryos: 1 Heating block to keep the LMP agarose at 40 °C. 2 LMP agarose 0.8% to immobilize the embryos. 3 Danieau/PTU/tricaine ready to use. 4 Danieau PTU to be added after agarose polymerization. 5 Petri dish filled with Danieau/PTU/tricaine. 6 Petri dish filled with Danieau/PTU and the embryos to be mounted. 7 Binoculars. 8 Tweezers to place the embryos within the LMP agarose drop. 9 Aspiration pipet used to transfer embryos from dish to dish. 10 Dark surface to be able to visualize the embryo. 11 Petri dish to mix the embryos in the drop of agarose. 12 Glass-bottomed petri dish compatible with imaging (MatTek). (B) Schematic view of the embryos aligned for injection and imaging in the MatTek dish. (C) Microneedle preparation and installation: (a) microinjector head, (b) microneedle (bottom) and microinjector with the piston out, (c) filling the microneedle with mineral oil, (d) microneedle mounted on the piston, (e) microinjector ready-to-use under the stereomicroscope. (D) Microinjection setup: 1 Stereomicroscope. 2 Camera. 3 Fluorescent illumination lamp. 4 Heating plate controller. 5 Computer with the Leica software. 6 Microinjector and its controller

microscope systems (Leica, either upright or inverted) which are used for confocal acquisition with an immersion 20× objective or a water-dipping 25× objective (HC FLUOTAR L 25×/0.95 W VISIR).

3 Methods

3.1 Zebrafish Embryos Handling

1. Zebrafish embryos should be maintained in 5–10 cm diameter petri dish, in Danieau 0.3× for the first 24 h post fertilization (hpf) and then transferred to Danieau/PTU for the rest of the experiments.
2. Embryos are carefully moved using plastic transfer pipet.
3. Dechorionate embryos at least two hours before mounting, using thin tweezers, to avoid any bending of the embryos during the mounting stage.

3.2 Zebrafish Mounting

Mounting can be performed using a simple and reproducible bench organization (Fig. 2a). The goal of the mounting step is to end up with immobilized embryos in a drop of LMP agarose, stuck on a glass-bottomed petri dish suitable for imaging.

1. Prepare the required solutions: Danieau/PTU, Danieau/PTU/tricaine (1 aliquot of 1 mL in 24 mL), melted and warm-kept LMP agarose supplemented with an aliquot of 1 mL tricaine.
2. Prepare tweezers, aspiration pipet, glass-bottom dish and a 10–15 cm diameter petri dish. To mount embryos efficiently, we realize sequentially the following steps as quickly as possible.
3. Transfer embryos from the Danieau/PTU to Danieau/PTU/tricaine under a binocular loupe, the anesthetic effect should be instantaneous (*see Note 6*).
4. Put a drop of agarose in a petri dish next to the binocular loupe.
5. Move the embryos from the Danieau/PTU/tricaine to the drop of agarose, in the smallest volume of Danieau/PTU/tricaine possible to avoid excessive agarose dilution.
6. Transfer the embryos (usually 8) with the agarose to the glass-bottomed dish.
7. Place the embryos as wished using tweezers, before the agarose solidifies (Fig. 2b, *see Note 7*).
8. After 1–2 min, the agarose should be solidified.
9. Add Danieau/PTU to keep the embryo in a liquid medium.
10. Store embryos in the incubator at 28 °C until injection and imaging.

3.3 Preparation of the Cells to Be Injected, at a Defined Concentration

1. Tumor cells (TCs) should be prepared for injection in their growing medium or in PBS.
2. Cells are usually concentrated at 10^8 cells per mL for injection, which roughly represents a final volume of 80 μ L of cell suspension from a confluent 10 cm culture dish. These parameters need to be adjusted and adapted to your cell line of interest.

3.4 Injection Preparation

For the injection of TCs, the Nanoject II (Drummond) is used in association with a fluorescence stereomicroscope (Fig. 2c, d).

1. Microneedles are pulled from capillaries and microforged extemporaneously using a capillary puller (Shutter Instrument) and a microforge to have an inner diameter of 20–25 μ m (*see Note 5*).
2. The microneedle is filled with mineral oil before inserting it around the Nanoject piston.
3. Five to ten microliters of cell suspension are deposited on a piece of Parafilm under the stereomicroscope, enabling a visual control during microneedle loading (Fig. 3a, *see Note 8*).

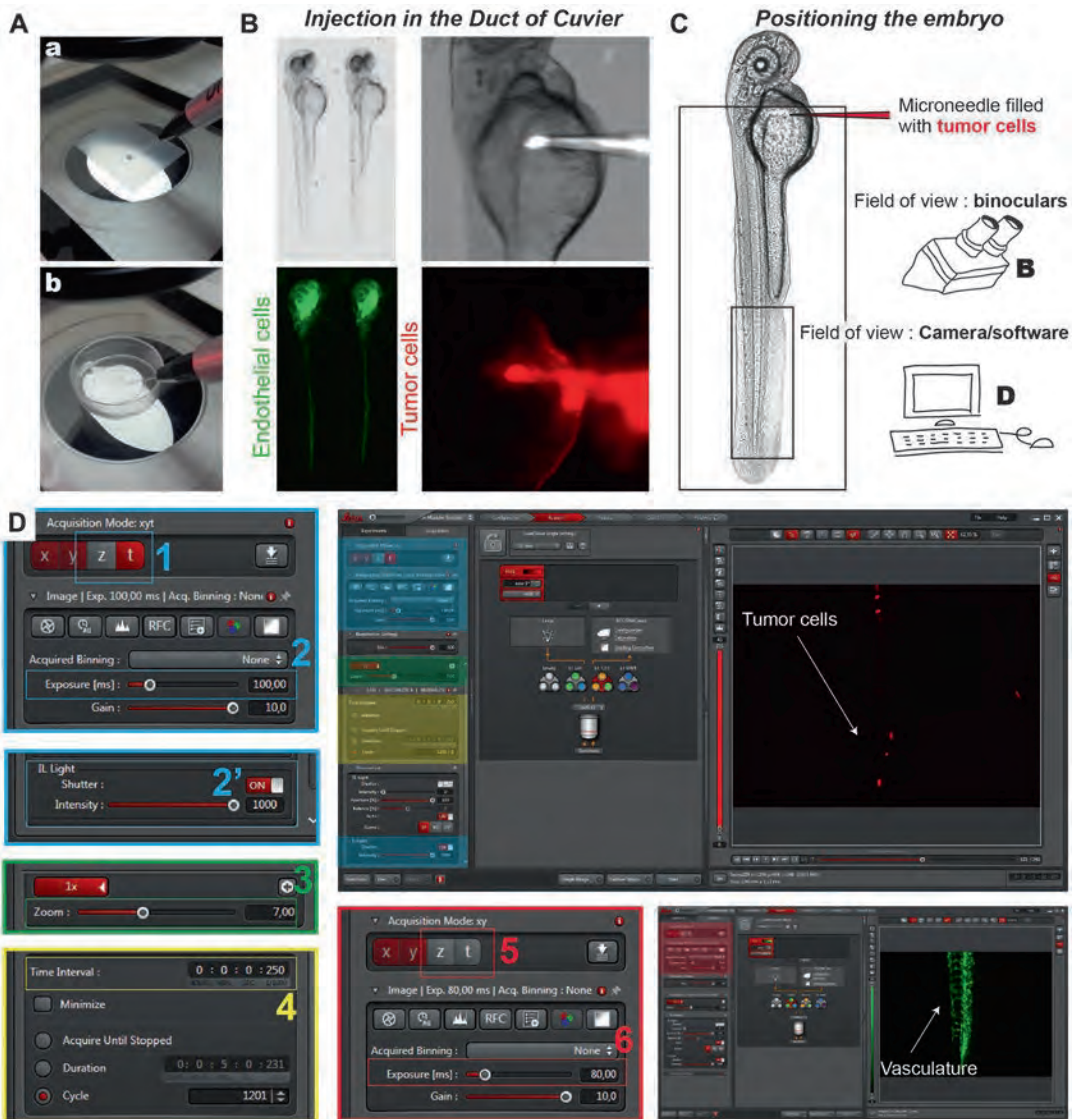


Fig. 3 Injection and live imaging setup. **(A)** Pictures showing the filling of the capillary with the solution containing tumor cells (a) and the rough positioning of the injector with a MatTek dish and zebrafish embryos (b). **(B)** Pictures showing the aligned fish, ready for injection under the stereomicroscope, with transmitted light and GFP filter (right); the position of the microneedle filled with cells for injecting in the duct of Cuvier with transmitted light and ET-C filter (left). **(C)** Schematic view of the situation for live injection imaging: with magnification optimized at $\times 7.0$, one will see the point of injection and the caudal plexus in the oculars, and at the same time, camera field of view will cover the entire plexus. **(D)** Software setting for live injection imaging: First, to do the time-lapse imaging, ET-C filter, Time (7) dimension set to on (1), Adapted exposure with maximal intensity (2,2'), Zoom on $\times 7.00$ (3), Time interval on 250 ms (4). Second, to record the endothelium (background image), GFP filter, Time dimension set to off (5), Adapted exposure (6)

3.5 Intravascular Injection of CTCs Coupled to Live Imaging (Fig. 3)

Our past experience demonstrated that most CTCs stop in the caudal plexus of the embryo [24]. Thus, we designed an imaging workflow such that injection of CTCs can be instantaneously coupled to live imaging of both the TCs and the vasculature in the caudal plexus of a developing ZF embryo (Fig. 3a–c). This offers several advantages such as the highly stereotyped vasculature of that region, which allows to observe multiple animals, cumulate and spatially correlate the observations made. Furthermore, this region is relatively thin, which allows to quantitatively track flowing CTCs in a vascular network that is rather flat. To perform simultaneous injection and imaging, the Leica LAS_AF software is used.

1. In order to capture flowing and arresting CTCs at a speed compatible with real time imaging, only the channel corresponding to the injected cell marker (red fluorescent protein) is recorded during injection. All the parameters are then set up to record this channel at the magnification of interest (light intensity, exposure, frame rate, etc.). In our case: maximal intensity, maximal gain, 100 ms exposure time allowing an acquisition at 4 frames per second) (Fig. 3d).
2. Place the microneedle at the site of injection within the duct of Cuvier (Fig. 3b).
3. Once the ZF embryo and the injector are properly positioned (Zoom $\times 7.00$, Fig. 3c), image capture is started simultaneously with the injection itself allowing to control the injection with the binoculars while recording the behavior of flowing CTCs using the software (Fig. 3c, d).
4. At the end of the live recording, a single image of the zebrafish vasculature is acquired, without moving the embryo. This image will be used as a background for the registered time-lapse recording of CTCs. The acquisition parameters are modified accordingly: the time-lapse mode is turned off, the light filter is changed to the GFP one and the exposure is lowered to 80 ms (Fig. 3d). In our experience, 5 min of recording is sufficient to document the earliest events such as CTC slowing, transient arrest events, and definitive arrest.

3.6 Time-Lapse Analysis in Image J

Once the time-lapse recording of the behavior of CTCs has been performed, the data obtained offers several angles of analysis. Here, we first propose a method for optimal movie rendering of the earliest steps of metastatic behavior (Fig. 4).

1. We use the ImageJ software. The single image of the zebrafish vasculature is duplicated n-time to match the number of recorded images on the injected cell channel. The following Java script can be used:

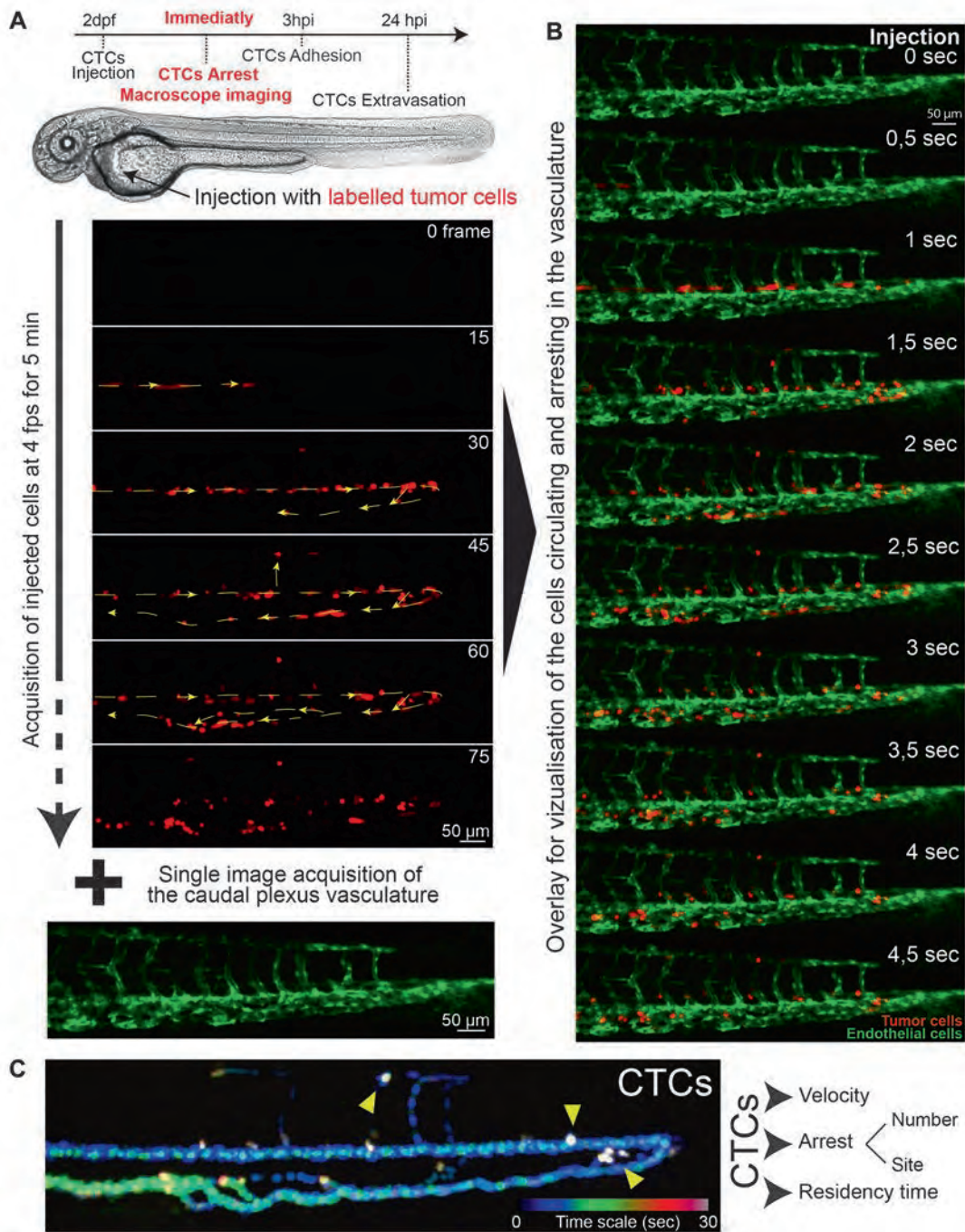


Fig. 4 Live injection imaging processing. **(a)** Timeline and schematic representation of the method: Single channel (red) acquisition is performed to live record the events with the maximal temporal resolution, followed by a single image acquisition in the green channel. **(b)** Processing with ImageJ allows the reconstruction of the injection movie. **(c)** Post-treatment with time color coding (ImageJ > Hyperstack > time color coding) allowing the qualitative and quantitative study of the movie

```

        title = "duplicate";
        Number_of_images=512;
        Dialog.create("New Parameters");
        Dialog.addNumber("Number_of_images:", 512);
        Dialog.show();
        title =Dialog.getString();
        Number_of_images = Dialog.getNumber();
        for (i = 1; i < Number_of_images; i++){
        run("Duplicate...", "title=ENDOTHELIUM");
        }
        run("Images to Stack", "name=endo title=[] use");
    
```

2. Merge the two stacks and optimize the color balance for each channel (Fig. 4b).
3. Post-treatment with time color coding (ImageJ > Hyperstack > time color coding) can be performed on the CTC channel (Fig. 4c; *see Note 9*).

3.7 Confocal Imaging to Record the Adhesion and Extravasation Pattern

1. Once early arrest of CTCs has been recorded, embryos can be placed back at 28 °C (incubator) and further studied to document subsequent important events of metastatic seeding. Here, we propose to further document, at high-throughput and spatial resolution, the stable intravascular adhesion of CTCs (Fig. 5a–c), as well as their capacity to extravasate and colonize the local parenchyma (Fig. 5d, e).
2. We have identified 3 hpi as an optimal timing for detecting and documenting stably attached intravascular TCs. We suggest using confocal imaging for studying the location of arrested TCs in relation to the vasculature. The caudal plexus is acquired sequentially for red (tumor cells) and green (endothelial cells) channels, coupled with transmitted light. Excitation/integration parameters are adjusted and 1.5 µm Z-step is selected.
3. For statistical analysis, a large batch of zebrafish caudal plexus can be acquired one after the other: We estimated the time for a single confocal stack (with a resolution of 1024 × 512) to be 5–8 min, depending on the width of the acquisition (*see Note 10*). Again, thanks to the highly stereotyped vasculature in that region, we have developed a method allowing the compilation of a high number of embryos, thereby providing a powerful statistical analysis of the behavior of metastatic cells in realistic conditions.

3.8 Image Preparation for High-Throughput Analysis Through Heat Mapping

Here, we propose a method for generating heat maps representing the density of TCs in a given region of the ZF embryo, over a high number of embryos. This method exploits the stereotyped vasculature of the embryo and uses a reference background image of the caudal plexus vasculature (Fig. 5b). The heat map is scaled from blue (lowest density of cells) to red (highest density). For display purposes,

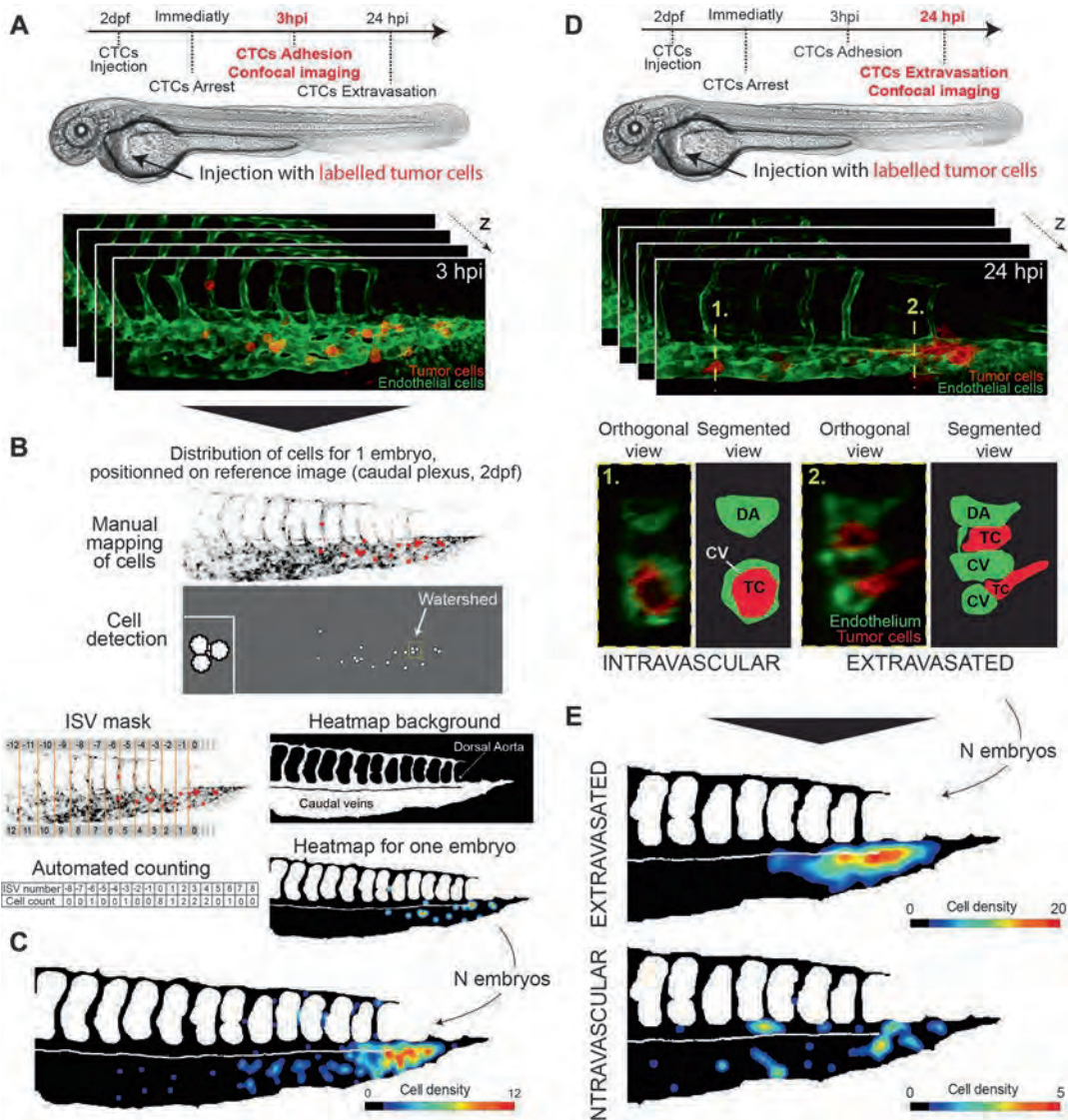


Fig. 5 Confocal imaging and analysis, at 3 and 24 hpi. **(a)** Schematic representation and timeline of the method: imaging at 3 hpi to record the stable adhesion pattern of tumor cells in the zebrafish caudal plexus. **(b)** Heat mapping protocol: From the manual mapping (top), to the automated counting of the cells per ISV and the heat map creation (bottom). Mapping automated recognition image is provided to illustrate the role of the watershed operation in the MatLab script (small insert show the watershed result, separating three cells). **(c)** Illustrative result from the heat mapping protocol at 3 hpi for several embryos. **(d)** Schematic representation and timeline of the method: imaging at 24 hpi for recording the extravasation pattern of tumor cells in the zebrafish plexus. Orthogonal views (ImageJ > Stack > Reslice) at different positions (yellow dashed lines) are provided to illustrate the best way to assess the cell situation (intravascular/extravasated). **(e)** Illustrative results from the heat-mapping protocol for intravascular versus extravasated cells

heat maps are revealed on the reference image (*see Note 11*) of the caudal plexus of a zebrafish embryo at 48 hpf.

1. Confocal stacks containing the position of each single CTC are projected into a single image (maximum projection tool of Image J).
2. The resulting image is used to relocate the exact positions over the reference image, using small red circle in ImageJ (Fig. 5b; brush tool, 5–10 pixels; *see Note 12*).
3. The localization images are saved as .tif and pooled in a single stack in ImageJ.

3.9 Heat Mapping Procedure

The heat map derived from the stack of localization images is created using a MatLab script (also compatible with Octave). For the sake of readability, the gray bright field image of the reference fish is processed using thresholds and morphological transformations to produce a black and white representation of the embryo vasculature. We further added a white line in the image to highlight the localization of the dorsal aorta and distinguish it from the caudal veins (Fig. 5b). The stacks are processed image-by-image in order to get the cell localization data in each embryo.

1. First, we subtract the green channel from the red one to remove the reference background image and leave only a binary image of the cells (previously displayed as red circles).
2. A watershed operation is used to individualize cells that are very close one to another and could be analyzed as a single cell (*see Note 12*).
3. Once the cells are individualized, we extract the position data using the *bwlabel* and *regionprops* functions. The script then processes this position data to produce a heat map built by adding a circle with a dimensional Gaussian shape intensity distribution.
4. For each point where a cell has been detected, the script adds a circle centered at the found position with a dimensional Gaussian intensity distribution with a maximal value of unity and a width of 6 (approximation of the real cell size at the resolution used here, *see Note 13*). The values of all the curves are added for each point in space, resulting in an image that represents the density of cells/pixel (Fig. 5c, e).
5. The color scale can then be adjusted to display a maximum (in red) where the largest cell density is observed (*see Note 14*).
6. The script also produces a table (saved as a .csv file) gives a quantitative analysis of cell locations data. The script then compares the position of a cell to the position of the ISVs and

gives its absolute value. This is automatically done for each fish and provides a file containing a line for each image/fish.

7. We propose here to divide the caudal plexus in several regions (Fig. 5c), based on the intersegmental vessels (ISV) stereotyped positions. The latter are registered from $-n$ to n : n being the number of ISVs in the reference image with negative values corresponding to positions within the dorsal aorta, positive values corresponding to positions within the caudal veins, and 0 representing the arteriovenous junction (see Note 15).

3.10 Tracking Tumor Metastasis at High Spatiotemporal Resolution

The experimental metastasis assay that we propose here is further compatible with a fine analysis of single CTC behavior. Here, we propose two angles of analysis that we have developed and used in our studies [24] for investigating various parameters of successful metastatic outgrowth (Fig. 6a). First, provided that one has access to fast confocal imaging (see Note 16), high-speed time lapse analysis of blood flow can be performed in vascular regions undergoing arrest or extravasation events of CTCs (Fig. 5b–e). While confocal imaging allows to capture, at high spatial resolution, the position and behavior of single CTC in relation to the vasculature, high-speed imaging (and subsequent tracking) of flowing red blood cells allows to document the hemodynamic environment of such an event, and study its potential influence on the extravasation process. We have recently shown that blood flow actively contributes to the arrest and extravasation of CTCs [24]. In addition, the ZF embryo is perfectly suited for tracking events such as arrest and extravasation at very high resolution using Correlative Light and Electron Microscopy methods [25, 26] (Fig. 5g). We have developed in the past protocols for achieving correlation of events imaged within living ZF embryos with high-resolution of Electron Microscopy [26]. When applied to single CTCs imaged within the ZF embryos, at different stages of the extravasation process, i.e., arrest, extravasation, or metastatic growth), this methodology allows to provide a high-resolution view of subcellular regions and organelles of cells, as well as of neighboring stromal cells such as endothelial or immune cells (Fig. 5g).

4 Notes

1. Many other lines (expressing fluorescent reporters in various cell types) are compatible with the following protocol. One is free to use any line of interest depending on the aims of the experimental approach. A long list of transgenic lines can be found on the ZFIN database (<https://zfin.org/action/fish/search>).

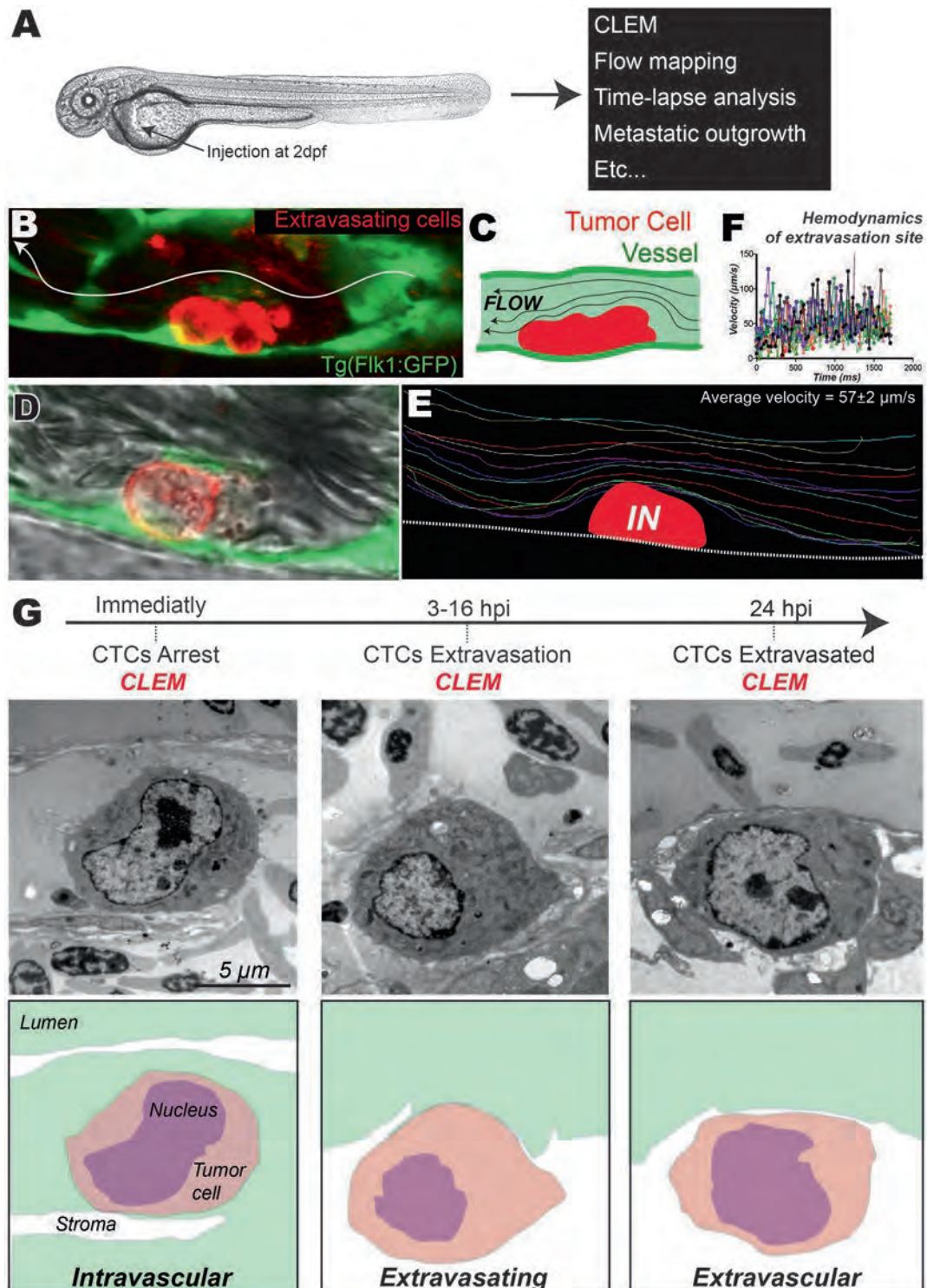


Fig. 6 Zebrafish embryo as a versatile experimental metastasis model. **(a)** Nonexhaustive list of the applications of the described method. **(b)** Zoom in a cluster of arrested tumor cells with confocal imaging. **(c)** Schematic of the arrested cluster of cells in the circulation from **(b)**. **(d)** Confocal imaging with transmitted light allowing the visualization of the blood cells. **(e)** Representation of the blood cell tracking on the confocal images. **(f)**

2. PTU (phenylthiourea—used to prevent melanogenesis) is rather unstable at 28 °C. Store Danieau/PTU at room temperature for 2 weeks.
3. Tricaine (used to anesthetize the embryos) is unstable at room temperature and 40 °C. Prepare fresh solutions from your frozen stock 25× for each experiment.
4. Mineral oil is an incompressible fluid, nonmiscible with water that allows a perfect transmission of the piston movement during injection.
5. The microneedle tip can also be broken with tweezers, under a stereomicroscope, but we recommend to do this step with a prototype obtained with a microforge for careful comparison.
6. As tricaine gets slightly more diluted for each mounted dish, it progressively loses its anesthetic power. At some point, do not hesitate to change to fresh Danieau/PTU/tricaine.
7. The best option for injection and imaging is to have all the embryos as close as possible, with one single orientation, in the center of the glass coverslip. During the mounting, if you are not fast enough to arrange the embryos, you can redo the mounting easily by adding some Danieau/PTU/tricaine in the glass-bottomed dish. Then, pipet the embryos back to the Danieau/PTU/tricaine and start again the mounting.
8. This is the utmost critical step for a successful injection session. If at any moment during capillary filling, one can see any resistance, bubble formation, etc., it means that the filling step is compromised. We advise changing the capillary for a new one and restart the filling step.
9. Because the vasculature is mostly planar in that region of the ZF embryo, this method allows to reconstruct a fine time-lapse analysis of the very first events of intravascular CTCs seeding in perfused blood vessels. The highly stereotyped architecture of the ZF vasculature in that region further offers the possibility to analyze a high number of embryos upon 5 min of time-lapse recording. This method thus offers the first, unprecedented, protocol for studying the arrest, at high throughput and spatiotemporal resolution, of CTCs in realistic vascular environments.
10. Alternatively, one can start a time-lapse for several hours to follow the evolution of a single event (or multiple events using the multiposition tool). From our experience, zebrafish embryos can handle more than 18 h of time-lapse recording in a thermostatic chamber.

Fig. 6 (continued) Tracking results allowing a fine flow dissection around the tumor cells in the vasculature. (g) Experimental timeline with Correlative Light and Electron Microscopy (CLEM) allowing high-resolution dissection of the extravasation process. Transmitted electron microscopy images (top) and their segmentation (bottom) are provided to illustrate several steps of the metastatic cascade

11. This can be changed by entering the name of your own background image (line 26 of the Matlab script), keeping in mind that this image has to be the reference image for all the data (the same dimension is critical).
12. We advise to use a small dot diameter for the manual localization. Indeed, if the marks are overlapping too much, the watershed operation will not be able to distinguish and dissociate the cells. There is a risk that the script will produce errors by detecting one cell instead of a cluster of several cells. The script cannot work with smaller diameters than 5 pixels but this size is enough to prevent most of the critical overlaps.
13. This can be changed by changing the sigma value (line 42 of the Matlab script).
14. Any MatLab color scale can be used and modified for better readability (line 59 of the Matlab script).
15. This approach is further compatible with confocal acquisitions performed 24 hpi, aiming to document the extravasation behavior of TCs. Here, the intravascular (versus extravascular) location of cells is assessed by displaying the confocal acquisitions as orthogonal views (Fig. 5d). We suggest using this method for confidently attributing intravascular versus extravascular localization of recorded cells. Doing so and applying the previously described heat-mapping protocol, this will lead to two distinct heat maps for a single embryo: a heat map for intravascular cells, a heat map for extravascular cells (Fig. 5e). This step implies the creation of two heat maps for each embryo: one with the extravasated cells and one with the intravascular cells for each embryo.
16. Fast blood flow imaging can be performed using, for example, SP5/SP8 confocal microscopes equipped with resonant scanner. We usually record the displacement of red blood cells using transmitted light at a scanning speed of about 100 fps.

Acknowledgments

We thank all members of the Goetz Lab for helpful discussions throughout the development of this technology. We are grateful to Sofia AZEVEDO and Nina FEKONJA for their help in various aspects of this method. We are very much grateful to Francesca PERI (EMBL) and Kerstin RICHTER (EMBL) for providing zebrafish embryos. This work has been funded by Plan Cancer (OptoMetaTrap, to J.G. and S.H) and CNRS IMAG'IN (to S.H., J.G., and C.P.) and by institutional funds from INSERM and University of Strasbourg. G.F. is supported by La Ligue Contre le Cancer. N.O is supported by Plan Cancer. G.A. was supported by FRM (Fondation pour la Recherche Médicale).

References

1. Massagué J, Obenauf AC (2016) Metastatic colonization by circulating tumour cells. *Nature* 529:298–306
2. Katt ME, Placone AL, Wong AD, Xu ZS, Searson PC (2016) In vitro tumor models: advantages, disadvantages, variables, and selecting the right platform. *Front Bioeng Biotechnol* 4:12
3. Cheung KJ, Gabrielson E, Werb Z, Ewald AJ (2013) Collective invasion in breast cancer requires a conserved basal epithelial program. *Cell* 155:1639–1651
4. Karreman MA, Hyenne V, Schwab Y, Goetz JG (2016) Intravital correlative microscopy: imaging life at the nanoscale. *Trends Cell Biol* 26:848–863
5. Kienast Y et al (2010) Real-time imaging reveals the single steps of brain metastasis formation. *Nat Med* 16:116–122
6. Cheung KJ et al (2016) Polyclonal breast cancer metastases arise from collective dissemination of keratin 14-expressing tumor cell clusters. *Proc Natl Acad Sci U S A* 113: E854–E863
7. Cheon D-J, Orsulic S (2011) Mouse models of cancer. *Annu Rev Pathol* 6:95–119
8. Deryugina EI, Kiosses WB (2017) Intratumoral cancer cell intravasation can occur independent of invasion into the adjacent stroma. *Cell Rep* 19:601–616
9. Leong HS et al (2014) Invadopodia are required for cancer cell extravasation and are a therapeutic target for metastasis. *Cell Rep* 8:1558–1570
10. Amatruda JF, Shepard JL, Stern HM, Zon LI (2002) Zebrafish as a cancer model system. *Cancer Cell* 1:229–231
11. Stoletov K, Klemke R (2008) Catch of the day: zebrafish as a human cancer model. *Oncogene* 27:4509–4520
12. Stoletov K, Montel V, Lester RD, Gonias SL, Klemke R (2007) High-resolution imaging of the dynamic tumor cell–vascular interface in transparent zebrafish. *Proc Natl Acad Sci U S A* 104:17406–17411
13. Stoletov K et al (2010) Visualizing extravasation dynamics of metastatic tumor cells. *J Cell Sci* 123:2332–2341
14. White RM et al (2008) Transparent adult zebrafish as a tool for in vivo transplantation analysis. *Cell Stem Cell* 2:183–189
15. Heilmann S et al (2015) A quantitative system for studying metastasis using transparent zebrafish. *Cancer Res* 75:4272–4282
16. Kaufman CK et al (2016) A zebrafish melanoma model reveals emergence of neural crest identity during melanoma initiation. *Science* 351:aad2197
17. Tang Q et al (2016) Imaging tumour cell heterogeneity following cell transplantation into optically clear immune-deficient zebrafish. *Nat Commun* 7:10358
18. Kim IS et al (2017) Microenvironment-derived factors driving metastatic plasticity in melanoma. *Nat Commun* 8:14343
19. Corey DR, Abrams JM (2001) Morpholino antisense oligonucleotides: tools for investigating vertebrate development. *Genome Biol* 2:reviews1015
20. Zhang Y, Huang H, Zhang B, Lin S (2016) TALEN- and CRISPR-enhanced DNA homologous recombination for gene editing in zebrafish. *Methods Cell Biol* 135:107–120
21. De Santis F, Di Donato V, Del Bene F (2016) Clonal analysis of gene loss of function and tissue-specific gene deletion in zebrafish via CRISPR/Cas9 technology. *Methods Cell Biol* 135:171–188
22. Ablain J, Zon LI (2016) Tissue-specific gene targeting using CRISPR/Cas9. *Methods Cell Biol* 135:189–202
23. Lawson ND, Weinstein BM (2002) In vivo imaging of embryonic vascular development using transgenic zebrafish. *Dev Biol* 248:307–318
24. Follain G, Osmani N, Azevedo S, Allio G, Mercier L, Karreman MA, Solecki G, Garcia-Leon MJ, Lefebvre O, Fekonja N, Hille C, Chabannes V, Dollé G, Metivet T, Der Hovsepian F, Prudhomme C, Ruthensteiner B, Kemmling A, Siemonsen S, Schneider T, Fiehler J, Glatzel M, Winkler F, Schwab Y, Pantel K, Harlepp S, Goetz JG (2017) Hemodynamic forces tune the arrest, adhesion and extravasation of circulating tumor cells. *Dev Cell*. <https://doi.org/10.1101/183046>
25. Goetz JG et al (2014) Endothelial cilia mediate low flow sensing during zebrafish vascular development. *Cell Rep* 6:799–808
26. Goetz JG, Monduc F, Schwab Y, Vermot J (2015) Using correlative light and electron microscopy to study zebrafish vascular morphogenesis. *Methods Mol Biol* 1189:31–46

**ANNEX 3: HEMODYNAMIC FORCES CAN BE ACCURATELY MEASURED IN VIVO
WITH OPTICAL TWEEZERS**

Hemodynamic forces can be accurately measured in vivo with optical tweezers

Sébastien Harlepp^{a,b,c,*}, Fabrice Thalmann^{a,d}, Gautier Follain^{a,e,f,g}, and Jacky G. Goetz^{a,e,f,g,*}

^aUniversité de Strasbourg, 67000 Strasbourg, France; ^bIPCMS, UMR7504, 67200 Strasbourg, France; ^cLabEx NIE and ^fLabEx Medalis, Université de Strasbourg, 67000 Strasbourg, France; ^dICCS, UPR22, 67034 Strasbourg, France; ^eInserm UMR_S1109, MN3T, 67200 Strasbourg, France; ^gFédération de Médecine Translationnelle de Strasbourg (FMTS), 67000 Strasbourg, France

ABSTRACT Force sensing and generation at the tissue and cellular scale is central to many biological events. There is a growing interest in modern cell biology for methods enabling force measurements *in vivo*. Optical trapping allows noninvasive probing of piconewton forces and thus emerged as a promising mean for assessing biomechanics *in vivo*. Nevertheless, the main obstacles lie in the accurate determination of the trap stiffness in heterogeneous living organisms, at any position where the trap is used. A proper calibration of the trap stiffness is thus required for performing accurate and reliable force measurements *in vivo*. Here we introduce a method that overcomes these difficulties by accurately measuring hemodynamic profiles in order to calibrate the trap stiffness. Doing so, and using numerical methods to assess the accuracy of the experimental data, we measured flow profiles and drag forces imposed to trapped red blood cells of living zebrafish embryos. Using treatments enabling blood flow tuning, we demonstrated that such a method is powerful in measuring hemodynamic forces *in vivo* with accuracy and confidence. Altogether this study demonstrates the power of optical tweezing in measuring low range hemodynamic forces *in vivo* and offers an unprecedented tool in both cell and developmental biology.

Monitoring Editor

Manuel Théry
CEA, Hopital Saint Louis

Received: Jun 15, 2017

Revised: Sep 5, 2017

Accepted: Sep 6, 2017

INTRODUCTION

Integration of biomechanics in cell biology studies has grown exponentially in the past few years. The early observation that mechanical signals drive and modulate signaling pathways within cells through mechano-transduction has led to a paradigm shift when approaching cell biological phenomena. Developmental biologists have led the way and undertook a series of mechanical manipulations and measurements to grasp the interplay between biomechanics and tissue morphogenesis (Petridou *et al.*, 2017).

Accurate manipulation, measurement, and quantification of tissue and cellular forces *in vivo* are essential to such task. There are several research fields where quantification of forces *in vivo* is central. For example, the progression of many diseases such as cancer, cardiomyopathies, and myopathies is tightly linked to biomechanics. Much attention has been given to the interplay between static forces such as tissue elasticity and tumor progression (Jain *et al.*, 2014). However, the biological ramifications of fluid forces, in development (Freund *et al.*, 2012) and disease progression (Provenzano and Hingorani, 2013), are obvious, and methods are needed for fine probing of these forces *in vivo*. Metastatic extravasation of circulating tumor cells (CTCs) is strongly influenced by mechanical inputs such as shear and adhesion forces, as well as vascular architecture (Wirtz *et al.*, 2011; Azevedo *et al.*, 2015). Similar to the extravasation of immune cells in an inflammatory context, efficient adhesion of CTCs to the vascular wall is needed before engaging in extravasation (Reymond *et al.*, 2013). While experiments have been largely performed *in vitro* (Chang *et al.*, 2016; Labernadie *et al.*, 2017), there is a growing need for establishing similar approaches *in vivo* enabling high-accuracy measurements of forces in realistic physio-pathological situations.

This article was published online ahead of print in MBoC in Press (<http://www.molbiolcell.org/cgi/doi/10.1091/mbc.E17-06-0382>) on September 13, 2017.

*Address correspondence to: Sébastien Harlepp (harlepp@unistra.fr) or Jacky G. Goetz (jacky.goetz@inserm.fr; www.goetzlab.com, twitter: @GoetzJacky).

© 2017 Harlepp *et al.* This article is distributed by The American Society for Cell Biology under license from the author(s). Two months after publication it is available to the public under an Attribution-Noncommercial-Share Alike 3.0 Unported Creative Commons License (<http://creativecommons.org/licenses/by-nc-sa/3.0/>).

Abbreviations used: AFM, atomic force microscopy; CTC, circulating tumor cell; DA, dorsal aorta; dpf, days postfertilization; ISV, intersegmental vein; OT, optical tweezers; PIV, particle image velocimetry; RBC, red blood cell; ZF, zebrafish.

"ASCB®," "The American Society for Cell Biology®," and "Molecular Biology of the Cell®" are registered trademarks of The American Society for Cell Biology.

However, performing such experiments *in vivo* needs to overcome two major hurdles: it should be noninvasive and also should be able to reach deep tissues. Such limitations prevent the use of several contact techniques such as atomic force microscopy (AFM), but led to the development of noninvasive and noncontact tools such as magnetic tweezers (Desprat *et al.*, 2008; Brunet *et al.*, 2013) or optical tweezers (OT) (Ashkin and Dziedzic, 1987; Hörner *et al.*, 2017).

Optical tweezers suffer from the inconvenience of calibration *in vivo* and from limitation in the application in deep tissues. While trapping cells *in vivo*, one needs to calibrate the setup for every single cell that is trapped. Indeed, heterogeneity of cell size and of the refractive index prevents us from applying a single calibration to multiple situations. Nevertheless, OT permits a dynamic analysis of the mechanical properties of cells (Huang *et al.*, 2003; Monachino *et al.*, 2017) and tissues (Lopez-Quesada *et al.*, 2014; Gao *et al.*, 2016) without altering embryonic development. Optical tweezing thus offers a wide palette for trapping and potentially measuring fluid forces *in vivo*. Recent pioneer work has shown that red blood cells (RBCs) can be trapped using optical tweezing in capillary vessels from mouse ears (Zhong *et al.*, 2013). In this study, the authors moved the trapped RBC through the capillary vessel and thereby induced artificial clots in the circulation. Although very powerful and promising, such a technique remains limited when studying events located deep in tissues.

The recent emergence of the zebrafish (ZF) embryo allows, due to its relative optical transparency, the use of a wide plethora of optical tools. Taking advantage of that property, Johansen *et al.* (2016) recently demonstrated the power of optical tweezing in a living ZF embryo. They trapped and displaced multiple cell types in the blood flow, such as RBCs or macrophages and brought these cell types in contact with the vascular wall. Although this interesting study shows a large panel of potential applications, it does not provide an accurate quantification of the range of forces exerted or applied on the different objects. A few years earlier, we used a similar approach for quantifying the importance of the viscoelasticity of the arterial walls in ZF embryos by trapping RBCs at different positions of the vasculature (Anton *et al.*, 2013). To our knowledge, this study was the first providing quantitative values from optical tweezing *in vivo*. We further used this approach to address the adhesion of epicardial cells to the pericardium during cardiac development in the ZF embryo (Peralta *et al.*, 2013). More recently, oscillating OT deforming cell junctions on the *Drosophila* embryo (Bambardekar *et al.*, 2015; Sugimura *et al.*, 2016) allowed the authors to accurately measure the tension forces between adjacent cells around 44pN.

Nevertheless, all these studies face a major obstacle, that is, the calibration of the optical trap, which limits the use of OT *in vivo* contexts. Recently calibration of OT *in situ* has been achieved (Staunton *et al.*, 2017). We provide here a mean to achieve accurate calibration in the context of probing hemodynamic forces in the ZF embryo. We first describe how to reach and quantify the physical parameters of the system by using high-speed imaging methods combined with image processing. Then we describe how trapping of RBCs at different positions in the vasculature is processed in order to quantify the trap stiffness and to calculate the associated forces. We provide a numerical approach allowing us to solve the differential equation of the movement and compare the numerical data with the experimental ones to confirm the power of such calibration. Finally, we validate our approach by tuning heart pacemaker activity and by measuring its impact on hemodynamic forces.

RESULTS AND DISCUSSION

Fine measurement of velocity profiles for calibration of optical tweezers *in vivo*

Accurate calibration of OT *in vivo* requires a fine assessment of the physical parameters over time and space. Here we introduce a method for accurate measurements of hemodynamic profiles in the ZF embryo. Hemodynamic profiles are measurements of velocity as a function of time, at a clearly located position in the ZF embryo. Such a method could be very useful in understanding the role played by hemodynamic forces in vascular morphogenesis, and also in pathological scenarios such as intravascular arrest and extravasation of CTCs or immune cells. We focused our analysis on the caudal plexus region of the ZF embryo (Figure 1A), whose optical characteristics and relative three-dimensional (3D) structure make it optimal for high-speed imaging of the blood flow. We first perform high-speed imaging of the blood flow, at 200 frames per second (fps) and at intermediate magnification. Such a frame rate is optimal for fine tracking individual RBCs in the vasculature (Supplemental Movie S1). Raw acquisitions are processed to enhance the contrast of RBCs in the blood flow (Figure 1B and Supplemental Movie S1). Subsequently the processed data set is analyzed through a PIV (particle imaging velocimetry) plug-in developed on ImageJ that is well-suited for automatic analysis of the blood flow movie (Figure 1B and Supplemental Movie S1). The PIV allows a fine measurement of the velocity amplitudes and profiles at any position within the vasculature at a given time. Such a step is of utmost importance while studying hemodynamics with a Poiseuille-type distribution where velocity profiles vary significantly along a cross-section of a single vessel (Figure 1B). However, PIV analysis requires several parameters to be adjusted manually. While these parameters can potentially influence the measured velocities, we undertook a parallel approach aiming to extract the flow profiles of several RBCs using manual tracking performed in Fiji and rendered using Imaris software (Figure 1C and Supplemental Movie S2). Because most of the RBCs follow the central streamline (Amini *et al.*, 2014), manual tracking of individual RBCs allows us to determine the flow profiles in the center of the measured vessel. We then compare these profiles to the ones obtained upon PIV treatment. The comparison of the two methods allows us to estimate the accuracy of our measurements, which is around 50 $\mu\text{m/s}$ for the determination of the blood flow velocity. We then fitted the PIV experimental curves with theoretical profiles (Figure 1C). The function used is adapted from our previous work (Anton *et al.*, 2013) and can be written as follows:

$$v(t) = v_{\max} \cdot \text{abs} \left(\tanh \left(3 \cdot \sin(\pi \cdot (f \cdot t - \varphi)) \right) \right) - \tanh \left(3 \cdot \sin(\pi \cdot (f \cdot t - \varphi) - (\pi / 4)) \cdot e^{(-\tau)} \right) + v_0$$

where v_{\max} represents the maximal velocity, f the heart beat frequency, φ the phase shift representing the arbitrary origin of the experimental signal, v_0 the minimal velocity, and τ the damping during the diastolic phase linked to the endothelial barrier viscoelastic behavior.

Combining these different methods allows for a very accurate assessment of velocity profiles at any position within the vasculature. This further permits us to model the profile theoretically and to adjust an equation whose parameters can be further used in the numerical simulation. Nevertheless, before performing numerical simulation of blood flow behavior in the ZF embryo, one should assess the efficacy of optical tweezing of circulating RBCs in developing blood vessels.

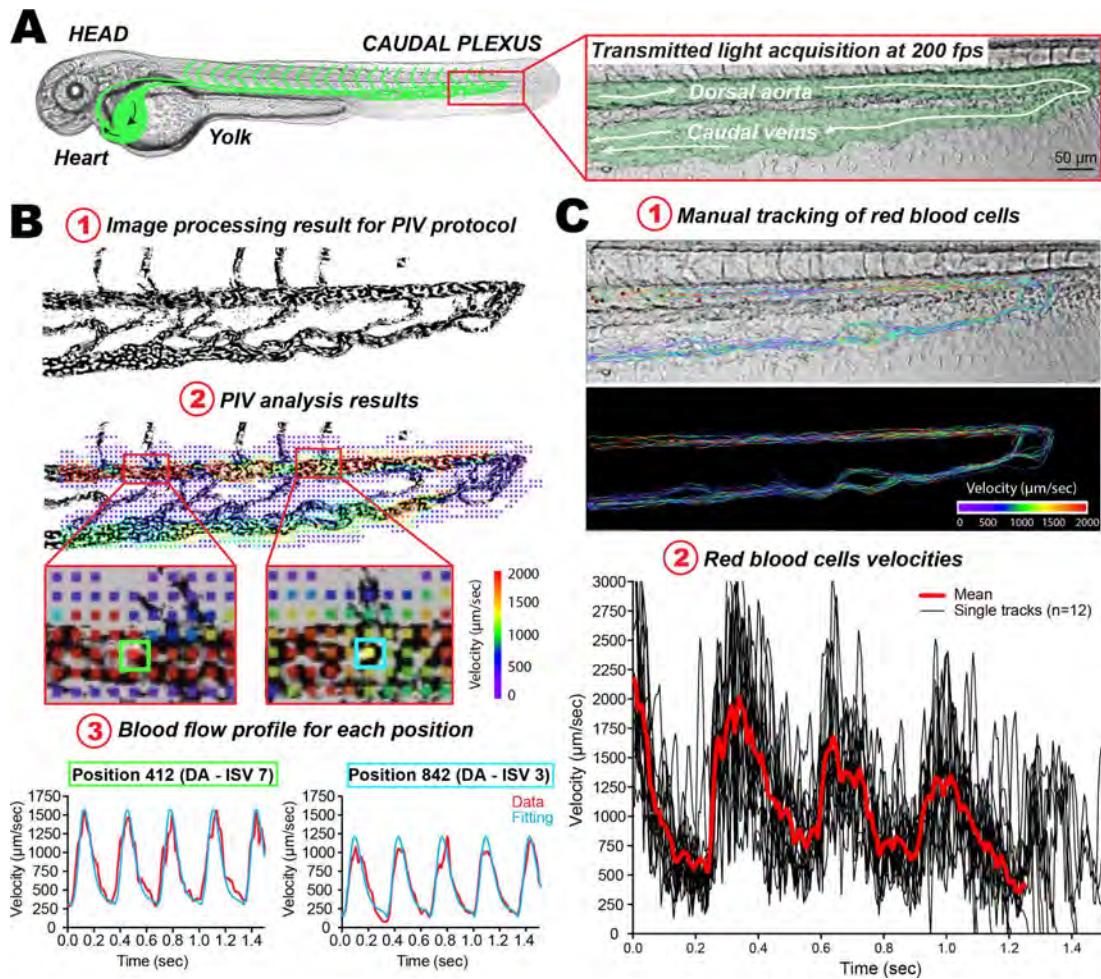


FIGURE 1: Fine measurements of blood flow velocities in the ZF embryo. (A) Experimental workflow: a representative image of a 48 hpf ZF embryo image is presented (the vasculature network is schematized in green), and a zoom of the caudal plexus region is presented in a separate box. (B) PIV analysis: 1) the images resulting from high-speed acquisition of the blood flow (200 fps) were processed such that high contrast is obtained for circulating RBCs. 2) The PIV analysis provides a color-coded velocity map over the entire image, in any region of interest. Flow profiles can thus be extracted at any given position. This further allows theoretical analysis of the flow values, which will be used in the simulation used for measuring the trap stiffness. 3) Here two positions, with distinct flow profiles and separated by roughly 250 μ m, are presented. Note the different flow profiles that can be observed and fitted. (C) Particle tracking analysis. Manual tracking of individual RBCs in perfused vessels can be performed. 1) Several tracks obtained over 12 RBCs are displayed. Tracks are color-coded according to their instantaneous velocity. Note the higher values and pulsatility obtained in the DA. 2) Instantaneous velocity frame after frame is plotted over a track spanning the entire caudal plexus, for 12 RBCs.

Optical trapping of RBCs, image analysis, and photodiode measurements

Although it is technically possible to trap RBCs (or other cells) anywhere in the ZF embryo (see Peralta *et al.*, 2013), we mostly performed optical tweezing in the caudal plexus. Here, in comparison to high-speed recording of the blood flow, a high magnification and numerical aperture objective is used to optically trap the RBCs in the flow (Figure 2A and Supplemental Movie S3). These trapped RBCs are mostly subjected to the dragging force of the blood flow and the restoring force of the OT (Jun *et al.*, 2014). We record the displacement of the RBCs within the optical trap on a quadrant photodiode at high frequency (more than 4 kHz) (Figure 2B). This temporal acquisition mirrors the cellular displacement from the trap center and is expressed in volts. Here we convert this displacement expressed in volts to displacement expressed in

micrometers by applying a conversion factor extracted from the two curves, allowing us to superimpose this curve to the displacement measured with the camera (Figure 2C). We further compute it as the power spectral density of the fluctuations (Figure 2B, black track), over which one can fit the OT behavior of a trapped cell in the absence of flow (as described in the Supplemental Methods). The parameters that are obtained allow us to extract a first approximation of the trap stiffness, which is $k = 4.7 \times 10^{-5}$ N/m. A similar temporal trapped RBC acquisition is simultaneously performed at 200 fps. The resulting kymograph shows the cellular displacement within the trap (Figure 2C) where accurate distances can be extracted (micrometers). From the cellular displacement in the trap and the measured stiffness, one can now convert the displacement track into an accurate force measurement (Figure 2D). When repeating the acquisition over the caudal plexus of the

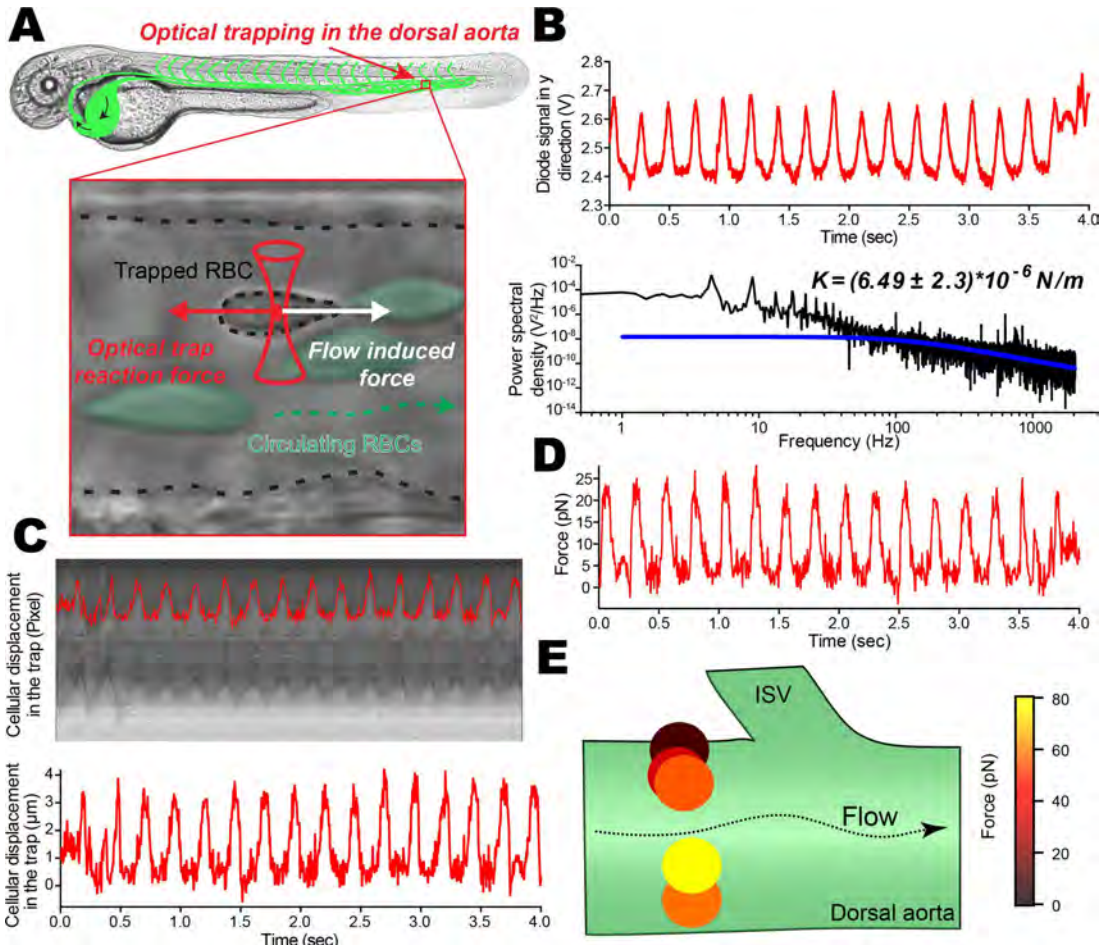


FIGURE 2: Optical trapping of circulating RBCs, image analysis and photodiode measurements. (A) Scheme of the experiment where the optical trap is located in the caudal plexus (DA) of the ZF embryo. The trapped RBC is subjected to the blood flow–driven dragging force as well as to the restoring force from the optical trap. (B) Thanks to the flow pulsatility occurring in arterial vessels, the time trace of the optically trapped RBC is followed on the quadrant diode. The time trace is further treated to access the power spectrum (black curve), revealing peaks of pulsatility as well as a corner frequency f_c around 250 Hz. This is highlighted with the theoretical curve for steady optical trapping experiments (blue curve). The cutoff frequency, obtained from a Lorentzian approximation, provides a first approximation of the trap stiffness, which is $\sim 4.7 \times 10^{-5}$ N/m. (C) A kymographic analysis of a single trapped RBC imaged at 200 fps is performed. Kymographs allow fine tracking of RBC displacement within the optical trap, thereby providing a real time track in micrometers. (D) A mirror force track over time is obtained and results from the use of the theoretical trap stiffness derived from the cutoff frequency (theoretical curve). (E) Any given position in the ZF vasculature can be probed, providing an accurate measure of hemodynamic forces. Here a few trapping RBCs in a cross-section of the DA permit appreciation of the behavior of a Poiseuille-type of flow.

2 dpf (days postfertilization) ZF embryo, we are now capable of drawing a hemodynamic force map (personal communication; Follain et al., 2017). From the forces extracted with this method, it is also possible to elaborate the flow profile and thus to extract the shear stress one cell has to overcome once attached to the endothelium. In addition, one can now observe and highlight the Poiseuille flow profile of the developing dorsal aorta (DA) of a 2 dpf ZF embryo (Figure 2E). This allows quantifying both the velocity and the shear stress in close proximity to the endothelial walls. It is important to note at this stage that the calibration of OT was here performed in a blood vessel with pulsatile flow (DA). Such a parameter could greatly influence the measured trap stiffness, as well as the ways to measure it. However, our workflow now allows conducting numerical simulations that can be compared with the previous data.

Performing numerical simulations for accurate measurement of the trap stiffness

Before starting running simulations of *in vivo* experiments, one needs to verify and assess the robustness of the code (see the Supplemental Methods). We first performed simulations in the absence of external flow and tuned the trap stiffness from 10^{-5} to 10^{-4} N/m (Figure 3A). The model predicts that an increase in the trap stiffness should lead to a decrease in the fluctuations of the cell within the trap as well as an increase in the cutoff frequency. We next considered the presence of a pulsatile flow for which we imposed fixed velocity, frequency, and damping values while only tuning the trap stiffness again from 10^{-5} to 10^{-4} N/m. The flow parameters are the following: maximal velocity of $1300 \mu\text{m/s}$, frequency of 2.1 Hz , and damping $\tau = 0.8$ (the latter value corresponds to an average value obtained through the caudal plexus) (Figure 3, B and C). As expected, the trap

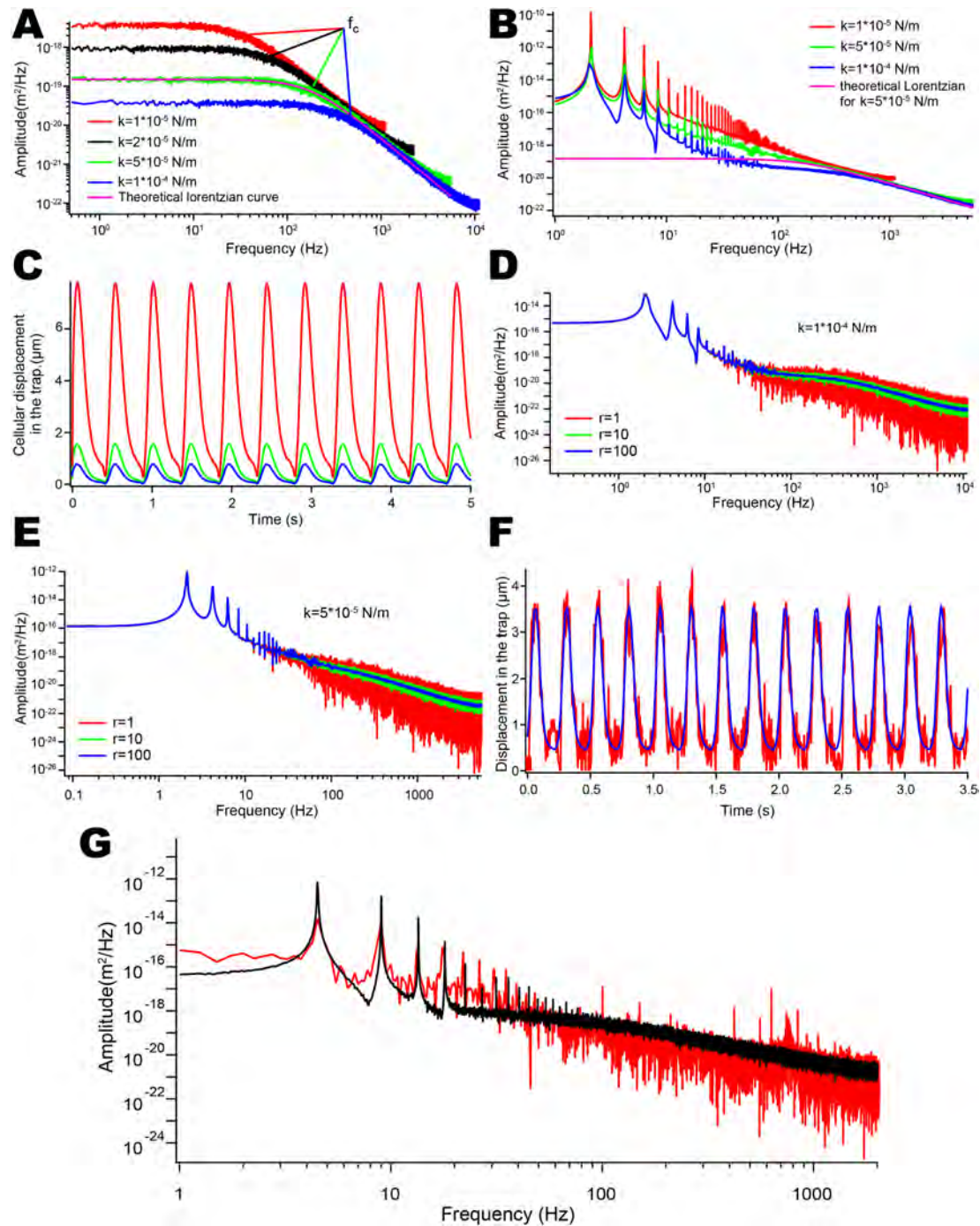


FIGURE 3: Numerical simulations. (A) Power spectrum of different tracks is represented graphically. No external pulsatile flow was applied, and the trap stiffness was modulated from 10^{-5} to 10^{-4} N/m to show that global fluctuations in the trap decreased when the stiffness was increased (ordinate at the origin) and that the cutoff frequency increases to higher frequency from 50 to 350 Hz. (B) Power spectral representations of different tracks resulting from same pulsatile flow. The trap stiffness is modulated from 10^{-5} to 10^{-4} N/m. The cutoff frequency increases to higher frequency when the stiffness increases as shown in A. The amplitude of the peaks at 2 Hz and its harmonics diminishes when the stiffness increases. (C) Movement of RBCs within the optical trap is tracked and plotted over time. Low trap stiffness allows trapped RBCs to reach 6 μm oscillations that are bigger than the cellular diameter and would lead to RBCs escaping the trap over time. (D) Three different power spectrum with constant velocity and physical parameters $k = 10^{-4}$ N/m, but with different spectral averaging from 1 to 100, are represented. While the signal-to-noise ratio is increasing as the square of the averages the cutoff frequency due to the trap stiffness was visible without averaging. (E) Three different power spectra with constant velocity and physical parameters $k = 5 \times 10^{-5}$ N/m, but with different averaging from 1 to 100. As in D, the signal-to-noise ratio is increasing as the square of the number of averages, nevertheless the cutoff frequency (around 150 Hz) is hardly visible even after 100 spectral averages. This is due to the overlap of the

stiffness affects the cutoff frequency in a manner similar to those obtained in the absence of flow (Figure 3B). In addition, we observed and measured a significant decrease in the peak amplitude with increasing trap stiffness, confirming that the fluctuations of the cell within the trap are directly linked to the stiffness (Figure 3B). The simulation allows us to extract also the displacement of the RBCs over time, and these displacements clearly demonstrated the impact of the trap stiffness on the cellular movement (Figure 3C). More precisely, we observed a displacement of 7.7 μm within the trap when the stiffness was set to 10^{-5} N/m and a displacement of 770 nm when the stiffness was set to 10^{-4} N/m. A cellular displacement of 7.7 μm within the trap, which exceeds the radius of individual RBCs, will inevitably lead to the RBCs escaping from the trap. Such simulations confirm that stiffness of the trap impacts the cutoff frequency and linearly impacts the overall amplitude of fluctuations at low frequencies that are mainly driven by the amplitude of the flow. It is important to note at this stage that these simulations were run by averaging the spectral density over 100 runs. A major bottleneck of such an experiment is, however, the acquisition time, which should be as low as possible to exclude or prevent external perturbations such as drift of the sample/embryo or trapped RBCs that are being ejected from the trap by collision with other circulating RBCs. We therefore assessed the sensitivity of this method by modulating the number of temporal averages from 100 to 1 while keeping all the other parameters constant. We ran a first series of simulations at high trap stiffness ($k = 10^{-4}$ N/m) and observed that the trap cutoff frequency remains well defined when compared with the flow-driven frequency dependence (Figure 3D). We thus concluded that the number of acquisitions is irrelevant. Nevertheless, in a second experiment where the trap stiffness was set to 5×10^{-5} N/m (Figure 3E), we observed that such stiffness leads to a trap cutoff frequency that cannot be extracted from the flow-driven frequency dependence. Here a simulation averaging of 100 times is required to reach the trap cutoff frequency. In other words, probing forces at such parameters is incompatible with experimental recording that would require acquisition of ~ 100 s or more. For this reason, we rely now on the developed numerical code (Supplemental Methods) as well as on the fine flow mapping described previously (Figure 1). A combination of numerical code and fine flow mapping allows us to calibrate the optical trap from the experimental data by applying a fit to the obtained curves. First, we extract the experimental data from the signal obtained on the quadrant diode and transform them into a real displacement in micrometers (Figure 3F, red plot). We run the simulation with the flow parameters extracted from the previous PIV experiment and adjust the trap stiffness until the simulated displacement adjusts the experimental one (Figure 3F, blue plot). This theoretical curve gives a good approximation on the beating frequency and the endothelial damping. The values obtained from fine flow mapping (PIV + tracking; Figure 1) are fed into the numerical simulation as input parameters before running the fit and superimposing the power spectral density curves obtained experimentally (Figure 3G, red) and theoretically (Figure 3G, black). This example demonstrates the good accordance between velocity peaks induced by flow pulsatility and the appearance of the cutoff frequency around

250 Hz. Altogether this demonstrates that the calibration of the setup is achieved. This now gives access to fine blood flow force mapping at any position in the developing ZF embryo.

Blood flow tuning can be accurately assessed with optical tweezers *in vivo*

A proper calibration of the OT allows envisioning fine flow mapping in the ZF embryo. To demonstrate the power of such a method, we tuned the pacemaker activity using a previously described pharmacological treatment and measured its impact on flow profiles and applied forces. Lidocaine, a sodium channel blocker, has been shown to reduce significantly the pacemaker activity of 2 dpf ZF embryos (Cummins, 2007; Vermot *et al.*, 2009). Using high-speed imaging of heart beats, we observed that lidocaine reduced the pacemaker activity by 30–35% (data not shown; Follain *et al.*, 2017, personal communication) and impacted the flow velocity accordingly. These behaviors are in good agreement with previous work performed with lidocaine (Vermot *et al.*, 2009; Anton *et al.*, 2013; Heckel *et al.*, 2015). Optical tweezing of single RBCs was performed at two different positions in the caudal region of the DA of control and lidocaine-treated embryos (Figure 4, A and B). Before optical tweezing, flow profiles at each respective position were probed using high-speed imaging (200 fps) followed by PIV analysis. Flow mapping indicates a significant decrease in flow velocities imposed by lidocaine and the underlying reduction in pacemaker activity. Both flow pulsatility as well as velocity amplitude are reduced at both positions (Figure 4, C and D). We then trapped single RBCs at the two positions and tracked the cellular movement within the trap over time (Figure 4, E and F). Kymographic analysis revealed RBC oscillations within the trap, which can be plotted over time (Figure 4, G and H). The profiles that are obtained perfectly mirror the velocity profiles from the PIV analysis, with a marked decrease in both pulse frequency and flow amplitude. Nevertheless, as shown previously, the trap stiffness controls the amplitude of movement of RBCs within the trap. We thus adjusted the laser power such that RBCs would be held in the trap without escaping in the control experiments. We thus increased the laser power in the control condition compared with the lidocaine condition. We then extracted the trap stiffness from the power spectra adjusted using our previously described numerical model and plotted the force tracks that are associated with cellular displacements (Figure 4, I and J). Such an analysis allows us to accurately measure flow forces and, in that case, to probe the impact of a reduction in pacemaker activity on hemodynamic forces at high accuracy.

In conclusion, we have described here a fast and straightforward method to probe and measure hemodynamic forces *in vivo*. By combining flow profile dissection, power spectrum acquisition, and numerical analysis of the experimental data, we could extract the stiffness of the optical trap that is essential for correlating the trapping effect to the imposed force. The power of this method and analysis is that the numerical simulation provides a fast and reliable mean to assess trap stiffness and the underlying forces. As described previously (Zhong *et al.*, 2013) and detailed in the Supplemental Methods, one can neglect inertia. Indeed, the temporal

flow contribution in the power spectrum and the cutoff frequency due to trap stiffness making its distinction complicated. (F) Displacement of a single RBC within the optical trap is tracked and plotted over time. The blue curve represents the theoretical function of the flow pulses, which perfectly matches the experimental data. The obtained function is later used to model and fit the experimental power spectrum. (G) Experimental power spectrum is obtained from a trapped RBC. The black curve represents the fitting of the experimental red curve with the numerical model. Such fitting permits extraction with high accuracy the trap stiffness.

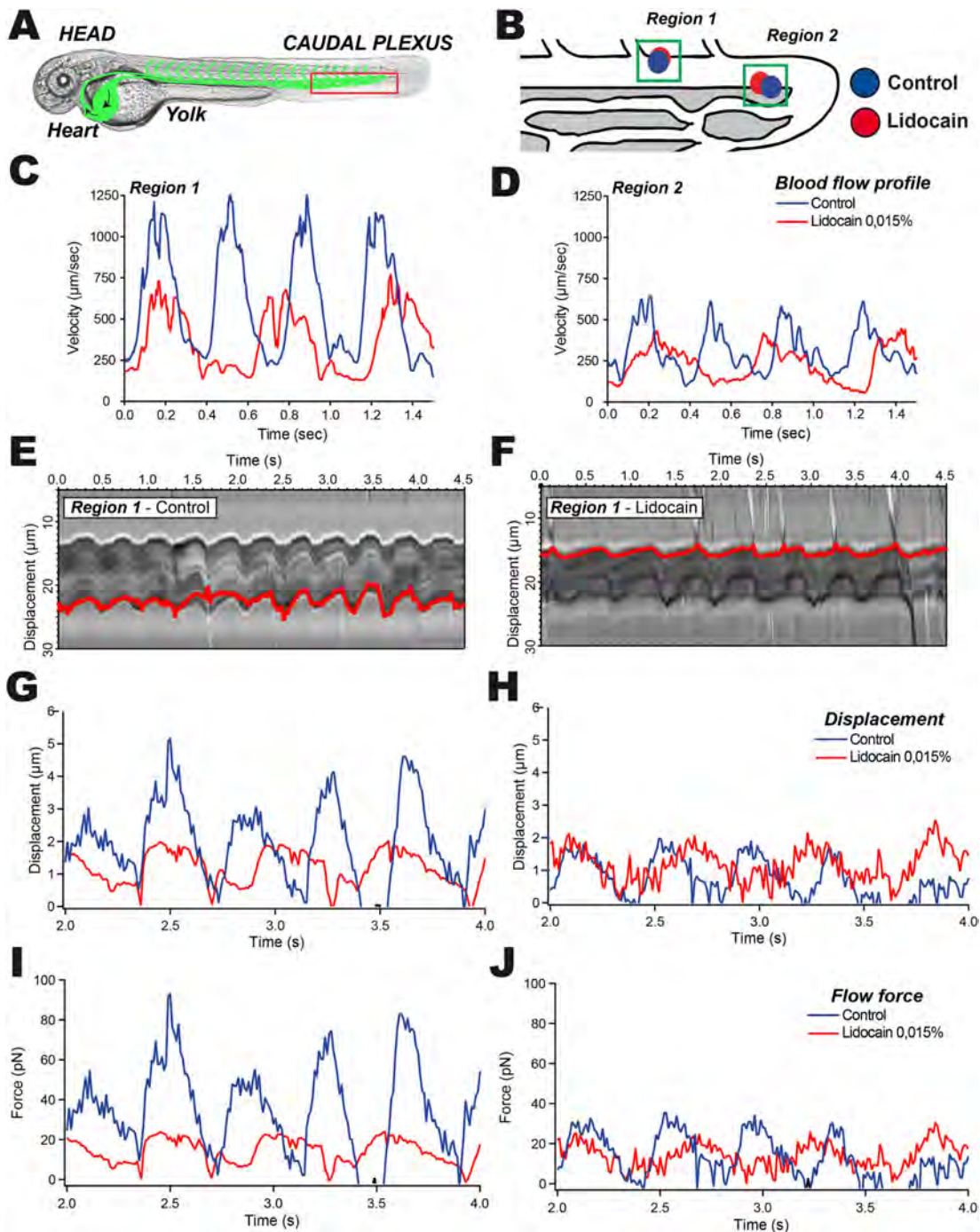


FIGURE 4: The impact of blood flow tuning on hemodynamic forces can be accurately measured using calibrated optical tweezing. (A) A representative image of the ZF embryo at 48 hpf is provided; the region of interest is highlighted in red. Blood flow tuning is achieved by pretreating the embryos with lidocaine (0.0015%). (B) Two positions within the caudal region of the DA are probed with OT. (C, D) PIV tracks are obtained from high-speed imaging and analysis of region 1 (C) and region 2 (D). (E, F) Kymographic analysis of the optically trapped RBC in region 1 in control (E) and lidocaine-treated (F) embryos. The displacement track is represented in red. (G, H) Displacement of the trapped RBC is measured and plotted in region 1 (G) and region 2 (H). (I, J) Force curves from region 1 (I) and 2 (J) are extracted from the displacement of RBCs within the calibrated optical trap.

resolution of imaging of the blood flow is limited and leads to two major forces: the restoring force exerted by the optical trap to the trapped object (i.e., a RBC) and the dragging force from the blood flow. These two forces have separated frequency responses. While the restoring force acts at high frequency (100–1000 Hz), the drag-

ging force, in the case of the ZF embryo, is closely linked to the heart beat frequency (around 2–3 Hz). In these conditions, previous work demonstrated analytically that two signals with frequency domains sufficiently separated could be solved in the Fourier domain as a sum of the two contributions (Seth Roberts *et al.*, 2007). In

that work they imposed oscillations at frequency far from the cutoff frequency to the trapped bead with an electrical field. From the collected oscillation, they plotted the power spectrum presenting a defined peak at the oscillation frequency. The amplitude of this peak due to its distance from the cutoff frequency was directly proportional to the number of charges created.

Our method suffers from two limitations. First, we consider RBCs as spherical objects from which the corresponding dragging force is derived. This consideration does not take into account RBC deformations. Second, we do not precisely measure the distance separating RBCs from the vessel wall and thus consider a constant viscosity instead of Faxen's law (Jun *et al.*, 2014). We therefore introduce underestimations in the resulting calibration. These underestimations represent an error on the force of ~20% close to the endothelial wall.

Altogether we have shown here that precise probing of hemodynamic forces using optical tweezing *in vivo* can be achieved. Such measurements, when applied to the understanding of hemodynamics in vascular morphogenesis (Sugden *et al.*, 2017), atherosclerosis (Namdee *et al.*, 2014), or thrombosis (Karachaliou *et al.*, 2015) events could provide unexpected insights into the contribution of fluid mechanics. When using the trapping function of OT, one can also redirect circulation of RBCs in the ZF embryo and unravel the importance of vascular architecture in driving its perfusion (Sugden *et al.*, 2017). Another important question that could be solved using this tool is the potential contribution of hemodynamics to intravascular arrest of immune or CTCs. Probing the shear stress in very close proximity to the vessel wall could help in understanding whether rolling of immune or tumor cells, usually attributed to selectin adhesion (Brunk and Hammer, 1997; Lawrence *et al.*, 1997; Sun *et al.*, 2015), can be tuned by hemodynamics. During their journey in the blood circulation, CTCs are subjected to shear forces and collisions with host cells. Only CTCs that overcome or exploit these forces will eventually arrest in vascular regions, preceding metastatic outgrowth. A major advantage provided by calibrated optical tweezing lies in the ability to probe hemodynamic forces precisely at the vessel wall. These regions cannot be reached with other classical flow mapping methods, although they are of utmost importance in the context of intravascular arrest of tumor or immune cells. Assessing, using calibrated optical tweezing, the impact of flow forces on such events, and many others, is thus within reach and could lead to very important observations in the near future.

MATERIALS AND METHODS

ZF handling and mounting for high-speed imaging

Tg(fli1a:eGFP) ZF (*Danio rerio*) embryos used in this study come from a Tübingen background. Embryos were maintained at 28°C in Danieau 0.3X medium (17.4 mM NaCl, 0.2 mM KCl, 0.1 mM MgSO₄, 0.2 mM Ca(NO₃)₂) buffered with HEPES 0.15 mM (pH = 7.6), supplemented with 200 μM of 1-phenyl-2-thiourea (Sigma-Aldrich) after 24 hpf. At 48 hpf, embryos were freed from their chorion and mount in an agarose drop (0.8%) deposited on a glass-bottomed dish (MatTek) compatible with high-resolution imaging. The embryos were positioned in the microscopic framework in order to overlap the DA longitudinal axis with the x-axis and the intersegmental vein (ISV) with the y-axis. For lidocaine treatment experiments, embryos were incubated in Danieau with 0.0015% lidocaine versus control vehicle (EtOH) for 2 h before mounting and imaging. Pacemaker activity of the heart was assessed using a USB 3.0 uEye IDS charge-coupled device (CCD) camera (IDEX) mounted on a DMIRE2 inverted microscope (Leica) using transmitted light. Heartbeats were acquired at 80 fps. Kymographic analysis was performed for extracting the beat frequency.

High-speed acquisition and PIV analysis

For the PIV analysis, high-speed recordings of the blood flow were performed using a Thorlabs DCC3240C Cmos camera at 200 fps mounted on the inverted microscope coupled with a UPLFLN 20X/0.4 objective (Olympus). The RBC positions at each frame were cross-correlated to the next frame using an adapted PIV protocol from ImageJ software available online (<https://sites.google.com/site/qingzongtseng/piv>). The individual displacements as well as the associated frame rate give then access to the individual velocity profiles of the blood cells in the bloodstream. These results were compared with results generated from manual particle tracking (ImageJ) sequences on the same movies. This allows to fine-tuning of the PIV parameters in order to access to the velocity distribution in the vasculature.

Optical trapping

A 1064 nm laser (Navigator 1064-7Y Spectra Physics) feeds the back aperture of the UPLFLNP 100X/1.3 objective (Olympus) to generate an optical trap; the objective is mounted on a thermostated inverted microscope. Trapping of RBCs was performed as described in Anton (2013) in a thermoregulated chamber ensuring the embryos to remain at 28°C. We acquired the displacement with the Thorlabs Cmos camera at 200 fps and simultaneously acquire the temporal signal on a quadrant photodiode at 20 kHz to calibrate the setup to reconstruct the power spectrum and thus allow the calibration of the trap.

Numerical simulation

A full and detailed description is provided in the Supplemental Methods. A general Langevin equation describing the Brownian evolution of a particle combined to an external flow reads

$$m\ddot{x}(t) = \xi[\dot{x}(t) - u_e(t)] - Kx(t) + \Gamma(t)$$

In the present case, let us assume that the parameters are $\xi = 4.5 \times 10^{-8}$ N·s·m⁻¹ the Stokes friction coefficient of the cell, $K = 1 \times 10^{-4}$ N·m⁻¹ the OT spring stiffness, $u_e(t)$ the external pulsatile flow with a velocity of the order of a few millimeters per second, and $m = 2.1 \times 10^{-14}$ kg the mass of a blood cell of radius 1.5 μm and volume mass 1500 kg/m³ (in the absence of hydrodynamic corrections). $\Gamma(t)$ is the random noise, or Langevin force. This random force is supposed to be white, stationary, and Gaussian, with the standard time correlations.

$$\langle \Gamma(t)\Gamma(t') \rangle = 2kBT\xi\delta(t - t')$$

The overall process is Markovian. Considering now the effect of a periodic external force acting on the cell, one observes that three different regimes emerge, delimited by two characteristic frequencies $\omega_s/(2\pi)$ and $\omega_i/(2\pi)$. For $\xi\omega_s = K$, the friction force matches the tweezer restoring force, while for $\xi\omega_i = m\omega_i^2$ friction and inertia come out even. Straightforward numerical estimates lead to $\omega_s/(2\pi) = 350$ Hz and $\omega_i/(2\pi) = 340$ kHz.

At low frequencies ($f < 300$ Hz), the position of the cell in the optical trap follows closely the external drag force $\xi \cdot u_e$. At these frequencies, the trapped cell follows the regime dominated by the external flow and the optical trap stiffness. Inertia can be safely neglected in the range of frequencies $f < 10^4$ Hz for which experimental sampling is done. At frequencies between 300 and 10^4 Hz, the position of the cell in the optical trap is dominated by thermal fluctuations and is represented on the power spectrum by a -2 power law. The frequency with which the cellular position switches from the dragging and trapping regime to the thermal fluctuations regime is called the cutoff frequency.

We therefore consider the overdamped, or Smoluchowsky, limit of the Langevin equation

$$-\xi(\dot{x}(t) - ue(t)) + Kx(t) + \Gamma(t) = 0$$

This equation represents the master equation used to run the numerical simulations.

ACKNOWLEDGMENTS

We thank all members of the Goetz lab for helpful discussions. We thank Julien Vermot for the original experiments in the ZF embryo. We are grateful to Pascal Kessler (Institut de Génétique et de Biologie Moléculaire et Cellulaire) for his help with the Imaris software. This work has been funded by labex NIE (S.H. and J.G.), Plan Cancer (OptoMetaTrap; J.G. and S.H.), and Centre National de la Recherche Scientifique (CNRS) IMAG'IN (S.H., J.G.) and by institutional funds from the Institut National de la Santé et de la Recherche Médicale (INSERM) and the University of Strasbourg. G.F. is supported by a PhD fellowship from La Ligue Contre le Cancer.

REFERENCES

Amini H, Lee W, Di Carlo D (2014). Inertial microfluidic physics. *Lab Chip* 14, 2739.

Anton H, Harlepp S, Ramspacher C, Wu D, Monduc F, Bhat S, Liebling M, Paoletti C, Charvin G, Freund JB, et al. (2013). Pulse propagation by a capacitive mechanism drives embryonic blood flow. *Development* 140, 4426–4434.

Ashkin A, Dziedzic J (1987). Optical trapping and manipulation of viruses and bacteria. *Science* 235, 1517–1520.

Azevedo S, Follain G, Pathabhiraman S, Harlepp S, Goetz JG (2015). Metastasis of circulating tumor cells: favorable soil or suitable biomechanics, or both? *Cell Adh Migr* 9, 345–356.

Bambadekar K, Clément R, Blanc O, Chardès C, Lenne P-F (2015). Direct laser manipulation reveals the mechanics of cell contacts in vivo. *Proc Natl Acad Sci USA* 112, 1416–1421.

Brunet T, Bouquet A, Ahmadi P, Mitrossilis D, Driuez B, Brunet A-C, Henry L, Seran F, Béalle G, Ménager C, et al. (2013). Evolutionary conservation of early mesoderm specification by mechanotransduction in Bilateria. *Nat Commun* 4, 2821.

Brunk DK, Hammer DA (1997). Quantifying rolling adhesion with a cell-free assay: E-selectin and its carbohydrate ligands. *Biophys J* 72, 2820.

Chang AC, Mekhdjian AH, Morimatsu M, Denisik AK, Pruitt BL, Dunn AR (2016). Single molecule force measurements in living cells reveal a minimally tensioned integrin state. *ACS Nano* 10, 10745–10752.

Cummins TR (2007). Setting up for the block: the mechanism underlying lidocaine's use-dependent inhibition of sodium channels. *J Physiol* 582, 11.

Desprat N, Supatto W, Pouille P-A, Beaurepaire E, Farge E (2008). Tissue deformation modulates twist expression to determine anterior midgut differentiation in *Drosophila* embryos. *Dev Cell* 15, 470–477.

Follain G, Osman N, Azevedo S, Allio G, Mercier L, Karreman M, Solecki G, Fekonja N, Hille C, Chabannes V, et al. (2017). Hemodynamic forces tune the arrest, adhesion and extravasation of circulating tumor cells. *bioRxiv* doi: 10.1101/183046.

Freund JB, Goetz JG, Hill KL, Vermot J (2012). Fluid flows and forces in development: functions, features and biophysical principles. *Development* 139, 3063.

Gao H, Metz J, Teanby NA, Ward AD, Botchway SW, Coles B, Pollard MR, Sparkes I (2016). In Vivo quantification of peroxisome tethering to chloroplasts in tobacco epidermal cells using optical tweezers. *Plant Physiol* 170, 263–272.

Heckel E, Boselli F, Roth S, Krudewig A, Belting H-G, Charvin G, Vermot J (2015). Oscillatory flow modulates mechanosensitive klf2a expression through trpv4 and trpp2 during heart valve development. *Curr Biol* 25, 1354–1361.

Hörner F, Meissner R, Polali S, Pfeiffer J, Betz T, Denz C, Raz E (2017). Holographic optical tweezers-based in vivo manipulations in zebrafish embryos. *J Biophoton*, doi:10.1002/jbio.201600226.

Huang W, Anvari B, Torres JH, LeBaron RG, Athanasiou KA (2003). Temporal effects of cell adhesion on mechanical characteristics of the single chondrocyte. *J Orthop Res* 21, 88–95.

Jain RK, Martin JD, Stylianopoulos T (2014). The role of mechanical forces in tumor growth and therapy. *Annu Rev Biomed Eng* 16, 321–346.

Johansen PL, Fenaroli F, Evensen L, Griffiths G, Koster G (2016). Optical micromanipulation of nanoparticles and cells inside living zebrafish. *Nat Commun* 7, 10974.

Jun Y, Tripathy SK, Narayananreddy BRJ, Mattson-Hoss MK, Gross SP (2014). Calibration of optical tweezers for in vivo force measurements: how do different approaches compare. *Biophys J* 107, 1474–1484.

Karachaliou N, Pilotto S, Bria E, Rosell R (2015). Platelets and their role in cancer evolution and immune system. *Transl Lung Cancer Res* 4, 713.

Labernadie A, Kato T, Brugués A, Serra-Picamal X, Derzsi S, Arwert E, Weston A, González-Tarragó V, Elosegui-Artola A, Albertazzi L, et al. (2017). A mechanically active heterotypic E-cadherin/N-cadherin adhesion enables fibroblasts to drive cancer cell invasion. *Nat Cell Biol* 19, 224–237.

Lawrence MB, Kansas GS, Kunkel EJ, Ley K (1997). Threshold levels of fluid shear promote leukocyte adhesion through selectins (CD62L, P, E). *J Cell Biol* 136, 717–727.

Lopez-Quesada C, Fontaine A-S, Farré A, Joseph M, Selva J, Egea G, Ludevid MD, Martín-Badosa E, Montes-Usategui M (2014). Artificially-induced organelles are optimal targets for optical trapping experiments in living cells. *Biomed Opt Express* 5, 1993.

Monachino E, Spenkelink LM, van Oijen AM (2017). Watching cellular machinery in action, one molecule at a time. *J Cell Biol* 216, 41–51.

Namdee K, Thompson AJ, Golinski A, Mochera S, Bouis D, Eniola-Adefeso O (2014). In vivo evaluation of vascular-targeted spheroidal microparticles for imaging and drug delivery application in atherosclerosis. *Atherosclerosis* 237, 279–286.

Peralta M, Steed E, Harlepp S, González-Rosa JM, Monduc F, Ariza-Cosano A, Cortés A, Rayón T, Gómez-Skarmeta J-L, Zapata A, et al. (2013). Heartbeat-driven pericardial fluid forces contribute to epicardium morphogenesis. *Curr Biol* 23, 1726–1735.

Petridou NI, Spiró Z, Heisenberg C-P (2017). Multiscale force sensing in development. *Nat Cell Biol* 19, 581–588.

Provenzano PP, Hingorani SR (2013). Hyaluronan, fluid pressure, stromal resistance in pancreas cancer. *Br J Cancer* 108, 1–8.

Reymond N, d'Águia BB, Ridley AJ (2013). Crossing the endothelial barrier during metastasis. *Nat Rev Cancer* 13, 858–870.

Seth Roberts G, Wood TA, Frith WJ, Bartlett P (2007). Direct measurement of the effective charge in nonpolar suspensions by optical tracking of single particles. *J Chem Phys* 126, 194503.

Staunton JR, Blehm B, Devine A, Tanner K (2017). In situ calibration of position detection in an optical trap for active microrheology in viscous materials. *Optics Express* 25, 1746.

Sugden WW, Meissner R, Aegeerter-Wilmsen T, Tsaryk R, Leonard EV, Bussmann J, Hamm MJ, Herzog W, Jin Y, Jakobsson L, et al. (2017). Endoglin controls blood vessel diameter through endothelial cell shape changes in response to haemodynamic cues. *Nat Cell Biol* 19, 653–665.

Sugimura K, Lenne P-F, Graner F (2016). Measuring forces and stresses in situ in living tissues. *Development* 143, 186–196.

Sun G, Liu K, Wang X, Liu X, He Q, Hsiao C-D (2015). Identification and expression analysis of zebrafish (*Danio rerio*) E-selectin during embryonic development. *Molecules* 20, 18539–18550.

Vermot J, Forouhar AS, Liebling M, Wu D, Plummer D, Gharib M, Fraser SE (2009). Reversing blood flows act through klf2a to ensure normal valvogenesis in the developing heart. *PLoS Biol* 7, e1000246.

Wirtz D, Konstantopoulos K, Searson PC (2011). The physics of cancer: the role of physical interactions and mechanical forces in metastasis. *Nat Rev Cancer* 11, 512–522.

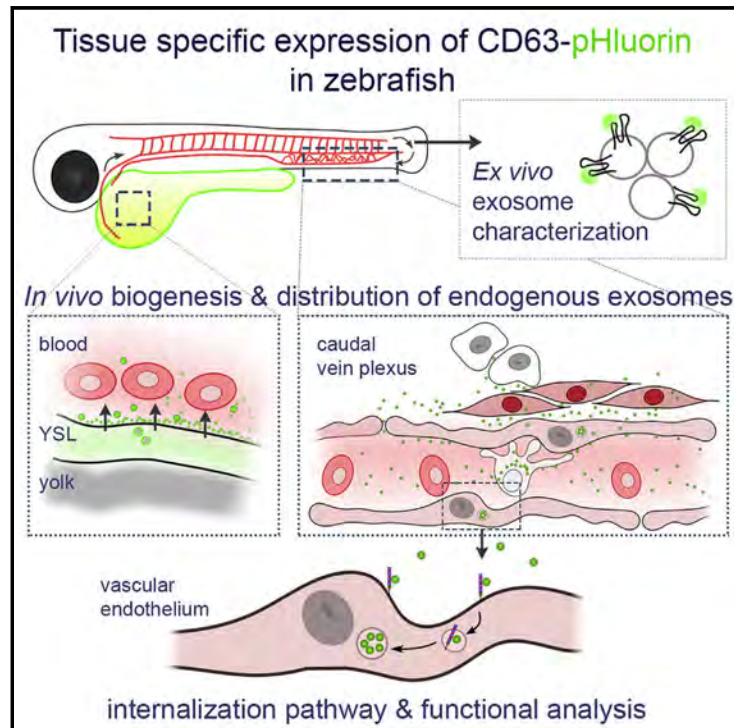
Zhong M-C, Wei X-B, Zhou J-H, Wang Z-Q, Li Y-M (2013). Trapping red blood cells in living animals using optical tweezers. *Nat Commun* 4, 1768.

**ANNEX 4: LIVE TRACKING OF INTER-ORGAN COMMUNICATION BY
ENDOGENOUS EXOSOME *IN VIVO***

Developmental Cell

Live Tracking of Inter-organ Communication by Endogenous Exosomes *In Vivo*

Graphical Abstract



Authors

Frederik J. Verweij, Celine Revenu, Guillaume Arras, ..., Filippo Del Bene, Graça Raposo, Guillaume van Niel

Correspondence

frederik.verweij@inserm.fr (F.J.V.), guillaume.van-niel@inserm.fr (G.v.N.)

In Brief

Verweij et al. develop an *in vivo* model using zebrafish embryos to live-track the production, journey, and fate of individual exosomes. Using a combination of imaging methods and proteomic analysis, they investigate the composition of endogenous exosomes and the molecular mechanisms controlling their biogenesis, fates, and functions in receiving cells.

Highlights

- Single endogenous EVs can be live-visualized in the zebrafish embryo with CD63-pHluorin
- Syntenin in the YSL regulates exosome release into the blood for further dissemination
- YSL exosomes are taken up by macrophages and endothelial cells in the tail of the embryo
- Uptake is scavenger receptor- and dynamin-dependent and provides trophic support



Live Tracking of Inter-organ Communication by Endogenous Exosomes *In Vivo*

Frederik J. Verweij,^{1,2,*} Celine Revenu,³ Guillaume Arras,⁴ Florent Dingli,⁴ Damarys Loew,⁴ D. Michiel Pegtel,⁵ Gautier Follain,⁶ Guillaume Allio,⁶ Jacky G. Goetz,⁶ Pascale Zimmermann,⁷ Philippe Herbomel,⁸ Filippo Del Bene,³ Graça Raposo,¹ and Guillaume van Niel^{1,2,9,*}

¹Institut Curie, PSL Research University, CNRS UMR144, Paris 75005, France

²Institute for Psychiatry and Neuroscience Paris, Hopital Saint-Anne, Université Descartes, INSERM U894, Paris 75014, France

³Institut Curie, PSL Research University, INSERM U934, CNRS UMR3215, Sorbonne Université, Paris 75005, France

⁴Institut Curie, PSL Research University, Centre de Recherche, Laboratoire de Spectrométrie de Masse Protéomique, Paris, France

⁵Department of Pathology, Cancer Center Amsterdam, the Netherlands

⁶INSERM UMR_S1109, Université de Strasbourg, Fédération de Médecine Translationnelle de Strasbourg, Strasbourg, France

⁷Centre de Recherche en Cancérologie de Marseille, Aix-Marseille Université, Marseille 13284, France

⁸Institut Pasteur, Department of Developmental & Stem Cell Biology, 25 rue du Dr Roux, Paris 75015, France

⁹Lead Contact

*Correspondence: frederik.verweij@inserm.fr (F.J.V.), guillaume.van-niel@inserm.fr (G.v.N.)

<https://doi.org/10.1016/j.devcel.2019.01.004>

SUMMARY

Extracellular vesicles (EVs) are released by most cell types but providing evidence for their physiological relevance remains challenging due to a lack of appropriate model organisms. Here, we developed an *in vivo* model to study EV function by expressing CD63-pHluorin in zebrafish embryos. A combination of imaging methods and proteomic analysis allowed us to study biogenesis, composition, transfer, uptake, and fate of individual endogenous EVs. We identified a subpopulation of EVs with exosome features, released in a syntenin-dependent manner from the yolk syncytial layer into the blood circulation. These exosomes are captured, endocytosed, and degraded by patrolling macrophages and endothelial cells in the caudal vein plexus (CVP) in a scavenger receptor- and dynamin-dependent manner. Interference with exosome biogenesis affected CVP growth, suggesting a role in trophic support. Altogether, our work represents a system for studying endogenous EV function *in vivo* with high spatiotemporal accuracy, demonstrating functional inter-organ communication by exosomes.

INTRODUCTION

Extracellular vesicles (EVs) collectively include exosomes, 50–200 nm diameter membranous vesicles secreted from multivesicular endosomes (MVEs) fusing with the plasma membrane (PM), and microvesicles (MVs), 50–1 μ m diameter membranous vesicles that bud from the PM. Exosomes and MVs are released by a wide variety of cell types and are found in all organisms investigated so far (van Niel et al., 2018). Their implication in an increasing number of major physiological and pathological processes supports their putative role as essential intercellular mes-

sengers (Lo Cicero et al., 2015; Tkach and Théry, 2016). Most of the data on the function of EVs such as exosomes, however, are gathered from transformed cancer cells and rely on the use of a heterogeneous population of EVs purified from cell culture supernatant or liquid biopsies. Consequently, the propagation of endogenous exosomes *in vivo* is largely unknown, and data on their biogenesis and role in normal developing tissue and adult tissue homeostasis distinctly lag behind. Understanding EV biogenesis, transfer, and fate in recipient cells, however, is of prime importance not only from a fundamental point of view but also to assess their relevance in pathological conditions as well as their use as therapeutic delivery systems (Fais et al., 2016). This apparent hiatus is largely due to the shortage of suitable models to visualize and track single endogenous EVs and in particular exosomes *in vivo* from their site of production to their final destination in target cells (Hyenne and Goetz, 2017). Previous studies visualizing EV release and transfer have been limited to the detection of larger extracellular structures or their transfer from transplanted transformed cells (Lai et al., 2015; Zomer et al., 2015).

Our main aim was to develop an integrated model to study EV release, transfer, and function, which combines *in vivo* imaging with sub-cellular resolution while retaining the *in toto* imaging scale. Due to their small size and transparency, zebrafish embryos elegantly match the single-cell precision of *C. elegans* research in a vertebrate system with relevant architectural homology with mice and human. We show here that zebrafish embryos can be used to track exosomes *in vivo* by expression of the CD63-pHluorin reporter. This fluorescent reporter is specifically targeted to (late-) endosomes and secreted on exosomes, allowing live visualization of exosome release in single cells *in vitro* (Verweij et al., 2018). Expression of CD63-pHluorin in zebrafish embryos revealed massive release of exosomes from the yolk syncytial layer (YSL) into the blood flow that could be tracked *in vivo* throughout the animal up to their final destination. These exosomes are arrested and taken up by macrophages and endothelial cells of the caudal vein plexus (CVP) in a dynamin-dependent manner for degradation in lysosomes. Interference with syntenin-dependent exosome biogenesis in the YSL affected CVP growth, supporting a trophic role of these exosomes. Altogether,



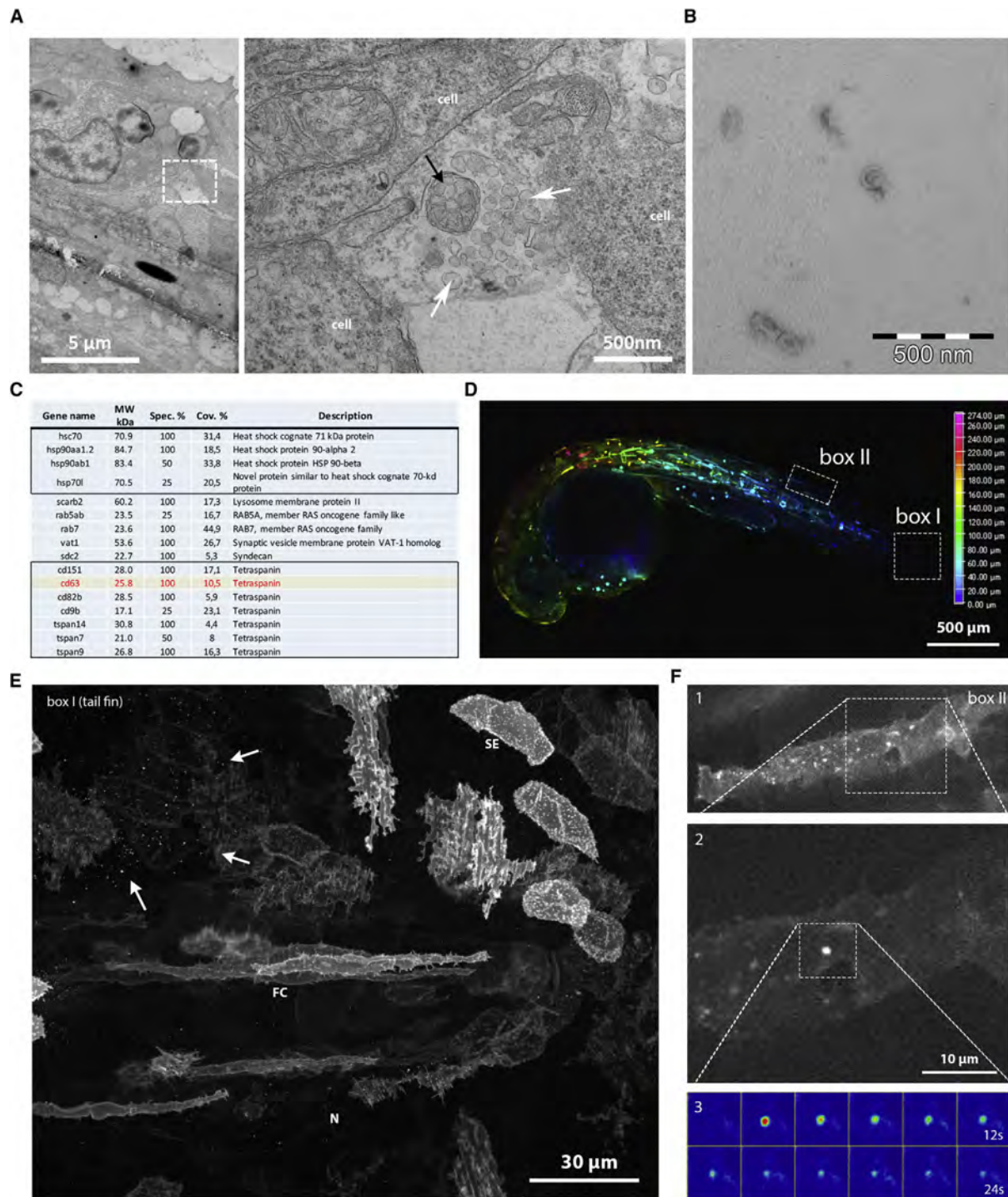


Figure 1. Identification and *In Vivo* Visualization of EVs in Zebrafish

(A) Electron microscopic analysis of a 3 dpf zebrafish embryo showing heterogeneous EVs between basal epidermal cells. White arrows indicate exosome-like vesicles, and black arrow indicates an enwrapped cluster of vesicles.

(B) Electron microscopy observation of EVs purified by ultra-centrifugation from the supernatant of AB.9 caudal fibroblast cells.

(C) Mass spectrometry analysis of AB.9-derived EVs (excerpt, complete list in Table S1).

(legend continued on next page)

these data reveal for the first time the secretion, journey, and uptake in target cells of individual endogenous exosomes secreted *in vivo* and key molecular mediators of these processes.

RESULTS

Zebrafish Cells Secrete EVs Containing Exosomal Proteins

To investigate whether zebrafish could serve as a relevant model to study exosomes, we first assessed the presence of EVs in zebrafish embryos 3 days post-fertilization (dpf) by electron microscopy (EM). EM analysis revealed the presence of 100 to 200 nm diameter vesicles clustered and enwrapped or free in the extracellular space (Figure 1A). We also processed the cell-culture supernatant of the zebrafish fibroblast AB.9 cell line with a differential ultra-centrifugation protocol (Théry et al., 2006). Using EM, we detected various vesicles in the size range of exosomes (~100 nm) (Figure 1B). Proteomic analysis on the same preparations identified a variety of zebrafish homolog proteins traditionally found in mammalian exosomes, including tetraspanins CD63, CD9, and CD82, and several heat shock proteins (HSPs), including HSP70 and HSP90 (Figure 1C; Table S1), and similar to the markers identified in exosomes derived from Zmel cells, a zebrafish melanoma cell line (Henne et al., 2019, this issue of *Developmental Cell*). This demonstrates that zebrafish cells release EVs that are enriched in the CD63 zebrafish ortholog, and supports the application in zebrafish of the fluorescent reporter hCD63-pHluorin, which we recently used to visualize the fusion of MVEs with the PM *in vitro*, (Verweij et al., 2018). Due to its pH-sensitivity, CD63-pHluorin primarily reports its “extracellular pool” (i.e., PM and EVs) but obscures CD63 large intracellular pool present in acidic endosomal compartments (Sung et al., 2015). Injection of ubi:hCD63-pHluorin plasmid-DNA (pDNA) at the single-cell stage of Casper zebrafish embryos resulted in mosaic, transient expression of CD63-pHluorin in multiple cell types, including epithelial, endothelial, neuronal, red blood cells, and muscle cells without obvious developmental defect of the embryo (Figures 1D and 1E). CD63-pHluorin-associated fluorescence was localized at the PM of these cell types and to small, dotty structures potentially corresponding to CD63-pHluorin-positive released EVs (Figure 1E, arrows). As previously shown in cell lines (Verweij et al., 2018), we could detect MVE-PM fusion events (Figure 1F, boxes 2 and 3) *in vivo*, which were pretty rare (~1 every 10 min) but with similar duration when compared to our observations in various cell lines *in vitro* (i.e., 20–30 s) (Verweij et al., 2018). Current technical limitations of imaging restricted the detection of MVE-PM fusion events *in vivo* to flat, stretched cells close to the dermis such as long-stretched fibroblast-like cell types (Figure 1F).

A Major Pool of CD63-Positive EVs Is Present in the Bloodstream of Zebrafish Embryos

One of the postulated assets of EVs is their potential as extracellular carriers in long-range communication *in vivo* by entering the

circulation (Thomou et al., 2017; Tkach and Théry, 2016). Despite circumstantial evidence, this has never been studied directly in a relevant physiological *in vivo* model. In zebrafish embryos, the cardiovascular system develops with a heartbeat and a first transient wave of erythrocytes as early as at 24 h post-fertilization (Hermkens et al., 2015). Strikingly, in 3 dpf zebrafish larvae expressing CD63-pHluorin, we could detect a large pool of CD63-pHluorin-positive membranous structures carried by the blood flow in different parts of the vasculature throughout the body, including the brain and the gills (Figures 2A and 2B; Video S1). EM analysis on blood vessels of ubi:CD63-pHluorin plasmid (p)DNA-expressing embryos confirmed the presence of numerous single EVs in the size range of exosomes (~100 nm), but also a minor fraction of trapped vesicles and multivesicular structures that labeled positive for immunogold associated to anti-GFP antibody (Figures 2C–2E). While the initial observations were done on 3 dpf embryos, we could detect CD63-positive EVs as early as 24 h (1 dpf), at the onset of the blood flow (data not shown). This observation opened the opportunity to track individual endogenous EVs *in vivo*.

The Yolk Syncytial Layer Releases CD63-pHluorin-Positive Exosomes in the Bloodstream

Next, we aimed to identify the cellular origin of the CD63-positive EVs detected in the bloodstream. The large surface area of the YSL, its highly differentiated secretory apparatus, high lysosomal activity, and cytoplasmic multivesicular structures by EM (Walzer and Schönenberger, 1979) made a plausible candidate for the vast number of EVs detected in the blood flow. Moreover, until the duct of Cuvier closes at day 2.5, then forming the common cardinal vein (CV), the YSL is in direct contact with the blood flow (Helker et al., 2013). Video-enhanced Nomarski microscopy revealed numerous EVs in the large interstitial space between the YSL and the overlying epidermis, at and even before the onset of blood circulation (Figure S1A). Injection of ubi:CD63-pHluorin pDNA directly in the YSL at the 1,000-cell stage (4 hpf) (Figure S1B) allowed for tissue-specific expression of CD63-pHluorin and circumvented the need for tissue-specific promoters (Figure 3A). Immunogold labeling for GFP on thin cryosections of YSL CD63-pHluorin expressing 3 dpf zebrafish embryos showed a massive number of vesicles ranging from 80 to 200 nm in size immediately above the YSL and in direct contact with the blood (Figures 3B–3C and S1C). Consistently, CD63-pHluorin-positive EVs were detected in the blood flow after tissue-specific expression of CD63-pHluorin in the YSL (Video S2), and EM analysis of the blood vessels confirmed the nature of the fluorescent structures as single vesicles enriched in CD63-pHluorin in the size range of exosomes (~100–150 nm) (Figure 3D). Moreover, YSL-derived EVs that were observed in the blood flow accumulated in the CVP only in embryos with a detectable bloodstream (Figure 3E). This indicates that YSL-derived EVs enriched in CD63-pHluorin are continuously released in the blood flow and can circulate through the entire embryo to reach their remote destination.

(D) Transient mosaic expression of ubi:CD63-pHluorin in 35 hpf zebrafish embryo, pseudo-colored for depth.

(E) Example of cell types in caudal fin targeted by transient mosaic expression of CD63-pHluorin (3 dpf). Identified as, among others, skin epithelial (SE), neuronal (N), and fibroblast cells (FC). Arrows point at labeled EV.

(F) Example of a fusion event observed in a fibroblast-like cell (1), with zoom in (2), and time-lapse heatmap of the event (3).

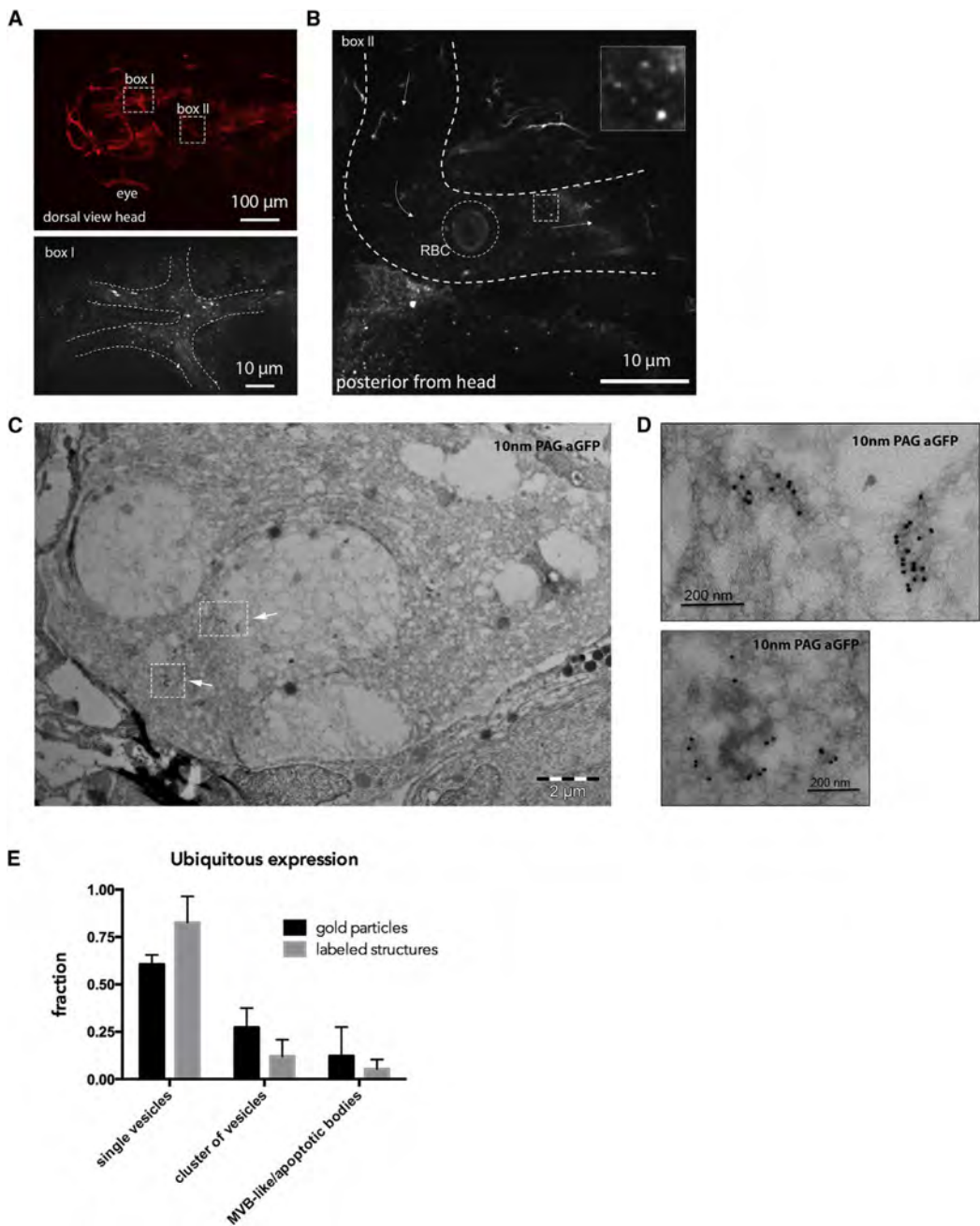


Figure 2. EVs Travel through the Blood Flow

(A) Dorsal view of the vasculature in the head of a *Tg(kdrl:Hsa.HRAS-mCherry)* 3 dpf zebrafish larva expressing CD63-pHluorin after injection of ubi:CD63-pHluorin pDNA at the 1-cell stage. Boxes I and II indicate areas of interest imaged for CD63-pHluorin, shown in (A) (lower panel) and (B).

(B) Still of time-lapse sequence shown in Video S1A, indicating the approximate vasculature wall (dashed white lines), a red blood cell (RBC), and in the dotted box, a sample of EVs seen in the bloodstream, which is magnified in the insert. Arrows indicate the direction of the blood flow.

(C) IEM on the vasculature of ubi:CD63-pHluorin pDNA-injected fish (transient mosaic expression), labeled with gold particles directed to GFP (10 nm), showing (D) single vesicle (upper panel) and clusters (lower panel) of vesicles, corresponding to the dotted boxes in (C).

(E) Quantification of vesicle labeling and appearance (single/clustered) of EVs as in (C) (mean \pm SD, >25 different fields, $n = 2$).

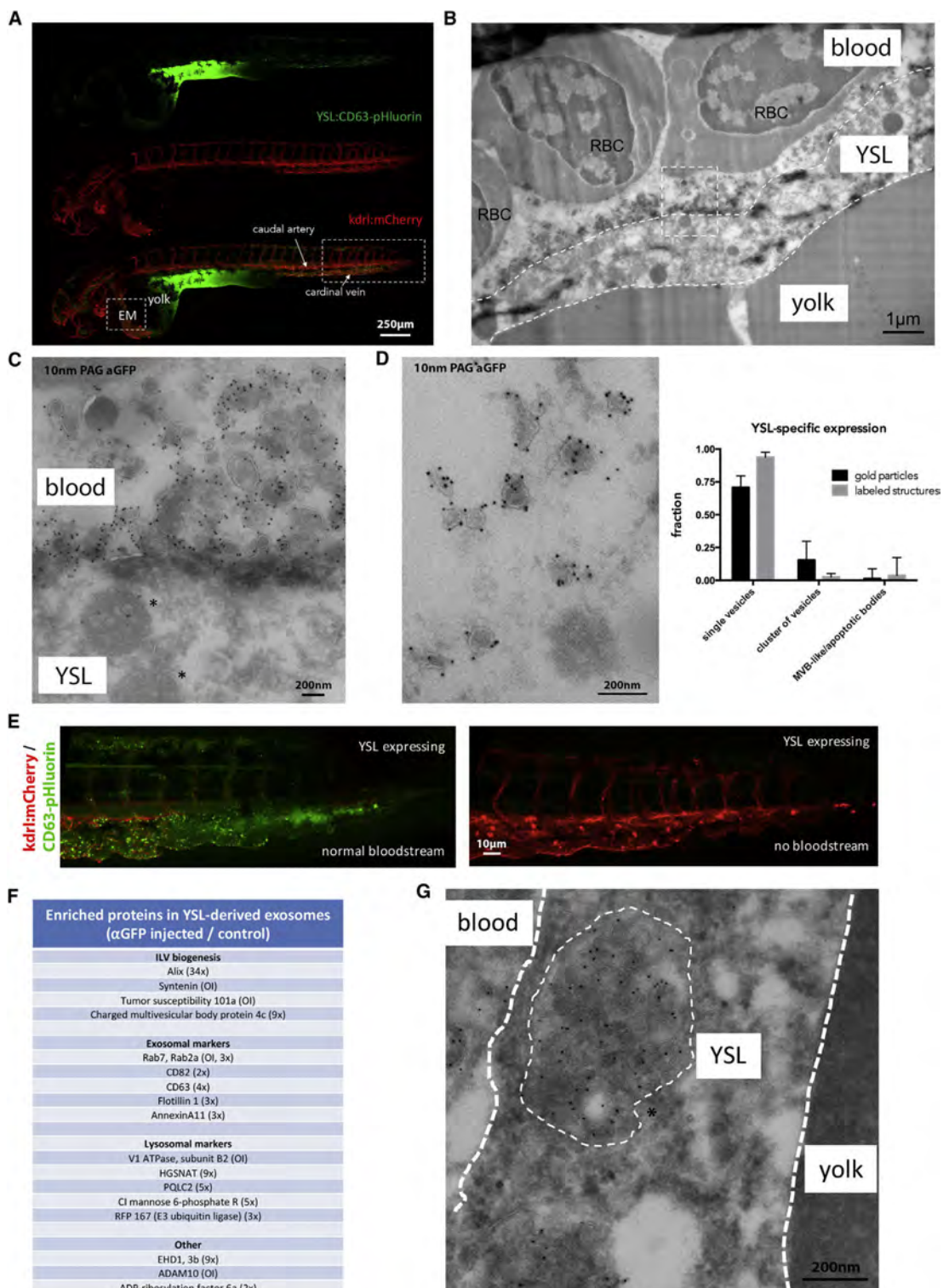


Figure 3. Origin and Composition of Exosomes in the Blood Flow

(A, B, D, and E) Fluorescence image of a 3 dpf *Tg(kdrl:hsa.HRAS-mCherry)* embryo injected with *ubi:CD63-pHluorin* in the YSL, green channel (top), red channel (middle), and merge (bottom). Box [EM] indicates the approximate region for EM analysis, shown in (B) and (D). Box to the right indicates the area shown in (E).

(legend continued on next page)
Developmental Cell 48, 573–589, February 25, 2019 577

Next, we characterized the nature of these fluorescent EVs by dissociating 3 dpf CD63-pHluorin YSL-expressing and YSL-non-expressing control embryos using Collagenase I treatment and isolating EVs from the supernatant with a differential ultra-centrifugation protocol (Théry et al., 2006). Immunogold labeling followed by EM observation of the CD63-pHluorin YSL-expressing-embryos-derived pellet (Figure S1C) confirmed the presence of vesicles heavily labeled for CD63-pHluorin with a morphology and a size (80–120 nm) comparable to those observed by EM *in situ* (Figure 3D). Whereas larger EVs were visible in the pellets, less than 5% of the labeled vesicles was larger than 150 nm in size (Figures S1C and S1D). Nanoparticle tracking analysis (Figure S1E) of the 100,000 g pellet of both conditions did not show significant differences in terms of size and number, suggesting that the expression of CD63-pHluorin in the YSL did not profoundly affect the release of EVs compared to basal condition. Pellets from both conditions were then further processed by immunoprecipitation against GFP using GFP-Trap agarose beads, followed by quantitative label-free proteomic analysis of the pull-down fraction. We quantified enrichment of specific proteins using non-injected zebrafish-derived EV pellet as background. The most enriched proteins were syntenin-a, TSG101, Rab7, ADAM10, and V1 ATPase subunit B2, which were only detected in the injected YSL EV-fraction and Alix (34×). Other YSL EV-enriched proteins included CMHP4c, EHD1, Cation-Independent Mannose 6-phosphate Receptor, Flotillin 1, CD63, CD82, the lysosomal acetyltransferase HGSNAT, and the lysosomal amino acid transporter PQLC2. (Figure 3F; Table S2). Of note, several of the enriched proteins are implicated in one of the machineries involved in exosome biogenesis in endosomes *in vitro* (Baietti et al., 2012). These data strongly support an endosomal origin of YSL-derived EVs. This conclusion was reinforced by the presence of large MVEs that contain CD63-pHluorin-positive intraluminal vesicles (ILVs) (Figure 3G) in the YSL. Thus, CD63-pHluorin-positive YSL-EVs present all the characteristics of endosome-derived exosomes as previously defined (Gould and Raposo, 2013). Finally, these YSL-exosomes were enriched for Molecular function Gene Oncology (GO) terms “Anion binding,” “Small molecule binding,” and “Transporter activity,” with the latter being characterized by the presence of several solute carrier family proteins, including zinc and amino acid transporters slc30a1a and slc3a2b. YSL-derived exosomes displayed similarities with the composition of the AB.9 caudal fibroblast-derived exosomes and to a certain extent with Zmel zebrafish cell line-derived EVs (Table S1; Hyenne et al., 2019), as they both contain major actors of exosome biogenesis (Alix, TSG101, Chmp4C, and tetraspanins). Nevertheless, physiological (this study) and pathological (Hyenne et al., 2019) exosomes

differed by their composition that could be linked to their respective (patho)physiology (Table S2). Altogether, these data strongly suggest that expression of CD63-pHluorin in the YSL reveals the release of exosomes in the bloodstream of developing embryos.

YSL-Derived CD63-Positive Exosomes Adhere to Endothelial Cells of the Caudal Plexus and Are Actively Endocytosed by Patrolling Macrophages

Having determined a cell layer of origin and transportation route of CD63-positive exosomes, we live-tracked them in the blood vasculature to identify potential target cells. Our data revealed an accumulation of dotty signals (Figure 3A) likely corresponding to immobilized exosomes in the blood, in particular in the caudal part of the vasculature. This area comprises the caudal artery (CA) and a complex, venous vascular network in between and originating from the CV, called the CVP (Figure 4A).

A maximum projection time-lapse movie of this region at higher magnification suggested an interaction between the labeled exosomes and the vessel wall (Figure 4A; Video S3A). Indeed, high-speed imaging of the CV confirmed the transient interaction of exosomes passing through the blood vessels with the PM of endothelial cells (Figure 4B; Video S3B). To visualize the extent and the exact localization of exosomes that adhere in the caudal part of the vasculature, we created a heatmap overlay of 6 individual YSL CD63-pHluorin pDNA-injected embryos at 3 dpf (Figure 4C). Strikingly, the vast majority of exosomes were selectively arrested in the venous plexus and the caudal vein but not in the CA. This behavior is remarkably similar to what was observed for intravenously injected Zmel1 EVs (Hyenne et al., 2019), suggesting a common behavior for EVs of distinct origin and labeled with different tags in the blood flow of zebrafish embryos. In high-magnification images, we identified motile cells that crawled on the surface of the endothelial vessels and that contained labeled exosomes in intracellular compartments, likely resulting from their endocytosis (Figure 4D). Apart from endothelial cells, the lumen of the CVP hosts a number of embryonic macrophages that continuously scavenge their environment and stand out by their relative high motility (Murrayama et al., 2006). In *Tg(kdrl:HRAS-mCherry)* zebrafish embryos, these macrophages can be distinguished by their mCherry-positive compartments, probably as a result of endocytosis of (apoptotic) fragments of mCherry-expressing endothelial cells. By exploiting a *Tg(mpeg1:mCherryF)* fish line that specifically labels macrophages in red, we could identify these exosome-internalizing cells as patrolling macrophages (Figure 4E; Video S4A). Subsequent time-lapse imaging of macrophages in the caudal plexus of *Tg(kdrl:HRAS-mCherry)* fish expressing CD63-pHluorin in the YSL revealed an active form of

(B) IEM image of the YSL of a 3 dpf *Tg(kdrl:Hsa.HRAS-mCherry)* embryo injected with ubi:CD63-pHluorin in the YSL labeled with gold particles directed to GFP (10 nm). Dashed white lines indicate the approximate membranes of the YSL. Dashed line box indicates area shown enlarged in (C). RBC, red blood cell.

(C) Zoom in of area indicated in (B), showing MVE (asterisk) in the YSL, and EVs labeled for gold particles directed to GFP (10 nm) on top of the YSL.

(D) (Left panel) IEM image of exosome-sized EVs observed in blood vessel lumen, labeled with gold particles directed to GFP (10 nm). Graph on the right: quantification of vesicle labeling and appearance as in Figure 2E (mean \pm SD, >25 different fields, $n = 2$).

(E) Zoom in on area indicated with rectangular box on the right in (A). (Left panel) Fish with blood flow; (Right panel) fish without blood flow, both expressing CD63-pHluorin in the YSL.

(F) Mass-spectrometry analysis of enriched proteins in YSL-derived EVs (excerpt, complete list in Table S2) (numbers between bracket indicated the rate of enrichment in injected embryos compared to control embryos; OI, only detected in injected embryos).

(G) IEM image of an MVE in the YSL area, labeled with gold particles directed to GFP (10 nm). Thin dashed white circle indicates an MVE. YSL, yolk syncytial layer; MVE, multivesicular endosome.

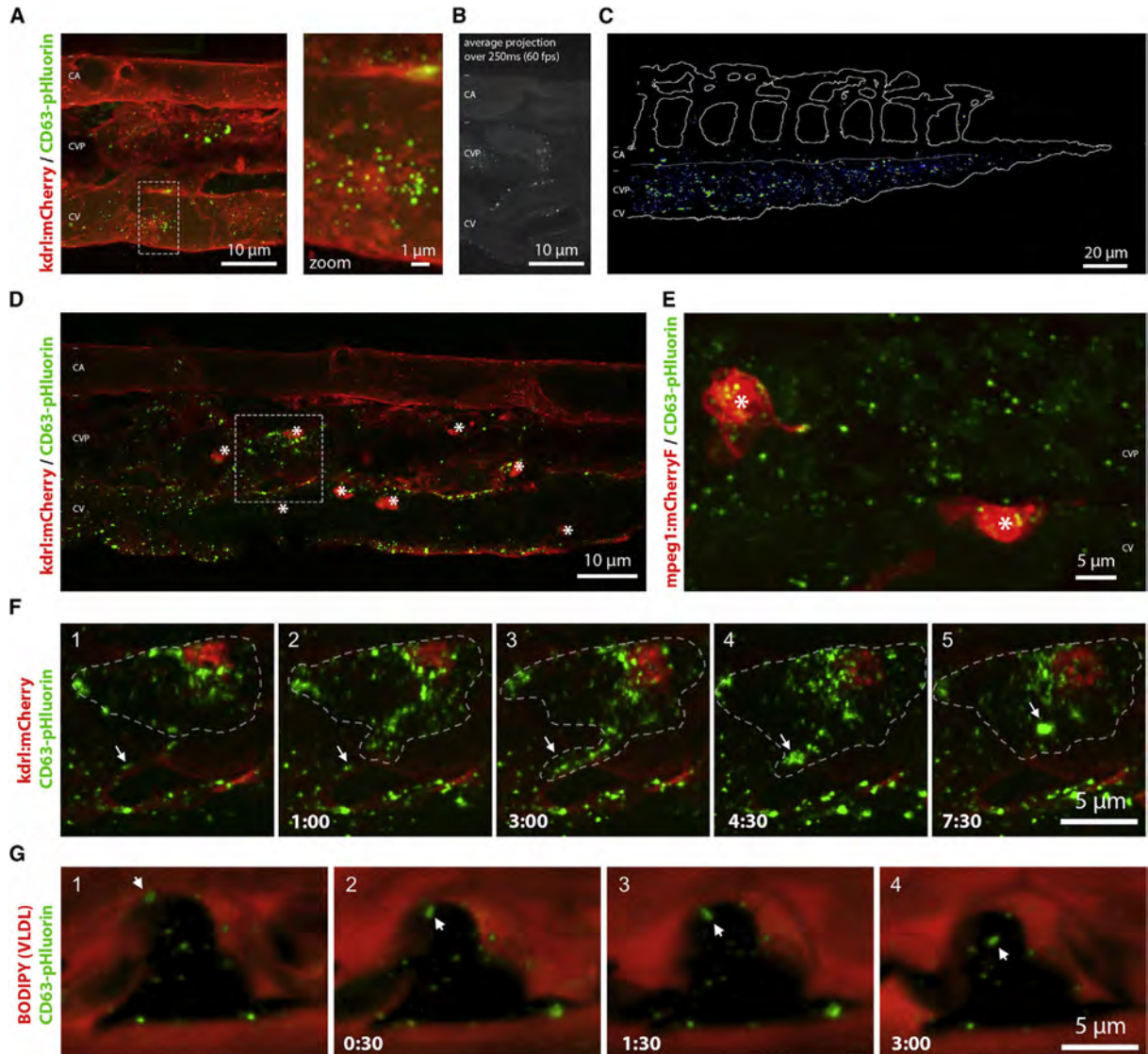


Figure 4. Distribution and Target Cells of YSL Exosomes

(A) Still of time-lapse shown in [Video S3A](#) of the CVP of a 3 dpf *Tg(kdr:Hsa.HRAS-mCherry)* embryo expressing CD63-pHluorin in the YSL. Dashed box indicates area shown at higher magnification to the right.

(B) Average projection of 15 sequential frames of [Video S3B](#), showing caudal artery (CA), CVP, and the cardinal vein (CV) in 3 dpf zebrafish embryos expressing CD63-pHluorin in the YSL.

(C) Heatmap of CD63-pHluorin signal in CVP of 6 3 dpf *Tg(kdr:Hsa.HRAS-mCherry)* zebrafish embryos expressing CD63-pHluorin in the YSL.

(D) CVP of a 3 dpf *Tg(kdr:Hsa.HRAS-mCherry)* embryo expressing CD63-pHluorin in the YSL. Stars indicate macrophages. Dashed box indicates area shown in [Video S4B](#) and (F). Asterisks indicate macrophages.

(E) Still of [Video S4A](#), showing the CVP of a 3 dpf *Tg(mpeg1:mCherryF)* expressing CD63-pHluorin in the YSL. Asterisks indicate macrophages.

(F) Time-lapse of a macrophage in a 3 dpf *Tg(kdr:Hsa.HRAS-mCherry)* zebrafish embryo expressing CD63-pHluorin in the YSL, shown in [Video S4B](#).

(G) Time-lapse of macrophage in a BODIPY-C12 injected 3 dpf zebrafish embryo expressing CD63-pHluorin in the YSL, shown in [Video S4C](#). CA, caudal artery; YSL, yolk syncytial layer; CVP, caudal vein plexus.

uptake of exosomes by macrophages that projected dendrites or pseudopodia, able to interact and “harvest” exosomes from the surface of endothelial cells (Figure 4F; [Video S4B](#)). Similar “harvesting” by patrolling macrophages was also observed for melanoma-derived exogenous EVs (Hyenne et al., 2019), sug-

gesting common mechanisms for the uptake of EVs of distinct origin.

To further investigate the specificity of the uptake of labeled exosomes by macrophages of the CVP, we injected the yolk of CD63-pHluorin YSL expressing Casper embryos at 1 dpf with

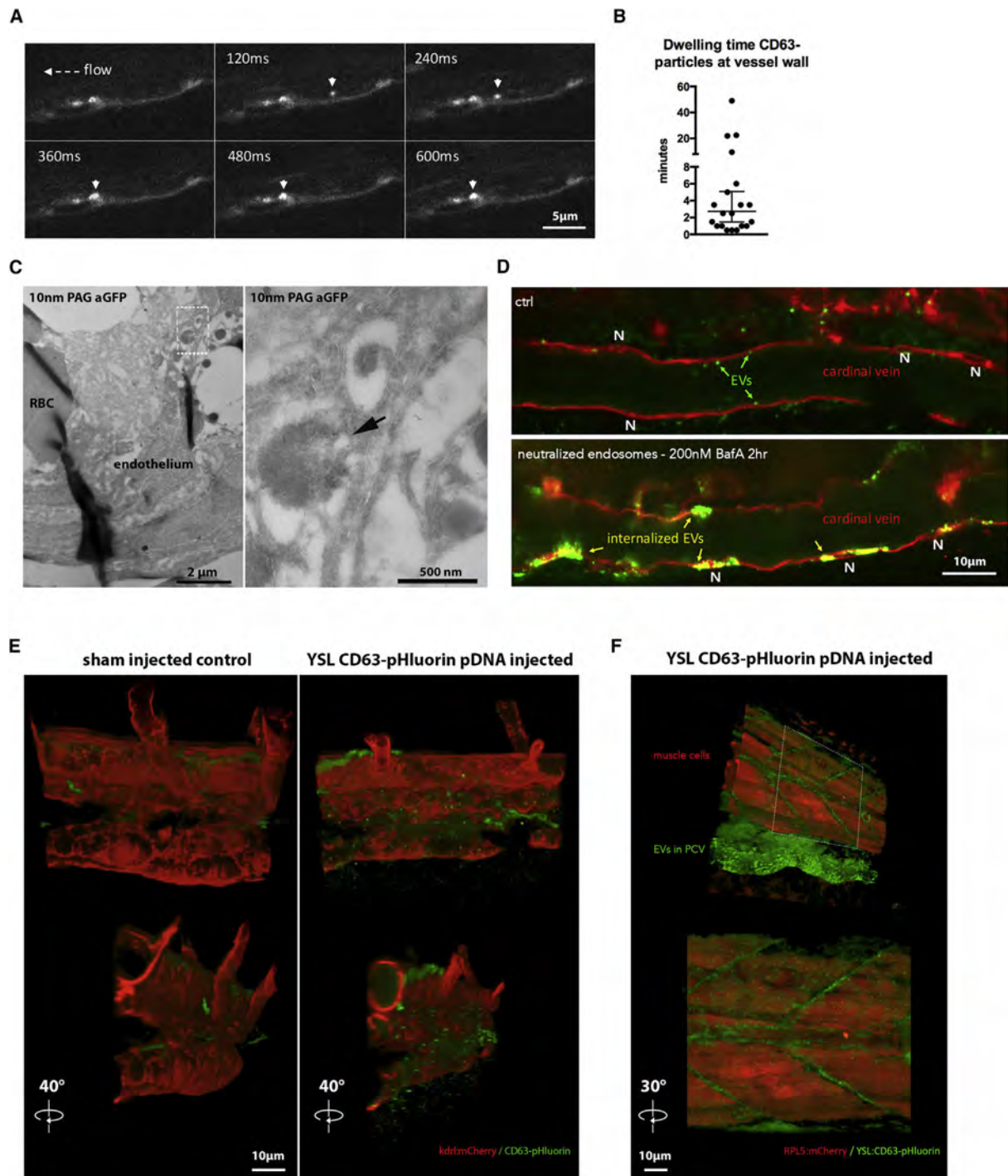


Figure 5. Interaction of YSL-Exosomes with Endothelium and Presence of YSL-Exosomes in ISF

(A) Time-lapse of [Video S5A](#), showing the rolling and arrest of exosomes in the cardinal vein of 3 dpf zebrafish embryo expressing CD63-pHluorin in the YSL.

(B) Quantification of dwelling time of CD63-pHluorin exosomes at the vascular wall (mean \pm SD, n = 20 events).

(C) EM image of the CVP of a 3 dpf zebrafish embryo expressing CD63-pHluorin in the YSL, labeled with gold particles directed to GFP (10 nm). Insert indicates area shown at higher magnification to the right. Arrow indicates internalized CD63-pHluorin exosomes in endo-lysosomal compartment of endothelial cell.

(legend continued on next page)

1.5 ng/nL BODIPY-C12 to specifically label the high amount of very-low-density lipoprotein (VLDL) particles produced by the YSL and released in the blood flow and to visualize the lumen of the blood vessels (Miyares et al., 2014). The BODIPY fluorescence was readily visible in the vasculature but was not overlapping with CD63-pHluorin labeling in the blood flow, confirming the nature of CD63-pHluorin-positive EV as exosomes and not as derivatives of VLDL. Moreover, we did not observe any BODIPY signal in macrophages, while exosomes were again actively endocytosed (Figure 4G; Video S4C). We did not observe an early decrease in fluorescence signal of CD63-pHluorin early (~3 min) after uptake (Figure 4G), in line with the observation of a large number of exosomes in the lumen of macrophages (Figures 4E and 4F), suggesting temporal “storage” and/or a delayed targeting to acidic endosomal compartments. Altogether, these data revealed a specific uptake of exosomes by macrophages in intracellular compartments that become acidic at later time point and/or that initially maintain connection with the cellular exterior.

YSL-Exosomes Are Taken Up and Degraded by Endothelial Cells

The specific interaction of labeled exosomes with the venous (Video S3), but not the arterial vasculature (Figure 4C), suggested potential implication of different shear forces exerted on EVs (Hyenne et al., 2019) between the venous and arterial blood flows. Drug treatment decreasing pacemaker activity (Vermot et al., 2009), and consequently the shear-force of the blood flow, did not lead to a visible increase of the association of exosomes with the CA (Figure S1F). This indicates the implication of additional factors, such as expression of adhesion molecules, in this interaction.

We further analyzed the dynamic of interaction between exosomes and the endothelium by using high-speed imaging of the caudal vein of YSL CD63-pHluorin pDNA-injected embryos 3 dpf. We observed rolling, arrest, and accumulation of exosomes on the endothelial wall of the vein (Figure 5A; Video S5A). Quantification of the duration of the interaction between exosomes and the venous vessel wall indicated that exosomes stay attached for an average duration of 3 min (Figure 5B). This behavior is similar to that of exogenous melanoma-derived EVs (Hyenne et al., 2019) and reinforced potential molecular interactions between exosomes and specific receptors at the surface of venous endothelial cells.

We observed that exosomes interacted transiently with endothelial cells and then disappeared (Figure 5B; Videos S3 and S5A), suggesting either their uptake by endothelial cells and targeting to acidic endosomal compartments, their re-entry into the blood flow, or dispersion outside of the vasculature. EM analysis of YSL CD63-pHluorin pDNA-injected zebrafish revealed, qualitatively, that the former occurs as we observed clusters of YSL derived exosomes immunogold labeled for GFP and mixed with dense aggregates in endo-lysosomal structures in endothelial

cells of the caudal plexus (Figure 5C). This suggested a degradative fate of exosomes that we further investigated by treating zebrafish embryos with a specific inhibitor of the vacuolar H(+)-ATPase, Bafilomycin A1 (BafA), which elevates endosomal pH and decreases lysosomal degradation (Christensen et al., 2002). Strikingly, incubation for 2 h with 100 nM BafA showed that, consistent with sites of exosome-endothelium interaction (Figure 4C), endothelial cells of the vein plexus and CV but not the CA endocytosed considerable amounts of CD63-pHluorin exosomes over time, mostly concentrating at peri-nuclear areas (Figure 5D, nuclei indicated with (N)). This accumulation, after only two h of treatment, suggests that exosomes are mainly and continuously taken up by endothelial cells to be degraded in acidic endo-lysosomes.

We then tested whether exosomes could propagate beyond vascular endothelial walls. For this, we imaged the area of the CVP and clearly observed labeled exosomes outside of the posterior cardinal vein (PCV) (Figures 5E and 5F; Video S5B). Even though we observed some of the larger fluorescent exosome clusters concentrated adjacent to the CVP, we detected high levels of fluorescent exosomes outside of the vasculature throughout the whole embryo, notably visible where covering the muscle segments and flowing in the neural tube (Videos S5B and S5C). The motility of the exosomes we observed outside the vasculature was irregular and resembled Brownian motion, clearly distinct from the dynamics of intracellular endosomal transport (Video S5B). However, in muscle cells, Bafilomycin A treatment (Video S5D) did not show accumulation of YSL derived exosomes as observed for endothelial cells. The large majority of endocytosed exosomes was thus observed in endothelial cells and to a lesser extent in patrolling macrophages but not in other cell types, highlighting the specificity for targeted cells.

Uptake of YSL-Derived Exosomes by Endothelial Cells Relies on Scavenger Receptors and Dynamin-Dependent Endocytosis

This specific interaction of exosomes with target cell types likely relied on specific receptors (van Niel et al., 2018). The visualization of internalized CD63-pHluorin exosomes with BafA treatment, allowed us to interfere with general uptake mechanisms by inhibiting dynamin, a key regulator of clathrin dependent and independent endocytosis (Ferguson and De Camilli, 2012). We treated 2 dpf YSL CD63-pHluorin expressing *Tg(kdrl:HRAS-mCherry)* embryos, expressing mCherry in the vasculature, with 3 μ M of dynamin inhibitor Pyrimidyn-7 prior to BafA treatment. Strikingly, we observed a near complete block of exosome uptake by endothelial cells (Figure 6A), excluding the uptake mechanisms of exosomes via dynamin independent pathways and possibly macropinocytosis (Harper et al., 2013). Mander's coefficient (M2) of the green signal (exosomes) overlapping with the red signal (endothelium) revealed an average decrease of more than 10-fold of the uptake (Figure 6B). Comparison of

(D) Close up of the cardinal vein of 3 dpf *Tg(kdrl:Hsa.HRAS-mCherry)* zebrafish embryos expressing CD63-pHluorin in the YSL, control-treated (DMSO), or treated with bafilomycin A (BafA) to neutralize acidic compartments.

(E) CVP area of 3 dpf *Tg(kdrl:Hsa.HRAS-mCherry)* zebrafish embryos sham-injected or injected with CD63-pHluorin pDNA in the YSL.

(F) Mid-trunk segment of 3 dpf zebrafish embryos expressing CD63-pHluorin in the YSL and mCherry under the ubiquitous RPL5 promoter. At this exposure level in the red channel, mostly muscle cells are visible. YSL, yolk syncytial layer; CVP, caudal vein plexus; PCV, posterior cardinal vein.

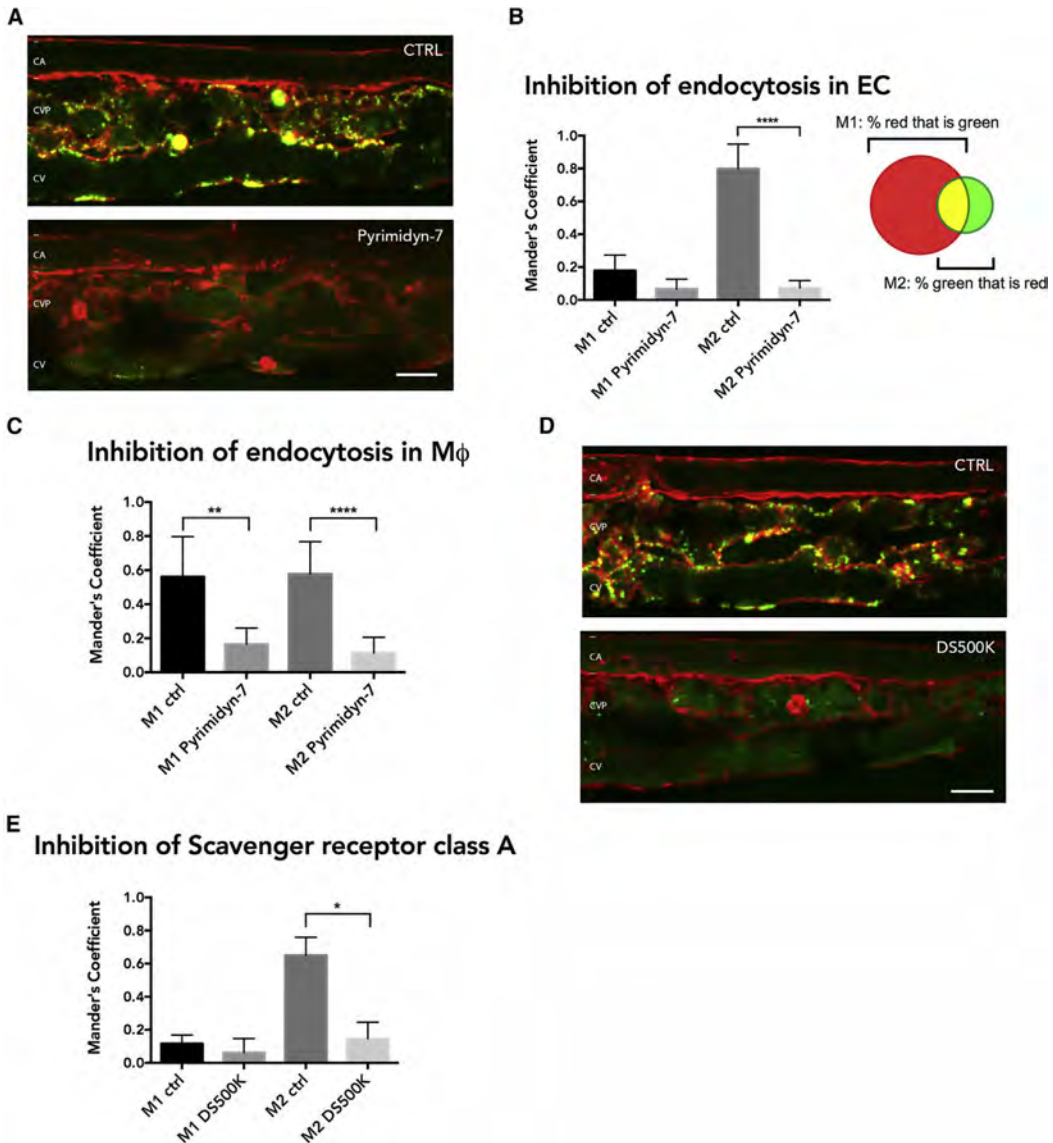


Figure 6. Characterization of Uptake Mechanism YSL-Exosomes by Endothelial Cells

(A) Close up of the CVP area of 3 dpf *Tg(kdrl: HsA.HRAS-mCherry)* zebrafish embryos expressing CD63-pHluorin in the YSL, treated with BafA to show internalized EVs and co-treated with DMSO (CTRL) or dynamin-inhibitor Pyrimidyn-7 (Pyrimidyn-7).

(B) Quantification of experiments as performed in (A), showing the overlap coefficient of red with green (M1) and green with red (M2) signal (mean \pm SD, ***p \leq 0.0001; n \geq 3; unpaired t test with equal SD).

(C) As in (B), but for macrophages alone (mean \pm SD, ***p \leq 0.0001; 7 macrophages per condition, n \geq 3; unpaired t test with equal SD).

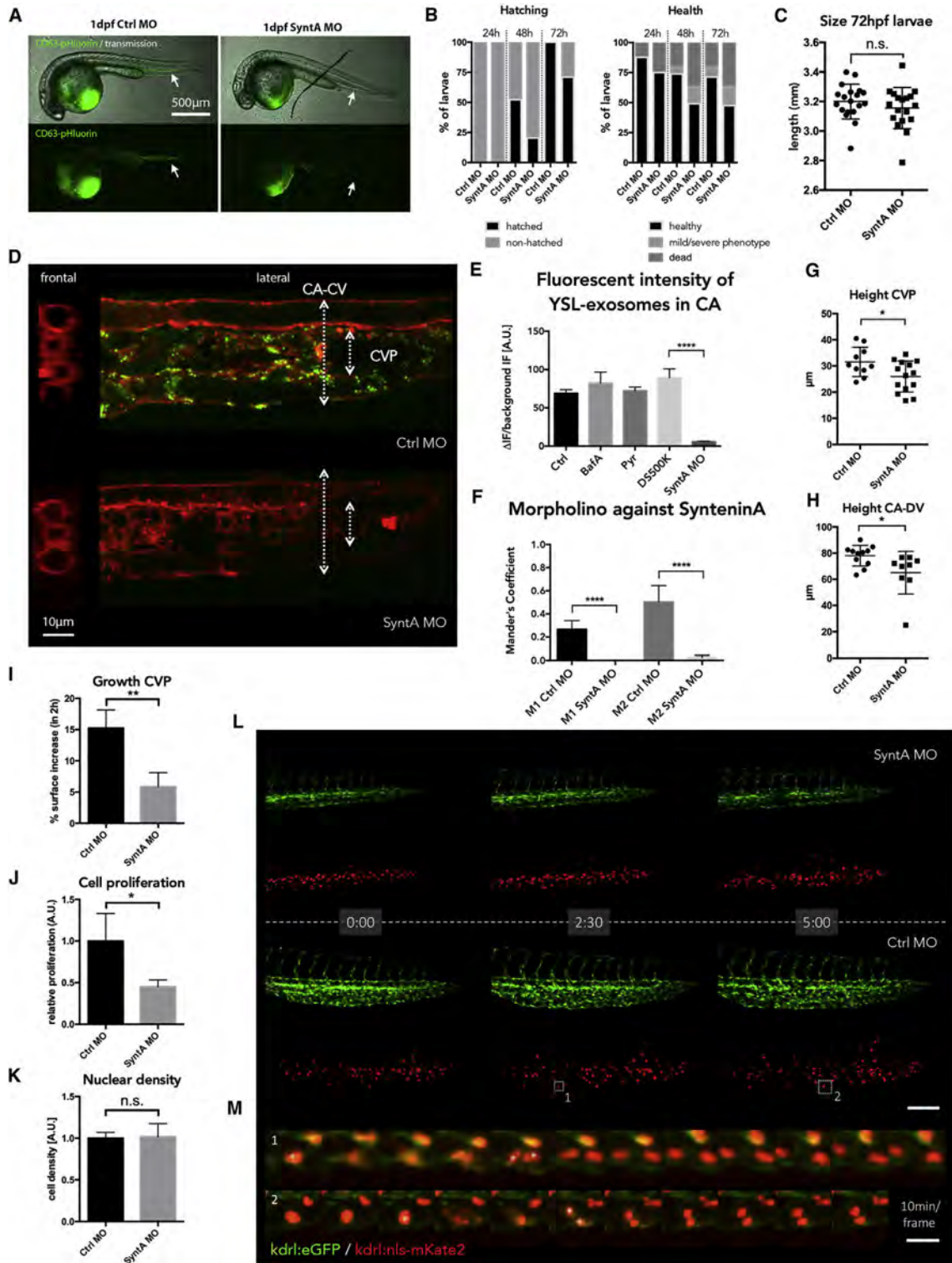
(D) Close up of the CVP area of 3 dpf *Tg(kdrl: HsA.HRAS-mCherry)* zebrafish embryos expressing CD63-pHluorin in the YSL treated with BafA to show internalized exosomes and non-injected or injected with 500K Dextran Sulfate (DS500K).

(E) Quantification of experiments as performed in (D) (mean \pm SD, *p \leq 0.05; n \geq 2; unpaired t test with equal SD). YSL, yolk syncytial layer; BafA, baflomycin A; CVP, caudal vein plexus. Scale bars represent 10 μ m.

Mander's coefficient after 180-degree rotation excluded potential interference of random overlap (Figure S1G). Similar quantification in ctrl or Pyrimidyn-7 condition showed a 5-fold reduction of uptake in macrophages (Figure 6C).

To assess the efficiency of exosome uptake, we performed 4D imaging of the CV of 3 dpf YSL CD63-pHluorin expressing

Tg(kdrl:HRAS-mCherry) embryos treated with 100 nM BafA. Time-lapse imaging indicated that exosomes accumulated over the \sim 1 h time-courses imaged (Video S6A), whereas a z-stack and a 3D rendering of the same z-stack showed a substantial presence of internalized exosomes per cell (Video S6B). Similar findings were obtained at 2 dpf (data not shown).



(legend on next page)

Together, this indicates that exosome uptake by the ECs of the CVP is not a sporadic event, but occurs in a continuous fashion. We next focused on potential receptors able to specify this endocytosis to endothelial cells.

Interestingly, the CVP area harbors scavenger endothelial cells (SECs) that interact in a scavenger-receptor mediated manner with liposomes of 100 nm injected in the circulation (Campbell et al., 2018). Scavenger receptors have also been reported *in vitro* to mediate exosome uptake (Plebanek et al., 2015); are expressed on endothelial cells and macrophages, and are conserved in teleost (Poynter et al., 2015); and mediate dynamin-dependent endocytosis (Jang et al., 2014). To investigate whether scavenger receptors are implicated in exosome uptake *in vivo*, we injected dextran sulfate (DexSO₄-500K), a known competitive ligand for scavenger receptors (Lysko et al., 1999), intravenously in CD63-pHluorin YSL expressing *Tg(kdrl:HRAS-mCherry)* embryos prior to BafA treatment. Strikingly, we observed a decrease of more than 4-fold of the green signal (EVs) overlapping with the red signal (endothelium) (Figures 6D and 6E), indicating that endogenous exosomes competed with DexSO₄-500K for their uptake by the same class of receptors. We did not observe a significant decrease in uptake in macrophages (Figure S1H).

This set of data revealed that *in vivo*, endogenous exosomes are specifically internalized by specialized venous endothelial cells in a dynamin- and scavenger receptor dependent pathway to be targeted to lysosomes for degradation.

Production of YSL-Derived Exosomes Relies on a Syntenin-Dependent Biogenesis Pathway and Supports Vasculogenesis of the Caudal Vein Plexus

The enrichment for a syntenin-ALIX mediated machinery in YSL-exosomes (Figure 3F) led us to interfere with their generation and further investigate their potential function *in vivo*. A previous study in zebrafish reported the expression of syntenin-a, notably in YSL, at different stages of development (Lamberts et al., 2012). Depletion of syntenin-a in the whole embryo in the same study revealed defects in epiboly progression and body-axis formation during early zebrafish development, whereas depleting syntenin-a solely in the YSL only affected epiboly in 30% of the embryos and resulted in a well-formed axis in all embryos. We

co-injected one of these morpholino (MO) oligonucleotides, validated in conformity to recently published guidelines (Stainier et al., 2017), targeting the translation start site in syntenin-a transcripts (SyntA MO) or control MO (Ctrl MO) together with CD63-pHluorin pDNA specifically in the YSL of *Tg(kdrl:HRAS-mCherry)* embryos 4 hpf. Of note, in our experiments most embryos displayed normal development but showed a small delay in hatching and increase in mortality (Figures 7A–7C). When considering only embryos with normal development (>50% in both conditions), whole body analysis showed expression of CD63-pHluorin in the YSL (Figure 7A) but a profoundly diminished number of fluorescent exosomes in the blood flow for the SyntA MO compared to the Ctrl MO condition (Figures 7D and 7E) that could be rescued by co-injection of MO-insensitive wt syntenin-a plasmid DNA (Figures S2A and S2B). This suggests that syntenin is implicated in CD63 positive exosome biogenesis in the YSL *in vivo* and that endogenous exosome biogenesis can be manipulated. Incubation of these embryos for 2 h with 100 nm BafA confirmed the near absence of exosomes in the CVP, corresponding with a 20-fold reduction of the uptake of exosomes by endothelial cells in this region (Figure 7F). While we did not observe any major defect in angiogenesis or growth of SyntA MO embryos at 3 dpf (Figure 7C), we did observe a decrease of ~18% in the height of the CVP between SyntA MO and Ctrl MO treated embryos (Figures 7G and 7H), suggesting a role of exosomes produced from the YSL in the development of the CVP by taking them up and targeting them to lysosomes. Finally, we aimed to further assess the effect of YSL-exosome depletion on CVP growth. For this, we performed imaging of YSL SyntA MO and Ctrl MO injected embryos over time between 35–40 hpf and quantified the number of nuclei and the expansion of the vascular bed (Figures 7I–7M). While the nuclear density was comparable, the growth of the CVP as well as the cell proliferation was lower in SyntA MO YSL-injected compared to Ctrl MO YSL-injected embryos (Figures 7I–7K), whereas cellular motility seemed unaffected. Together, this indicates that YSL exosomes support CVP growth, mainly by affecting cell proliferation.

Collectively, these data demonstrate that endogenous biogenesis of exosomes can be modulated, revealing physiological effects in defined target cells.

Figure 7. Functional Analysis of YSL-Exosomes

- (A) Transmission and fluorescent images of Ctrl MO- or SyntA MO-treated 1 dpf zebrafish embryos.
- (B) Quantification of morphological features of Ctrl MO- or SyntA MO-treated 1–3 dpf (24–72 h) zebrafish embryos. To the left, hatched versus non-hatched comparison. To the right, health status comparison with normal morphology (healthy), mild or severe developmental defects, and mortality. Sample size ≥ 120 .
- (C) Size (length) of Ctrl MO- or SyntA MO-treated 3 dpf zebrafish embryos (scatter-dot plot, mean \pm SD; $n = 19$, $n = 18$, respectively).
- (D) Close up of the CVP area of 3 dpf *Tg(kdrl:Hsa.HRAS-mCherry)* zebrafish embryos expressing CD63-pHluorin in the YSL, co-injected with Ctrl MO or SyntA MO in the YSL. Left panel: frontal view; right panel: lateral view. CA, caudal artery; CV, cardinal vein.
- (E) Fluorescent intensity of GFP signal in CA measured during different treatments. BafA, baflomycin-A; Pyr, Pyrimidin-7; DS500K, 500 KDa dextran sulfate; SyntA MO, syntenin-a morpholino; A.U., arbitrary units. mean \pm SD; ***p ≤ 0.0001 ; all conditions show at least triplicates of $n \geq 3$; unpaired t test with equal SD.
- (F) Quantification of overlap-coefficient of red with green (M1) and green with red (M2) in Ctrl MO- or SyntA MO-treated 3 dpf *Tg(kdrl:Hsa.HRAS-mCherry)* zebrafish embryos, as shown in (D) (mean \pm SD; ***p ≤ 0.0001 ; $n = 5$; unpaired t test with equal SD).
- (G and H) Quantification of height of caudal part of vasculature, specifically for the CVP at second intersegmental vessel (ISV), or (H) measured from CA to CV (scatter-dot plot, mean \pm SD; *p ≤ 0.05 ; $n \geq 10$, $n \geq 9$ resp; unpaired t test with equal SD).
- (I–K) *Tg(kdrl:eGFP /nls-mKate2)* embryos injected with control (Ctrl MO) or syntenin-a (SyntA MO) morpholinos in the YSL, analyzed for growth (I), proliferation (J), and nuclear density (K) in the CVP between 35 and 40 hpf (mean \pm SD; *p ≤ 0.05 ; **p ≤ 0.01 ; $n = 4$; unpaired t test with equal SD).
- (L) Time-lapse of *Tg(kdrl:eGFP /nls-mKate2)* embryos between 35 and 40 hpf. Boxes indicate 2 examples of proliferating cells, as shown in (M). Scale bar represents 40 μ m.
- (M) Two examples of dividing cells are shown. Scale bar represents 15 μ m. YSL, yolk syncytial layer; CVP, caudal vein plexus.

DISCUSSION

Until now, the development of a model to explore the release, journey, and targets of endogenous exosomes *in vivo* had been hampered by the small size of the exosomes and the lack of appropriate methods to label them. A recent study reported the use of CD63-GFP in transgenic rats (Yoshimura et al., 2016) that demonstrated its usefulness for the *ex vivo* analysis of EV transfer to organs and bodily fluids but that was limited in its suitability for *in vivo* imaging. Here, we sought to fill that void by exploring a vertebrate model suitable for *in toto* imaging while maintaining sub-cellular and even supra-optical resolution. The CD63-pHluorin strategy has recently been shown to be an accurate *in vitro* model to explore new facets of the molecular mechanisms that control the biogenesis and secretion of exosomes (Verweij et al., 2018). Our study demonstrates that the CD63-pHluorin reporter can be used *in vivo* to investigate the molecular regulation of exosome secretion. However, this approach is currently still limited by a technological latch that hinders quantitative observation of bursts of fluorescence in cells that are not flat. In our model, we observed a relatively limited number of fusion events compared to transformed cell lines *in vitro*, which is in line with *in vitro* experiments indicating lower fusion activity for non-transformed cells (Verweij et al., 2018) as well as increased presence of exosomes in bodily fluids of cancer patients (Galindo-Hernandez et al., 2013; Logozzi et al., 2009). Interestingly, the transposition of this tool *in vivo* also provided a model allowing single vesicle tracking from their site of production to their final destination and might be useful to investigate the dynamics of body fluid flows with high precision (Bachy et al., 2008).

We observed a large number of fluorescent vesicles in the blood after ubiquitous expression of CD63-pHluorin. IEM labeling confirmed that CD63-pHluorin was associated to vesicular structures (Figures S1C and S2D). Using tissue-specific expression, we could trace the origin of these exosomes and identified the YSL, a secretory cell layer in direct contact with the blood, as one of the providers of endogenous exosomes that reach the rest of the organism. Mass spectrometry analysis of EVs derived from cell lines (AB.9, Zmel), embryos in our study, and in (Henne et al., 2019) showed a common composition and highlights a consistent presence of proteins involved in exosome biogenesis by the syntenin-Alix-ESCRT-III pathway, previously reported *in vitro* (Baietti et al., 2012). Our data strongly suggest that the EVs followed in this study are likely of endosomal origin, although we cannot exclude the contribution of the PM of the YSL as a source of EVs. Of note, treatment of embryos with GW4869 did not affect exosome release from the YSL (Figure S2E), suggesting that at least for this source of exosomes, ceramide is not a major regulator of their biogenesis (Trajkovic et al., 2008). These data suggest that *in vivo*, the syntenin-ALIX-ESCRT-III pathway is among one of the essential pathways for exosome biogenesis, opening avenues to interfere with EV generation and function *in vivo*.

Our initial explorations uncovered endothelial cells and patrolling macrophages as recipient cells, strengthening the notion of targeted communication by exosomes. Although we cannot exclude a specific role of YSL-derived exosomes once taken up by macrophages, these scavenger cells may harvest exo-

somes dwelling at the surface of endothelial cells to regulate the steady-state level of EVs in the circulation (Imai et al., 2015). However, we also observed that the internalizing compartments containing EVs (1) do not immediately acidify (Figure 4G) and (2) might be internalized slower, as we did not need to use baflomycin A treatment to visualize uptake in macrophages and still observed green EVs in macrophages after prolonged incubation with DS500K (Figure S1H). This would be compatible with a functional interaction between the EVs and the macrophage, recently demonstrated in a cancer setting (Gabrusiewicz et al., 2018), and might be part of an immune surveillance function analogous to Kupffer cells (Jenne and Kubes, 2013). In zebrafish, we show that endogenous exosomes are mainly targeted to the venous endothelial cells of the CV(P). These cells show functional homology with specialized liver sinusoidal endothelial cells (LSECs) in higher vertebrates (Campbell et al., 2018), indicating inter-species correlation with the targeting of injected EVs to the liver in murine models (Charoenviriyakul et al., 2017; Wiklander et al., 2015). LSECs clear soluble macromolecules and small particles from the circulation and, in humans, possess the highest endocytic capacity of all cells (Poisson et al., 2017). In older vertebrates, jawless, cartilaginous, and bony fish, cells resembling the LSEC are located at different locations outside the liver and are collectively called SECs that are similarly central to the removal and catabolism of a variety of macromolecules from the circulation (Sternes et al., 2002).

We show that the uptake mechanisms of EVs by endothelial cells in the CV(P) implicate scavenger receptors and dynamin-dependent endocytosis. Indeed, various scavenger receptors internalize their ligands in a dynamin-dependent manner and traffic to lysosomes (Fukuda et al., 2011). Scavenger receptors, such as Stabilin-2, have been recently described as mediating the uptake of 100-nm-sized anionic liposomes in zebrafish (Campbell et al., 2018). This suggests that exosomes, having a negative z-potential (due to the presence of anionic lipids), could bind in a similar fashion to these receptors, independently of a specific ligand present on the exosomal membrane.

The lysosomal fate of YSL-derived exosomes in endothelial cells echoes data showing that uptake and catabolism of exosomes in lysosomal compartments is likely a major fate as described *in vitro* (Tian et al., 2010). This pathway would allow catabolism of EV content and provide a source of amino acids, nucleic acids, lipids, and ions to recipient cells. Although we cannot rule out a structural function of YSL-derived EVs during development, e.g., in patterning or differentiation (McGough and Vincent, 2016), the effect we observed on CV and CVP development when interfering with EVs biogenesis also suggests that endothelial cells may uptake and process EVs in lysosomes to use them as a source of macromolecules for their own development (Yao et al., 2017). It is also possible that these exosomes provide an extracellular source of membrane to allow for expansion of the vascular bed, analogous to the involvement of late endo/lysosomes in protrusions and neurite outgrowth (Naegeli et al., 2017; Raiborg et al., 2015). In accordance with this, we observed a lower proliferation rate of CVP endothelial cells with reduced levels of CD63 exosomes coming from the YSL (Figure 7J). These data raise the possibility that uptake of exosomes by LSEC, beyond a simple removal role of exosomes

from the circulation, indeed may support a trophic link between the YSL and LSCEs.

The presence of numerous EVs in the bloodstream but also in the interstitial fluid (ISF) of developing zebrafish embryos strengthens *ex vivo* observations of the presence of EVs in both fluids (Gromov et al., 2013; Johnstone et al., 1989). Recent evidence indicates that exosomes or EVs containing miRNAs can also in- and extravasate biological barriers to access ISF under physiological conditions (Thomou et al., 2017), but the YSL in zebrafish is directly connected with the ISF, providing a direct way for exosomes from YSL to access the ISF. The motility of the CD63-pHluorin-positive exosomes we observed outside the vasculature was irregular and resembled Brownian motion (Video S5B), clearly distinct from the dynamics of intracellular endosomal transport. Of note, baflomycin A treatment (as in Figure 5D) did not show accumulation of YSL-derived exosomes in other cells such as the highly abundant muscle cells (Video S5D). These observations would exclude uptake and lysosomal degradation as a major way to use EVs as a source of macromolecules by other cells than endothelial cells. Of note, our proteomic analysis revealed the presence and enrichment for various lipid, amino acid, and ion transporters that could support a role of YSL-derived exosomes as “macromolecule dispenser” to the surrounding cells, as these transporters could potentially mediate the bioavailability of exosomal contents (Allen and Cullis, 2013). All in all, the presence of these EVs in various bodily fluids supports a general role in metabolism, e.g., in nutrient delivery, and makes a specific role in other YSL functions, e.g., embryonic patterning, less likely. Nevertheless, we cannot exclude that these EVs are used to exchange genetic information between cells *in vivo* as shown recently (Ashley et al., 2018; Pastuzyn et al., 2018; Zomer et al., 2015), and future development of adapted tools as described *in vitro* (Yim et al., 2016) is required to explore these functions in detail.

Despite its several advantages, we cannot exclude that in this model expression of this reporter might affect exosome secretion or composition. Nevertheless, nanoparticle tracking did not show a significant change in the number of particles between non-injected and CD63-pHluorin YSL-expressing embryos, and proteomics indicated the presence of endogenous zCD63 in the YSL-CD63-pHluorin labeled exosomes. Another potential downside of our approach might be that expression of a TSPAN-reporter may only label a subpopulation of YSL-derived exosomes as CD63 may not be equally enriched in all exosome subpopulation (Kowal et al., 2016). Larger (>150 nm) vesicles, predominantly negative for CD63-pHluorin, suggest the presence of different subpopulations in our model. Isolating a subpopulation from the heterogenous family of EVs with this reporter presents, however, the advantage to target specific fate or functions. Future studies using other TSPAN-pHluorin markers, including CD81, CD82, or CD9 (Verweij et al., 2018), could aid to cover the whole spectrum of EVs. The present study was restricted to the YSL, excluding from our observation all EVs released by other cell types that might represent up to 90% of the pelleted vesicles from dissociated fishes (Figures S1C and S2D). Development of future strains with cell-type-specific expression will allow investigation of the various roles of exosomes secreted under physiological and pathological conditions by nearly all cell types investigated so far. In addition, combining cell-type-spe-

cific expression of TSPAN-pHluorin markers with proteomic analysis of immuno-isolated exosomes could potentially be used to discover pathological biomarkers for each producing cell type targeted *in vivo*. What might also be considered as a drawback in some applications is that we use a pH-sensitive GFP, meaning that EVs that are taken up in recipient cells will in most cases likely end up in acidified compartments, resulting in quenching of their fluorescence. However, in this study, we do show that baflomycin treatment reverts this acidification and consequently quenching of fluorescent EVs and the addition of a pH-insensitive fluorescent label to CD63-pHluorin can also be considered.

In this study, we opted for the MO strategy to achieve a tissue-specific knockdown of syntenin-a in the YSL. Although generally targeted mutagenesis using CRISPR/Cas9 would be the method of choice, the generation of a null allele would not affect maternal contribution of syntenin-a mRNA (Lambaerts et al., 2012) until reaching F3, and maternal-zygotic mutants will likely have too broad effects to address our specific point. While we did initiate the generation of a null line (data not shown), we realized that since exosome secretion from the YSL could be observed as early as 1 dpf, the use of MO injected in the YSL was preferred to (1) be able to affect maternal contribution of syntenin-a mRNA and (2) achieve tissue-specific knockdown of syntenin-a. We are well aware that the application of MO in zebrafish has to be approached with caution, and proper controls are needed to distinguish specific phenotypes from off-target effects, as outlined in recently published guidelines (Stainier et al., 2017). The specific MO we applied has been used in a previous publication and complies with the additional guidelines as recently set out (Lambaerts et al., 2012; Stainier et al., 2017). In addition, we titrated the MO for its ability to sufficiently block exosome secretion while minimizing mortality and performed an additional rescue experiment (Figure S2A). Future studies with syntenin-a KO lines will be indispensable to deepen our understanding of the contribution of this exosome biogenesis pathway to exosome physiology *in vivo* but might require tissue-specific KO.

Importantly, the study of Hyenne et al. (2019) also used zebrafish embryos to investigate the behavior and fate of systemically injected exogenous exosomes originating from zebrafish melanoma cells. Whereas previous studies have indicated how tumor-exosome integrins determine their organotropism (Hoshino et al., 2015), the combination of both models presented here reveals common uptake mechanisms between (exogenous) pathological exosomes and (endogenous) physiological exosomes, an interesting phenotype that has never been explored before at this scale. How circulating EVs target specific cell types at distance remains to be solved, mostly because this step could not be visualized before, but the *in vivo* models presented here pave new avenues to unveil such mechanisms under physiological and pathological conditions. The genetic and structural homologies between zebrafish and human open new perspectives to validate exosome-mediated intercellular communication in the complex architecture of the organism, notably inter-organ communication and their ability to cross biological barriers. The fast development of disease models in zebrafish also provides the opportunity to tackle putative roles of exosomes in several pathologies (Yáñez-Mó et al., 2015), which involves a complex network of cell types. Therefore, the zebrafish

embryo-expressing fluorescent proteins associated with exosomes (e.g., CD63-pHluorin) are a relevant model to study endogenous EVs *in vivo* to unravel fundamental aspects in EV physiology and to assess their clinical applications. Together, our study showcases the variety of questions that could likely be investigated in model organisms to validate the numerous *in vitro* studies on the biology and function of EVs so far.

STAR★METHODS

Detailed methods are provided in the online version of this paper and include the following:

- **KEY RESOURCES TABLE**
- **CONTACT FOR REAGENT AND RESOURCE SHARING**
- **EXPERIMENTAL MODEL AND SUBJECT DETAILS**
 - Zebrafish Strains
 - Cell Lines
- **METHOD DETAILS**
 - Construction of pUbi-CD63-pHluorin
 - Morpholino Injection
 - Plasmid DNA Injections
 - VLDL Labeling
 - Decreasing Pace-Maker Activity
 - Live Fluorescent Imaging
 - DIC Video-Microscopy/‘Nomarski’
 - Electron Microscopy
 - Image Analysis
 - Generation of EV-Heatmap in Zebrafish Embryo
 - Exosome Preparation from *In Vitro* Cultured Cells
 - Exosome Isolation from Zebrafish Embryos
 - NTA Measurements
 - Label-free Mass-Spectrometry
 - Analysis of Growth in the CVP
- **QUANTIFICATION AND STATISTICAL ANALYSIS**
- **DATA AND SOFTWARE AVAILABILITY**

SUPPLEMENTAL INFORMATION

Supplemental Information includes two figures, two tables, and six videos and can be found with this article online at <https://doi.org/10.1016/j.devcel.2019.01.004>.

ACKNOWLEDGMENTS

We acknowledge Vincent Fraisier, Ludovic Leconte, Laetitia Pidial, and Christine Viaris for technical assistance and Karine Duroure and Mylène Lancino for assistance and helpful discussions. The authors greatly acknowledge the Cell and Tissue Imaging (PICT-IBISA) and Nikon Imaging Centre, Institut Curie, member of the French National Research Infrastructure France-BioImaging (ANR10-INBS-04), the NeurImag imaging platform at the IPNP, and the Zebrafish Platform at Institut Curie. Financing support has been provided by Fondation pour la Recherche Médicale (contract AJE20160635884) to G.v.N., the European Molecular Biology Organization grant (EMBO ALTF 1383-2014) to F.J.V., the Fondation ARC pour la Recherche sur le Cancer fellowship (PJA 20161204808) to F.J.V., LabEx CelTisPhyBio to G.v.N. and F.J.V., and a “Région Ile-de-France” grant to D.L.

AUTHOR CONTRIBUTIONS

Conceptualization, F.J.V. and G.v.N.; Methodology, F.J.V., G.v.N., F.D.B., and D.M.P.; Validation, F.J.V.; Formal Analysis, F.J.V., G.v.N., G. Arras, and G. Alilio; Investigation, F.J.V., C.R., F.D., G.F., and G.v.N.; Resources, F.D.B., P.H.,

J.G.G., and P.Z.; Data Curation, F.J.V. and G.A.; Writing – Original Draft, F.J.V. and G.v.N.; Writing – Review & Editing, F.J.V., G.v.N., D.M.P., G.R., P.H., F.D.B., C.R., and J.G.G.; Visualization, F.J.V.; Supervision, G.v.N., F.D.B., and D.L.; Project Administration, G.v.N.; Funding Acquisition, F.J.V. and G.v.N.

DECLARATION OF INTERESTS

The authors declare no competing interests.

Received: March 15, 2018

Revised: December 21, 2018

Accepted: December 31, 2018

Published: February 7, 2019

REFERENCES

Allen, T.M., and Cullis, P.R. (2013). Liposomal drug delivery systems: From concept to clinical applications. *Adv. Drug Deliv. Rev.* **65**, 36–48.

Ashley, J., Cordy, B., Lucia, D., Fradkin, L.G., Budnik, V., and Thomson, T. (2018). Retrovirus-like gag protein Arc1 binds RNA and traffics across synaptic boutons. *Cell* **172**, 262–274.e11.

Bachy, I., Koziraki, R., and Wassef, M. (2008). The particles of the embryonic cerebrospinal fluid: how could they influence brain development? *Brain Res. Bull.* **75**, 289–294.

Baietti, M.F., Zhang, Z., Mortier, E., Melchior, A., Degeest, G., Geeraerts, A., Ivarsson, Y., Depoortere, F., Coomans, C., Vermeiren, E., et al. (2012). Syndecan-syntenin-ALIX regulates the biogenesis of exosomes. *Nat. Cell Biol.* **14**, 677–685.

Campbell, F., Bos, F.L., Sieber, S., Arias-Alpizar, G., Koch, B.E., Huwyler, J., Kros, A., and Bussmann, J. (2018). Directing nanoparticle biodistribution through evasion and exploitation of Stab2-dependent nanoparticle uptake. *ACS Nano* **12**, 2138–2150.

Charoenviriyakul, C., Takahashi, Y., Morishita, M., Matsumoto, A., Nishikawa, M., and Takakura, Y. (2017). Cell type-specific and common characteristics of exosomes derived from mouse cell lines: yield, physicochemical properties, and pharmacokinetics. *Eur. J. Pharm. Sci.* **96**, 316–322.

Christensen, K.A., Myers, J.T., and Swanson, J.A. (2002). PH-dependent regulation of lysosomal calcium in macrophages. *J. Cell Sci.* **115**, 599–607.

Ellett, F., Pase, L., Hayman, J.W., Andrianopoulos, A., and Lieschke, G.J. (2011). mpeg1 promoter transgenes direct macrophage-lineage expression in zebrafish. *Blood* **117**, e49–e56.

EV-TRACK Consortium, Van Deun, J., Mestdagh, P., Agostinis, P., Akay, Ö., Anand, S., Anckaert, J., Martinez, Z.A., Baetens, T., Beghein, E., et al. (2017). EV-TRACK: transparent reporting and centralizing knowledge in extracellular vesicle research. *Nat. Methods* **14**, 228–232.

Fais, S., O’Driscoll, L., Borras, F.E., Buzas, E., Camussi, G., Cappello, F., Carvalho, J., Cordeiro da Silva, A., Del Portillo, H., El Andaloussi, S., et al. (2016). Evidence-based clinical use of nanoscale extracellular vesicles in nanomedicine. *ACS Nano* **10**, 3886–3899.

Ferguson, S.M., and De Camilli, P. (2012). Dynamin, a membrane-remodelling GTPase. *Nat. Rev. Mol. Cell Biol.* **13**, 75–88.

Fukuda, M., Ohtani, K., Jang, S.J., Yoshizaki, T., Mori, K., Motomura, W., Yoshida, I., Suzuki, Y., Kohgo, Y., and Wakamiya, N. (2011). Molecular cloning and functional analysis of scavenger receptor zebrafish CL-P1. *Biochim. Biophys. Acta* **1810**, 1150–1159.

Gabrusiewicz, K., Li, X., Wei, J., Hashimoto, Y., Marisetty, A.L., Ott, M., Wang, F., Hawke, D., Yu, J., Healy, L.M., et al. (2018). Glioblastoma stem cell-derived exosomes induce M2 macrophages and PD-L1 expression on human monocytes. *Oncoimmunology* **7**, e1412909.

Galindo-Hernandez, O., Villegas-Comonfort, S., Candaleno, F., González-Vázquez, M.C., Chavez-Ocaña, S., Jimenez-Villanueva, X., Sierra-Martinez, M., and Salazar, E.P. (2013). Elevated concentration of microvesicles isolated from peripheral blood in breast cancer patients. *Arch. Med. Res.* **44**, 208–214.

Gould, S.J., and Raposo, G. (2013). As we wait: coping with an imperfect nomenclature for extracellular vesicles. *J. Extracell. Vesicles* 2, 20389.

Gromov, P., Gromova, I., Olsen, C.J., Timmermans-Wielenga, V., Talman, M.L., Serizawa, R.R., and Moreira, J.M.A. (2013). Tumor interstitial fluid — A treasure trove of cancer biomarkers. *Biochim. Biophys. Acta* 1834, 2259–2270.

Harper, C.B., Popoff, M.R., McCluskey, A., Robinson, P.J., and Meunier, F.A. (2013). Targeting membrane trafficking in infection prophylaxis: dynamin inhibitors. *Trends Cell Biol.* 23, 90–101.

Helker, C.S.M., Schuermann, A., Karpanen, T., Zeuschner, D., Belting, H.G., Affolter, M., Schulte-Merker, S., and Herzog, W. (2013). The zebrafish common cardinal veins develop by a novel mechanism: lumen ensheathment. *Development* 140, 2776–2786.

Hermkens, D.M.A., Duckers, H.J., and Schulte-Merker, S. (2015). Vascular development in the zebrafish. In *Endothelial Signaling in Development and Disease*, M.H.H. Schmidt and S. Liebner, eds. (Springer), pp. 47–64.

Hoshino, A., Costa-Silva, B., Shen, T.-L., Rodrigues, G., Hashimoto, A., Tesic Mark, M., Molina, H., Kohsaka, S., Di Giannatale, A., Ceder, S., et al. (2015). Tumour exosome integrins determine organotropic metastasis. *Nature* 527, 329–335.

Hurbain, I., Geerts, W.J., Boudier, T., Marco, S., Verkleij, A.J., Marks, M.S., and Raposo, G. (2008). Electron tomography of early melanosomes: implications for melanogenesis and the generation of fibrillar amyloid sheets. *Proc. Natl. Acad. Sci. U S A.* 105, 19726–31.

Hyenne, V., Ghoroghi, S., Collot, M., Bons, J., Follain, G., Harlepp, S., Mary, B., Bauer, J., Mercier, L., Busnelli, I., et al. (2019). Studying the fate of tumor extracellular vesicles at high spatiotemporal resolution using the zebrafish embryo. *Dev. Cell* 48. Published online February 7, 2019. <https://doi.org/10.1016/j.devcel.2019.01.014>.

Hyenne, V., and Goetz, J.G. (2017). Extracellular vesicles on the wire. *Cell Adh. Migr.* 11, 121–123.

Imai, T., Takahashi, Y., Nishikawa, M., Kato, K., Morishita, M., Yamashita, T., Matsumoto, A., Charoenviriyakul, C., and Takakura, Y. (2015). Macrophage-dependent clearance of systemically administered B16BL6-derived exosomes from the blood circulation in mice. *J. Extracell. Vesicles* 4, 26238.

Jang, S., Ohtani, K., Fukuoh, A., Mori, K., Yoshizaki, T., Kitamoto, N., Kim, Y., Suzuki, Y., and Wakamiya, N. (2014). Scavenger receptor CL-P1 mediates endocytosis by associating with AP-2μ2. *Biochim. Biophys. Acta* 1840, 3226–3237.

Jenne, C.N., and Kubes, P. (2013). Immune surveillance by the liver. *Nat. Immunol.* 14, 996–1006.

Jin, S.W., Beis, D., Mitchell, T., Chen, J.N., and Stainier, D.Y. (2005). Cellular and molecular analyses of vascular tube and lumen formation in zebrafish. *Development* 132, 5199–5209.

Johnstone, R.M., Bianchini, A., and Teng, K. (1989). Reticulocyte maturation and exosome release: transferrin receptor containing exosomes shows multiple plasma membrane functions. *Blood* 74, 1844–1851.

Kowal, J., Arras, G., Colombo, M., Jouve, M., Morath, J.P., Primdal-Bengtson, B., Dingli, F., Loew, D., Tkach, M., and Théry, C. (2016). Proteomic comparison defines novel markers to characterize heterogeneous populations of extracellular vesicle subtypes. *Proc. Natl. Acad. Sci. USA* 113, E968–E977.

Lai, C.P., Kim, E.Y., Badr, C.E., Weissleder, R., Mempel, T.R., Tannous, B.A., and Breakefield, X.O. (2015). Visualization and tracking of tumour extracellular vesicle delivery and RNA translation using multiplexed reporters. *Nat. Commun.* 6, 7029.

Lamberts, K., Van Dyck, S., Mortier, E., Ivarsson, Y., Degeest, G., Luyten, A., Vermeiren, E., Peers, B., David, G., and Zimmermann, P. (2012). Syntenin, a syndecan adaptor and an Arf6 phosphatidylinositol 4,5-bisphosphate effector, is essential for epiboly and gastrulation cell movements in zebrafish. *J. Cell Sci.* 125, 1129–1140.

Lenard, A., Ellerstsdottir, E., Herwig, L., Krudewig, A., Sauteur, L., Belting, H.G., and Affolter, M. (2013). In vivo analysis reveals a highly stereotyped morphogenetic pathway of vascular anastomosis. *Dev. Cell.* 25, 492–506.

Lo Cicero, A., Stahl, P.D., and Raposo, G. (2015). Extracellular vesicles shuffling intercellular messages: for good or for bad. *Curr. Opin. Cell Biol.* 35, 69–77.

Logozzi, M., De Milito, A., Lugini, L., Borghi, M., Calabro, L., Spada, M., Perdicchio, M., Marino, M.L., Federici, C., Iessi, E., et al. (2009). High levels of exosomes expressing CD63 and caveolin-1 in plasma of melanoma patients. *PLoS One* 4, e5219.

Lysko, P.G., Weinstock, J., Webb, C.L., Brawner, M.E., and Elshourbagy, N.A. (1999). Identification of a small-molecule, nonpeptide macrophage scavenger receptor antagonist. *J. Pharmacol. Exp. Ther.* 289, 1277–1285.

McGough, I.J., and Vincent, J.P. (2016). Exosomes in developmental signaling. *Development* 143, 2482–2493.

Miyares, R.L., de Rezende, V.B., and Farber, S.A. (2014). Zebrafish yolk lipid processing: a tractable tool for the study of vertebrate lipid transport and metabolism. *Dis. Model. Mech.* 7, 915–927.

Mosimann, C., Kaufman, C.K., Li, P., Pugach, E.K., Tamplin, O.J., and Zon, L.I. (2011). Ubiquitous transgene expression and Cre-based recombination driven by the ubiquitin promoter in zebrafish. *Development* 138, 169–177.

Murayama, E., Kissa, K., Zapata, A., Mordelet, E., Briolat, V., Lin, H.F., Handin, R.I., and Herbomel, P. (2006). Tracing hematopoietic precursor migration to successive hematopoietic organs during zebrafish development. *Immunity* 25, 963–975.

Naegeli, K.M., Hastie, E., Garde, A., Wang, Z., Keeley, D.P., Gordon, K.L., Pani, A.M., Kelley, L.C., Morrissey, M.A., Chi, Q., et al. (2017). Cell invasion in vivo via rapid exocytosis of a transient lysosome-derived membrane domain. *Dev. Cell* 43, 403–417.e10.

van Niel, G., D'Angelo, G., and Raposo, G. (2018). Shedding light on the cell biology of extracellular vesicles. *Nat. Rev. Mol. Cell Biol.* 19, 213–228.

Pastuzyn, E.D., Day, C.E., Kearns, R.B., Kyrke-Smith, M., Taibi, A.V., McCormick, J., Yoder, N., Belnap, D.M., Erlendsson, S., Morado, D.R., et al. (2018). The neuronal gene arc encodes a repurposed retrotransposon gag protein that mediates intercellular RNA transfer. *Cell* 172, 275–288.

Plebanek, M.P., Mutharasan, R.K., Volpert, O., Matov, A., Gatlin, J.C., and Thaxton, C.S. (2015). Nanoparticle targeting and cholesterol flux through scavenger receptor Type B-1 inhibits cellular exosome uptake. *Sci. Rep.* 5, 15724.

Poisson, J., Lemoinne, S., Boulanger, C., Durand, F., Moreau, R., Valla, D., and Rautou, P.E. (2017). Liver sinusoidal endothelial cells: physiology and role in liver diseases. *J. Hepatol.* 66, 212–227.

Poulet, P., Carpentier, S., and Barillot, E. (2007). myProMS, a web server for management and validation of mass spectrometry-based proteomic data. *Proteomics* 7, 2553–2556.

Poynter, S.J., Weleff, J., Soares, A.B., and DeWitte-Orr, S.J. (2015). Class-A scavenger receptor function and expression in the rainbow trout (*Oncorhynchus mykiss*) epithelial cell lines RTgutGC and RTgill-W1. *Fish Shellfish Immunol.* 44, 138–146.

Raiborg, C., Wenzel, E.M., Pedersen, N.M., Olsvik, H., Schink, K.O., Schultz, S.W., Vietri, M., Nisi, V., Bucci, C., Brech, A., et al. (2015). Repeated ER–endosome contacts promote endosome translocation and neurite outgrowth. *Nature* 520, 234–238.

Raposo, G., Tenza, D., Murphy, D.M., Berson, J.F., and Marks, M.S. (2001). Distinct protein sorting and localization to premelanosomes, melanosomes, and lysosomes in pigmented melanocytic cells. *J. Cell Biol.* 152, 809–824.

Seternes, T., Sørensen, K., and Smedsrød, B. (2002). Scavenger endothelial cells of vertebrates: a nonperipheral leukocyte system for high-capacity elimination of waste macromolecules. *Proc. Natl. Acad. Sci. USA* 99, 7594–7597.

Stainier, D.Y.R., Raz, E., Lawson, N.D., Ekker, S.C., Burdine, R.D., Eisen, J.S., Ingham, P.W., Schulte-Merker, S., Yelon, D., Weinstein, B.M., et al. (2017). Guidelines for morpholino use in zebrafish. *PLoS Genet.* 13, e1007000.

Sung, B.H., Ketova, T., Hoshino, D., Zijlstra, A., and Weaver, A.M. (2015). Directional cell movement through tissues is controlled by exosome secretion. *Nat. Commun.* 6, 7164.

Théry, C., Amigorena, S., Raposo, G., and Clayton, A. (2006). Isolation and characterization of exosomes from cell culture supernatants and biological fluids. *Curr. Protoc. Cell Biol.* 3, 22.

Thomou, T., Mori, M.A., Dreyfuss, J.M., Konishi, M., Sakaguchi, M., Wolfrum, C., Rao, T.N., Winnay, J.N., Garcia-Martin, R., Grinspoon, S.K., et al. (2017). Adipose-derived circulating miRNAs regulate gene expression in other tissues. *Nature* 542, 450–455.

Tian, T., Wang, Y., Wang, H., Zhu, Z., and Xiao, Z. (2010). Visualizing of the cellular uptake and intracellular trafficking of exosomes by live-cell microscopy. *J. Cell. Biochem.* 111, 488–496.

Tkach, M., and Théry, C. (2016). Communication by extracellular vesicles: where we are and where we need to go. *Cell* 164, 1226–1232.

Trajkovic, K., Hsu, C., Chiantia, S., Rajendran, L., Wenzel, D., Wieland, F., Schwille, P., Brügger, B., and Simons, M. (2008). Ceramide triggers budding of exosome vesicles into multivesicular endosomes. *Science* 319, 1244–1247.

Valot, B., Langella, O., Nano, E., and Zivy, M. (2011). MassChroQ: a versatile tool for mass spectrometry quantification. *Proteomics* 11, 3572–3577.

Vermot, J., Forouhar, A.S., Liebling, M., Wu, D., Plummer, D., Gharib, M., and Fraser, S.E. (2009). Reversing blood flows act through klf2a to ensure normal valvulogenesis in the developing heart. *PLoS Biol.* 7, e1000246.

Verweij, F.J., Bebelman, M.P., Jimenez, C.R., Garcia-Vallejo, J.J., Janssen, H., Neeffes, J., Knol, J.C., de Goeij-de Haas, R., Piersma, S.R., et al. (2018). Quantifying exosome secretion from single cells reveals a modulatory role for GPCR signaling. *J Cell Biol.* 217, 1129–1142.

Vizcaíno, J.A., Deutsch, E.W., Wang, R., Csordas, A., Reisinger, F., Ríos, D., Dianes, J.A., Sun, Z., Farrah, T., Bandeira, N., et al. (2014). ProteomeXchange provides globally coordinated proteomics data submission and dissemination. *Nat. Biotechnol.* 32, 223–226.

Walzer, C., and Schönenberger, N. (1979). Ultrastructure and cytochemistry of the yolk syncytial layer in the alevin of trout (*Salmo fario trutta* L. and *Salmo* gairdneri R.) after hatching. II. The cytoplasmic zone. *Cell Tissue Res.* 196, 75–93.

Westerfield, M. (2000). *The Zebrafish Book. A Guide for the Laboratory Use of Zebrafish (Danio rerio)* (University of Oregon Press).

White, R.M., Sessa, A., Burke, C., Bowman, T., LeBlanc, J., Ceol, C., Bourque, C., Dovey, M., Goessling, W., Burns, C.E., and Zon, L.I. (2008). Transparent adult zebrafish as a tool for *in vivo* transplantation analysis. *Cell Stem Cell* 2, 183–189.

Wiklander, O.P.B., Nordin, J.Z., O'Loughlin, A., Gustafsson, Y., Corso, G., Mäger, I., Vader, P., Lee, Y., Sork, H., Seow, Y., et al. (2015). Extracellular vesicle *in vivo* biodistribution is determined by cell source, route of administration and targeting. *J. Extracell. Vesicles* 4, 26316.

Yáñez-Mó, M., Siljander, P.R., Andreu, Z., Zavec, A.B., Borràs, F.E., Buzas, E.I., Buzas, K., Casal, E., Cappello, F., Carvalho, J., et al. (2015). Biological properties of extracellular vesicles and their physiological functions. *J. Extracell. Vesicles* 4, 27066.

Yao, Y., Jones, E., and Inoki, K. (2017). Lysosomal regulation of mTORC1 by amino acids in mammalian cells. *Biomolecules* 7, 51.

Yim, N., Ryu, S.W., Choi, K., Lee, K.R., Lee, S., Choi, H., Kim, J., Shaker, M.R., Sun, W., Park, J.H., et al. (2016). Exosome engineering for efficient intracellular delivery of soluble proteins using optically reversible protein–protein interaction module. *Nat. Commun.* 7, 12277.

Yoshimura, A., Kawamata, M., Yoshioka, Y., Katsuda, T., Kikuchi, H., Nagai, Y., Adachi, N., Numakawa, T., Kunugi, H., Ochiya, T., et al. (2016). Generation of a novel transgenic rat model for tracing extracellular vesicles in body fluids. *Sci. Rep.* 6, 31172.

Zomer, A., Maynard, C., Verweij, F.J., Kamermans, A., Schäfer, R., Beerling, E., Schiffelers, R.M., de Wit, E., Berenguer, J., Ellenbroek, S.I.J., et al. (2015). *In vivo* imaging reveals extracellular vesicle-mediated phenocopying of metastatic behavior. *Cell* 161, 1046–1057.

STAR★METHODS

KEY RESOURCES TABLE

REAGENT or RESOURCE	SOURCE	IDENTIFIER
Antibodies		
Rabbit anti-GFP	Molecular Probes	Cat# A-11122; RRID: AB_221569
GFP-trap	ChromoTek	Cat# gtma-20; RRID: AB_2631358
Chemicals, Peptides, and Recombinant Proteins		
Lidocaine	Sigma-Aldrich	L7757
Tricaine	Sigma-Aldrich	MS-222
Bafilomycin-A1	Sigma-Aldrich	SML1661
Dextran Sulfate 500 kDa	Sigma-Aldrich	D8906
BODIPY C12 558/568	Life Technologies SAS	D3835
Collagenase I	ThermoFisher	17018029
25% glutaraldehyde	EMS	16220
Cacodylate 100 g	EMS	12300
Osmium 4%	EMS	19170
PFA	EMS	15710
Phosphate buffer (NaH ₂ PO ₄)	Sigma-Aldrich	S8282
EPON	TAAB	T024
Deposited Data		
Proteomics data	PRIDE Repository	PXD011258
EV related experimental details	EV-track consortium	EV180009
Experimental Models: Organisms/Strains		
Zebrafish: Casper	White et al., 2008	N/A
Zebrafish: <i>kdr1:Hsa.HRAS-mCherry</i> : Tg(<i>kdr1</i> : <i>Hsa.HRAS-mCherry</i>)s916	Stainier lab	ZFIN: ZDB-ALT-090506-2
Zebrafish: <i>mpeg1:mCherryF</i> : Tg(<i>mpeg1</i> : <i>mCherryF</i>)	Ellett et al., 2011	ZFIN: ZDB-ALT-120117-2
Zebrafish: <i>kdr1:EGFP</i> : Tg(<i>kdr1</i> : <i>EGFP</i>)	Stainier lab; Jin et al., 2005	ZFIN: ZDB-ALT-061120-6
Zebrafish: <i>kdr1:nls-mKate2</i> : Tg(<i>kdr1</i> : <i>nls-mKate2</i>)	Lenard et al., 2013	ZFIN: ZDB-FISH-150901-2655
Oligonucleotides		
Primers for cloning CD63-pHluorin into pDONR221	This paper	N/A
For 5'-GGGGACAAGTTGTACAAAAAAGCAGGCTGGatggcggtgaa aggagga-3'		
Rev 5'-GGGGACCACTTGTACAAGAAAGCTGGGTcatacatcaccc gtacccactct-3'		
zSyntenin-A Morpholino (SyntA MO) 5'-TACAACGACATCCTTCT GCTTCA-3'	Lambaerts et al., 2012	N/A
Ctrl Morpholino (Ctrl MO) 5'- CCTCTTACCTCAGTTACAATTATA-3'	Gene Tools	PCO-StandardControl-100
Recombinant DNA		
pCMV-CD63-pHluorin	Verweij et al., 2018	N/A
pDONR221	Invitrogen	N/A (Gateway)
p5E-ubi	Mosimann et al., 2011 Addgene	27320
p3E-polyA 153	Invitrogen	N/A (Gateway)
pCS2-zSyntenin-a wt 83-11	Zimmermann lab/this paper	1561
pDEST R4-R3	Invitrogen	N/A (Gateway)
pUbi-CD63-pHluorin	this paper	N/A
Software and Algorithms		
Fiji / ImageJ	NIH	RRID:SCR_002285
Metamorph	Molecular Devices	N/A
GraphPad PRISM	GraphPad Software	N/A

(Continued on next page)

Continued

REAGENT or RESOURCE	SOURCE	IDENTIFIER
Other		
Polypropylene centrifuge tubes, 11 x 34 mm	Beckman Coulter	347287
Polypropylene centrifuge tubes, 25 x 89 mm	Beckman Coulter	326823

CONTACT FOR REAGENT AND RESOURCE SHARING

Further information and requests for resources and reagents should be directed to and will be fulfilled by the Lead Contact, Guillaume van Niel (guillaume.van-niel@inserm.fr).

EXPERIMENTAL MODEL AND SUBJECT DETAILS**Zebrafish Strains**

Zebrafish were staged and cared for according to standard protocols (Westerfield, 2000). All fish are housed in the fish facility of our laboratory, which was built according to the local animal welfare standards. All animal procedures were performed in accordance with French and European Union animal welfare guidelines. We performed our analyses at 3 dpf. At this developmental stage, sex ratios cannot be determined (gonad differentiation begins around 25 dpf). Adult density was maintained at ~7-8 fish/L, and fish were fed twice daily with artemia and dry food (SDS-400, DIETEX France). Water temperature was maintained at 28°C.

Cell Lines

AB.9 (ATCC CRL-2298) cells are fibroblast obtained from the caudal fin of an adult AB strain zebrafish. AB.9 cultures were grown in Leibovitz-L15 CO₂-independent medium supplemented with 15% heat-inactivated bovine serum at 28°C and passaged when reaching 90% confluence (1-2 times/week).

METHOD DETAILS**Construction of pUbi-CD63-pHluorin**

pUbi-CD63-pHluorin was constructed by first cloning CD63-pHluorin (human CD63; sequence identical to Verweij et al., 2018) using primer pairs 5'-GGGGACAAGTTGTACAAAAAGCAGGCTGGatggcggtggaggaga-3' (fwd) and 5'-GGGGACCACTTTGTACAA GAAAGCTGGGTCCtacatcacccgttagccacttct-3' (rev) into pDONR221 (Gateway, Invitrogen). pDONR221-CD63-pHluorin was subsequently recombined with p5E-ubi (Addgene plasmid # 27320), p3E-polyA 153, and pDEST R4-R3 (Gateway, Invitrogen) to create pUbi-CD63-pHluorin.

Morpholino Injection

The MO against zSyntenin-A, and Standard Control oligo were purchased from GeneTools, used at 1:4 dilution from a 1 mM stock, and injected at 0.5-1.0 nL. The Synt-a MO has been previously validated for its effect on the YSL (Lambaerts et al., 2012). To minimize potential off-targets effects in the current study, the optimal MO concentration for YSL-injection was titrated as the minimal concentration causing the studied phenotype while minimizing mortality or phenotypic abnormalities compared to control.

Plasmid DNA Injections

To induce expression of CD63-pHluorin, embryos were injected at the one-cell stage (for ubiquitous expression) or at 4h in the YSL (for YSL-specific expression). On the next day, injected embryos were inspected under a stereomicroscope. Only embryos that developed normally were assayed.

VLDL Labeling

BODIPY C12 was dissolved in canola oil as lipid (slow release) carrier at 1.5 µg/µl; approximately 5nL was injected in the yolk per embryo.

Decreasing Pace-Maker Activity

Lidocaine was dissolved in ethanol and used at 640µM. After 2h incubation, zebrafish pace-maker activity was assessed by recording the heart-beat for 20 seconds at high speed (30Hz) using a video microscope with stage incubator maintained at 28°C.

Live Fluorescent Imaging

Embryos were anesthetized with tricaine and embedded in 1.5% low melting point agarose. For most experiments, embryos were imaged at 3 dpf. Recordings were performed at 28°C using a Nikon TSi spinning-wide (Yokogawa CSU-W1) microscope, equipped with a 60x CFI Plan Apo IR SR W NA 1.27, a sCMOS 1200x1200 Prime95B from Photometrics (pixel size:11 μ m) and a sCMOS 2048x2048 Orca Flash 4 v2 from Hamamatsu (pixel size:6.5 μ m).

DIC Video-Microscopy/‘Nomarski’

Embryos were examined with a Reichert Polyvar 2 microscope with DIC optics and equipped with a Hitachi HV-C20 tri-CCD camera. All contrast-dampening functions were set off, so that with the $\times 100$ (oil immersion) objective, the final magnification on a 26-cm video screen was $\times 4000$ with excellent contrast, such that mitochondria and intracellular vesicle trafficking could be observed. Video-sequences were recorded from the Y/C output of the camera by a Sony DHR1000 tape recorder in Digital Video (DV) format. Single video images were captured and stored on a PC from the DV videotapes, through the Sony DVK2000 capture board.

Electron Microscopy

For conventional EM, Zebrafish embryos 3 dpf were fixed in 2.5% glutaraldehyde in 0.1 M cacodylate buffer for 24 h, post-fixed with 1% osmium tetroxide, dehydrated in ethanol and embedded in epon as described (Raposo et al., 2001). Epon embedding was performed as described (Hurbain et al., 2008). Ultrathin sections of zebrafish were prepared with a Reichert UltracutS ultramicrotome (Leica Microsystems) and contrasted with uranyl acetate and lead citrate.

For ultrathin cryosectioning and immunogold labeling, zebrafish were fixed in 2% PFA, 0.2% glutaraldehyde in 0.1M phosphate buffer pH 7.4. Zebrafishes were processed for ultracyromicotomy and immunogold labeled using PAG 10 as described (Raposo et al., 2001).

Exosome pellets were deposited on carbonated grids and fixed in 2% PFA in 0.1 M phosphate buffer, pH 7.4. The grids were then processed for single immunogold labeled using PAG10 (Raposo et al., 2001) and embedded in methyl-cellulose Uranyl Acetate 0.4%.

All samples were examined with a FEI Tecnai Spirit electron microscope (FEI Company), and digital acquisitions were made with a numeric camera (Quemesa; Soft Imaging System).

Image Analysis

All imaging data was analyzed using ImageJ. Mander’s overlap coefficient was determined using the JACoP plugin.

Generation of EV-Heatmap in Zebrafish Embryo

The heatmap was generated using Fiji and MATLAB software. After image acquisition, the particles (immobilized EVs at the endothelial walls) were identified after analyses of the z-stacks with Fiji for each fish. The positions of these events were registered on a gray-level support image of a 3 dpf zebrafish plexus by drawing dots at the position of the events. Next, all support images were put together in a z-stack, one layer corresponding to each fish. The next step was to read this support-image z-stack layer by layer with MATLAB, where the dots representing the particles were automatically detected with the function HoughCircles (Yuan-Liang Tang, Department of Information Management, Chaoyang University of Technology, Taichung, Taiwan) using the Circular Hough Transform based algorithm, giving the coordinates of the detected dots as output. Gaussian spots were then created at these coordinates, with an amplitude of each spot equal to 1. A sum projection of the different layers was generated, after which a black and white mask created with the gray level support image was applied to this sum projection. The gaussian spot amplitudes of each layers were summed to produce the heatmap. The areas of the sum projection where the gaussian spot amplitudes are higher corresponds to high density areas of events. To produce the final heatmap, a custom colormap, inspired by the jet colormap, was applied to the sum projection. The colormap goes from black (no event) to red (high density areas).

Exosome Preparation from *In Vitro* Cultured Cells

Exosomes were prepared from the supernatant of 24h cultured AB.9 cells as described before (Théry et al., 2006). Briefly, exosomes were purified from the cultured media with exosome-free serum. Differential centrifugations at 500 x g (2 x 10 min) and 2,000 x g (2 x 15min) were carried out in a standard lab culture centrifuge using 50mL tubes. Subsequent steps were carried out in an ultracentrifuge, using polyallomer tubes listed above. The 10,000 x g (2 x 30min) steps eliminated cellular debris and centrifugation at 100,000 x g (60 min) pelleted exosomes. The exosome pellet was washed once in a PBS, centrifuged at 100,000 x g for 1 h and re-suspended in 50-200 μ L PBS, depending on the starting volume.

Exosome Isolation from Zebrafish Embryos

50 zebrafish embryos 3 dpf were anesthetized and with Collagenase I, used at a concentration 200mg/mL in a total volume of 500 μ L. Sample was incubated at 29°C for 30-45 min under slow agitation on a heating block, while the sample was intermittently triturated with a sterile 200 μ l tip, every 10 minutes until large clumps disappeared. EDTA was added to stop the Collagenase activity. The final volume was adjusted to 1mL, and transferred to 11 x 34 mm centrifuge tubes.

Differential centrifugations at 500 g (2 x 10 min), 2,000 g (2 x 15min), 10,000g (2 x 30min) eliminated cellular debris and centrifugation at 100,000 g (60 min) pelleted exosomes. The exosome pellet was washed once in a PBS, centrifuged at 100,000 g for 1 h and re-suspended in 50-200 μ L PBS, depending on the starting volume.

NTA Measurements

For NTA measurements of EV-size and concentration, concentrated samples were pre-diluted 2000x, and analyzed using a Nano-sight (LM10). Samples were measured at 5 different positions in the chamber for 1 min each, with stage temperature control set at 27°C. The videos were then processed by the Nanosight software (NTA 3.2 Dev Build 3.2.16).

Label-free Mass-Spectrometry

Exosomes were purified by differential ultracentrifugation as described above, and followed (for YSL derived exosomes) by an IP for GFP using GFP-trap magnetic agarose beads (Chromotek). Pull-downs were performed in biological replicates (n = 3) under agitation overnight at 4°C.

To characterize the exosome proteins, we qualitatively and quantitatively analyzed them by Orbitrap Fusion Tribrid mass spectrometry, by using a label free approach. For exosome quantification, SDS/PAGE was used without separation as a clean-up step, and only one gel slice was excised otherwise proteins were separated on SDS/PAGE and four gel slices were excised. Subsequently, gel slices were washed and proteins were reduced with 10 mM DTT before alkylation with 55 mM iodoacetamide. After washing and shrinking the gel pieces with 100% MeCN, we performed in-gel digestion using trypsin/LysC (Promega) overnight in 25 mM NH4HCO3 at 30°C. Peptide were then extracted using 60/35/5 MeCN/H2O/HCOOH and vacuum concentrated to dryness

Samples were chromatographically separated using an RSLCnano system (Ultimate 3000, Thermo Scientific) coupled to an Orbitrap Fusion Tribrid mass spectrometer (Thermo Scientific).

Peptides were loaded onto a C18 column (75-μm inner diameter × 2 cm; nanoViper Acclaim PepMapTM 100 or 300 μm x 5 mm PepMapTM 100, 5 μm, Thermo Scientific), separated and MS data acquired using Xcalibur software. Peptides separation was performed over a linear gradient of 100 min from 5% to 25% or 5% to 35% MeCN (75-μm inner diameter × 50 cm; nanoViper C18, 2 μm or 5 μm, 100Å, Acclaim PepMapTM RSLC, Thermo Scientific). Full-scan MS was acquired in the Orbitrap analyzer with a resolution set to 120,000 and ions from each full scan were HCD fragmented and analyzed in the linear ion trap.

For identification the data were searched against the UniProtKB Zebrafish database using Sequest through proteome discoverer. Enzyme specificity was set to trypsin and a maximum of two missed cleavage site were allowed. Oxidized methionine, N-terminal acetylation, and carbamidomethyl cysteine were set as variable modifications. Maximum allowed mass deviation was set to 10 ppm for monoisotopic precursor ions and 0.6 Da for MS/MS peaks. The resulting files were further processed using myProMS (Poulet et al., 2007). FDR calculation used Percolator and was set to 1%. The label free quantification was performed by peptide Extracted Ion Chromatograms (XICs) computed with MassChroQ version 1.2.1 (Valot et al., 2011). Global MAD normalization was applied on the total signal to correct the XICs for each biological replicate. Protein ratios were computed as the geometrical mean of related peptides. To estimate ratio significance, a two-tailed t test was performed and p values were adjusted with a Benjamini–Hochberg FDR procedure with a control threshold set to 0.05. Fold change-based GO enrichment analysis was performed as in Kowal et al. (Kowal et al., 2016).

Analysis of Growth in the CVP

For height measurements, the longest distance through the z-stack was used, obtained by maximum projection in z and using a fixed point (second ISV from the right). For measurements of the (relative) surface area increase, likewise a maximum projection in z was used and compared over time. To measure proliferation, the number of nuclei were counted at different time points. As a slight mosaicism of the kdrl:nls-mKate2 line could not be fully excluded, we expressed proliferation relative to the control.

QUANTIFICATION AND STATISTICAL ANALYSIS

We performed statistical analysis (Student's two-tailed t test for significance) using GraphPad Prism version 6.0 (GraphPad software). Unpaired analysis was used unless specified otherwise. Data distribution was assumed to be normal but this was not formally tested. Sample sizes, statistical test and P values are indicated in the figures or figure legends.

DATA AND SOFTWARE AVAILABILITY

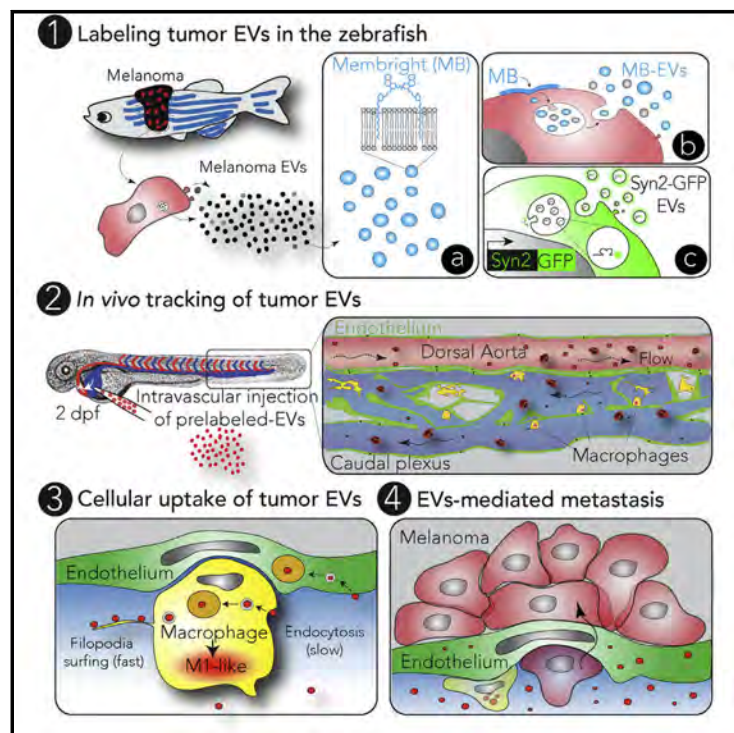
The mass spectrometry proteomics data have been deposited to the ProteomeXchange Consortium (Vizcaíno et al., 2014) via the PRIDE partner repository with the dataset identifier PXD011258. We have submitted all relevant data of our experiments to the EV-TRACK knowledgebase (EV-TRACK ID: EV180009) (Van Deun et al., 2017).

ANNEX 5: STUDY THE FATE OF TUMOR EXTRACELLULAR VESICLES AT HIGH SPATIOTEMPORAL RESOLUTION USING THE ZEBRAFISH EMBRYO

Developmental Cell

Studying the Fate of Tumor Extracellular Vesicles at High Spatiotemporal Resolution Using the Zebrafish Embryo

Graphical Abstract



Authors

Vincent Hyenne, Shima Ghoroghi, Mayeul Collot, ..., Christine Carapito, Andrey S. Klymchenko, Jacky G. Goetz

Correspondence

hyenne@unistra.fr (V.H.), jacky.goetz@inserm.fr (J.G.G.)

In Brief

Tumor extracellular vesicles (EVs) promote tumor progression. However, their behavior in body fluids remains mysterious. Hyenne et al. show that the zebrafish embryo can be used to track and assess the function of circulating tumor EVs *in vivo* and provide a high-resolution description of their dissemination and uptake.

Highlights

- MemBright allows for bright and specific staining of EVs
- The zebrafish embryo allows tracking of tumor EVs at high spatiotemporal resolution
- Circulating tumor EVs are mostly taken up by endothelial cells and patrolling macrophages
- Zebrafish melanoma EVs favor metastatic outgrowth in zebrafish embryos



Studying the Fate of Tumor Extracellular Vesicles at High Spatiotemporal Resolution Using the Zebrafish Embryo

Vincent Hyenne,^{1,2,3,4,12,*} Shima Ghoroghi,^{1,2,3} Mayeul Collot,⁵ Joanna Bons,⁶ Gautier Follain,^{1,2,3} Sébastien Harlepp,^{1,2,3} Benjamin Mary,^{1,2,3} Jack Bauer,^{1,2,3} Luc Mercier,^{1,2,3} Ignacio Busnelli,^{1,2,3} Olivier Lefebvre,^{1,2,3} Nina Fekonja,^{1,2,3} Maria J. Garcia-Leon,^{1,2,3} Pedro Machado,⁷ François Delalande,⁶ Ana Amor López,⁸ Susana Garcia Silva,⁸ Frederik J. Verweij,^{9,10} Guillaume van Niel,^{9,10} Farida Djouad,¹¹ Héctor Peinado,⁸ Christine Carapito,⁶ Andrey S. Klymenko,⁵ and Jacky G. Goetz^{1,2,3,*}

¹INSERM UMR_S1109, Strasbourg 67200, France

²Université de Strasbourg, Strasbourg 67200, France

³Fédération de Médecine Translationnelle de Strasbourg, Strasbourg 67200, France

⁴CNRS SNC5055, Strasbourg 67200, France

⁵Laboratoire de Biophotonique et Pharmacologie, UMR CNRS 7213, Université de Strasbourg, Illkirch 67000, France

⁶CNRS, Laboratoire de Spectrométrie de Masse Bio-Organique (LSMBO), IPHC, UMR 7178, Université de Strasbourg, Strasbourg 67087, France

⁷Electron Microscopy Core Facility, European Molecular Biology Laboratory, Heidelberg 69117, Germany

⁸Microenvironment and metastasis group. Department of Molecular Oncology, Spanish National Cancer Research Center (CNIO), Madrid, Spain

⁹Institut Curie, PSL Research University, CNRS UMR144, Paris 75005, France

¹⁰Center for Psychiatry and Neuroscience, Hôpital Saint-Anne, Université Descartes, INSERM U894, Paris 75014, France

¹¹IRMB, Université de Montpellier, INSERM, Montpellier, France

¹²Lead Contact

*Correspondence: hyenne@unistra.fr (V.H.), jacky.goetz@inserm.fr (J.G.G.)

<https://doi.org/10.1016/j.devcel.2019.01.014>

SUMMARY

Tumor extracellular vesicles (EVs) mediate the communication between tumor and stromal cells mostly to the benefit of tumor progression. Notably, tumor EVs travel in the bloodstream, reach distant organs, and locally modify the microenvironment. However, visualizing these events *in vivo* still faces major hurdles. Here, we describe an approach for tracking circulating tumor EVs in a living organism: we combine chemical and genetically encoded probes with the zebrafish embryo as an animal model. We provide a first description of tumor EVs' hemodynamic behavior and document their intravascular arrest. We show that circulating tumor EVs are rapidly taken up by endothelial cells and blood patrolling macrophages and subsequently stored in degradative compartments. Finally, we demonstrate that tumor EVs activate macrophages and promote metastatic outgrowth. Overall, our study proves the usefulness and prospects of zebrafish embryo to track tumor EVs and dissect their role in metastatic niches formation *in vivo*.

INTRODUCTION

Over the past two decades, extracellular vesicles (EVs) have emerged as novel mediators of cell-cell communication due to

their capacity to carry functional molecules coupled with their ability to travel in biological fluids (Raposo and Stoorvogel, 2013). EVs are heterogeneous in content and origin, as they can either arise from plasma membrane budding (then called microvesicles) or originate from a late endosomal compartment, the multi-vesicular body (MVB) (i.e., exosomes) (van Niel et al., 2018). EVs are known to be important in tumor progression and metastasis, where the complex tumor microenvironment requires a permanent cross-communication between cells (Hyenne et al., 2017). EVs secreted by tumor cells are enriched in pro-tumoral and pro-metastatic factors (proteins, mRNAs, miRNAs, and other non-coding RNAs) and can modify the phenotype of both tumor and stromal cells, mostly to the benefit of tumor growth and metastasis formation (Hyenne et al., 2017). For instance, tumor EVs were shown to transfer oncogenic traits from more aggressive to less aggressive tumor cells (Al-Nedawi et al., 2008). Importantly, tumor EVs can differentiate macrophages or fibroblasts into tumor-associated macrophages or fibroblasts, thereby promoting tumor growth and invasion (Chow et al., 2014; Gu et al., 2012; Paggetti et al., 2015). This pro-metastatic EV-mediated communication can occur within the primary tumor or at distance in physically far-off organs (Peinado et al., 2017). Remarkably, repeated injection of EVs isolated from metastatic cells into the mouse blood circulation induces the formation of a pre-metastatic niche, even in the absence of tumor cells (Costa-Silva et al., 2015; Grange et al., 2011; Hoshino et al., 2015; Liu et al., 2016; Peinado et al., 2012). The ability of circulating tumor EVs to alter the microenvironment of a given organ is particularly relevant with regard to (1) the increased amounts of tumor EVs present in the blood circulation of patients with cancer (Baran et al., 2010; Galindo-Hernandez et al., 2013;



Logozzi et al., 2009), and (2) the fact that elevated levels of EV proteins have been associated with poor prognosis in metastatic melanoma patients (Peinado et al., 2012). Therefore, it is crucial to precisely understand the mechanisms governing tumor EV dispersion and uptake in the blood circulation.

However, local or distant dissemination of tumor EVs has only been sparsely characterized in living organisms (Hoshino et al., 2015; Lai et al., 2015; Pucci et al., 2016). In particular, how EVs circulate in the blood flow and how specifically they are internalized by stromal cells during the priming of pre-metastatic niches remain poorly understood. EVs are nanoscale objects and are thus difficult to track *in vivo*. Moreover, mouse models are not fully suited for real time and *in vivo* EV tracking. In mice, EVs can either be followed after bulk injections (Lai et al., 2014; Takahashi et al., 2013) or with increased resolution through intravital imaging procedures (Lai et al., 2015; Van Der Vos et al., 2016; Zomer et al., 2015). However, such approaches have not yet been able to describe the behavior of tumor EVs in the blood circulation. An ideal animal model suited to accurately dissect the behavior of tumor EVs *in vivo* would allow their tracking in the circulation and their uptake and, at the same time, be amenable for modeling tumor and metastasis progression.

Interestingly, the zebrafish embryo largely complies with all these needs. Indeed, zebrafish has recently emerged as a potent model in cancer biology (White et al., 2013). The molecular pathways driving cancer progression and the anatomo-pathological features of tumorigenesis are essentially conserved between human and fish. In addition, the zebrafish embryo is transparent, possesses a stereotyped vasculature, a maturing immune system and is therefore perfectly suited for intravital imaging with high spatial and temporal resolution. For these reasons, the zebrafish embryo appears as an adequate model to study tumor EVs *in vitro*.

Here, we show that zebrafish melanoma EVs are similar to human melanoma EVs and demonstrate how their fate can be tracked in the zebrafish embryo. For efficient staining of EVs, we used MemBright, a recently developed cyanine-based membrane probe with improved brightness and specificity (Collot et al., 2019). Using this tool, and EVs from genetically engineered cells in parallel, we provide the first description of EVs' dynamics in the blood circulation. We subsequently examined the transit routes and arrest sites of tumor EVs and identified endothelial cells and patrolling macrophages as major EVs-recipient cells. Importantly, these cells have also been identified in a parallel study describing endogenous EVs dispersion in the zebrafish embryo (Verweij et al., 2019). We further show that these cell types have increased uptake efficiency toward tumor EVs, and found that patrolling macrophages internalize tumor EVs through at least two distinct endocytic mechanisms, before storing them in acidic compartments. Using correlated light and electron microscopy (CLEM), we precisely identified the cells uptaking EVs and finely described their morphology as well as the storage or degradative compartments at the electron microscopy level. In addition, we demonstrate that it is possible to track naturally released EVs *in vivo* in the zebrafish embryo using either pre-labeling with MemBright or genetically engineered cells. Finally, we show that melanoma EVs activate macrophages and promote metastatic outgrowth in zebrafish.

RESULTS

Zebrafish Melanoma EVs Are Similar to Human and Mouse Melanoma EVs

To study tumor EVs in zebrafish, we first characterized EVs released by a melanoma cell line (Zmel1) derived from a transgenic *mitfa-BRAF(V600E);p53(−/−)* zebrafish line (Heilmann et al., 2015) (Figure 1A). EVs were isolated from a cell culture supernatant following an established protocol of differential centrifugation (Théry et al., 2006), and EVs present in the 100,000 g pellet were characterized by nanoparticle tracking analysis (NTA) and electron microscopy. We found that Zmel1 EVs have an average diameter of 150 nm in solution and 90 nm after chemical fixation (Figures 1B and 1C). Subsequently, we characterized the protein content of these EVs by mass spectrometry and identified 794 proteins present in Zmel1 EVs (Table S1A). This list includes several proteins typically found in extracellular vesicles, such as ALIX, CD81, Flotillin 1, TSG101, CD9, RalA, Hsc70, HSP90, syntenin 2, integrins α 5 and β 1, and others (of note, CD63 was absent from Zmel1 EVs) (Figure 1D; Table S1A). We then wondered whether the content of zebrafish melanoma EVs was comparable to the ones of human or mouse melanoma EVs. We compared proteins present in Zmel1 EVs with proteins identified in the EVs isolated from six human (451-LU, SK-Mel28, SK-Mel147, SK-Mel103, WM35, and WM164) (Tables S1B–S1G) and three mouse (B16-F0, B16-F1, and B16-F10) (Tables S1H–S1J) melanoma cell lines. Protein content comparison revealed that 65% and 40% of Zmel1 proteins were also identified in human or mouse melanoma EVs, respectively (Figure 1E). Zmel1 EVs are closer to human melanoma EVs than to mouse melanoma EVs. We identified a core list of 82 proteins found in melanoma EVs from either zebrafish, mice, or human (Table S1K). Altogether, these data demonstrate that Zmel1 EVs derived from an established zebrafish melanoma cell line are highly similar to mammalian melanoma EVs and therefore constitute a good model to study human melanoma EVs.

In addition, we compared proteins present in Zmel1 EVs with proteins present in two other types of zebrafish EVs identified in a parallel study (Verweij et al., 2019). First, 17% of Zmel1 EVs proteins are also present in EVs from AB9 fibroblastic cell line (Table S1L). Then, we compared Zmel1 EVs with CD63-positive EVs secreted by a zebrafish embryonic epithelium, the yolk syncytial layer (YSL), and isolated from zebrafish embryos (Verweij et al., 2019). Interestingly, we found a relatively low similarity between these two types of zebrafish EVs (1–2% of Zmel1 EV proteins are present in YSL CD63+EVs; 10% of YSL CD63+EV proteins are present in Zmel1 EVs) (Table S1M). This difference illustrates the cell-type specificity of EV cargo enrichment. However, the mechanism of biogenesis of these two EV types could be partially similar, as 5 of the 12 proteins common to Zmel1 EVs and YSL EVs have been shown to affect, positively or negatively, exosome secretion in mammalian cells: TSG101, ALIX, Syntenin 2, Flotillin 1, and Rab2 (Baietti et al., 2012; Colombo et al., 2013; Okabayashi and Kimura, 2010; Ostrowski et al., 2010).

The MemBright Dye Specifically and Brightly Labels Tumor EVs

In order to fluorescently label Zmel1 EVs and follow them *in vivo*, we used new membrane probes, MemBright (Collot et al., 2019).

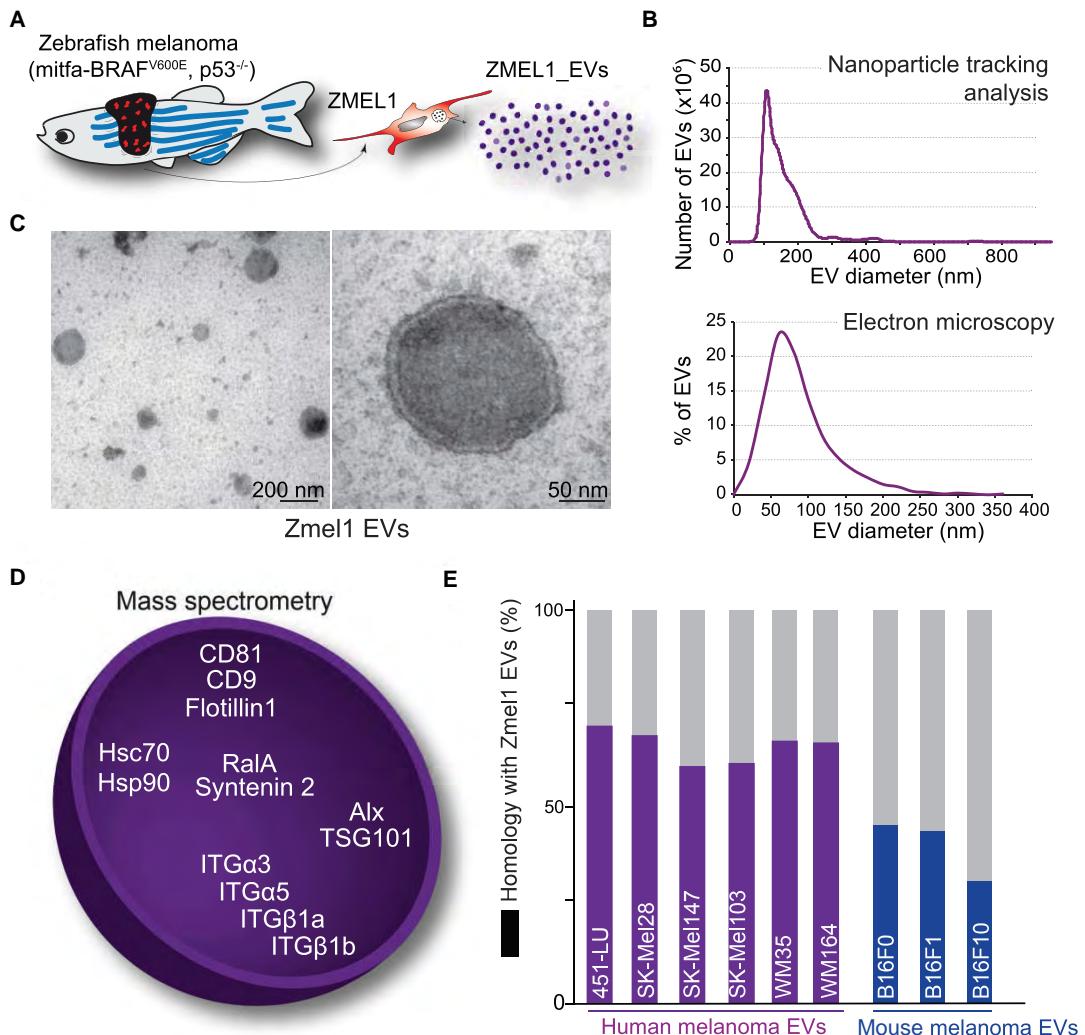


Figure 1. EVs Secreted by Zmel1 Zebrafish Melanoma Cells Are Similar to Mouse and Human Melanoma EVs

(A) Zebrafish melanoma EVs were isolated from Zmel1 cells by differential centrifugation (Heilmann et al., 2015).
 (B) Histogram of a nanoparticle tracking analysis of Zmel1 EVs showing the number of EVs (y axis) versus their diameter (nm, x axis).
 (C) Electron microscopy images of Zmel1 EVs and a histogram showing the percentage of total EVs (y axis) versus their diameter (nm, x axis).
 (D) Illustration of some of the classical EV proteins present among the 794 proteins identified in ZMEL1 EVs by mass spectrometry (see Table S1).
 (E) Histogram showing the percentage of Zmel1 EVs proteins common with EV proteins from various human or mouse cell lines (using human orthologs).

They differ significantly from existing commercial dyes because they bear two amphiphilic groups composed of zwitterions and alkyl chains, which insert the dye into the membrane bilayer (Figure 2A). Moreover, MemBright is available in several colors, which therefore enables multi-color approach in EV imaging (Figures S2G–S2I). To assess the value of MemBright in EV labeling, we first globally compared the MemBright-labeled EVs to identical EVs labeled with PKH-26, a commercially available and widely used dye for EV labeling (Hoshino et al., 2015; Imai et al., 2015). Zmel1 EVs were incubated with MemBright-Cy3 (at 0.2 μ M) or with PKH-26 (at 2 μ M, according to manufacturer's instructions), washed and isolated by ultracentrifugation. Using fluorescence spectroscopy, we observed that PKH-labeled

EVs display a broad absorption spectrum, with a blue shifted peak typically indicating the presence of H-aggregation (Figure 2B) (Würthner et al., 2011). By contrast, MemBright-labeled EVs show an absorption spectrum identical to the solubilized form of the probe (Figures 2B and S1A), revealing that the MemBright is efficiently embedded in EV membranes. MemBright-labeled EVs are as bright as PKH-labeled EVs even though the MemBright was 10-fold less concentrated than PKH (Figures 2B, 2C, and S1D). When both dyes were used at similar dilutions (0.2 μ M), the MemBright labeled EVs were much brighter than the PKH ones (Figure S1E). Indeed, MemBright displays >20-fold higher quantum yield than the PKH: 0.42 versus 0.02 (Table S2). Since MemBright-Cy3 and

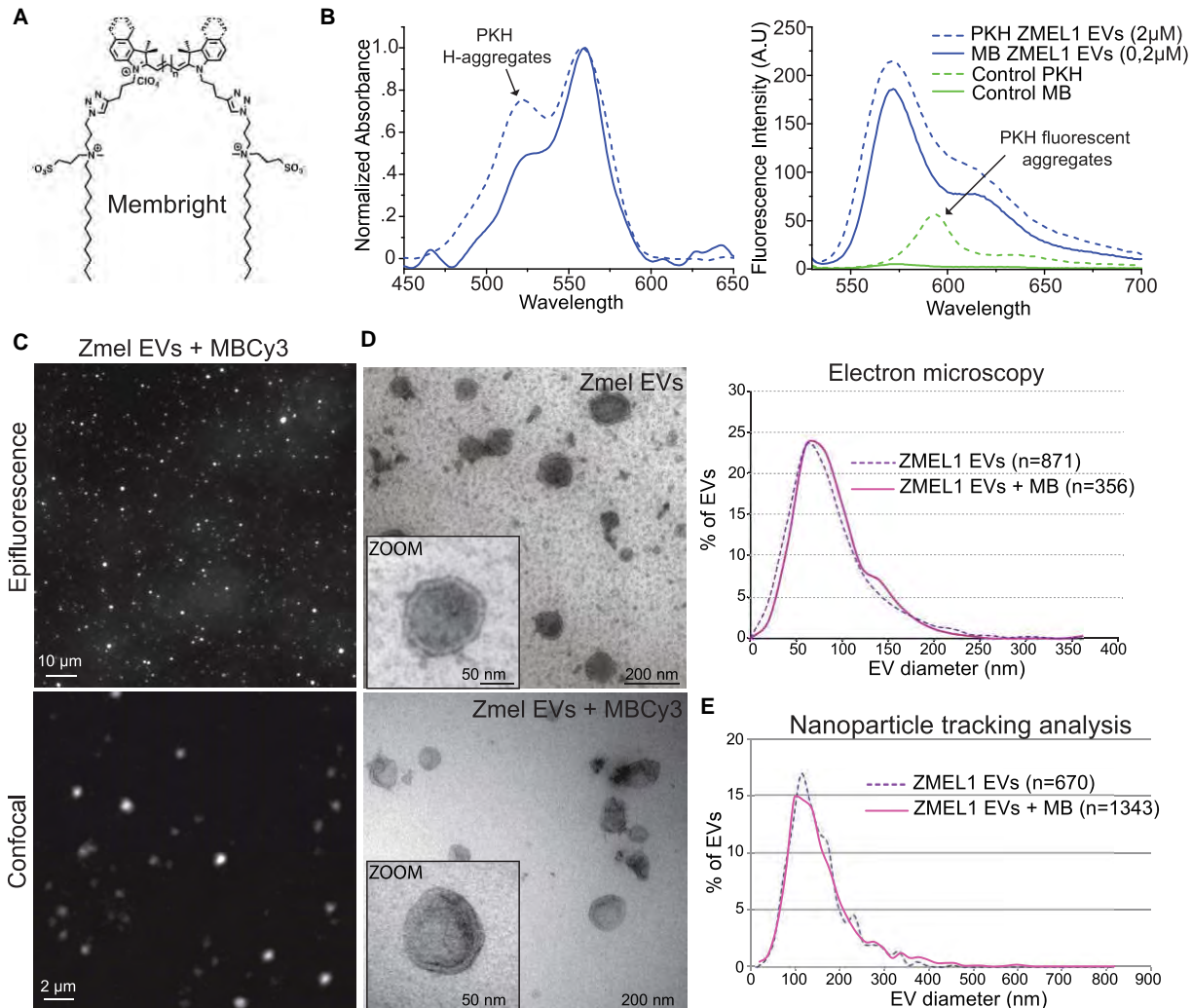


Figure 2. EVs Can Be Brightly and Specifically Labeled with MemBright

(A) Molecular structure of the membrane binding probe MemBright.

(B) Histograms showing a spectroscopy analysis of MemBright (MB) and PKH labeled Zmel1 EVs describing the absorbance (left histogram, y axis) and the fluorescence intensity (right histogram, y axis) versus the wavelength (nm, x axis). Arrows indicate the presence of PKH aggregates in labeled EVs (left) as well as in control PKH alone (right).

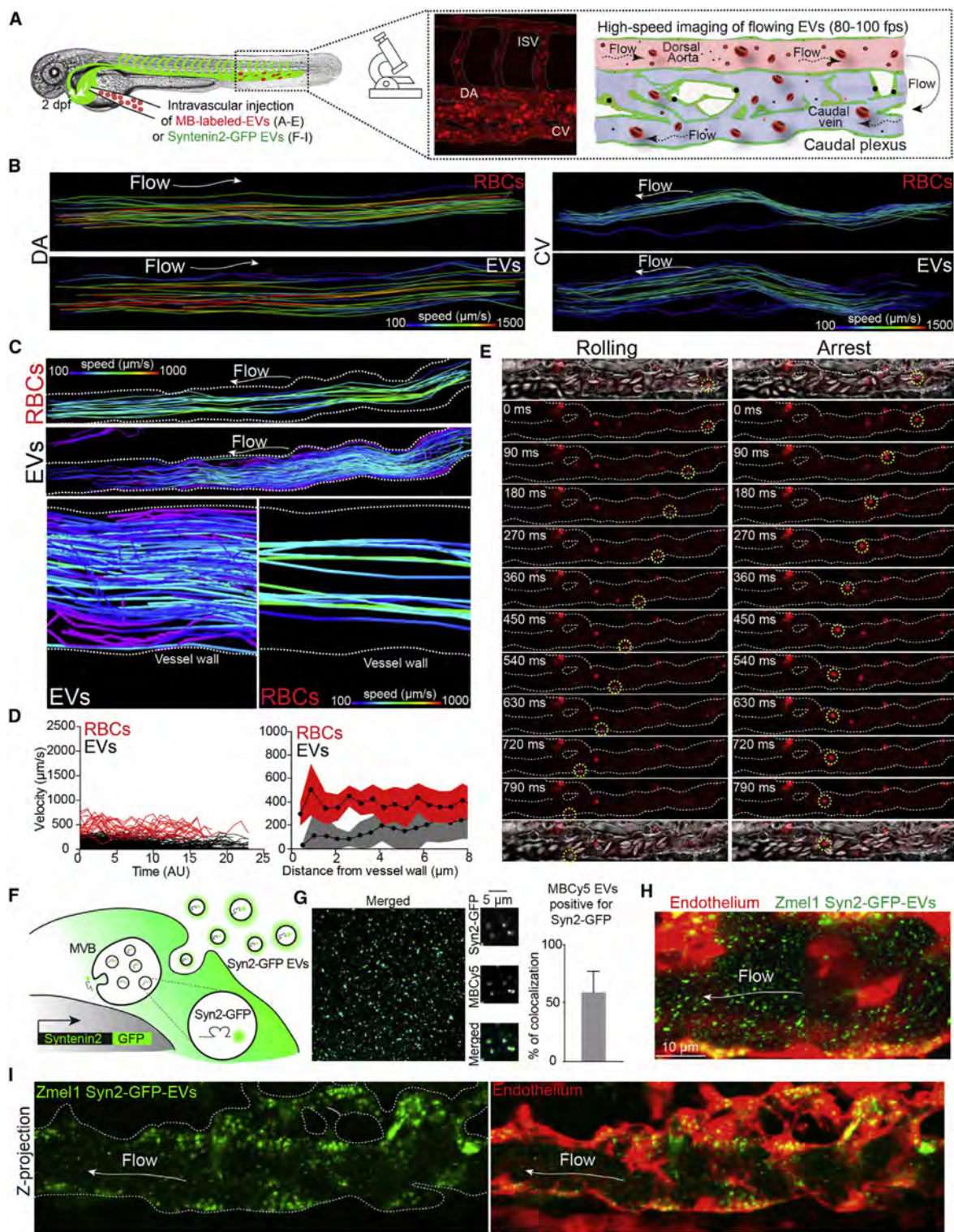
(C) Zmel1 EVs labeled with MemBright Cy3 (MBCy3) observed by Epifluorescence (upper) and confocal (lower).

(D) Electron microscopy of non-labeled (upper) and labeled (lower) Zmel1 EVs and histogram showing the percentage of labeled and non-labeled Zmel1 EVs (y axis) versus their diameter (x axis, nm) by electron microscopy (right graph).

(E) Nanoparticle tracking analysis of MemBright-labeled and non-labeled Zmel1 EVs showing the number of EVs (y axis) versus their diameter (nm, x axis).

PKH26 contain the same Cy3-based fluorophore, such remarkable difference in the quantum yield suggests inefficient partitioning of PKH into EV membranes. This poor partitioning probably arises from the aggregation of PKH in aqueous media, in line with characteristic short-wavelength shoulder in the absorption spectrum in the samples of EVs (Figure S1B). This is not the case for MemBright. Interestingly, a similar spectroscopic experiment conducted without EVs reveals the presence of a red-shifted fluorescence peak with PKH alone but not with MemBright alone (Figure S1C). These fluorescent PKH aggregates have an average diameter of 80 nm (\pm 10 nm), as analyzed

by fluorescence correlation spectroscopy (FCS), which is in the range of EVs and therefore could lead to artifacts. To complement these studies, we analyzed MemBright-labeled EVs by electron microscopy and NTA and found that neither their morphology nor their size was affected, when compared to non-labeled EVs (Figure 2D). Importantly, no larger size aggregates were detected in MemBright-labeled EVs (Figure 2E). Finally, we demonstrated the versatility of MemBright by labeling EVs isolated from 4T1 mouse mammary carcinoma cells. Spectroscopy (Figure S1B; Table S2) and electron microscopy analysis (data not shown) confirmed the advantages of the



(legend on next page)

MemBright probes. Furthermore, separation of MemBright-labeled 4T1 EVs by density gradient revealed that the majority of the fluorescent MemBright is present in the fractions where most EVs are found, as confirmed by the presence of ALIX and TSG101 (Figure S1F). Altogether, these experiments prove that labeling EVs with MemBright does not lead to soluble fluorescent aggregates that can be confounded with labeled EVs. In addition, given its high quantum yield, MemBright can be used at a relatively low concentration to efficiently label isolated EVs.

Tumor EVs Can Be Individually Tracked in the Living Zebrafish Embryo

We next investigated whether MemBright labeling could be used for tracking tumor EVs *in vivo*. We injected zebrafish embryos at 2 days post-fertilization with MemBright-labeled EVs in the blood circulation. Fluorescent EVs were observed essentially in the tail region of the embryo, which is composed of the dorsal aorta and the venous caudal plexus (Figure 3A). Minutes following injection, we observed several fluorescent EVs that were either still flowing or that were already arrested along the endothelium (Figure 3A; Video S1A). We first assessed the apparent size of EVs by comparing them to 100 nm fluorescent polystyrene beads. *In vitro* and upon injection in the circulation of zebrafish embryos, we found that MemBright-labeled EVs and 100 nm fluorescent beads display similar apparent sizes, which correspond to the resolution limits of confocal microscopy (Figures S2A–S2D). Furthermore, MemBright-labeled EVs do not adhere to red blood cells (RBCs), and no leakage of MemBright from EVs to RBCs could be observed *in vitro* or *in vivo* (Figures S2E and S2F). These observations suggest that MemBright in combination with our microscopy set-up allow imaging of fluorescent objects of the size of an individual EV. At this stage, however, we cannot assess whether bigger spots result from bigger EVs or clusters of small EVs. In addition, MemBright can be used to co-inject different types of EVs labeled with different colors (Cy3, Cy5) and specifically track their fate. As a proof of concept, we co-injected Zmel1 tumor EVs (labeled with MemBright-Cy5) with 4T1 mouse tumor EVs (labeled with MemBright-Cy3) in zebrafish embryos and observed both specific localizations for each EVs population as well as a common uptake in isolated cells (Figures S2H and S2I). This suggests that MemBright could be used to follow specific internalization routes of distinct types of EVs that might be on the basis of their function and message delivery.

We then aimed to describe the over-looked behavior of tumor EVs in the blood circulation. To do that, we performed high-speed confocal acquisitions of flowing tumor EVs (and of co-flowing RBCs) in different regions of the vasculature of living zebrafish embryos (Figure 3A; Videos S1B and S1C). When tracking both tumor EVs and RBCs, we first found that EVs have a higher velocity in the aorta than in the caudal veins, in accordance with the hydrodynamic profiles previously described in this region of the zebrafish embryo vasculature (Figure 3B) (Follain et al., 2018a). Second, when analyzing co-motion of tumor EVs and RBCs in a single vessel, we noticed that EVs have a reduced velocity compared to RBCs. These observations are not restricted to Zmel1 EVs since 4T1 EVs display a higher velocity in the dorsal aorta than in the caudal veins but a slower velocity than RBCs (Figures 3C and 3D). Interestingly, we observed that the hemodynamic behavior of tumor EVs differs in regions close to the vessel wall, from which RBCs are mostly excluded. Indeed, when we plotted the velocity of tumor EVs as a function of their position with regards to vessel walls, we observed that tumor EVs explore the vicinity of vessel walls with a reduced velocity (Figures 3C and 3D). Thus, it seems that tumor EVs follow a Poiseuille flow, which predicts that objects displaced by a laminar flow would have a reduced velocity because of frictional forces, along the border of the vessel wall. Such a behavior, in addition to their potential adhesive capacity, could thus favor the arrest of tumor EVs. Indeed, individual inspection of EVs in close proximity to the vessel wall reveals that they are either flowing, rolling on the surface of the endothelium, or arresting (Figure 3E). We observed arrest of EVs following a rolling behavior, suggesting that it could be driven by progressive activation of adhesion molecules, as well as the sharp arrest of flowing EVs, without a rolling phase (Video S2). A very similar behavior was observed for endogenous EVs (Verweij et al., 2019). Altogether, we provide the first accurate description of circulating tumor EVs in the vasculature.

In addition, we used a complementary genetic approach. We expressed Syntenin2 (a major cargo detected in Zmel1 EVs by mass spectrometry, Figure 1D) fused to GFP in Zmel1 cells and showed that these cells secrete GFP-positive EVs (Figures 3F and 3G). Upon intravascular injection in zebrafish embryos, the Syntenin2-GFP EVs can be tracked in the circulation similar to MemBright-labeled EVs (Figures 3H and 3I). Altogether, we document that both genetically and chemically labeled tumor

Figure 3. Hemodynamic Characterization of Individual EVs Tracked in the Circulation of Zebrafish Embryo

(A) Experimental setup used to track circulating EVs: two days post-fertilization zebrafish embryos are injected in the duct of Cuvier with fluorescent EVs (left) and observed in the caudal plexus with high-speed confocal microscopy. Middle: Z projection of MemBright-Cy3 Zmel1 EVs in the caudal plexus right after injection. Right: schematic representation of the caudal plexus showing the direction of the blood flow in the dorsal aorta (pink) and the venous plexus (blue).

(B) Individual tracks of red blood cells (RBC) or Zmel1 EVs in the dorsal aorta (DA, left) and in the caudal vein (CV, right).

(C) Upper: Individual tracks of red blood cells (RBC) or 4T1 EVs in the CV. Lower: Zoom on individual tracks of red blood cells (RBC, right) or 4T1 EVs (left) in the CV in proximity of the vessel wall (white lines). (B) and (C): Color coding represents velocities.

(D) Left: histogram showing the velocity (y axis, $\mu\text{m/s}$) versus the time (x axis, AU) of RBCs (red) and EVs (black) in the CV. Right: histogram showing the velocity (y axis, $\mu\text{m/s}$) versus the distance to the vessel wall (x axis, μm) of RBCs (red) and EVs (gray) in the CV.

(E) Examples of individual EVs rolling (left) or arresting (right) in the circulation of the CV.

(F) Schematic representation of Zmel1 cells expressing Syntenin2-GFP.

(G) EVs isolated from Zmel1 Syntenin2-GFP cells and labeled with MemBright; the diagram indicates the colocalization between GFP and MemBright (mean and standard deviation).

(H) Temporal projection of a time-lapse of *Tg(Fl:Gal4, UAS:RFP)* embryos injected with Zmel1 Syntenin2-GFP EVs imaged immediately after injection.

(I) Z-projection of *Tg(Fl:Gal4, UAS:RFP)* embryos injected with Zmel1 Syntenin2-GFP EVs imaged 1h after injection.

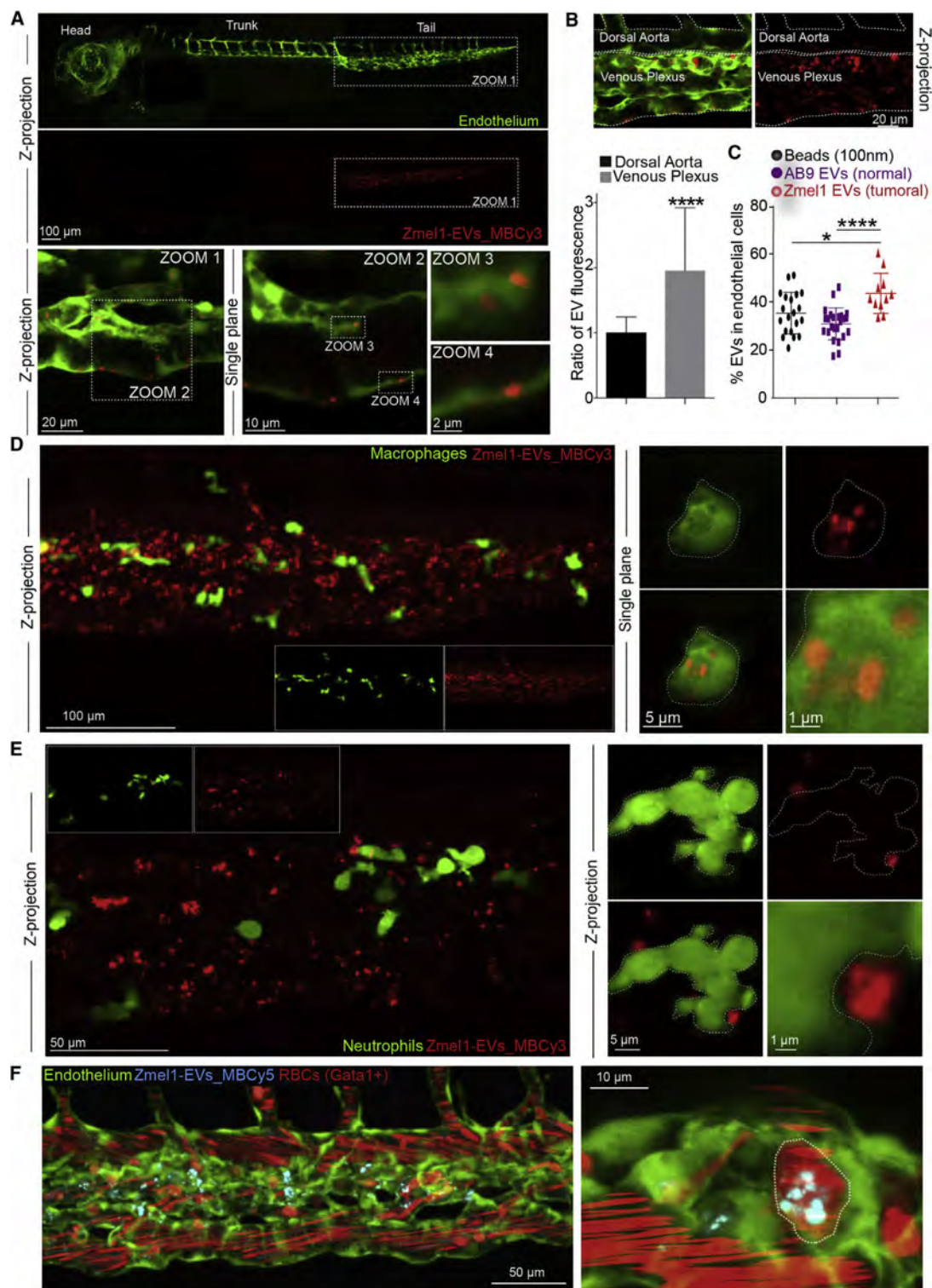


Figure 4. Zmel1 EVs Are Mainly Taken Up by Endothelial Cells, Macrophages, and Hematopoietic Stem Cells but Not by Neutrophils
 (A) Confocal images of MemBright-Cy3 labeled Zmel1 EVs 3 h post-injection (hpi) in *Tg(Flt1:GFP)* embryos (endothelium specific expression). The upper panels were stitched from several individual images to allow a large region to be visualized.

(legend continued on next page)

EVs can be tracked in the bloodstream of zebrafish embryos, allowing the study of their hemodynamic behavior and intravascular arrest.

Circulating Tumor EVs Are Mostly Taken Up by Endothelial Cells and Patrolling Macrophages

How circulating tumor EVs target specific cell types at distance remains a mystery, mostly because this step could not be captured before. Here, most of the tumor EVs are found arrested, exclusively in the tail region of the fish, only 10 to 15 min following injection (Figure 4A). In addition, we found that most of the uptake by endothelial cells occurs in the venous region (Figure 4B), suggesting that the permissive flow profiles of this particular region favor arrest and uptake of tumor EVs, as they do for circulating tumor cells (Follain et al., 2018a). Syntenin2-GFP EVs arrest similarly in *Tg(Fli:Gal4, UAS:RFP)* embryos (Figure 3) and similar observations have been done for endogenous EVs (Verweij et al., 2019). To assess which cell types could uptake tumor EVs, we used four transgenic zebrafish lines with different tissue-specific fluorescent expression *Tg(Fli1:GFP)* for the endothelium (Figure 4A), *Tg(mpeg1:GFP)* for macrophages (Figure 4D), *Tg(mpo:GFP)* for neutrophils (Figure 4E), and *Tg(gata1:dsRed)* for RBCs and putative hematopoietic stem cells (Figure 4F). We found that tumor EVs are rapidly taken up by endothelial cells, macrophages, and immobile Gata1-positive cells (putative hematopoietic stem cells) but not by neutrophils that are known to have a reduced phagocytic activity (Figures 4A, 4D, 4E, and 4F) (Le Guyader et al., 2008). Embryos injected with the MemBright dye alone do not show any signal that could arise from soluble fluorescent aggregates (Figure S3). In addition, endothelial cells and macrophages take up equivalent proportions of Zmel1 EVs, 43% (n = 19 fish) and 38% (n = 11) respectively. Together, this represents the large majority of arrested EVs in the zebrafish embryo at that stage. Importantly, a similar behavior is observed for endogenous CD63-positive EVs (Verweij et al., 2019), suggesting again that circulating EVs of different origins share common mechanisms of arrest *in vivo*. Interestingly, although inert polystyrene beads and non-tumoral EVs (from AB9 zebrafish fibroblasts) can be taken up by macrophages and endothelial cells, they show a reduced accumulation compared to Zmel1 EVs (Figures 4C and 5C). This suggests that both unspecific and specific uptake mechanisms co-exist *in vivo*.

In mice, tumor EVs are internalized by different types of monocytes and macrophages (Whiteside, 2016). In the zebrafish embryo, we noticed that tumor EVs are mostly taken up by small round mpeg1-positive cells (Figures 5A and 5B). In non-injected embryos, these round cells are in direct contact with the blood flow (Figure 5A), which they scan using long protrusions (Figure 5D; Video S3). They also display a reduced velocity (Figure 5E; Video S4). Therefore, the morphology, location, and

dynamics of these cells are reminiscent of patrolling monocytes, which are known to play an important role in tumor progression and metastasis in mice and humans (Auffray et al., 2007; Carlin et al., 2013; Hanna et al., 2015). To confirm this observation and gain insight into the ultrastructure of these cells, we used our established CLEM procedure (Goetz et al., 2014; Karreman et al., 2016b) in *Tg(mpeg1:GFP)* embryos injected with tumor EVs labeled with MemBright-Cy3 (Figure 5F; Video S5). We targeted two typical mpeg1:GFP positive cells that have taken up circulating tumor EVs in the living zebrafish embryo (see STAR Methods; Figures S4A and S4B). Fine segmentation of EM images revealed that macrophages localize in a cavity of the lumen of the vessel, where they form tight contacts with the endothelium and extend wide protrusions in the lumen (Figure 5F; Video S5). Interestingly, the region of the endothelium that contacts the macrophages is enriched of endocytic structures, suggesting active exchange between those two cell types (Figure 5G). The macrophages that have taken up tumor EVs extend long and dynamic protrusions in the lumen of the vessel (Figures 5D and 5H), as shown for patrolling monocytes in mice (Carlin et al., 2013). Surprisingly, analysis of the serial sections reveals that their height can be $>3\text{ }\mu\text{m}$ and that these protrusions are actually forming large flat sheets deployed in the lumen. Altogether, our data show that circulating tumor EVs are rapidly taken up by patrolling macrophages in the zebrafish embryo, which suggests that it can be used to track the mechanisms of delivery of tumor EVs at high spatiotemporal resolution.

Internalized Tumor EVs Are Targeted to Late Endosomal Compartments

To gain further insight into the mechanisms through which patrolling macrophages uptake tumor EVs, we then imaged the dynamics of circulating tumor EVs (Video S6A). On one hand, EVs arrest at the surface of the macrophage and undergo a slow internalization that can be tracked at optimal spatiotemporal resolution (Figures 6A and 6C; Video S6B). The timing of this uptake (~ 30 s) is in the range of classical endocytosis (Figure 6A) (Idrissi and Geli, 2014; Taylor et al., 2011). On the other hand, tumor EVs are first caught by a protrusion extending from the macrophage, and then crawl back toward the cell center before being internalized at the basis of the protrusion (Figures 6B and 6C; Video S6C). This second mechanism of internalization is significantly faster (< 5 s) (Figure 6C).

Next, we wondered which intracellular compartments are targeted by uptaken EVs. For this, we incubated *Tg(mpeg1:GFP)* zebrafish embryos with the Lysotracker to label late endosome-lysosomes (LELs). Rapidly after injection, several Zmel1 EVs already colocalize with Lysotracker, although the majority does not (Figure 6D). This colocalization increases over time and 3 h post-injection (hpi), most EV signal is found in

(B) Z-projections showing the borders of the dorsal aorta (DA) and the venous plexus (VP), and a histogram showing the EV fluorescence per surface in DA and VP (mean and standard deviation; $p < 0.0001$; Mann-Whitney test).

(C) Quantification of the proportion of 100 nm polystyrene beads, fibroblasts AB9 EVs, or Zmel1 melanoma EVs taken up by endothelial cells 3 hpi (Zmel1 EVs Vs beads: $p = 0.015$, unpaired t test; Zmel1 EVs Vs AB9 EVs: $p < 0.0001$, unpaired t test).

(D) Confocal images of MemBright-Cy3 labeled Zmel1 EVs 3 hpi in *Tg(mpeg1:GFP)* (macrophage specific expression).

(E) Confocal images of MemBright-Cy3 labeled Zmel1 EVs 3 hpi in *Tg(mpo:GFP)* (neutrophil-specific expression).

(F) Confocal images of MemBright-Cy5 labeled Zmel1 EVs 3 hpi in *Tg(Fli1:GFP; Gata1:RFP)* (GFP: endothelium; Gata1: red blood cells and hematopoietic stem cells).

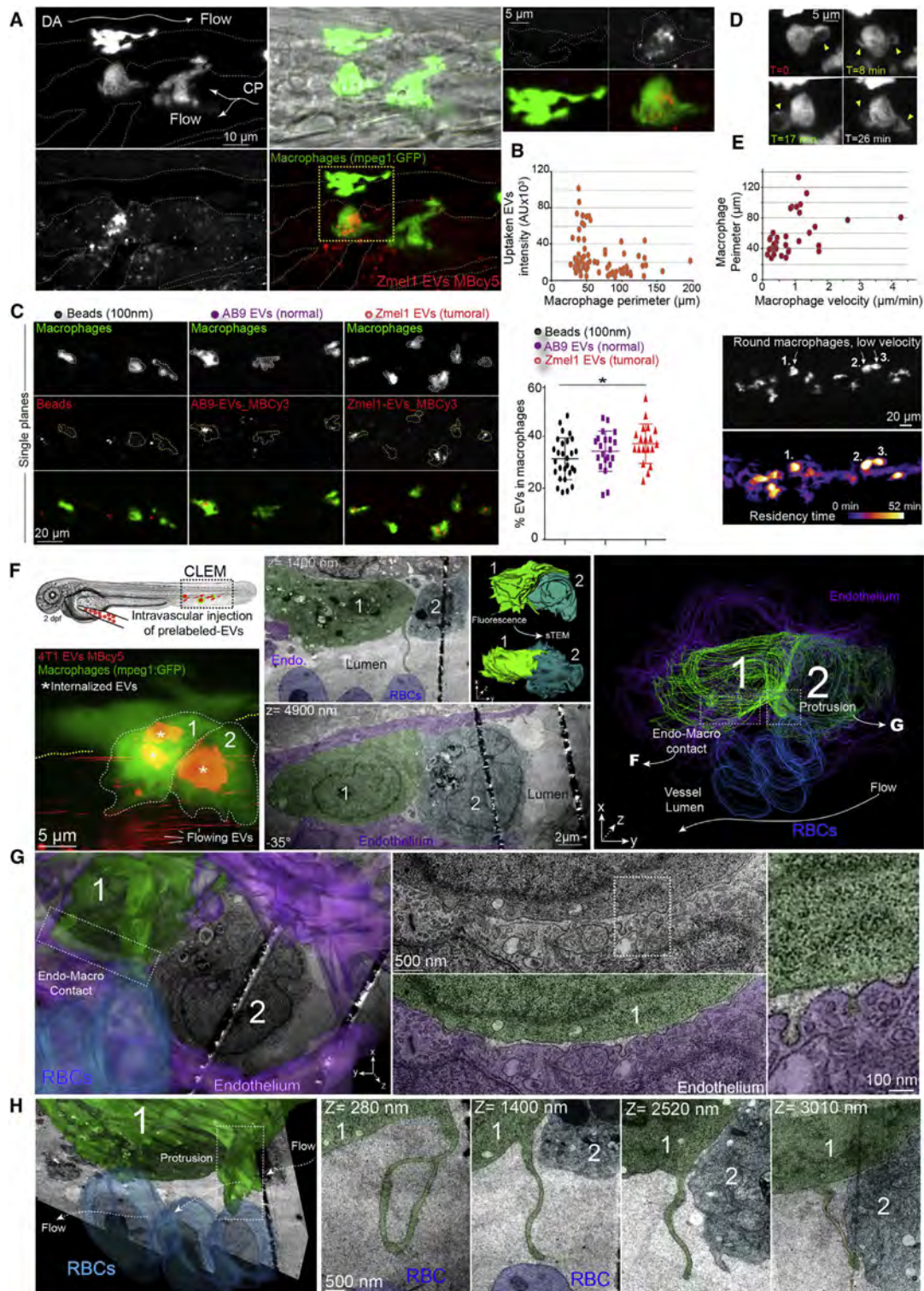


Figure 5. Circulating EVs Are Taken Up by Patrolling Macrophages

(A) Confocal Z projection images of MemBright-Cy3 labeled Zmel1 EVs injected in *Tg(mpeg1:GFP)* (left) with zoom on elongated macrophages devoid of EVs and round macrophages accumulating EVs (right).

(legend continued on next page)

endosome-lysosome compartments (Figure 6D). Of note, 24 hpi, the MemBright signal is still visible and fully colocalizes with Lysotracker (Figure 6D). Although this approach provides a dynamic view of EVs trafficking in zebrafish embryos, Lysotracker labeling does not distinguish between MVBs, late endosomes, and lysosomes. To complement this study, we again exploited our established CLEM procedure on *Tg(mpeg1:GFP)* embryos injected with tumor EVs (Figures 5F–5H and 6E). We generated a 3D model of MemBright-labeled EVs in each macrophage, based on the confocal fluorescent data (called fluorescent 3D model, Figure 6F, upper panel). In parallel, based on TEM serial sections of the same cells, we segmented all the MVBs, late endosomes, and lysosomes that we could locate, and generated a 3D model of these compartments (called TEM 3D model) (Figure 6F, lower panel; Video S5). When comparing the two models, we found that the 3D model created from the fluorescent tumor EVs overlaps with the model from serial TEM sections of LELs (Video S5). This suggests that the internalized tumor EVs are stored within these MVBs, LELs compartments that we imaged at high-resolution (Figure 6E, lower panels). Besides, close examination of the EM stack revealed EVs present in the lumen of the vessel, in close proximity of macrophage protrusions, as well as putative EVs present in endosomes (Figures S4C–S4E). Altogether, this demonstrates the power of the zebrafish embryo to track, at multiple scales, the fate of nanometer-sized objects such as tumor EVs.

Tracking the Release of EVs *In Vivo* Using MB and Genetically Engineered Cells

We focused so far on tumor EVs that were previously isolated and labeled *in vitro* and subsequently tracked *in vivo*. This strategy, however, does not allow tracking of tumor EVs shed from *in-vivo*-grown tumors. Interestingly, we noticed that EVs can be labeled by incubating the secreting cells with the MemBright dye. MemBright quickly and exclusively accumulates in late endosomal compartments of Zmel1 cells in culture (Figure 7A). Upon extensive washing, these cells release fluorescently labeled EVs (Figure 7B) whose morphologies and diameters are similar to EVs from non-labeled cells (Figure 7B). When this approach was used on 4T1 cells expressing CD63-GFP, we could detect EVs positive for both MemBright and CD63, proving that the MemBright can label exosomes (Figure S5). We observed puncta positive for CD63-GFP but not for MemBright and vice-versa. This suggests that the MemBright dye does not label all EVs equally and illustrates the heterogeneity of EVs, which has recently been described (Kowal et al., 2016). Altogether, these experiments suggest that the MemBright is

rapidly endocytosed, targeted to MVBs, and incorporated into the membrane of intra-luminal vesicles before being subsequently released outside of the cells attached to the membrane of exosomes. Such a behavior is extremely useful since it allows labeling and tracking of naturally released EVs by pre-incubating cells with MemBright. To prove this, we co-cultured Zmel1 pre-labeled with MemBright-Cy5 with Zmel1 cells expressing cytoplasmic tdTomato. After a week, we observed several Cy5 fluorescent puncta accumulating in the cytoplasm of Zmel1 tdTomato cells, suggesting that indirectly labeled EVs successfully transferred between neighboring cells (Figure 7B). Such a result opens the door to *in vivo* experiments where pre-labeled tumor cells would be grafted in zebrafish embryos (Figures 7C and 7D). To test local EVs transfer, tdTomato Zmel1 cells were pre-labeled with MemBright-Cy5 and subsequently injected into the circulation of *Tg(mpeg1:GFP)* zebrafish embryos. We observed macrophages crawling around arrested Zmel1 tumor cells, and containing Cy5-positive fluorescent puncta (Figure 7C; Video S7), suggesting local EVs transfer between tumor cells and macrophages. These puncta are negative for tdTomato, revealing a different mechanism than the transfer of cytoplasmic material between melanoma cells and macrophages (Roh-Johnson et al., 2017). In addition, we tested the distant transfer of EVs by injecting tdTomato Zmel1 cells pre-labeled with MemBright-Cy5 in the yolk region and imaging macrophages present in the caudal plexus. Similar to the previous experiment, we detected Cy5 fluorescence in macrophages, suggesting the existence of a distant transfer of EVs that exploits the blood circulation for shedding and targeting at distance (Figure 7D). We further validated the ability to detect secreted EVs *in vivo* by intravascular injection of Syntenin2-GFP expressing Zmel1 cells. Upon injection of these cells in the bloodstream, we followed successful extravasation and metastatic outgrowth overtime, which was accompanied by an increased secretion of tumor EVs. While the release of fluorescent EVs was not observed around recently extravasated cells (4 hpi), growing metastatic foci gradually released increasing amounts of Syn2-GFP EVs, which were either mobile or immobile (Figure 7E). Altogether, these experiments demonstrate that the zebrafish embryo allows tracking of the release and transfer of chemically and genetically labeled EVs from tumor to stromal cells *in vivo*.

Tumor EVs Activate Macrophages and Promote Metastatic Growth in Zebrafish

In contrast to inert objects, tumor EVs are loaded with signaling molecules that are likely to affect the fate or behavior of cells that

(B) EVs are mostly taken up by small macrophages. Histogram showing the intensity of taken up EVs (y axis, arbitrary units) versus the perimeter of the macrophages (x axis, μm). Each dot represents one macrophage.

(C) Macrophages internalize tumor EVs more efficiently than 100 nm polystyrene beads (mean and standard deviation; $p = 0.016$, unpaired t test).

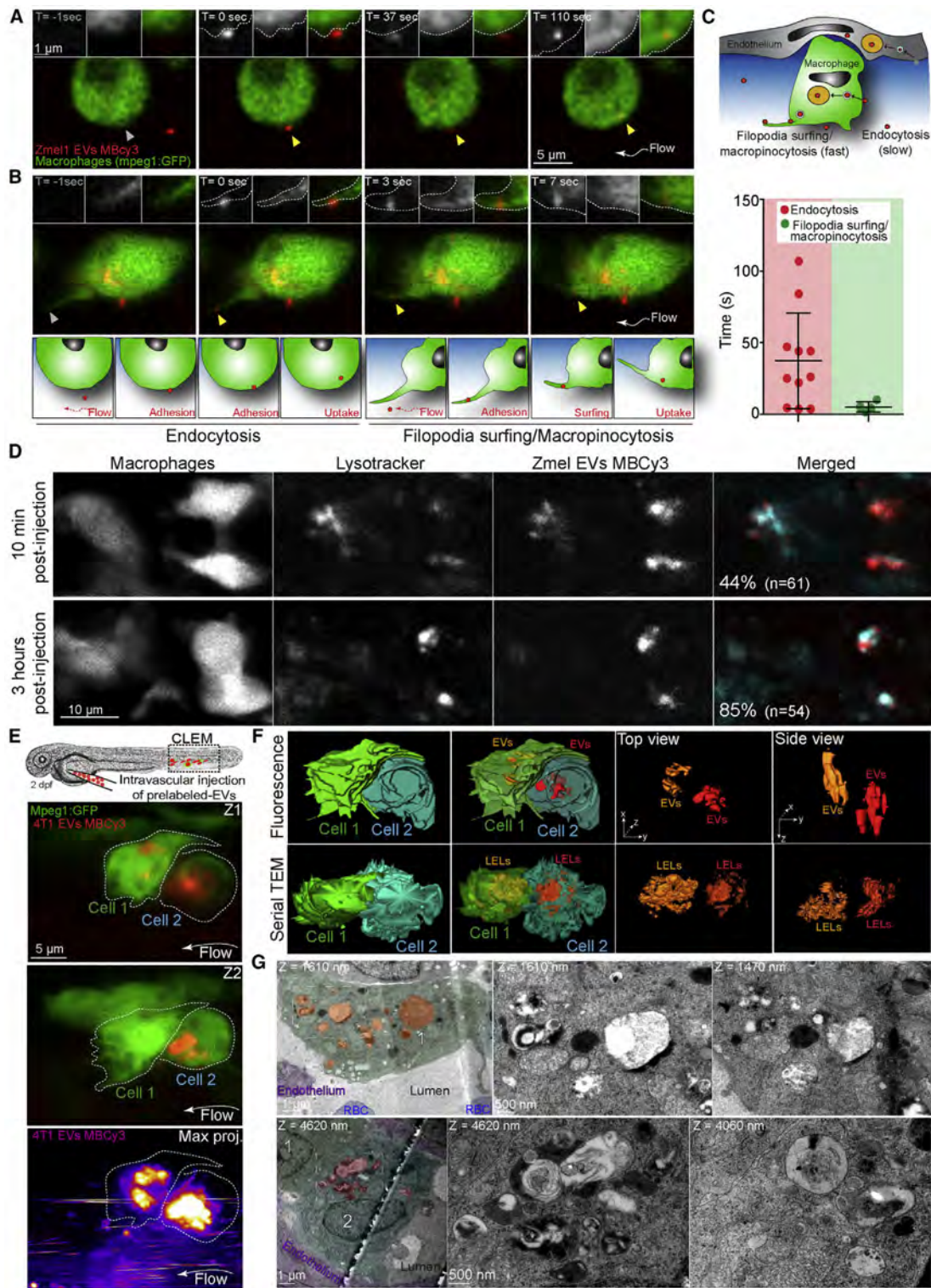
(D) Individual time points of single plane confocal images showing the dynamics of the protrusions in round macrophages.

(E) Histogram showing the perimeter of macrophages (y axis, μm) versus their velocity (x axis, $\mu\text{m/s}$) (left) and images at the beginning ($T = 0$) and the end ($T = 60$ min) of a representative time-lapse. Velocities of migration of *Tg(mpeg1:GFP)*-positive cells are represented with a color code. Three round *Tg(mpeg1:GFP)*-positive cells (1, 2, and 3) show very little displacement during one h.

(F) CLEM experiment on *Tg(mpeg1:GFP)* embryos injected with MemBright-Cy3 4T1 EVs imaged by confocal right after injection (left, Z projection). Middle: electron microscopy images on two different Z planes showing the same cells. Right: 3D model showing the two macrophages (green), the endothelium (purple), and three red blood cells (blue).

(G) Electron microscopy images of the contact between the endothelium and the macrophage, showing the accumulation of endocytic structures on the endothelium side.

(H) 3D model and electron microscopy images of one protrusion sent by the macrophage into the lumen. This protrusion is visible over several microns in Z.



(legend on next page)

internalize them. We thus assessed whether Zmel1 EVs could modify the behavior of receiving cells. We focused on macrophages, which are taking up most of the circulating EVs, and first analyzed their velocities upon uptake. The uptake of tumor EVs by patrolling macrophages significantly reduced their motility when compared to macrophages that had internalized control beads (Figure 8A). Since macrophage velocity has been associated with their activation status *in vitro* (Vogel et al., 2014), we chose to evaluate the impact of Zmel1 EVs on macrophage activation. To do this, we used a recently described transgenic line that relies on the expression of TNF- α to discriminate between pro-inflammatory “M1-like” and “M2-like” polarized macrophages (Nguyen-Chi et al., 2015). Strikingly, most embryos injected with Zmel1 EVs showed M1 activated macrophages 20 hpi (Figures 8B and 8C). Such switches were rarely observed when embryos were injected with 100 nm control polystyrene beads, which clearly demonstrates that circulating Zmel1 EVs can modify the behavior of receiving cells at distance. Tumor EVs can educate receiving cells and confer them pro-metastatic characteristics (Peinado et al., 2017). Inspired by such experiments mostly performed in mice, we next assessed whether circulating tumor EVs could tune metastatic outgrowth. We first “primed” embryos with intravascular injection of either Zmel1 EVs (or 100 nm polystyrene beads). After 12 h, the same embryos were injected with Zmel1 cells in a classical experimental metastasis assay as previously performed (Follain et al., 2018a). Metastatic growth was assessed 7 days later by measuring fluorescence in the caudal plexus. We observed a marked and significant increase in metastatic outgrowth when embryos were primed with Zmel EVs, and not with inert beads (Figure 8D). Furthermore, metastatic foci of embryos primed with tumor Zmel EVs were strikingly more invasive and displayed colonization of the fin parenchyma (Figures 8D and 8E). Altogether, these experiments demonstrate that (1) tumor EVs transform the phenotypes of macrophages and (2) favor metastatic outgrowth and invasiveness by modifying the microenvironment. In addition to demonstrating that labeling EVs with MemBright does not perturb their function, this further validates the use of zebrafish embryos to dissect, with high spatiotemporal resolution, the cascade of events induced by circulating tumor EVs and leading to pre-metastatic niche formation *in vivo*.

DISCUSSION

The work presented here establishes the zebrafish embryo as a new animal model to study tumor EVs *in vivo*. It demonstrates the

proximity of zebrafish melanoma EVs to human melanoma EVs and shows how a new membrane probe, the MemBright, specifically and brightly labels EVs. Using this probe, but also genetically labeled EVs, we were able to precisely track their fate and behavior at high spatiotemporal resolution *in vivo*. This allowed us to provide a description of the behavior of tumor EVs circulating in the blood flow and to track their fate upon arrest. We identify the three main cell types taking up circulating tumor EVs (endothelial cells, patrolling macrophages, and putative hematopoietic stem cells) and unravel their uptake mechanisms. Besides, we describe two complementary methods, a conventional genetic approach and the pre-labeling of secreting cells by MemBright, allowing to track the release and transfer of EVs *in vivo*. Finally, we provide evidence for a functional role of tumor EVs in altering the metastatic microenvironment and promoting metastatic outgrowth in zebrafish embryos.

In a parallel study, Verweij and colleagues examine the fate of CD63 positive EVs secreted by the YSL in zebrafish embryo (Verweij et al., 2019). They track endogenous EVs, genetically labeled and naturally secreted during zebrafish development, while we tracked exogenous MemBright-labeled injected tumor EVs. Yet, both studies reach similar conclusions. They both show that (1) endogenous and tumor EVs mainly arrest in the caudal plexus, in regions of low blood flow, (2) EVs are mostly taken up by endothelial cells and patrolling macrophages, and (3) EVs are stored in acidic compartments. Together, our reports establish the zebrafish embryo (*Danio rerio*) as a new model to study fundamental aspects of EVs biology *in vivo*. It thus represents a precious and complementary tool to invertebrate models *Drosophila* and *C. elegans*, which already contributed to better understand the mechanisms of EV secretion as well as their function (Beer and Wehman, 2017).

In addition, we propose the zebrafish embryo as a new and complementary model to murine and human cell culture systems for studying the fate and the function of tumor EVs during the priming of metastatic niches at distance. Compared to *in vitro* systems, zebrafish embryo offers an invaluable complex microenvironment, where different cell types known to contribute to tumor progression are present and can be tracked using established fluorescent transgenic lines. Its transparency allows visualization of individual tumor EVs dispersion and uptake in living zebrafish with unprecedented spatiotemporal resolution, which represents a major advantage over the mouse, where more complex intravital imaging procedures are required in order to visualize single EVs (Lai et al., 2015; Van Der Vos et al., 2016; Zomer et al., 2015). The zebrafish embryo is also amenable to CLEM,

Figure 6. EVs Are Taken Up through Different Mechanisms and Accumulate in Late Endosomal Compartments

(A and B) Single-plane confocal images of *Tg(mpeg1:GFP)* embryos injected with Zmel1 MemBright-Cy3 (MBCy3) EVs extracted from time-lapses generated immediately after injection and showing: (A) the attachment and uptake of EVs by endocytosis and (B) the sliding of EVs on the macrophage protrusion and its fast internalization.

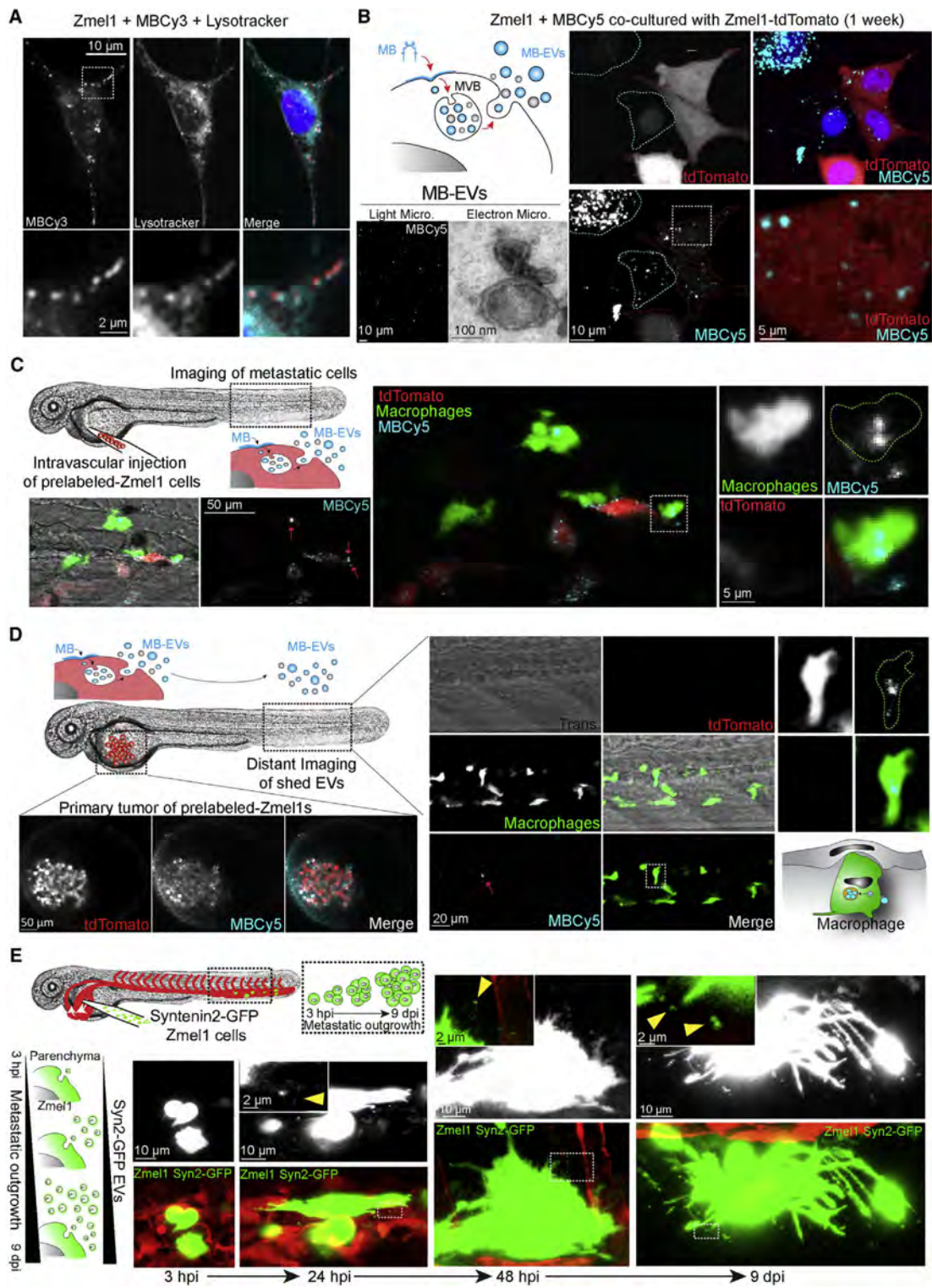
(C) Schematic representation of the modes of uptake by macrophages (upper) and histogram showing the duration (y axis, s) of those two mechanisms (mean and standard deviation).

(D) Single plane confocal images of *Tg(mpeg1:GFP)* embryos injected with Zmel1 MBCy3 EVs and incubated with Lysotracker.

(E) CLEM experiment on *Tg(mpeg1:GFP)* embryos injected with MemBright-Cy3 4T1 EVs imaged by confocal (2 single confocal planes of the GFP and the MBCy3 channels and Z projection of the EV channel (lower)).

(F) 3D model of the two cells and the taken up EVs generated from the confocal data (upper panel, fluorescence), and 3D model of the two cells and the MVBs-late endosomes-lysosomes compartments (LELs) generated from the serial transmission electron microscopy data (lower panel, serial TEM).

(G) Global view of each macrophage highlighting the MVBs-late endosomes-lysosomes compartments (orange and red, left). Zooms of those compartments are shown on the right in two different Z positions of the same region.



(legend on next page)

through procedures which are simplified compared to the mouse (Goetz et al., 2015; Karreman et al., 2016b). In the future, nano-scale imaging should unravel how tumor EVs secreted by a primary tumor reach the blood circulation before crossing the endothelium when reaching a given organ but also to grasp the details of their uptake and trafficking at a subcellular level.

Here, we show that most tumor EVs are internalized by a subset of macrophages. We consider these cells as functionally similar to murine and human patrolling monocytes for the following reasons: (1) they are positive for the mpeg1 promoter, which is expressed both by monocytes and macrophages in human (Spilsbury et al., 1995), (2) they are small, round and have a slow migration velocity when compared to elongated differentiated macrophages, and (3) they are sending highly dynamic protrusions toward the lumen of the vessels and show areas of direct cell-cell contacts with the endothelial wall, as previously shown (Murayama et al., 2006). These last two aspects match the main characteristics of human and mice patrolling monocytes (Auffray et al., 2007; Carlin et al., 2013). Notably, CLEM analysis reveals that the dynamic protrusions observed in live imaging are actually flat sheets of several microns that scan the vessel lumen and could function as butterfly nets to catch tumor EVs deep in the vessel lumen. Such structures are specific to macrophages, allowing them to internalize fluid-borne objects, unlike neutrophils that only phagocytose surface-bound ones (Colucci-Guyon et al., 2011). Once they have contacted the protrusion, the EVs quickly slide toward the cell body through unknown mechanisms, which could be similar to the filopodia surfing recently described (Heusermann et al., 2016). Those protrusions could also participate in macropinocytic uptake of EVs, similar to what has been observed by microglia (Fitzner et al., 2011). EVs are then internalized at the basis of the protrusions, probably in regions of active endocytosis. Interestingly, our EM data revealed several EVs present at the basis of protrusions (see Figure S4C). Alternatively, circulating EVs can directly bind to the macrophage surface before being endocytosed. The capacity of patrolling macrophages to rapidly uptake circulating EVs explains the very short half-life (10–20 min) of circulating EVs after their injection in the blood circulation of either mouse (Morishita et al., 2015; Saunderson et al., 2014; Takahashi et al., 2013) or zebrafish (our work). This is in agreement with the observation that chemical depletion of monocytes and macrophages in mice dramatically increases the stability of circulating EVs (Imai et al., 2015).

Tumor EVs are then rapidly stored in acidic degradative compartments, similar to what has been described for macrophages *in vitro* (Feng et al., 2010). Determining whether and how internal-

ized EVs deliver signaling molecules to the receiving cell, although they are mostly targeted to degradative compartments, is a central question in the EV field. It will be particularly important to address it in the case of tumor EVs taken up by patrolling macrophages. It is interesting to note that uptake mechanisms and compartments are similar between exogenous tumor EVs (this study) and endogenous EVs (Verweij et al., 2019). This suggests that tumor EVs are internalized using universal mechanisms and further demonstrates that the zebrafish embryo is a perfect model for dissecting such behavior.

In addition, the zebrafish embryo allows a direct comparison of EVs with distinct sizes, contents, or origins. This will be essential to better understand the heterogeneity of EVs, as it is now clear that multiple sub-populations (or sizes) of EVs co-exist with different cargo contents and presumably different functions (Kowal et al., 2016). Co-injection of different types of EVs can, for instance, be used to precisely dissect the involvement of one given EV transmembrane or cargo protein, or to compare tumor EVs from patients at different stages of tumor progression. Using multi-color MemBright probes (Cy3, 5, or 7) to label EVs, it is possible to directly compare the behavior of co-injected populations of EVs. Labeling EVs with membrane probes after their isolation is fast and allows obtaining bright fluorescent EVs regardless of their origin. It is particularly relevant for EVs isolated from cell lines reluctant to gene expression manipulation, from animal body fluids, or, importantly, in the case of tumor EVs from samples of cancer patients. However, the use of membrane probes requires the assurance of labeling specificity. This is particularly essential for studies aiming to track EVs dispersion and uptake, as dye aggregates can easily be confounded with EVs, due to their small sizes (Lai et al., 2015; Takov et al., 2017). Here, using spectroscopic and microscopic approaches, we have shown that the MemBright does not form such fluorescent aggregates, in contrast to commonly used PKH. In addition, it is brighter and can therefore be used at reduced concentrations, minimizing again the risk of false-positive results. The key difference of MemBright from PKH is the presence of amphiphilic groups, which favor efficient transfer of the fluorophore from aqueous media to lipid membranes (Collot et al., 2015; Kucherak et al., 2010). Therefore, MemBright can be used to confidently track EV dispersion and uptake.

Finally, our work demonstrates that zebrafish can be used to dissect the causal relationship between circulating tumor EVs uptake and formation of metastatic niches. While most studies performed in mice demonstrate correlations between bulk injection of EVs and emergence of a pre-metastatic niche, the zebrafish embryo, by allowing continuous imaging, allows direct

Figure 7. Tracking EVs Released by Zebrafish Melanoma Cells

- (A) Confocal images of Zmel1 cells incubated with MemBright-Cy3 and stained with Lysotracker.
- (B) Schematic representation of the experimental procedure: MemBright added to cells in culture accumulates in MVBs and is subsequently released in exosomes. Such EVs can be observed by electron microscopy. Confocal images of Zmel1 cells pre-labeled with MemBright-Cy5 and co-cultured with Zmel1 tdTomato cells, showing the transfer of MemBright in Z projections (left) and single planes (right).
- (C) Confocal images of tdTomato Zmel1 cells pre-labeled with MemBright-Cy5 injected in the circulation of *Tg(mpeg1:GFP)* embryos and imaged in the caudal plexus two days post-injection, showing the local transfer of MemBright-Cy5 to macrophages.
- (D) Confocal images of tdTomato Zmel1 cells pre-labeled with MemBright Cy5 injected above the yolk of *Tg(mpeg1:GFP)* embryos and imaged in the yolk region (primary tumor, left) and in the caudal plexus (distant imaging of shed EVs, right) two days post-injection, showing the long distance transfer of MemBright-Cy5 to macrophages.
- (E) *In vivo* release of Syntenin2-GFP EVs. Zmel1 Syntenin2-GFP cells injected in the circulation of *Tg(Fl:Gal4, UAS:RFP)* embryos and imaged by confocal in the following days.

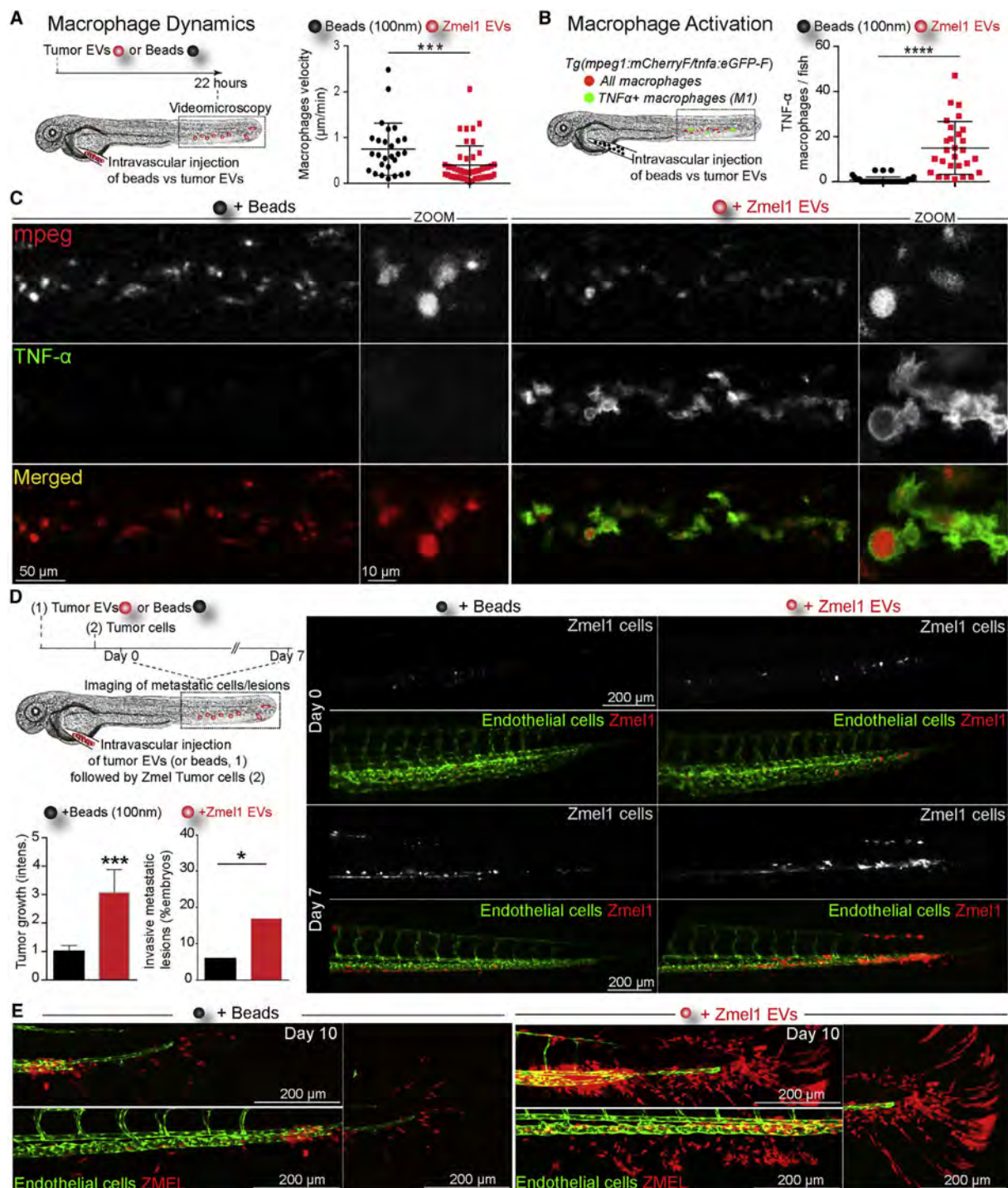


Figure 8. Melanoma EVs Activate Macrophages and Promote Tumor Growth in Zebrafish

(A) 22 h following injection of Zmel1 EVs or 100 nm beads, the dynamics of *mpeg1*:GFP macrophages was measured by time-lapse. Histogram showing that the velocity of macrophages 22 h after injection (one dot represents one macrophage; mean and standard deviation; $p = 0.0009$, Mann-Whitney test).

(B) *Tg(mpeg1:mCherry/TNF α :eGFP-F)* injected with Zmel1 EVs or 100 nm beads and imaged 20 h post-injection. Histogram showing the number of TNF α :GFP positive cells per fish caudal plexus (one dot represents one embryo; mean and standard deviation; $p < 0.0001$, Mann-Whitney test).

(C) Confocal images of *Tg(mpeg1:mCherry/TNF α :eGFP-F)* injected with Zmel1 EVs or 100 nm beads and imaged 20 h post-injection.

(legend continued on next page)

quantitative assessment of how metastatic niches are formed and how they can contribute to metastatic outgrowth. In this work, we show that injection of tumor EVs in the circulation is rapidly followed by expression of TNF α , reminiscent of their activation into a pro-inflammatory “M1-like” phenotype. These results are consistent with *in vitro* studies showing that EVs from breast cancer cells or oral squamous carcinoma cells stimulate an M1 macrophage inflammatory response (including TNF induction) (Xiao et al., 2018; Chow et al., 2014). Other studies, however, show that tumor EVs, for instance from prostate tumors, induce an M2 activation (Halin Bergström et al., 2016). Although the M1/M2 binary polarization model of macrophages has been challenged (Aras and Zaidi, 2017), pro-inflammatory macrophages have been reported to exert pro- or anti-tumoral effects depending on the context (Engblom et al., 2016). Further work is thus needed to better understand how tumor EVs tune macrophages’ fate during metastatic progression. Here, the zebrafish model offers the opportunity to revisit the interactions between tumor EVs, macrophages and other immune cells (and their activation status), and tumor cells during extravasation and metastatic outgrowth. Recent work performed in mice, which exploited intravital imaging, revealed close interactions between tumor cells arrested in the circulation and myeloid cells and the exchange of microvesicles promoting extravasation (Headley et al., 2016). Complementary usage of these two models, based on intravital imaging, is thus likely to bring important insights into how tumor EVs can tune metastatic outgrowth.

Importantly, we show that pre-treatment of zebrafish with Zmel1 tumor EVs enhances metastatic outgrowth, leading to a more invasive phenotype. This phenotype is reminiscent of several mice studies showing that pre-injection of EVs from either melanoma, pancreatic ductal adenocarcinoma, or breast tumors promotes metastasis of their respective tumors cells injected in the circulation (Costa-Silva et al., 2015; Hoshino et al., 2015; Plebanek et al., 2017). In Zmel1 EVs pre-treated fish, we also observed that tumor cells were more efficient at actively invading the caudal fin. Such a phenotype could result from increased extravasation efficiency or from EV-mediated increased proliferation. Alternatively, it could arise from tumor EVs that can directly alter the extracellular matrix in pre-metastatic niches (Costa-Silva et al., 2015), or induce the secretion of pro-migratory factors by activated pro-inflammatory macrophages (Xiao et al., 2018).

Altogether, our work on the tracking of exogenous tumor EVs (this study) and of endogenous EVs (Verweij et al., 2019) set the zebrafish embryo as a new and highly attractive *in vivo* model to track EVs at the single EV scale. Interestingly, both studies identified similar mechanisms of transit and uptake for physiological and pathological extracellular vesicles, which further validate the zebrafish embryo as a reliable animal model for studying the biology of EVs. Finally, we believe that the zebrafish embryo will open new avenues for EV biology, as it offers adapted time and space scales to the study of small organelles *in vivo*.

(D) Zmel1-tdTomato tumor growth is enhanced in *Tg(Fli1:GFP)* embryos that were pre-injected with Zmel1 EVs. Histograms showing tumor growth at 7 days (left; $p = 0.0004$, Mann-Whitney test) and invasive lesions at 10 days (right; $p < 0.05$; chi-squared test). Epifluorescent images of tumor growth in the caudal plexus, right panels.

(E) Confocal images of tumor cell invasion in embryos.

STAR★METHODS

Detailed methods are provided in the online version of this paper and include the following:

- **KEY RESOURCES TABLE**
- **CONTACT FOR REAGENT AND RESOURCE SHARING**
- **EXPERIMENTAL MODEL AND SUBJECT DETAILS**
 - Zmel1, Zmel1 tdTomato and Zmel1 Syntenin2-GFP
 - AB9 Cells
 - 4T1 Cells and 4T1 CD63-GFP
 - B16-F0, F1 and F10
 - 451-LU, SK-Mel28, SK-Mel147, SK-Mel103, WM35 and WM164
 - Zebrafish
- **METHOD DETAILS**
 - Cell Line Generation
 - EV Isolation and Analysis
 - Shotgun Proteomics
 - Protein Comparisons
 - MemBright and PKH Labeling of EVs
 - Spectroscopy
 - Fluorescence Correlation Spectroscopy (FCS)
 - MemBright Labeling of Cells
 - Intravascular Injection of Zebrafish Embryo
 - Confocal Imaging and Analysis
 - Semi-automated Method to Determine the Proportion of Internalized EVs
 - Quantification of EVs in Aorta vs Vein Regions
 - Flow Analysis for Red Blood Cells
 - Flow Analysis of EVs
 - EVs and RBCs Distance and Velocity from the Endothelial Barrier
 - Sample Preparation for Correlative Light and Electronic Microscopy of ZF Embryos
- **QUANTIFICATION AND STATISTICAL ANALYSIS**
 - Statistical Tests
 - Zebrafish Experiments
 - EVs Experiments
- **DATA AND SOFTWARE AVAILABILITY**

SUPPLEMENTAL INFORMATION

Supplemental Information includes five figures, two tables, and seven videos and can be found with this article online at <https://doi.org/10.1016/j.devcel.2019.01.014>.

ACKNOWLEDGMENTS

We thank all members of the Goetz Lab for helpful discussions. We are indebted to K. Richter and F. Peri (EMBL, Heidelberg, Germany) as well as to P. Hanns and C. Lengerke (University Hospital Basel, Switzerland) for supplying zebrafish embryos. We are grateful to R. White (MSKCC, New York, USA) for the Zmel1 (native and tdTomato) cells, to Dr. D.C. Bennett (St. George’s University of London, U.K.) and Dr. M. Soengas (CNIO, Madrid, Spain) for mammalian melanoma cells, and to P. Zimmerman (CRCM,

Marseille, France) for the Syntenin-2 construct. We thank A. Michel (EFS, Strasbourg, France) and C. Spiegelhalter (IGBMC, Illkirch, France) for EM assistance, Y. Schwab for advice during CLEM analysis (EMBL, Heidelberg), E. Guiot and Y. Lutz (IGBMC, Illkirch, France) for advice on confocal imaging, and A. Audfray (Malvern Instruments) for NTA. We thank the CNIO proteomics core for performing the mass spectrometry on mouse and human melanoma EVs. We thank P. Herbomel for critical reading of the manuscript. This work was supported by a fellowship from IDEX (University of Strasbourg) to S.G.; by grants from La Ligue contre le Cancer, Canceropole Grand-Est, INCa (MetaCLEM) and Roche to J.G.G.; and by institutional funds from University of Strasbourg, INSERM, and ANR (to CC, French Proteomics Infrastructure ProFI; ANR-10-INBS-08-03).

AUTHOR CONTRIBUTIONS

V.H. and J.G.G. planned the project. V.H. designed and conducted most of the experiments with contributions from S.G., B.M., G.F., M.J.G-L., and J.B. M.C. synthesized the MemBright and led the spectroscopy experiments, with A.S.K. S.H. designed the automated EV tracking and the EV colocalization analysis. O.L. engineered the fluorescent cell lines. F.De., J.B., and C.C. conducted the mass spectrometry on Zmel1 EVs. A.I.A., S.G.S., and H.P. lead the mass spectrometry analysis on human and mice melanoma EVs. F.V. and G.v.N. generated the mass spectrometry data on AB9 and endogenous zebrafish EVs. N.F. prepared the samples for CLEM and P.M. did the serial sectioning and the microCT. F.Dj. provided the *Tg(mpeg:mCherry,tnf:GFP)* zebrafish line and advised its use. L.M. and I.B. performed image analysis. V.H. and J.G.G. wrote the manuscript with insights from all authors.

DECLARATION OF INTERESTS

The authors declare no competing interests.

Received: March 15, 2018

Revised: October 19, 2018

Accepted: January 10, 2019

Published: February 7, 2019

REFERENCES

Al-Nedawi, K., Meehan, B., Micallef, J., Lhotak, V., May, L., Guha, A., and Rak, J. (2008). Intercellular transfer of the oncogenic receptor EGFRvIII by microvesicles derived from tumour cells. *Nat. Cell Biol.* 10, 619–624.

Aras, S., and Zaidi, M.R. (2017). TAMEless traitors: macrophages in cancer progression and metastasis. *Br. J. Cancer* 117, 1583–1591.

Auffray, C., Fogg, D., Garfa, M., Elain, G., Join-Lambert, O., Kayal, S., Sarnacki, S., Cumano, A., Lauvau, G., and Geissmann, F. (2007). Monitoring of blood vessels and tissues by a population of monocytes with patrolling behavior. *Science* 317, 666–670.

Baietti, M.F., Zhang, Z., Mortier, E., Melchior, A., Degeest, G., Geeraerts, A., Ivarsson, Y., Depoortere, F., Coomans, C., Vermeiren, E., et al. (2012). Syndecan-syntenin-ALIX regulates the biogenesis of exosomes. *Nat. Cell Biol.* 14, 677–685.

Baran, J., Baj-Krzyworzeka, M., Weglarczyk, K., Szatanek, R., Zembala, M., Barbasz, J., Czupryna, A., Szczepanik, A., and Zembala, M. (2010). Circulating tumour-derived microvesicles in plasma of gastric cancer patients. *Cancer Immunol. Immunother.* 59, 841–850.

Beer, K.B., and Wehman, A.M. (2017). Mechanisms and functions of extracellular vesicle release in vivo—what we can learn from flies and worms. *Cell Adh. Migr.* 11, 135–150.

Carapito, C., Burel, A., Guterl, P., Walter, A., Varrier, F., Bertile, F., and Van Dorselaer, A. (2014). MSDA, a proteomics software suite for in-depth mass spectrometry Data Analysis using grid computing. *Proteomics* 14, 1014–1019.

Cardona, A., Saalfeld, S., Schindelin, J., Arganda-Carreras, I., Preibisch, S., Longair, M., Tomancak, P., Hartenstein, V., and Douglas, R.J. (2012). TrakEM2 software for neural circuit reconstruction. *PLoS One* 7, e38011.

Carlin, L.M., Stamatides, E.G., Auffray, C., Hanna, R.N., Glover, L., Vizcay-Barrena, G., Hedrick, C.C., Cook, H.T., Diebold, S., and Geissmann, F. (2013). Nr4a1-dependent Ly6C(low) monocytes monitor endothelial cells and orchestrate their disposal. *Cell* 153, 362–375.

Chow, A., Zhou, W., Liu, L., Fong, M.Y., Champer, J., Van Haute, D., Chin, A.R., Ren, X., Gugiu, B.G., Meng, Z., et al. (2014). Macrophage immunomodulation by breast cancer-derived exosomes requires Toll-like receptor 2-mediated activation of NF- κ B. *Sci. Rep.* 4, 5750.

Collot, M., Kreder, R., Tatarenko, A.L., Patsenker, L.D., Mely, Y., and Klymchenko, A.S. (2015). Bright fluorogenic squaraines with tuned cell entry for selective imaging of plasma membrane vs. endoplasmic reticulum. *Chem. Commun.* 51, 17136–17139.

Collot, M., Ashokkumar, P., Anton, H., Boutant, E., Faklaris, O., Galli, T., Mely, Y., Danglot, L., and Klymchenko, A.S. (2019). MemBright: a family of red to near-infrared fluorescent membrane probes for advanced cellular imaging and neuroscience. *Cell Chem. Biol.* 26, <https://doi.org/10.1016/j.chembiol.2019.01.009>.

Colombo, M., Moita, C., van Niel, G., Kowal, J., Vigneron, J., Benaroch, P., Manel, N., Moita, L.F., Théry, C., and Raposo, G. (2013). Analysis of ESCRT functions in exosome biogenesis, composition and secretion highlights the heterogeneity of extracellular vesicles. *J. Cell Sci.* 126, 5553–5565.

Colucci-Guyon, E., Tinevez, J.Y., Renshaw, S.A., and Herbomel, P. (2011). Strategies of professional phagocytes in vivo: unlike macrophages, neutrophils engulf only surface-associated microbes. *J. Cell Sci.* 124, 3053–3059.

Costa-Silva, B., Aiello, N.M., Ocean, A.J., Singh, S., Zhang, H., Thakur, B.K., Becker, A., Hoshino, A., Mark, M.T., Molina, H., et al. (2015). Pancreatic cancer exosomes initiate pre-metastatic niche formation in the liver. *Nat. Cell Biol.* 17, 816–826.

Cox, J., Hein, M.Y., Luber, C.A., Paron, I., Nagaraj, N., and Mann, M. (2014). Accurate Proteome-wide label-free quantification by delayed normalization and maximal peptide ratio extraction, termed MaxLFQ. *Mol. Cell Proteomics* 13, 2513–2526.

Van Deun, J., Mestdagh, P., Sormunen, R., Cocquyt, V., Vermaelen, K., Vandesompele, J., Bracke, M., De Wever, O., and Hendrix, A. (2014). The impact of disparate isolation methods for extracellular vesicles on downstream RNA profiling. *J. Extracell. Vesicles* 3, 1–14.

EV-TRACK Consortium, Van Deun, J., Mestdagh, P., Agostinis, P., Akay, Ö., Anand, S., Anckaert, J., Martinez, Z.A., Baetens, T., Beghein, E., et al. (2017). EV-TRACK: transparent reporting and centralizing knowledge in extracellular vesicle research. *Nat. Methods* 14, 228–232.

Engblom, C., Pfirschke, C., and Pittet, M.J. (2016). The role of myeloid cells in cancer therapies. *Nat. Rev. Cancer* 16, 447–462.

Feng, D., Zhao, W.L., Ye, Y.Y., Bai, X.C., Liu, R.Q., Chang, L.F., Zhou, Q., and Sui, S.F. (2010). Cellular internalization of exosomes occurs through phagocytosis. *Traffic* 11, 675–687.

Fitzner, D., Schnaars, M., van Rossum, D., Krishnamoorthy, G., Dibaj, P., Bakhti, M., Regen, T., Hanisch, U.K., and Simons, M. (2011). Selective transfer of exosomes from oligodendrocytes to microglia by macropinocytosis. *J. Cell Sci.* 124, 447–458.

Follain, G., Osmani, N., Azevedo, A.S., Allio, G., Mercier, L., Karreman, M.A., Solecki, G., Garcia León, M.J., Lefebvre, O., Fekonja, N., et al. (2018a). Hemodynamic forces tune the arrest, adhesion, and extravasation of circulating tumor cells. *Dev. Cell* 45, 33–52.

Follain, G., Osmani, N., Fuchs, C., Allio, G., Harlepp, S., and Goetz, J.G. (2018b). Using the zebrafish embryo to dissect the early steps of the metastatic cascade. *Methods Mol. Biol.* 1749, 195–211.

Galindo-Hernandez, O., Villegas-Comonfort, S., Candaleno, F., González-Vázquez, M.C., Chavez-Ocaña, S., Jimenez-Villanueva, X., Sierra-Martinez, M., and Salazar, E.P. (2013). Elevated concentration of microvesicles isolated from peripheral blood in breast cancer patients. *Arch. Med. Res.* 44, 208–214.

Goetz, J.G., Steed, E., Ferreira, R.R., Roth, S., Ramspacher, C., Boselli, F., Charvin, G., Liebling, M., Wyart, C., Schwab, Y., et al. (2014). Endothelial cilia mediate low flow sensing during zebrafish vascular development. *Cell Rep.* 6, 799–808.

Goetz, J.G., Monduc, F., Schwab, Y., and Vermot, J. (2015). Using correlative light and electron microscopy to study zebrafish vascular morphogenesis. *Methods Mol. Biol.* **1189**, 31–46.

Grange, C., Tapparo, M., Collino, F., Vitillo, L., Damasco, C., Dereigibus, M.C., Tetta, C., Bussolati, B., and Camussi, G. (2011). Microvesicles released from human renal cancer stem cells stimulate angiogenesis and formation of lung premetastatic niche. *Cancer Res.* **71**, 5346–5356.

Gu, J., Qian, H., Shen, L., Zhang, X., Zhu, W., Huang, L., Yan, Y., Mao, F., Zhao, C., Shi, Y., et al. (2012). Gastric cancer exosomes trigger differentiation of umbilical cord derived mesenchymal stem cells to carcinoma-associated fibroblasts through TGF- β /Smad pathway. *PLoS One* **7**, e52465.

Le Guyader, D., Redd, M.J., Colucci-Guyon, E., Murayama, E., Kiss, K., Briolat, V., Mordelet, E., Zapata, A., Shinomiya, H., and Herbolz, P. (2008). Origins and unconventional behavior of neutrophils in developing zebrafish. *Blood* **111**, 132–141.

Halin Bergström, S., Hägglöf, C., Thysell, E., Bergh, A., Wikström, P., and Lundholm, M. (2016). Extracellular vesicles from metastatic rat prostate tumors prime the normal prostate tissue to facilitate tumor growth. *Sci. Rep.* **6**, 31805.

Hanna, R.N., Čekic, C., Sag, D., Tacke, R., Thomas, G.D., Nowyhed, H., Herrley, E., Rasquinha, N., McArdle, S., Wu, R., et al. (2015). Patrolling monocytes control tumor metastasis to the lung. *Science* **350**, 985–990.

Headley, M.B., Bins, A., Nip, A., Roberts, E.W., Looney, M.R., Gerard, A., and Krummel, M.F. (2016). Visualization of immediate immune responses to pioneer metastatic cells in the lung. *Nature* **531**, 513–517.

Heilmann, S., Ratnakumar, K., Langdon, E.M., Kansler, E.R., Kim, I.S., Campbell, N.R., Perry, E.B., McMahon, A.J., Kaufman, C.K., Van Rooijen, E., et al. (2015). A quantitative system for studying metastasis using transparent zebrafish. *Cancer Res.* **75**, 4272–4282.

Heusermann, W., Hean, J., Trojer, D., Steib, E., von Bueren, S., Graff-Meyer, A., Genoud, C., Martin, K., Pizzato, N., Voshol, J., et al. (2016). Exosomes surf on filopodia to enter cells at endocytic hot spots and shuttle within endosomes to scan the ER. *J. Cell Biol.* **213**, 173–184.

Hoshino, A., Costa-Silva, B., Shen, T.L., Rodrigues, G., Hashimoto, A., Tesic Mark, M., Molina, H., Kohsaka, S., Di Giannatale, A., Ceder, S., et al. (2015). Tumour exosome integrins determine organotropic metastasis. *Nature* **527**, 329–335.

Hyenne, V., Lefebvre, O., and Goetz, J.G. (2017). Going live with tumor exosomes and microvesicles. *Cell Adh. Migr.* **11**, 173–186.

Idrissi, F.Z., and Gelli, M.I. (2014). Zooming in on the molecular mechanisms of endocytic budding by time-resolved electron microscopy. *Cell. Mol. Life Sci.* **71**, 641–657.

Imai, T., Takahashi, Y., Nishikawa, M., Kato, K., Morishita, M., Yamashita, T., Matsumoto, A., Charoenviriyakul, C., and Takakura, Y. (2015). Macrophage-dependent clearance of systemically administered B16BL6-derived exosomes from the blood circulation in mice. *J. Extracell. Vesicles* **4**, 26238.

Karreman, M.A., Mercier, L., Schieber, N.L., Solecki, G., Allio, G., Winkler, F., Ruthensteiner, B., Goetz, J.G., and Schwab, Y. (2016a). Fast and precise targeting of single tumor cells in vivo by multimodal correlative microscopy. *J. Cell Sci.* **129**, 444–456.

Karreman, M.A., Hyenne, V., Schwab, Y., and Goetz, J.G. (2016b). Intravital correlative microscopy: imaging life at the nanoscale. *Trends Cell Biol.* **26**, 848–863.

Kowal, J., Arras, G., Colombo, M., Jouve, M., Morath, J.P., Primdal-Bengtson, B., Dingli, F., Loew, D., Tkach, M., and Théry, C. (2016). Proteomic comparison defines novel markers to characterize heterogeneous populations of extracellular vesicle subtypes. *Proc. Natl. Acad. Sci. USA* **113**, E968–E977.

Kucherak, O.A., Oncul, S., Darwich, Z., Yushchenko, D.A., Arntz, Y., Didier, P., Mély, Y., and Klymenko, A.S. (2010). Switchable Nile red-based probe for cholesterol and lipid order at the outer leaflet of biomembranes. *J. Am. Chem. Soc.* **132**, 4907–4916.

Lai, C.P., Mardini, O., Ericsson, M., Prabhakar, S., Maguire, C.A., Chen, J.W., Tannous, B.A., and Breakefield, X.O. (2014). Dynamic biodistribution of extracellular vesicles in vivo using a multimodal imaging reporter. *ACS Nano* **8**, 483–494.

Lai, C.P., Kim, E.Y., Badr, C.E., Weissleder, R., Mempel, T.R., Tannous, B.A., and Breakefield, X.O. (2015). Visualization and tracking of tumor extracellular vesicle delivery and RNA translation using multiplexed reporters. *Nat. Commun.* **6**, 7029.

Liu, Y., Gu, Y., Han, Y., Zhang, Q., Jiang, Z., Zhang, X., Huang, B., Xu, X., Zheng, J., and Cao, X. (2016). Tumor exosomal RNAs promote lung pre-metastatic niche formation by activating alveolar epithelial TLR3 to recruit neutrophils. *Cancer Cell* **30**, 243–256.

Logozzi, M., De Milito, A., Lugini, L., Borghi, M., Calabro, L., Spada, M., Perdicchio, M., Marino, M.L., Federici, C., Iessi, E., et al. (2009). High levels of exosomes expressing CD63 and caveolin-1 in plasma of melanoma patients. *PLoS One* **4**, e5219.

Magde, D., Rojas, G.E., and Seybold, P.G. (1999). Solvent dependence of the fluorescence lifetimes of xanthene dyes. *Photochem. Photobiol.* **70**, 737–744.

Morishita, M., Takahashi, Y., Nishikawa, M., Sano, K., Kato, K., Yamashita, T., Imai, T., Saji, H., and Takakura, Y. (2015). Quantitative analysis of tissue distribution of the B16BL6-derived exosomes using a streptavidin-lactadherin fusion protein and iodine-125-Labeled biotin derivative after intravenous injection in mice. *J. Pharm. Sci.* **104**, 705–713.

Müller, P., Schwille, P., and Weidemann, T. (2014). PyCorrFit - generic data evaluation for fluorescence correlation spectroscopy. *Bioinformatics* **30**, 2532–2533.

Murayama, E., Kiss, K., Zapata, A., Mordelet, E., Briolat, V., Lin, H.F., Handin, R.I., and Herbolz, P. (2006). Tracing hematopoietic precursor migration to successive hematopoietic organs during zebrafish development. *Immunity* **25**, 963–975.

Nguyen-Chi, M., Laplace-Builhe, B., Travnickova, J., Luz-Crawford, P., Tejedor, G., Phan, Q.T., Duroux-Richard, I., Levraud, J.P., Kiss, K., Lutfalla, G., et al. (2015). Identification of polarized macrophage subsets in zebrafish. *Elife* **4**, e07288.

van Niel, G., D'Angelo, G., and Raposo, G. (2018). Shedding light on the cell biology of extracellular vesicles. *Nat. Rev. Mol. Cell Biol.* **19**, 213–228.

Okabayashi, S., and Kimura, N. (2010). LGI3 interacts with flotillin-1 to mediate APP trafficking and exosome formation. *NeuroReport* **21**, 606–610.

Oliveros, J.C. (2007). VENNY. An Interactive Tool for Comparing Lists with Venn Diagrams. BioinfoGP of CNB-CSIC, <http://bioinfogp.cnb.csic.es/tools/venny/>.

Ostrowski, M., Carmo, N.B., Krumeich, S., Fanget, I., Raposo, G., Savina, A., Moita, C.F., Schauer, K., Hume, A.N., Freitas, R.P., et al. (2010). Rab27a and Rab27b control different steps of the exosome secretion pathway. *Nat. Cell Biol.* **12**, 19–30.

Paggetti, J., Haderk, F., Seiffert, M., Janji, B., Distler, U., Ammerlaan, W., Kim, Y.J., Adam, J., Licher, P., Solary, E., et al. (2015). Exosomes released by chronic lymphocytic leukemia cells induce the transition of stromal cells into cancer-associated fibroblasts. *Blood* **126**, 1106–1117.

Peinado, H., Alečković, M., Lavotshkin, S., Matei, I., Costa-Silva, B., Moreno-Bueno, G., Hergueta-Redondo, M., Williams, C., García-Santos, G., Ghajar, C.M., et al. (2012). Melanoma exosomes educate bone marrow progenitor cells toward a pro-metastatic phenotype through MET. *Nat. Med.* **18**, 883–891.

Peinado, H., Zhang, H., Matei, I.R., Costa-Silva, B., Hoshino, A., Rodrigues, G., Psaila, B., Kaplan, R.N., Bromberg, J.F., Kang, Y., et al. (2017). Pre-metastatic niches: organ-specific homes for metastases. *Nat. Rev. Cancer* **17**, 302–317.

Plebanek, M.P., Angeloni, N.L., Vinokour, E., Li, J., Henkin, A., Martinez-Marin, D., Filleur, S., Bhowmick, R., Henkin, J., Miller, S.D., et al. (2017). Pre-metastatic cancer exosomes induce immune surveillance by patrolling monocytes at the metastatic niche. *Nat. Commun.* **8**, 1319.

Pucci, F., Garris, C., Lai, C.P., Newton, A., Pfirschke, C., Engblom, C., Alvarez, D., Sprachman, M., Evavold, C., Magnuson, A., et al. (2016). SCS macrophages suppress melanoma by restricting tumor-derived vesicle-B cell interactions. *Science* **1328**, 242–246.

Raposo, G., and Stoorvogel, W. (2013). Extracellular vesicles: exosomes, microvesicles, and friends. *J. Cell Biol.* 200, 373–383.

Roh-Johnson, M., Shah, A.N., Stonick, J.A., Poudel, K.R., Kargl, J., Yang, G.H., di Martino, J., Hernandez, R.E., Gast, C.E., Zarour, L.R., et al. (2017). Macrophage-dependent cytoplasmic transfer during melanoma invasion in vivo. *Dev. Cell* 43, 549–562.e6.

Saunders, S.C., Dunn, A.C., Crocker, P.R., and McLellan, A.D. (2014). CD169 mediates the capture of exosomes in spleen and lymph node. *Blood* 123, 208–216.

Schindelin, J., Arganda-Carreras, I., Frise, E., Kaynig, V., Longair, M., Pietzsch, T., Preibisch, S., Rueden, C., Saalfeld, S., Schmid, B., et al. (2012). Fiji: an open-source platform for biological-image analysis. *Nat. Methods* 9, 676–682.

Spilsbury, K., O'Mara, M.A., Wu, W.M., Rowe, P.B., Symonds, G., and Takayama, Y. (1995). Isolation of a novel macrophage-specific gene by differential cDNA analysis. *Blood* 85, 1620–1629.

Stoletov, K., Kato, H., Zardouzian, E., Kelber, J., Yang, J., Shattil, S., and Klemke, R. (2010). Visualizing extravasation dynamics of metastatic tumor cells. *J. Cell Sci.* 123, 2332–2341.

Takahashi, Y., Nishikawa, M., Shinotsuka, H., Matsui, Y., Ohara, S., Imai, T., and Takakura, Y. (2013). Visualization and in vivo tracking of the exosomes of murine melanoma B16-BL6 cells in mice after intravenous injection. *J. Biotechnol.* 165, 77–84.

Takov, K., Yellon, D.M., and Davidson, S.M. (2017). Confounding factors in vesicle uptake studies using fluorescent lipophilic membrane dyes. *J. Extracell. Vesicles* 6, 1388731.

Taylor, M.J., Perrais, D., and Merrifield, C.J. (2011). A high precision survey of the molecular dynamics of mammalian clathrin-mediated endocytosis. *PLoS Biol.* 9, e1000604.

Théry, C., Amigorena, S., Raposo, G., and Clayton, A. (2006). Isolation and characterization of exosomes from cell culture supernatants. *Curr. Protoc. Cell Biol.* 3.22.1–3.22.29.

Thomas, P.D., Campbell, M.J., Kejariwal, A., Mi, H., Karlak, B., Daverman, R., Diemer, K., Muruganujan, A., and Narechania, A. (2003). PANTHER: A library of protein families and subfamilies indexed by function. *Genome Res.* 13, 2129–2141.

Verweij, F., Revenu, C., Arras, G., Dingli, F., Loew, D., Pegtel, M., Follain, G., Allio, G., Goetz, J.G., Zimmermann, P., et al. (2019). Live tracking of inter-organ communication by endogenous exosomes in vivo. *Dev. Cell* 48, this issue, 573–589.

Vogel, D.Y.S., Heijnen, P.D.A.M., Breur, M., de Vries, H.E., Tool, A.T.J., Amor, S., and Dijkstra, C.D. (2014). Macrophages migrate in an activation-dependent manner to chemokines involved in neuroinflammation. *J. Neuroinflamm.* 11, 1–11.

Van Der Vos, K.E., Abels, E.R., Zhang, X., Lai, C., Carrizosa, E., Oakley, D., Prabhakar, S., Mardini, O., Crommentuijn, M.H.W., Skog, J., et al. (2016). Directly visualized glioblastoma-derived extracellular vesicles transfer RNA to microglia/macrophages in the brain. *Neuro. Oncol.* 18, 58–69.

White, R., Rose, K., and Zon, L. (2013). Zebrafish cancer: the state of the art and the path forward. *Nat. Rev. Cancer* 13, 624–636.

Whiteside, T.L. (2016). Exosomes and tumor-mediated immune suppression. *J. Clin. Invest.* 126, 1216–1223.

Würthner, F., Kaiser, T.E., and Saha-Möller, C.R. (2011). J-aggregates: From serendipitous discovery to supramolecular engineering of functional dye materials. *Angew. Chem. Int. Ed.* 50, 3376–3410.

Xiao, M., Zhang, J., and Chen, W., Chen W. (2018). M1-like tumor-associated macrophages activated by exosome-transferred THBS1 promote malignant migration in oral squamous cell carcinoma. *J. Exp. Clin. Cancer Res.* 37, 1–15.

Zomer, A., Maynard, C., Verweij, F.J., Kamermans, A., Schäfer, R., Beerling, E., Schiffelers, R.M., De Wit, E., Berenguer, J., Ellenbroek, S.I.J., et al. (2015). In vivo imaging reveals extracellular vesicle-mediated phenocopying of metastatic behavior. *Cell* 161, 1046–1057.

STAR★METHODS

KEY RESOURCES TABLE

REAGENT OR RESOURCE	SOURCE	IDENTIFIER
Chemicals, Peptides and Recombinant proteins		
MemBright	Collot et al. (2019)	N/A
PKH-26	Sigma-Aldrich	MINI26
100nm fluorescent beads	Phosphorex	2211
Antibodies		
Mouse monoclonal anti-Alix antibody	BD Biosciences	Cat# 611621; RRID: AB_2236941
Mouse monoclonal anti-TSG-101 antibody	GeneTex	Cat# GTX70255; RRID: AB373239
Anti-mouse IgG coupled to HRP	Fisher scientific	Cat# NC9491974
Deposited Data		
EV related experimental details	EV-track consortium	EV180078
EV proteomics	Exocarta	TBD
Experimental Models: Cell lines		
Zmel1	White lab (MSKCC)	N/A
Zmel1 tdTomato	White lab (MSKCC)	N/A
Zmel1 Syntenin2-GFP	This paper	N/A
AB9	ATCC	ATCC-CRL-2298
4T1		RRID: CVCL_0125
4T1 CD63-GFP	This paper	N/A
B16F0	ATCC	ATCC CRL-6322; RRID: CVCL_0604
B16F1	ATCC	ATCC CRL-6323; RRID: CVCL_0158
B16F10	ATCC	ATCC CRL-6475; RRID: CVCL_0159
451-LU	Soengas lab (CNIO)	RRID: CVCL_6357
SK-Mel28	Soengas lab (CNIO)	RRID: CVCL_0526
SK-Mel147	Soengas lab (CNIO)	RRID: CVCL_3876
SK-Mel103	Soengas lab (CNIO)	RRID: CVCL_6069
WM35	Soengas lab (CNIO)	RRID: CVCL_0580
WM164	Soengas lab (CNIO)	RRID: CVCL_7928
Experimental Models: Organisms/strains		
Zebrafish: <i>Tg(Fli1a:eGFP)</i>	Peri lab; EMBL zebrafish facility	N/A
Zebrafish: <i>Tg(mpeg1a:eGFP)</i>	Lengerke lab; Basel University zebrafish facility	N/A
Zebrafish: <i>Tg(mpo:eGFP)</i>	Lengerke lab; Basel University zebrafish facility	N/A
Zebrafish: <i>Tg(Fli1a:Gal4; UAS:RFP)</i>	Lengerke lab; Basel University zebrafish facility	N/A
Zebrafish: Casper <i>Tg(Flk:eGFP; Gata1:RFP)</i>	Vermot lab; IGBMC zebrafish facility	N/A
Zebrafish: <i>Tg(mpeg1:mCherry; TNFa:eGFP)</i>	Djouad lab; IRMB zebrafish facility	N/A
Recombinant DNA		
pSyntenin2-eGFP	Zimmermann lab (CRCM)	N/A
pCS2 Zf-Syntenin2-eGFP	This paper	N/A
pLenti CMV-CD63-AcGFP	This paper	N/A
Software and Algorithms		
Fiji / Image J	NIH	N/A
IMOD	University of Colorado	N/A
Amira for Life Sciences	ThermoFisher Scientific	N/A
GraphPad PRISM	GraphPad Software	N/A
MaxQuant	Max Planck Institute of Biochemistry	N/A
PyCorrFit software	Max Planck Institute of Biochemistry	N/A

(Continued on next page)

Continued

REAGENT OR RESOURCE	SOURCE	IDENTIFIER
Other		
Transmitted electron microscope CM12	Philips	N/A
Transmitted electron microscope CM120	Philips	N/A
Biotwin CM120 (FEI) TEM	Philips	
Nanosight NS300	Malvern Instruments	N/A
ZetaView	Particle Metrix	N/A
NanoAcuity UPLC device	Waters	N/A
NanoLC-Ultra 1D+ system	Eksigent	N/A
Cary 400 Scan ultraviolet-visible spectrophotometer	Varian	N/A
FluoroMax-4 spectrofluorometer	Horiba Jobin Yvon	N/A
M205 FA stereomicroscope	Leica	N/A
Inverted TCS SP5 confocal microscope	Leica	N/A
Upright SP8 confocal microscope	Leica	N/A

CONTACT FOR REAGENT AND RESOURCE SHARING

Further information and requests for resources and reagents should be directed to and will be fulfilled by the Lead Contact, Vincent Hyenne (hyenne@unistra.fr).

EXPERIMENTAL MODEL AND SUBJECT DETAILS**Zmel1, Zmel1 tdTomato and Zmel1 Syntenin2-GFP**

Zebrafish melanoma Zmel1 and Zmel1 td Tomato Kindly provided by Richard White (Memorial Sloan Kettering Cancer Center, New York) ([Heilmann et al., 2015](#)). Zmel1 Syntenin2-GFP generated in the laboratory. Culture condition: 28°C, 5% CO₂, DMEM high glucose (HG), 10% FBS, 1% NEAA-MEM, 1% penicillin-streptomycin.

AB9 Cells

Zebrafish fibroblasts obtained from the caudal fin of an adult AB strain zebrafish (ATCC CRL-2298). Culture condition: 28°C, 5% CO₂, DMEM HG, 10% FBS, 1% NEAA-MEM, 1% Penstrep.

4T1 Cells and 4T1 CD63-GFP

Mouse mammary gland carcinoma (BALB/c female) (CVCL_0125). 4T1 CD63-GFP generated in the laboratory. Culture condition: 37°C, 5%CO₂, RPMI 1640 with 10% FBS, 1% penicillin-streptomycin. Authentication: Injection in the nipple of mammary gland of BALB/c mice lead to mammary tumor.

B16-F0, F1 and F10

Mouse melanoma cell lines, purchased from ATCC (ATCC CRL-6322; ATCC CRL-6323; ATCC CRL-6475). Culture condition: 37°C, 5%CO₂. DMEM supplemented with 10% (v/v) EV-depleted fetal bovine serum (EV-d-FBS), glutamine 2mM and gentamicin

451-LU, SK-Mel28, SK-Mel147, SK-Mel103, WM35 and WM164

Human melanoma cells, kindly provided by Dr. M. Soengas (CNIO, Madrid). Culture condition: 37°C, 5%CO₂. DMEM with 10% EV-d-FBS.

Zebrafish

Zebrafish embryos were obtained from the following strains: *Tg(fli1a:eGFP)*, *Tg(mpeg1:eGFP)*, *Tg(mpo:eGFP)*, *Tg(Flt1:Gal4; UAS:RFP)*, Casper *Tg(Gata1:RFP; flk:GFP)*, *Tg(mpeg:mCherry; TNF- α :GFP)*. Embryos were grown in our laboratory or kindly provided by F. Peri's (EMBL, Heidelberg, Germany) and C. Lengerke's laboratories (University Hospital Basel, Switzerland). Embryos were maintained at 28° in Danieau 0.3X medium, supplemented with 1-Phenyl-2-thiourea (Sigma-Aldrich) after 24 h post fertilization (hpf). For all Zebrafish experiments, the offspring of one single cross was selected, based on anatomical/developmental good health. Embryos were split randomly between experimental groups. All injection experiments were carried at 48 hpf and imaged between 48 hpf and 72 hpf. All animal procedures were performed in accordance with French and European Union animal welfare guidelines and supervised by local ethics committee (Animal facility #A6748233; APAFIS #2018092515234191).

METHOD DETAILS

Cell Line Generation

To generate Zmel1 cells expressing Syntenin2-GFP, Syntenin2 (a gift from P.Zimmerman) was first cloned in pCS2 eGFP Ires Blast vector. Then, 2 millions of Zmel dark cells were transfected with 2 μ g of plasmid pCS2 Zf-Syntenin2-eGFP Ires Blast cut with NotI using 4 μ l of JetPrime according to manufactory instructions (PolyPlus, Illkirch, France). After 1 week, cells with stable integration of the construct were selected using 4 μ g/ml of blasticidin (Sigma Aldrich, St. Quentin Fallavier, France). 4T1 cells expressing CD63-GFP were generated as follows. Briefly, human CD63 cDNA was fused to AcGFP cDNA by In-Fusion cloning (Takara, Ozyme, Saint-Quentin-en-Yvelines, France) and introduced in pLenti CMV-MABBXXS mPGK-Blast vector. Lentiviruses were obtained by HEK293T cells (ATCC CRL-3216; cultured in DMEM, 10% FCS, 1% penicillin-streptomycin) transfection (Invitrogen, Life Technologies, Saint Aubin, France) with pLenti CMV-CD63-acGFP mPGK-Blast together with pLP1, pLP2 and pLP/VSVG lentiviral packaging plasmids to obtain lentiviral particles. After 48 hours, conditioned media was collected, filtered through a 0.22 μ m filter to remove cell debris, and used to transduce 4T1 cells cultured in DMEM supplemented with 10% fetal calf serum and 1% penicillin-streptomycin (Gibco, USA) in the presence of 5 μ g/mL polybrene (Sigma Aldrich, Lyon, France), followed by selection with puromycin (1 μ g/mL, Sigma Aldrich, Lyon, France). Human blood was collected from healthy donors using 3.8% (v/v) sodium citrate (1:9) as anticoagulant. Human erythrocyte rich pellet was obtained by centrifugation at 250 rpm during 15 minutes at room temperature.

EV Isolation and Analysis

For Zmel1 and 4T1 EVs isolation, cells were cultured in EV depleted medium (obtained by overnight ultracentrifugation at 100,000g, using a Beckman, XL-70 centrifuge with a Ti70 rotor) for 24h before supernatant collection. Extracellular medium was concentrated using a Centricon Plus-70 centrifugal filter (10k; Millipore) and EVs were isolated by successive centrifugation at 4°C: 5 minutes at 300 g, 10 minutes at 2,000 g, 30 minutes at 10,000 g and 70 minutes at 100,000 g (using a Beckman XL-70 centrifuge with a SW28 rotor). EVs pellets were washed in PBS, centrifuged again at 100,000 g for 70 minutes, resuspended in PBS and stored at 4°C. For *in vivo* experiments, EVs were used immediately after isolation or kept 4°C at and used the next day.

For mouse and human melanoma EVs isolation, cells were cultured in media supplemented with 10% EV-depleted FBS (FBS, Hyclone). FBS was depleted of bovine EVs by ultracentrifugation at 100,000xg for 70 min. EVs were isolated from conditioned media collected after 72 h of cell cultures by successive centrifugation at 10°C: 5 minutes at 300 g, 10 minutes at 500 g, 20 minutes at 12,000 g and 70 minutes at 100,000 g (using a Beckman Optima X100 with a Beckman 70Ti rotor). EVs pellets were washed in PBS, centrifuged again at 100,000 g for 70 minutes, and resuspended in PBS. Protein content was measured by bicinchoninic acid assay (BCA assay).

For transmitted electron microscopy analysis, 3 μ l of EV extracts were allowed to dry on formvar coated grids for 20 minutes, fixed in 3% PFA for 10 minutes, rinsed in water and contrasted in a uranyl acetate (0.4%)/ methylcellulose (2%) mix for 10 minutes on ice. EVs were observed either with an Orius 100 charge-coupled device camera (Gatan) mounted on a Philips CM12 microscope operated at 80kV or with a Veleta 2kx2k side-mounted TEM CDD Camera (Olympus Soft Imaging Solutions) mounted on a Philips CM120 microscope operated at 120kV.

NTA was performed on Zmel1 EVs diluted 10 times with sterile PBS, using a Nanosight NS300 (Malvern Instruments) or a ZetaView (Particle Metrix). The measurement was repeated three times.

For density gradient analysis, EVs isolated in the 100,000 g pellet were loaded on top of a 5-40% iodixanol (Optiprep) density gradient prepared as previously described (Van Deun et al., 2014). The gradient was centrifuged for 18 hours at 100,000g and 4°C (using a Beckman XL-70 centrifuge with a SW28 rotor). Gradient fractions of 1ml were collected from the top of the gradient. Fractions 1 to 4, 5 to 10 and 11 to 16 were pooled, diluted to 16 ml in PBS and centrifuged for 3 hours at 100,000g and 4°C. The resulting pellet was resuspended in 50 μ l of PBS. For western blotting analysis, 10 μ l of EV extracts were loaded on 4-20% polyacrylamide gels (Biorad), under denaturing conditions. The following antibodies were used: Alix (BD Biosciences 611621) and TSG101 (GeneTex GTX70255). Acquisitions were done using a PXi system (Syngene).

Shotgun Proteomics

Sample Preparation of Zmel1 EVs Protein Content

After having determined protein concentration (RC-DC™; Bio-Rad, Hercules, CA), 20 μ g samples were denatured at 95°C for 5 min in Laemmli buffer and then concentrated in one stacking band using a 5% SDS-PAGE gel. The gel was fixed with 50% ethanol/3% phosphoric acid and stained with colloidal Coomassie Brilliant Blue. Each band was excised, cut in five pieces, and transferred into a 96-well microtiter plate. Gel slices were washed with 3 cycles of incubations in 100 μ L of 50:50 (v/v) 25 mM NH₄HCO₃/ACN for 10 min. Gel bands were then dehydrated with 50 μ L 100% ACN and then reduced with 50 μ L 10 mM DTT for 30 min at 60°C, followed by 30 min at RT. Proteins were then alkylated with 50 μ L 55 mM iodoacetamide for 20 min in the dark at RT, and then 100 μ L ACN were added for 5 min. Samples were washed with 50 μ L 25 mM NH₄HCO₃ for 10 min, and then 50 μ L ACN for 5 min, before being dehydrated with two cycles of incubations in 50 μ L ACN for 5 min. Proteins were digested overnight with a modified porcine trypsin (Promega, Madison, WI) solution at a 1:100 (w/w) enzyme/protein ratio at 37°C. Tryptic peptides were extracted under agitation at RT with 60 μ L 60% ACN/0.1% FA for 45 min, and then 100% ACN for 10 min. The extraction supernatants were pooled and vacuum-dried, before re-suspension in 40 μ L 2% ACN/0.1% FA.

Nano-LC-MS/MS Analysis of Zmel1 EVs Protein Content

Nano-LC-MS/MS analysis was performed on a nanoAcuity UPLC device (Waters, Milford, MA) coupled to a Q-Exactive Plus mass spectrometer (Thermo Fisher Scientific, Bremen, Germany). The solvents consisted of 0.1% FA in H₂O (solvent A) and 0.1% in ACN (solvent B). 1 μ L of the samples was loaded onto a Symmetry C18 pre-column (20 mm \times 180 μ m, 5 μ m diameter particles; Waters, Milford, MA) over 3 min at 5 μ L/min with 1% solvent B. Peptides were eluted on a Acuity UPLC BEH130 C18 column (250 mm \times 75 μ m, 1.7 μ m particles; Waters, Milford, MA) at 450 μ L/min with the following gradient of solvent B: linear from 1% to 8 % in 2 min, linear from 8% to 35% in 77 min, linear from 35% to 90% in 1 min, isocratic at 90% for 5 min, down to 1% in 2 min, isocratic at 1% for 2 min.

The Q-Exactive Plus was operated in data-dependent acquisition mode by automatically switching between full MS and consecutive MS/MS acquisitions. Full-scan MS spectra were collected from 300-1,800 m/z at a resolution of 70,000 at 200 m/z with an automatic gain control target fixed at 3×10^6 ions and a maximum injection time of 50 ms. The top 10 precursor ions with an intensity exceeding 2×10^5 ions and charge states ≥ 2 were selected on each MS spectrum for fragmentation by higher-energy collisional dissociation. MS/MS spectra were collected at a resolution of 17,500 at 200 m/z with a fixed first mass at 100 m/z, an automatic gain control target fixed at 1×10^5 ions and a maximum injection time of 100 ms. A dynamic exclusion time was set to 60 s.

Sample Preparation of Mammalian EVs Cargo

Proteins were solubilized using 8 M urea in 100 mM Tris-HCl pH 8.0. Samples (7.5 μ g) were digested by means of the standard FASP protocol. Briefly, proteins were reduced (10 mM DTT, 30 min, RT), alkylated (55 mM IA, 20 min in the dark, RT) and sequentially digested with Lys-C (Wako) (protein:enzyme ratio 1:50, o/n at RT) and trypsin (Promega) (protein:enzyme ratio 1:100, 6 h at 37° C). Resulting peptides were desalting using C₁₈ stage-tips.

Nano-LC-MS/MS Analysis of Mammalian EVs Cargo

LC-MS/MS was done by coupling a nanoLC-Ultra 1D+ system (Eksigent) to a LTQ Orbitrap Velos mass spectrometer (Thermo Fisher Scientific) via a Nanospray Flex source (Thermo Fisher Scientific). Peptides were loaded into a trap column (NS-MP-10 BioSphere C18 5 μ m, 20 mm length, Nanoseparations) for 10 min at a flow rate of 2.5 μ L/min in 0.1% FA. Then peptides were transferred to an analytical column (ReproSil Pur C18-AQ 2.4 μ m, 500 mm length and 0.075 mm ID) and separated using a 120 min linear gradient (buffer A: 4% ACN, 0.1% FA; buffer B: 100% ACN, 0.1% FA) at a flow rate of 250 nL/min. The gradient used was: 0-2 min 6% B, 2-103 min 30% B, 103-113 min 98% B, 113-120 min 2% B. The peptides were electrosprayed (1.8 kV) into the mass spectrometer with a PicoTip emitter (360/20 Tube OD/ID μ m, tip ID 10 μ m) (New Objective), a heated capillary temperature of 325° C and S-Lens RF level of 60%. The mass spectrometer was operated in a data-dependent mode, with an automatic switch between MS and MS/MS scans using a top 15 method (threshold signal ≥ 800 counts and dynamic exclusion of 60 s). MS spectra (350-1500 m/z) were acquired in the Orbitrap with a resolution of 60,000 FWHM (400 m/z). Peptides were isolated using a 1.5 Th window and fragmented using collision induced dissociation (CID) with linear ion trap read out at a NCE of 35% (0.25 Q-value and 10 ms activation time). The ion target values were 1E6 for MS (500 ms max injection time) and 5000 for MS/MS (100 ms max injection time).

Nano-LC-MS/MS Data Interpretation

Raw files were processed with MaxQuant (versions 1.6.0.16) (Cox et al., 2014) against an in-house concatenated *Danio rerio*-*Bos taurus* (UniProtKB, February 2017, 90,922 entries) supplemented with contaminants for Zmel1 EVs proteins and generated with the database toolbox from MSDA (Carapito et al., 2014), or a human protein database (UniProtKB/Swiss-Prot, August 2014, 20,187 sequences) supplemented with contaminants for mammalian EVs cargo. Label-free quantification was done with the match between runs option activated (match window of 0.7 min and alignment window of 20 min). Carbamidomethylation of cysteines was set as a fixed modification whereas oxidation of methionines and protein N-term acetylation were set as variable modifications. Minimal peptide length was set to 7 amino acids and a maximum of two tryptic missed-cleavages were allowed.

Protein Comparisons

To compare the Zmel1 protein content with mammalian EV content, each protein list was concatenated and duplicate proteins were deleted. Ortholog proteins were searched using the ortholog protein files predicted by the PANTHER classification system (<ftp://ftp.pantherdb.org/ortholog/13.0/> (Thomas et al., 2003)). Only proteins referred as “Least diverged ortholog” or “Ortholog” were considered. All comparisons between Zmel1 EVs and mammalian EVs were done using human orthologs and the lists of common proteins was obtained using Venny 2.1 (Oliveros, 2007).

MemBright and PKH Labeling of EVs

Isolated EVs were incubated with MemBright-Cy3 or Cy5 at 200nM (final concentration) in PBS for 30 minutes at room temperature in the dark. They were then rinsed in 15ml of PBS and centrifuged at 100,000g with a SW28 rotor in a Beckman XL-70 centrifuge. Pellets were resuspended in 50 μ L PBS and stored at 4° C. For *in vivo* experiments, EVs were used immediately after isolation or stored overnight at 4° C and injected the next day. For PKH-26 labeling EVs were treated according to the manufacturer’s instructions (2 μ M final concentration). Briefly, EVs in 200 μ L of PBS were first mixed with 300 μ L of Diluent C, then with 500 μ L of Diluent C containing 4 μ L of PKH and finally incubated for 30 minutes at room temperature in the dark. PKH labeled EVs were then processed as MemBright labeled EVs. As a control, PBS alone was processed similarly to EVs, labeled with MemBright or PKH and analysed by microscopy or spectroscopy.

For photonic microscopy analysis, 3 μ L of labeled EV extracts were allowed to settle on poly-L lysine coated coverslips and then imaged on a Zeiss Imager Z2 with a 63X objective (N.A. 1.4) or with a SP5 confocal (Leica) with a 40X objective (N.A. 1.25).

Spectroscopy

EVs labeled with either MemBright-Cy3 or PKH-26, or control MemBright-Cy3 or control PKH (diluted in PBS as described above), as well as the dyes directly diluted in Milli-Q water (Millipore) or ethanol were analyzed by spectroscopy. Absorption and emission spectra were recorded at 20°C in quartz cuvettes on a Cary 400 Scan ultraviolet-visible spectrophotometer (Varian) and a FluoroMax-4 spectrofluorometer (Horiba Jobin Yvon) equipped with a thermostated cell compartment, respectively. For standard recording of fluorescence spectra, excitation was at 520 nm and the emission was collected 10 nm after the excitation wavelength (530 nm to 700 nm). All the spectra were corrected from wavelength-dependent response of the detector. The scattering due to the EVs was corrected with a baseline correction using Origin software. Quantum yields were determined using rhodamine B in water (QY= 0.31) as a reference (Magde et al., 1999).

Fluorescence Correlation Spectroscopy (FCS)

To characterize the size of PKH aggregates, FCS measurements were performed on PKH26 (diluted at 5 μ M) using a home-built confocal set-up based on a Nikon inverted microscope with a Nikon 60x 1.2NA water immersion objective. Excitation was provided by a cw laser diode (532 nm, Oxxius) and photons were detected with a fibered Avalanche Photodiode (APD SPCM-AQR-14-FC, Perkin Elmer) connected to an on-line hardware correlator (ALV7000-USB, ALV GmbH, Germany). Typical acquisition time was 5 min (10 \times 30 s) with an excitation power of 1.1 μ W at the sample level. The data were analyzed using the PyCorrFit software (Müller et al., 2014).

MemBright Labeling of Cells

Sub-confluent cells in 10cm culture dishes were rinsed twice with warm serum free medium and then incubated for 30 minutes at 28°C (Zmel1 cells) or at 37°C (4T1 cells) with MemBright quickly diluted in serum free medium (200nM final). To eliminate all possible traces of unbound MemBright, cells were then rinsed three times with serum free medium, rinsed with EDTA and trypsinized. Cells were then either injected in zebrafish embryos, seeded in a triple flask for EV production, or seeded in glass bottom microwell dishes (MatTek Corporation) pre-coated with fibronectin from bovine plasma at 10 μ g/ml (Sigma F-1141) for imaging.

Intravascular Injection of Zebrafish Embryo

At 48h post-fertilization (hpf), zebrafish embryos were dechorionated and mounted in 0.8% low melting point agarose pad containing 650 μ M of tricaine (ethyl-3-aminobenzoate-methanesulfonate) to immobilize them. Pre-labelled EVs, polystyrene beads (Phosphorex) or tumors cells were injected with a Nanoject microinjector 2 (Drummond) and microforged glass capillaries (25 to 30 μ m inner diameter) filled with mineral oil (Sigma). 27,6 nL of a EV, beads or cell suspension (at 100.10 6 cells) per ml were injected into the duct of Cuvier of the embryos under the M205 FA stereomicroscope (Leica), as previously described (Follain et al., 2018b; Stolletov et al., 2010). For the priming experiments, 32hpf embryos were injected with either Zmel1 EVs or 100nm polystyrene beads (together with fluorescent dextran to assess the efficiency of injection). 14h post-injection, embryos were injected in the circulation with Zmel1 tdTomato tumor cells. Larvae were grown for a week and imaged at 7 days post-injection. For late endosome/lysosome labeling, embryos were incubated with Lysotracker Deep Red (Thermo Fisher Scientific) diluted at 5 μ M in Danieau 0,3X medium for 2 hours at 28°C before injection.

Confocal Imaging and Analysis

Confocal imaging was alternatively performed with an inverted TCS SP5 with HC PL APO 20X/0,7 IMM CORR CS objective (Leica) or an upright SP8 confocal microscope with a HC FLUOTAR L 25X/0,95 W VISIR objective (Leica). For high speed imaging of EVs in the blood flow, embryos were imaged right after injection; acquisitions were done at 80-100 frames per second for 1 minute, using the resonant scanner in a single Z plane, with an opened pinhole of more than 1 airy unit. To identify the cell types uptaking EVs, the caudal plexus region of mpeg1:GFP, mpo:GFP or Fli1a:GFP was imaged 3h post-injection with a z-step of 1 μ m. To quantify the proportion of EVs arrested in the dorsal aorta vs venous plexus regions, images were acquired similarly in Fli1:GFP embryos. For each case, quantification is described in the next paragraphs. To image the dynamics of macrophage protrusions, short time lapses of mpeg1:GFP embryos were acquired at 5 to 10 Z stacks per minute (z-step of 0,5 μ m, stack covering the macrophage). To image the dynamics of macrophages, long time lapses of mpeg1:GFP embryos were acquired at 1 Z stack per minute for one hour (z-step of 2 μ m, stack covering the venous plexus). To image the uptake of EVs by macrophage, mpeg1:GFP embryos short time lapses were generated right after injection at 3 to 8 images per second on single Z planes. Image analysis and processing were performed using Fiji (Schindelin et al., 2012) as described in the following paragraphs.

Semi-automated Method to Determine the Proportion of Internalized EVs

To determine the proportion of EVs internalized by either endothelial or macrophages, we used the Z-stacks obtained from either Fli1:GFP or mpeg1:GFP embryos injected with Zmel1-MemBright EVs. Using Fiji, we split the cell and EVs channels and merged them in a single RGB image. From the merged channel, we made a binary stack followed by a Z-projection with maximal intensity. We used this as a reference image where all the EVs and cells are apparent. After normalizing this image to 1 we multiplied each stack (respectively EVs and Cell) by this projection. In both stacks, we thus kept only the positions that colocalize either with the EV position or the Cells position (all other positions possess a null value). We then made a binary from the Cell stack, applied close and dilated before normalizing it to 1. The multiplication of this stack with the EV one lead to a new stack that keeps only the particle enclosed in

the cellular compartments. Getting back to the Cell stack, we apply an inversion of the intensity values before subtracting 254. The resulting stack was then multiplied by the EV stack and the created new stack let only apparent the EVs that did not colocalize with the cells. Further analyses of the intensities from the two stacks allowed us to access the ratiometric values of EVs uptaken by the different cell lines.

Quantification of EVs in Aorta vs Vein Regions

Each region (dorsal aorta and venous plexus) was manually delimited on Z-projections, using vessels visible in Fli1:GFP channels. Total EV intensity was then measured in each region and reported to the area. A ratio of EV fluorescence in the venous plexus over dorsal aorta was then measured for each fish.

Flow Analysis for Red Blood Cells

Flow analysis of red blood cells

We first globally enhanced the contrast of the whole stack. Then we performed a Z-projection with the average intensity and subtracted the obtained image to the stack. The remaining stack exhibits only the moving objects i.e. the red blood cells in this case. Then we applied a binarisation to the stack before applying a bandpass filter with the correct values to remove the background noise and keeping only the flowing blood cells. This stack was then further analyzed with the Mosaic 2D/3D particle tracker plugin. We thus accessed the positions of each blood cell for the different frames and we computed the velocities of each individual track.

Flow Analysis of EVs

Time-lapses of EVs were first thresholded and binarized. We then inverted the stack before running the 2D spot enhancing Filter plugin. We used the resulting stack to perform a second binarisation and then launched the Mosaic 2D/3D particle tracker plugin. We thus accessed the positions of each EV for the different frames and we computed the velocities of each individual track

EVs and RBCs Distance and Velocity from the Endothelial Barrier

In order to access to the distance of the EVs or red blood cells to the endothelial barrier, we first drew the endothelial wall using the transmitted light and extracted its coordinates to a table. From the analysis described in the previous paragraph, we extracted the coordinates and the velocity EVs and red blood cells. We ran a macro where we compared for all the position X_{EV} and Y_{EV} of the EV the closest position X_{endo} and Y_{endo} by comparing all the possible distances d by calculating :

$$d = \sqrt{(X_{EV} - X_{endo})^2 + (Y_{EV} - Y_{endo})^2}$$

and keeping the smallest distance.

This allowed us to plot the EV or the red blood cells velocities as a function of the distance from the endothelial wall.

Sample Preparation for Correlative Light and Electronic Microscopy of ZF Embryos

Correlative Light and Electron Microscopy was performed as previously described (Goetz et al., 2014; Karreman et al., 2016a). Transgenic mpeg1:GFP embryos were injected with MemBright-Cy3 4T1 EVs and imaged alive with a Leica SP8 confocal microscope (see “Confocal imaging and analysis section”). Z stack was performed on two patrolling macrophages having uptaken EVs. After imaging, the embryo was chemically fixed with 2,5% glutaraldehyde and 4% paraformaldehyde in 0.1 M Cacodylate buffer (the fish tail was cut off in the fixative). The sample was kept in fixative at room temperature for 1-2h and stored in fixative at 4°C overnight or until further processing. The sample was rinsed in 0.1M Cacodylate buffer for 2x5min and post-fixed using 1% OsO4 in 0.1 M Cacodylate buffer, for 1h at 4°C. Then, sample was rinsed for 2x10 min in 0.1M Cacodylate buffer and secondary post-fixed with 4% water solution of uranyl acetate, 1h at room temperature. Rotation was used at all steps of sample processing. Followed by 5 min wash in MilliQ water, the sample was stepwise dehydrated in Ethanol (25%, 50% each 15min, 95%, 3X100% each 20 min) and infiltrated in a graded series of Epon (Ethanol/Epon 3/1, 1/1, 1/3, each 45 min). Sample was left in absolute Epon (EmBed812) overnight. The following day, sample was placed in a fresh absolute Epon for 1h and polymerized (flat embedded) at 60°C for 24-48h. Once polymerized, most surrounding Epon was cut off using razorblade and sample was mounted on empty Epon blocks (samples flat on the top of the blocks) and left at 60°C for 24h-48h. Samples were attached to an imaging pin with dental wax and mounted into the Bruker Skyscan 1272 for microCT imaging. Data were acquired over 188° with 0.2° angular step and a pixel size of 9 μm. Karreman et al. thoroughly details the process of how the microCT data enables the correlation of fluorescent imaging to 3D EM of voluminous samples (Karreman et al., 2016a). Retrieval of the region of interest is described in Figure S4. The region of interest was targeted by ultramicrotome, sections stained with toluidine blue and compared with the MicroCT and LM datasets. After targeting, serial 70nm sections were collected in formvar coated slot grids. The sections were post stained with uranyl acetate (4%) and lead citrate. The sections were imaged in a Biotwin CM120 Philips (FEI) TEM at 80kV with a SIS 1K KeenView. Stitches of the 70 sections were aligned using the Track EM plugin in Fiji (Cardona et al., 2012). Segmentation and 3D reconstruction were done using the IMOD software package (Boulder Laboratory, University of Colorado) and Amira.

QUANTIFICATION AND STATISTICAL ANALYSIS

Statistical Tests

Statistical analysis of the results was performed using the GraphPad Prism program version 5.04. The Shapiro-Wilk normality test was used to confirm the normality of the data. The statistical difference of Gaussian data sets was analyzed using the Student unpaired two-tailed t test, with Welch's correction in case of unequal variances. For data not following a Gaussian distribution, the Mann-Whitney test was used. Illustrations of these statistical analyses are displayed as the mean +/- standard deviation (SD). p-values smaller than 0.05 were considered as significant. *, p<0.05, **, p < 0.01, ***, p < 0.001, ****, p < 0.0001.

Zebrafish Experiments

Measurements of EVs displacement in the dorsal aorta and in the caudal vein of zebrafish embryos (Figures 3B-3E) was performed on four zebrafish embryos. Measurements of EV uptake in aorta versus venous plexus was repeated three times (n=17; Figure 4B). Comparison of the uptake of beads, AB9 EVs and Zmel1 EVs by endothelial cells (n=20, 24 and 11 respectively; Figure 4C) and macrophages (n=28, 21 and 19 respectively; Figure 5C) was repeated three times each. The correlation between Zmel1 uptake intensity and macrophages perimeter was done on 73 macrophages (13 embryos; Figure 5B). The velocity of non-injected macrophages was measured on 35 macrophages (6 embryos; Figure 5E). The colocalization between taken EVs and lysotracker in macrophages at 10 min and 3h post-injection was performed on 61 and 54 puncta, respectively (n=6 and 7 fish, respectively; Figure 6D). The dynamics of macrophages injected with either beads or Zmel1 EVs was measured on 27 and 47 macrophages, respectively (5 and 8 embryos; Figure 8A). The activation of M1 macrophages after beads or Zmel1 EVs injection was repeated twice (n=38 and 28 fish, respectively; Figures 8B and 8C). The metastatic outgrowth of Zmel1 cells in zebrafish embryos injected with either beads or Zmel1 EVs was repeated five times (n=55 and 57 fish, respectively; Figure 8D).

EVs Experiments

Measurements of the diameters of Zmel1 EVs (Figure 1B) and Zmel1 EVs labeled with MemBright (Figure 2E) by NTA was repeated three times. Analysis of Zmel1 EVs (Figures 1C and 2D) and Zmel1 EVs labeled with MemBright (Figure 2D) by TEM was repeated each three times (n= 871 and 356, respectively). Spectroscopic analysis of PKH and MemBright labeled EVs (Figure 1B) was performed once, at different concentrations. Measurements of the fluorescence of PKH or MemBright labeled EVs was repeated three times (Figures S2A and S2B). The number of puncta measured is indicated in the graph bars. The density gradient isolation of EVs was repeated twice (Figure S1F). The measurements of the apparent EV diameter Vs beads diameter by confocal was repeated three times *in vitro* and *in vivo* (Figure S2). The number of individual puncta measured is indicated in the graphs. Mass spectrometry of EVs was performed on triplicates (Figure 1E; Table S1).

DATA AND SOFTWARE AVAILABILITY

The proteomics data have been deposited on Exocarta. All relevant data regarding the EVs experiments have been deposited on the EV-TRACK knowledgebase (EV-Track ID:EV180078) (Van Deun et al., 2017).

**ANNEX 6: FLUORESCENT POLYMER NANOPARTICLES FOR CELL BARCODING
IN VITRO AND IN VIVO**

Fluorescent Polymer Nanoparticles for Cell Barcoding In Vitro and In Vivo

Bohdan Andreiuk, Andreas Reisch,* Marion Lindecker, Gautier Follain, Nadine Peyriéras, Jacky G. Goetz, and Andrey S. Klymchenko*

*Fluorescent polymer nanoparticles for long-term labeling and tracking of living cells with any desired color code are developed. They are built from biodegradable poly(lactic-co-glycolic acid) polymer loaded with cyanine dyes (DiO, DiI, and DiD) with the help of bulky fluorinated counterions, which minimize aggregation-caused quenching. At the single particle level, these particles are \approx 20-fold brighter than quantum dots of similar color. Due to their identical 40 nm size and surface properties, these nanoparticles are endocytosed equally well by living cells. Mixing nanoparticles of three colors in different proportions generates a homogeneous RGB (red, green, and blue) barcode in cells, which is transmitted through many cell generations. Cell barcoding is validated on 7 cell lines (HeLa, KB, embryonic kidney (293T), Chinese hamster ovary, rat basophilic leukemia, U97, and D2A1), 13 color codes, and it enables simultaneous tracking of co-cultured barcoded cell populations for >2 weeks. It is also applied to studying competition among drug-treated cell populations. This technology enabled six-color imaging *in vivo* for (1) tracking xenografted cancer cells and (2) monitoring morphogenesis after microinjection in zebrafish embryos. In addition to a robust method of multicolor cell labeling and tracking, this work suggests that multiple functions can be co-localized inside cells by combining structurally close nanoparticles carrying different functions.*

B. Andreiuk, Dr. A. Reisch, M. Lindecker,
Dr. A. S. Klymchenko
Laboratoire de Biophotonique et Pharmacologie
UMR 7213 CNRS
Faculté de Pharmacie
Université de Strasbourg
74, Route du Rhin, BP 60024, 67401 Illkirch, France
E-mail: reisch@unistra.fr; andrey.klymchenko@unistra.fr
G. Follain, Dr. J. G. Goetz
MN3T
Inserm U1109
LabEx Medalis
Fédération de Médecine Translationnelle de Strasbourg (FMTS)
Université de Strasbourg
Strasbourg 67000, France
Dr. N. Peyriéras
CNRS USR3695 BioEmergences
Avenue de la Terrasse, 91190 Gif-sur-Yvette, France

 The ORCID identification number(s) for the author(s) of this article can be found under <https://doi.org/10.1002/smll.201701582>.

DOI: [10.1002/smll.201701582](https://doi.org/10.1002/smll.201701582)



1. Introduction

The current trend in nanotechnology for biological applications is the implementation of multiple functions within the same nanoparticle (NP). One should mention multimodal NP probes that enable simultaneous use of several imaging modalities, such as magnetic, X-ray, and/or fluorescence.^[1] Another example is co-encapsulation of a drug with an imaging agent, which enables developing highly promising tools for theranostics.^[1b,2] Finally, in optical imaging, which is currently undergoing remarkable growth, multiple colors are included within the same particles, thus providing them with unique color fingerprints (barcodes) for multiplex detection.^[3] However, implementation of multiple functions within the same NP requires complicated synthetic protocols, which have to be revalidated for the whole system once a single function is changed, added, or removed. Moreover, these protocols do not always allow achieving high reproducibility of nanoparticle properties, so that the important challenges related to cost, effectiveness, and toxicity of these NPs in

the biomedical context are still to be addressed.^[4] A totally different approach is to implement multiple functions separately into different NPs of practically identical characteristics, and then to combine them together to achieve a desired multifunctional effect in biological samples. In this case, the similar size and surface properties of the NPs ensure their identical delivery in biological samples so that multiple functions of these NPs are co-localized. This approach could be realized within optical modality, where structurally close NPs of different colors, undergoing identical delivery into live cells, could generate any desired barcode for long-term cell tracking *in vitro* and *in vivo*, something that has not been realized to date.

Long-term fluorescence staining of living cells in multiple colors is of high importance for tracking different cell populations *in vitro* and *in vivo*, and in this way helps to address key questions in cancer research, cell differentiation, cell therapy, regenerative medicine, embryogenesis.^[5] However, due to the relatively broad absorption and emission bands of organic dyes, fluorescent nanoparticles and fluorescent proteins standard fluorescent microscopy can distinguish only four to five individual colors. A recently proposed concept, named “Brainbow,”^[6] overcomes this problem by using RGB (red, green, and blue) optical (color) coding, where a practically unlimited number of barcodes can be generated by co-expressing blue, green, and red fluorescent proteins in a stochastic and thus unique combination. This method has been successfully used for visualizing neuronal networks *in vitro* and *in vivo*^[7] and cellular organization and development in small animals,^[8] and was recently proposed for stem cells^[9] and cancer research.^[10] However, color coding of living cells without their genetic modification is underexplored. To develop such a method, several fundamental problems have to be addressed: (i) long-term cell staining should be achieved; (ii) this implies that staining should be sufficiently bright despite multiple cellular divisions; (iii) the individual colors should be stable and well resolved, so that each color code and thus each cell population could be recognized even after several weeks; (iv) the staining should not produce toxic effects, especially in the view of long-term studies. Organic dyes, such as hydrophobic cyanine dyes (DiO, DiI, DiR, and PKH families) and the specially designed CellTracker and CellTrace families (CFSE, CM-DiI, CMTMR, etc.) can be used for long-term cell staining.^[11] However, the staining generally remains for only about 3 d.^[12] Moreover, no reports showed that these dyes could be used in combination to generate multiple colors, as it is done by Brainbow using fluorescent proteins. New possibilities emerge with fluorescent nanoparticles.^[4b,13] Recent reports described long-term staining using NPs based on aggregation-induced emission of dyes,^[14] although their application for RGB color coding has not been shown. Studies of color coding using nanoparticles were mainly focused on multiplex detection of biomolecules in solution.^[15] The only attempts to barcode living cells using NPs were performed with quantum dots (QDs).^[16] However, due to the stochastic nature of their internalization,^[17] cell labeling by QDs of three different colors generated randomly distributed color codes within the same population of cells.^[16b] At the moment, there is no method

for exogenous cell labeling that can generate in a whole cell population a defined RGB barcode readable directly by fluorescence microscopy. One solution is to use fluorescent dye-loaded polymer NPs, which attracted attention due to their extreme brightness (>10 brighter than QDs), color variability, biodegradability, and low toxicity.^[18] Significant efforts have been done to design multicolored dye-loaded polymer nanoparticles through encapsulation of multiple dyes within the same NPs, which ensures cascade Förster resonance energy transfer (FRET) and multiband emission.^[3a,19] One of these systems was applied for RGB color coding, where two cell populations were distinguished without long-term measurements.^[3a] Recently, we developed 40 nm polymer NPs based on the biodegradable polymer poly(lactic-co-glycolic acid) (PLGA).^[20] To achieve high dye loading with excellent brightness, we combined a hydrophobic cationic dye, octadecyl rhodamine, with bulky fluorinated counterions. These NPs showed very fast internalization into cells by endocytosis, thus providing efficient cellular labeling.^[20] We hypothesized that the counterion approach could be expanded to other cationic dyes, such as cyanines, so that we could generate NPs bearing three well-separated absorption/emission bands. Then, if these NPs are of similar size and surface properties, they may present identical internalization inside cells, so that their co-incubation with cells in different proportions could generate labeled cells of any desired color far beyond the commonly used three colors. Presently, we successfully realized this hypothesis, where the obtained ultrabright NPs of three different colors could label living cells with at least 13 different RGB barcodes. These color codes are transmitted through many cell generations, so that the cells could be tracked in culture for >2 weeks. In addition, we showed that such barcoded cells can be easily tracked in living animals such as zebrafish embryos.

2. Results

2.1. Preparation and Characterization of Nanoparticles

To obtain fluorescent polymer NPs of small size, we used our recently developed protocol of charge-controlled nanoprecipitation,^[20,21] where a diluted solution of a polymer bearing one charged group per chain and a dye in an organic solvent are rapidly added into aqueous media. In case of PLGA, bearing one negatively charged carboxylate at the polymer terminus, NPs of 35–40 nm diameter can be obtained. To generate NPs of three distinct colors, we selected cyanine dyes, which are known to exhibit sharp absorption and emission bands. For successful encapsulation inside polymer NPs, the dyes should be hydrophobic, so that they will co-precipitate together with the polymer. Hence, we selected cyanine derivatives bearing two octadecyl chains: DiO, DiI, and DiD (**Figure 1A**). The choice of the counterion was of high importance for obtaining small NPs. While the use of small inorganic counterion (e.g., chloride or perchlorate) led to a strong increase in NP size, using bulky hydrophobic tetraphenylborate counterions (F0, F5, and F12; Figure 1A) led to a minimal dependence of the size of NPs on the dye loading

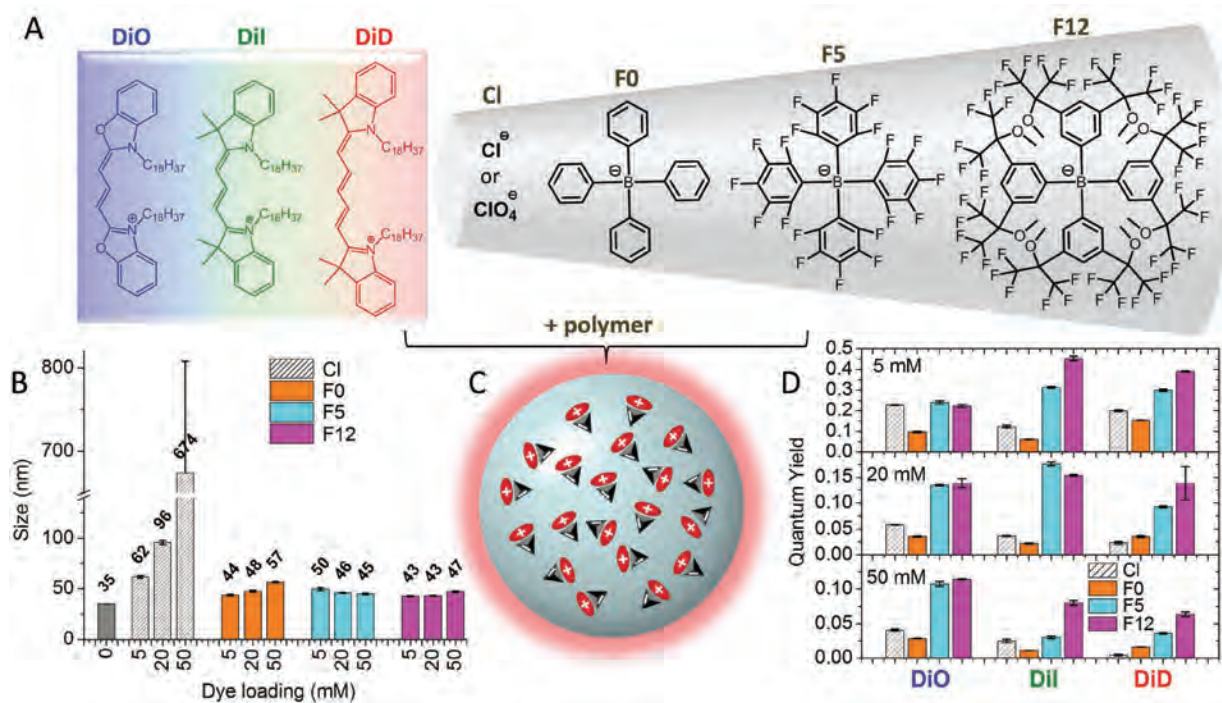


Figure 1. Polymer NPs loaded with cyanine dyes using different counterions. A) Chemical structures of cationic cyanine dyes (blue, green, and red) and their counterions (in black). B) Effect of dye loading on the hydrodynamic diameter of NPs doped with DiO bearing inorganic (perchlorate) or different bulky organic counterions (F0, F5, and F12). C) Schematic presentation of dye-loaded polymer nanoparticles. D) Fluorescent quantum yields of NPs loaded at different concentration with three cyanine dyes: role of counterions for preventing self-quenching. The error bars are standard error of the mean ($n = 3$).

(Figure 1C; Tables S1 and S2, Supporting Information). The best results were obtained with the fluorinated counterions F5 and F12, showing that the super-hydrophobicity of fluorinated compounds^[22] plays a key role in efficient encapsulation of cationic dyes into polymer NPs. Increase in the dye loading produced a systematic decrease in the fluorescence quantum yield (QY) of NPs (Figure 1D) and broadening of absorption bands (Figures S1–S3, Supporting Information), which are clearly related to aggregation caused quenching (ACQ).^[23] However, these unwanted effects were minimized by using the fluorinated counterions F5 and F12 (Figure 1D; Figures S1–S3, Supporting Information). The most efficient in this respect was the largest counterion F12, as the QY values were the highest for most of the formulations, notably in the case of Cy5, where F12 allowed obtaining QYs of 14% even at 20×10^{-3} M loading.

Based on the obtained results, we selected 20×10^{-3} M loading of cyanine dyes with the F12 counterion and further characterized the obtained NPs in detail. Absorption spectra of these NPs presented maxima at 488, 553, and 651 nm (Figure 2A), which corresponded well to those of DiO, Dil, and DiD dyes in methanol (Figures S1–S3, Supporting Information) and matched the most common laser lines at 488, 561, and 640 nm. The emission bands were rather sharp for DiI–F12 and DiD–F12 dye loaded NPs (Figure 2A), similar to those in methanol (Figures S1–S3, Supporting Information), which confirmed minimal aggregation of dyes at this high loading. Despite a broader emission spectrum of DiO–F12 NPs, it is clear that, using appropriate excitation

wavelengths and emission filters, it would be possible to detect each of these three types of NPs, without crosstalk in the detection (Figure 2A). Transmission electron microscopy (TEM) revealed that, independently of the loaded dye, NPs displayed the same size and spherical structure (Figure 2B,C). Moreover, the dye-loaded NPs showed practically the same zeta potential of around -40 mV as the corresponding blank NPs (Figure 2B). Therefore, we can conclude that encapsulation of dyes did not alter the surface properties of the NPs. Thus, we obtained fluorescent NPs of three different colors presenting the same size and surface properties. In wide-field fluorescence microscopy, all three types of NPs appeared as bright fluorescent dots (Figure 2D). Remarkably, the brightness of DiI–F12 NPs was 22-fold larger than that of QDs of similar color (QD585, Figure 2E).

2.2. Cell Labeling by NPs

For labeling, the cells were incubated with NPs for 3 h at 37°C , followed by rinsing and transfer to chambered microscope slides. Then, the cells were imaged using three excitation/detection channels (displayed in blue, green, and red) corresponding to the DiO–F12, DiI–F12, and DiD–F12 NPs, using similar laser powers and detection sensitivities. In order to delimit the cells, they were additionally stained with the violet membrane probe F2N12SM^[24] (displayed in gray). In total, we tested our NPs on six cell lines: HeLa (studied the most extensively), KB, embryonic kidney (293T), astrocytoma

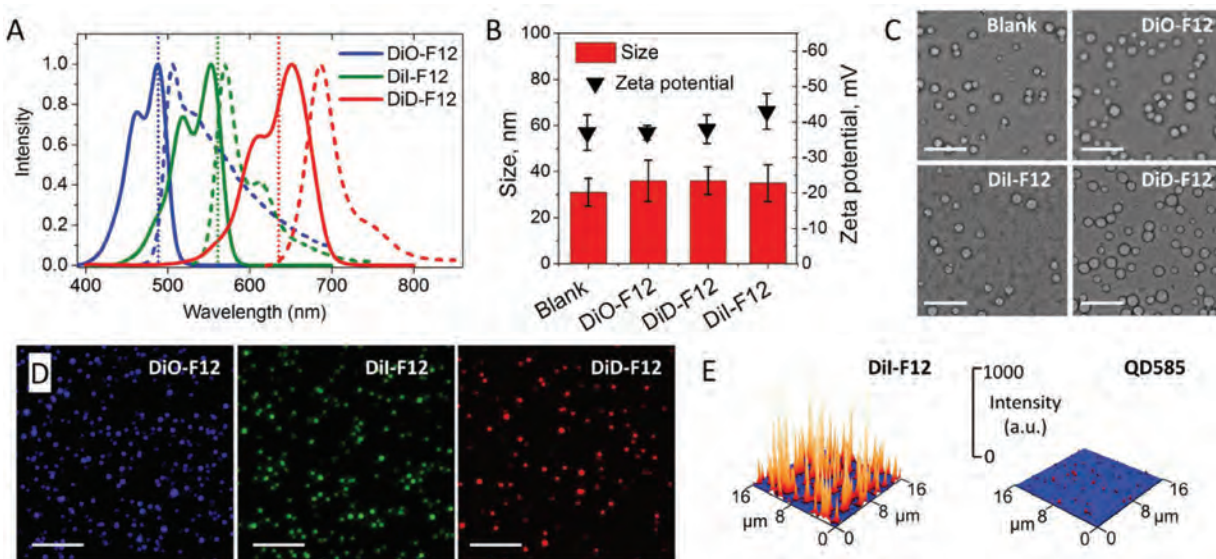


Figure 2. Properties of the three types of NPs loaded with the three cyanine dyes DiO, Dil, and DiD and the F12 counterion at $20 \times 10^{-3} \text{ M}$. A) Normalized absorption and fluorescence spectra of cyanine-loaded polymer NPs. B) Diameter based on TEM images and zeta potential of these NPs. The error bars are standard error of the mean ($n = 3$). C) Electron microscopy of blank and dye-loaded NPs. Scale bar is 200 nm. D) Wide-field fluorescence microscopy images of dye-loaded NPs. Scale bar is 5 μm . Illumination power was 1 W cm^{-2} at 488 nm (DiO-F12), 532 nm (Dil-F12), and 645 nm (DiD-F12). E) 3D representation of the fluorescence image of Dil-F12 NPs in comparison to quantum dots QD585. Excitation wavelength was 532 nm.

(U87), rat basophilic leukemia (RBL), and Chinese hamster ovary (CHO). Fluorescence microscopy revealed homogeneous staining of virtually all imaged cells (Figure 3A), and this phenomenon was observed for the three types of NPs in all six cell lines (Figures S4 and S5, Supporting Information). Moreover, the signal from the labeled cells was observed only in the corresponding blue, green, or red channel (Figure 3A), indicating minimal crosstalk of the channels. Finally, analysis of fluorescence images revealed similar intensities of the cells labeled with all three types of NPs (Figure S6, Supporting Information). Flow cytometry analysis confirmed the observed similar staining of cells by NPs of different colors and showed that practically all cells were labeled (Figure S7, Supporting Information). These results suggest that internalization of NPs is independent of the encapsulated dyes, in agreement with invariant sizes and surface properties of these NPs.

A closer look in the case of KB and HeLa cells (Figure 3B,C) revealed that after 24 h, the NPs were mainly located in the perinuclear regions in form of bright spots. This is in agreement with an endosomal entry of these NPs, as we have shown earlier for the same type of PLGA NPs loaded with a rhodamine dye.^[20] The observed high contrast between the perinuclear regions and the rest of the cells suggested minimal dye leaching from NPs even after 24 h of incubation. By contrast, when NPs were loaded with DiO perchlorate (i.e., without hydrophobic counterion), the images showed a diffuse fluorescence throughout the cell, probably due to leaching of the poorly encapsulated dye from the NPs (Figure S8, Supporting Information).

We then estimated the number of NPs per cell using two methods: (i) the fluorescence emission of labeled cells

was measured in suspension using a fluorometer and compared to the emission of solutions of the corresponding NPs of known concentrations (Figure S9, Supporting Information); (ii) the intensities of total fluorescence emission per cell were determined from confocal microscopy images at low magnification (20 \times objective) and compared to that of standard 200 nm beads (Figure S10, Supporting Information). The two methods gave remarkably close results, respectively, 9400 and 10 500 NPs per HeLa cell 24 h after labeling with $0.15 \times 10^{-9} \text{ M}$ of Dil-F12 NPs (0.002 g L^{-1} of polymer). The analyzed per cell fluorescence revealed a relatively narrow distribution of the number of NPs per cell (Figure S10, Supporting Information). Increasing the particle concentration to 0.45 and $1.5 \times 10^{-9} \text{ M}$ (corresponding to 0.006 and 0.02 g L^{-1} of polymer) led to an increase in the labeling intensity (Figure S11A, Supporting Information), corresponding to 23 000 and 45 000 NPs per cell.

Finally, according to MTT cell viability assay, the NPs did not show significant cytotoxicity after 72 h of incubation with HeLa cells at concentrations more than ten times those used for labeling (Figure S12, Supporting Information). Thus, our NPs can internalize equally well into all cells, independently of the encapsulated dye and display minimal crosstalk between the RGB channels, high stability, and low toxicity over extended periods of culture.

2.3. RGB Barcoding of Living Cells

The described unique properties of our NPs gave the possibility to label cells by a variety of color codes simply by incubating the cells with different mixtures of these NPs

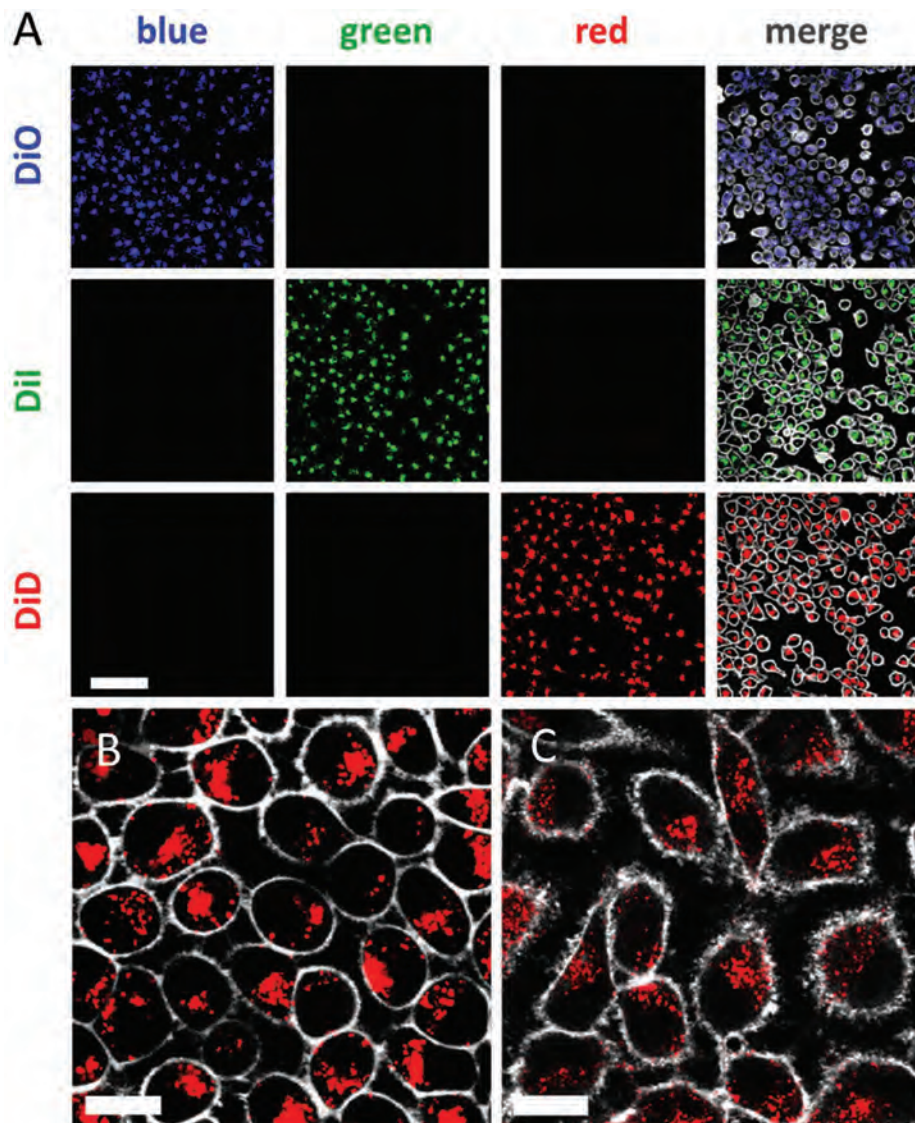


Figure 3. Fluorescence micrographs of cells incubated for 3 h with nanoparticles. A) KB cells labeled with DiO-F12 (top row), Dil-F12 (middle row), and DiD-F12 (bottom row) NPs. The images obtained in the different channels are shown (blue, green, and red). Merged images from all three channels are shown on the right; membrane staining is shown in gray. A 20 \times objective was used; scale bar is 100 μ m. Localization of DiD-F12 NPs in B) KB and C) HeLa cells. The membrane was labeled with F2N12SM. Before imaging, the cells were incubated with NPs for 3 h, rinsed, transferred into microscopy chambers and then incubated for 24 h. A 63 \times objective was used; scale bar is 20 μ m.

(**Figure 4**). For example, to achieve an orange labeling, we mixed DiI-F12 NPs and DiD-F12 NPs in a 0.25–0.75 ratio in Opti-MEM, followed by incubation for 3 h. After 24 h of culture, the labeled cells showed an intensity of the DiD channel about three times that of the DiI channel and negligible signal in the DiO channel (Figure 4B), so that the merged images yielded an orange color for all the imaged cells. Applying this procedure to different mixtures of NPs resulted in cell populations labeled homogeneously with 13 clearly distinguished colors (Figure 4C), while keeping all the instrumental and analysis setting identical. The colors of the individual cells were then analyzed quantitatively. Owing to the perinuclear localization of the NPs, each labeled cell appeared as a separate region of high density of dots, which facilitated greatly

an automated image analysis using an ImageJ macro (File S1, Supporting Information). The measured relative intensities of the three channels provided RGB barcodes for each cell, which were then represented in a ternary diagram of an RGB color triangle (Figure 4D). Analysis of over 2000 cells showed 13 well-separated populations, which implies robust color coding of live cells by at least 13 different barcodes. It should be noted that incubation of cells with a simple mixture of dyes (DiI and DiD) without nanoparticles resulted rather heterogeneous color code (Figure S13, Supporting Information). The latter could be explained by very poor solubility of these dyes in water, so that the aggregates of these dyes in water do not provide as homogeneous cell staining as PLGA NPs loaded with these dyes.

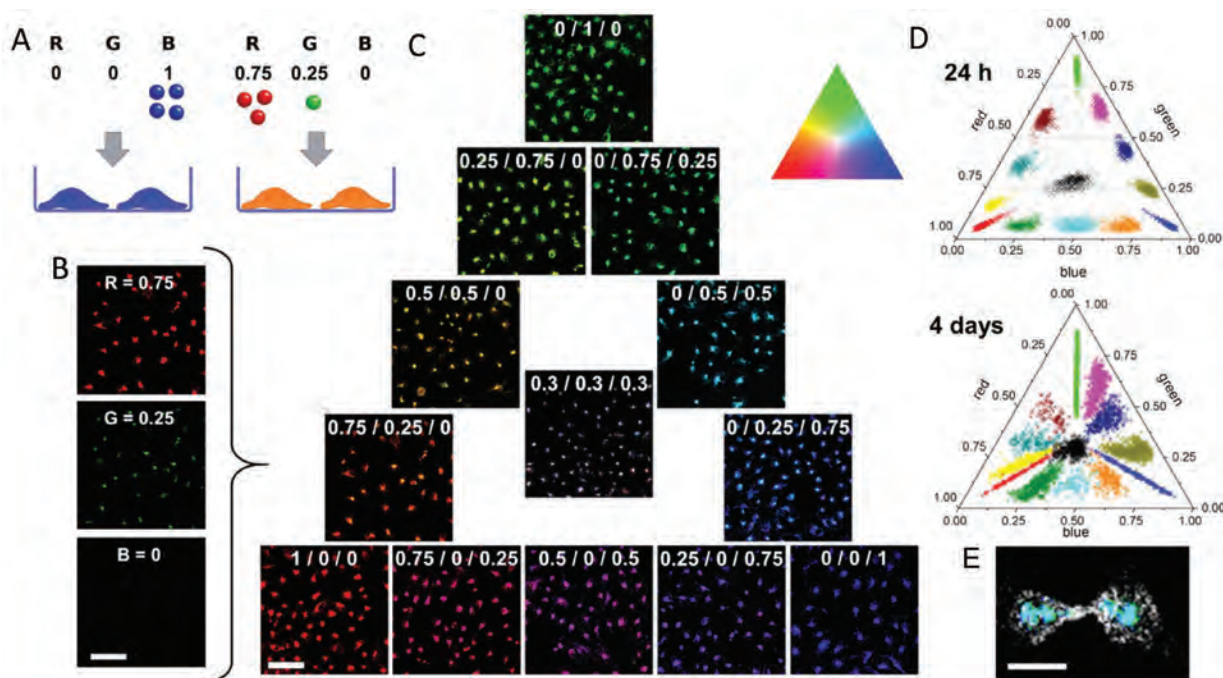


Figure 4. Multicolor labeling of HeLa cells. A) Principle of cell color coding by NPs. B) Example of cells labeled with orange: the images on the left show the three channels, and the single image in the color triangle corresponds to the superposition of the three. C) Images of cells after labeling with the different NP mixtures (13 colors). Scale bar is 100 μ m. D) Representation of the relative intensities of DiO (blue), Dil (green), and DiD (red) channels of individual cells in a ternary diagram at 1 and 4 d after labeling with 13 colors. The relative intensities were determined for about 200 cells per condition. Only the basic colors, red, green, and blue, are represented in these colors, and all other colors are false colors in order to facilitate the distinction of adjacent colors. E) Confocal image of selected dividing cell.

2.4. Transmission of RGB Barcode to Daughter Cells

When HeLa cells labeled with different colors were cultured separately for longer periods, the color of each cell population was preserved, so that 13 colors remained easily distinguishable at 4 d (lower part of Figure 4D) and even at 8 d (Figure S14, Supporting Information) after labeling. However, the decrease in the intensity of the signal produced some displacement of the color codes toward the center of the color triangle (Figure 4D). The preservation of the colors of cell populations after such long periods requires the NPs of different colors to be transmitted to the daughter cells in equal proportions. Indeed, in the observed cases of dividing cells (Figure 4E; Figure S15, Supporting Information), both daughter cells displayed very similar fluorescence intensities and identical RGB barcodes. On the other hand, this implies that the mean fluorescence intensity of individual cells should decrease twofold after each division, which ultimately limits the overall time over which RGB barcodes were detectable. Consistently, the mean number of NPs per cell, as determined from microscopy, was 10 500 after 1 d, 3300 after 3 d, and 600 after 7 d. Taking day 1 as the first cell generation, we could estimate that on days 3 and 7, we observed 2.7th and 5th generation of HeLa cells, which is a reasonable division rate (about 0.8 times per 24 h).

2.5. Distinguishing Mixed Populations of Cells by Color

When three cell populations labeled with NPs of different colors were mixed together, they could be easily distinguished after 1 d and even after 14 d of co-culture (Figure 5A,B). This result implied that the cells did not exchange their internalized NPs and thus did not mix the colors. The color mixing was also not observed for higher NP concentration (0.45×10^{-9} M), which enabled observation of distinct cell populations even after 19 d (Figure S16, Supporting Information). However, at the highest used concentration (1.5×10^{-9} M) the color mixing was detectable already after 24 h (Figure S11B, Supporting Information), which shows the upper concentration limit of this method. Then, we mixed seven populations of barcoded cells, and after 4 d, all of them were easily distinguishable both visually (Figure 5C) and as distinct regions in the color triangle (Figure S17, Supporting Information), which should enable their automatized identification. Strikingly, our method also worked to distinguish 13 barcoded cell populations co-cultured at least for 24 h (Figure S18, Supporting Information).

We then applied our labeling method to barcode six different cell lines: HeLa, KB, 293T, U87, RBL, and CHO cells. These cell lines were labeled with six different RGB barcodes and then either incubated separately or together by mixing in equal numbers for 24 h before imaging. Within the individual cell lines, the applied barcode was identical in all imaged

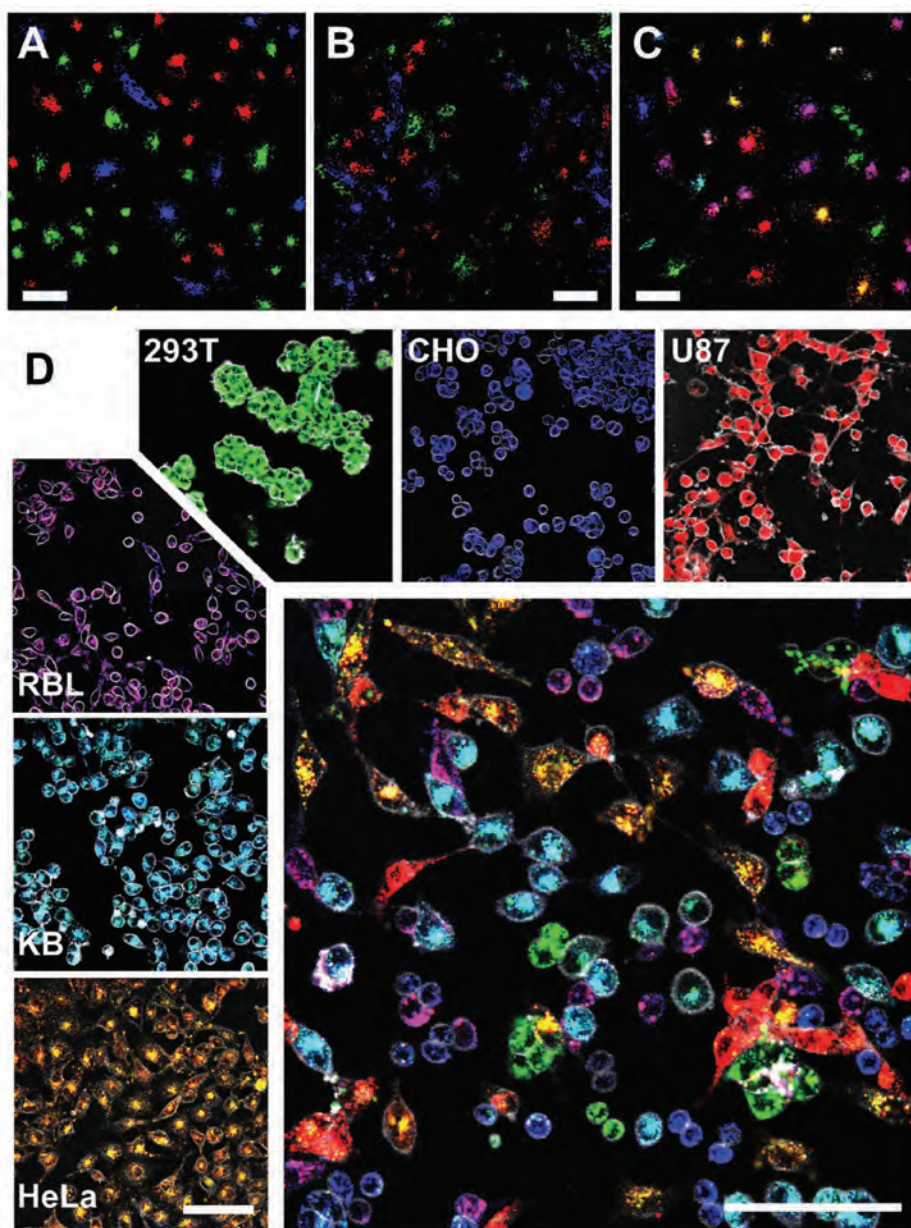


Figure 5. Co-culture of mixed RGB barcoded cell populations. A,B) Confocal image of a mixture of three cell populations labeled with the three different NPs, respectively, A) 1 d and B) 14 d after labeling. Scale bar is 60 μ m. C) Confocal image of a mixture of seven cell populations of different colors 4 d after labeling. D) The large micrograph shows a confocal image six cell types (HeLa, KB, 293T, U87, RBL, and CHO) mixed and co-cultured for 24 h. Each cell type was labeled with an RGB barcode (orange, cyan, green, red, magenta, and blue, respectively), also shown separately in the smaller images. Images are superpositions of the three NP channels with identical settings and of the membrane channel in gray. Scale bar is 100 μ m.

cells. In the mixture of cell lines, each cell type could be easily recognized by its color code as well as by its expected morphology (Figure 5D; Figure S19, Supporting Information).

2.6. Competition among Mixed Cell Populations after Drug Treatment

Finally, we used this method to distinguish the behavior of HeLa cells that underwent different doxorubicin treatments

in direct competition for adhesion to the surface. Six populations of HeLa cells, where individual color corresponded to the level of doxorubicin treatment, were seeded in chambered microscope slides for 4 h and then imaged at different heights from the surface (Figure S20, Supporting Information). We found that nontreated cells in green had an approximately equal relative distribution throughout the three imaged z -planes. However, HeLa cells that had undergone a doxorubicin treatment at low concentration (magenta) were significantly more present close to the surface and showed a

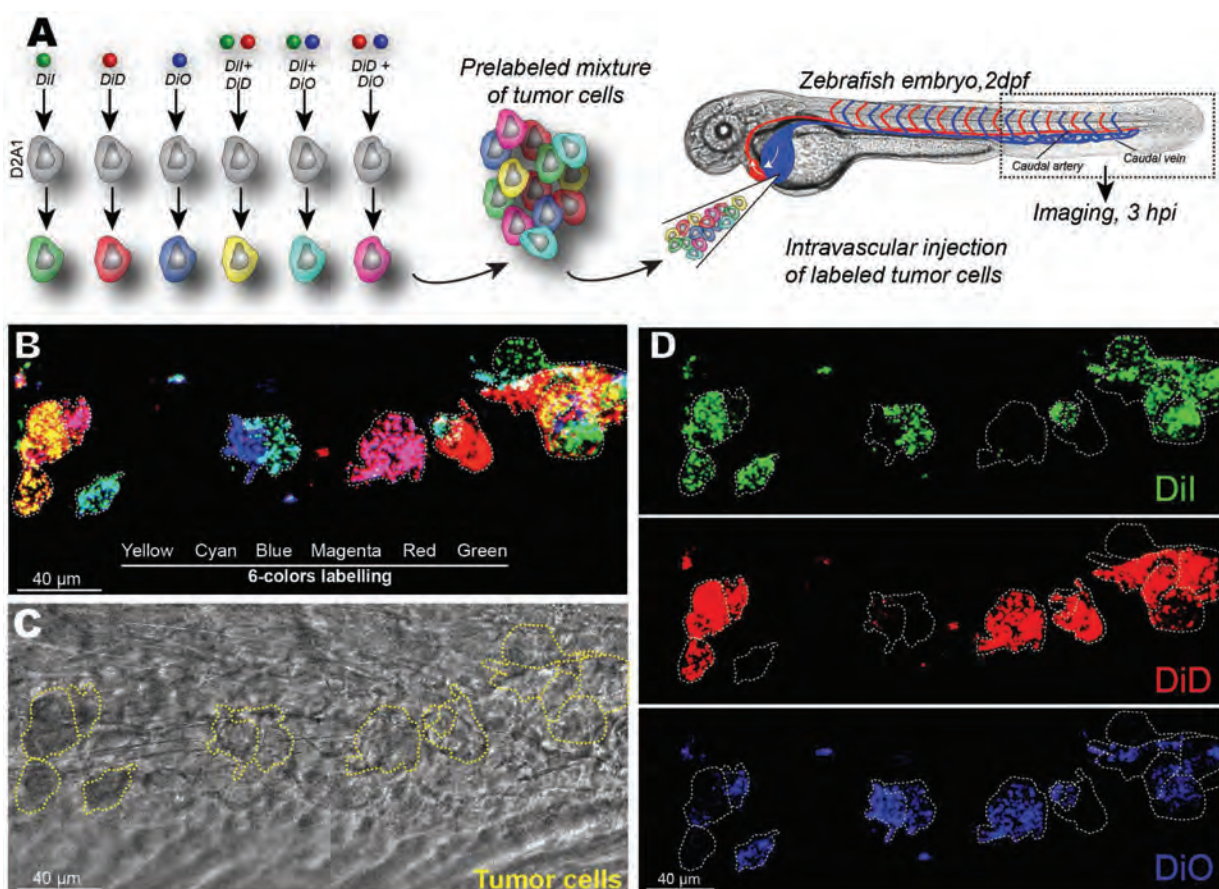


Figure 6. Tracking RGB barcoded cancer cells in zebrafish embryo. A) Experimental design: six batches of D2A1 cells were labeled with fluorescent NPs generating RGB barcodes (green, red, blue, yellow, magenta, and cyan). Labeled cells were then mixed and injected intravascularly in 2 dpf zebrafish embryos. B-D) Tumor cells that arrested in the vasculature are imaged, at 3 hpi, in the caudal plexus region of the zebrafish embryo. Clusters and individual cells can be found and distinguished based on their color.

more surface-spread morphology. By contrast, those treated with intermediate concentrations (blue) were relatively more abundant further away from the surface and showed rather rounded shapes at the surface. Higher doxorubicin concentrations decreased significantly the cell fraction at all studied distances from the surface, probably because of fast cell death and aggregation (Figure S21, Supporting Information).

2.7. Multicolor Tumor Cell Tracking in Living Animals

We then applied our color-coding approach to the tracking of tumor cells (D2A1, murine mammary carcinoma cells) directly in a living animal. To this end, six cell populations of tumor cells were labeled by distinct RGB barcodes of our NPs (Figure 6A) and then injected in the duct of Cuvier of zebrafish embryos (2 d postfertilization, 2 dpf) and imaged 3 h post-injection (3 hpi). Single cells and clusters of injected tumor cells can be found in the caudal plexus regions of the zebrafish embryo and are easily distinguishable based on their color (Figure 6B-D). Importantly, according to the images in three channels (Figure 6D) and the merged image (Figure 6B), all six colors are clearly defined without

appearance of other colors (except cases of cell overlap). This means that the RGB barcode is well preserved inside the cells without leakage in vivo.

2.8. Cell Tracking in the Developing Embryo

We further investigated the usefulness of our cell-labeling technology for developmental studies using zebrafish embryos. To do so, solutions of our NPs and NP mixtures were injected directly into the cytoplasm of distinct cells at the four- or eight-cell stage (Figure 7). Using this procedure, the NPs distributed homogeneously throughout the cytoplasm of the injected cells (Figure 7A,C), which was clearly different from cell staining through endocytosis (Figure 3B,C). After embryo development, populations of daughter cells of the same color code were observed for both three and six color staining protocols (Figure 6B,D). Again, even for the six color protocol, all colors could be readily identified, indicating minimal exchange of the NPs among the cells. These results showed that upon cell division, the NPs were equally shared by the daughter cells, leading to a homogeneous, bright staining of all cells derived from a given cell

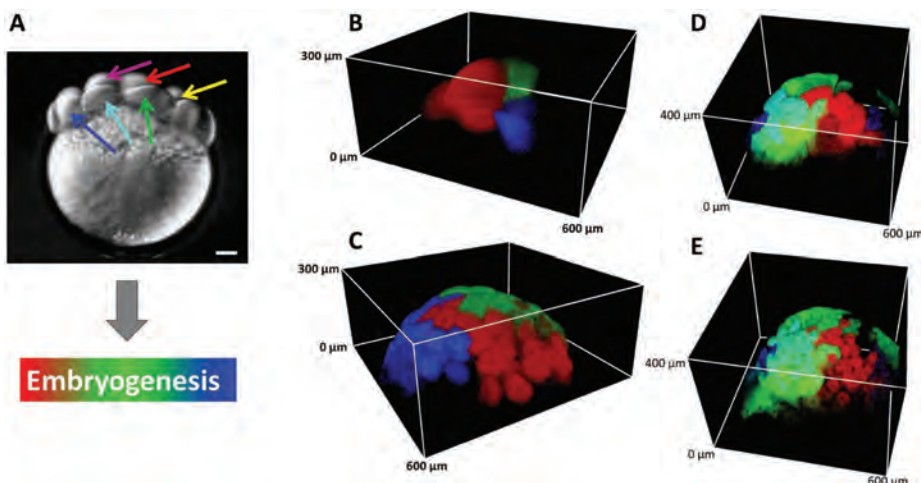


Figure 7. Imaging of the development of zebrafish embryos labeled by intracellular injection of fluorescent NPs. A) Scheme of experiment: multiple intracellular injections of NPs into eight-cell stage zebrafish embryos. Transmission image is shown; scale bar is 100 μ m. B,C) 3D reconstruction of embryos labeled with, respectively, DiO, Dil, and DiD NPs through microinjection inside the cytoplasm of three distinct cells at the four-cell stage imaged B) 30 min after injection and C) 80 min after injection. 3D reconstruction of embryos labeled with six NP mixtures (red: DiD NPs, green: Dil NPs, blue: DiO NPs, cyan: DiO NPs and Dil NPs, magenta: DiD NPs and DiO NPs, yellow: DiD NPs and Dil NPs) through microinjection inside the cytoplasm of six distinct cells at the eight-cell stage imaged D) 75 min after injection and E) 135 min after injection.

during embryonic morphogenesis. Labelling with our NPs thus provides an easy way of tracing the distribution of cells throughout the whole embryo for several hours, and this can be done for at least six cell populations simultaneously.

3. Discussion and Conclusions

For successful multicolor labeling of cells, we needed fluorescent NPs having three distinct absorption and emission colors, identical sizes, and surface properties. To achieve this, we designed polymer NPs loaded with hydrophobic cyanine dyes, DiO, Dil, and DiD, corresponding to the most frequently used laser lines. However, encapsulation of these cationic dyes with inorganic counterions (chloride or perchlorate) increased the size of the NPs, probably due to dye adsorption at the particle surface leading to neutralization of the particle negative charge, as we observed earlier with rhodamine derivatives.^[20] Remarkably, when these counterions were replaced by bulky hydrophobic counterions, no influence of the dye loading on the size of the NPs was observed. In this case, more hydrophobic dye salts are expected to form, which are better integrated into NPs. The identical size for different colors is a key advantage of our NPs compared to QDs, where color is directly linked to the size of the NPs.^[25] Moreover, bulky counterions significantly decreased ACQ of cyanines. F12 performed particularly well, especially for the longest dye DiD, probably because it isolates better the dyes from direct π -stacking.^[26] The F12 counterion thus allowed obtaining QYs of 14% for DiD at 20 m^{-3} loading, in contrast to only 2% for DID 4-chlorobenzenesulfonate^[27] and for DiD chloride at the same loading. The use of bulky counterions is probably a generic approach to better encapsulate and prevent ACQ of cationic dyes in polymer NPs, as the concept works for both cyanines and octadecyl rhodamine

B.^[20] Importantly, single particle measurements suggest that obtained Dil-F12 NPs are \approx 20-fold brighter than QDs. Taking into account the expected number of Dil-F12 dyes per NP (\approx 300), their extinction coefficient of 94 000 $\text{m}^{-1} \text{cm}^{-1}$ at 532 nm excitation and a fluorescence quantum yield of 0.15, the expected brightness is $300 \cdot 94\ 000 \cdot 0.15 = 4.2 \cdot 10^6 \text{ m}^{-1} \text{cm}^{-1}$. For QDs585, the brightness at 532 nm excitation is $2.1 \cdot 10^5 \text{ m}^{-1} \text{cm}^{-1}$, which is 20-fold lower than that of our Dil-F12 NPs. The other two types of NPs should present similar brightness, because of close values of their size, QY, and the extinction coefficients of the loaded dyes.

The optimized NPs showed efficient internalization into the cells within 3 h of incubation. The observed perinuclear localization of NPs in form of dots, especially in HeLa and KB cells, together with previous results on rhodamine-loaded PLGA NPs showing their lysosomal localization,^[20] suggests an endocytic pathway. As PLGA NPs biodegrade on the time scale of several months,^[28] they remain entrapped inside lysosomes similarly to other NPs,^[29] which enables their long-term imaging. Moreover, the perinuclear localization of the NPs facilitated greatly the automatic recognition of cells and the analysis of their color codes.

The simple incubation of cells with our NPs thus led to a bright, homogeneous, and long-term labeling of virtually all cells of a given population, and this for all the six different cell types tested. Owing to the same size and surface properties, NPs of three distinct colors exhibit similar internalization, so their mixing in different combinations enabled RGB coding of cells with at least 13 colors. Remarkably, each cell of the population received the same combination of RGB NPs and, therefore, the identical barcode. The behavior of our NPs is different from that reported for QDs, where stochastic combination of color codes was observed for cells within the same population.^[16b] Importantly, the color code generated by our NPs can be transmitted through many generations of

daughter cells. As every division decreases twice the number of NPs, the method can be used to track cell division, as it is done by the fluorescein-based probe CFSE,^[30] but in our case, multiple color codes can be used. Finally, multiple populations of cells bearing different RGB barcodes can be co-incubated together for weeks without signs of color mixing. Remarkably, the method works well even for a mixture of 13 barcoded cell populations, showing that it can be readily used to study complex multicellular systems. Although we did not test more than 13 barcodes, it is clear that the method could be further extended to a larger number of color codes.

The long-term color coding by NPs is suitable to study the organization and interactions of different cell types in complex co-cultures as was demonstrated on two examples. First, we showed that up to six different cell lines labeled with different colors could be readily distinguished in co-cultures. Second, it enabled monitoring competition within six cell populations differently treated by doxorubicin. Our observations suggest that at very small doxorubicin concentrations, the capacity of the cells to adhere could be similar or even higher than that of nontreated cells, while higher concentrations of the drug inhibit cell adherence. This experiment not only shows the effect of drug on the cell behavior, but it may also reveal the heterogeneous nature of the cells in culture.^[31] Indeed, whereas some fraction of the cells was killed by low concentrations ($0.2 - 10^{-6}$ M) of doxorubicin (Figure S20, Supporting Information), the surviving fraction showed excellent adhesion properties. Understanding the reasons for this heterogeneity and distinct adhesion behaviors of the drug-treated cells is outside the scope of this work. However, we showed that it is a powerful method to study multiple cell populations in direct contact and competition, and it enables new ways to test drugs, such as high-content screening.^[32]

The experiments performed in the zebrafish embryo showed that the new methodology of cell labeling allows also multiple applications *in vivo*. The first one relies on the fast and efficient fluorescent labeling of cells prior to transplantation *in vivo* to map up to six different cell populations and potentially track individual cells. Multicolor labeling of distinct populations of tumor cells should allow fine tracking of single population's behavior, where one could tune gene expression or metastatic abilities, for example. Such a protocol should be of choice to study invasion and metastasis of prelabeled tumor cells, and further assess drug resistance using intravital imaging.^[33] Second, we showed that NPs can be used to directly label cells *in vivo* with at least six different colors to follow individual cells and cell populations during embryonic development. Intracellular injection of NPs at the early developmental stage proved to be suitable to explore cell behavior in morphogenetic processes in zebrafish embryos and should be useful in other species as well, especially those not amenable to genetic engineering. The high brightness of our NPs and their homogenous distribution in the cytosol after intracellular microinjection ensure high performance in terms of signal-to-noise ratio and spatial and temporal resolution in large 3D field of views.

Compared to RGB coding of cells by fluorescent proteins, as, for instance, realized by Brainbow,^[6] our method, based

on fluorescent NPs, presents several important features: (i) it does not require genetic modification; (ii) it is extremely easy, fast, and can, in principle, operate in any cell type, and the brightness of labeling can be tuned much easier compared to fluorescent proteins in rainbow-type animals. The fast labeling without genetic modification is particularly promising to study primary cell cultures. It is also important in early embryogenesis studies, where multiple division cycles take places within hours.^[34] In our method, a given cell population bears an identical RGB barcode, whereas Brainbow labeling generates a variety of color codes within the same population. Thus, these two methods are complementary. In the method presented here, cell division leads to a reduction of the number of NPs per cell, which ultimately limits the observation time in rapidly dividing cells (like HeLa). Nevertheless, by optimizing the NPs' concentration we could detect labeled HeLa cells for at least 19 d. This is significantly longer than the 1 week labeling reported earlier for QDs,^[5b] probably because our NPs are much brighter. Moreover, in contrast to the stochastic distribution of colors within the same labeled population using QDs,^[16b] our approach generates a uniform color code within the same population stable throughout multiple generations. Finally, our NP-based method is advantageous over direct cell labeling by dyes (1). Cell trackers work efficiently only for a few days.^[12] Encapsulation of dyes inside NPs, on the other hand, prevents dye leakage from cells and prolongs staining for weeks. This feature minimizes the loss of staining and enables co-culture of multiple cell populations with different barcodes with minimized exchange of colors (2). It features homogeneous cell staining, while classical dyes, like DiD or CellVue Claret (PKH type), provide rather heterogeneous cell staining because of their poor water solubility.^[35] Therefore, as we observed in this work, simple mixing of two different dyes (DiI and DiD) does not generate a homogeneous color code within the same cell population. All these points probably explain why organic dyes have never been used, to date, to generate multiple color codes transmittable to daughter cells. The only examples are limited to color coding of fixed cells.^[36] Thus, the proposed method of multicolor coding, being complementary to Brainbow, does not have analogs in literature and opens the way to a variety of applications related to long-term cell tracking *in vitro* and *in vivo*.

Finally, this work provides new insights into interfacing nanotechnology and biology. Rather than creating complex multimodal nanoparticles bearing simultaneously multiple functions, we propose to implement different functions/modalities (colors in our case) separately into "homologous" nanoparticles of identical size and surface properties. The latter ensure their identical delivery into live cells, where these NPs can then combine forces to perform sophisticated tasks.

4. Experimental Section

Synthesis of Dye Salt: DiI-Cl and DiD-Cl were synthesized according to a previously described procedure.^[37] Synthesis of all ion pairs of cyanine dyes with tetraphenyl borate counterions

was done by ion exchange of corresponding dye chloride with a borate salt in dichloromethane followed by purification by column chromatography. The details are described in the Supporting Information.

Preparation of Fluorescent NPs: PLGA (lactide:glycolide, 1:1, mole:mole, $M_n = 24\,000$) was dissolved at 2 mg mL⁻¹ in acetonitrile containing different amounts of dye. These solutions were added quickly and under stirring (shaking) using a micropipette to a ten-fold volume excess of 20 10⁻³ M phosphate buffer at pH 7.4. The particle solution was then quickly diluted fivefold with the same buffer.

Characterization of NPs: Dynamic light scattering (DLS) measurements were performed on a Zetasizer Nano series DTS 1060 (Malvern Instruments S.A.). Electron microscopy was performed on a Philips CM120 transmission electron microscope. Absorption and emission spectra were recorded on a Cary 400 Scan ultraviolet-visible spectrophotometer (Varian) and a FluoroMax-4 spectrophotometer (Horiba Jobin Yvon) equipped with a thermostated cell compartment, respectively. QYs were calculated using rhodamine B in methanol^[38] (QY = 0.7) for Dil series, fluorescein in 0.1 M NaOH^[39] (QY = 0.92) for DiO series and DiD in MeOH^[40] (QY = 0.33) for DiD series.

Cell Labeling: For labeling, cells were seeded in six-well plates at 200 000 cells per well (21 000 cells cm⁻²) or at 500 000 cells per well in 25 cm² cell culture flasks (20 000 cells cm⁻²). After letting the cells adhere for 18 h, the cell culture medium was removed, and the cells were rinsed twice with opti-MEM, followed by incubation with a freshly prepared solution of the NPs (0.15 10⁻⁹ M in particles, 2.5 mL for six-well plates, 10 mL for 25 cm² cell culture flasks). NP suspensions for cell labeling were prepared starting from stock solutions in 20 10⁻³ M phosphate buffer at a pH of 7.4 with a particle concentration of 3 10⁻⁹ M (0.04 g L⁻¹ of polymer). Depending on the desired color, the stock solutions were mixed in the needed proportions (e.g., DiO:Dil:DiD 1:0:0 for “blue” or 0.5:0.5:0 for “cyan”) and diluted in opti-MEM to a concentration of 0.15 10⁻⁹ M (0.002 g L⁻¹ of polymer). After 3 h of incubation, the NP suspension was removed, and the cells were rinsed first with opti-MEM, then with phosphate buffered saline (PBS), and finally with the corresponding cell culture medium.

The resulting cells were then either cultured for longer periods, mixed, or transferred for imaging. For transfer or mixing, the wells were rinsed twice with PBS followed by incubation for 2–5 min with 0.4 mL of trypsin at 37 °C, and collection of the detached cells in 3 mL of the corresponding medium. After centrifugation and redispersion in 1–5 mL of medium (depending on the obtained number of cells), the cells were counted. For mixing of different cell populations, equal numbers of cells were combined in a centrifugation tube and thoroughly mixed before further use (for example “blue,” “green,” and “red” cells or HeLa, KB, and CHO cells). For imaging, the cells, after the desired labeling, mixing, and time of culture, were seeded in LabTek 8 well plates at 60 000 cells per well and left to adhere for at least 18 h.

Confocal Microscopy: Fluorescence imaging of the cells in chambered microscope slides (LabTek or Ibidi eight-well plates) was performed on a Leica TSC SPE confocal microscope using either a 20 air objective or a 63 oil immersion objective. The different channels were recorded as follows: excitation 405 nm, emission recorded from 430 to 480 nm; excitation 488 nm, emission recorded from 495 to 560 nm; excitation 561 nm, emission

recorded from 570 to 610 nm; and excitation 635 nm, emission recorded from 650 to 750 nm. The power of the 405 nm laser was adjusted as needed. The power of the 488, 561, and 635 nm lasers was set either to 10% or to 20% of the nominal power (same for all three), and the gain and offset were set to the same value for all three. Three successive sequences were recorded for each image.

Image Analysis: Image analysis was performed using the Fiji software and, for data analysis, the R software. The three consecutive images were averaged for each channel. The intensity levels were set to the same levels for the three NP channels for all images presented here. An ImageJ macro was programmed to determine automatically the colors of the individual cells (macro code can be found in the Supporting information). Briefly, the macro combines the intensities from the three NP channels in a single grayscale image. This image was then used to detect the locations of the individual cells and so to create a mask, which allows measuring the intensities of the three channels for each individual cell. The intensities were then normalized to 1 in order to obtain the RGB barcode of each cell.

Tracking Cancer Cells in Zebrafish Embryos: Wild-type *golden* zebrafish embryos (48 h postfertilization (hpf)) were anesthetized in Danieau containing 650 10⁻⁶ M tricain and mounted in 0.8% low melting point agarose. Meanwhile, unlabeled D2A1 cells (murine mammary carcinoma cells) were cultured in six-well plates and incubated for 3 h at 37 °C/5% CO₂ with NPs (2 mg L⁻¹) of different colors and their one-to-one mixtures (red: DiD NPs; green: Dil NPs; blue: DiO NPs; cyan: DiO NPs and Dil NPs; magenta: DiD NPs and DiO NPs; yellow: DiD NPs and Dil NPs) before being trypsinized. A mixture of RGB barcoded cells at equal quantities was prepared at a concentration of 100 10⁶ M mL⁻¹. Embryos were injected under a stereomicroscope (LEICA M205 FA) equipped with a fluorescence module. The mixture of barcoded cells was loaded in a microforged glass capillary, and 18 nL of the mixture was injected in the duct of Cuvier of the embryos using a microinjector (Nanoject, Drummond). Injected embryos were then imaged at 3 h postinjection using a confocal microscope (Leica TCS SP5, 25X/ON 0.95 N.A. water immersion objective).

Labeling and Imaging Early Zebrafish Embryos: Wild-type *Danio rerio* (zebrafish) embryos were reared and staged as described elsewhere.^[34b] Embryos were collected at the one-cell stage and kept in embryo medium at 28.5 °C until the desired stage.^[34a] Intracellular injection at the four-cell or eight-cell stage was performed into chorionated embryos with solutions of DiO, Dil, and DiD NPs or one-to-one mixtures to generate three or six RGB barcodes (red: DiD NPs, green: Dil NPs, blue: DiO NPs, cyan: DiO NPs and Dil NPs, magenta: DiD NPs and DiO NPs, yellow: DiD NPs and Dil NPs), all at global NP concentrations of 0.2 g L⁻¹. The injected volume was about 1 nL per cell. Injected embryos were immediately mounted in a 3 cm Petri dish with a glass coverslip bottom, sealing a hole of 0.5 mm at the dish center, where a Teflon tore (ALPHAnov) with a hole of 780 μm received the dechorionated embryo. The embryo was maintained and properly oriented (animal pole up) by infiltrating around it 0.5% low-melting-point agarose (Sigma) in embryo medium as described elsewhere.^[34b] 3D+time imaging was performed with a Zeiss LSM780 confocal upright microscope with a high numerical aperture, water dipping lens objective (either 20 or 25) for up to 12 h. Temperature control was achieved with the Okolab chamber (26 °C in the Petri dish). All the investigations using the zebrafish model were carried

out in compliance with the European and international guidelines on animal welfare (Directive 2010/63/EU).

Supporting Information

Supporting Information is available from the Wiley Online Library or from the author.

Acknowledgements

This work was supported by the European Research Council ERC Consolidator grant BrightSens 648528. B.A. was supported by LabEx Chimie des Systèmes Complexes. G.F. was supported by La Ligue Contre le Cancer. The authors thank Y. Mely and P. Didier for providing access to wide-field fluorescence microscopy and C. Ruhmann for help with electron microscopy. The authors also thank Romain Vauchelles for help with image analysis using the ImageJ software and Claudine Ebel for help with flow cytometry. The authors are very much grateful to Francesca PERI (EMBL) and Kerstin RICHTER (EMBL) for providing zebrafish embryos. The authors thank the BioEmergences platform and FBI ANR-10-INBS-04 for injections and 3D+time imaging.

Conflict of Interest

The authors declare no conflict of interest.

- [1] a) J. H. Gao, H. W. Gu, B. Xu, *Acc. Chem. Res.* **2009**, *42*, 1097; b) D. E. Lee, H. Koo, I. C. Sun, J. H. Ryu, K. Kim, I. C. Kwon, *Chem. Soc. Rev.* **2012**, *41*, 2656; c) N. Lee, D. Yoo, D. Ling, M. H. Cho, T. Hyeon, J. Cheon, *Chem. Rev.* **2015**, *115*, 10637; d) S. K. Yen, D. Janczewski, J. L. Lakshmi, S. Bin Dolmanan, S. Tripathy, V. H. B. Ho, V. Vijayaraghavan, A. Hariharan, P. Padmanabhan, K. K. Bhakoo, T. Sudhaharan, S. Ahmed, Y. Zhang, S. T. Selvan, *ACS Nano* **2013**, *7*, 6796; e) H. M. Kim, H. Lee, K. S. Hong, M. Y. Cho, M. H. Sung, H. Poo, Y. T. Lim, *ACS Nano* **2011**, *5*, 8230.
- [2] a) E. K. Lim, T. Kim, S. Paik, S. Haam, Y. M. Huh, K. Lee, *Chem. Rev.* **2015**, *115*, 327; b) C. M. Spillmann, J. Naciri, W. R. Algar, I. L. Medintz, J. B. Delehanty, *ACS Nano* **2014**, *8*, 6986.
- [3] a) A. Wagh, F. Jyoti, S. Mallik, S. Qian, E. Leclerc, B. Law, *Small* **2013**, *9*, 2129; b) Y. W. C. Cao, R. C. Jin, C. A. Mirkin, *Science* **2002**, *297*, 1536; c) G. Wang, Y. K. Leng, H. J. Dou, L. Wang, W. W. Li, X. B. Wang, K. Sun, L. S. Shen, X. L. Yuan, J. Y. Li, J. S. Han, H. S. Xiao, Y. Li, *ACS Nano* **2013**, *7*, 471; d) S. Giri, E. A. Sykes, T. L. Jennings, W. C. W. Chan, *ACS Nano* **2011**, *5*, 1580.
- [4] a) Z. Cheng, A. Al Zaki, J. Z. Hui, V. R. Muzykantov, A. Tsourkas, *Science* **2012**, *338*, 903; b) P. D. Howes, R. Chandrawati, M. M. Stevens, *Science* **2014**, *346*, 1247390.
- [5] a) A. Taylor, K. M. Wilson, P. Murray, D. G. Fernig, R. Levy, *Chem. Soc. Rev.* **2012**, *41*, 2707; b) J. K. Jaiswal, H. Matoussi, J. M. Mauro, S. M. Simon, *Nat. Biotechnol.* **2003**, *21*, 47; c) T. J. Wu, Y. K. Tzeng, W. W. Chang, C. A. Cheng, Y. Kuo, C. H. Chien, H. C. Chang, J. Yu, *Nat. Nanotechnol.* **2013**, *8*, 682; d) K. M. Dupont, K. Sharma, H. Y. Stevens, J. D. Boerckel, A. J. Garcia, R. E. Guldberg, *Proc. Natl. Acad. Sci. USA* **2010**, *107*, 3305.
- [6] a) J. Livet, T. A. Weissman, H. N. Kang, R. W. Draft, J. Lu, R. A. Bennis, J. R. Sanes, J. W. Lichtman, *Nature* **2007**, *450*, 56; b) D. Cai, K. B. Cohen, T. Luo, J. W. Lichtman, J. R. Sanes, *Nat. Methods* **2013**, *10*, 540.
- [7] a) J. P. Card, O. Kobiler, J. McCambridge, S. Ebdahad, Z. Y. Shan, M. K. Raizada, A. F. Sved, L. W. Enquist, *Proc. Natl. Acad. Sci. USA* **2011**, *108*, 3377; b) D. Hadjieconomou, S. Rotkopf, C. Alexandre, D. M. Bell, B. J. Dickson, I. Salecker, *Nat. Methods* **2011**, *8*, 260; c) S. Hampel, P. Chung, C. E. McKellar, D. Hall, L. L. Looger, J. H. Simpson, *Nat. Methods* **2011**, *8*, 253.
- [8] Y. A. Pan, T. Freundlich, T. A. Weissman, D. Schoppik, X. C. Wang, S. Zimmerman, B. Ciruna, J. R. Sanes, J. W. Lichtman, A. F. Schier, *Development* **2013**, *140*, 2835.
- [9] N. Di Girolamo, S. Bobba, V. Raviraj, N. C. Delic, I. Slapetova, P. R. Nicovich, G. M. Halliday, D. Wakefield, R. Whan, J. G. Lyons, *Stem Cells* **2015**, *33*, 157.
- [10] J. W. Wu, R. Turcotte, C. Alt, J. M. Runnels, H. Tsao, C. P. Lin, *Sci. Rep.* **2016**, *6*, 24303.
- [11] C. R. Parish, *Immunol. Cell Biol.* **1999**, *77*, 499.
- [12] S. K. Lee, M. S. Han, C. H. Tung, *Small* **2012**, *8*, 3315.
- [13] a) O. S. Wolfbeis, *Chem. Soc. Rev.* **2015**, *44*, 4743; b) S. Liu, L. M. Tay, R. Anggara, Y. J. Chuah, Y. Kang, *ACS Appl. Mater. Interfaces* **2016**, *8*, 11925.
- [14] a) Y. Yu, C. Feng, Y. Hong, J. Liu, S. Chen, K. M. Ng, K. Q. Luo, B. Z. Tang, *Adv. Mater.* **2011**, *23*, 3298; b) D. Ding, D. Mao, K. Li, X. M. Wang, W. Qin, R. R. Liu, D. S. Chiam, N. Tomczak, Z. M. Yang, B. Z. Tang, D. L. Kong, B. Liu, *ACS Nano* **2014**, *8*, 12620.
- [15] a) S. Rana, N. D. B. Le, R. Mout, K. Saha, G. Y. Tonga, R. E. S. Bain, O. R. Miranda, C. M. Rotello, V. M. Rotello, *Nat. Nanotechnol.* **2015**, *10*, 65; b) M. Y. Han, X. H. Gao, J. Z. Su, S. Nie, *Nat. Biotechnol.* **2001**, *19*, 631; c) K. Ming, J. Kim, M. J. Biondi, A. Syed, K. Chen, A. Lam, M. Ostrowski, A. Rebbapragada, J. J. Feld, W. C. W. Chan, *ACS Nano* **2015**, *9*, 3060.
- [16] a) L. C. Mattheakis, J. M. Dias, Y. J. Choi, J. Gong, M. P. Bruchez, J. Q. Liu, E. Wang, *Anal. Biochem.* **2004**, *327*, 200; b) P. Rees, J. W. Wills, M. R. Brown, J. Tonkin, M. D. Holton, N. Hondow, A. P. Brown, R. Brydson, V. Millar, A. E. Carpenter, H. D. Summers, *Nat. Methods* **2014**, *11*, 1177.
- [17] H. D. Summers, P. Rees, M. D. Holton, M. R. Brown, S. C. Chappell, P. J. Smith, R. J. Errington, *Nat. Nanotechnol.* **2011**, *6*, 170.
- [18] a) K. Li, B. Liu, *Chem. Soc. Rev.* **2014**, *43*, 6570; b) A. Reisch, A. S. Klymchenko, *Small* **2016**, *12*, 1968.
- [19] a) J. Chen, P. Zhang, G. Fang, P. Yi, F. Zeng, S. Wu, *J. Phys. Chem. B* **2012**, *116*, 4354; b) J. Chen, F. Huang, H. Wang, Y. Li, S. Liu, P. Yi, *J. Appl. Polym. Sci.* **2015**, *132*, 41492.
- [20] A. Reisch, P. Didier, L. Richert, S. Oncul, Y. Arntz, Y. Mely, A. S. Klymchenko, *Nat. Commun.* **2014**, *5*, 4089.
- [21] A. Reisch, A. Runser, Y. Arntz, Y. Mely, A. S. Klymchenko, *ACS Nano* **2015**, *9*, 5104.
- [22] a) M. Cametti, B. Crousse, P. Metrangolo, R. Milani, G. Resnati, *Chem. Soc. Rev.* **2012**, *41*, 31; b) I. T. Horváth, *Acc. Chem. Res.* **1998**, *31*, 641.
- [23] Y. N. Hong, J. W. Y. Lam, B. Z. Tang, *Chem. Soc. Rev.* **2011**, *40*, 5361.
- [24] R. Kreder, S. Oncul, O. A. Kucherak, K. A. Pyrshev, E. Real, Y. Mely, A. S. Klymchenko, *RSC Adv.* **2015**, *5*, 22899.
- [25] a) A. P. Alivisatos, *Science* **1996**, *271*, 933; b) I. L. Medintz, H. T. Uyeda, E. R. Goldman, H. Mattossi, *Nat. Mater.* **2005**, *4*, 435.
- [26] I. Shulov, S. Oncul, A. Reisch, Y. Arntz, M. Collot, Y. Mely, A. S. Klymchenko, *Nanoscale* **2015**, *7*, 18198.
- [27] A. Wagh, S. Y. Qian, B. Law, *Bioconjugate Chem.* **2012**, *23*, 981.
- [28] N. Samadi, A. Abbadessa, A. Di Stefano, C. F. van Nostrum, T. Vermonden, S. Rahimian, E. A. Teunissen, M. J. van Steenbergen, M. Amidi, W. E. Hennink, *J. Controlled Release* **2013**, *172*, 436.
- [29] G. Sahay, D. Y. Alakhova, A. V. Kabanov, *J. Controlled Release* **2010**, *145*, 182.

[30] A. B. Lyons, C. R. Parish, *J. Immunol. Methods* **1994**, *171*, 131.

[31] a) B. Snijder, R. Sacher, P. Ramo, E. M. Damm, P. Liberali, L. Pelkmans, *Nature* **2009**, *461*, 520; b) B. Snijder, L. Pelkmans, *Nat. Rev. Mol. Cell Biol.* **2011**, *12*, 119.

[32] F. Zanella, J. B. Lorens, W. Link, *Trends Biotechnol.* **2010**, *28*, 237.

[33] R. White, K. Rose, L. Zon, *Nat. Rev. Cancer* **2013**, *13*, 624.

[34] a) C. B. Kimmel, W. W. Ballard, S. R. Kimmel, B. Ullmann, T. F. Schilling, *Dev. Dyn.* **1995**, *203*, 253; b) E. Faure, T. Savy, B. Rizzi, C. Melani, O. Stasova, D. Fabreges, R. Spir, M. Hammons, R. Cunderlik, G. Recher, B. Lombardot, L. Duloquin, I. Colin, J. Kollar, S. Desnoulez, P. Affaticati, B. Maury, A. Boyreau, J. Y. Nief, P. Calvat, P. Vernier, M. Frain, G. Lutfalla, Y. Kergosien, P. Suret, M. Remesikova, R. Doursat, A. Sarti, K. Mikula, N. Peyreras, P. Bourgine, *Nat. Commun.* **2016**, *7*, 8674.

[35] M. Collot, R. Kreder, A. L. Tatarets, L. D. Patsenker, Y. Mely, A. S. Klymchenko, *Chem. Commun.* **2015**, *51*, 17136.

[36] P. O. Krutzik, G. P. Nolan, *Nat. Methods* **2006**, *3*, 361.

[37] X. J. Peng, Z. G. Yang, J. Y. Wang, J. L. Fan, Y. X. He, F. L. Song, B. S. Wang, S. G. Sun, J. L. Qu, J. Qi, M. Yang, *J. Am. Chem. Soc.* **2011**, *133*, 6626.

[38] R. A. Velapoldi, H. H. Tønnesen, *J. Fluoresc.* **2004**, *14*, 465.

[39] D. Magde, R. Wong, P. G. Seybold, *Photochem. Photobiol.* **2002**, *75*, 327.

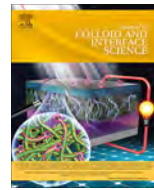
[40] I. Texier, M. Goutayer, A. Da Silva, L. Guyon, N. Djaker, V. Josserand, E. Neumann, J. Bibette, F. Vinet, *J. Biomed. Opt.* **2009**, *14*, 054005.

Received: May 14, 2017

Revised: June 26, 2017

Published online: August 9, 2017

**ANNEX 7: WRAPPED STELLATE SILICA NANOCOMPOSITES AS
BIOCOMPATIBLE LUMINESCENT NANOPARTICLES ASSESSED IN VIVO**



Regular Article

Wrapped stellate silica nanocomposites as biocompatible luminescent nanoplatforms assessed *in vivo*

Francis Perton ^a, Sébastien Harlepp ^b, Gautier Follain ^b, Ksenia Parkhomenko ^c, Jacky G. Goetz ^b,
Sylvie Bégin-Colin ^{a,*}, Damien Mertz ^{a,*}

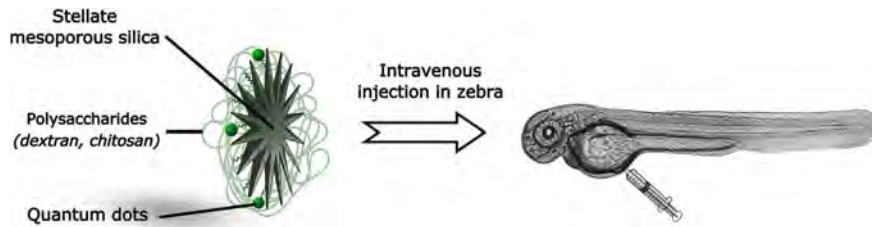
^a Institut de Physique et Chimie des Matériaux de Strasbourg (IPCMS), UMR-7504, CNRS-Université de Strasbourg, 23 rue du Loess, BP 34 67034, Strasbourg Cedex 2, France

^b INSERM UMR_S1109, Tumor Biomechanics, Strasbourg, Université de Strasbourg, Fédération de Médecine Translationnelle de Strasbourg (FMTS), 67000 Strasbourg, France

^c Institut de Chimie et Procédés pour l'Énergie l'Environnement et la Santé, 25 rue Becquerel, 67087 Strasbourg, France



GRAPHICAL ABSTRACT



ARTICLE INFO

Article history:

Received 24 October 2018

Revised 14 January 2019

Accepted 22 January 2019

Available online 23 January 2019

Keywords:

Stellate mesoporous silica
Quantum dots
Isobutyramide binders
Protective coatings
Polysaccharide shell
Cell viability
Zebrafish
In vivo cell tracking

ABSTRACT

The engineering of luminescent nanoplatforms for biomedical applications displaying ability for scaling-up, good colloidal stability in aqueous solutions, biocompatibility, and providing an easy detection *in vivo* by fluorescence methods while offering high potential of functionalities, is currently a challenge. The original strategy proposed here involves the use of large pore (*ca.* 15 nm) mesoporous silica (MS) nanoparticles (NPs) having a stellate morphology (denoted STMS) on which fluorescent InP/ZnS quantum dots (QDs) are covalently grafted with a high yield ($\geq 90\%$). These nanoplatforms are after that further coated to avoid a potential QDs release. To protect the QDs from potential release or dissolution, two wrapping methods are developed: (i) a further coating with a silica shell having small pores (≤ 2 nm) or (ii) a tight polysaccharide shell deposited on the surface of these STMS@QDs particles via an original isobutyramide (IBAM)-mediated method. Both wrapping approaches yield to novel luminescent nanoplatforms displaying a highly controlled structure, a high size monodispersity (*ca.* 200 and 100 nm respectively) and colloidal stability in aqueous solutions. Among both methods, the IBAM-polysaccharide coating approach is shown the most suitable to ensure QDs protection and to avoid metal cation release over three months. Furthermore, these original STMS@QDs@polysaccharide luminescent nanoplatforms are shown biocompatible *in vitro* with murine cancer cells and *in vivo* after injections within zebrafish (ZF) translucent embryos where no sign of toxicity is observed during their development over several days. As assessed by *in vivo* confocal microscopy imaging, these nanoplatforms are shown to rapidly extravasate from blood circulation to settle in neighboring tissues, ensuring a remanent fluorescent labelling of ZF tissues *in vivo*. Such fluorescent and hybrid STMS composites are envisioned as novel luminescent nanoplatforms for *in vivo* fluorescence tracking applications and offer a versatile degree of additional functionalities (drug delivery, incorporation of magnetic/plasmonic core).

© 2019 Elsevier Inc. All rights reserved.

* Corresponding authors.

E-mail addresses: sylvie.begin@ipcms.unistra.fr (S. Bégin-Colin), damien.mertz@ipcms.unistra.fr (D. Mertz).

1. Introduction

Despite the low cost of fluorescent molecular dyes such as fluorescein, one major issue with their use is their limited photostability (photobleaching) and their broad emission spectra that may lead to fluorescence overlapping [1]. Quantum dots (QDs) are a suitable alternative to molecular dyes because of their higher quantum efficiency, long-term photostability, and finely tunable narrow emission fluorescence [2]. However, the most efficient QDs are made of CdSe or InP/ZnS nanoparticles (NPs) and thus contain toxic elements. The non- or limited release of heavy metals such as cadmium or indium is highly required for their use as biosensors for biological issues as well as for environmental applications for example, to detect pollutants or to follow the path of effluents. The strategy proposed here is to ensure a strong anchoring of QDs on a suitable silica support and then to encapsulate such hierarchical clusters within a protective and biocompatible matrix to avoid the release of toxic cations with the aim to apply such nanoclusters for biological applications as for example the fluorescent labelling of tissues *in vivo*, which will be demonstrated here.

Since two decennia, the development of multifunctional nanostructures made of non-porous and mesoporous silica (MS) encapsulating plasmonic, magnetic or luminescent inorganic cores has attracted a huge interest for a broad range of applications such as catalysis, energy and drug delivery [3–8]. Various core-shells, constituted of gold, magnetic NPs, or QDs as the core and encapsulated within silica, have been investigated because of the great chemical stability and biocompatibility of silica. The coating of inorganic nanocrystals with non-porous silica shells were essentially developed as protective shells to prevent inorganic core from potential oxidation or dissolution and it affords a high colloidal stability in water [6]. It was usually done according to two methods: the well-known classical sol-gel (Stöber) process mostly developed for water soluble inorganic crystals [9–11] and the reverse (or water in oil (w/o)) emulsion, suitable for inorganic NPs stabilized with apolar ligands in an organic solvent [12,13]. However some drawbacks are noticed like the difficult control of the silica thickness for the Stöber method and the weak yield of the silica NPs (typically less than 100 mg) synthesis associated with long-time process (48 h) for the emulsion route. Magnetic NPs and QDs were also coated with MS shells by using cetyltrimethylammonium bromide (CTAB) micelles acting as pore structure directing agents [14]. However here too, a lack of uniform encapsulation of both NPs and a weak yield of synthesis were noticed. All these strategies may thus have limitations for scaling-up and industrial processing which are key features to foster the development of luminescent nanoprobes whether for biomedical or depollution applications. There is thus a strong need for investigating new encapsulation strategies and here, the wrapping of small luminescent NPs (such as QDs) in silica shells and also polymers is addressed.

Indeed, besides the encapsulation of QDs within silica, another interesting alternative is to extend strategies involving the capping of tightly adsorbed or cross-linked polymer, from various chemical approaches, at the surface of sub-micron size porous or non-porous silica particles. Such approaches were importantly developed this last decennia for polymer surface functionalization or to form, after dissolution of the silica –used as sacrificial templates – fully impermeable templated polymer-based capsules [15–17]. In recent works, we and co-workers introduced a pioneering strategy to provide very strongly anchored polymer nanocoatings at silica surface by using original isobutyramide (IBAM) linkers [18,19]. Indeed, IBAM groups grafted at silica surfaces were shown to behave as versatile non-covalent surface binders to form a tight and physically stable cross-linked nanofilm, through a single step adsorption of macromolecules without the need of an additional cross-linking

step or other adjuvant. After removal of the silica used as sacrificial templates, the nanofilms are physically cross-linked enough to ensure the formation of self-supported micron or submicron size polymer capsules or spheres which can be used for drug delivery applications [20]. Such an approach for polymer coating would thus provide a second protection and also favor good biocompatibility and colloidal stability.

Hence, the challenges in nanocomposite design and polymer nanoassembly, as described above, highlight the needs to develop new strategies towards efficient luminescent nanoplatforms for biomedical applications made according to: (i) a rapid and simplified procedure with high yield synthesis (superior to 1 g/day of synthesised materials) able to be scaled-up for industrial applications; (ii) a high level of control of the nanocomposite structure and homogeneity of dispersion with composite particles displaying controlled monodispersity, pore size, composition and biocompatibility and (iii) new methods of biocompatible polymer coatings for QDs encapsulation.

Herein, we report on an original wrapping strategy for the design of novel luminescent nanoplatforms. They consist of stellate mesoporous silica (STMS) encapsulating InP/ZnS QDs with a very high efficiency ($\geq 90\%$), which are then protected by applying two different wrapping methods based either on an additional silica coating, or a tight polymer capping (see scheme in Fig. 1). In a first common step of these approaches, large pore STMS NPs having a well-controlled morphology (ca. 100 nm size, 15 nm pore size) are synthesized according to a rapid, facile, and large scale synthesis method developed recently [21]. To date, no encapsulation of inorganic NPs or polymer capping have been performed within such silica nanostructures. These STMS NPs are modified with (aminopropyl)triethoxysilane (APTS) and water dispersible carboxylate-modified QDs are then covalently grafted using a carbodiimide approach within the large pores of the STMS and with a high efficiency. To prevent toxic degradation of QDs, two encapsulation approaches are investigated. The first route consists of building a second silica layer having small pores (denoted SPS for small pore silica), which increases the colloidal stability, limits the ion diffusion and allows the possibility to further functionalize the SPS shell. The second route aims at capping the STMS NPs with polysaccharides which are biocompatible natural polymers by using the IBAM-polymer assembly. In this work, the structure, colloidal stability, surface charge and fluorescence imaging properties of these novel luminescent nanocomposites are deeply investigated. Furthermore, the biocompatibility of such polysaccharide-coated STMS@QDs is assessed *in vitro* in murine cancer cells through cell viability assays and *in vivo* by injecting the nanocomposites within zebrafish (ZF) embryos and following embryo development over several days. Zebrafish (*Danio rerio*) embryos present several advantages including short generation time and fast development, large number of offspring and optical transparency, the latter being perfectly suited to assessment of *in vivo* fluorescence. The fate and fluorescent tracking of such fluorescent nanoprobes *in vivo* in ZF is then investigated by confocal microscopy.

2. Experimental

2.1. Materials

Tetraethyl orthosilicate (TEOS), cetyltrimethylammonium bromide (CTAB) (Roth, >98%), cetyltrimethylammonium tosylate (CTA-Tos), 2-amino-2-hydroxymethyl-1,3-propanediol (AHMPD), aminopropyltriethoxysilane (APTS) (Sigma Aldrich), 1-Ethyl-3-(3-dimethylaminopropyl)carbodiimide (EDC), *N*-hydroxysuccinimide (NHS), isobutyramide chloride (IBC) (Sigma Aldrich), ammonium

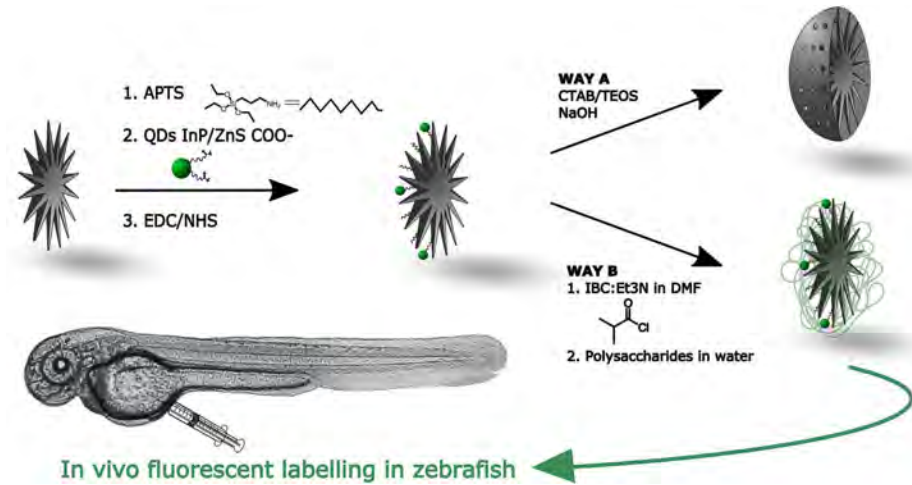


Fig. 1. Scheme showing the design of luminescent STMS grafted with QDs and the two strategies of protective coatings: small pore silica or IBAM-polysaccharide coatings.

hydroxide (25% in water) (Fluka), triethylamine (Sigma Aldrich), sodium hydroxide (Carlo Elba), ammonium nitrate (Sigma Aldrich, >99%), dimethylformamide (DMF) (Carlo Elba), Quantum dots InP/ZnS (MK Nano, 1 mg mL⁻¹), Dextran (Sigma Aldrich) and Chitosan (Sigma Aldrich) were used as received, without further purification.

2.2. Synthesis procedures

2.2.1. Synthesis of large pore stellate mesoporous silica (STMS)

On a 500 mL flask, 3.8 g of CTATOs, 0.436 g AHMPD and 200 mL of water were introduced and stirred at 80 °C up to full dissolution (about 1 h30). Next, 30.2 g of TEOS was added to mixture, and stirred for 2 h at 80 °C. A white precipitate was formed, and filtered under vacuum. The precipitate was washed three times with distilled water, and dried overnight. The resulted powder was calcined at 550 °C for 6 h in order to remove the CTATOs. 7706 g of a white powder was obtained and crushed with a mortar. 0.981 g of the crushed powder was added to 50 mL of ethanol in a centrifuge tube. About half of the particles aggregated and fallen on the bottom of the tube. In order to quickly eliminate those aggregates, a centrifuge cycle (1000 g × 1 min) was performed. These aggregates (0.477 g) were recovered, crushed again, and put again in 50 mL of ethanol. Almost all the aggregates dispersed again were stable in ethanol after the second crushing.

2.2.2. APTS grafting

5 mL of stellate silica in ethanol at 50 mg mL⁻¹ was added to 27 mL of ethanol in a tube with 1.2 mL of NH₃ (0.7 M). The mixture was stirred for five minutes, and 5 mL of 3-aminopropyltriethoxysilane (APTS) was added. The tube was mixed for 2 h and washed twice with 15 mL ethanol.

2.2.3. QDs grafting

For a typical procedure, 0.5 mL of carboxylate modified InP/ZnS QDs at 1 mg mL⁻¹ was added in a tube containing the previous STMS@APTS dispersed in 5 mL of water at pH 7. To tune the amount of QDs grafted, various amounts of QDs were used onto silica. The mixture was left to stir for 24 h. Then, 100 equivalents of EDC and 250 equivalents of NHS vs carboxylate functions of InP/ZnS QDs, were added to the previous mixture, with 500 mL of PBS buffer. After 4 h of stirring, the mixture was centrifuged at 8000 g for 8 min. The supernatant was analysed by spectrofluorimetry and

the STMS@QDs nanocomposites were washed three times with water.

2.2.4. Coating of a small pore silica shell

In a 500 mL Erlenmeyer, 50 mL of a solution of CTAB at 27.4 mM (0.5 mg) was prepared by succession of stirring and sonification at 60 °C until the CTAB was fully dissolved. After cooling to room temperature, 5 mL of STMS@QDs at 10 mg mL⁻¹ in ethanol was added and stirred for 30 min. 150 mL of a basic solution (60 µL of NaOH 2 M) was mixed with the previous mixture. The solution was then heated at 70 °C for 30 min. 1.5 mL of TEOS and 2.5 mL ethyl acetate were successively added, and the solution was let under stirring for 3 h. The synthesized particles were washed several times with water by centrifugation. CTAB was extracted by mixing with ammonium nitrate at 60 °C, and followed by zeta potential measurement.

2.2.5. Coating of polysaccharides on STMS@QDs by IBAM grafting strategy

The previously synthesized STMS@QDs were dispersed in a tube with 14 mL of DMF and 1.4 mL of Et₃N. In another tube, 1.9 mL of IBC was mixed with the same amount of DMF. Both tubes are put together and stirred for 2 h. A precipitate of organic salt, triethylamine chloride hydrate was formed during the reaction, so in the end, a small amount of water (around 2 mL) was added up to its dissolution. The solution was washed three times with 10 mL of DMF, and finally dispersed in a small amount of DMF (1 mL). Then CHI and DEX polysaccharides were all two used as coating materials. 10 mL solution of each polymer at 1 mg mL⁻¹ was prepared, and mixed with previously made solution of STMS@QDs@IBAM in DMF. The mixture was left under stirring for 2 h, and washed with 15 mL of water and dispersed in water.

2.3. Characterization methods

2.3.1. TEM microscopy

Nanoparticle morphology and size were characterized by transmission electron microscopy (TEM) with a JEOL 2100 ultra-high resolution microscope operating at 200 kV. TEM samples were prepared by depositing one or two droplet of about 1 mg mL⁻¹ nanoparticle solutions on carbon-coated copper grids. The size distribution was determined using ImageJ software on at least 100 particles.

2.3.2. Dynamic light scattering (DLS) and zeta potential (ZP)

DLS and zeta potential measurements were performed on Zetasizer Nano ZS by Malvern Instruments. The concentration of the particles in solvents for DLS measurements was adjusted in order to have suitable signals and pH of solutions were adjusted with KOH 0.1 M and HCl 0.1 M solutions to reach buffer between pH 3 and pH 12.

2.3.3. Fluorescence microscopy

Fluorescence of the particles containing QDs was visualized by microscopy on an Olympus microscope IX73 with a Hamamatsu OrcaFlash Cmos camera, being exciting by a white LED light (Xcite 110Led), filtered at 490 nm to have to correct excitation wavelength. 5 μ L of the solution were deposited onto a microscopic flake, and observed after solvent evaporation.

2.3.4. Steady state luminescence measurement

Photoluminescence measurements were conducted on Quanta-Master 300, with a LPS 220B lamp and a Motor Driver MD 5020. Standard sample of 3 mL were prepared by dilution of the stock solution of QDs from MK Nano (1 mg mL^{-1}) into water, with an excitation wavelength of 490 nm.

2.3.5. N_2 adsorption-desorption

For the determination of mesoporosity of STMS, N_2 adsorption desorption measurements were conducted onto a Tristar 3000, with an adsorption analyser of Micromeritics instruments. Specific surfaces were calculated according to BET (Brunauer-Emmett-Teller) theory and pore size according to BJH (Barrett-Joyner-Halenda) model.

For the determination of micro and mesoporosity of STMS@SPMS, the textural properties of the prepared of STMS@SPS were studied by N_2 adsorption-desorption measurements at -196°C using two analysers of Micromeritics-Tristar 3000 and ASAP 2420. The nanoparticles were degassed under vacuum at 100°C for 6 h to desorb the moisture before analysis. Specific surface area was calculated by BET method. Pore volume and pore distribution were determined using desorption branch by the BJH method. Horvath-Kawazoe model was used for determining pore-size distribution in a micropore analysis from a single adsorption isotherm (dosing of nitrogen 1 cm^3 , stability time 3 h).

2.3.6. Inductively coupled plasma mass spectrometry (ICP-MS)

Supernatant of STMS@QDs NP samples were diluted with 1% trace metals grade nitric acid (TraceSELECT, Fluka). The amount of Zn and In was measured with an ICP-MS Agilent 7500 instrument. Intensities were measured at m/z 66 for Zn and at m/z 115 for In and compared to intensities of standards (1 – 5–25 – 100 $\mu\text{g L}^{-1}$) prepared from certified standards (1000 mg L^{-1} , CPI International) and using Rh (m/z 103) at 10 $\mu\text{g L}^{-1}$ as internal standard.

2.3.7. Thermogravimetric analysis (TGA)

TGA were performed on a TA SDT 600 instrument to measure the amount of organic compound grafted on functionalized inorganic nanoparticle.

2.4. Cell culture, zebrafish manipulation and imaging

2.4.1. Cell culture

Murine D2A1 cells stably expressing LifeAct-RFP or LifeAct-YPET were grown as previously described [22], in DMEM with 4.5 g/l glucose (Dutscher) supplemented with 5% FBS, 5% NBCS, 1% NEAA and 1% penicillin-streptomycin (Gibco). The MTS experiments were performed in triplicate over 72 h with three different time points at 24, 48 and 72 h incubation with the NP in 96 well plates. The NP concentration ranged from 50 $\mu\text{g mL}^{-1}$ to

0.39 $\mu\text{g mL}^{-1}$ and each well was seeded with 4000 cells. Upon incubation at 37°C , 5% of CO_2 for the given time needed to assess the desired timepoints, Cell density was assessed using CellTiter 96[®] AQueous provided by Promega and following the provided protocol and revealed with a plate reader (MultiskanEx, Thermo Fisher).

2.4.2. Zebrafish handling

Tg (fl1a:RFP) Zebrafish (*Danio rerio*) embryos were used [23]. Embryos were maintained in Danieau 0.3X medium (17.4 mM NaCl, 0.2 mM KCl, 0.1 mM MgSO₄, 0.2 mM Ca(NO₃)₂) buffered with HEPES 0.15 mM (pH = 7.6), supplemented with 200 μM of 1-Phenyl-2-thiourea (Sigma-Aldrich) to inhibit the melanogenesis, as previously described [24].

2.4.3. Intravascular injection of NPs in the zebrafish embryo

48 h post-fertilization (hpf) *Tg(Fl1a:RFP)* embryos were mounted in 1% low melting point agarose containing 650 μM of tricain (ethyl-3-aminobenzoate-methanesulfonate) to immobilize the embryos. The NP were injected with a Nanoject microinjector 2 (Drummond) and microforged glass capillaries (25 to 30 μm inner diameter) filled with mineral oil (Sigma). 23 nL of a NP suspension at 5 mg/ml were injected in the duct of Cuvier of the embryos under the M205 FA stereomicroscope (Leica), as previously described [25,26].

2.4.4. Confocal imaging and analysis

Confocal imaging was performed with an upright TCS SP5 confocal microscope with a HC FLUOTAR L 25X/0.95 W VISIR (Leica). The caudal plexus (around 50 μm depth) and the head (around 150 μm depth) were imaged with a z-step of 1 μm . The acquisition of the different color channels was performed sequentially to avoid cross talks between the acquisition channels.

2.4.5. Macroscopy

Developmental stages of the zebrafish embryos upon NP injection were assessed using macroscopy imaging. All the experiments were done in triplicate over a population of 8 embryos per condition.

2.4.6. Image analysis

The confocal images were processed with ImageJ. All the confocal images are Z projections of the maximal intensity.

3. Results and discussion

3.1. Synthesis of stellate mesoporous silica and surface modification with aminosilane

The large pore stellate mesoporous silica (STMS) nanoparticles were synthesized by performing a sol-gel process according to the previous work of Zhang et al. [21]. This method allowed the synthesis of STMS with a mean ca. 15 nm pore size, according to an easy, reproducible and rapid sol-gel method (see Materials and Methods section). Briefly, cetyltrimethylammonium tosylate (CTA⁺, Tos⁻) is used as the porogen surfactant instead of the usual CTA⁺, bromide (CTA⁺, Br⁻) and is reported to ensure the control of the silicate polymerization and pore size. The authors explained the formation of larger pores in the STMS by a stronger binding of Tos⁻ compared with Br⁻ to the cationic CTA⁺ micelles and by the silicate polymerization around stacked CTA micelles. After the synthesis of STMS NPs, their transmission electron microscopy (TEM) imaging showed monodisperse nanoparticles with a mean diameter of 103 \pm 10 nm (see TEM image at low magnification in Fig. 2A). Besides, the large porosities were clearly visible as seen in the TEM image at higher magnification in Fig. 2B. Brunauer-Emmet-Teller (BET) nitrogen

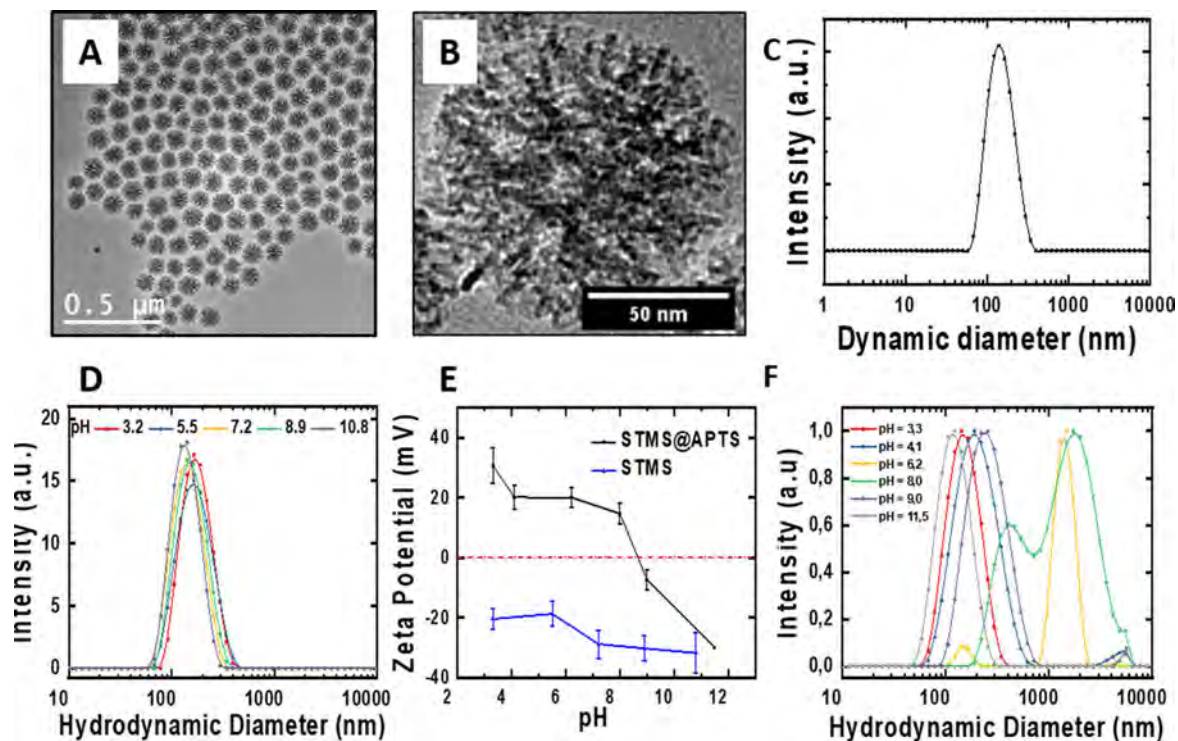


Fig. 2. TEM images of STMS NPs (A) at low and (B) high magnification with a zoomed image on an unique particle showing the large porosity. (C) DLS size distribution in EtOH of the STMS NPs. (D) DLS size distributions in water as a function of the pH of non-modified STMS. (E) Zeta potential values for STMS and STMS@APTS NPs in water as function of the pH. (F) DLS size distributions in water as a function of the pH of STMS after APTS grafting.

adsorption-desorption analysis (Fig. S1) confirmed a specific surface of $477 \text{ m}^2 \text{ g}^{-1}$ with a *ca.* 16 nm mean pore size in agreement with the values found by Zhang et al.

Furthermore, dynamic light scattering (DLS) measurement (intensity mode) confirmed the high colloidal stability of the STMS nanoparticles, in ethanol even for several days, with a size distribution centered at *ca.* 150 nm (Fig. 2C) indicating that the STMS NPs suspension displays good colloidal stability. These bare STMS NPs were then dispersed in water and a study of the colloidal stability was conducted for different pH values. DLS and zeta potential (ZP) measurements were performed for pH ranging from pH = 3 to 12. Mean hydrodynamic diameters of the STMS NPs were measured in the range of 100–150 nm, evidencing an excellent colloidal stability also in water on a wide pH range (Fig. 2D). ZP values measured in the range of -20 mV (pH = 3) to -40 mV (pH = 12) showed an isoelectric point (IEP) below pH 3 (Fig. 2E, blue curve) explaining this high colloidal stability ensured by electrostatic repulsions. Indeed, the surface charge of silica originated from the presence of hydroxide groups at its surface which are amphoteric and deprotonated (negative charge) and it is generally accepted that mesoporous silica is negatively charged above its isoelectric point (pH 2–3).

Then, the grafting of APTS on STMS was performed according to a well-established procedure of surface silanization. DLS and ZP measurements were also carried out in the same pH range in water. From DLS measurements, the STMS NPs form a stable colloidal suspension below pH = 6 and above pH = 8 (Fig. 2F). That was confirmed by ZP measurements as a function of pH which showed that after the APTS grafting on the silica surface, IEP moved from low pH (below 3) to pH = 8. Such a shift of the IEP (Fig. 2E, black curve) proved the grafting of APTS and explained why the APTS-grafted STMS aggregated in the pH range 6–8. Indeed, the pKa of the amine group in APTS is around 9 and when pH increases

up to 8, the ammonium charge decreases until the particles do not carry anymore net charge and at this point, the electrostatic repulsions which stabilized the STMS NPs are not strong enough, so the NPs aggregated, and the hydrodynamic size strongly increased (Fig. 2F).

3.2. Grafting of quantum dots (QDs) on stellate silica

To functionalize the STMS NPs by QDs, carboxylate modified InP/ZnS QDs were covalently grafted on stellate silica by an ethyl-3-(3-dimethylaminopropyl)carbodiimide (EDC)/N-hydroxysuccinimide (NHS) coupling. This coupling involved a reaction between the carboxylate group and the carbodiimide EDC, to form a very reactive but also unstable intermediary compound, o-acylsourea. The use of NHS limited the side reactions, because a more stable amine-reactive ester is formed by reaction with the o-acylsourea. In order to quantify the amount of QDs anchored within the STMS NPs, photoluminescence (PL) intensity measurements were conducted. First, standard samples of QDs, with different concentrations (at 2, 4, 9, 18, 35, 70 $\mu\text{g mL}^{-1}$ in water) were prepared. Their photoluminescence intensities were recorded to draw a calibration curve (Fig. S2A). Analysis of the fluorescence intensity of the supernatant of the STMS@QDs (Fig. S2B) just after the grafting and centrifugation of the STMS NPs allowed to quantify the amount of grafted QDs per mass of STMS denoted as grafting rate and also to evaluate the grafting yield of the QDs whose expressions are given below:

$$\text{Grafting Rate} = \frac{m_{\text{QDs encapsulated}}}{m_{\text{silica}}}$$

$$\text{Grafting Yield} = \frac{m_{\text{QDs encapsulated}}}{m_{\text{QDs introduced}}}$$

The grafting rate and grafting efficiency were investigated as a function of the introduced concentration in QDs. For that, different amount of QDs (0.1, 0.2 and 0.4 mg) were incubated with the same mass of STMS (50 mg). Grafting rates of 1.6, 3.6 and 7.4 $\mu\text{g QDs mg}^{-1}$ STMS were obtained leading to respectively grafting yields of 80, 89 and 93%. A summary of the results obtained is provided in Table 1.

To confirm the effective fluorescence property of these new clusters, fluorescence microscopy imaging was performed on the STMS@QDs suspensions. Fig. S3 shows images of STMS@QDs in transmission (Fig. S3A) and fluorescence (Fig. S3B) microscopy and the co-localisation of both (Fig. S3C). These images showed that the lighting in fluorescence comes from the silica STMS NPs, proving that QDs are well grafted in the silica and remained fluorescent in this environment. Indeed, several works reported that silica particles embedded with QDs did not display any effect of QDs quenching or change in their fluorescence emission properties [27,28].

3.3. Way A. Capping of STMS@QDs with a small pore silica shell

As seen above, STMS@APTS(@QDs) did not display good colloidal stability in aqueous solution at pH 7. To avoid possible QDs un-anchoring or dissolution in water with time and to ensure the colloidal stability at this important physiological pH, the STMS@QDs NPs surface was covered with an additional porous silica shell having small pores (denoted SPS, small pore silica). STMS@APTS were thus dispersed in water at pH = 11 in a CTAB solution (27.4 mM), which ensured good colloidal stability. Then, TEOS was added to the CTAB/STMS mixture, and the SPS shell was grown. Besides the role of protecting the QDs inside the porous silica matrix, one advantage of this SPS shell is also to bring the possibility to load further the pores with small functional molecules. The morphology and the size of the resulting coated STMS@QDs NPs coated with SPS (denoted STMS@QDs@SPS NPs) were investigated by TEM (Fig. 3). After the SPS coating, the mean diameter increased from 100 to 180 nm (Fig. 3A for a low magnification image and Fig. 3B for the size statistic measurement). Furthermore, imaging at higher magnification of individual particles shows that the stellate structure disappeared and was fully filled by the SPS granular structure (Fig. 3C).

To understand the mechanism of this additional porous silica layer coating around STMS@APTS NPs, we investigated the chemical stability of STMS@APTS NPs in the basic conditions of the sol-gel process. Some works in the literature report that polymer assisted-silica etching [29,30] can be achieved already at pH 10–11. However, these reports indicate that these processes are performed at an elevated T (in the range 90–100 °C) with etching times usually superior to 2–3 h while in our process, the contact of the STMS@APTS with basic media is made in milder conditions (30 min/ambient T and then 30 min. at 70 °C). To firmly understand how the additional silica layer coat around STMS NPs, we assessed potential etching of the STMS in the basic conditions of this work. After incubation of the STMS@APTS at pH = 11, at amb. T (30 min) and then at 70 °C (30 min), these samples were imaged by TEM. TEM imaging reveals no difference observed before and

after incubation in this basic media (see Fig. S4). This clearly demonstrates that the original STMS NPs do not dissolve upon these basic conditions of this work. We hypothesize thus that a silica layer of small porosities fill the large pore of STMS@APTS@QDs (making them disappear) and then create an homogenous layer of small pore silica.

To validate this mechanism and characterize the nature of the porosity (micro or mesoporosity), we have performed BET nitrogen adsorption-desorption-isotherms. The surface area and porosity properties of the STMS@SPS NPs were investigated by the implementation of two complementary methods: the usual Barrett, Joyner and Halenda (BJH) method to assess mesoporosity (for pore size superior to 2 nm) and the additional Horwath-Kawazoe (H-K) method suitable for the analysis of the microporosity (for pore size inferior to 2 nm). As compared to the large mesopores found for stellate STMS NPs, isotherms curves of nitrogen adsorption and desorption as well as the pore size distribution of these samples show both a decrease in surface area and the loss of the large pore mesoporosity. (see Fig. S5). Indeed, after the silica coating, the BET specific surface area of the samples decreased from 477 to 146 $\text{m}^2 \text{g}^{-1}$. Moreover, it was observed that the large pores of the STMS (in the range of ca. 10–15 nm) disappeared completely and the graph of the pore size distribution (BJH) indicates only the presence of small pores around 2 nm, which allow suggesting a pore size contribution close (\leq) to 2 nm. This would be in agreement with the process of CTAB surfactant mediated assembly of porous silica (micelles size formed of CTAB are of 2–2.5 nm in diameter). Additionally, by Horvath-Kawazoe method, it was observed the presence of micropores with a bimodal distribution of 7 and 8 Å. Comparing the pores size distribution from both analyses, it is evident to conclude that the material after the silica coating has a multiple microporous structure in the range of 0.5–2 nm. Thus, the loss of specific surface area and of the large pores have impacted significantly the initial stellate materials porous structure. The TEM image of the resulting STMS@SPS (Fig. 3C) presents at the NP border a granular porous amorphous morphology with estimated pores or channels size having size below 2 nm, supporting the results of nitrogen adsorption-desorption analysis that the stellate morphology was filled with a microporous silica granular layer.

With the aim to assess the colloidal stability of these STMS@QDs@SPS particles, DLS measurements were also performed (Fig. 3D) in water at pH = 7. The results showed a great colloidal stability at pH 7, with a mean hydrodynamic diameter of ca. 200 nm by contrast to the STMS@APTS NPs before the SPS coating displaying hydrodynamic sizes larger than 1000 nm at this pH. These results are in agreement with evolutions of ZP measurements as a function of the pH found for these two surface modifications (Fig. 3E). Worthy to note is that for STMS@QDs@SPS NPs, an IEP of ca. 4.5 was found which is slightly higher than the IEP of silica suggesting that some CTAB are still adsorbed at the silica surface, even after several extraction steps.

To address the fluorescence properties of the resulting STMS@QDs@SPMS NPs composites, fluorescence microscopy imaging was performed. Optical transmission and fluorescence images showed that good correspondence was found between transmission (left images) and fluorescence (middle images) and that both superposed very well (right images). Moreover, a signal is still detected, even when the concentration is divided by ca. a factor 11, going from 23 $\mu\text{g QDs mL}^{-1}$ water (Fig. 4A–C) to 2 $\mu\text{g QDs mL}^{-1}$ (Fig. 4D–F).

It was expected that the SPS shell prevent the release of the QDs, and then strongly diminish the toxicity of the sensor. In order to assess this property, two samples with the same amount of grafted QDs (1% wt, 10 $\mu\text{g/mL}$) were prepared, one with an SPS shell and one without. Both samples have been stored for three

Table 1

Results of the QDs encapsulation within stellate mesoporous silica as a function of the QDs concentration.

QDs initial amount [mg]	Amount of STMS0 [mg]	Grafting rate [$\mu\text{g QDs mg}^{-1}$ STMS]	Grafting yield (%)
0.1	50	1.6 ± 0.1	80 ± 5
0.2	50	3.6 ± 0.1	89 ± 5
0.4	50	7.4 ± 0.1	93 ± 5

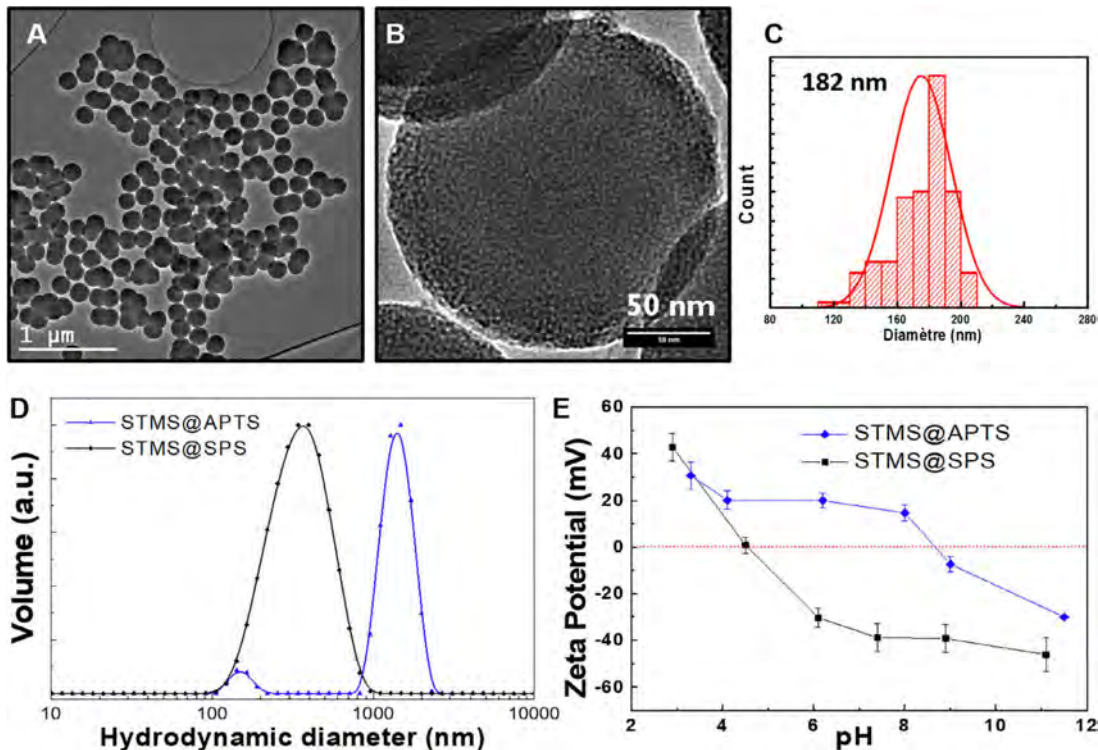


Fig. 3. TEM picture of STMS@SPS at low magnification (A), and its associated size distribution (B). TEM picture at high magnification on an individual NP (C). DLS at ca. pH 6.2 (D) and ZP measurements (E) in water as a function of the pH of the STMS@SPS NPs compared with STMS@APTS.

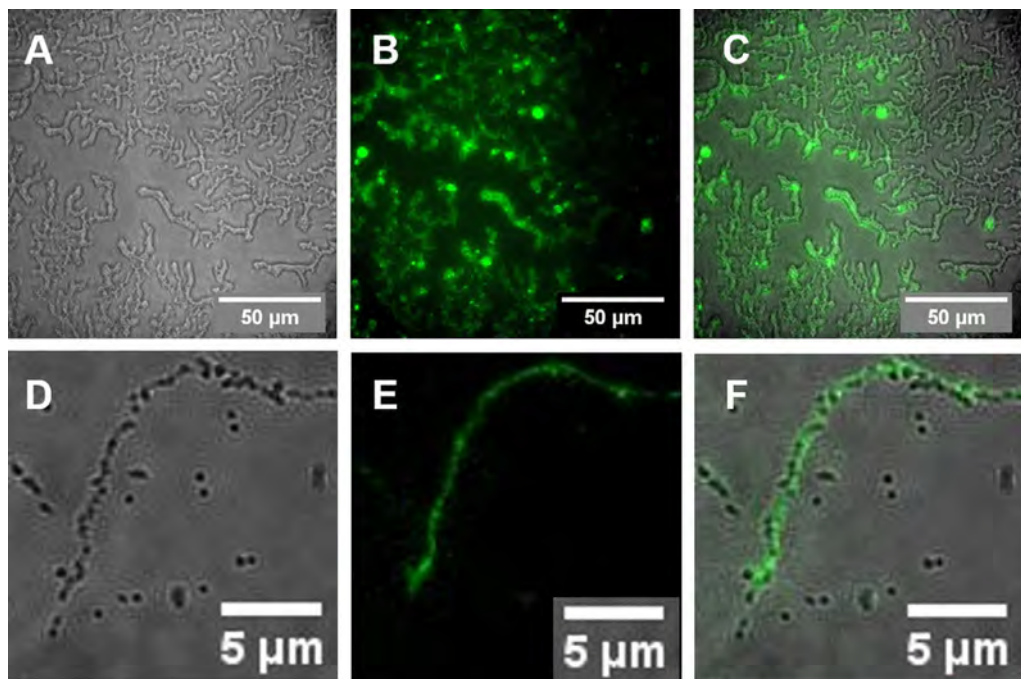


Fig. 4. From left to the right, transmission-fluorescence and combined fluorescence microscopy images of STMS@QDs@SPS having (A, B, C) $23 \mu\text{g QDs mL}^{-1}$ (top panel images) water or (D, E, F) $2 \mu\text{g QDs mL}^{-1}$ (bottom panel images).

months in a fridge, and after this time were centrifuged. The supernatants were collected and the amount of Zn and In was determined by inductively coupled plasma mass spectrometry (ICP-MS) (Table 2) in order to figure out if the QDs were desorbed or dissolved during these three months.

It is worth noting that the amount of Zn and In without any capping is already quite low, showing the good stability of both the QDs and the amide bond between the silica and the QDs. When capped with a SPS shell, no In was detected during the analysis, whereas a level of Zn in the supernatant was found moderately

Table 2

Summary of the ICP-MS analysis performed on sample with and without small pore silica coating.

	[Zn] in supernatant [µg/L]	[In] in supernatant [µg/L]	[InPZnS] in the STMS suspension [µg/L]
STMS@QDs	138 ± 8	32 ± 0.1	10 000
STMS@QDs@SPS	1089 ± 113	<0.1	10 000

high, demonstrating the efficiency of the coating to prevent the release of In but not Zn. The Zn release may be attributed to potential dissolution of the ZnS shell upon contact to the basic media during the surfactant mediated sol-gel reaction. If some pore were filled with water at high local pH, it may trigger the continuous release of $Zn(OH)_4^{2-}$ anions with time [31]. In the next section, an alternative method to the silica coating was investigated to cover the STMS NPs which consisted in capping the STMS@QDs with a tight polymer shell.

3.4. Way B. Capping of STMS@QDs with different polysaccharides coatings

Another approach addressed here to protect the QDs from desorption/un-anchoring and limit ions release is to encapsulate directly the STMS@QDs NPs within a polymer nanoassembly and then to assess their potential for fluorescence imaging. For that, we used an original strategy making use of IBAM surface binders. IBAM was thus grafted onto APTS modified silica by reacting STMS NPs with isobutyryl chloride in DMF (see Fig. 1). Two well-known biocompatible and natural polymers: chitosan (CHI) and dextran (DEX) polysaccharides were then adsorbed in aqueous solutions on IBAM-modified STMS@QDs according to a procedure adapted from previous works [18,19]. Their resulting colloidal stability was compared to those of bare and APTS modified stellate silica NPs. The DLS size distributions of STMS@QDs coated by the two IBAM-polysaccharides in water at pH = 7 are shown in Fig. 5. The DLS measurements revealed an important improvement of the colloidal dispersion of STMS@QDs after their coating with both polysaccharides compared to the APTS grafting. The slight increase of the hydrodynamic diameter for both STMS@QDs@DEX and STMS@QDs@CHI is consistent with a polymeric shell coating the surface.

To assess and quantify the grafting of polysaccharides, thermogravimetric analysis (TGA) experiments were conducted (see Fig. 6) from RT to 600 °C at 5 °C/min with bare STMS, STMS@CHI

and STMS@DEX, on dried sample (48 h at 50 °C). A change in behaviour is noticed between the silica NPs with and without polysaccharide. Considering that the physisorbed water will be removed once a 70 °C temperature is reached, we can estimate the weight percentage of polysaccharides effectively coated on the particles. Since the APTS and IBAM moieties are responsible for 19% of the total particle weight, we achieved a coverage of the particle with 5% wt of polysaccharides, while a solution containing 20% wt was introduced, meaning that a quarter of the polysaccharides were effectively coated on the STMS@QDs@IBAM particles.

These samples were imaged by optical transmission and fluorescence imaging and aggregation was observed on glass support induced by drying effect. However, fluorescence microscopy imaging (Fig. 7) showed that the fluorescence was not affected by the polymeric shell. Moreover, the fluorescence signal was co-localized with the silica cluster visible in transmission microscopy. As done with the Way A, the sample STMS@QDs@DEX and STMS@QDs@CHI with a concentration of 1 mg mL⁻¹ in NPs (and so 10 µg QDs/mL⁻¹) have been left to rest in the fridge for three months. The supernatants were then collected and analysed via ICP-MS (Table 3). Once again, no In was detected in the supernatant, even after three months, validating the stability of the both coatings and the protection that they ensure towards QDs dissolution and toxic ions release. Regarding Zn release, a very limited amount were found for both coatings with a higher retention with CHI compared to DEX which could be attributed to the formation of complexes of Zn cations with CHI in the polymer shell [32]. Hence, this polysaccharide coating strategy is helpful to avoid heavy metal toxicity by blocking their release. Noteworthy, it may be also attractive to limit cytotoxic effects due to reactive oxygen species generation by metals such as Zn [33].

3.5. Biocompatibility of the STMS nanocomposites and potential use as fluorescent labels

To assess whether these latter STMS composites are biocompatible, we first performed confocal imaging of D2A1 cells genetically modified to express the red fluorescent protein, and incubated with the green fluorescent composites: STMS@QDs, STMS@QDs@DEX and STMS@QDs@CHI NPs. In Fig. 8A and B, we present the localisation of the nanocomposites (denoted QDs in the confocal image, green channel) and the cells (red channel) separately before merging the images, after 24 h (A) and 48 h (B) incubation times. Overall, these images indicate that treated D2A1 cells are healthy and

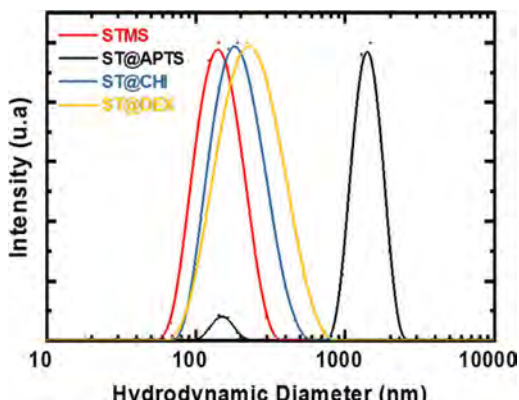


Fig. 5. DLS size distributions of STMS (red curve), STMS@APTS (black curve) and STMS@QDs@IBAM coated with two different polysaccharides: CHI (blue curve) or DEX (yellow curve) in water at pH 7.

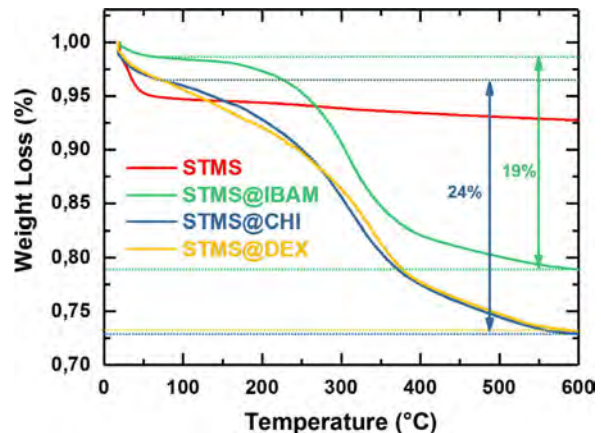


Fig. 6. Thermogravimetric analysis of bare STMS (red curve), STMS@IBAM (green curve), STMS@CHI (blue curve) and STMS@DEX (yellow curve), from room T to 600 °C.

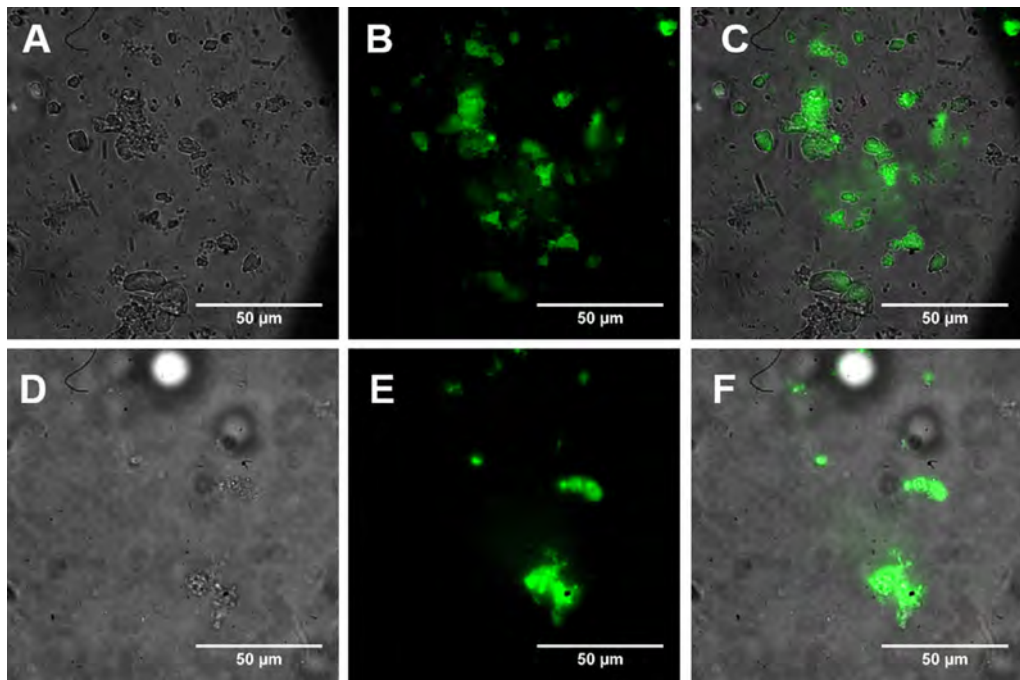


Fig. 7. From left to right, transmission, fluorescence and combined fluorescence microscopy images of STMS@QDs@CHI (top) and STMS@QDs@DEX (bottom) loaded with $23 \mu\text{g mL}^{-1}$ QDs in water.

Table 3

Summary of the ICP-MS analysis performed on sample with and without polysaccharides coating after three months storage.

	[Zn] in supernatant [$\mu\text{g/L}$]	[In] in supernatant [$\mu\text{g/L}$]	[InPZnS] in the STMS suspension [$\mu\text{g/L}$]
STMS@QDs	138 ± 8	32 ± 0.1	10,000
STMS@QDs@DEX	44 ± 1	< 0.1	10,000
STMS@QDs@CHI	< 20	< 0.1	10,000

continue to proliferate independently on the NP treatment. After 24 h of incubation (Fig. 8A) the co-localisation between the cells and the different nanocomposites is slightly visible. After 48 h (Fig. 8B) the co-localisation is clearly visible and the nanocomposites are located mostly on the cellular membrane. We next performed cell proliferation assays upon loading of STMS@QDs, STMS@QDs@DEX and STMS@QDs@CHI NPs on murine cancer cells (D2A1 cells, murine breast tumor cells). First, upon incubation with STMS@QDs NPs, the cell growth was assessed over 24 h and displayed no significant difference, independently of the nanocomposite NP concentration used (range concentration: $0.39\text{--}50 \mu\text{g}$ nanocomposite NPs mL^{-1}). (Fig. 8C). Similarly, no effect on cell proliferation was observed after 72 h of incubation with these STMS@QDs NPs (Fig. 8D). A similar behaviour was observed when using STMS@QDs@DEX NPs (Fig. 8E and F) or STMS@QDs@CHI NPs (Fig. 8G and H). To generalize this trend, the quantification of the normalised optical density over time (at 24, 48, 72 h) demonstrates that none of the formulations affect the cell proliferation. (Fig. 8I respectively for STMS@QDs, STMS@QDs@DEX and STMS@QDs@CHI NPs, from left to right). Thus, these three types of STMS NPs did not affect cellular growth over 24 h and 72 h in the range of the NPs concentration used (at $50 \mu\text{g/ml}$ or less). In the previous paragraphs, we have shown that the IBAM-polysaccharide coatings with CHI or DEX allowed to efficiently prevent the release of In over three months which is a much longer

period than the time of the cell toxicity study used here. The good biocompatibility for all three composites is thus more explained by the NPs concentration range which is well adapted for the next fluorescence study and also by the very slow kinetics of dissolution and/or diffusion of In cations. Hence, by demonstrating a good biocompatibility in a suitable concentration range, these cellular data bring information about the formulation which is not toxic for cells. Moreover, there are advantages to use the polysaccharide coating approach as compared to STMS@QDs which are: their improved colloidal stability and their prevention of In release over long time periods (three months).

We next assessed whether the three STMS nanocomposites would affect the development of an entire organism, by investigating the growth of zebrafish (ZF) embryos loaded with these NPs. Zebrafish embryos are perfectly suited to address potential toxicity issues. Indeed, the rapid embryonic development of zebrafish (all major organs are formed within 24 h, embryos are autonomous and look for food after only 3 days post-fertilization) allows us to question toxicity of our NPs. To do so, we performed intravascular injection of different STMS@QDs NPs at 48 h post fertilization (hpf) and followed the development of the ZF embryos upon 120 h post fertilisation. As shown in Fig. 9, evolution of the ZF embryo length was similar for all three types of STMS NPs as compared to an injection of PBS as a control. Hence, injection of the three types of STMS NPs did not affect the developmental growth of ZF embryos. Altogether, this demonstrates that our NPs are biocompatible and well tolerated by small organisms such as the ZF embryo.

Since all three types of STMS NPs are well tolerated by ZF embryos, we went on testing whether they could be used as *in vivo* fluorescent tracers. Noteworthy that the ZFs are genetically modified to express the red fluorescent protein (RFP) under the control of an endothelial promoter (Fli1a) allowing thus to visualize their vasculature in red fluorescence ($\lambda_{\text{exc}}/\lambda_{\text{em}} = 542/550\text{--}600 \text{ nm}$) while the STMS NPs are visualized in green fluorescence ($\lambda_{\text{exc}}/\lambda_{\text{em}} = 488/500\text{--}530 \text{ nm}$). We injected then STMS NPs into

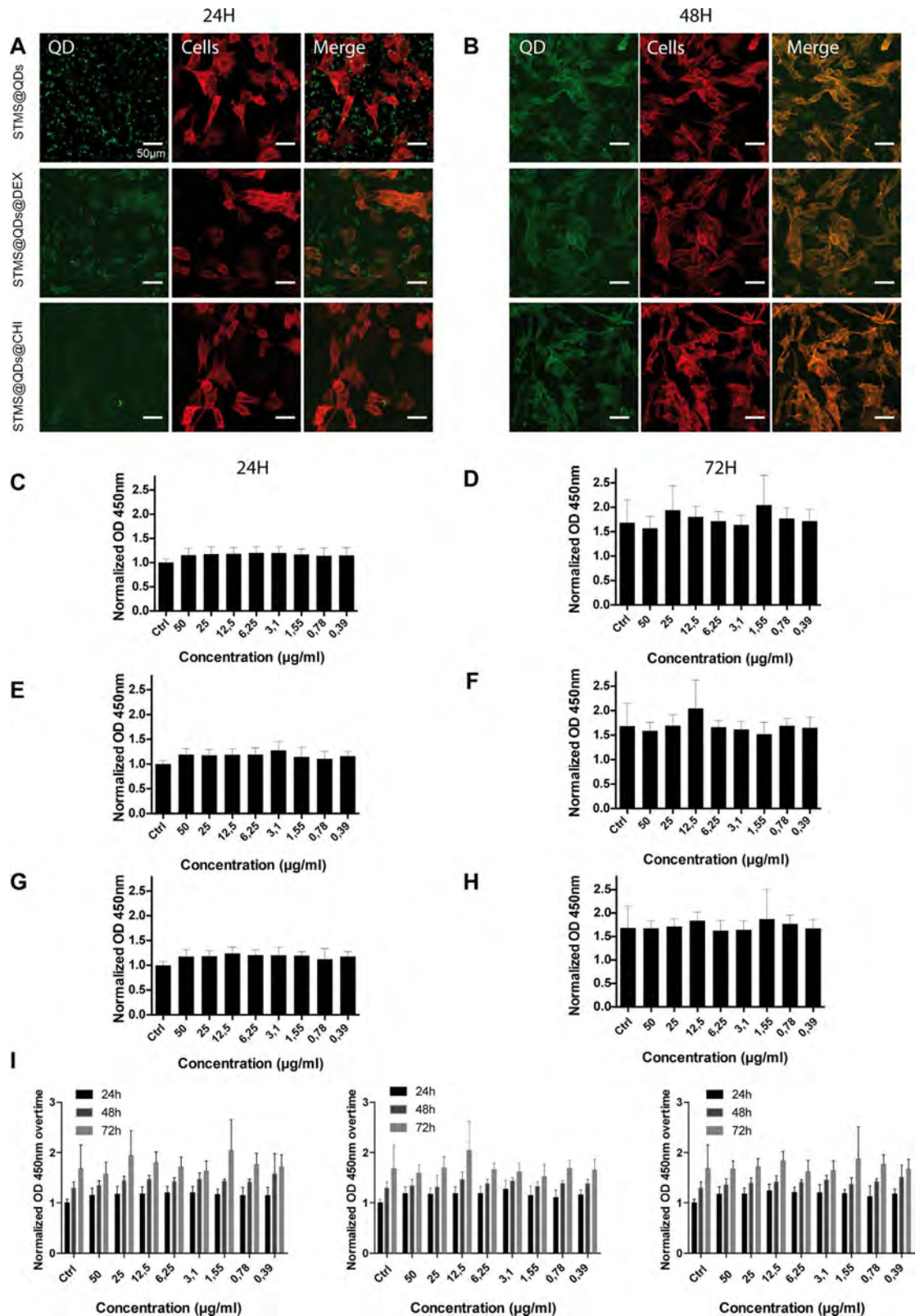


Fig. 8. Cell toxicity assays. Confocal images of D2A1 cells (red fluorescence) incubated with $50 \mu\text{g mL}^{-1}$ nanocomposites grafted with QDs (green fluorescence), and the merged images after 24 h incubation (A) and 48 h (B). Normalized optical density graphs at 450 nm of the D2A1 cells incubated at different concentrations of: STMS@QDs after 24 h (C) and 72 h (D), STMS@QDs@DEX after 24 h (E) and 72 h (F) and STMS@QDs@CHI after 24 h (G) and 72 h (H). I. Optical density of the cells over time at 24, 48 and 72 h when incubated respectively with STMS@QDs, STMS@QDs@DEX and STMS@QDs@CHI. (For interpretation of the references to color in this figure legend, the reader is referred to the web version of this article.)

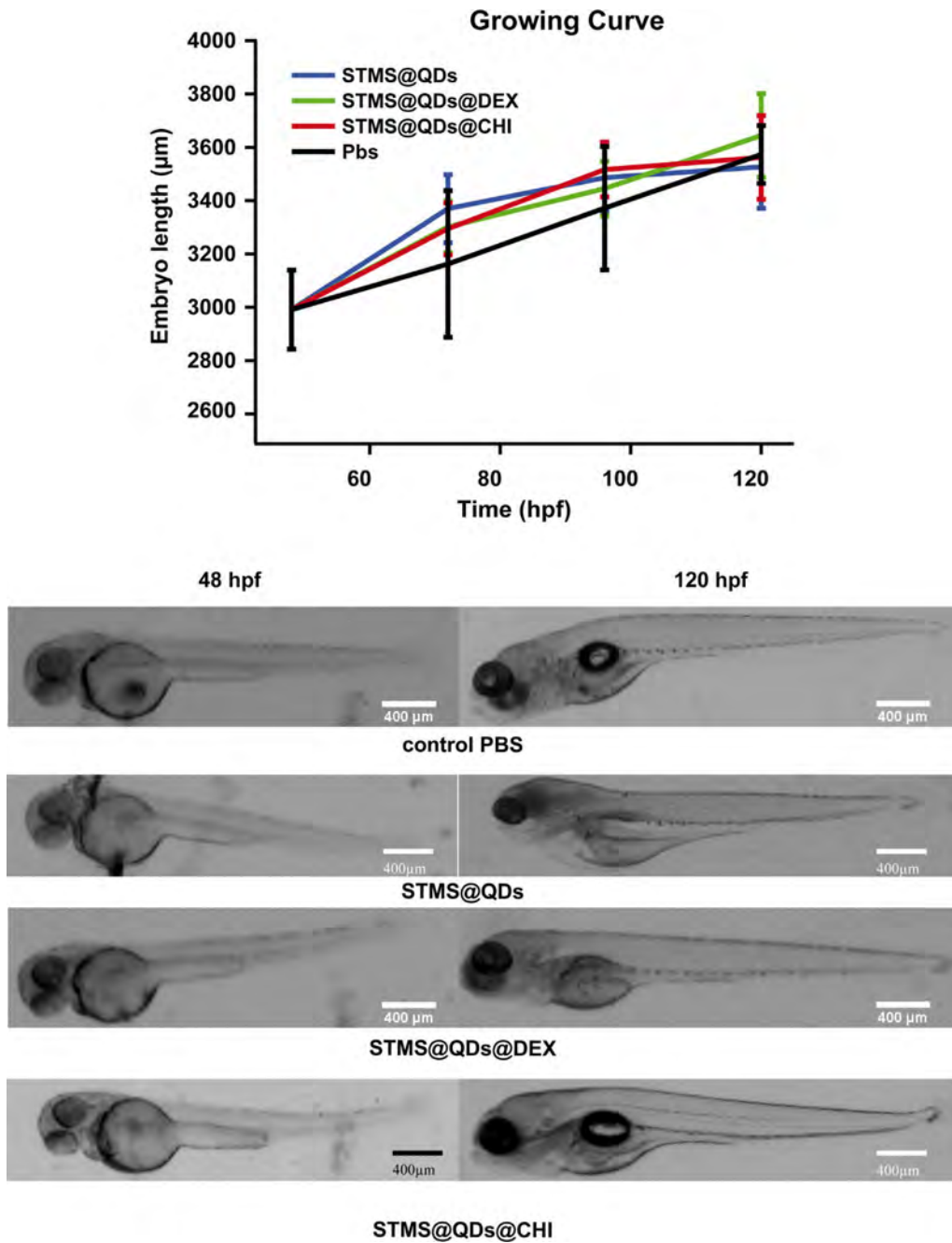


Fig. 9. Evolution of the embryo length (μm) with time (hpf) after injection of the three types of NPs suspensions: STMS@QDs, STMS@QDs@DEX, and STMS@QDs@CHI as compared with PBS injection as a control. The injection was performed at 48 hpf. Below, microscopy images showing the development of the ZF embryos when treated with the three types of NPs and PBS at 120 hpf. The same behavior is observed for all three types of NPs.

the blood circulation of ZF embryos (Fig. 10A), and imaged the embryos upon 6 h post-injection (Fig. 10B–D). The three different NP type: STMS@QDs, STMS@QDs@DEX and STMS@QDs@CHI display a very similar behavior: the NPs rapidly leak from the blood-stream and extravasate to accumulate in the surrounding tissues. NPs rapidly disseminate in regions close to vascular regions, and seem to quickly label resident cells that very likely take up, through phagocytosis, the NPs (Fig. 10B–D). We performed similar imaging at 24 h post-injection to follow over one day the behavior in the organism. As shown on Fig. 10E–G, for all three types of STMS NPs, the NPs are still visible in the caudal plexus of the ZF

embryo, within somites, proving that the NPs remain and label tissues in the ZF embryo for at least 24 h post-injection. In addition, NPs rapidly accumulate in head regions as well (Fig. 10H and I). Interestingly, the NPs preferentially label residing cells that could be either microglial or neuronal populations that are extravascular, as shown by the distinct pattern from the labeled vasculature.

Altogether, by using two biological models (cultured cells and zebrafish embryo), we have shown that our stellate mesoporous silica nanoplatforms do not affect cellular growth, neither embryonic development over 4 days of treatment, in the concentration range assessed (up to 50 μ g mL⁻¹ NPs). In addition, the fluorescence

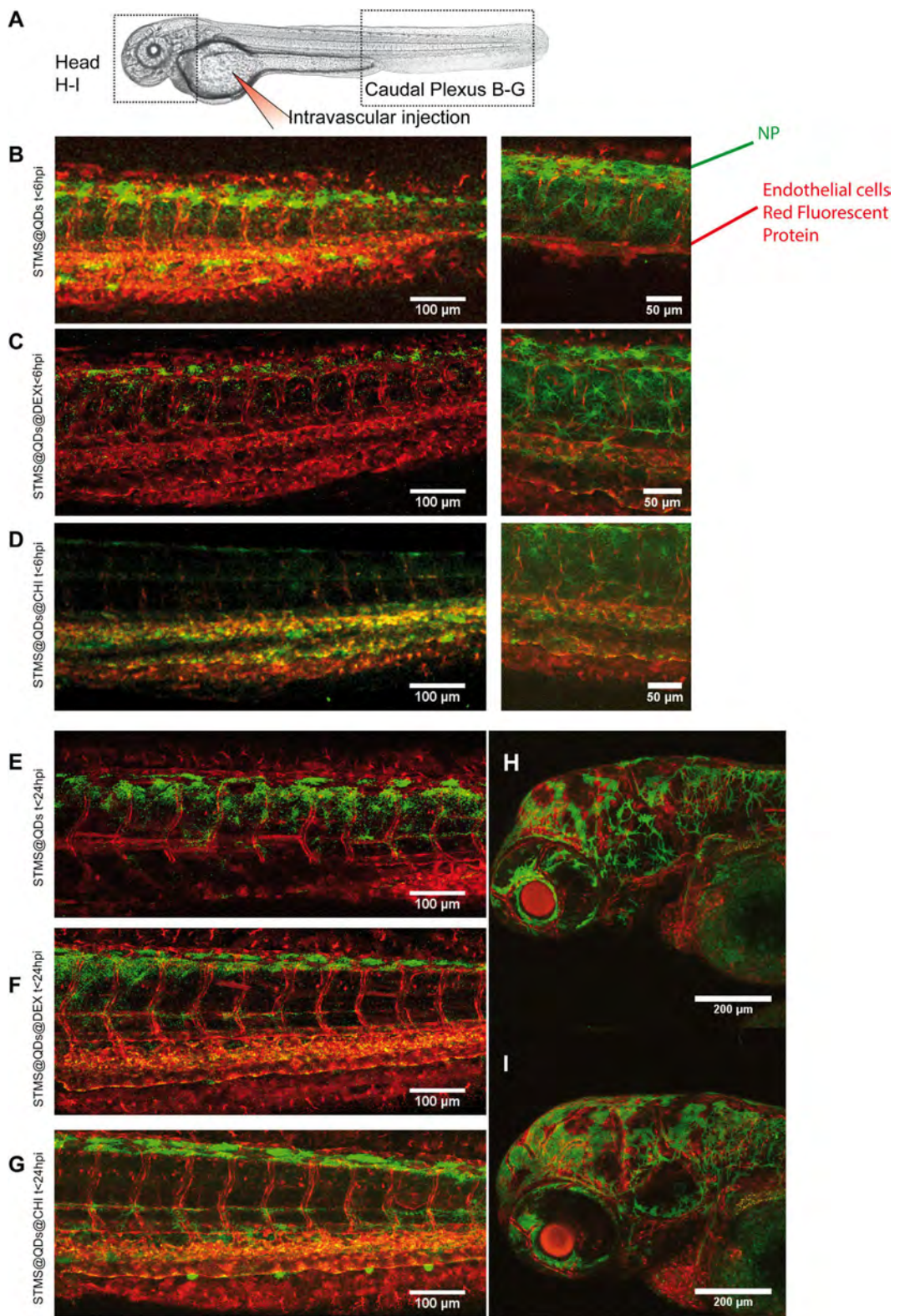


Fig. 10. A represents a scheme of the ZF with the injection spots and the different areas imaged. B–D left panel are low magnification confocal images showing respectively the distribution of STMS@QDs, STMS@QDs@DEX, and STMS@QDs@CHI NPs in the ZF embryo 6 h post-injection. The right panel corresponds to high magnification images at the same time points. E–G are low magnification images representing the distribution of the three NPs in the ZF at 24 h post-injection. H and I are the distribution at 24 h post injection of the STMS@QDs, and STMS@QDs@CHI in the ZF head.

tracking of injected NPs is shown to be highly feasible in the ZF embryo.

Some studies have investigated previously the use of fluorescent silica nanoparticles in zebrafish. They are mainly non porous, encapsulate fluorescent dyes and do not bear functional polymer coating that may be useful for additional functionalities. Hence, one work reported the uptake and toxicity of fluorescent silica nanoparticles doped with Ru complexes in zebrafish (*Danio rerio*) early life stages [34]. Authors indicated that up to 200 $\mu\text{g mL}^{-1}$, these nanoparticles were mainly accumulated on the chorion of embryos and exhibited no embryo-toxicity (mortality or deformity). In another study, the exposure of zebra fish larvae to silica nanoparticles were shown to cause embryonic (edema, tail and head) malformations by increasing doses in the range 25–200 $\mu\text{g mL}^{-1}$ [35]. These two different behaviors illustrate that it is rather difficult to address a general trend of the effect of silica nanoparticles in zebrafish especially because of the highly specific chemistry of the nanoparticles and the biological conditions of the experiments.

4. Conclusion

In this work, we investigated the design of hierarchically assembled silica nanoplateform made by a wrapping approach and we assessed their biodistribution *in vivo* in zebrafish embryo by luminescence bioimaging. Such stellate silica nanocomposites, grafted with quantum dots (QDs), were capped either with a further silica shell or with an original IBAM-polysaccharide coating. Interestingly, this latter polysaccharide coating method is shown the most suitable wrapping method to limit the release of indium and zinc cations in aqueous solution over three months. Regarding biological applications, these silica based nanoplateform demonstrated a good biocompatibility, as shown by cell culture or embryonic development assays and demonstrated a great potential to be used as fluorescent cell trackers in the zebrafish embryo.

Hence, given the large porosities offered by the stellate silica, and the possibility to graft QDs and to deposit inorganic or biopolymer coatings at their surface, these novel hybrid nanoplateform let envision further functionalities for theranostic applications (imaging, surface protection, drug release etc.) that cannot be obtained with QDs alone.

The main improvements as compared to other current functionalized silica nanoplateform are the facility to synthesize highly controlled and functionalized stellate silica nanoparticles (size, monodispersity) and the high potential for scaling-up as a typical synthetic procedure is rapid (2 h) and allows to synthesize several g of stellate silica nanoparticles. A main originality of this work is also the use of IBAM-polysaccharide coatings providing good colloidal stability to the nanoplateform and a high level of protection towards cation release over a long period of time (three months) which can be attractive for long-term storage of samples.

Future works will concern the development of further functionalities to the silica nanoplateform which may be combined to their luminescence properties. Hence we envision to investigate drug loading into these large pore and/or the incorporation of a magnetic core to afford MRI imaging and therapy by magnetic hyperthermia. Regarding biological aspects, the fluorescent labelling of more specific tissues *in vivo* and studies with mice which is the next step beyond zebrafish models will be envisioned.

Acknowledgements

The authors thank for financial and personal supports the «NANOTRANSMED» project which is co-funded by the European Regional Development Fund (ERDF) in the framework of the

INTERREG V Upper Rhine program «Transcending borders with every project». The «NANOTRANSMED» project is co-funded by the Swiss Confederation and the Swiss cantons of Aargau, Basel-Landschaft and Basel-Stadt. The Institut National du Cancer (INCa) is also acknowledged for the financial support (project PRTK14, THERAMAG 2014–225). The authors thank Dr A. Boos and P. Ronot (UMR 7178 - Institut Pluridisciplinaire Hubert Curien, Plateforme analytique des Inorganiques, Strasbourg) for ICP-MS measurements. Work in the Goetz lab (Tumor biomechanics) is supported by institutional funds from INSERM and University of Strasbourg. GF is a recipient of a PhD fellowship (from La ligue contre le Cancer). The Goetzlab is also thankful to INCa and Plan Cancer (OPTo-MetaTrap) for financial support.

Appendix A. Supplementary material

Supplementary data to this article can be found online at <https://doi.org/10.1016/j.jcis.2019.01.098>.

References

- [1] U. Resch-Genger, M. Grabolle, S. Cavaliere-Jaricot, R. Nitschke, T. Nann, Quantum dots versus organic dyes as fluorescent labels, *Nat. Method* 5 (2008) 763–775.
- [2] W.Y. William, E. Chang, R. Drezek, V.L. Colvin, Water-soluble quantum dots for biomedical applications, *Biochem. Biophys. Res. Commun.* 348 (2006) 781–786.
- [3] P. Yang, S. Gai, J. Lin, Functionalized mesoporous silica materials for controlled drug delivery, *Chem. Soc. Rev.* 41 (2012) 3679–3698.
- [4] F. Tang, L. Li, D. Chen, Mesoporous silica nanoparticles: synthesis, biocompatibility and drug delivery, *Adv. Mater.* 24 (2012) 1504–1534.
- [5] J. Liu, S.Z. Qiao, Q.H. Hu, Magnetic nanocomposites with mesoporous structures: synthesis and applications, *Small* 7 (2011) 425–443.
- [6] A. Guerrero-Martinez, J. Pérez-Juste, L.M. Liz-Marzán, Recent progress on silica coating of nanoparticles and related nanomaterials, *Adv. Mater.* 22 (2010) 1182–1195.
- [7] Y. Wang, H. Gu, Core–shell-type magnetic mesoporous silica nanocomposites for bioimaging and therapeutic agent delivery, *Adv. Mater.* 27 (2015) 576–585.
- [8] D. Mertz, O. Sandre, S. Bégin-Colin, Drug releasing nanoplateform activated by alternating magnetic fields, *Biochim. Biophys. Acta BBA – Gen. Subj.* 2017 (1861) 1617–1641.
- [9] L.M. Liz-Marzán, M. Giersig, P. Mulvaney, Synthesis of nanosized gold–silica core–shell particles, *Langmuir* 12 (1996) 4329–4335.
- [10] Y. Lu, Y. Yin, B.T. Mayers, Y. Xia, Modifying the surface properties of superparamagnetic iron oxide nanoparticles through a sol–gel approach, *Nano Lett.* 2 (2002) 183–186.
- [11] S.L. Pinho, G.A. Pereira, P. Voisin, J. Kassem, V. Bouchaud, L. Etienne, J.A. Peters, L. Carlos, S. Mornet, C.F. Geraldes, Fine tuning of the relaxometry of $\gamma\text{-Fe}_2\text{O}_3@ \text{SiO}_2$ nanoplateform by tweaking the silica coating thickness, *ACS Nano*, 4 (2010) 5339–5349.
- [12] D.K. Yi, S.T. Selvan, S.S. Lee, G.C. Papaefthymiou, D. Kundaliya, J.Y. Ying, Silica-coated nanocomposites of magnetic nanoparticles and quantum dots, *J. Am. Chem. Soc.* 127 (2005) 4990–4991.
- [13] D.K. Yi, S.S. Lee, G.C. Papaefthymiou, J.Y. Ying, Nanoparticle architectures templated by $\text{SiO}_2/\text{Fe}_2\text{O}_3$ nanocomposites, *Chem. Mater.* 18 (2006) 614–619.
- [14] J. Kim, J.E. Lee, J. Lee, J.H. Yu, B.C. Kim, K. An, Y. Hwang, C.-H. Shin, J.-G. Park, J. Kim, Magnetic fluorescent delivery vehicle using uniform mesoporous silica spheres embedded with monodisperse magnetic and semiconductor nanocrystals, *J. Am. Chem. Soc.* 128 (2006) 688–689.
- [15] J. Cui, M.P. van Koeverden, M. Müllner, K. Kempe, F. Caruso, Emerging methods for the fabrication of polymer capsules, *Adv. Colloid Interface Sci.* 207 (2014) 14–31.
- [16] B.G. De Geest, N.N. Sanders, G.B. Sukhorukov, J. Demeester, S.C. De Smedt, Release mechanisms for polyelectrolyte capsules, *Chem. Soc. Rev.* 36 (2007) 636–649.
- [17] J. Cui, Y. Yan, Y. Wang, F. Caruso, Templated assembly of pH-labile polymer-drug particles for intracellular drug delivery, *Adv. Funct. Mater.* 22 (2012) 4718–4723.
- [18] D. Mertz, P. Tan, Y. Wang, T.K. Goh, A. Blencowe, F. Caruso, Bromoisobutyramide as an intermolecular surface binder for the preparation of free-standing biopolymer assemblies, *Adv. Mater.* 23 (2011) 5668–5673.
- [19] D. Mertz, J. Cui, Y. Yan, G. Devlin, C. Chaubaroux, A. Dochter, R. Alles, P. Lavalle, J.C. Voegel, A. Blencowe, Protein capsules assembled via isobutyramide grafts: sequential growth, biofunctionalization, and cellular uptake, *ACS Nano*, 6 (2012) 7584–7594.
- [20] D. Mertz, H. Wu, J.S. Wong, J. Cui, P. Tan, R. Alles, F. Caruso, Ultrathin, bioresponsive and drug-functionalized protein capsules, *J. Mater. Chem.* 22 (2012) 21434–21442.

[21] K. Zhang, L.-L. Xu, J.-G. Jiang, N. Calin, K.-F. Lam, S.-J. Zhang, H.-H. Wu, G.-D. Wu, B. Albela, L. Bonneviot, Facile large-scale synthesis of monodisperse mesoporous silica nanospheres with tunable pore structure, *J. Am. Chem. Soc.* 135 (2013) 2427–2430.

[22] T. Shibu, M.W. Brooks, R.A. Weinberg, An integrin-linked machinery of cytoskeletal regulation that enables experimental tumor initiation and metastatic colonization, *Cancer Cell.* 24 (2013) 481–498.

[23] P. Corti, S. Young, C.-Y. Chen, M.J. Patrick, E.R. Rochon, K. Pekkan, B.L. Roman, Interaction between alk1 and blood flow in the development of arteriovenous malformations, *Development* (2011). dev-060467.

[24] J.G. Goetz, E. Steed, R.R. Ferreira, S. Roth, C. Ramspacher, F. Boselli, G. Charvin, M. Liebling, C. Wyart, Y. Schwab, J. Vermot, Endothelial cilia mediate low flow sensing during zebrafish vascular development, *Cell Rep.* 6 (2014) 799–808.

[25] G. Follain, N. Osmani, A.S. Azevedo, G. Allio, L. Mercier, M.A. Karreman, G. Solecki, M.J. Garcia León, O. Lefebvre, N. Fekonja, C. Hille, V. Chabannes, G. Dollé, T. Metivet, F.D. Hovsepian, C. Prudhomme, A. Pichot, N. Paul, R. Carapito, S. Bahram, B. Ruthensteiner, A. Kemmling, S. Siemonsen, T. Schneider, J. Fiehler, M. Glatzel, F. Winkler, Y. Schwab, K. Pantel, S. Harlepp, J.G. Goetz, Hemodynamic forces tune the arrest, adhesion, and extravasation of circulating tumor cells, *Dev. Cell.* 45 (2018) 33–52, e12. <https://doi.org/10.1016/j.devcel.2018.02.015>.

[26] G. Follain, N. Osmani, C. Fuchs, G. Allio, S. Harlepp, J.G. Goetz, Using the Zebrafish Embryo to Dissect the Early Steps of the Metastasis Cascade, in: *Cell Migr.*, Springer, 2018, pp. 195–211.

[27] Y. Chan, J.P. Zimmer, M. Stroh, J.S. Steckel, R.K. Jain, M.G. Bawendi, Incorporation of luminescent nanocrystals into monodisperse core–shell silica microspheres, *Adv. Mater.* 16 (2004) 2092–2097.

[28] M. Darbandi, R. Thomann, T. Nann, Single quantum dots in silica spheres by microemulsion synthesis, *Chem. Mater.* 17 (2005) 5720–5725.

[29] Q. Zhang, T. Zhang, J. Ge, Y. Yin, Permeable silica shell through surface-protected etching, *Nano Lett.* 8 (2008) 2867–2871, <https://doi.org/10.1021/nl8016187>.

[30] L. You, T. Wang, J. Ge, When mesoporous silica meets the alkaline polyelectrolyte: a controllable synthesis of functional and hollow nanostructures with a porous shell, *Chem.- Eur. J.* 19 (2013) 2142–2149.

[31] G. Ren, Z. Lin, B. Gilbert, J. Zhang, F. Huang, J. Liang, Evolution of ZnS nanostructure morphology under interfacial free-energy control, *Chem. Mater.* 20 (2008) 2438–2443.

[32] X. Wang, Y. Du, H. Liu, Preparation, characterization and antimicrobial activity of chitosan–Zn complex, *Carbohydr. Polym.* 56 (2004) 21–26.

[33] J. Shi, H.L. Karlsson, K. Johansson, V. Gogvadze, L. Xiao, J. Li, T. Burks, A. Garcia-Bennett, A. Uheida, M. Muhammed, S. Mathur, R. Morgenstern, V.E. Kagan, B. Fadeel, Microsomal glutathione transferase 1 protects against toxicity induced by silica nanoparticles but not by zinc oxide nanoparticles, *ACS Nano.* 6 (2012) 1925–1938.

[34] K. Fent, C.J. Weisbrod, A. Wirth-Heller, U. Pieles, Assessment of uptake and toxicity of fluorescent silica nanoparticles in zebrafish (*Danio rerio*) early life stages, *Aquat. Toxicol.* 100 (2010) 218–228.

[35] J. Duan, Y. Yu, H. Shi, L. Tian, C. Guo, P. Huang, X. Zhou, S. Peng, Z. Sun, Toxic effects of silica nanoparticles on zebrafish embryos and larvae, *PloS One* 8 (2013) e74606.

**ANNEX 8: ZIKA VIRUS ENHANCES MONOCYTE ADHESION AND
TRANSMIGRATION, FAVORING VIRAL DISSEMINATION TO THE CNS**

1 **Zika virus enhances monocyte adhesion and transmigration,**
2 **favoring viral dissemination to the CNS**

3

4 Nilda Vanesa Ayala-Nunez^{1,2}, Gautier Follain³, François Delalande⁴, Aurélie Hirschler⁴, Emma
5 Partiot¹, Gillian L. Hale⁵, Brigid C. Bollweg⁵, Judith Roels⁶, Maxime Chazal⁷, Florian Bakoa⁷,
6 Margot Carocci⁸, Sandrine Bourdoulous⁹, Orestis Faklaris¹⁰, Sherif R. Zaki⁵, Anita Eckly⁸,
7 Béatrice Uring-Lambert¹¹, Frédéric Doussau¹², Sarah Cianferani⁴, Christine Carapito⁴, Frank
8 M.J. Jacobs⁶, Nolwenn Jouvenet⁷, Jacky G. Goetz³, Raphael Gaudin^{1,2,*}.

9

10 ¹ Institut de Recherche en Infectiologie de Montpellier (IRIM), CNRS, Université de Montpellier,
11 34293 Montpellier, France

12 ² Université de Strasbourg, INSERM, 67000 Strasbourg, France

13 ³ INSERM U1109 and FMTS, 67000 Strasbourg, France

14 ⁴ Laboratoire de Spectrométrie de Masse Bio-Organique, IPHC, UMR 7178, CNRS-Université de
15 Strasbourg, ECPM, 67087 Strasbourg, France

16 ⁵ Infectious Diseases Pathology Branch, Division of High-Consequence Pathogens and Pathology,
17 National Center for Emerging and Zoonotic Infectious Diseases (NCEZID), Centers for Disease Control
18 and Prevention, 1600 Clifton Rd NE, MS: G32, Atlanta, GA 30329-4027, USA

19 ⁶ University of Amsterdam, Swammerdam Institute for Life Sciences, Science Park 904, 1098XH
20 Amsterdam, The Netherlands

21 ⁷ Viral Genomics and Vaccination Unit, UMR3569 CNRS, Virology Department, Institut Pasteur, 75015
22 Paris, France

23 ⁸ Université de Strasbourg, INSERM, EFS Grand Est, BPPS UMR-S1255, FMTS, 67000 Strasbourg,
24 France

25 ⁹ Université Paris Descartes, Sorbonne Paris Cité, CNRS UMR 8104, INSERM U1016, Institut Cochin,
26 Paris, France

27 ¹⁰ MRI Core facility, Biocampus, CNRS UMS 3426, 34293 Montpellier, France

28 ¹¹ Hôpitaux universitaires de Strasbourg, laboratoire central d'immunologie, 67000 Strasbourg,
29 France

30 ¹² CNRS UPR 3212, Institut des Neurosciences Cellulaires et Intégratives, Strasbourg, France

31

32 * Corresponding author:
33 Raphael Gaudin, PhD
34 Institut de Recherche en Infectiologie de Montpellier (IRIM)
35 CNRS UMR9004
36 1919 route de Mende, 34293 Montpellier, France
37 Phone: +33 4 34 35 94 63
38 Email: raphael.gaudin@irim.cnrs.fr
39

40 **Running title:** Monocyte-mediated ZIKV brain invasion

41

42 **Keywords:** virus-host interaction; Flavivirus; neurological disorder; zebrafish; organoids

43

44 **Abstract (150 words max)**

45 Zika virus (ZIKV) invades and persists in the central nervous system (CNS), causing severe neurological
46 diseases. Yet, the viral particle journey, from the bloodstream to tissues through a mature
47 endothelium, remains unclear. Here, we show that ZIKV-infected monocytes represent suitable
48 carriers for the viral dissemination to the CNS using human primary monocytes, cerebral organoids
49 derived from embryonic stem cells, organotypic mouse cerebellar slices, a xenotypic human-
50 zebrafish model, and human fetus brain samples. We found that ZIKV-exposed monocytes exhibit
51 higher expression of adhesion molecules, higher abilities to attach onto the vessel wall and
52 transmigrate across endothelia. This phenotype was associated to enhanced monocyte-mediated
53 ZIKV dissemination to neural cells. Together, our data shows that ZIKV manipulates the monocyte
54 adhesive properties and enhances monocyte transmigration and viral dissemination to neural cells.
55 Monocytes transmigration may represent an important mechanism requires for viral tissue invasion
56 and persistence that could be specifically targeted for therapeutic intervention.

57

58

59

60 **Introduction**

61 Zika virus (ZIKV) is a major public health concern worldwide¹. Currently no approved vaccine nor
62 drugs are available for treatment. The virus is a blood-borne pathogen from the *Flaviviridae* family
63 that is transmitted through the bite of an infected mosquito but also from human-to-human sexual
64 transmission, blood transfusion and mother-to-child transfer during pregnancy or at delivery²⁻⁶. The
65 most severe complications include fetal microcephaly in pregnant women, Guillain-Barré syndrome,
66 as well as other neurological disorders in fetuses, but also in newborns, infants and adults^{1,7-10},
67 severe thrombocytopenia¹¹ and testicular damage and atrophy^{12,13}. Moreover, ZIKV establishes
68 persistent infection in multiple tissues and body fluids such as in the brain, blood, saliva, urine and
69 semen¹⁴⁻¹⁸. The wide dissemination of the virus within the body suggests that molecular and cellular
70 mechanisms from the host are subverted to allow ZIKV virions to travel from their port of entry
71 toward tissues. This is particularly important for the difficult-to-access brain sanctuary. ZIKV
72 efficiently invades and persists within the brain^{15,17,19} and exhibits a preferential tropism for human
73 neural progenitor cells (hNPCs), which are key players in the development of ZIKV-induced
74 neurological diseases^{3,7,20,21}, cranial neural crest cells and microglia²²⁻²⁵. However, the mechanism by
75 which ZIKV travels towards and spreads into the brain remains unknown.

76 Although endothelial blood-to-tissue permeability may allow diffusive virus spreading in a first-
77 trimester fetus, it is not clear how ZIKV would invade hard-to-reach tissues exhibiting a mature,
78 impermeable endothelium. Yet, ZIKV efficiently reaches and remains within the brain of hosts with a
79 mature blood-brain barrier (BBB)^{15,17,26-29}. The BBB is an extremely tight endothelium separating
80 bloodstream-circulating incoming virions from the neural target cells. The “Trojan horse” strategy,
81 consisting of the infection of circulating leukocytes that carry virus through endothelial monolayers,
82 has been proposed for numerous viruses in various *in vitro* infection assays³⁰⁻³⁵, but never highlighted
83 in an *in vivo* context. Monocytes are considered as well-suited viral carriers since they exhibit potent
84 transmigrating abilities over endothelial barriers, including the BBB^{36,37}. It was recently shown that
85 circulating monocytes harbor ZIKV *in vitro* and in patients³⁸⁻⁴⁰, but no further role was attributed to
86 these cells in the physiopathology of the infection.

87 Here, we show that ZIKV-infected monocytes are found in the CNS of a human fetus with
88 microcephaly and we assessed monocyte-driven ZIKV dissemination and damage in *ex vivo* culture
89 models including human embryonic stem cell (hESCs)-derived cerebral organoids and organotypic
90 mouse cerebellar slices. Moreover, we found that exposure of human monocytes to ZIKV triggers
91 higher expression of adhesion molecules, higher capacities to spread and adhere to different
92 substrates, and higher abilities to attach and transmigrate through endothelia *in vitro* and in a

93 zebrafish embryo model. Finally, we correlated the increased transmigration phenotype to higher
94 dissemination rates to hESC-derived cerebral organoids compared to cell-free virus infection.

95

96 **Results**

97 *ZIKV-infected monocyte-derived cells are found in the CNS of a human fetus*

98 First, we asked whether ZIKV-infected monocyte-derived cells could be detected in human brain
99 samples. Brain slices of a ZIKV-positive human fetus (5 months) diagnosed with microcephaly were
100 stained for the viral protein NS1 together with the leukocyte marker CD45, the monocytic marker
101 CD14, and the myeloid markers CD68 or CD163. Numerous cells expressing these markers in the
102 perivascular area were found positive for ZIKV NS1 (Fig. 1a-d and controls in Suppl Fig. S1).
103 Importantly, although endothelial cells have been reported to be targets of ZIKV *in vitro*⁴¹⁻⁴³, we did
104 not observe any infection of these cells from the BBB of a naturally ZIKV-infected human fetus with
105 microcephaly (Fig. 1e).

106 *Monocytes are productively infected by ZIKV*

107 To assess for the susceptibility of leukocytes to ZIKV infection, we isolated total PBMCs from three
108 human healthy donors infected *in vitro* by ZIKV strains isolated in 2015 in Colombia (ZIKV^C) and
109 Panama (ZIKV^P) that share 99.5% similarity. Flow cytometry analysis was performed to define the
110 permissiveness of CD4⁺ T lymphocytes, CD8⁺ T lymphocytes, B lymphocytes, monocytes, natural killer
111 (NK) cells and NKT cells (Suppl Fig. S2a). A primary labeled anti-NS2B antibody that recognizes a non-
112 structural ZIKV protein (that is not contained into incoming virions) was used to identify cells
113 supporting active ZIKV replication (as opposed to non-infected cells carrying incoming particles). All
114 cell types showed some level of ZIKV infection, in a strain- and donor-dependent manner (Suppl Fig.
115 S2a). Monocytes were the most permissive cell type overall, in agreement with previous reports³⁸⁻⁴⁰.
116 Moreover, ZIKV induces a shift of the monocyte population from a CD14⁺ CD16⁻ toward a CD14⁺
117 CD16⁺, preferentially infecting them (Suppl Fig. S2b-c), which correlates with studies that previously
118 showed that the CD14⁺ CD16⁺ monocytic subset is particularly permissive to infection by other Asian
119 ZIKV strains^{38,39}.

120 Given the variability observed among the three blood donors examined, we then purified monocytes
121 from PBMCs of these 3 donors (donors A to C) as well as from 4 additional donors (donors D-G). Flow
122 cytometry analyses revealed that monocytes were permissive to ZIKV^C in 6 out of 7 donors and to
123 ZIKV^P in 5 out of 7 donors (Fig. 2a). In the subsequent experiments, we worked solely with the ZIKV^C
124 strain, which shows better infectiveness, and will be referred to as ZIKV.

125 To determine whether the absence of NS2B staining in some donors was due to low fluorescence
126 sensitivity, we performed RT-qPCR analysis on monocytes from three donors at different time post-
127 infection. No significant infection was detected by RT-qPCR for one donor (not shown), but successful
128 replication was observed in the two other donors (Fig. 2b). Specifically, the amount of viral RNA was
129 first decreasing from 2 to 24 hpi, indicative of the expected incoming viral RNA degradation, followed
130 by an increase at 48 hpi. Such increase represents viral replication. Thus, ZIKV replication in
131 monocytes is slow as compared to the 24-hour cell cycle usually reported for Flaviviruses in other cell
132 types (see for instance ⁴⁴). This late timing was also observed at the protein level, where NS2B was
133 successfully detected at 48 hpi but not at 24 hpi (Suppl Fig. S3a). Detection of ZIKV RNA by
134 fluorescence *in situ* hybridization (FISH) in monocytes isolated from two donors further
135 demonstrated the ability of the virus to replicate in this cell type (Fig. 2c). In agreement with flow
136 cytometry and qPCR data, very little cells were positive for viral RNA, suggesting that only a small
137 subset of monocytes is susceptible to infection. Finally, productive monocyte infection was
138 established by measuring infectious viral particle release and we found that monocytes shed a low
139 amount of infectious ZIKV (Fig. 2d). ZCL278, a Cdc42 inhibitor⁴⁵ and a broad-spectrum entry
140 inhibitor⁴⁶, abolished ZIKV infection of monocytes (Fig. 2d and Suppl Fig. S3b). In all the conditions
141 tested, we measured the amount of LDH released from dying cells as an indirect measurement of
142 cytotoxicity and found that neither ZIKV nor ZCL278 induced cell death (Suppl Fig. S3c).

143 *ZIKV-infected monocytes disseminate the infection and alter the cytoarchitecture of the cerebellum*
144 As monocytes are productively infected (Fig. 2), we then addressed whether they could disseminate
145 ZIKV to target cells. Therefore, we grew cerebral organoids from hESCs as we previously
146 described^{47,48} (see Material & Methods for details). At 3 weeks post differentiation (wpd), the cells
147 composing the cerebral organoids were mostly Pax6-positive, indicative of neural precursor cells
148 (Suppl Fig. S4a). At 6 wpd, the organoids contained Pax6-positive cells organized as Rosetta and a
149 high number of terminally differentiated neurons, as shown by the increased number of CTIP2-
150 positive cells (Suppl Fig. S4a-b). The hESC-derived cerebral organoids were incubated with cell-free
151 ZIKV or ZIKV-infected monocytes for 2 days, and analyzed by flow cytometry to measure the
152 percentage of live ZIKV-infected cells among the CCR2-negative population (to exclude the
153 monocytes). Strikingly, we observed that ZIKV-infected monocytes isolated from two donors were
154 successful at disseminating the infection to the organoids as early as 2 days post-contact, while the
155 ability of cell-free virus to disseminate the infection was marginal to null (Fig. 3a). By 3D confocal
156 imaging, the infected cells were mostly positive for Pax6 (Fig. 3b). When the infection was allowed
157 for 9 days, the organoids infected with cell-free virus were successfully infected as well (Suppl Fig.
158 S4c), suggesting that monocytes accelerate the kinetics of ZIKV dissemination to cerebral organoids.

159 To further explore the functional relevance of the presence of infected monocyte in the CNS, we
160 used an organotypic culture of mouse cerebellar slices as we previously described⁴⁹, a method of
161 choice for the *ex vivo* study of viral infection⁵⁰. ZIKV was shown to induce abnormal cerebellum
162 anatomy in mice⁵¹ and thus, organotypic culture provides a tissue that maintains cellular
163 composition, tissue architecture, and function of a *bona fide* cerebellum⁴⁹. The cerebellar slices were
164 incubated for 4 days with non-infected human monocytes, ZIKV-infected monocytes or cell-free virus
165 in the presence or absence of ZCL278 (scheme in Fig. 3c). Staining of the Purkinje cell layer and nuclei
166 showed relatively well-conserved tissue architecture in untreated conditions (Fig. 3d). Quantification
167 of the proportion of altered, intermediate, or healthy lobules highlighted that the cerebellar slices
168 incubated with ZIKV-infected monocytes represent the only condition in which altered
169 cytoarchitecture of the cerebellar lobules was significantly increased (Fig. 3e), suggesting that cell-
170 associated viral dissemination favors neuropathogenesis. This phenotype was completely reversed by
171 the use of the antiviral ZCL278.

172 *ZIKV-infected monocytes exhibit higher transmigration abilities*

173 To test whether ZIKV could influence circulating monocytes to cross the BBB, transwell inserts were
174 seeded with the human cerebellar microvascular endothelial cells D3 (hCMEC/D3)⁵² (see scheme Fig.
175 4a). Under our culturing conditions, hCMEC/D3 cells form a tight monolayer exhibiting robust
176 impermeability (Suppl Fig. S5a-b), within the range of expected tightness^{53,54}. ZIKV-infected
177 monocytes, cell-free virus and ZCL278 treatment did not significantly perturb endothelial
178 impermeability (Fig. 4b). No viral replication was observed in hCMEC/D3 monolayer during the
179 course of the experiment (Fig. 4c). However, a significantly greater percentage of monocytes that
180 transmigrated were ZIKV-positive (bottom chamber, green) compared to the one that did not
181 transmigrate (top chamber, red; Fig. 4d). Consistently, scanning confocal microscopy analysis
182 revealed that a significantly greater proportion of monocytes were found under the endothelial
183 monolayer when exposed to ZIKV (Fig. 4e-f).

184 In conclusion, our data indicates that ZIKV readily enhances the ability of monocytes to transmigrate,
185 while the permeability of the endothelial layer remained unaffected.

186 *ZIKV-exposed monocytes exhibit higher adhesion properties*

187 To further investigate the impact of ZIKV on human primary monocytes, we performed differential
188 quantitative proteome profiling using highly sensitive and robust liquid chromatography coupled to
189 tandem mass spectrometry (LC-MS/MS). A total of 521 proteins were differentially expressed (191
190 upregulated and 330 downregulated) between mock and ZIKV-exposed monocytes from 2 donors (in
191 quadruplicates, FDR 0.05; see Suppl Table 1). Upon parallel analyses using STRING⁵⁵ (highest

192 confidence 0.9) and GSEA⁵⁶ (“biological process” and “cellular component” pathways), we observed
193 that ZIKV induced a significant enrichment of proteins associated with adhesion, vesicular transport
194 (clathrin-mediated endocytosis and cytoskeleton-related proteins), and RNA processing and
195 translation (Fig. 5a-b). Specifically, integrins ($\beta 1$, $\alpha 5$, αM), ICAM3, PECAM1, IQGAP1, catenin,
196 myosins, actinin, KIF5B, vinculin, talin, and filamin A and B that are involved in cell adhesion and/or in
197 the establishment of focal adhesion sites, were upregulated by ZIKV (Suppl Table 1). Proteins
198 associated with the immune system response were not significant upregulated in monocytes upon
199 ZIKV infection. By comparison, monocytes exposed to HIV-1, which is unrelated to flaviviruses, or to
200 the closely related Dengue 2 virus (DENV2), elicited a enrichment of proteins involved in antiviral
201 immune responses, but no modulation of adhesion-related proteins (Suppl Fig. S6). Thus, the
202 increase of expression of adhesion proteins in monocytes seems specific of ZIKV infection.

203 To determine whether the ZIKV-induced expression of adhesion molecules was over-represented at
204 their functional location, *i.e.* the cell surface, we next assessed by flow cytometry the monocyte’s
205 surface expression levels of a panel of well-known adhesion molecules. We found that 10 out of the
206 22 proteins tested were significantly upregulated at the surface of monocytes from 3 donors (Fig. 5c).
207 Interesting, productive infection was not strictly required as non-infected bystander cells (Fig. 5d),
208 and UV-inactivated ZIKV (Fig. 5e and Suppl Fig. S7) also significantly induced the overexpression of
209 the adhesion-associated protein CD99. Of note, UV-inactivated virus exposure induced an early
210 overexpression of CD99 at the surface of monocytes (Fig. 5e) and therefore, the molecular
211 mechanism behind this increase could differ from the one observed in ZIKV-infected monocytes.
212 Interestingly, while CD99 and ITGAL were significantly overexpressed at the cell surface of monocytes
213 (Fig. 5c-e), we observed a decreased expression of the mRNA coding for these proteins (Suppl Fig.
214 S8). As ZIKV enhances RNA processing and translation related proteins (Fig. 5a-b), one could
215 hypothesize that ZIKV lower transcription levels and favor translation by an unknown mechanism.

216 We next investigated whether the observed ZIKV-induced adhesion phenotype would have a
217 functional role on monocyte’s attachment. Upon ZIKV infection, adhesion of monocytes was
218 significantly increased on different substrates and on hCMEC/D3 endothelial cells (Fig. 5f-h). This
219 increased attachment was specific for ZIKV, since infection with HIV-1 and treatment with hGM-CSF
220 did not result in such an increase (Fig. 5f).

221 *ZIKV-exposed monocytes exhibit an increased spread out morphology*

222 From the imaging in Fig. 5g and 3D reconstructions in Fig. 6a, we noticed that exposure to ZIKV
223 correlated with an extended spread morphology of the monocytes. Quantification of the cell’s area
224 and circularity upon attachment to endothelial cells in ZIKV-exposed monocytes confirmed that ZIKV

225 induces a dramatic spread out morphology compared to naïve monocytes (Fig. 6b-c and Suppl Fig.
226 S9).

227 Given the importance of Cdc42 on integrin-mediated cell adhesion, spreading and transmigration^{56,57},
228 we tested the small molecule ZCL278, which activity was initially reported to suppress Cdc42-
229 dependent cell motility⁴⁵, as an inhibitor of ZIKV-induced transmigration. Remarkably, ZCL278, when
230 added post-infection, selectively prevented transmigration of monocyte the monocytes exposed to
231 ZIKV (Fig. 6d), while non-infected cells were insensitive to the drug.

232 Together, our data shows that ZIKV induces higher adhesion, spreading and transmigration of human
233 primary monocytes across an *in vitro* BBB-like model.

234 *ZIKV-exposed monocytes exhibit higher transmigration properties in vivo*

235 We next aimed at demonstrating the relevance of this phenotype *in vivo*. Since transmigration is a
236 very challenging process to study in mammals, we tested whether zebrafish embryos could represent
237 a suitable alternative. To this end, we developed a novel quantitative xenotypic system based on a
238 procedure designed to dissect the early behavior of circulating cells in the zebrafish embryo
239 bloodstream^{57,58}. Monocytes were infected with ZIKV alone or ZIKV in the presence of a pan-flavivirus
240 antibody known to increase infection through “antibody-dependent enhancement” (ADE)⁵⁹⁻⁶² (Suppl
241 Fig. S10). Transgenic zebrafish embryos *Tg(fli:EGFP)* modified to express EGFP in endothelial cells⁶³
242 were injected with pre-labeled human primary monocytes (see Fig. 7a-b, Suppl Movie 1, and Material
243 & Methods for details) and imaged \approx 6 h post-injection, a timing sufficient to observe the monocytes
244 inside, outside, and transmigrating through the vasculature (Fig. 7c). Mapping the location of the
245 monocytes that successfully transmigrated out of the vascular caudal plexus did not show significant
246 differences between the different conditions (Fig. 7d). However, the percentage of extravasated cells
247 was significantly increased when monocytes were previously exposed to ZIKV for all three donors
248 tested (Fig. 7e). Transmigration efficiency was not linked to the percentage of ZIKV-infected cells as
249 ADE-ZIKV had no significant further effect on monocytes transmigration compared to monocytes
250 infected in the absence of ADE.

251 *ZIKV-exposed monocytes exhibit higher arresting properties in vivo*

252 To further determine the mechanism by which ZIKV promotes monocyte transmigration *in vivo*, we
253 defined the hemodynamic behavior of circulating human monocytes in the bloodstream of zebrafish
254 embryos upon injection. Three main dynamic phenotypes could be monitored: circulating, stopping
255 and rolling-like motion (Fig. 8a and Suppl Movie 2). Automated tracking of circulating monocytes
256 revealed that previous exposure to ZIKV significantly increased monocyte track duration (Fig. 8b). In

257 parallel, the speed of ZIKV-exposed monocytes was drastically diminished (Fig. 8c-e). These
258 measurements correlated with a greater percentage of ZIKV-exposed monocytes immobilized onto
259 the endothelial vasculature compared to monocytes that were not in contact with the virus (Fig. 8f).
260 However, once immobilized on the vessel wall, the average time of monocyte arrest was
261 independent of the infection status of the cell (Fig. 8g). Of note, enhancing ZIKV infection of
262 monocytes through ADE did not potentiate these behaviors.

263 These data suggest that exposure to ZIKV promotes the initial attachment of human primary
264 monocytes to the endothelial cell wall without impacting their arrest duration.

265 *Transmigrated monocytes efficiently disseminate infection to cerebral organoids*

266 We then intended to directly link monocyte transmigration to viral dissemination and CNS
267 neuroinvasion. We thus established a co-culture transmigration assay, in which transwells coated
268 with an endothelial monolayer of hBMEC/D3 cells, were incubated with cell-free ZIKV or ZIKV-
269 associated monocytes in the top chamber, and with 6-wpd cerebral organoids in the bottom
270 chamber (scheme Fig. 9a). In this setting, and in the absence of chemokine addition in the organoid-
271 containing bottom chamber, we observed that the proportion of monocytes that transmigrated was
272 higher when exposed to ZIKV than in the absence of virus (Suppl Fig. S11a), consistent with our
273 previous observations indicating that ZIKV enhances monocyte transmigration (Fig. 4). The transwell
274 inserts were removed at the end of the overnight transmigration process, at a time that did not allow
275 infection of endothelial cells (Fig. 4c), and the cerebral organoids were collected 48 h later. Flow
276 cytometry analysis of the dissociated organoids revealed that the cerebral cells were more
277 permissive to infection driven by ZIKV-infected monocytes than by cell-free virus (Fig. 9b-c).
278 Nevertheless, at 9 dpi, no difference in the percentage of cerebral infected cells was observed (Suppl
279 Fig. S11b), suggesting that cell-free virus can cross endothelium in the absence of leukocyte carriers,
280 but with delayed viral dissemination.

281 Together these data indicate that ZIKV-induced monocyte transmigration promotes viral
282 dissemination across the vessel wall.

283

284 **Discussion**

285 In this study, we propose a model in which ZIKV productively infects a subset of blood-circulating
286 monocytes and induces phenotypical and morphological changes, which in turn leads to higher
287 monocyte adhesion and transmigration abilities. Upon transmigration, monocytes-associated ZIKV
288 shows faster infectiveness kinetics toward reconstituted “mini-brains” than cell-free virus.

289 We have shown that cells derived from circulating monocytes are host targets in the brain of a ZIKV-
290 infected human fetus. Resident perivascular macrophages (CD163⁺) and microglia (CD68⁺) originate
291 from the embryonic yolk sac or from blood-circulating monocytes that differentiate upon
292 transmigration⁶⁴⁻⁶⁶. The importance of the recruitment of circulating monocytes to the CNS during
293 the course of an infection by the West Nile Virus (WNV), a ZIKV-related Flavivirus, was previously
294 demonstrated in mice⁶⁷. This study indicates that the infiltrated myeloid cells in the CNS originate
295 from blood circulating monocytes. A recent study showed that the recombinant NS1 protein of
296 several Flaviviruses induces transient endothelial permeability⁶⁸. This work convincingly highlighted
297 the presence of vascular leakage in mice injected with recombinant NS1, and further *in vivo* studies
298 using ZIKV infection models that recapitulate the physiopathology of a natural infection in humans
299 will be required. Negligible BBB disruption was found in WNV-infected mice with encephalitis⁶⁷ and
300 our *in vitro* data failed to detect endothelial permeability following ZIKV exposure (Fig. 4b), similarly
301 to previously published data⁴³. Moreover, ZIKV is mostly asymptomatic in humans and does not
302 induce hemorrhagic fever nor cytokine storm^{10,69}, suggesting that endothelial leakage may not be a
303 major feature of ZIKV physiopathology.

304 Endothelial cells have also been reported to be targets of ZIKV *in vitro*⁴¹⁻⁴³ using different viral strains
305 and/or cell lines. However, we did not observe infection nor disruption of endothelial cells from the
306 BBB of a naturally ZIKV-infected human fetus with microcephaly (Fig. 1e and in our experimental
307 design, hCMEC/D3 cells were not infected by ZIKV (Fig. 4c). Thus, the viral main access to the CNS
308 remains to be further characterized as several models, including endothelial cell infection, the Trojan
309 horse hypothesis and transient BBB permeability remains plausible and not mutually exclusive.
310 Further work will also be required to assess whether ZIKV could subvert other pathways, such as
311 transcytosis, to cross the BBB.

312 We and others have observed that ZIKV does not induce a robust immune response in monocytes
313 (our proteomics data in Fig. 5a-b and ⁷⁰⁻⁷³), in sharp contrast to DENV2 and HIV-1^{74,75}. It could be
314 explained by the capacity of the NS5 protein of ZIKV to suppress interferon signaling⁷⁶. However, ZIKV
315 infection is not fully immunologically silent in all cell types and higher production of MCP-1, a
316 monocyte chemoattractant, in mice and in macaques has also been reported^{77,78}. Moreover, the
317 work by O'Connors *et al.* established that monocytes are targeted by the virus in macaques and that
318 these cells are recruited to tissues, promoting viral persistence⁷⁷. Therefore, ZIKV-infected monocytes
319 could represent a *bona fide* "Trojan horse"-like carrier used by ZIKV to cunningly disseminate into the
320 CNS. Therefore, monocytes may represent an important systemic mediator of tissue invasion and
321 viral persistence and additional *in vivo* studies will help to evaluate the relative contribution of
322 monocytes in the ZIKV neuroinvasion process.

323 ZIKV enhances monocytes adhesion and transmigration through the vessel wall, inducing higher
324 expression of adhesion molecules at the monocyte surface (Fig. 4). This mechanism of action is
325 specific to ZIKV as we did not observe adhesion-related pathway upregulation in HIV-1 and DENV2
326 infection of monocytes. HIV-1 also enhances transmigration to the CNS (not shown and ⁷⁹), but the
327 underlying molecular mechanism likely differs from the one of ZIKV, as HIV-infected monocytes do
328 not adhere significantly more than controls (Fig. 5f-h). Dengue virus does not trigger transmigration
329 of J774 monocytic cells⁸⁰, further highlighting the specificity of ZIKV-monocyte interactions that we
330 reported here. The impact of ZIKV-infected monocytes on the adhesion molecule profile of
331 endothelial cells would also be relevant to address in future work, as monocyte-endothelial
332 communication plays an important role in adhesion⁸¹.

333 Transmigration induced by ZIKV was prevented by treating cells with an inhibitor of Cdc42 function
334 (Fig. 6d). A previous report pointed out that Cdc42 was not required for physiological monocyte
335 adhesion and spreading⁸², and thus, ZIKV could engage a Cdc42-dependent actin remodeling
336 program that is not usually implicated in physiological monocyte transmigration. This observation
337 may have important implication for the design of treatments with selective activity. The dual action
338 of ZCL278 as a Cdc42 inhibitor and as a potent antiviral molecule may be a promising antiviral option
339 that requires further investigations.

340 Live cell imaging of leukocyte circulation, arrest, rolling and transmigration is very challenging to
341 perform in complex mammals, such as in mice, as elegantly exemplified recently⁸³. The technical
342 limitations include body hindrance under the microscope, heartbeat repetitive pulses, lack of
343 transparency and loss of the injected cells into body parts that are not accessible to imaging.
344 Although powerful 3D organoid models that mimic blood vessels are being developed^{84,85}, they
345 represent *in vitro* systems that do not fully recapitulate the complexity of a living organism. In this
346 context, the zebrafish embryo represents a promising *in vivo* alternative, previously used to study
347 mammalian viruses⁸⁶⁻⁸⁸. Indeed, the zebrafish embryo is relatively transparent, easy to handle,
348 displays fast growth kinetics, and numerous tools for genetic manipulation are available. Moreover,
349 the zebrafish embryo represents a classical approach to study cancer cell extravasation^{52,89,90}, but has
350 never been employed, to our knowledge, to study virus-induced transmigration. Here, we have
351 developed a xenotypic system, injecting human primary monocytes into zebrafish embryos (Fig. 7-8).
352 We showed that human primary cells retained their capacity to undergo diapedesis through a
353 zebrafish endothelial barrier, suggesting that active molecular interactions between these cells are
354 taking place despite the species' gap. This experimental *in vivo* model was recently exploited to
355 perform extensive human monocyte phenotyping upon injection in zebrafish⁹¹. The development of
356 this robust and easy-to-manipulate *in vivo* model allowed quantitative analyses of monocyte

357 transmigration under hemodynamically relevant conditions that would not have been achieved with
358 other animal models.

359 The cerebral organoid model derived from hESCs was previously characterized and used in the
360 context of ZIKV infection^{92,93} as these organoids recapitulate much of the architecture of the fetal
361 brain, modeling whole brain development⁹⁴. A limitation however is that cerebral organoids do not
362 spontaneously develop a functional vasculature (unless transplanted⁹⁵), and we thus had to engineer
363 a tranwell-organoid system to allow the combined investigations of both transmigration and
364 dissemination (Fig. 9). In this system, we found that cell-free virus had slower kinetics of
365 dissemination than monocyte-associated virus, suggesting that monocytes could accelerate viral
366 spreading toward tissues.

367 In conclusion, using various *in vitro*, *ex vivo* and *in vivo* models, we have shown that ZIKV enhances
368 monocyte transmigration to efficiently cross endothelial barriers and promotes viral dissemination.
369 Our findings are of importance in regard of our current understanding of ZIKV-host interactions and
370 highlight monocyte transmigration as a process that could be specifically targeted for therapeutic
371 intervention.

372

373

374 **Acknowledgments**

375 We thank Dr. Philippe Benaroch for his critical reading of our study, Lucie Klughertz for her technical
376 support, and Dr. Camille Ducloy for her helpful insights on flow cytometry techniques. We
377 acknowledge the imaging facility MRI, member of the national infrastructure France-BioImaging
378 supported by the French National Research Agency (ANR-10-INBS-04, “Investments for the future”).
379 This work has received funding from the French State via the French National Research Agency (ANR)
380 as part of the program “Investissements d’avenir” (IdEx Université de Strasbourg) to RG. This work
381 was supported by an ATIP-AVENIR starting grant to RG. The research leading to these results has
382 received funding from the People Program (Marie Curie Actions) of the European Union’s Seventh
383 Framework Program (FP7/2007-2013) under REA grant agreement n. PCOFUND-GA-2013-609102,
384 through the PRESTIGE program coordinated by Campus France, and from the French Agency for
385 Research on AIDS and Viral Hepatitis (ANRS), both attributed to NVAN. Experiments conducted by GF
386 and JGG were funded by Plan Cancer (OptoMetaTrap), Ligue contre le Cancer, Idex Attractivités
387 (University of Strasbourg), and by institutional funds from INSERM and University of Strasbourg. GF
388 was supported by a doctoral fellowship from Ligue Contre le Cancer. Mass spectrometry experiments
389 were supported by the French Proteomic Infrastructure (ProFI; ANR-10-INBS-08-03). FB is recipient of
390 a PhD grant provided by ANRT (Association Nationale de la Recherche et de la Technologie). NJ is
391 funded by Agence Nationale pour la Recherche (ANR-16-CE15-0025-01), Centre National de la
392 Recherche Scientifique (CNRS) and Institut Pasteur.

393 CDCs contributions to this manuscript written and edited by GLH and BCB in their private capacity.
394 No official support or endorsement by the Centers for Disease Control and Prevention, Department
395 of Health and Human Services is intended, nor should be inferred. All authors read, provided
396 feedback and approved the manuscript. The findings and conclusions in this report are those of the
397 authors and do not necessarily represent the official position of the Centers for Disease Control and
398 Prevention.

399 The following reagent was obtained through the NIH AIDS Reagent Program, Division of AIDS, NIAID,
400 NIH: HIV-1 NL4-3 AD8 Infectious Molecular Clone (pNL(AD8)) from Dr. Eric O. Freed (cat# 11346).

401

402 **Author Contributions**

403 NVAN and RG conceived the experiments. NVAN performed the experiments involving viruses and
404 monocytes. NVAN, EP and RG analyzed flow cytometry data. RT-qPCR analyses were performed by FB
405 and FISH imaging was undertaken by MCh. MCa produced concentrated Zika virus. GLH, BCB and SRZ

406 designed and performed experiments associated to human fetal brain. FD and AH performed mass
407 spectrometry and associated data analyses were undertaken by FD, CC, SC and RG. NVAN and GF
408 performed the zebrafish experiments and image analyses were undertaken by NVAN, GF, JGG and
409 RG. JR and FMJJ prepared and provided expertise on cerebral organoids. NVAN, RG and AE
410 performed SEM. OF, BUL, SB, and NJ provided reagents and expertise. RG wrote the manuscript and
411 NVAN, NJ and JGG edited and commented on the manuscript.

412

413 **Declaration of Interests**

414 The authors declare no competing interests.

415

416 **Methods**

417 ***Cell culture***

418 Purified human primary monocytes were cultured in RPMI 1640 (Gibco) supplemented with 2% FBS
419 (Dutscher) and 1% Penicillin-Streptomycin (Gibco). Cells were cultured into round bottom tissue
420 culture treated 96-well plates. The human Cerebellar Microvascular Endothelial Cells D3 (hCMEC/D3)
421 cells⁹⁶ were cultured using EndoGRO-MV Complete Culture Media (Millipore) supplemented with 1
422 ng/mL bFGF (Sigma) and 1% Penicillin-Streptomycin (Gibco). Cells were plated and cultured in dishes
423 coated with rat collagen-I (R&D Systems). Lithium Chloride (10 mM) and Resveratrol (10 μ M) were
424 added when seeding the cells in the culture inserts (cf. transmigration assay). Vero cells (ATCC) were
425 cultivated in High-glucose DMEM media with L-Glutamine (Hyclone), 10% FBS, and 1% Penicillin-
426 Streptomycin. All cell types were maintained at 37°C in a humidified atmosphere containing 5% CO₂.

427 ***Monocyte purification***

428 Buffy coats were obtained from adult healthy blood donors (EFS Strasbourg, France) where all donors
429 signed informed consent allowing the use of their blood for research purpose. PBMCs were purified
430 on a Ficoll density gradient (GE Healthcare). Monocytes were isolated by positive selection using
431 CD14⁺ microbeads and magnetic columns from Miltenyi Biotec.

432 ***Viruses***

433 The ZIKV strains were obtained through BEI Resources, NIAID, NIH: Zika Virus, FLR, NR-50183 (ZIKV^C)
434 and Zika Virus, H/PAN/2015/CDC-259359, NR-50219 (ZIKV^P). ZIKV^C and ZIKV^P were isolated in
435 December 2015 from the blood of infected patients from Colombia and Panama, respectively. The
436 ZIKV strain PRVABC59, which was used as a control for immunohistochemistry experiments,
437 originated from a human serum specimen in December of 2015 in Puerto Rico (NCBI Accession No.
438 KU501215). ZIKV^C and ZIKV^P were grown on Vero cells for 72 h. The cleared supernatant was stored
439 at -80°C and used for infection experiments. To obtain concentrated virus, the ZIKV-containing
440 supernatant was passed through a 0.45 μ m filter (Millipore) and ultracentrifugation at 30000g for 15
441 h using a SW28 rotor (Beckman Coulter). In all experiments, supernatant from non-infected Vero
442 cells was used as non-infected controls. The multiplicity of infection (MOI) was calculated by virus
443 titration on Vero cells using standard plaque assay to measure plaque forming unit per ml of virus
444 (PFU/ml). All experiments involving infectious ZIKV were performed in a BSL-3 facility. DENV2 strain
445 16681 was obtained from the Biological Resource Center of Institut Pasteur. Viral stocks were
446 prepared on C6/36 cells. Virus titers were assessed by focus forming assays on Vero cells, as

447 described previously⁴⁴. HIV-1 was obtained from the supernatant of HEK 293T cells transfected with
448 pNL(AD8)⁹⁷.

449 ***Flow cytometry and antibodies***

450 To process the cells for flow cytometry analysis, the samples were first blocked with 10% FBS in PBS.
451 Human FcR Blocking Reagent (Miltenyi Biotec) was added to prevent unspecific binding of IgGs to Fc
452 receptors (FcR). To label cell surface markers, samples were stained with a cocktail of primary labeled
453 antibodies at 4°C. To detect intracellular proteins, cells were fixed in 4% paraformaldehyde (PFA) and
454 permeabilized using 0.1% Triton X-100 (Sigma) and 0.5% BSA (Euromedex). PBMC samples were
455 acquired with a 10-channel Navios flow cytometer (Beckman Coulter) with a combination of 405,
456 488, 640 nm lasers. The other samples were acquired with a LSR II flow cytometer (BD Biosciences), a
457 MACS Quant flow cytometer (Miltenyi Biotec), a Cytoflex flow cytometer (Beckman Coulter), or a
458 Novocyte (ACEA Biosciences). All data were analyzed using FlowJo, LLC software version v10.4.2.

459 Fluorophore-coupled antibodies anti-CD3-PB, -CD4-AF750, -CD8-AF700, -CD14-PC7, -CD16-PE, -CD19-
460 ECD, -CD45-KO, -CD56-PC5.5, and -CD144-AF647 were purchased from Beckman Coulter. The CD45-
461 VioBright515, CD156a-APC, CD62E-APC, CD62L-FITC, CD62P-APC, CD54-APC, CD102-APC, CD106-FITC,
462 CD31-FITC, CD146-FITC, CD11a-FITC, CD11b-APC-Vio770, CD11c-FITC, CD49d-FITC, CD29-FITC, CD18-
463 FITC, CD43-FITC, CD47-FITC, CD162-FITC, CD169-APC, CD209-FITC, and CD99-FITC were purchased
464 from Miltenyi Biotech. The mouse anti CD144-A647 was purchased from BD Biosciences. The rabbit
465 anti-NS2B and anti-NS1 antibodies were purchased from GeneTex. The mouse and rabbit Anti-
466 Flavivirus group antigen [D1-4G2-4-15 (4G2)] was purchased from Absolute Antibody. Antibodies
467 were labeled with Alexa Fluor 488 or 647 using an antibody labeling kit (Molecular Probes).

468 ***Reagents***

469 ZCL278 was purchased from Tocris and diluted in DMSO at 50 mM. ICAM-1 recombinant protein
470 (#ADP4-050), fibronectin isolated from human plasma (1918-FN-02M) were purchased from R&D
471 Systems. The type I solution of rat collagen, Lucifer Yellow CH dilithium salt and Resveratrol, and
472 Lithium Chloride were purchased from Sigma-Merck. The recombinant human CCL2/MCP-1 Protein
473 from R&D Systems and Miltenyi Biotec,

474 ***Human subjects***

475 The human fetal brain tissues used in this study were obtained from a PCR-confirmed case of
476 congenital ZIKV; gestational age 22 weeks⁹⁸. The use of these tissues for the research presented in
477 this paper was determined to be outside the scope of human subjects oversight, and institutional
478 review board (IRB) was not required.

479 **Immunohistochemistry**

480 Immunohistochemical assays were performed using a peroxidase and alkaline-phosphatase detection
481 system. Briefly, 4 μ m tissue sections were placed on slides. The sections were deparaffinized in
482 xylene and rehydrated through graded alcohol solutions. Colorimetric detection of antibodies was
483 performed using the EnVision G|2 Doublestain System Rabbit/Mouse (DAB+/Permanent Red)
484 (Agilent). Heat induced epitope retrieval (HIER) using EDTA based buffer was performed (Biocare
485 Medical) using the Biocare NxGen decloaker program #5 (110°C for 15 min). All slides were then
486 treated according to the Dako EnVision G|2 Doublestain System procedure. Slides were incubated in
487 Endogenous Enzyme block for 5 min, primary antibody for 10 min, HRP-Polymer for 10 minutes and
488 DAB working solution for 10 min. Doublestain block was then applied for 3 min, and the second stain
489 procedure consisted of the other primary antibody for 10 min, followed by the Rabbit/Mouse Link,
490 AP-Polymer and Permanent Red working solution for 10 min each. Slides were double stained with a
491 ZIKV specific anti NS1 monoclonal antibody (clone 3C2) at 1:500 (CDC Immuno-Diagnostic
492 Development Team, manuscript in preparation) and one of the following markers: CD68 at 1:100
493 (Leica # NCL-L-CD68), CD163 at 1:50 (Leica # NCL-L-CD163), CD14 at 1:100 (Abcam # ab183322) or
494 CD45 at 1:100 (Leica # NCL-L-LCA). In each double stain, CD markers and Zika virus were each labeled
495 with Permanent Red and DAB in serial sections. Appropriate negative control serum was run in
496 parallel. Slides were counterstained in Mayer's Hematoxylin (Polyscientific) and blued in Lithium
497 carbonate (Polysciences). Slides were cover slipped with aqueous mounting medium (Polysciences).
498 All steps of the staining procedure, with the exception of the HIER, were performed at room
499 temperature.

500 **Human cortical organoid**

501 *Culture and differentiation.* Cortical organoids were generated from H9 human embryonic stem cells
502 (hESC; female, WA09, WiCell) as described previously⁴⁸. Briefly, H9 hESCs were grown on mitomycin-
503 C treated MEF feeding layers in ESC culture medium: DMEM/F12 + L-glutamine (Thermofisher) with
504 20% KnockOut serum replacement (Thermofisher), 1X non-essential amino acids (Thermofisher), 100
505 μ M β -mercaptoethanol (Thermofisher) and 1X Penicillin-Streptomycin (Thermofisher). The hESC
506 culture medium was changed daily and freshly supplemented with 8 ng/ml human bFGF (Sigma). For
507 organoid differentiation, the culture medium was replaced with differentiation medium: ESC culture
508 medium with 1X Sodium Pyruvate (Thermofisher) but without addition of human bFGF. Colonies of
509 approximately 2 mm in diameter were manually lifted using a Corning cell lifter and were transferred
510 to a 60 mm ultra-low attachment dish (Corning). After 24 hours (day 0), embryoid bodies had formed
511 and half of the medium was replaced with differentiation medium supplemented with 3 μ M IWR-1-

512 Endo (Sigma), 1 μ M Dorsomorphin (Sigma), 10 μ M SB-431542 (Sigma) and 1 μ M Cyclopamine
513 (Sigma). Medium was replaced every other day until the harvest. From day 3 onwards, 60 mm dishes
514 with organoids were placed on a belly button shaker in the incubator. From day 18 onwards,
515 organoids were cultured in Neurobasal medium (Thermofisher) with 1X N2 supplement
516 (Thermofisher), 2 mM L-glutamine, 1X pen-strep and 1 μ M Cyclopamine. From day 24 onwards,
517 Cyclopamine was not added anymore.

518 *Infection and processing.* Cerebral organoids were co-cultured with ZIKV-infected monocytes, non-
519 infected monocytes, cell-free ZIKV or mock for either 2 or 9 days. The media was replaced every
520 other day. At the indicated timepoints, the organoids were processed for flow cytometry or
521 immunofluorescence. For the flow cytometry analysis, the organoids were dissociated with trypsin,
522 stained with Viability 405/502 (Miltenyi), fixed with 4% PFA for 20 min at RT, permeabilized and
523 stained. For immunofluorescence, the cerebral organoids were fixed with 4% PFA for 1 h at RT,
524 permeabilized with 1% Triton X-100 (2 days at RT), labeled for 1 day at RT with primary antibodies
525 and fluorescent secondary antibodies as necessary, and clarified overnight at RT using RapiClear 1.52
526 reagent (Sunjin Lab). The clarification was observed to be important to perform in-depth whole
527 organoid imaging, as the clarification medium homogenizes the refractive index of the organoid and
528 diminishes scattering of the emitted photons. All stainings were done in the presence of human FcR
529 blocking reagent and nuclei were labeled with Dapi. Image acquisition was performed on a spinning
530 disk confocal microscope (Dragonfly, Oxford Instruments) equipped an ultra-sensitive 1024x1024
531 EMCCD cameras (iXon Life 888, Andor) and four laser lines (405, 488, 561 and 637 nm). A 20x, NA 0.8
532 air objective was used for whole organoid imaging and a 40x, NA 1.15 (Nikon) water immersion long
533 distance (0.6 mm) objective was used for in-depth imaging of selected areas of the organoid. For the
534 z-stacks a z step of 1 μ m was used. Images were processed using Imaris x64 (Bitplane) version 9.2.

535 **Organotypic cultures of mouse cerebellar slices**

536 Organotypic cerebellar slices were prepared from P10-P12 mice as previously described^{99,100}. Briefly,
537 after decapitation, the cerebellum was dissected out in minimum essential medium (MEM) with 25
538 mM Hepes, 4 g l⁻¹ D-Glucose, 50 UI ml⁻¹ penicillin and 50 μ g ml⁻¹ streptomycin. Isolated cerebella
539 were cut into 350 μ m parasagittal slices using a McIlwain tissue chopper (MickleLab). Slices were
540 transferred onto 30 mm culture inserts with 0.4 μ m pore size (Millicell, Merk Millipore). Inserts were
541 placed in six-well plates containing 1 ml of culture medium per well. Culture medium was composed
542 of 50% MEM with 25 mM Hepes, 25% basal medium eagle, 25% heat-inactivated horse serum
543 supplemented with 2.10–3 M GlutaMAX®, 50 UI ml⁻¹ penicillin, 50 μ g ml⁻¹ streptomycin and 4 g l⁻¹
544 D-glucose. Slices cultures were incubated at 37°C in a humidified incubator equilibrated with 95%

545 air/5% CO₂. The medium was refreshed every 2 days. D-Glucose, penicillin and streptomycin were
546 from Sigma-Aldrich. Culture media, horse serum and GlutaMAX® were from ThermoFisher.

547 One week after culture, the slices were treated with 10⁶ monocytes/slice (infected or not infected).
548 The cell-free virus condition was performed using 10⁶ PFUs of ZIKV, corresponding to the amount
549 used to infect monocytes at a MOI of 1. Monocytes and virus preparations were applied dropwise to
550 the top (air interface) of each slice.

551 Individual organotypic cerebellar slices were fixed using paraformaldehyde 4% in phosphate buffer
552 solution (PBS) for 30 min at room temperature. Then, slices were transferred to a saturation solution
553 containing PBS with 0.2% Triton, 2% bovine serum albumin (Sigma-Aldrich) and 10% goat serum
554 (Merk Millipore) for a minimum of 12 hours. Purkinje cells were specifically labeled using an anti-
555 calbindin antibody (mouse monoclonal, 1:1500, Sigma-Aldrich). The secondary antibody was an
556 Alexa-488 donkey anti-rabbit (1:1000, Invitrogen). Primary and secondary antibodies were prepared
557 in PBS supplemented with 0.2% Triton, 2% bovine serum albumin and 5% normal goat serum (Merk
558 Millipore) and labeling at each step was performed for a minimum of 24 hours at 4°C. Slices were
559 mounted on glass coverslips with Prolong Gold® antifade reagent (Invitrogen, USA). Confocal images
560 were produced at the imaging facility service of the Neuropole (CNRS, UPS 3156, Strasbourg, France)
561 using a Leica SP5II inverted confocal microscope (10x; 20x or 63x objectives). Fields were acquired
562 using 488 nm argon laser and 561 nm Diode pumped solid-state laser.

563 ***Detection of Zika RNA in infected cells by fluorescent in situ Hybridization (FISH) assays.***

564 Cells were attached on #1.5 glass coverslips using Poly-L-lysine, and FISH was performed using the
565 QuantiGene ViewRNA ISH Assay Kit following the manufacturer's instruction (Affymetrix) and a
566 specific probe recognizing ZIKV plus strand RNA (Affymetrix VF1-19981). Cell DNA was stained with
567 Nucblue (Thermo Fisher). Images were acquired with an inverted confocal microscope (Zeiss LSM
568 700) and processed with Zen2 (blue edition) software (Zeiss).

569 ***RT-qPCR***

570 Total RNA was extracted from monocytes with the NucleoSpin RNA II kit (Macherey-Nagel). First-
571 strand complementary DNA synthesis was performed with the SuperScript III First-Strand Synthesis
572 System Reverse Transcriptase (Invitrogen). Quantitative real-time PCR was performed on a real-time
573 PCR system (ABI PRISM 7900HT) with SYBR Green PCR Master Mix (Life Technologies). Data were
574 analyzed with the 2-DDCT method¹⁰¹, with all samples normalized to GAPDH. The ZIKV forward and
575 reverse primers used were 5' – AARTACACATACCAACAAAGTGGT – 3' and 5' –
576 TCCRCTCCCYCTYTGGTCTTG – 3' as previously published¹⁰². The GAPDH forward and reverse primers

577 used were 5' – GGTCGGAGTCAACGGATTG – 3' and 5' – ACTCCACGACGTACTCAGCG – 3'. The CD99
578 forward and reverse primers used were 5' – CTCTTCCCCTTCTTCCTGTG – 3' and 5' –
579 CAAATCCAAACCCCAACCAC – 3'. The ITGAL forward and reverse primers used were 5' –
580 TCATACACCACGTCAACCTTC – 3' and 5' – CTCTTCCATGTTCAGCCTCTG – 3'.

581 ***Transmigration assay***

582 The hCMEC/D3 cells were seeded at a density of 40-50,000 cells/cm² (6-wells) hanging cell culture
583 inserts (PET, 5 µm pores, Millipore) pre-coated with rat collagen type 1 (Sigma). The cells were kept
584 in culture for 7 days until ready for the transmigration and permeability assays. Infected monocytes
585 were extensively washed in RPMI 10% FBS media prior addition to the transwell inserts containing
586 the hCMEC/D3 cells. In parallel, the media in the bottom chamber was replaced with fresh media
587 containing 200 ng/mL MCP-1 (Miltenyi Biotech). Transmigration was allowed to occur overnight
588 (about 17 h). Monocytes were recovered from the top and bottom chambers of the insert and
589 prepared for flow cytometry analysis.

590 ***Lucifer yellow permeability assay***

591 On day 7 of culture in the transwell, permeability was assessed by adding 50 µM Lucifer yellow in the
592 top chamber. After 120 min at 37°C, media was collected from the top and bottom chambers of the
593 insert. In parallel, a calibration curve of Lucifer yellow was prepared (50, 25, 12.5 and 6.25 µM).
594 Quantification of fluorescence was done using a microplate reader (Mithras LB 940 Multimode
595 Microplate Reader, Berthold Technologies) with excitation at 488 nm and emission filter at 520 nm.
596 The permeability coefficient (Pc) was calculated as described in ⁵³.

597 ***Cell viability***

598 Cell viability was assessed using the Pierce LDH Cytotoxicity Assay Kit (Thermofisher Scientific)
599 according to the manufacturer's instructions. Absorbance was measured with a Mithras LB 940
600 Multimode Microplate Reader (Berthold Technologies).

601 ***Immunofluorescence***

602 ZIKV-infected monocytes co-cultured with either hCMEC/D3 cells or hNPCs grown on coverslips were
603 fixed with PFA 4%, permeabilized with 0.1% Triton X-100 and 0.5% BSA and labeled with primary
604 antibodies and fluorescent secondary antibodies as necessary. The staining was done in the presence
605 of human FcR blocking reagent and nuclei were labeled with Dapi. Coverslips were mounted on slides
606 using Fluoromount Aqueous Mounting (Sigma). Image acquisition was performed on an
607 AxioObserver.Z1 inverted microscope (Zeiss) mounted with a spinning disc head (Yokogawa), a back-

608 illuminated EMCCD camera (Evolve, Photometrics) and a X63 or X100, 1.45 NA oil objective (Zeiss).
609 Images were processed using Fiji (ImageJ software version 1.51h) and the 3D reconstruction was
610 performed using Imaris x64 version 9.2.

611 The goat anti Human VE-Cadherin antibody was purchased from R&D Systems. The secondary
612 donkey anti-mouse antibody coupled to Alexa Fluor 488 was purchased from Invitrogen.

613 ***Adhesion assay***

614 Adhesion assays were performed either in plastic 96-wells plates (flat bottom) or on glass coverslips.
615 The coating of the substrate was done with 150 µg/mL of collagen, type I solution from rat tail
616 (Sigma), 12.5 µg/mL of recombinant Human ICAM-1/CD54 (R&D Systems), or 5 µg/cm² of human
617 fibronectin from R&D Systems. Primary monocytes were added to the coated substrate and
618 incubated for 2 h at 37°C. Afterwards, the cells were processed for immunofluorescence staining
619 with Phalloidin A568 (Invitrogen), or analyzed for cell viability with the CellTiter-Glo Luminescent Cell
620 Viability Assay (Promega).

621 ***Scanning electron microscopy***

622 ZIKV-infected monocytes co-cultured with hCMEC/D3 cells on coverslips were washed twice with
623 Cacodylate buffer (pre-warmed), and fixed with Glutaraldehyde 2.5% for 1 h at RT. The samples were
624 dehydrated in a graded alcohol, coated with platinum, and imaged with a Phenom ProX Desktop
625 scanning electron microscope (Thermo Fisher).

626 ***Quantitative proteomics***

627 *Sample preparation.* The protein concentration of all samples was determined using the RC-DC
628 protein assay (Bio-Rad) according to the manufacturer's instructions and a standard curve was
629 established using BSA. Five µg of protein lysate for each sample and a sample pool for quality control
630 (QC) were heated at 95°C for 5 min and concentrated on a stacking gel band. The gel bands were cut,
631 washed with ammonium hydrogen carbonate and acetonitrile, reduced and alkylated before trypsin
632 digestion (Promega). The generated peptides were extracted with 60% acetonitrile in 0.1% formic
633 acid followed by a second extraction with 100% acetonitrile. Acetonitrile was evaporated under
634 vacuum and the peptides were resuspended in 10 µL of H₂O and 0.1% formic acid before nanoLC-
635 MS/MS analysis.

636 *NanoLC-MS/MS analysis.* NanoLC-MS/MS analyses were performed on a nanoACQUITY Ultra-
637 Performance LC system (Waters, Milford, MA) coupled to a Q-Exactive Plus Orbitrap mass
638 spectrometer (ThermoFisher Scientific) equipped with a nanoelectrospray ion source. The solvent
639 system consisted of 0.1% formic acid in water (solvent A) and 0.1% formic acid in acetonitrile (solvent

640 B). Samples were loaded into a Symmetry C18 precolumn (0.18 x 20 mm, 5 μ m particle size; Waters)
641 over 3 min in 1% solvent B at a flow rate of 5 μ L/min followed by reverse-phase separation (ACQUITY
642 UPLC BEH130 C18, 200 mm x 75 μ m id, 1.7 μ m particle size; Waters) using a linear gradient ranging
643 from 1% to 35% of solvent B at a flow rate of 450 nL/min. The mass spectrometer was operated in
644 data-dependent acquisition mode by automatically switching between full MS and consecutive
645 MS/MS acquisitions. Survey full scan MS spectra (mass range 300-1800) were acquired in the
646 Orbitrap at a resolution of 70K at 200 m/z with an automatic gain control (AGC) fixed at 3.10⁶ and a
647 maximal injection time set to 50 ms. The ten most intense peptide ions in each survey scan with a
648 charge state \geq 2 were selected for fragmentation. MS/MS spectra were acquired at a resolution of
649 17,5K at 200 m/z, with a fixed first mass at 100 m/z, AGC was set to 1.10⁵, and the maximal injection
650 time was set to 100 ms. Peptides were fragmented by higher-energy collisional dissociation with a
651 normalized collision energy set to 27. Peaks selected for fragmentation were automatically included
652 in a dynamic exclusion list for 60 s. All samples were injected using a randomized and blocked
653 injection sequence (one biological replicate of each group plus pool in each block). To minimize carry-
654 over, a solvent blank injection was performed after each sample. A sample pool comprising equal
655 amounts of all proteins extracts was constituted and regularly injected 4 times during the course of
656 the experiment, as an additional QC. Protein identification rates and coefficients of variation (CV)
657 monitoring of this QC sample revealed very good stability of the system: 2597 of the 2805 identified
658 proteins, namely 92%, showed a CV value lower than 25% considering all 4 injections.

659 *Data interpretation.* Raw MS data processing was performed using MaxQuant software¹⁰³ v1.6.0.16.
660 Peak lists were searched against a database including *Homo sapiens* protein sequences extracted
661 from SwissProt (06-03-2019; 20 410 sequences, Taxonomy ID 9606) using the MSDA software
662 suite¹⁰⁴.

663 MaxQuant parameters were set as follows: MS tolerance set to 20 ppm for the first search and 5
664 ppm for the main search, MS/MS tolerance set to 40 ppm, maximum number of missed cleavages set
665 to 1, Carbamidomethyl (C) set as fixed modification, Oxidation (M) set as variable modification. False
666 discovery rates (FDR) were estimated based on the number of hits after searching a reverse database
667 and were set to 1% for both peptide spectrum matches (with a minimum length of seven amino
668 acids) and proteins. Data normalization and protein quantification was performed using the LFQ
669 (label free quantification) option implemented in MaxQuant using a “minimal ratio count” of one.
670 The “Match between runs” option was enabled using a 2 min time window after retention time
671 alignment. All other MaxQuant parameters were set as default. To be considered, proteins must be
672 identified in all four replicates of at least one condition and a minimum of 2 unique peptides. The
673 imputation of the missing values and differential data analysis were performed using the open-

674 source ProStaR software¹⁰⁵. Two runs of imputation were applied, the “SLA” mode was applied for
675 the partially observed values (POV) and the “det quantile” for the missing in the entire condition
676 (MEC)¹⁰⁶. A Limma moderated *t*-test was applied on the dataset to perform differential analysis. The
677 adaptive Benjamini-Hochberg procedure was applied to adjust the p-values and FDR values under 1%
678 or 5% depending on the comparisons were achieved. Data analyses were performed using the
679 STRING online tool⁵⁵, using highest confidence (0.9 interaction score). The unlinked proteins were
680 excluded from the network shown in Fig. 5a. The same data were also processed using the GSEA
681 online tool⁵⁶, using features from gene ontology “biological process” and “cellular component”.
682 Complete dataset has been deposited to the ProteomeXchange Consortium via the PRIDE partner
683 repository¹⁰⁷ with the dataset identifier PXD014002.

684 ***Antibody-dependent enhancement assay***

685 For virus-antibody complex formation, virus particles (MOI 5) were incubated for 30 min at 37 °C in
686 presence of serial 10-fold dilutions of 4G2 antibody in RPMI medium containing 2% FBS. The virus-
687 antibody complexes were then added to primary monocytes and incubated at 37°C with 5% CO₂. At
688 48 hpi, the cells were thoroughly washed, fixed, and processed for flow cytometry analysis as
689 described below.

690 ***Zebrafish experiments***

691 Tg(*fli1a:eGFP*) Zebrafish (*Danio rerio*) embryos (ZFIN ID: ZDB-FISH-150901-3654) were used in all
692 experiments. Embryos were maintained in Danieau 0.3X medium (17,4 mM NaCl, 0,2 mM KCl, 0,1
693 mM MgSO₄, 0,2 mM Ca(NO₃)₂) buffered with HEPES 0.15 mM (pH = 7.6), supplemented with 200 mM
694 of 1-Phenyl-2-thiourea (Sigma-Aldrich) to inhibit the melanogenesis, as previously described¹⁰⁸. For
695 all Zebrafish experiments, the offspring of one single cross was selected, based on
696 anatomical/developmental good health. Embryos were split randomly between experimental groups.
697 48 h post-fertilization (hpf), embryos were mounted in a 0.8% low melting point agarose pad
698 containing 650 mM of tricain (ethyl-3-aminobenzoate-methanesulfonate) to immobilize them. Pre-
699 labelled primary human CD14⁺ monocytes were injected with a Nanoject microinjector 2
700 (Drummond) and microforged glass capillaries (20 µm inner diameter) filled with mineral oil (Sigma)
701 and 14 nL of a cell suspension at 10⁸ cells per mL were injected in the duct of Cuvier of the embryos
702 under the M205 FA stereomicroscope (Leica) similarly to what we previously described⁵⁸. At 5 to 7 h
703 post-injection, confocal imaging was performed with an inverted TCS SP5 confocal microscope with a
704 HC PL IRAPO 20X NA0.75 objective (Leica). The experiment was carried 3 independent times using 3
705 different monocyte donors with n = 10 embryos per condition (exception: n = 5 for second donor,

706 condition ADE-ZIKV). The monocytes were labeled with CellTrace Yellow (Invitrogen) according to
707 manufacturer's instructions.

708 For live recording of the injection, a stereomicroscope with a DFC3000 G camera (Leica) was used. To
709 capture flowing and arresting monocytes in real time, only the red channel (corresponding to
710 injected prelabeled monocytes) was recorded during injection. After 5 min, a single image of the
711 zebrafish vasculature was acquired and used as an overlay background for the registered time-lapse
712 recording of monocytes.

713 Cell dispersion was manually counted and localized in the caudal plexus using the stereotype
714 patterning of intersegmental vessels (ISVs) as a reference. The data were compiled to generate
715 heatmaps using a custom-made MATLAB plugin⁵⁸. Post-processing was performed using ImageJ and
716 Imaris x64 version 9.2 for segmentation, 3D reconstruction, and tracking.

717

718 **References**

719

- 720 1 Lessler, J. *et al.* Assessing the global threat from Zika virus. *Science* **353**, aaf8160, doi:10.1126/science.aaf8160 (2016).
- 722 2 Turmel, J. M. *et al.* Late sexual transmission of Zika virus related to persistence in the semen. *Lancet* **387**, 2501, doi:10.1016/S0140-6736(16)30775-9 (2016).
- 724 3 Yockey, L. J. *et al.* Vaginal Exposure to Zika Virus during Pregnancy Leads to Fetal Brain Infection. *Cell* **166**, 1247-1256 e1244, doi:10.1016/j.cell.2016.08.004 (2016).
- 726 4 Mansuy, J. M. *et al.* Zika virus: high infectious viral load in semen, a new sexually transmitted pathogen? *The Lancet. Infectious diseases* **16**, 405, doi:10.1016/S1473-3099(16)00138-9 (2016).
- 729 5 Harrower, J. *et al.* Sexual Transmission of Zika Virus and Persistence in Semen, New Zealand, 2016. *Emerging infectious diseases* **22**, 1855-1857, doi:10.3201/eid2210.160951 (2016).
- 731 6 Musso, D. *et al.* Potential sexual transmission of Zika virus. *Emerging infectious diseases* **21**, 359-361, doi:10.3201/eid2102.141363 (2015).
- 733 7 Li, H., Saucedo-Cuevas, L., Shresta, S. & Gleeson, J. G. The Neurobiology of Zika Virus. *Neuron* **92**, 949-958, doi:10.1016/j.neuron.2016.11.031 (2016).
- 735 8 Baud, D., Gubler, D. J., Schaub, B., Lanteri, M. C. & Musso, D. An update on Zika virus infection. *Lancet*, doi:10.1016/S0140-6736(17)31450-2 (2017).
- 737 9 da Silva, I. R. F., Frontera, J. A., Bispo de Filippis, A. M. & Nascimento, O. Neurologic Complications Associated With the Zika Virus in Brazilian Adults. *JAMA neurology*, doi:10.1001/jamaneurol.2017.1703 (2017).
- 740 10 Pierson, T. C. & Diamond, M. S. The emergence of Zika virus and its new clinical syndromes. *Nature* **560**, 573-581, doi:10.1038/s41586-018-0446-y (2018).
- 742 11 Sharp, T. M. *et al.* Zika Virus Infection Associated With Severe Thrombocytopenia. *Clinical infectious diseases : an official publication of the Infectious Diseases Society of America* **63**, 1198-1201, doi:10.1093/cid/ciw476 (2016).
- 744 12 Uraki, R. *et al.* Zika virus causes testicular atrophy. *Science advances* **3**, e1602899, doi:10.1126/sciadv.1602899 (2017).

747 13 Ma, W. *et al.* Zika Virus Causes Testis Damage and Leads to Male Infertility in Mice. *Cell* **167**, 748 1511-1524 e1510, doi:10.1016/j.cell.2016.11.016 (2016).

749 14 Lustig, Y., Mendelson, E., Paran, N., Melamed, S. & Schwartz, E. Detection of Zika virus RNA in 750 whole blood of imported Zika virus disease cases up to 2 months after symptom onset, Israel, 751 December 2015 to April 2016. *Euro surveillance : bulletin European sur les maladies 752 transmissibles = European communicable disease bulletin* **21**, doi:10.2807/1560-7917.ES.2016.21.26.30269 (2016).

753 15 Aid, M. *et al.* Zika Virus Persistence in the Central Nervous System and Lymph Nodes of 754 Rhesus Monkeys. *Cell* **169**, 610-620 e614, doi:10.1016/j.cell.2017.04.008 (2017).

755 16 Paz-Bailey, G. *et al.* Persistence of Zika Virus in Body Fluids - Preliminary Report. *The New 756 England journal of medicine*, doi:10.1056/NEJMoa1613108 (2017).

757 17 Hirsch, A. J. *et al.* Zika Virus infection of rhesus macaques leads to viral persistence in 758 multiple tissues. *PLoS pathogens* **13**, e1006219, doi:10.1371/journal.ppat.1006219 (2017).

759 18 Musso, D. *et al.* Detection of Zika virus in saliva. *Journal of clinical virology : the official 760 publication of the Pan American Society for Clinical Virology* **68**, 53-55, 761 doi:10.1016/j.jcv.2015.04.021 (2015).

762 19 Bhatnagar, J. *et al.* Zika Virus RNA Replication and Persistence in Brain and Placental Tissue. 763 *Emerging infectious diseases* **23**, 405-414, doi:10.3201/eid2303.161499 (2017).

764 20 Li, H. *et al.* Zika Virus Infects Neural Progenitors in the Adult Mouse Brain and Alters 765 Proliferation. *Cell stem cell* **19**, 593-598, doi:10.1016/j.stem.2016.08.005 (2016).

766 21 Tang, H. *et al.* Zika Virus Infects Human Cortical Neural Progenitors and Attenuates Their 767 Growth. *Cell stem cell* **18**, 587-590, doi:10.1016/j.stem.2016.02.016 (2016).

768 22 Lum, F. M. *et al.* Zika Virus Infects Human Fetal Brain Microglia and Induces Inflammation. 769 *Clinical infectious diseases : an official publication of the Infectious Diseases Society of 770 America* **64**, 914-920, doi:10.1093/cid/ciw878 (2017).

771 23 Mesci, P. *et al.* Modeling neuro-immune interactions during Zika virus infection. *Human 772 molecular genetics*, doi:10.1093/hmg/ddx382 (2017).

773 24 Vermillion, M. S. *et al.* Intrauterine Zika virus infection of pregnant immunocompetent mice 774 models transplacental transmission and adverse perinatal outcomes. *Nature communications* 775 **8**, 14575, doi:10.1038/ncomms14575 (2017).

776 25 Bayless, N. L., Greenberg, R. S., Swigut, T., Wysocka, J. & Blish, C. A. Zika Virus Infection 777 Induces Cranial Neural Crest Cells to Produce Cytokines at Levels Detrimental for 778 Neurogenesis. *Cell host & microbe* **20**, 423-428, doi:10.1016/j.chom.2016.09.006 (2016).

779 26 Silveira, E. L. V. *et al.* Immune Cell Dynamics in Rhesus Macaques Infected with a Brazilian 780 Strain of Zika Virus. *J Immunol* **199**, 1003-1011, doi:10.4049/jimmunol.1700256 (2017).

781 27 Mavigner, M. *et al.* Postnatal Zika virus infection is associated with persistent abnormalities 782 in brain structure, function, and behavior in infant macaques. *Sci Transl Med* **10**, 783 doi:10.1126/scitranslmed.aaa6975 (2018).

784 28 Deng, Y. Q. *et al.* Intranasal infection and contact transmission of Zika virus in guinea pigs. 785 *Nature communications* **8**, 1648, doi:10.1038/s41467-017-01923-4 (2017).

786 29 Manangeeswaran, M., Ireland, D. D. & Verthelyi, D. Zika (PRVABC59) Infection Is Associated 787 with T cell Infiltration and Neurodegeneration in CNS of Immunocompetent Neonatal 788 C57Bl/6 Mice. *PLoS pathogens* **12**, e1006004, doi:10.1371/journal.ppat.1006004 (2016).

789 30 Yewdell, J. W. & Brooke, C. B. Monocytes, viruses and metaphors: hanging the Trojan horse. 790 *Cell Cycle* **11**, 1748-1749, doi:10.4161/cc.20311 (2012).

791 31 Gras, G. & Kaul, M. Molecular mechanisms of neuroinvasion by monocytes-macrophages in 792 HIV-1 infection. *Retrovirology* **7**, 30, doi:10.1186/1742-4690-7-30 (2010).

793 32 Laval, K., Favoreel, H. W., Poelaert, K. C., Van Cleemput, J. & Nauwynck, H. J. Equine 794 Herpesvirus Type 1 Enhances Viral Replication in CD172a+ Monocytic Cells upon Adhesion to 795 Endothelial Cells. *Journal of virology* **89**, 10912-10923, doi:10.1128/JVI.01589-15 (2015).

796 33 Lim, J. K. *et al.* Chemokine receptor Ccr2 is critical for monocyte accumulation and survival in 797 West Nile virus encephalitis. *J Immunol* **186**, 471-478, doi:10.4049/jimmunol.1003003 (2011).

798

799 34 Paul, A. M. *et al.* Osteopontin facilitates West Nile virus neuroinvasion via neutrophil "Trojan
800 horse" transport. *Scientific reports* **7**, 4722, doi:10.1038/s41598-017-04839-7 (2017).

801 35 Peluso, R., Haase, A., Stowring, L., Edwards, M. & Ventura, P. A Trojan Horse mechanism for
802 the spread of visna virus in monocytes. *Virology* **147**, 231-236 (1985).

803 36 Kamei, M. & Carman, C. V. New observations on the trafficking and diapedesis of monocytes.
804 *Curr Opin Hematol* **17**, 43-52, doi:10.1097/MOH.0b013e328333949 (2010).

805 37 Gerhardt, T. & Ley, K. Monocyte trafficking across the vessel wall. *Cardiovascular research*
806 **107**, 321-330, doi:10.1093/cvr/cvv147 (2015).

807 38 Michlmayr, D., Andrade, P., Gonzalez, K., Balmaseda, A. & Harris, E. CD14+CD16+ monocytes
808 are the main target of Zika virus infection in peripheral blood mononuclear cells in a
809 paediatric study in Nicaragua. *Nature microbiology*, doi:10.1038/s41564-017-0035-0 (2017).

810 39 Foo, S. S. *et al.* Asian Zika virus strains target CD14+ blood monocytes and induce M2-skewed
811 immunosuppression during pregnancy. *Nature microbiology*, doi:10.1038/s41564-017-0016-
812 3 (2017).

813 40 Lum, F. M. *et al.* A Sensitive Method for Detecting Zika Virus Antigen in Patients' Whole-
814 Blood Specimens as an Alternative Diagnostic Approach. *The Journal of infectious diseases*
815 **216**, 182-190, doi:10.1093/infdis/jix276 (2017).

816 41 Liu, S., DeLallo, L. J., Isakson, B. E. & Wang, T. T. AXL-Mediated Productive Infection of Human
817 Endothelial Cells by Zika Virus. *Circulation research* **119**, 1183-1189,
818 doi:10.1161/CIRCRESAHA.116.309866 (2016).

819 42 Richard, A. S. *et al.* AXL-dependent infection of human fetal endothelial cells distinguishes
820 Zika virus from other pathogenic flaviviruses. *Proceedings of the National Academy of Sciences of
821 the United States of America* **114**, 2024-2029, doi:10.1073/pnas.1620558114
822 (2017).

823 43 Mladinich, M. C., Schwedes, J. & Mackow, E. R. Zika Virus Persistently Infects and Is
824 Basolaterally Released from Primary Human Brain Microvascular Endothelial Cells. *mBio* **8**,
825 doi:10.1128/mBio.00952-17 (2017).

826 44 Chazal, M. *et al.* RIG-I Recognizes the 5' Region of Dengue and Zika Virus Genomes. *Cell
827 reports* **24**, 320-328, doi:10.1016/j.celrep.2018.06.047 (2018).

828 45 Friesland, A. *et al.* Small molecule targeting Cdc42-intersectin interaction disrupts Golgi
829 organization and suppresses cell motility. *Proceedings of the National Academy of Sciences of
830 the United States of America* **110**, 1261-1266, doi:10.1073/pnas.1116051110 (2013).

831 46 Chou, Y. Y. *et al.* Identification and Characterization of a Novel Broad-Spectrum Virus Entry
832 Inhibitor. *Journal of virology* **90**, 4494-4510, doi:10.1128/JVI.00103-16 (2016).

833 47 Coulter, M. E. *et al.* The ESCRT-III Protein CHMP1A Mediates Secretion of Sonic Hedgehog on
834 a Distinctive Subtype of Extracellular Vesicles. *Cell reports* **24**, 973-986 e978,
835 doi:10.1016/j.celrep.2018.06.100 (2018).

836 48 Fiddes, I. T. *et al.* Human-Specific NOTCH2NL Genes Affect Notch Signaling and Cortical
837 Neurogenesis. *Cell* **173**, 1356-1369 e1322, doi:10.1016/j.cell.2018.03.051 (2018).

838 49 Doussau, F. *et al.* Organotypic cultures of cerebellar slices as a model to investigate
839 demyelinating disorders. *Expert Opin Drug Discov* **12**, 1011-1022,
840 doi:10.1080/17460441.2017.1356285 (2017).

841 50 Dionne, K. R. & Tyler, K. L. Slice culture modeling of central nervous system (CNS) viral
842 infection. *Methods Mol Biol* **1078**, 97-117, doi:10.1007/978-1-62703-640-5_9 (2013).

843 51 Cui, L. *et al.* Visual and Motor Deficits in Grown-up Mice with Congenital Zika Virus Infection.
844 *EBioMedicine* **20**, 193-201, doi:10.1016/j.ebiom.2017.04.029 (2017).

845 52 Weksler, B., Romero, I. A. & Couraud, P. O. The hCMEC/D3 cell line as a model of the human
846 blood brain barrier. *Fluids and barriers of the CNS* **10**, 16, doi:10.1186/2045-8118-10-16
847 (2013).

848 53 Eigenmann, D. E. *et al.* Comparative study of four immortalized human brain capillary
849 endothelial cell lines, hCMEC/D3, hBMEC, TY10, and BB19, and optimization of culture

850 conditions, for an in vitro blood-brain barrier model for drug permeability studies. *Fluids and*
851 *barriers of the CNS* **10**, 33, doi:10.1186/2045-8118-10-33 (2013).

852 54 Youdim, K. A., Avdeef, A. & Abbott, N. J. In vitro trans-monolayer permeability calculations:
853 often forgotten assumptions. *Drug discovery today* **8**, 997-1003 (2003).

854 55 Szklarczyk, D. *et al.* STRING v10: protein-protein interaction networks, integrated over the
855 tree of life. *Nucleic acids research* **43**, D447-452, doi:10.1093/nar/gku1003 (2015).

856 56 Subramanian, A. *et al.* Gene set enrichment analysis: a knowledge-based approach for
857 interpreting genome-wide expression profiles. *Proceedings of the National Academy of*
858 *Sciences of the United States of America* **102**, 15545-15550, doi:10.1073/pnas.0506580102
859 (2005).

860 57 Follain, G. *et al.* Hemodynamic Forces Tune the Arrest, Adhesion, and Extravasation of
861 Circulating Tumor Cells. *Dev Cell* **45**, 33-52 e12, doi:10.1016/j.devcel.2018.02.015 (2018).

862 58 Follain, G. *et al.* Using the Zebrafish Embryo to Dissect the Early Steps of the Metastasis
863 Cascade. *Methods Mol Biol* **1749**, 195-211, doi:10.1007/978-1-4939-7701-7_15 (2018).

864 59 Khandia, R. *et al.* Modulation of Dengue/Zika Virus Pathogenicity by Antibody-Dependent
865 Enhancement and Strategies to Protect Against Enhancement in Zika Virus Infection. *Front*
866 *Immunol* **9**, 597, doi:10.3389/fimmu.2018.00597 (2018).

867 60 Li, M. *et al.* Dengue immune sera enhance Zika virus infection in human peripheral blood
868 monocytes through Fc gamma receptors. *Plos one* **13**, e0200478,
869 doi:10.1371/journal.pone.0200478 (2018).

870 61 Zimmerman, M. G. *et al.* Cross-Reactive Dengue Virus Antibodies Augment Zika Virus
871 Infection of Human Placental Macrophages. *Cell host & microbe* **24**, 731-742 e736,
872 doi:10.1016/j.chom.2018.10.008 (2018).

873 62 Langerak, T. *et al.* The possible role of cross-reactive dengue virus antibodies in Zika virus
874 pathogenesis. *PLoS pathogens* **15**, e1007640, doi:10.1371/journal.ppat.1007640 (2019).

875 63 Lawson, N. D. & Weinstein, B. M. In vivo imaging of embryonic vascular development using
876 transgenic zebrafish. *Dev Biol* **248**, 307-318 (2002).

877 64 Faraco, G., Park, L., Anrather, J. & Iadecola, C. Brain perivascular macrophages:
878 characterization and functional roles in health and disease. *J Mol Med (Berl)* **95**, 1143-1152,
879 doi:10.1007/s00109-017-1573-x (2017).

880 65 Solomon, J. N. *et al.* Origin and distribution of bone marrow-derived cells in the central
881 nervous system in a mouse model of amyotrophic lateral sclerosis. *Glia* **53**, 744-753,
882 doi:10.1002/glia.20331 (2006).

883 66 Goldmann, T. *et al.* Origin, fate and dynamics of macrophages at central nervous system
884 interfaces. *Nature immunology* **17**, 797-805, doi:10.1038/ni.3423 (2016).

885 67 Getts, D. R. *et al.* Ly6c+ "inflammatory monocytes" are microglial precursors recruited in a
886 pathogenic manner in West Nile virus encephalitis. *The Journal of experimental medicine*
887 **205**, 2319-2337, doi:10.1084/jem.20080421 (2008).

888 68 Puerta-Guardo, H. *et al.* Flavivirus NS1 Triggers Tissue-Specific Vascular Endothelial
889 Dysfunction Reflecting Disease Tropism. *Cell reports* **26**, 1598-1613 e1598,
890 doi:10.1016/j.celrep.2019.01.036 (2019).

891 69 Tappe, D. *et al.* Cytokine kinetics of Zika virus-infected patients from acute to convalescent
892 phase. *Medical microbiology and immunology* **205**, 269-273, doi:10.1007/s00430-015-0445-7
893 (2016).

894 70 Vielle, N. J. *et al.* Silent infection of human dendritic cells by African and Asian strains of Zika
895 virus. *Scientific reports* **8**, 5440, doi:10.1038/s41598-018-23734-3 (2018).

896 71 Bowen, J. R. *et al.* Zika Virus Antagonizes Type I Interferon Responses during Infection of
897 Human Dendritic Cells. *PLoS pathogens* **13**, e1006164, doi:10.1371/journal.ppat.1006164
898 (2017).

899 72 Bowen, J. R., Zimmerman, M. G. & Suthar, M. S. Taking the defensive: Immune control of Zika
900 virus infection. *Virus Res* **254**, 21-26, doi:10.1016/j.virusres.2017.08.018 (2018).

901 73 Yoshikawa, F. S. Y. *et al.* Zika Virus Infects Newborn Monocytes Without Triggering a
902 Substantial Cytokine Response. *The Journal of infectious diseases*, doi:10.1093/infdis/jiz075
903 (2019).

904 74 Burdo, T. H., Lackner, A. & Williams, K. C. Monocyte/macrophages and their role in HIV
905 neuropathogenesis. *Immunol Rev* **254**, 102-113, doi:10.1111/imr.12068 (2013).

906 75 Wong, K. L. *et al.* Susceptibility and response of human blood monocyte subsets to primary
907 dengue virus infection. *PLoS one* **7**, e36435, doi:10.1371/journal.pone.0036435 (2012).

908 76 Grant, A. *et al.* Zika Virus Targets Human STAT2 to Inhibit Type I Interferon Signaling. *Cell host*
909 & *microbe* **19**, 882-890, doi:10.1016/j.chom.2016.05.009 (2016).

910 77 O'Connor, M. A. *et al.* Early cellular innate immune responses drive Zika viral persistence and
911 tissue tropism in pigtail macaques. *Nature communications* **9**, 3371, doi:10.1038/s41467-
912 018-05826-w (2018).

913 78 Garcez, P. P. *et al.* Zika virus impairs the development of blood vessels in a mouse model of
914 congenital infection. *Scientific reports* **8**, 12774, doi:10.1038/s41598-018-31149-3 (2018).

915 79 Williams, D. W., Eugenin, E. A., Calderon, T. M. & Berman, J. W. Monocyte maturation, HIV
916 susceptibility, and transmigration across the blood brain barrier are critical in HIV
917 neuropathogenesis. *Journal of leukocyte biology* **91**, 401-415, doi:10.1189/jlb.0811394
918 (2012).

919 80 Velandia-Romero, M. L., Calderon-Pelaez, M. A. & Castellanos, J. E. In Vitro Infection with
920 Dengue Virus Induces Changes in the Structure and Function of the Mouse Brain
921 Endothelium. *PLoS one* **11**, e0157786, doi:10.1371/journal.pone.0157786 (2016).

922 81 Tang, N., Sun, B., Gupta, A., Rempel, H. & Pulliam, L. Monocyte exosomes induce adhesion
923 molecules and cytokines via activation of NF- κ B in endothelial cells. *FASEB J* **30**, 3097-
924 3106, doi:10.1096/fj.201600368RR (2016).

925 82 Wojciak-Stothard, B., Williams, L. & Ridley, A. J. Monocyte adhesion and spreading on human
926 endothelial cells is dependent on Rho-regulated receptor clustering. *The Journal of cell*
927 *biology* **145**, 1293-1307 (1999).

928 83 Entenberg, D. *et al.* A permanent window for the murine lung enables high-resolution
929 imaging of cancer metastasis. *Nat Methods* **15**, 73-80, doi:10.1038/nmeth.4511 (2018).

930 84 Bergmann, S. *et al.* Blood-brain-barrier organoids for investigating the permeability of CNS
931 therapeutics. *Nat Protoc* **13**, 2827-2843, doi:10.1038/s41596-018-0066-x (2018).

932 85 Jeon, J. S. *et al.* Human 3D vascularized organotypic microfluidic assays to study breast
933 cancer cell extravasation. *Proceedings of the National Academy of Sciences of the United*
934 *States of America* **112**, 214-219, doi:10.1073/pnas.1417115112 (2015).

935 86 Passoni, G. *et al.* Imaging of viral neuroinvasion in the zebrafish reveals that Sindbis and
936 chikungunya viruses favour different entry routes. *Dis Model Mech* **10**, 847-857,
937 doi:10.1242/dmm.029231 (2017).

938 87 Antoine, T. E., Jones, K. S., Dale, R. M., Shukla, D. & Tiwari, V. Zebrafish: modeling for herpes
939 simplex virus infections. *Zebrafish* **11**, 17-25, doi:10.1089/zeb.2013.0920 (2014).

940 88 Palha, N. *et al.* Real-time whole-body visualization of Chikungunya Virus infection and host
941 interferon response in zebrafish. *PLoS pathogens* **9**, e1003619,
942 doi:10.1371/journal.ppat.1003619 (2013).

943 89 Benjamin, D. C. & Hynes, R. O. Intravital imaging of metastasis in adult Zebrafish. *BMC Cancer*
944 **17**, 660, doi:10.1186/s12885-017-3647-0 (2017).

945 90 Stoletov, K. *et al.* Visualizing extravasation dynamics of metastatic tumor cells. *J Cell Sci* **123**,
946 2332-2341, doi:10.1242/jcs.069443 (2010).

947 91 Paul, C. D. *et al.* Human macrophages survive and adopt activated genotypes in living
948 zebrafish. *Scientific reports* **9**, 1759, doi:10.1038/s41598-018-38186-y (2019).

949 92 Garcez, P. P. *et al.* Zika virus impairs growth in human neurospheres and brain organoids.
950 *Science* **352**, 816-818, doi:10.1126/science.aaf6116 (2016).

951 93 Zhou, T. *et al.* High-Content Screening in hPSC-Neural Progenitors Identifies Drug Candidates
952 that Inhibit Zika Virus Infection in Fetal-like Organoids and Adult Brain. *Cell stem cell* **21**, 274-
953 283 e275, doi:10.1016/j.stem.2017.06.017 (2017).

954 94 Qian, X., Nguyen, H. N., Jacob, F., Song, H. & Ming, G. L. Using brain organoids to understand
955 Zika virus-induced microcephaly. *Development* **144**, 952-957, doi:10.1242/dev.140707
956 (2017).

957 95 Lancaster, M. A. Brain organoids get vascularized. *Nat Biotechnol* **36**, 407-408,
958 doi:10.1038/nbt.4133 (2018).

959 96 Weksler, B. B. *et al.* Blood-brain barrier-specific properties of a human adult brain
960 endothelial cell line. *FASEB J* **19**, 1872-1874, doi:10.1096/fj.04-3458fje (2005).

961 97 Freed, E. O., Englund, G. & Martin, M. A. Role of the basic domain of human
962 immunodeficiency virus type 1 matrix in macrophage infection. *Journal of virology* **69**, 3949-
963 3954 (1995).

964 98 Ritter, J. M., Martines, R. B. & Zaki, S. R. Zika Virus: Pathology From the Pandemic. *Archives of
965 pathology & laboratory medicine* **141**, 49-59, doi:10.5858/arpa.2016-0397-SA (2017).

966 99 Wioland, L. *et al.* Epsilon toxin from Clostridium perfringens acts on oligodendrocytes
967 without forming pores, and causes demyelination. *Cellular microbiology* **17**, 369-388,
968 doi:10.1111/cmi.12373 (2015).

969 100 Stoppini, L., Buchs, P. A. & Muller, D. A simple method for organotypic cultures of nervous
970 tissue. *Journal of neuroscience methods* **37**, 173-182 (1991).

971 101 Livak, K. J. & Schmittgen, T. D. Analysis of relative gene expression data using real-time
972 quantitative PCR and the 2(-Delta Delta C(T)) Method. *Methods* **25**, 402-408,
973 doi:10.1006/meth.2001.1262 (2001).

974 102 Faye, O. *et al.* Quantitative real-time PCR detection of Zika virus and evaluation with field-
975 caught mosquitoes. *Virol J* **10**, 311, doi:10.1186/1743-422X-10-311 (2013).

976 103 Cox, J. *et al.* Accurate proteome-wide label-free quantification by delayed normalization and
977 maximal peptide ratio extraction, termed MaxLFQ. *Mol Cell Proteomics* **13**, 2513-2526,
978 doi:10.1074/mcp.M113.031591 (2014).

979 104 Carapito, C. *et al.* MSDA, a proteomics software suite for in-depth Mass Spectrometry Data
980 Analysis using grid computing. *Proteomics* **14**, 1014-1019, doi:10.1002/pmic.201300415
981 (2014).

982 105 Wieczorek, S. *et al.* DAPAR & ProStaR: software to perform statistical analyses in quantitative
983 discovery proteomics. *Bioinformatics* **33**, 135-136, doi:10.1093/bioinformatics/btw580
984 (2017).

985 106 Wieczorek, S., Combes, F., Borges, H. & Burger, T. Protein-level statistical analysis of
986 quantitative label-free proteomics data with ProStaR. *Methods In Molecular Biology* (in
987 press).

988 107 Deutsch, E. W. *et al.* The ProteomeXchange consortium in 2017: supporting the cultural
989 change in proteomics public data deposition. *Nucleic Acids Res* **45**, D1100-D1106,
990 doi:10.1093/nar/gkw936 (2017).

991 108 Goetz, J. G. *et al.* Endothelial cilia mediate low flow sensing during zebrafish vascular
992 development. *Cell reports* **6**, 799-808, doi:10.1016/j.celrep.2014.01.032 (2014).

993

994

995 **Figure legend**

996 **Figure 1. Monocyte-derived cells, but not endothelial cells, are infected by ZIKV in the CNS of a**
997 **human fetus with microcephaly.** (a-e) Immunohistochemical staining was performed on human fetal
998 brain tissues from a PCR-confirmed case of congenital ZIKV (gestational age 22 weeks). All slides were
999 counterstained in Mayer's Hematoxylin and blued in Lithium carbonate. The tissue slices were
1000 stained for ZIKV-NS1 in combination with (a) CD45 (left panel: 63x, right panel: 40x), (b) CD14 (20x),
1001 (c) CD68 (upper panel: 63x, lower left panel: 100x, lower right panel: 40x), or (d) CD163 (upper panel:
1002 40x, lower left panel: 100x, lower right panel: 63x). (e) The endothelial cells of slices from the same
1003 tissue appear morphologically intact and were never found positive for ZIKV-NS1 staining. The black
1004 arrowheads indicate ZIKV-infected cells. BV: blood vessel.

1005 **Figure 2. Human primary monocytes are productively infected by ZIKV.** (a) Monocytes purified from
1006 7 healthy blood donors were inoculated with Colombian (ZIKV^C) or Panama (ZIKV^P) ZIKV strains at
1007 MOI 1 (+) or 5 (++) for 48 h. Cells were fixed, permeabilized and stained. Flow cytometry was
1008 performed and the percentage of ZIKV-infected cells (NS2B⁺) was plotted as a function of the strain
1009 and amount of ZIKV used. Each dot corresponds to the mean +/- SD of ZIKV-infected cells for each
1010 donor and each condition in two individual samples. (b) Monocytes purified from 3 healthy donors
1011 were infected for indicated time with ZIKV (MOI 1) for 48 h. Total RNA was extracted and RT-qPCR
1012 was performed using ZIKV and GAPDH specific primers. The graph represents the fold change of ZIKV
1013 RNA with respect to GAPDH of a triplicate +/- SD. Two-tailed p value was < 0.05 (*). Only two donors
1014 were represented as the third one did not show any detectable ZIKV RNA. (c) Monocytes infected
1015 with ZIKV for 48 h were fixed and fluorescence *in situ* hybridization (FISH) was performed using a
1016 ZIKV-specific RNA probe (magenta) and nuclei were stained with Dapi (blue). (d) Monocytes purified
1017 from 4 healthy donors were untreated or pre-treated or 50 µM ZCL278 for 30 min at 37 °C and the
1018 cells were then infected with ZIKV (MOI 1) in the presence or absence of ZCL278. The inoculum was
1019 removed at 4 h post-infection after which the cells were washed and re-incubated in complete media
1020 for 48 h. Supernatant was harvested and plaque assay on Vero cells was performed to titrate ZIKV
1021 production. ZCL278 treatment inhibited ZIKV infection of monocytes by 93% (+/- 7). Two-tailed p
1022 value was < 0.05 (*).

1023 **Figure 3. ZIKV-infected monocytes promote viral dissemination to cerebral organoids and induce**
1024 **tissue damage.** (a-b) Cerebral organoids were co-cultured with either ZIKV-infected monocytes, not-
1025 infected monocytes, cell-free ZIKV or mock for 2 days. The organoids were fixed at 3 or 6 weeks
1026 post-differentiation (wpd) and processed for (a) flow cytometry or (b) immunofluorescence. The bar
1027 graph shows the mean of an experiment performed in duplicate +/- SD from two donors. Two-tailed
1028 p value < 0.05 (*). (c-e) Organotypic cultures of mouse cerebellar slices in the presence or absence of
1029 cell-free ZIKV or ZIKV-infected monocytes +/- ZCL278. (c) Experimental design. (d) A staining with an
1030 anti-calbindin antibody (green) and Dapi (blue) was done to observe the tissue cytoarchitecture. (e)
1031 The cytoarchitecture index is a measurement of the degree of tissue injury. Three categories were
1032 defined: healthy (part of the lobule with a regular alignment of Purkinje), intermediate (partially
1033 damaged, sparse Purkinje, mild on the graph, this category can be regrouped with the category
1034 "altered") or altered (absence of Purkinje, impaired on the slice). For each condition, the length of
1035 the healthy, intermediate or altered regions was measured using ImageJ and the proportion of each
1036 category was plotted. The condition in which cerebellar slices were incubated with ZIKV-infected
1037 monocytes is the only one that significantly differed from the others. Two-tailed p value < 0.05 (*).

1038 **Figure 4. ZIKV-infected monocytes exhibit higher transmigration properties.** (a) Representative
1039 scheme of the transwell transmigration assay. (b) A Lucifer Yellow permeability assay was performed
1040 under indicated conditions in order to measure a permeability coefficient according to standard
1041 calculations⁵³. Shown are the mean +/- SD of the fold change with respect to the non-treated (NT)
1042 control (ns = no significant difference). (c) After a transmigration assay was performed in a transwell
1043 system, the hCMEC/D3 monolayer was harvested from the transwell membrane, fixed, and
1044 processed for flow cytometry. The cells were stained with a NS2B antibody to assess for viral
1045 infection. The graph shows the mean +/- SD of triplicates. ns, not-significant. (d) Monocytes were
1046 non-infected or infected with ZIKV^C at MOI 1 for 24 h. Upon extensive washes, monocytes were
1047 added on top of a transwell insert onto which hCMEC/D3 endothelial cells were plated 7 days prior
1048 addition. Transmigration was allowed to occur for \approx 17 h. Monocytes from the top and bottom
1049 chambers were harvested, fixed and stained. Flow cytometry analysis was performed to determine
1050 the percentage of ZIKV-infected cells (NS2B⁺) among the monocytes that did not transmigrate (top,
1051 green) or did transmigrate (bottom, red). The graph shows two individual experiments from three
1052 donors. One replicate was not shown because no infected cells were detected in both conditions.
1053 Monocytes from the top and bottom come from the same transwell. The fold-change of the
1054 percentage of infected cells in the top and bottom chambers was significantly greater (two-way
1055 Anova = 0.039). (e-f) ZIKV-infected or non-infected (NI) monocytes isolated from two donors were
1056 co-cultured for 17 h with hCMEC/D3 cells previously grown on glass coverslips. Upon fixation and
1057 staining with a fluorescently labeled anti-CD45 antibody, the number of monocytes located above,
1058 intermediate, or under the endothelial layer (as depicted in e) was quantified by confocal
1059 microscopy. (f) The pie charts correspond to the number of monocytes counted per 10 fields of view
1060 from two individual experiments.

1061 **Figure 5. ZIKV-exposed monocytes exhibit higher adhesion properties.** (a-b) Monocytes isolated
1062 from two healthy donors were infected with ZIKV (MOI 1). At 48 hpi, the cells were thoroughly
1063 washed and processed for quantitative proteome profiling using liquid chromatography coupled to
1064 tandem mass spectrometry (LC-MS/MS). Cluster and ontology analyses of the upregulated proteins
1065 (virus over mock) were identified using STRING (a) and GSEA (b) methods. The list of the proteins
1066 modulated upon ZIKV infection using a 5% FDR (p value < 0.0085) is provided in Suppl Table 1. (c)
1067 Flow cytometry analysis assessing the cell surface expression of a panel of 22 adhesion molecules
1068 upon ZIKV infection. Each dot corresponds to the average fold change of duplicates for individual
1069 donors. The red lines correspond to the mean from three donors. NI, not infected. Two-tailed p value
1070 < 0.05 (*). The grey dashed line indicate a fold of 1 (no differential expression between infected and
1071 non-infected monocytes). (d) The expression of CD99 (MIC2) was measured in monocytes treated
1072 with mock, and in monocytes exposed to the virus for 48. In the latter, the CD99 expression was
1073 quantified within the not-infected and the infected population. Infection was defined by an NS2B
1074 staining. (e) Expression of CD99 was measured over time on primary monocytes treated with mock,
1075 ZIKV (MOI 1) and UV-inactivated ZIKV. At the indicated timepoints, the cells were fixed and processed
1076 for flow cytometry. The bar graphs show the fold change of CD99 expression with respect to the
1077 mock condition (mean +/- SD). Two-tailed p value was non-significant (ns) or < 0.05 (*). (f) Non-
1078 infected (NI) or ZIKV-infected monocytes were plated in wells coated with type I collagen, ICAM-1
1079 protein, or fibronectin for 2 h at 37°C. The relative number of cells was measured using CellTiter-Glo.
1080 Each bar graph corresponds to an experiment performed on monocytes from 2 healthy donors
1081 showing the mean +/- SD from two individual experiments. Two-tailed p value was non-significant

1082 (ns) or < 0.005 (**) or < 0.0005 (***). NI, not infected. NT, no cytokine treatment. (g-h) ZIKV-infected
1083 or non-infected (NI) monocytes of two donors were co-cultured with hCMEC/D3 cells previously
1084 grown on glass coverslips, co-cultured for 17 h. Upon fixation and staining with a fluorescently
1085 labeled anti-CD45 antibody, the number of adherent monocytes was quantified by epifluorescence
1086 microscopy (g and Suppl Fig. S9a-b). (h) The bar graph corresponds to the mean +/- SD of the number
1087 of monocytes counted per 10 fields of view from two individual experiments for two donors. Two-
1088 tailed p value was < 0.05 (*).

1089 **Figure 6. ZIKV induces a spread out morphology of monocytes.** (a) Non-infected (NI) or ZIKV-
1090 infected monocytes were plated in wells coated with fibronectin for 2 h at 37°C. Upon fixation, cells
1091 were permeabilized and stained with Phalloidin A568 (yellow) and Dapi (blue). Images were acquired
1092 with a spinning disk confocal microscope. For each condition, the images show a top view of
1093 unprocessed fluorescence signal of a field of view (upper right) and the raw and isosurface-processed
1094 3D reconstructions a side view. (b) ZIKV-infected or non-infected (NI) monocytes from two healthy
1095 donors were added to hCMEC/D3 and processed as mentioned in Fig. 5g. The relative projected area
1096 (area covered by the surface of individual monocytes) was measured at the indicated times post
1097 monocyte addition. Each bar graph corresponds to an experiment performed on monocytes from
1098 two donors showing the mean +/- SD from two individual experiments. Two-tailed p value was non-
1099 significant (ns) or < 0.05 (*) or < 0.0005 (***). (c) Circularity of individual monocytes was measured
1100 17 h after monocyte-hCMEC/D3 co-culture using ImageJ. Each dot corresponds to a single monocyte
1101 and the red bars correspond to the mean +/- SEM from two individual experiments from two donors.
1102 A circularity value of 1 indicates a perfect circle and as the value approaches 0, it indicates an
1103 increasingly elongated polygon. Two-tailed p value < 0.0001 (**). (d) Non-infected (NI) or 48 h ZIKV-
1104 infected (ZIKV) monocytes were incubated in a hCMEC/D3-coated transwell system in the presence
1105 or absence of 50 μ M ZCL278. Shown is the ratio of transmigrating cells between ZCL278-treated and
1106 untreated samples. Each dot corresponds to an individual donor. Two-tailed p value was < 0.05 (*).

1107 **Figure 7. ZIKV enhances monocyte transmigration in zebrafish embryos.** (a) Representative scheme
1108 of the experimental design associated to the zebrafish model. Human primary monocytes were non-
1109 infected (NI), or infected for 48 h with ZIKV in the absence (ZIKV) or presence (ADE-ZIKV) of 20 ng/ml
1110 of the 4G2 enhancing pan-*Flaviviridae* antibody (see Suppl Fig. S10), stained with CellTrace, and
1111 injected into the duct of Cuvier of *Tg(fli1a:eGFP)* zebrafish embryos (GFP-labeled endothelial cells⁶³).
1112 (b) Zebrafish imaging was done at 6-8 h post injection by scanning confocal microscopy.
1113 Representative 3D confocal image of the monocytes' distribution within the tail of a zebrafish
1114 embryo vasculature (associated to Movie 1) 6 h post-injection. (c) Three-dimensional reconstruction
1115 of endothelium (green) and monocytes (magenta) that remained in the blood stream (left panel,
1116 intravascular), transmigrated (middle panel, extravascular), or in the process of transmigrating (right
1117 panel). (d) Zebrafish *Tg(fli1a:eGFP)* embryos were injected with non-infected (NI), ZIKV-infected
1118 monocytes in the absence (ZIKV) or presence (ADE-ZIKV) of the 4G2 enhancing antibody. Six hours
1119 post-injection, the embryos were imaged by confocal microscopy. Cell dispersion was manually
1120 counted and localized in the caudal plexus using the stereotype patterning of intersegmental vessels
1121 (ISVs) as a reference. The data were compiled to generate heatmaps using a custom-made MATLAB
1122 plugin. (e) Quantification of the mean +/- SD of the ratio of extravasated monocytes at 6-8 h post-
1123 injection. Each cross represents the ratio calculated from all the monocytes tracked within a fish.
1124 Acquisition of the different conditions was performed in random order. Two-tailed p value < 0.05 (*),
1125 < 0.005 (**) and < 0.0001 (***).

1126 **Figure 8. ZIKV favors monocyte arrest onto zebrafish embryos' vessel wall, but does not affect their**
1127 **arresting time.** Human primary monocytes treated and injected as in Fig. 7a and imaged with an
1128 epifluorescence microscope immediately after injection (0-5 min). **(a)** Micrographs representing the
1129 three types of monocyte behaviors observed (see also Suppl Movie S2). White arrowheads indicate
1130 the monocyte's behavior described: circulating (left panels), stopping (middle panels) or undergoing
1131 a rolling-like movement (right panels). Note that timescales are different for each behavior. The red
1132 arrows represent the direction of the blood stream. **(b)** Monocytes were automatically tracked over
1133 time using the Bitplane Imaris software and the mean track length of monocytes was quantified (NI n
1134 = 2 fish; ZIKV n = 3 fish; ADE-ZIKV n = 3 fish). Each dot corresponds to a single monocyte tracked over
1135 \approx 5 min. Two-tailed p value < 0.05 (*) and < 0.0001 (***). **(c)** Color-coded representation of monocyte
1136 speed with the zebrafish vasculature. Red tracks indicate arrested monocytes. **(c)** Quantification of
1137 the mean track length of monocytes (NI n = 2 fish; ZIKV n = 3 fish; ADE-ZIKV n = 3 fish). Each dot
1138 corresponds to a single monocyte tracked over \approx 5 min. Two-tailed p value < 0.05 (*) and < 0.0001
1139 (***). **(d)** The graph is representative of the mean track speed +/- SD of single monocytes (red dots)
1140 measured in one fish per condition. **(e)** Quantification of the mean track speed +/- SD of monocytes
1141 tracked over \approx 5 min under the indicated conditions (NI n = 2 fish, ZIKV n = 3 fish and ADE-ZIKV n = 3
1142 fish). Two-tailed p value < 0.0001 (***). **(f)** The bar graph represents the mean +/- SEM of the
1143 percentage of monocytes that arrested for more than 2 seconds. Two-tailed p value < 0.005 (**) and
1144 < 0.0001 (***). **(g)** The bar graph represents the mean +/- SEM of the arrest length among the
1145 monocytes that arrested for more than 2 seconds. ns = non-significant.

1146 **Figure 9. Transmigrated ZIKV-infected monocytes promote viral dissemination to cerebral**
1147 **organoids.** **(a)** Representative scheme of the experimental design. Neural organoids were located
1148 under a transwell where hCMEC/D3 cells were previously grown for 7 days. On top of a transwell,
1149 either ZIKV-infected monocytes, not-infected monocytes, cell-free ZIKV or mock were added. After
1150 an overnight incubation, the transwells were removed and the organoids were cultured for 2 or 9
1151 days, when they fixed and processed for **(b)** immunofluorescence or **(c)** flow cytometry. The bar
1152 graph shows the mean of an experiment performed in duplicate +/- SD. Two-tailed p value < 0.05 (*).

1153

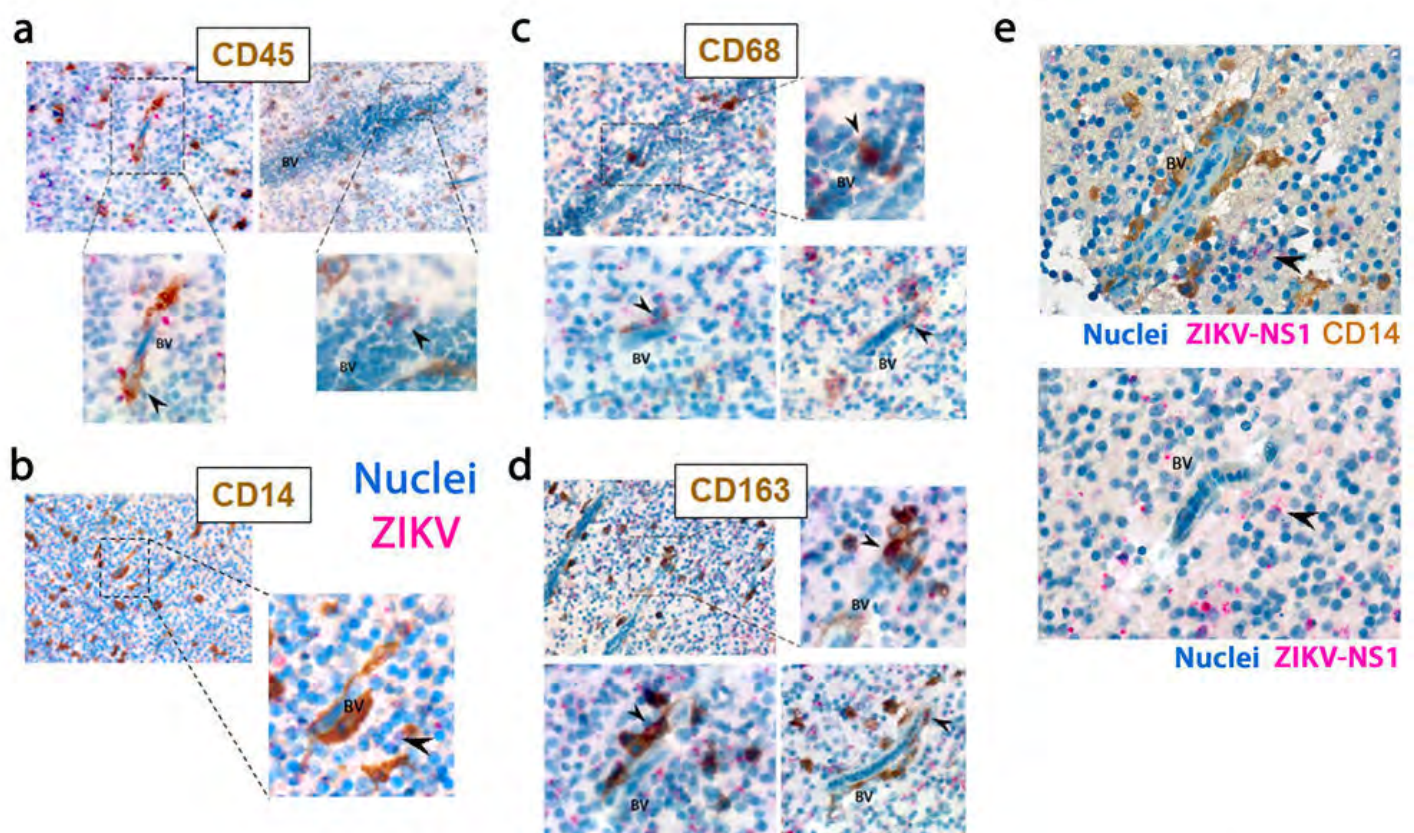


Figure 1. Ayala-Nunez *et al.*

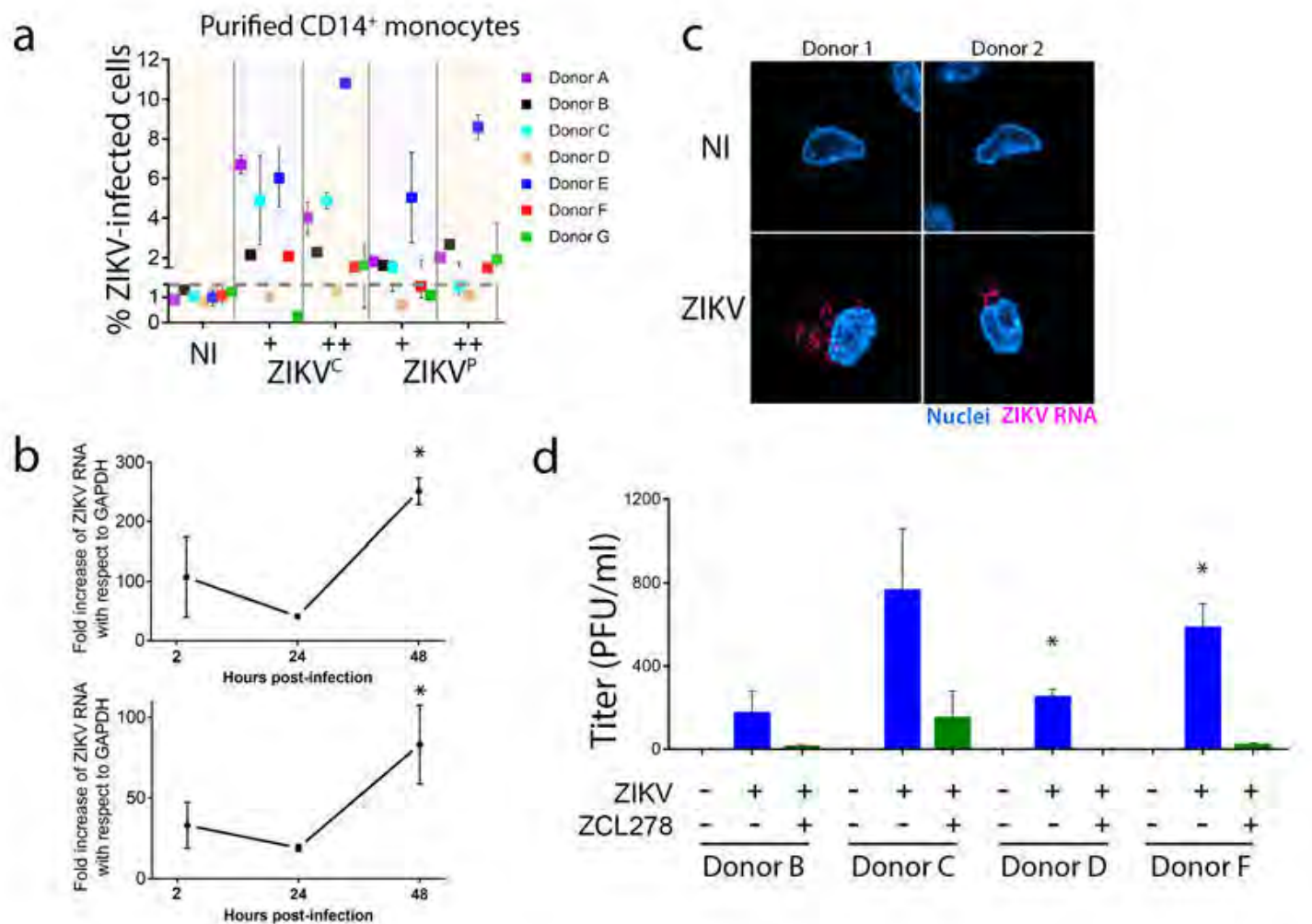


Figure 2. Ayala-Nunez *et al.*

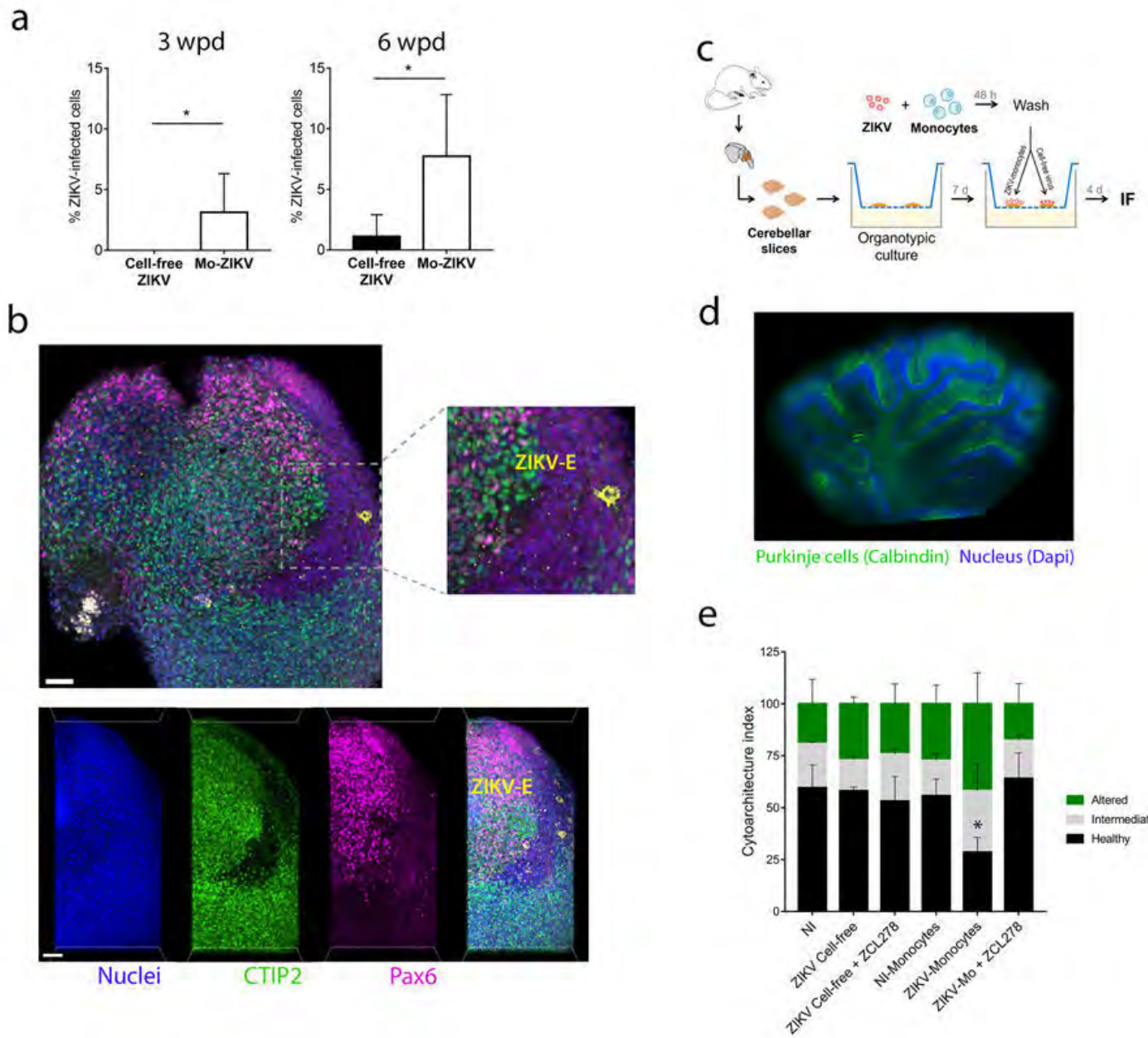


Figure 3. Ayala-Nunez *et al.*

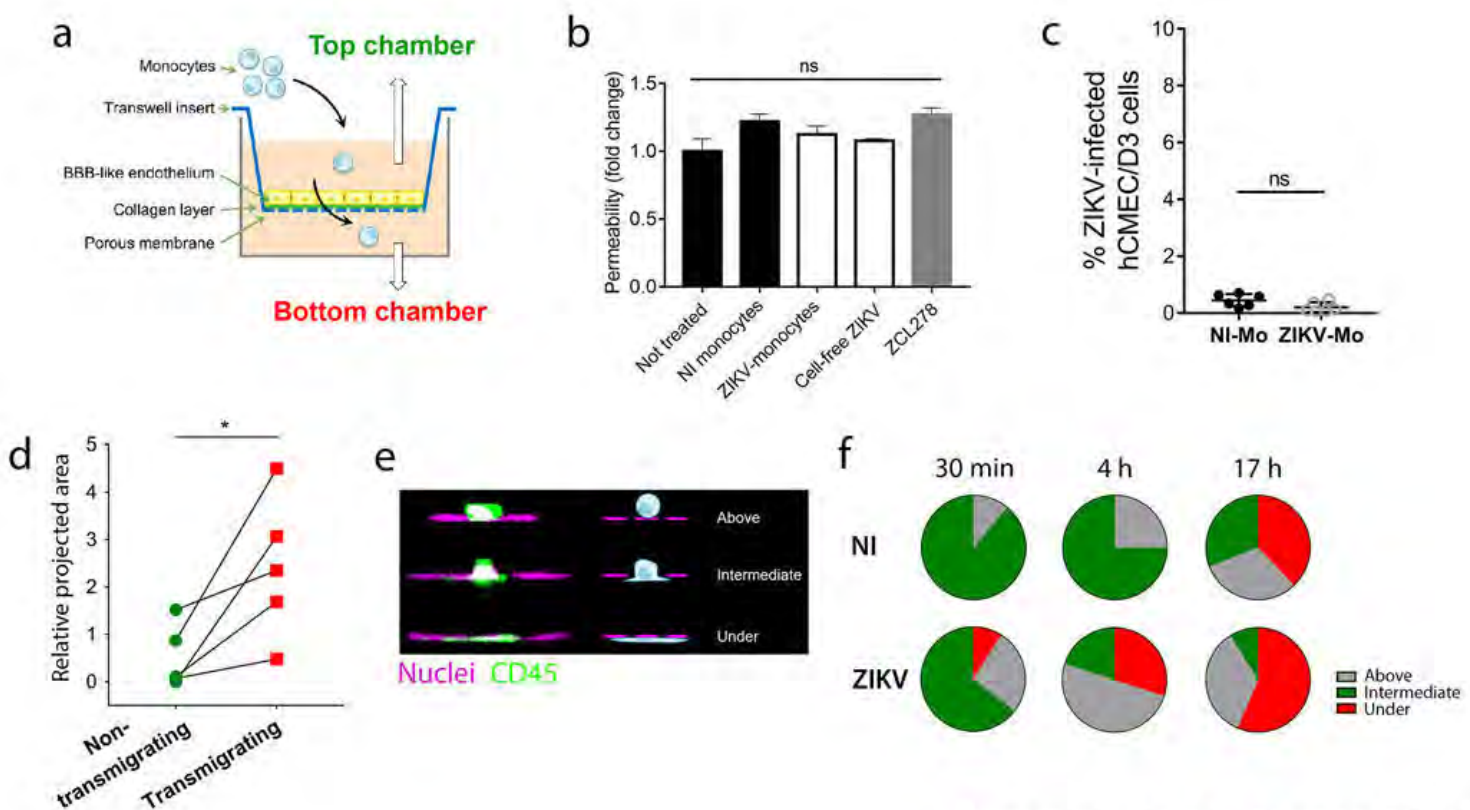


Figure 4. Ayala-Nunez *et al.*

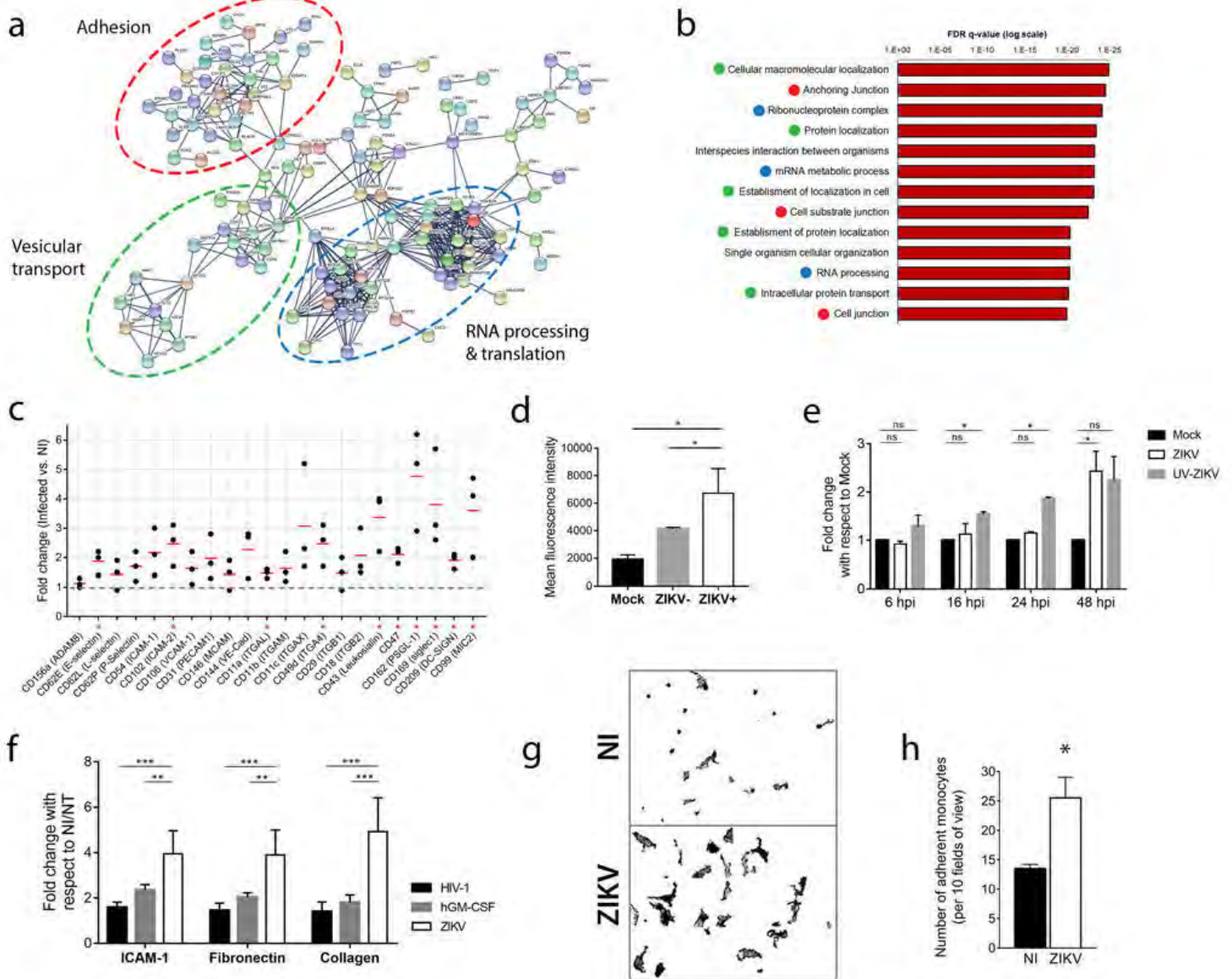


Figure 5. Ayala-Nunez *et al.*

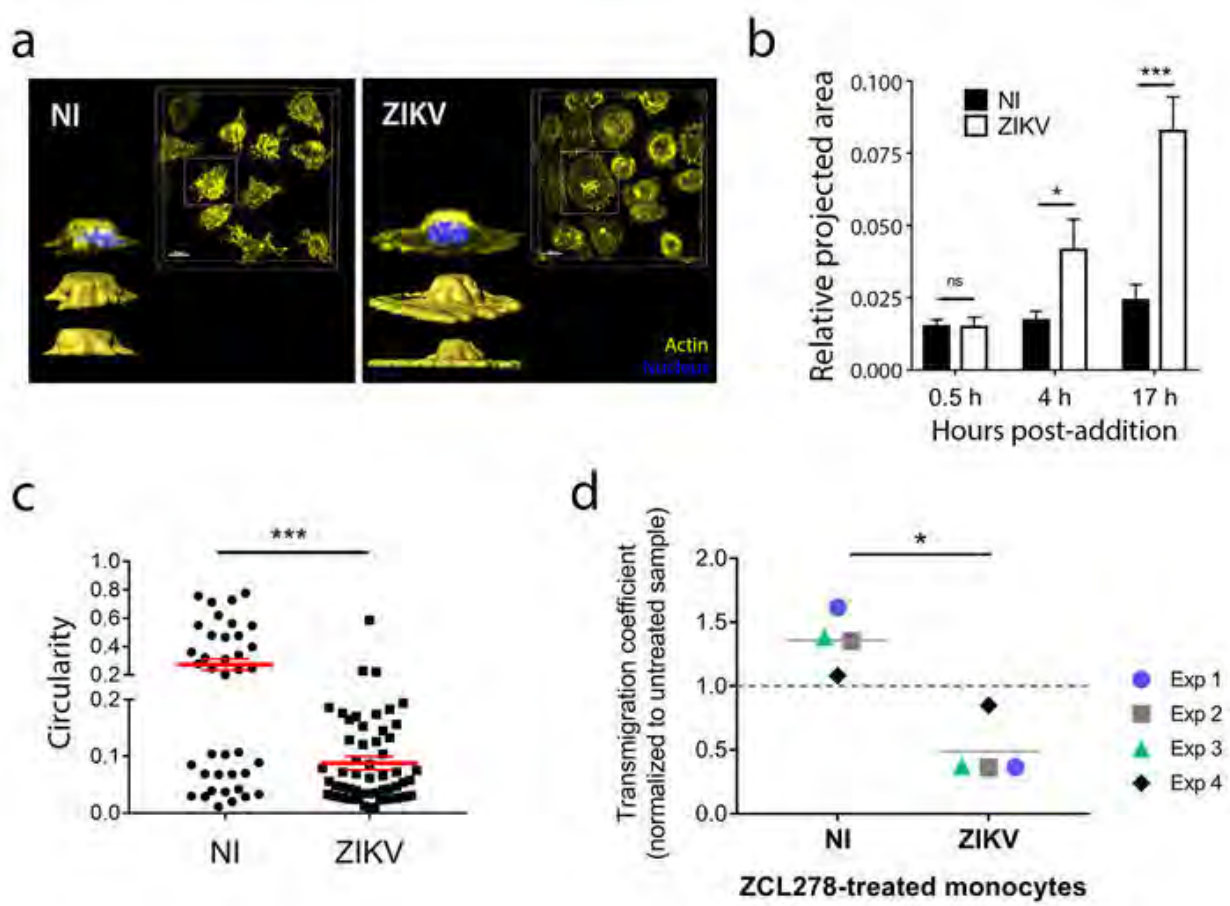


Figure 6. Ayala-Nunez *et al.*

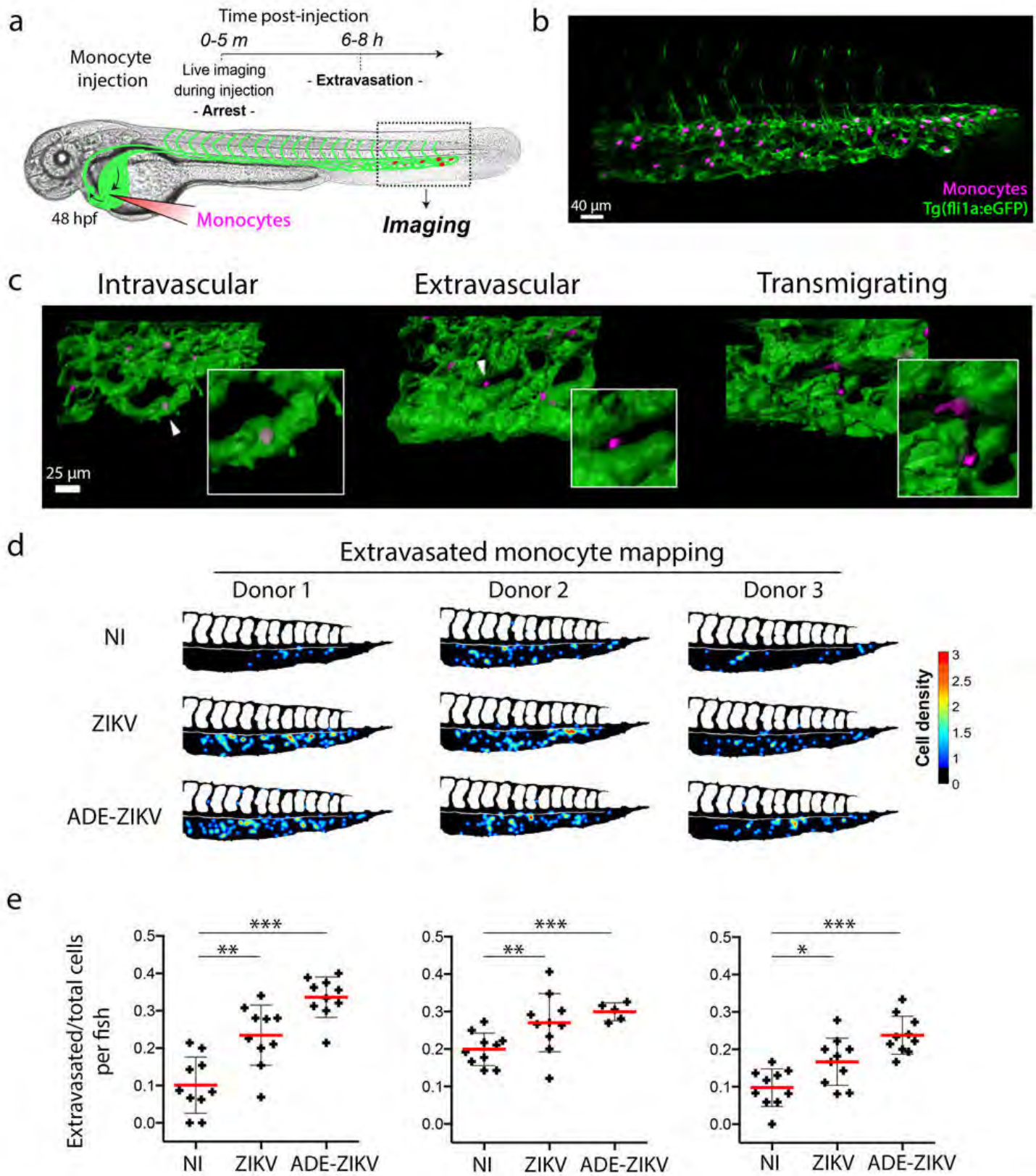


Figure 7. Ayala-Nunez *et al.*

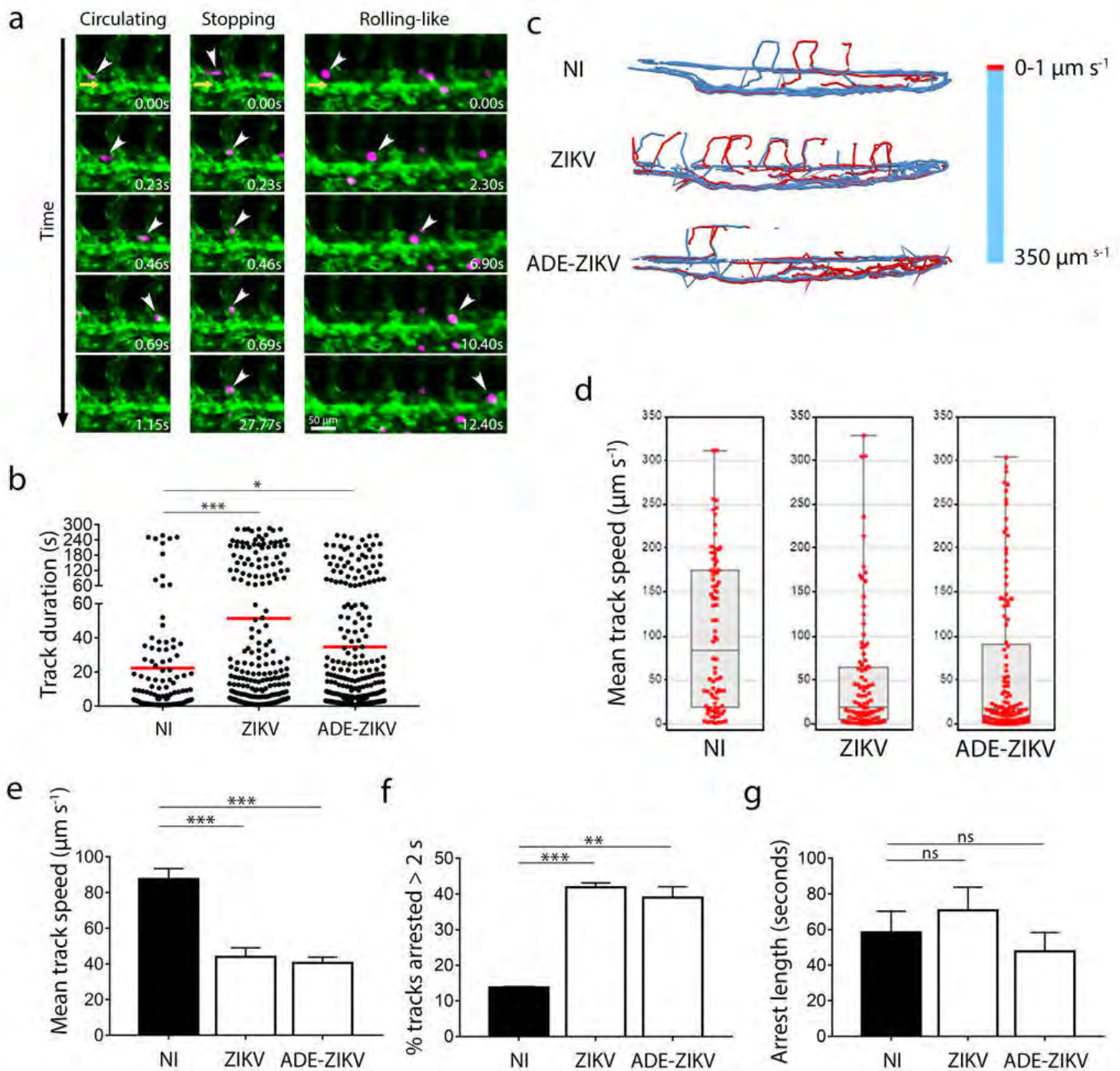


Figure 8. Ayala-Nunez *et al.*

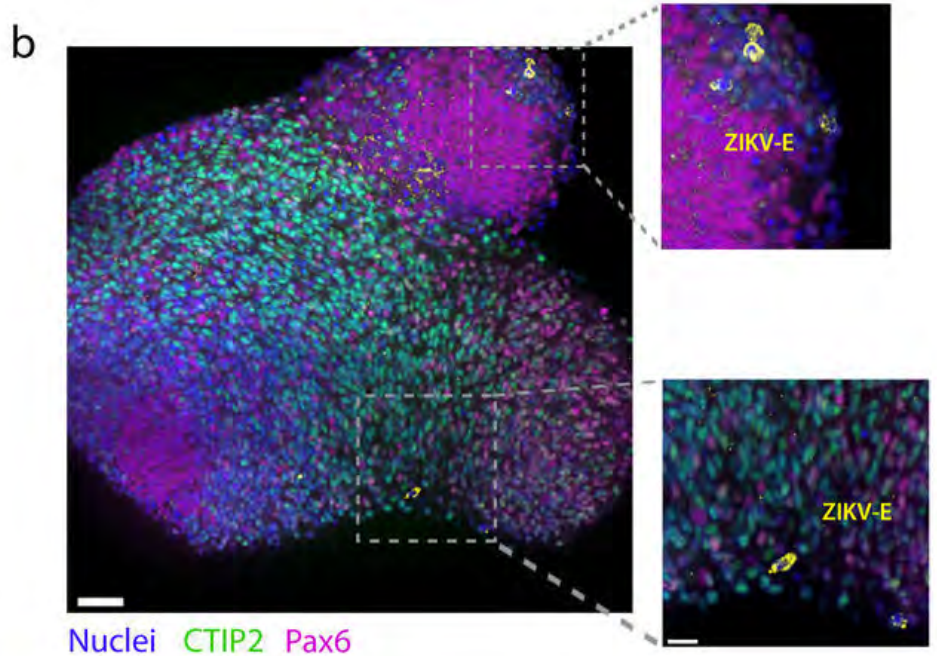
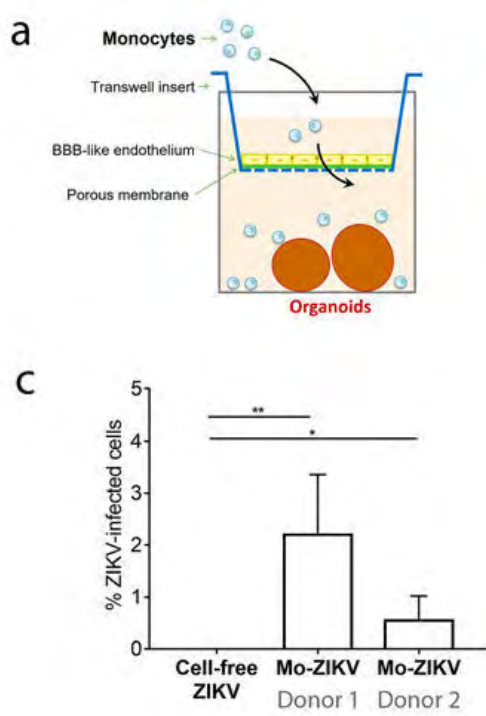


Figure 9. Ayala-Nunez *et al.*